frontiers | Research Topics

Seeing convergent margin processes through metamorphism

Edited by
Yi Chen, Qiuli Li, Guibin Zhang, Tatsuki Tsujimori
and Richard M. Palin

Published in
Frontiers in Earth Science

ISSN 1664-8714
ISBN 978-2-83250-030-9
DOI 10.3389/978-2-83250-030-9

About Frontiers

Frontiers is more than just an open access publisher of scholarly articles: it is a pioneering approach to the world of academia, radically improving the way scholarly research is managed. The grand vision of Frontiers is a world where all people have an equal opportunity to seek, share and generate knowledge. Frontiers provides immediate and permanent online open access to all its publications, but this alone is not enough to realize our grand goals.

Frontiers journal series

The Frontiers journal series is a multi-tier and interdisciplinary set of open-access, online journals, promising a paradigm shift from the current review, selection and dissemination processes in academic publishing. All Frontiers journals are driven by researchers for researchers; therefore, they constitute a service to the scholarly community. At the same time, the *Frontiers journal series* operates on a revolutionary invention, the tiered publishing system, initially addressing specific communities of scholars, and gradually climbing up to broader public understanding, thus serving the interests of the lay society, too.

Dedication to quality

Each Frontiers article is a landmark of the highest quality, thanks to genuinely collaborative interactions between authors and review editors, who include some of the world's best academicians. Research must be certified by peers before entering a stream of knowledge that may eventually reach the public - and shape society; therefore, Frontiers only applies the most rigorous and unbiased reviews. Frontiers revolutionizes research publishing by freely delivering the most outstanding research, evaluated with no bias from both the academic and social point of view. By applying the most advanced information technologies, Frontiers is catapulting scholarly publishing into a new generation.

What are Frontiers Research Topics?

Frontiers Research Topics are very popular trademarks of the *Frontiers journals series*: they are collections of at least ten articles, all centered on a particular subject. With their unique mix of varied contributions from Original Research to Review Articles, Frontiers Research Topics unify the most influential researchers, the latest key findings and historical advances in a hot research area.

Find out more on how to host your own Frontiers Research Topic or contribute to one as an author by contacting the Frontiers editorial office: frontiersin.org/about/contact

Seeing convergent margin processes through metamorphism

Topic editors
Yi Chen — Institute of Geology and Geophysics, Chinese Academy of Sciences (CAS), China
Qiuli Li — Institute of Geology and Geophysics, Chinese Academy of Sciences (CAS), China
Guibin Zhang — Peking University, China
Tatsuki Tsujimori — Tohoku University, Japan
Richard M. Palin — University of Oxford, United Kingdom

Citation
Chen, Y., Li, Q., Zhang, G., Tsujimori, T., Palin, R. M., eds. (2023). *Seeing convergent margin processes through metamorphism*.
Lausanne: Frontiers Media SA. doi: 10.3389/978-2-83250-030-9

Table of contents

frontiers | Frontiers in Earth Science

TYPE Editorial
PUBLISHED 11 August 2022
DOI 10.3389/feart.2022.989889

OPEN ACCESS

EDITED AND REVIEWED BY
Michel Grégoire,
UMR5563 Géosciences Environnement Toulouse (GET), France

*CORRESPONDENCE
Yi Chen,
chenyi@mail.iggcas.ac.cn

SPECIALTY SECTION
This article was submitted to Petrology, a section of the journal Frontiers in Earth Science

RECEIVED 09 July 2022
ACCEPTED 13 July 2022
PUBLISHED 11 August 2022

CITATION
Chen Y, Li Q, Zhang G, Tsujimori T and Palin RM (2022), Editorial: Seeing convergent margin processes through metamorphism.
Front. Earth Sci. 10:989889.
doi: 10.3389/feart.2022.989889

Editorial: Seeing convergent margin processes through metamorphism

Yi Chen[1,2]*, Qiuli Li[1,2], Guibin Zhang[3], Tatsuki Tsujimori[4] and Richard M. Palin[5]

[1]State Key Laboratory of Lithospheric Evolution, Institute of Geology and Geophysics, Chinese Academy of Sciences, Beijing, China, [2]College of Earth and Planetary Sciences, University of Chinese Academy of Sciences, Beijing, China, [3]The Key Laboratory of Orogenic Belts and Crustal Evolution, MOE, School of Earth and Space Sciences, Peking University, Beijing, China, [4]Depertment of Earth Science, Graduate School of Science, Tohoku University, Sendai, Japan, [5]Department of Earth Sciences, University of Oxford, Oxford, United Kingdom

KEYWORDS

convergent plate margin, metamorphism, subduction, collision, carbon cycle, orogenic evolution

Editorial on the Research Topic
Seeing convergent margin processes through metamorphism

Introduction

Plate convergence can induce large-scale metamorphism and magmatism, reshape large parts of continental margins, and subsequently change regional climate and biodiversity. Metamorphic rocks in orogenic belts commonly record different metamorphic evolutions and temporal-spatial distributions at the regional scale, which are strongly influenced by convergent processes through time. In some cases, ultrahigh-pressure (UHP) and ultrahigh-temperature (UHT) metamorphic rocks are observed at both ancient and young convergent plate margins, marking the operation of extreme tectonism in the regime of plate tectonics. This Research Topic aims to understand how regional metamorphism operated at convergent plate margins through the study of field and petrographic observations, geochemical and petrological analysis, high-pressure experiments, and thermodynamic modeling. The scope is to gather new ideas and interpretations on the structure and processes of convergent plate margins.

Contributions in this Topic

This Research Topic assembles ten papers focusing on metamorphic processes in orogenic belts worldwide from the Neoarchean to Cenozoic.

Metamorphic response to tectonic transition in orogenic belts

Tectonic evolution of the early Earth can be seen from multiple metamorphism at Archean cratonic margins. Liu et al. present metamorphic conditions and geochronology for mafic granulites from the east Hebei terrane in the North China Craton. This paper establishes two-episode metamorphism in this region. The late Neoarchean (ca. 2. 5 Ga) UHT metamorphism with an anticlockwise P–T path reflects a vertical sagduction regime. In contrast, the Paleoproterozoic (ca. 1.8 Ga) HP granulite facies metamorphism with a clockwise P–T path corresponds to the continental collision process. Therefore, this study provides valuable information about the Neoarchean-Paleoproterozoic tectonic transition in the northern margin of the North China Craton.

Tectonic transition in orogens can be illustrated by changes in metamorphic thermal structure. Zhang et al. present an example of the tectonic transition from the termination of oceanic subduction to continental collision. This paper investigates two newly found garnet schists from the Ondor Sum Group mélanges (central Inner Mongolia), both of which record clockwise P-T paths but with different peak thermal gradients. The early Paleozoic HP metamorphism with a thermal gradient of ~8°C/km resulted from the terminal subduction of the Paleo-Asian oceanic plate, whereas the Devonian medium-pressure metamorphism with a thermal gradient of ~22°C/km points to the subsequent continental collision process.

How continental collision stems from subduction is a critical but unclear process in subduction zones. Chen et al. yield an eclogite-facies metamorphic age of ca. 31 Ma for the Stak HP massif in the western Himalayan syntaxis. Based on the comparison of peak P–T–t conditions of the Himalayan HP-UHP rocks, the authors find that the HP rocks record higher peak thermal gradients and younger ages than those of UHP rocks. These new data, combined with the regional geological and geophysical evidence, suggest that the Indian continental lithosphere underwent a coherent change in subduction dip angle in the middle Eocene. This study provides critical constraints on the change in subduction geometry responsible for the tectonic transition from continental subduction to collision.

Convergent margin processes trigger intracontinental orogeny

The dynamic mechanism of intracontinental orogens is still controversial. Zhao et al. investigate HP metabasites in the northeastern Cathaysia of the South China Block. Petrological and geochemical data indicate that these rocks originated from the continental crust and experienced eclogite-facies metamorphism during the early Triassic. Based on a comprehensive geological comparison around the South China Block, these high-grade rocks are interpreted to be formed in an intracontinental orogen triggered by far-field stress from margin convergence. This study provides a good case for intracontinental orogeny and constructs its connection with continental margin processes.

Evolution of the continental crust at convergent margins

Convergent margin processes play critical roles in the continental crust reworking. A common way is to investigate the behavior of crustal anatexis in orogens. Yang et al. present isotope geochemistry of Himalayan leucosome produced by partial melting of metasediments. The leucosome shows a broad range of Sr-Nd-Hf isotopes that deviate from the source. This isotopic disequilibrium might be caused by the different consumption (or dissolution) behaviors of muscovite, plagioclase, apatite, monazite, and zircon during crustal melting. This study highlights that isotopic disequilibrium may be common in low-temperature partial melting of metasediments.

Another crustal reworking study, by Gou et al., presents geochronology and metamorphic petrology from the Ramba gneiss dome in the northern Himalaya. The authors obtain a clockwise P–T path for garnet–mica schist in the dome. *In situ* biotite Rb–Sr geochronology yields two metamorphic ages of ca. 37 and 5.0 Ma, corresponding to the timing of retrograde cooling and the cooling age of the latest thermal resetting, respectively. This study provides valuable information on the tectonic evolution of the Ramba gneiss dome, from the Eocene crustal thickening during the India–Asia collision to the later exhumation.

The continental crust reworking can also be illustrated by the thermal structure of the crustal root. Zheng et al. present a large-scale (~10,000 km^2) thermal mapping, based on a Ti-in-quartz thermometer, for the Paleoproterozoic eastern Khondalite Belt, North China Craton. The new results highlight the hottest region in this belt, where UHT metamorphism closely correlates with abundant charnockite. This hottest region may represent the crustal root of a Paleoproterozoic large hot orogen. Further models for the mechanism of large-scale UHT metamorphism need to consider its close relation with charnockite.

Liu et al. present detrital zircon U-Pb geochronology and isotopic geochemistry from the northern Tibetan Plateau, aiming to investigate the continental crust evolution in the South Qilian, North Qaidam, and East Kunlun terranes. The results indicate that these three terranes show affinity to the western Yangtze Block and have undergone multiple Wilson cycles since the Paleoproterozoic. Based on geological comparison in the three terranes, the authors construct a detailed tectonic evolution of the northern Tibetan Plateau from the Neoproterozoic to Early Mesozoic.

Carbon cycle in subduction zones

Subduction zones act as a key region transporting supracrustal carbonates down to the deep mantle. How carbonates evolve at depths is crucial for understanding deep carbon flux and sequestration mechanisms. Gao et al. review prominent progress in the chemistry of carbonates under pressures up to the core-mantle boundary. This review highlights that several new polymorphs of carbonates would be stable at high pressure-temperature conditions, but metamorphic decarbonization and reduction reactions restrict subducting carbonates to the top-mid region of the lower mantle. This study shows more possibilities for carbon behavior in the mantle, which offers a strong handle on Earth's extraordinary history.

Methane (CH_4) is a critical carbon species in subduction zone fluids; however, its flux in subduction zones is still unknown. Using microanalysis techniques, Zhang et al. document the first case to estimate the abiotic CH_4 flux in the western Tianshan based on fluid inclusion compositions in eclogites. The authors estimate that the western Tianshan eclogites at least contain 113–342 Mt CH_4, and propose that cold subduction zones may be a hidden, huge reservoir of CH_4 on Earth. This study highlights that CH_4 flux must be considered further when evaluating carbon flux in global subduction zones.

Author contributions

YC wrote the draft manuscript with input from all authors.

Acknowledgments

We thank all the contributors to this Topic and the referees who spared their time to provide thoughtful and helpful comments.

Conflict of interest

The authors declare that the research was conducted in the absence of any commercial or financial relationships that could be construed as a potential conflict of interest.

Publisher's note

frontiers in Earth Science

ORIGINAL RESEARCH
published: 03 February 2022
doi: 10.3389/feart.2021.790999

Change in Subduction Dip Angle of the Indian Continental Lithosphere Inferred From the Western Himalayan Eclogites

Si Chen[1,2], Yi Chen[1,3], Stéphane Guillot[4] and Qiuli Li[1,3]*

[1]State Key Laboratory of Lithospheric Evolution, and Institutions of Earth Science, Institute of Geology and Geophysics, Chinese Academy of Sciences, Beijing, China, [2]Key Laboratory of Marine Mineral Resources, Ministry of Natural Resources, Guangzhou Marine Geological Survey, Guangzhou, China, [3]College of Earth and Planetary Sciences, University of Chinese Academy of Sciences, Beijin, China, [4]University Grenoble Alpes, University Savoie Mont-Blanc, CNRS, IRD, IFSTTAR, ISTerre, Grenoble, France

Edited by:
*Oliver Jagoutz,
Massachusetts Institute of Technology, United States*

Reviewed by:
*Xiao-Ping Xia,
Guangzhou Institute of Geochemistry (CAS), China
Andy Parsons,
University of Plymouth, United Kingdom*

***Correspondence:**
*Yi Chen
chenyi@mail.iggcas.ac.cn*

Specialty section:
*This article was submitted to Petrology,
a section of the journal
Frontiers in Earth Science*

Received: *07 October 2021*
Accepted: *16 December 2021*
Published: *03 February 2022*

Citation:
*Chen S, Chen Y, Guillot S and Li Q (2022) Change in Subduction Dip Angle of the Indian Continental Lithosphere Inferred From the Western Himalayan Eclogites.
Front. Earth Sci. 9:790999.
doi: 10.3389/feart.2021.790999*

The occurrence of ultrahigh-pressure (UHP) and high-pressure (HP) rocks in the Himalayan orogen has been conventionally attributed to the different subduction dip angles along the strike. The western Himalayan UHP eclogites point to a steep continental subduction in the Eocene. The present-day geophysical data show low subduction dip angles of the Indian lithosphere beneath southern Tibet and Karakoram, implying that a shift from steep to low-angle subduction probably happened in the western Himalaya. However, the timing and mechanism of such a subduction-angle change are still unknown. Here we present a combined analysis of zircon geochronology and geochemistry of eclogites and gneiss in the Stak massif, western Himalaya. Metamorphic zircons equilibrated with garnet and omphacite show flat heavy rare earth element patterns without Eu anomalies and, thus, yield similar eclogite-facie ages of ca. 31 Ma. The Stak HP eclogite-facie metamorphism is at least 15 Ma younger than those measured in the western Himalayan UHP eclogites, but broadly contemporaneous with other Himalayan HP rocks. Therefore, all the Himalayan HP rocks record higher peak geothermal gradients and younger ages than those of the UHP rocks. Our new data, combined with the magmatic lull observed in the Kohistan–Ladakh–Gangdese arc and with the convergent rate of the Indian plate, suggest a change in subduction dip angle over time. Consequently, we suggest that the entire Indian continental lithosphere experienced an approximately coherent shift from steep to low-angle subduction after the breakoff of the Neo-Tethyan slab since the middle Eocene. This critical change in subduction geometry is interpreted to be responsible for the transition from continental subduction to collision dynamics.

Keywords: Himalaya, Stak, eclogites, zircon chronology, subduction dip angle

INTRODUCTION

The Indo–Asia collision after the closure of the Neo-Tethys produced the present-day largest ongoing continent–continent collisional orogen of the Earth, the Himalayan orogen (Yin, 2006). Because subduction angle, convergence rate, and slab rollback/breakoff strongly influence the spatial and temporal distribution of metamorphic and magmatic rocks (Kay and Coira, 2009; Paterson and Ducea, 2015), the subduction style of the orogen can be revealed by studying these aspects.

High-pressure (HP) metamorphic rocks (blueschist, eclogite, HP granulite facies rocks, and HP garnet amphibolite facies rocks) are exposed along the Himalayan orogen (**Figure 1**). However, ultrahigh-pressure (UHP) eclogites only occur at Kaghan and Tso Morari in the western syntaxis (O'Brien et al., 2001; Sachan et al., 2004). The UHP eclogites in the western Himalaya were subducted earlier (53–46 Ma) and exhumed faster (45–40 Ma) than the HP rocks (buried at 38–15 Ma and exhumed at 25–13 Ma) in the central and eastern Himalaya (Parrish et al., 2006; Zhang et al., 2010; Donaldson et al., 2013; Rehman, 2019; Wang et al., 2021), possibly reflecting different subduction dip angles or depths of the Indian continental slab along strike (Guillot et al., 2008). Therefore, it is proposed that the Indo–Asia plates in the western syntaxis collided earlier followed by steep subduction, and that those in the central and eastern Himalaya collided later with low-angle subduction (Chemenda et al., 2000; Guillot et al., 2008; Zhang et al., 2015). Numerical models imply that a subduction angle decreases over time due to continental lithosphere buoyancy (Duretz and Gerya, 2013; Magni et al., 2017). Geophysical data point to the present-day low subduction angles (or underthrusting) of the Indian continental lithosphere beneath east and west Tibet and Karakoram (Hazarika et al., 2017; Parsons et al., 2020). If correct, the Indian continental slab underwent a shift from steep subduction to low-angle subduction or underthrusting in the western Himalaya. However, such a subduction-angle change has not been evidenced by the rocks in this region, making the timing and mechanism of such a process poorly resolved.

In addition to UHP eclogites, HP eclogites were discovered in the Stak massif in the western syntaxis (Le Fort et al., 1997). These HP–UHP eclogites record clockwise *P*-*T* paths (Wilke et al., 2010; Lanari et al., 2013; St-Onge et al., 2013) and, thus, define a large HP-UHP province (Guillot et al., 2008; Lanari et al., 2013). However, the Stak eclogite suffered a greater degree of overprint and recorded younger metamorphic zircon ages of 32 Ma (Kouketsu et al., 2016) than the UHP eclogites with peak metamorphic ages of 53–46 Ma (e.g., Rehman, 2019). Is this a reflection of zircon recrystallization during exhumation in Stak, or a real age of eclogite formation? It remains uncertain whether the western Himalayan HP–UHP eclogites were formed synchronously at different subducting depths and then experienced different exhumation histories or were formed by diachronous subduction of various continental slices.

Here we show, based on petrology, zircon geochronology, and geochemistry, that both the Stak eclogites and their country gneiss share the same peak metamorphic age of ca. 31 Ma. This age is younger than that of the UHP eclogites, but coeval to a magmatic lull in the entire Himalayan orogen. Steep subduction of the continental lithosphere, driven by downgoing oceanic lithosphere, would generate UHP metamorphism in the subducting crust (**Figure 2A**). However,

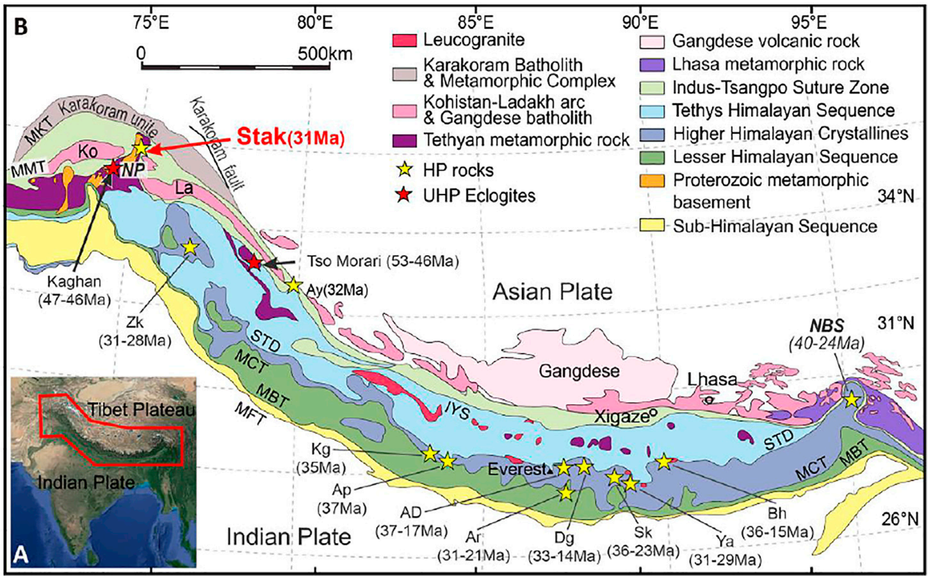

FIGURE 1 | (A) Location of the Himalayan orogen. **(B)** Geological map of Himalaya (modified after Ding et al., 2016a; Guillot et al., 2008) with locations and peak metamorphic ages of high-pressure (HP) and ultrahigh-pressure (UHP) metamorphic rocks. MKT, Main Karakoram Thrust; MMT, Main Mantle Thrust; IYS, Indus–Yarlung Suture; STD, South Tibetan Detachment; MCT, Main Central Thrust; MBT, Main Boundary Thrust; MFT, Main Frontal Thrust; AD, Ama Drime; Ap, Annapurna; Ar, Arun; Ay, Ayilari; Bh, Bhutan; Dg, Dinggye; Kg, Kali Gandaki; Ko, Kohistan arc unite; La, Ladakh arc unite; NBS, Namche Barwa Syntaxis; NPS, Nanga Parbat Syntaxis; Sk, Sikkim; Ya, Yadong; Zk, Zanskar. Detailed age data and sources are listed in **Supplementary Table S6**.

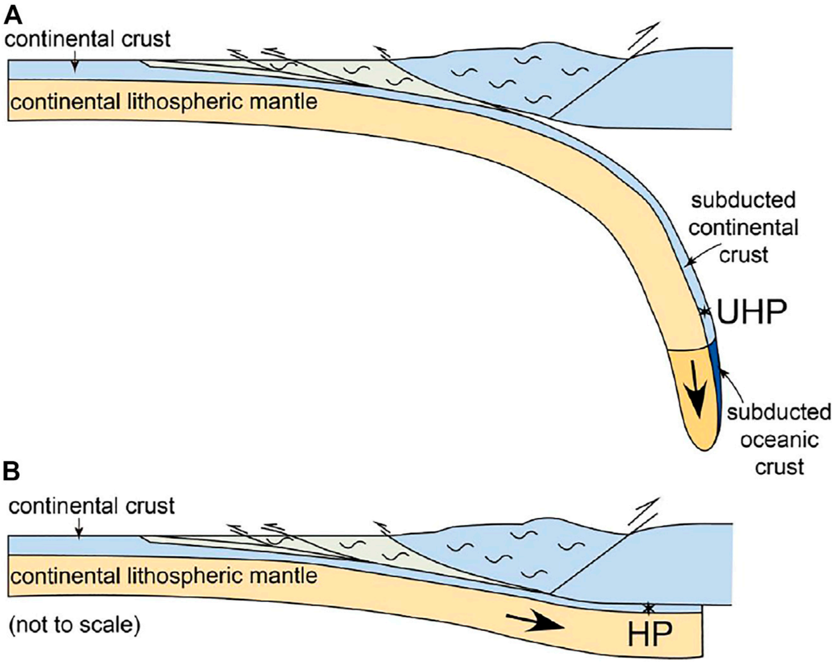

FIGURE 2 | Schematic diagrams showing the relation between subduction angle and metamorphism. **(A)** Steep subduction of continental lithosphere triggered by downgoing oceanic lithosphere would produce UHP metamorphism. **(B)** Low-angle (shallow) subduction leads to the underthrusting of continental lithosphere producing HP metamorphism.

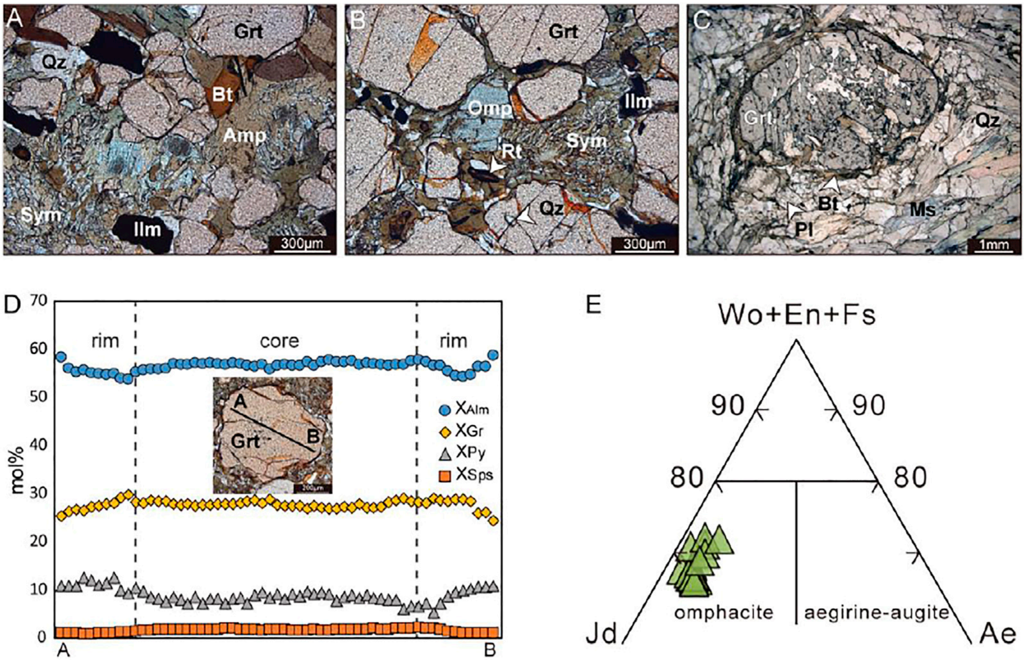

FIGURE 3 | Photomicrographs of the eclogites 16PK190 **(A)** and 16PK194 **(B)**, and gneiss 16PK181 **(C)**. **(D)** Zoning profile of a garnet in the eclogite 16PK194. **(E)** Ternary diagram showing the composition of omphacite in eclogite. Mineral abbreviations are after Whitney and Evans (2010).

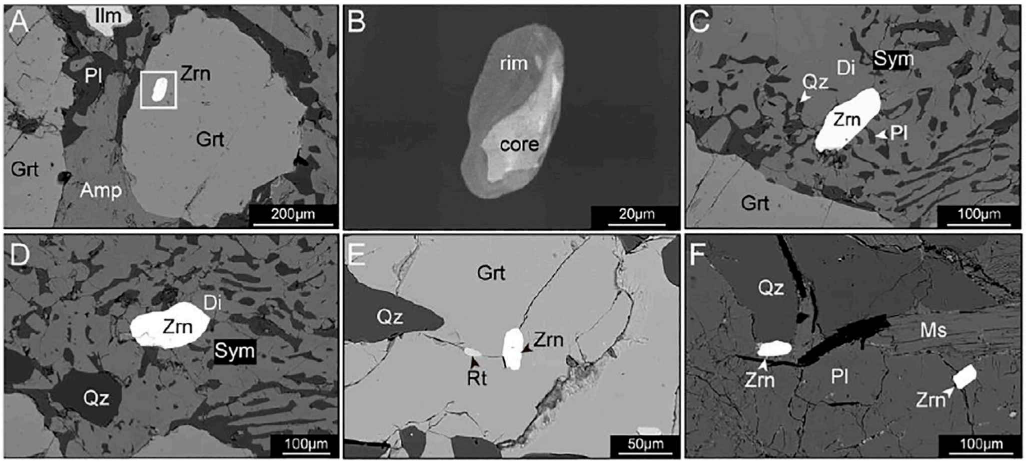

FIGURE 4 | Back-scattered electron (BSE) images showing microstructure of zircon in eclogites **(A,C,D)** and gneiss **(E,F)**; **(B)** Cathodoluminescence (CL) image of zircon inclusion in garnet enlarged for the square of **(A)**.

the continental lithosphere, without driven force from subducted oceanic lithosphere, would undergo low-angle subduction or underthrusting (Magni et al., 2017) and, thus, more likely produce HP metamorphism (**Figure 2B**). Based on geological and geophysical records, we further infer a uniform change in the subduction dip angle over 2,500 km throughout the Himalayan belt since the middle Eocene.

GEOLOGICAL SETTING AND SAMPLES

The Stak massif is located in the north Indian continental margin, northeast of the Nanga Parbat–Haramosh massif (NPHM), southwest of the Ladakh arc (**Figure 1B**), and close to the Main Mantle Thrust (MMT). This massif consists of gneisses, schists, metabasites, with minor marbles, and develops fold and imbricate structures (Guillot et al., 2008). Eclogites with extensive retrogression in the Stak massif occur as boudins or dikes in the gneisses. A detailed petrological study on the Stak eclogites yields HP peak conditions at ~750°C and ~2.5 GPa and retrograde conditions at 650°C–700°C and 0.9–1.6 GPa (Lanari et al., 2013). This retrograde temperature is slightly higher than those (<600°C at 1.0–1.7 GPa) of the Kaghan and Tso Morari UHP eclogites (Wilke et al., 2010; Wilke et al., 2015).

The peak metamorphic age of the Stak eclogite is still unknown. Sensitive high-resolution ion microprobe (SHRIMP) zircon U-Pb data yielded scattered ages between 70 and 50 Ma (Riel et al., 2008). However, Kouketsu et al. (2016) used the same method to show that a small cluster of low Th/U (<0.03) and Yb (<10 ppm) zircon ages are concentrated between 36 and 28 Ma with a lower intercept age of ~32 Ma. This age was interpreted as recrystallization after eclogite-facie metamorphism, which was possibly induced by heating from nearby NPHM at lower crustal levels (Kouketsu et al., 2016).

The present study focuses on the eclogite boudins (16PK190 and 16PK194) and country gneiss (16PK181) in the Stak massif. Both eclogite samples contain an eclogite-facies assemblage of garnet, omphacite, quartz, and rutile (**Figure 3**). Garnet is surrounded by amphibole and plagioclase kelyphite and has a compositionally homogeneous core ($\text{Alm}_{55-57}\text{Prp}_{7-13}\text{Grs}_{24-28}\text{Sps}_{1-2}$) (see the **Supplementary Table S1**) with a narrow retrograde zoning rim. Omphacite with a 23.4–30.0 mol.% jadeite component (**Supplementary Table S2**) is partially replaced by fine-grained symplectite of diopside + plagioclase + amphibole. The symplectite is rimmed by coarser (200–500 μm) amphibole and biotite. The eclogite sample zircons occur as inclusions within garnet and symplectite, and as an intergranular phase in the matrix (**Figure 4**). The zircon grains in the symplectite are larger (~100 μm) than the plagioclase and diopside grains, and show disequilibrium texture with these phases. The gneiss (16PK181) contains garnet, muscovite, biotite, plagioclase, and quartz with minor rutile and zircon (**Figure 3**). The garnet is surrounded by plagioclase and mica, and could be a relict eclogite-facie phase. The gneiss sample zircons exist as matrix phases and inclusions within garnet and muscovite (**Figure 4**).

MATERIALS AND METHODS

Mineral Major Elements

Major elements of rock-forming minerals were analyzed using an electron microprobe analyzer (EPMA, JEOL-JXA8100) at the IGG-CAS. The operating conditions were a 15-kV accelerating voltage, a 20-nA beam current, and 3-μm spot diameter. The counting time was 20 s at peak and 10 s at the lower and upper background positions, respectively. All data were corrected online using a modified ZAF (atomic number, absorption, and fluorescence) correction procedure. The detection limits (1σ) were in the range of 0.008–0.02wt%. The precision of the major element analysis was better than 1.0%.

Zircon U-Pb Isotopes and Trace Elements

Zircon grains were separated from samples by using conventional heavy liquid and magnetic separation techniques. Approximately

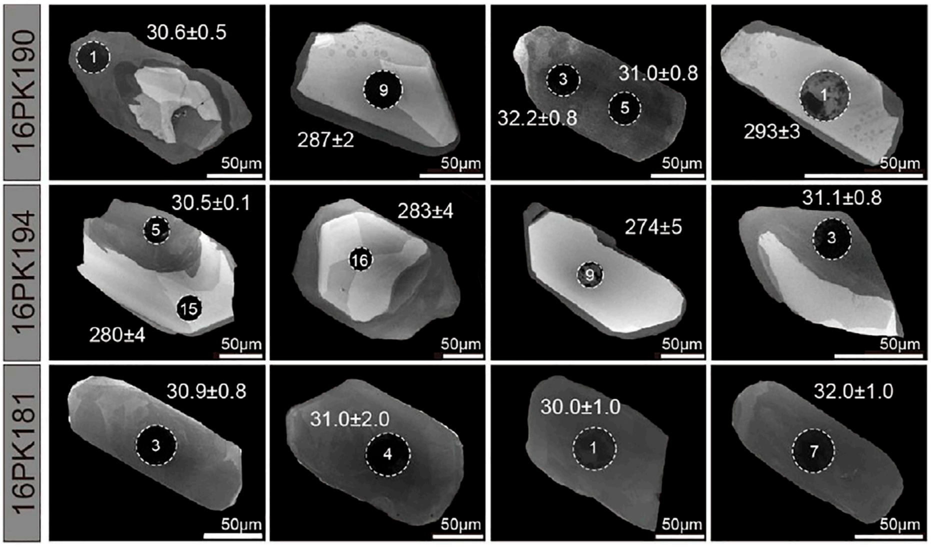

FIGURE 5 | Cathodoluminescence images of zircons from Stak samples. White digits are U-Pb ages, dashed cycles are analysis spots with analytical numbers. The age unit is Ma.

200 zircons of each sample were handpicked out from under a binocular microscope and mounted in epoxy resin together with zircon U-Pb age reference materials. Then the epoxy mounts were polished to expose the interior of the crystals. All grains were photographed in reflected and transmitted light under petrographic microscope to avoid fissures and inclusions. Cathodoluminescence (CL) and back-scattered electron (BSE) images were obtained using field emission scanning electron microscope (Nova NanoSEM 450) equipped with Gatan MomoCL4 at the Institute of Geology and Geophysics, Chinese Academy of Sciences (IGG-CAS). Mineral inclusions in zircon were identified using Raman spectroscopy at the IGG-CAS. Homogeneous zircons without inclusions or fissures were chosen for U-Pb dating and trace element analyses. Zircon U-Pb ages were determined by using secondary ion mass spectrometry (SIMS) and laser ablation-inductively coupled plasma-mass spectrometry (LA-ICP-MS). Zircon trace elements were acquired in the same run of age dating by LA-ICP-MS.

Secondary Ion Mass Spectrometry Zircon U-Pb Dating

Zircon U, Th, and Pb isotope analyses were performed with a Cameca IMS-1280HR SIMS at the IGG-CAS. Detailed instrumental parameters and analytical procedures are described by Li et al. (2009). The analytical spot is about 20 × 30 μm in size. Plešovice zircon standard (^{206}Pb/^{238}U age of 337.3 Ma; Sláma et al., 2008) was interspersed with unknown grains. Nonradiogenic ^{204}Pb was used for common Pb correction of measured compositions, and the present-day crustal common Pb composition is used in the model of Stacey and Kramers (1975). An inhouse zircon standard Qinghu was alternately analyzed together with other unknown zircons for the purpose of monitoring external uncertainties of SIMS U-Pb zircon dating calibrated by the Plešovice standard. Excel and the add-in Isoplot 2.49 program (Ludwig, 2001) were used for data calculation. Uncertainties on individual analyses in **Supplementary Table S3** are reported at 1σ level. The weighted mean U-Pb ages are quoted with 95% confidence interval. Seven measurements on Qinghu zircon yielded a Concordia age of 159.7 ± 1.8 Ma, which is identical within errors with the recommended value of 159.5 ± 0.2 Ma (Li et al., 2013).

Laser Ablation-Inductively Coupled Plasma-Mass Spectrometry Zircon U-Pb Dating and Trace Element Analyses

U-Pb dating combined with *in situ* trace element analyses of zircons were carried out in a single run by Agilent 7500a ICP-MS instrument equipped with Geolas-193 UV laser ablation system at the State Key Laboratory of Continental Dynamics, Northwest University, China. Operating conditions and data processing are described by Liu et al. (2007) in detail. The spot diameter is 32 μm for two eclogites (16PK190 and 16PK196) and 44 μm for gneiss (16PK181) with a laser repetition rate of 6 Hz. Helium was used as the carrier gas. Laboratory standards (GJ-1, 91500, NIST 610) were interspersed with unknown grains. U-Th-Pb isotope ratios and trace element contents were calculated using the GLITTER 4.0 program (Macquarie University). Harvard zircon 91500 was used as external standard. To monitor the external uncertainties of U-Pb zircon dating calibrated against 91500, a second zircon standard GJ-1 was analyzed as an unknown together with other unknown zircons. Trace element concentrations were calibrated by using ^{29}Si as internal standard and NIST 610 as external standard. Data reduction was carried out using Isoplot/Excel version 2.49 (Ludwig, 2001). Fifteen measurements on GJ-1 and 32 measurements on 91500 yielded weighted mean ^{206}Pb/^{238}U ages of 602 ± 3.7 Ma (1σ) and 1,062.5 ± 2.8 Ma (1σ), respectively,

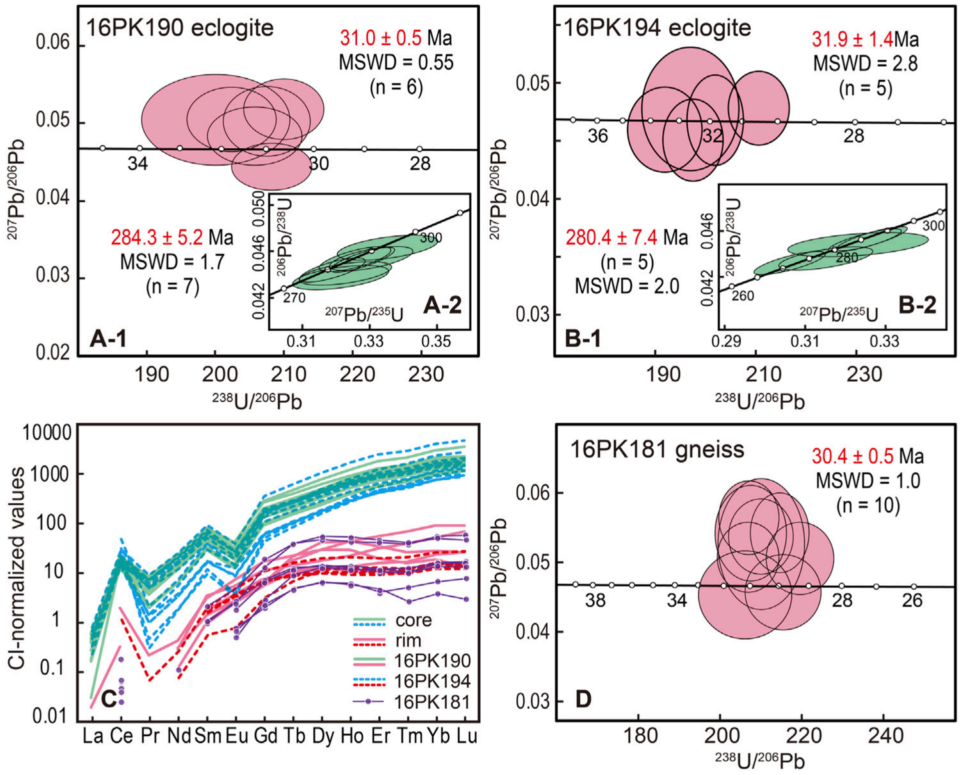

FIGURE 6 | Zircon U-Pb dates **(A,B,D)** and REE patterns **(C)**. **(A-1)**, **(B-1)**, **(D)** Tera-Wasserburg diagrams of metamorphic zircon U-Pb data uncorrected for common Pb. **(A-2)**, **(B-2)** Concordia diagrams for zircon cores of the Stak eclogites. **(C)** Chondrite-normalized REE patterns of zircons in the Stak samples. Chondrite data are from McDonough and Sun (1995). n, number of analyses; MSWD, mean square of weighted deviates.

which are in good agreement with the recommended value of 608 ± 0.4 Ma (Jackson et al., 2004) for GJ-1 and 1,065.4 ± 0.6 Ma (Wiedenbeck et al., 2004) for 91500.

RESULTS

The zircons from the two eclogites are mostly subhedral and consist of two major parts under cathodoluminescence (CL) images (**Figure 5**): 1) a core with relatively bright and slightly oscillatory zoning luminescence, and 2) a rim with relatively dark, homogeneous luminescence. Inclusions of diopside, amphibole, plagioclase, quartz, and apatite are common in the zircon cores, while the rims have garnet, rutile, and quartz inclusions without plagioclase and coesite (**Supplementary Figure S1**). Fourteen zircons from sample 16PK190 and 10 zircons from sample 16PK194 were dated by the SIMS method. The Th/U ratios of the zircon cores and rims are 2.05–3.17 and ≤0.05, respectively (**Supplementary Table S3**). The SIMS dating results show that the two eclogites, 16PK190 and 16PK194, have similar $^{206}Pb/^{238}U$ weighted mean ages of 284.3 ± 5.2 Ma (MSWD = 1.7, $n = 7$) and 280.4 ± 7.4 Ma (MSWD = 2.0, $n = 5$) for the zircon cores and 31.0 ± 0.5 Ma (MSWD = 0.55, $n = 6$), 31.9 ± 1.4 Ma (MSWD = 2.8, $n = 5$) for the zircon rims (**Figures 6A, B**). The LA-ICP-MS results (see the **Supplementary Figure S2**) are consistent with those of SIMS. The zircon cores have higher REE concentrations than the rims and are characterized by positive Ce anomalies, negative Eu anomalies, and steep heavy REE patterns (**Figure 6C**). The zircon rims for both samples show flat heavy REE patterns with a distinct lack of Eu anomalies (**Figure 6C**).

Zircons from the country gneiss 16PK181 are oval or prismatic crystals characterized by weak luminescence and patchy zoning under CL, with rare bright cores (**Figure 5**). All the analyses were conducted on the core-free zircons. They show low Th/U ratios (<0.01) (**Supplementary Table S3**) and REE concentrations (**Supplementary Table S5**), with flat heavy REE patterns and no negative Eu anomalies (**Figure 6C**). The SIMS dating result (30.4 ± 0.5 Ma, MSWD = 1.0, $n = 10$) (**Figure 6D**) is consistent with that of LA-ICP-MS (30.8 ± 0.8 Ma, MSWD = 0.46, $n = 7$) within errors (**Supplementary Figure S2**).

DISCUSSION

Timing of Eclogite-Facies Metamorphism

The $^{206}Pb/^{238}U$ weighted mean ages of ca. 284–280 Ma measured in the zircon cores from both eclogites represent the crystallization age of the magmatic protolith, which is demonstrated by their oscillatory zoning, high Th/U ratios, and steep REE patterns. This age is contemporaneous with the protolith formation of the Kaghan and Tso Morari UHP eclogites

(Rajkumar, 2015; Rehman et al., 2016), which is ascribed to the eruption of the Panjal Traps in the north Indian continental margin (Shellnutt, 2018). Our results, coupled with the similar whole-rock chemistry and Nd isotopic compositions between the Stak eclogites and the Panjal Traps volcanic rocks (Kouketsu et al., 2017), indicate that the western Himalayan eclogites likely shared the same protoliths during the Permian magmatism of the Panjal Traps.

The rims of the eclogite zircons exhibit metamorphic characteristics and equilibrium texture with HP phases. The date of ca. 31 Ma most likely reflects eclogite-facies zircon recrystallization because, 1) the zircon rims have inclusions of garnet and rutile without plagioclase, 2) the disequilibrium texture of zircon with symplectitic diopside and plagioclase implies zircon inclusions presented in preexisting omphacite (**Figure 4**), and 3) the REE data indicate recrystallization in the presence of garnet and absence of plagioclase (**Figure 6C**). A similar metamorphic age (ca. 32 Ma) reported by Koukestsu et al. (2016) was interpreted as a recrystallization time after eclogite-facies metamorphism. However, the low Yb concentrations in those zircons only reflect equilibration with garnet, which could occur both under eclogite- and granulite-facies conditions. Moreover, metamorphic zircons from the country gneiss show REE characteristics and ages similar to those from the eclogites (**Figures 6C,D**). Therefore, the Stak massif was coherently buried beneath the Asian plate and underwent eclogite-facies metamorphism at ca. 31 Ma.

The HP metamorphic time of the Stak massif is at least 15 Ma later than the UHP metamorphic time (53–46 Ma) in the Kaghan and Tso Morari massifs (de Sigoyer et al., 2000; Kaneko et al., 2003; Donaldson et al., 2013). Therefore, the HP-UHP massifs in the western Himalaya were asynchronously buried to ~2.5–3.8 GPa, indicating a continuous subduction/collision process spanning more than 15 Ma. After the Kaghan and Tso Morari massifs experienced UHP metamorphism (~46 Ma) and rapid exhumation to the middle to lower crustal levels (~44–40 Ma) (de Sigoyer et al., 2000; Parrish et al., 2006; Wilke et al., 2010), the Stak massif was buried to HP eclogite-facie conditions at ca. 31 Ma. Such a continuous burial process recorded by HP–UHP rocks is common in other collisional belts such as Dabie-Sulu (e.g., Zhang et al., 2009), Alps (e.g., Berger and Bousquet, 2008), and the Western Gneiss Region (e.g., Kylander-Clark et al., 2009). In the following section, we will focus on how this process proceeded through time.

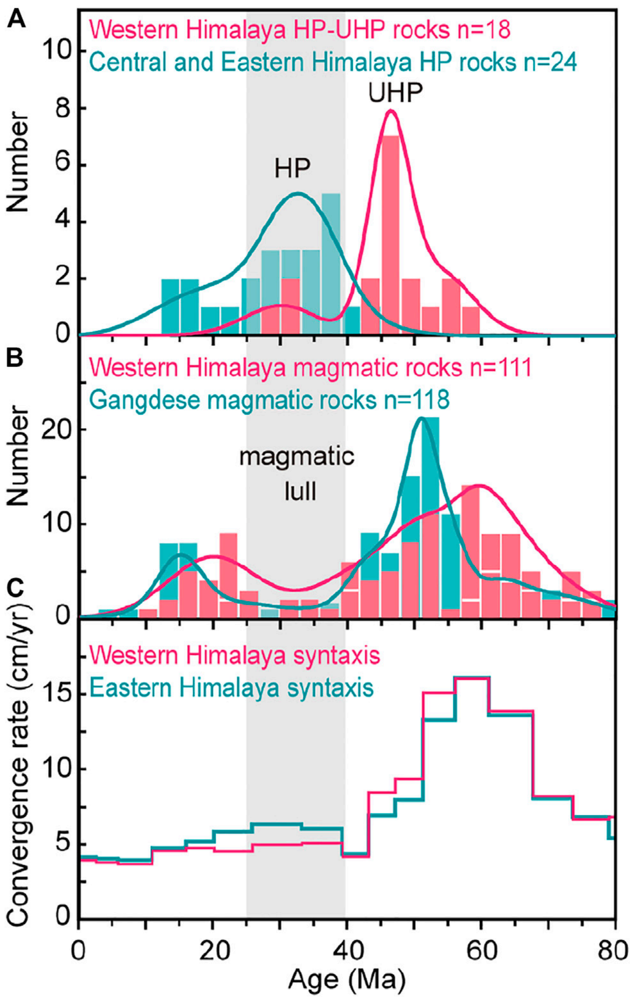

FIGURE 7 | (A) Cumulative probability curve and histogram showing the peak metamorphic ages of the HP and UHP rocks in the western (red) and central-eastern Himalayas (green). **(B)** Cumulative probability curve and histogram for the crystallization ages of the western Himalaya (South Karakoram, Kohistan–Ladakh Arc, red), and Gangdese (green) magmatic rocks. **(C)** India–Asia convergence rates. Detailed data and sources are listed in **Supplementary Table S6**.

Implications for change in subduction dip angle through time

The HP metamorphism of the Stak massif is broadly contemporaneous with that of quartz eclogites, HP granulites, and garnet amphibolites (mostly 40–25 Ma) in the central and eastern Himalayas (**Figure 7A**) (Corrie et al., 2010; Zhang et al., 2010; Rubatto et al., 2013; Wang et al., 2021). This indicates that the subducted Indian continental slab probably underwent a coherent process along the Indus–Yarlung Suture Zone since 40 Ma. However, UHP metamorphism spatially restricted to the western Himalaya (Kaghan and Tso Morari) was only recognized before ca. 46 Ma (Kaneko et al., 2003; Donaldson et al., 2013). The discrepancy of HP–UHP timing in the western and central Himalayas could be induced by continental subduction of a jagged Indian margin (Guillot et al., 2008), by different exhumation styles (residence times at crustal level) of eclogites (O'Brien, 2019; Rehman, 2019), or by changes in subduction dip angle (**Figure 2**). However, it is unlikely that an irregular northern margin of India would trigger the long discrepancy (>15 Ma) between UHP and HP peak metamorphic ages. The different *P-T*-t paths observed between UHP and HP eclogites were interpreted to result from the prolonged residence times in the central and eastern Himalayas but rapid exhumation of UHP rocks in the west (Rehman, 2019). However, the different exhumation styles are not the first-order mechanism responsible for the distinct peak metamorphic ages of

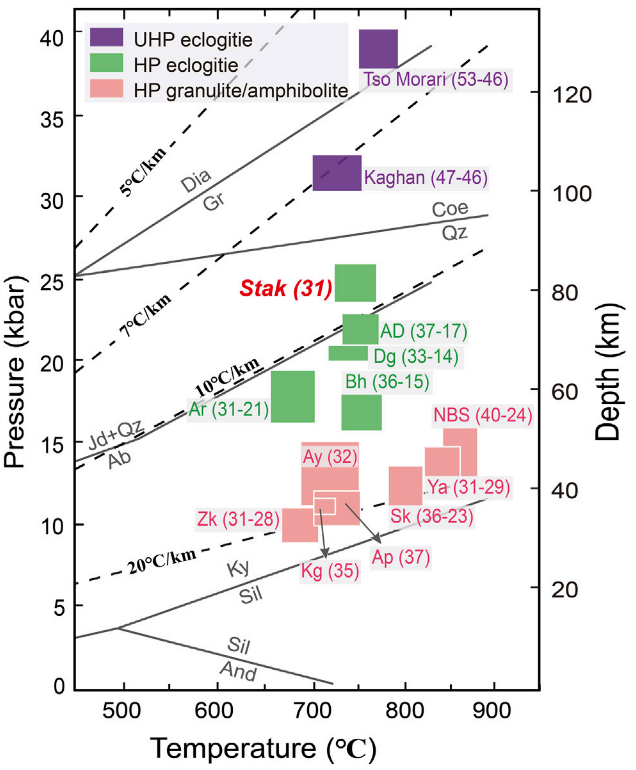

FIGURE 8 | Integrated peak *P-T* conditions and ages of eclogites and HP granulites in the Himalayan orogen. The age data sources are listed in **Supplementary Table S6**. Source references for *P-T* conditions: Annapurna (Ap) (Kohn and Corrie, 2011), Ama Drime (AD) (Li et al., 2018), Arun (Ar) (Corrie et al., 2010), Ayilari (Ay) (Chen et al., 2021), Bhutan (Bh) (Grujic et al., 2011), Dinggye (Dg) (Wang et al., 2017), Kaghan (Kaneko et al., 2003), Sikkim (Sk) (Faak et al., 2012), Stak (Lanari et al., 2013), Tso Morari (Mukherjee et al., 2005), Yadong (Ya) (Zhang et al., 2017), Namche Barwa Syntaxis (NBS) (Zhang et al., 2015), and Zanskar (Zk) (Vance and Harris, 1999).

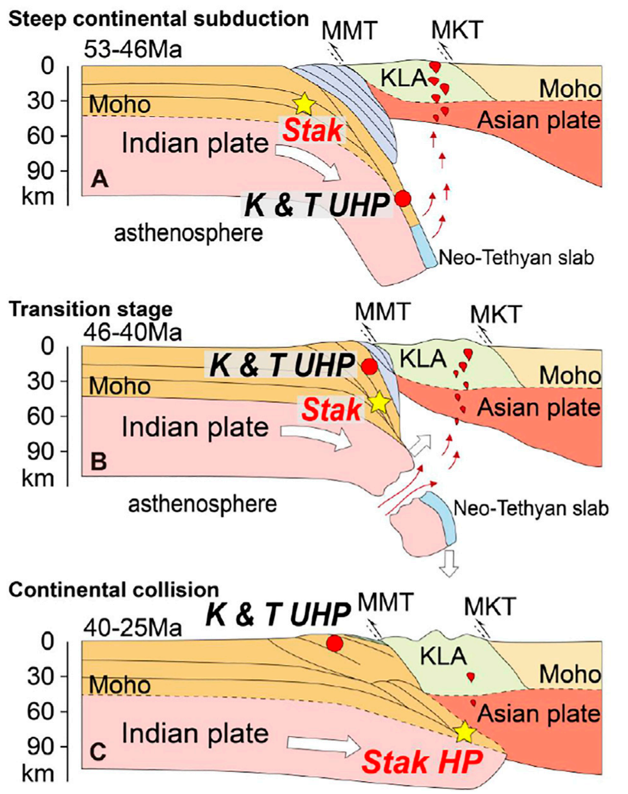

FIGURE 9 | Schematic diagrams illustrating the evolution process of the western Himalaya during the India–Asia collision. **(A)** Steep subduction and UHP metamorphism of the Indian continental slab at ca. 53–46 Ma. **(B)** Breakoff of the Neo-Tethyan lithosphere induced fast exhumation of UHP metamorphic rocks and then rebound of subducted Indian continental slab at ca. 46–40 Ma. **(C)** Continuous (ca. 40–25 Ma) low-angle underthrusting of the Indian continental slab during collision contributed to the HP metamorphism and magmatic lull. K & T, Kaghan and Tso Morari; KLA, Kohistan–Ladakh arc.

HP–UHP rocks. The ~31 Ma eclogite-facies metamorphic age in Stak is similar to those recorded in the central Himalayan HP eclogite (~30 Ma; Wang et al., 2021) and the Zanskar HP granulite (31–28 Ma; Vance and Harris, 1999) and the Ayilari garnet amphibolite (~32 Ma; Chen et al., 2021) in the western Himalaya (**Figure 1B**), indicating that these HP rocks were synchronously buried to shallow depths much later than the UHP rocks.

Notably, the old UHP eclogites and young HP rocks record different peak-pressure thermal gradients (temperature change with depth, referred to as metamorphic *T/P*) (**Figure 8**), implying a change in the subduction geometry of the Indian continental slab during 46–40 Ma. The subduction of oceanic lithosphere (Neo-Tethys) after the initial India–Asia collision (~60 Ma; e.g., Parsons et al., 2020) would continuously release fluids or melts, generate convective corner flow in the mantle wedge, and, thus, induce magmatism at convergent plate margins (**Figure 7B**). The successive steep subduction of Indian continental crust driven by slab pull of the Neo-Tethys underwent UHP metamorphism (low *T/P*) at 53–46 Ma (**Figures 2A** and **9A**). The steep subduction of the Indian continental slab is also supported by the presence of the UHP eclogite units in the western Himalaya now directly adjacent to the Indus–Tsangpo suture zone (O'Brien, 2019). However, after ~40 Ma, the sole occurrence of HP metamorphism (high *T/P*) along the strike reflects an increase of geothermal gradient that requires a change in subduction dip angle (**Figures 2B** and **9B**). These young HP rocks most likely resulted from low-angle underthrusting during continental collision (Guillot et al., 2008; Soret et al., 2021). Therefore, the change in subduction dip angle of the Indian continental slab during 46–40 Ma is critical for the transition from continental subduction to collision dynamics.

The change in subduction dip angle can be induced by the continuous subduction of buoyant continental lithosphere (Parsons et al., 2021) or by the breakoff of the oceanic (Neo-Tethyan) lithosphere (Davies and von Blanckenburg, 1995; Magni et al., 2017). Breakoff of the Neo-Tethyan lithosphere would lead to fast exhumation of UHP rocks (Kohn and Parkinson, 2002), uplifting of the buoyant continental lithosphere, and shifting to gently dipping subduction or underthrusting (Davies and von Blanckenburg, 1995;

Chemenda et al., 2000). In addition, slab breakoff mostly occurs at greater depths (~130–240 km) than the base of the overriding lithosphere and would not trigger significant magmatism at convergent margins (e.g., Freeburn et al., 2017), which is consistent with the weak magmatism within the Asian plate at 46–40 Ma (**Figure 7B**). There are many lines of evidence supporting the breakoff of the Neo-Tethyan slab around 46–40 Ma after the initial India–Asia collision. 1) According to paleomagnetic reconstructions and tomographical observations, Negredo et al. (2007) estimated the breakoff of oceanic slab occurring at 48–44 Ma. 2) The rapid exhumation of the Kaghan UHP eclogite from ~100 to ~35 km during 46–44 Ma (Parrish et al., 2006) also agrees with the breakoff model (Kohn and Parkinson, 2002). 3) Based on tomography, the Asian tectonics reconstructions and the Indian plate kinematics, Replumaz et al. (2014) proposed that the major breakoff between India and the Tethys ocean occurred at ~45 Ma. However, Parsons et al. (2021) proposed a different timing for slab breakoff based on interpretations of the same tomographic anomalies. 4) The occurrence of 42–40 Ma intraplate-type mafic dykes in eastern Tibet supports the breakoff of subducting Neo-Tethyan slab from the Indian continental slab during the middle Eocene (Xu et al., 2008). 5) The 45 Ma oceanic island basalt-type gabbro in southern Tibet was used to constrain the breakoff time of the Neo-Tethyan slab (Ji et al., 2016). Numerical studies suggest that the timing of slab breakoff after the onset of continental collision varies from 10 to 25 Ma, which is largely affected by the strength and age of the subducting oceanic slab (e.g., van Hunen and Allen, 2011). Our proposed slab breakoff timing (46–40 Ma) for the old Neo-Tethyan slab after the onset of continental collision (~60 Ma) broadly fits this modeled result. Therefore, we suggest that the different *T*/*P* and ages between the Himalayan UHP and HP rocks were induced by the breakoff of the Neo-Tethyan slab and subsequent transition from steep continental subduction to low-angle underthrusting (collision) at 46–40 Ma (**Figure 9B**).

The synchronous HP metamorphism induced by laterally large-scale low-angle underthrusting is also supported by palaeomagnetic and magmatic data. Since the Late Cretaceous, the India–Asia convergence rates in the eastern and western Himalayas show high consistency (**Figure 7C**), decreasing from 140–160 to 80–100 mm/year at 52–50 Ma and then decreasing to 40–60 mm/year at ca. 45 Ma (van Hinsbergen et al., 2011). The first deceleration is attributed to the initial India–Asia collision (van Hinsbergen et al., 2011), whereas the second most likely resulted from the loss of oceanic slab pull after breakoff (e.g., Bercovici et al., 2015; Ji et al., 2016) or the India–Asia second collision (45–40 Ma) after an earlier collision (~60 Ma) of either Indian continent + intraoceanic arc or greater India microcontinent + Asia (e.g., Parsons et al., 2020, 2021). A low convergence rate benefits sufficient heat exchange between the subducting plate and the overlying mantle, thus inducing HP metamorphism with high *T*/*P* (Guillot et al., 2008). In addition, the Himalayan magmatic activities from east to west were systematically complementary to the HP metamorphic events after 40 Ma. The Kohistan–Ladakh–Gangdese arc system and south Karakoram exhibit a coherent magmatic lull at 40–25 Ma (**Figure 7B**). The Stak eclogite in the western Himalaya and most of the other HP rocks in the central and eastern Himalaya also formed at this stage (**Figures 7A** and **9C**). The low-angle underthrusting after slab breakoff would have driven the asthenosphere beneath the Asian plate away and then shielded the active continental margin from convective heat, which would have led to the magmatic lull in the convergent margin (Chung et al., 2005; Ji et al., 2016; Ji et al., 2020). The driving force for the continuous convergence and underthrusting after the breakoff of the Neo-Tethyan slab could be subduction of Australian oceanic lithosphere (e.g., Parsons et al., 2021) or subduction of Indian continental lithosphere (e.g., Capitanio et al., 2010). In addition, the continuous low-angle underthrusting during continental collision at 40–25 Ma potentially enhanced crustal thickening (Soret et al., 2021) and elevated the thermal structure of orogenic wedge due to radiogenic heat production in the thickened crust (Berger et al., 2011), contributing to the high- or ultrahigh-temperature overprints in HP eclogites during exhumation (Wang et al., 2021). In this regard, the change in subduction dip angle of continental slab would have influenced both magmatic activities and peak geothermal gradients of HP–UHP rocks. To summarize, a lateral (>2,500 km) change in the subduction geometry of the Indian continental slab during the middle Eocene would be broadly consistent with the igneous and metamorphic records.

CONCLUSION

The Stak eclogites and their country gneiss in the western Himalayan syntexis provide insight into the change in subduction dip angle of the Indian continental lithosphere. Precise geochronological data show that the Stak massif underwent HP eclogite-facie metamorphism at ~31 Ma, which is at least ~15 Ma later than the Himalayan UHP metamorphism. Considering the discrepancies in peak ages and geothermal gradients between the Himalayan HP and UHP metamorphic rocks, we suggest that the Indian continental lithosphere underwent a coherent change in subduction dip angle during 46–40 Ma. Based on geological and geophysical evidence, this change in subduction geometry is likely induced by the breakoff of the Neo-Tethyan slab. We suggest that the change in subduction dip angle is a critical process controlling the transition from continental subduction to collision dynamics.

DATA AVAILABILITY STATEMENT

The original contributions presented in the study are included in the article/**Supplementary Materials**. Further inquiries can be directed to the corresponding author.

AUTHOR CONTRIBUTIONS

SC, YC, and QL performed the analyses. SC contributed to the data sorting and compilation. YC interpreted the data. YC, SC, and SG wrote the manuscript.

FUNDING

This work is financially supported by the National Natural Science Foundation of China (Nos. 41822202 and 41490614).

ACKNOWLEDGMENTS

We thank Profs. Lin Ding, Weiming Fan, Junmeng Zhao, Jamie Cutts, and Fulong Cai, Muhammad Qasim, Lin Chen, and Weiqiang Ji for inspiring discussion and constructive comments. D. Zhang, X.X. Ling, and C.R. Diwu are thanked for their help during the electron probe microanalysis, SIMS, and LA-ICP-MS analyses. Critical reviews by Andy Parsons and Xiao-Ping Xia and editorial handling by Oliver Jagoutz and Valerio Acocella helped to improve the manuscript.

SUPPLEMENTARY MATERIAL

The Supplementary Material for this article can be found online at: https://www.frontiersin.org/articles/10.3389/feart.2021.790999/full#supplementary-material

REFERENCES

Bercovici, D., Schubert, G., and Ricard, Y. (2015). Abrupt Tectonics and Rapid Slab Detachment with Grain Damage. *Proc. Natl. Acad. Sci. USA* 112 (5), 1287–1291. doi:10.1073/pnas.1415473112

Berger, A., and Bousquet, R. (2008). Subduction-related Metamorphism in the Alps: Review of Isotopic Ages Based on Petrology and Their Geodynamic Consequences. *Geol. Soc. Lond. Spec. Publications* 298, 117–144. doi:10.1144/SP298.7

Berger, A., Schmid, S. M., Engi, M., Bousquet, R., and Wiederkehr, M. (2011). Mechanisms of Mass and Heat Transport during Barrovian Metamorphism: A Discussion Based on Field Evidence from the Central Alps (Switzerland/northern Italy). *Tectonics* 30 (1). doi:10.1029/2009TC002622

Capitanio, F. A., Morra, G., Goes, S., Weinberg, R. F., and Moresi, L. (2010). India-asia Convergence Driven by the Subduction of the Greater Indian Continent. *Nat. Geosci* 3 (2), 136–139. doi:10.1038/ngeo725

Chemenda, A. I., Burg, J. P., and Mattauer, M. (2000). Evolutionary Model of the Himalaya-Tibet System: Geopoem: Based on New Modelling, Geological and Geophysical Data. *Earth Planet. Sci. Lett.* 174 (3–4), 397–409. doi:10.1016/S0012-821X(99)00277-0

Chen, X., Schertl, H.-P., Gu, P., Zheng, Y., Xu, R., Zhang, J., et al. (2021). Newly Discovered MORB-type HP Garnet Amphibolites from the Indus-Yarlung Tsangpo Suture Zone: Implications for the Cenozoic India-Asia Collision. *Gondwana Res.* 90, 102–117. doi:10.1016/j.gr.2020.11.006

Corrie, S. L., Kohn, M. J., and Vervoort, J. D. (2010). Young Eclogite from the Greater Himalayan Sequence, Arun Valley, Eastern Nepal: *P-T*-t Path and Tectonic Implications. *Earth Planet. Sci. Lett.* 289 (3–4), 406–416. doi:10.1016/j.epsl.2009.11.029

Davies, J. H., and von Blanckenburg, F. (1995). Slab Breakoff: a Model of Lithosphere Detachment and its Test in the Magmatism and Deformation of Collisional Orogens. *Earth Planet. Sci. Lette* . 129 (1–4), 85–102. doi:10.1016/0012-821X(94)00237-S

de Sigoyer, J., Chavagnac, V., Blichert-Toft, J., Villa, I. M., Luais, B., Guillot, S., et al. (2000). Dating the Indian continental Subduction and Collisional Thickening in the Northwest Himalaya: Multichronology of the Tso Morari Eclogites. *Geology* 28 (6), 487–490. doi:10.1130/0091-7613(2000)28<487:DTICSA>2.0.CO;2

Ding, H., Zhang, Z., Dong, X., Tian, Z., Xiang, H., Mu, H., et al. (2016a). Early Eocene (C . 50 Ma) Collision of the Indian and Asian Continents: Constraints from the North Himalayan Metamorphic Rocks, southeastern Tibet. *Earth Planet. Sci. Lett.* 435, 64–73. doi:10.1016/j.epsl.2015.12.006

Ding, H., Zhang, Z., Hu, K., Dong, X., Xiang, H., and Mu, H. (2016b). *P-T*-t-D Paths of the North Himalayan Metamorphic Rocks: Implications for the Himalayan Orogeny. *Tectonophysics* 683, 393–404. doi:10.1016/j.tecto.2016.06.035

Donaldson, D. G., Webb, A. A. G., Menold, C. A., Kylander-Clark, A. R. C., and Hacker, B. R. (2013). Petrochronology of Himalayan Ultrahigh-Pressure Eclogite. *Geology* 41 (8), 835–838. doi:10.1130/g33699.1

Duretz, T., and Gerya, T. V. (2013). Slab Detachment during continental Collision: Influence of Crustal Rheology and Interaction with Lithospheric Delamination. *Tectonophysics* 602, 124–140. doi:10.1016/j.tecto.2012.12.024

Faak, K., Chakraborty, S., and Dasgupta, S. (2012). Petrology and Tectonic Significance of Metabasite Slivers in the Lesser and Higher Himalayan Domains of Sikkim, India. *J. Metamorph. Geol.* 30 (6), 599–622. doi:10.1111/j.1525-1314.2012.00987.x

Freeburn, R., Bouilhol, P., Maunder, B., Magni, V., and van Hunen, J. (2017). Numerical Models of the Magmatic Processes Induced by Slab Breakoff. *Earth Planet. Sci. Lett.* 478, 203–213. doi:10.1016/j.epsl.2017.09.008

Grujic, D., Warren, C. J., and Wooden, J. L. (2011). Rapid Synconvergent Exhumation of Miocene-Aged Lower Orogenic Crust in the Eastern Himalaya. *Lithosphere* 3 (5), 346–366. doi:10.1130/L154.1

Guillot, S., Mahéo, G., de Sigoyer, J., Hattori, K. H., and Pêcher, A. (2008). Tethyan and Indian Subduction Viewed from the Himalayan High- to Ultrahigh-Pressure Metamorphic Rocks. *Tectonophysics* 451 (1–4), 225–241. doi:10.1016/j.tecto.2007.11.059

Hazarika, D., Wadhawan, M., Paul, A., Kumar, N., and Borah, K. (2017). Geometry of the Main Himalayan Thrust and Moho beneath Satluj valley, Northwest Himalaya: Constraints from Receiver Function Analysis. *J. Geophys. Res. Solid Earth* 122 (4), 2929–2945. doi:10.1002/2016jb013783

Jackson, S. E., Pearson, N. J., Griffin, W. L., and Belousova, E. A. (2004). The Application of Laser Ablation-Inductively Coupled Plasma-Mass Spectrometry to *In Situ* U-Pb Zircon Geochronology. *Chem. Geology.* 211 (1–2), 47–69. doi:10.1016/j.chemgeo.2004.06.017

Ji, W.-Q., Wu, F.-Y., Chung, S.-L., Wang, X.-C., Liu, C.-Z., Li, Q.-L., et al. (2016). Eocene Neo-Tethyan Slab Breakoff Constrained by 45 Ma Oceanic Island basalt-type Magmatism in Southern Tibet. *Geology* 44 (4), 283–286. doi:10.1130/g37612.1

Ji, W.-Q., Wu, F.-Y., Wang, J.-M., Liu, X.-C., Liu, Z.-C., Zhang, Z., et al. (2020). Early Evolution of Himalayan Orogenic belt and Generation of Middle Eocene Magmatism: Constraint from Haweng Granodiorite Porphyry in the Tethyan Himalaya. *Front. Earth Sci.* 8, 236. doi:10.3389/feart.2020.00236

Kaneko, Y., Katayama, I., Yamamoto, H., Misawa, K., Ishikawa, M., Rehman, H. U., et al. (2003). Timing of Himalayan Ultrahigh-Pressure Metamorphism: Sinking Rate and Subduction Angle of the Indian continental Crust beneath Asia. *J. Metamorph. Geol.* 21 (6), 589–599. doi:10.1046/j.1525-1314.2003.00466.x

Kay, S. M., and Coira, B. L. (2009). "Shallowing and Steepening Subduction Zones, continental Lithospheric Loss, Magmatism, and Crustal Flow under the Central Andean Altiplano-Puna Plateau," in *Backbone of the Americas: Shallow Subduction, Plateau Uplift, and Ridge and Terrane Collision*. Editors S. M. Kay, V. A. Ramos, and W. R. Dickinson (New York: Geol Soc Am Mem), 204, 229–259. doi:10.1130/2009.1204(11)

Kohn, M. J., and Corrie, S. L. (2011). Preserved Zr-Temperatures and U-Pb Ages in High-Grade Metamorphic Titanite: Evidence for a Static Hot Channel in the Himalayan Orogen. *Earth Planet. Sci. Lett.* 311 (1–2), 136–143. doi:10.1016/j.epsl.2011.09.008

Kohn, M. J., and Parkinson, C. D. (2002). Petrologic Case for Eocene Slab Breakoff during the Indo-Asian Collision. *Geol* 30 (7), 591–594. doi:10.1130/0091-7613(2002)030<0591:pcfesb>2.0.co;2

Kouketsu, Y., Hattori, K., and Guillot, S. (2017). Protolith of the Stak Eclogite in the Northwestern Himalaya. *Ijg* 136 (1), 64–72. doi:10.3301/IJG.2015.41

Kouketsu, Y., Hattori, K., Guillot, S., and Rayner, N. (2016). Eocene to Oligocene Retrogression and Recrystallization of the Stak Eclogite in Northwest Himalaya. *Lithos* 240-243, 155–166. doi:10.1016/j.Lithos.2015.10.022

Kylander-Clark, A. R. C., Hacker, B. R., Johnson, C. M., Beard, B. L., and Mahlen, N. J. (2009). Slow Subduction of a Thick Ultrahigh-Pressure Terrane. *Tectonics* 28, a–n. doi:10.1029/2007TC002251

Lanari, P., Riel, N., Guillot, S., Vidal, O., Schwartz, S., Pêcher, A., et al. (2013). Deciphering High-Pressure Metamorphism in Collisional Context Using Microprobe Mapping Methods: Application to the Stak Eclogitic Massif (Northwest Himalaya). *Geology* 41 (2), 111–114. doi:10.1130/G33523.1

Le Fort, P., Guillot, S., and Pêcher, A. (1997). HP Metamorphic belt along the Indus Suture Zone of NW Himalaya: New Discoveries and Significance. *Comptes Rendus de l'Académie des Sci. - Ser. IIA - Earth Planet. Sci.* 325 (10), 773–778. doi:10.1016/S1251-8050(97)82755-3

Li, Q., Zhang, L., Fu, B., Bader, T., and Yu, H. (2018). Petrology and Zircon U-Pb Dating of Well-preserved Eclogites from the Thongmön Area in central Himalaya and Their Tectonic Implications. *J. Metamorph. Geol.* 37 (2), 203–226. doi:10.1111/jmg.12457

Li, X.-H., Li, W.-X., Li, Z.-X., Lo, C.-H., Wang, J., Ye, M.-F., et al. (2009). Amalgamation between the Yangtze and Cathaysia Blocks in South China: Constraints from SHRIMP U-Pb Zircon Ages, Geochemistry and Nd-Hf Isotopes of the Shuangxiwu Volcanic Rocks. *Precambrian Res.* 174 (1-2), 117–128. doi:10.1016/j.precamres.2009.07.004

Li, X., Tang, G., Gong, B., Yang, Y., Hou, K., Hu, Z., et al. (2013). Qinghu Zircon: A Working Reference for Microbeam Analysis of U-Pb Age and Hf and O Isotopes. *Chin. Sci. Bull.* 58 (36), 4647–4654. doi:10.1007/s11434-013-5932-x

Liu, X., Gao, S., Diwu, C., Yuan, H., and Hu, Z. (2007). Simultaneous *In-Situ* Determination of U-Pb Age and Trace Elements in Zircon by LA-ICP-MS in 20 μm Spot Size. *Chin. Sci Bull* 52 (9), 1257–1264. doi:10.1007/s11434-007-0160-x

Ludwig, K. (2001). Users Manual for Isoplot/Ex Rev. 2.49: A Geochronological Toolkit for Microsoft Excel. *Calif. Berkeley Geochronol. Cent. Spec. Publ.* 1 (1), 56.

Magni, V., Allen, M. B., van Hunen, J., and Bouilhol, P. (2017). Continental Underplating after Slab Break-Off. *Earth Planet. Sci. Lett.* 474, 59–67. doi:10.1016/j.epsl.2017.06.017

McDonough, W. F., and Sun, S. -S. (1995). The Composition of the Earth. *Chem.Geol.* 120 (3–4), 223–253. doi:10.1016/0009-2541(94)00140-4

Mukheerjee, B., Sachan, H., and Ahmad, T. (2005). A New Occurrence of Microdiamond from Indus Suture Zone, Himalata: a Possible Origin. *Spec. Ext Abstrgéol Alp.* 44, 136.

Negredo, A. M., Replumaz, A., Villaseñor, A., and Guillot, S. (2007). Modeling the Evolution of continental Subduction Processes in the Pamir-Hindu Kush Region. *Earth Planet. Sci. Lett.* 259, 212–225. doi:10.1016/j.epsl.2007.04.043

O'Brien, P. J. (2019). Tso Morari Coesite Eclogite: Pseudosection Predictions V. The Preserved Record and Implications for Tectonometamorphic Models. *Geol. Soc. Lond. Spec. Publications* 474 (1), 5–24. doi:10.1144/SP474.16

O'Brien, P. J., Zotov, N., Law, R., Khan, M. A., and Jan, M. Q. (2001). Coesite in Himalayan Eclogite and Implications for Models of India-Asia Collision. *Geology* 29 (5), 352–438. doi:10.1130/0091-7613(2001)029<0435:CIHEAI>2.0.CO10.1130/0091-7613(2001)029<0435:ciheai>2.0.co;2

Parrish, R. R., Gough, S. J., Searle, M. P., and Waters, D. J. (2006). Plate Velocity Exhumation of Ultrahigh-Pressure Eclogites in the Pakistan Himalaya. *Geol* 34 (11), 989–992. doi:10.1130/G22796A.1

Parsons, A. J., Hosseini, K., Palin, R. M., and Sigloch, K. (2020). Geological, Geophysical and Plate Kinematic Constraints for Models of the India-Asia Collision and the post-Triassic central Tethys Oceans. *Earth-Science Rev.* 208, 103084. doi:10.1016/j.earscirev.2020.103084

Parsons, A. J., Sigloch, K., and Hosseini, K. (2021). Australian Plate Subduction Is Responsible for Northward Motion of the India-Asia Collision Zone and ~1,000 Km Lateral Migration of the Indian Slab. *Geophys. Res. Lett.* 48, e2021GL094904. doi:10.1029/2021gl094904

Paterson, S. R., and Ducea, M. N. (2015). Arc Magmatic Tempos: Gathering the Evidence. *Elements* 11 (2), 91–98. doi:10.2113/gselements.11.2.91

Rajkumar, A. (2015). *Prograde Histories in High-P to Ultra-high-P Metamorphic Rocks from Tibet and Northern India*. Ph.D. thesis. Sydney: The University of Sydney.

Rehman, H. U. (2019). Geochronological enigma of the HP-UHP Rocks in the Himalayan Orogen. *Geol. Soc. Lond. Spec. Publications* 474 (1), 183–207. doi:10.1144/SP474.14

Rehman, H. U., Lee, H.-Y., Chung, S.-L., Khan, T., O'Brien, P. J., and Yamamoto, H. (2016). Source and Mode of the Permian Panjal Trap Magmatism: Evidence from Zircon U-Pb and Hf Isotopes and Trace Element Data from the Himalayan Ultrahigh-Pressure Rocks. *Lithos* 260, 286–299. doi:10.1016/j.lithos.2016.06.001

Replumaz, A., Capitanio, F. A., Guillot, S., Negredo, A. M., and Villaseñor, A. (2014). The Coupling of Indian Subduction and Asian continental Tectonics. *Gondwana Res.* 26, 608–626. doi:10.1016/j.gr.2014.04.003

Riel, N., Hattori, K., Guillot, S., Rayner, N., Davis, B., Latif, M., et al. (2008). SHRIMP Zircon Ages of Eclogites in the Stak Massif, Northern Pakistan. *Himalayan J. Sci.* 5, 119–120. doi:10.3126/hjs.v5i7.1307

Rubatto, D., Chakraborty, S., and Dasgupta, S. (2013). Timescales of Crustal Melting in the Higher Himalayan Crystallines (Sikkim, Eastern Himalaya) Inferred from Trace Element-Constrained Monazite and Zircon Chronology. *Contrib. Mineral. Petrol.* 165 (2), 349–372. doi:10.1007/s00410-012-0812-y

Sachan, H. K., Mukherjee, B. K., Ogasawara, Y., Maruyama, S., Ishida, H., Muko, A., et al. (2004). Discovery of Coesite from Indus Suture Zone (ISZ), Ladakh, India: Evidence for Deep Subduction. *ejm* 16 (2), 235–240. doi:10.1127/0935-1221/2004/0016-0235

Shellnutt, J. G. (2018). The Panjal Traps. *Geol. Soc. Lond. Spec. Publications* 463, 59–86. doi:10.1144/SP463.4

Sláma, J., Košler, J., Condon, D. J., Crowley, J. L., Gerdes, A., Hanchar, J. M., et al. (2008). Plešovice Zircon - A New Natural Reference Material for U-Pb and Hf Isotopic Microanalysis. *Chem. Geology.* 249 (1–2), 1–35. doi:10.1016/j.chemgeo.2007.11.005

Soret, M., Larson, K. P., Cottle, J., and Ali, A. (2021). How Himalayan Collision Stems from Subduction. *Geology* 49, 894–898. doi:10.1130/G48803.1

St-Onge, M. R., Rayner, N., Palin, R. M., Searle, M. P., and Waters, D. J. (2013). Integrated Pressure-Temperature-Time Constraints for the Tso Morari Dome (Northwest India): Implications for the Burial and Exhumation Path of UHP Units in the Western Himalaya. *J. Meta. Geol.* 31 (5), 469–504. doi:10.1111/jmg.12030

Stacey, J. S., and Kramers, J. D. (1975). Approximation of Terrestrial lead Isotope Evolution by a Two-Stage Model. *Earth Planet. Sci. Lett.* 26 (2), 207–221. doi:10.1016/0012-821X(75)90088-6

van Hinsbergen, D. J. J., Steinberger, B., Doubrovine, P. V., and Gassmöller, R. (2011). Acceleration and Deceleration of India-Asia Convergence since the Cretaceous: Roles of Mantle Plumes and continental Collision. *J. Geophys. Res.* 116, B06101. doi:10.1029/2010jb008051

van Hunen, J., and Allen, M. B. (2011). Continental Collision and Slab Break-Off: A Comparison of 3-D Numerical Models with Observations. *Earth Planet. Sci. Lett.* 302, 27–37. doi:10.1016/j.epsl.2010.11.035

Vance, D., and Harris, N. (1999). Timing of Prograde Metamorphism in the Zanskar Himalaya. *Geol* 27 (5), 395–398. doi:10.1130/0091-7613(1999)027<0395:topmit>2.3.co;2

Wang, J.-M., Lanari, P., Wu, F.-Y., Zhang, J.-J., Khanal, G. P., and Yang, L. (2021). First Evidence of Eclogites Overprinted by Ultrahigh Temperature Metamorphism in Everest East, Himalaya: Implications for Collisional Tectonics on Early Earth. *Earth Planet. Sci. Lett.* 558, 116760. doi:10.1016/j.epsl.2021.116760

Wang, Y., Zhang, L., Zhang, J., and Wei, C. (2017). The Youngest Eclogite in central Himalaya: *P-T* Path, U-Pb Zircon Age and its Tectonic Implication. *Gondwana Res.* 41, 188–206. doi:10.1016/j.gr.2015.10.013

Whitney, D. L., and Evans, B. W. (2010). Abbreviations for Names of Rock-Forming Minerals. *Am. Mineral.* 95 (1), 185–187. doi:10.2138/am.2010.3371

Wiedenbeck, M., Hanchar, J. M., Peck, W. H., Sylvester, P., Valley, J., Whitehouse, M., et al. (2004). Further Characterisation of the 91500 Zircon crystal. *Geostand Geoanalyt Res.* 28 (1), 9–39. doi:10.1111/j.1751-908X.2004.tb01041.x

Wilke, F. D. H., O'Brien, P. J., Altenberger, U., Konrad-Schmolke, M., and Khan, M. A. (2010). Multi-stage Reaction History in Different Eclogite Types from the Pakistan Himalaya and Implications for Exhumation Processes. *Lithos* 114 (1–2), 70–85. doi:10.1016/j.lithos.2009.07.015

Wilke, F. D. H., O'Brien, P. J., Schmidt, A., and Ziemann, M. A. (2015). Subduction, Peak and Multi-Stage Exhumation Metamorphism: Traces from One Coesite-Bearing Eclogite, Tso Morari, Western Himalaya. *Lithos* 231, 77–91. doi:10.1016/j.lithos.2015.06.007

Xu, Y.-G., Lan, J.-B., Yang, Q.-J., Huang, X.-L., and Qiu, H.-N. (2008). Eocene Break-Off of the Neo-Tethyan Slab as Inferred from Intraplate-type Mafic

Dykes in the Gaoligong Orogenic belt, Eastern Tibet. *Chem. Geology.* 255, 439–453. doi:10.1016/j.chemgeo.2008.07.016

Yin, A. (2006). Cenozoic Tectonic Evolution of the Himalayan Orogen as Constrained by Along-Strike Variation of Structural Geometry, Exhumation History, and Foreland Sedimentation. *Earth-Science Rev.* 76 (1–2), 1–131. doi:10.1016/j.earscirev.2005.05.004

Zhang, R. Y., Liou, J. G., and Ernst, W. G. (2009). The Dabie-Sulu continental Collision Zone: A Comprehensive Review. *Gondwana Res.* 16, 1–26. doi:10.1016/j.gr.2009.03.008

Zhang, Z. M., Zhao, G. C., Santosh, M., Wang, J. L., Dong, X., and Liou, J. G. (2010). Two Stages of Granulite Facies Metamorphism in the Eastern Himalayan Syntaxis, South Tibet: Petrology, Zircon Geochronology and Implications for the Subduction of Neo-Tethys and the Indian Continent beneath Asia. *J. Metamorph. Geol.* 28 (7), . doi:10.1111/j.1525-1314.2010.00885.x

Zhang, Z., Xiang, H., Dong, X., Ding, H., and He, Z. (2015). Long-lived High-Temperature Granulite-Facies Metamorphism in the Eastern Himalayan Orogen, South Tibet. *Lithos* 212-215, 1–15. doi:10.1016/j.lithos.2014.10.009

Zhang, Z., Xiang, H., Dong, X., Li, W., Ding, H., Gou, Z., et al. (2017). Oligocene HP Metamorphism and Anatexis of the Higher Himalayan Crystalline Sequence in Yadong Region, East-central Himalaya. *Gondwana Res.* 41, 173–187. doi:10.1016/j.gr.2015.03.002

Conflict of Interest: The authors declare that the research was conducted in the absence of any commercial or financial relationships that could be construed as a potential conflict of interest.

The reviewer X-PX declared a past co-authorship with one of the authors, QL, to the handling editor.

frontiers
in Earth Science

REVIEW
published: 18 March 2022
doi: 10.3389/feart.2022.837775

Fate of Carbonates in the Earth's Mantle (10-136 GPa)

Jing Gao[1]*, *Xiang Wu*[2], *Xueyin Yuan*[3] and *Wen Su*[1]

[1]*State Key Laboratory of Lithospheric Evolution, Institutions of Earth Science, Institute of Geology and Geophysics, Chinese Academy of Sciences, Beijing, China,* [2]*State Key Laboratory of Geological Processes and Mineral Resources, China University of Geosciences, Wuhan, China,* [3]*MNR Key Laboratory of Metallogeny and Mineral Assessment, Institute of Mineral Resources, Chinese Academy of Geological Sciences, Beijing, China*

Earth carbon cycle shapes the evolution of our planet and our habitats. As a key region of carbon cycle, subduction zone acts as a sole channel transporting supracrustal carbonate rocks down to the mantle, balancing carbon budget between the Earth's surface and the interior, and regulating CO_2 concentration of the atmosphere. How carbonates evolve at depth is thus, a most fundamental issue in understanding carbon flux and carbon sequestration mechanism in the Earth. This study reviews prominent progresses made in the field of crystal chemistry of carbonates along subduction geotherms. It clearly finds that, in addition to common carbonates in the Earth's crust, several new polymorphs of carbonates have been discovered to be stable under high-pressure and high-temperature conditions. This opens possibilities for oxidized carbon species in the deep Earth. However, metamorphic decarbonatation and reduction reactions restrict subducting carbonates to the top-mid region of the lower mantle. Specifically, subsolidus decarbonatation in the form of carbonates reacting with silicates has been proposed as an efficient process releasing CO_2 from slabs to the mantle. Besides, carbonate reduction in the metal-saturated mantle likely results in generation of super-deep diamonds and a considerable degree of carbon isotope fractionation. Review of these novel findings leads us to consider three issues in the further studies, including *1*) searching for new chemical forms of carbon in the mantle, *2*) determining the reduction efficiency of carbonates to diamonds and the accompanying carbon isotope fractionation and *3*) concerning carbon cycle in subduction of continental crust.

Keywords: phase relation, crystal chemistry, diamond, graphite, decarbonatation

Edited by:
Guibin Zhang,
Peking University, China

Reviewed by:
Renbiao Tao,
Center for High Pressure Science and Technology Advanced Research, China
Yi-Xiang Chen,
University of Science and Technology of China, China
Michel Grégoire,
UMR5563 Géosciences Environnement Toulouse (GET), France

***Correspondence:**
Jing Gao
gaojing@mail.iggcas.ac.cn

Specialty section:
This article was submitted to Petrology, a section of the journal Frontiers in Earth Science

Received: *17 December 2021*
Accepted: *18 January 2022*
Published: *18 March 2022*

Citation:
Gao J, Wu X, Yuan X and Su W (2022) Fate of Carbonates in the Earth's Mantle (10-136 GPa). Front. Earth Sci. 10:837775. doi: 10.3389/feart.2022.837775

INTRODUCTION

Carbon is a basic element that forms the Earth and the biosphere. Earth carbon cycle ties closely with the global climate, the origin and evolution of life and the carbon-based energy resources. The present review focuses on the carbon cycle in subduction zones. The crustal carbon is carried down to the Earth's interior *via* subduction processes, modifying the redox state of the mantle, and the deep carbon exchanges with the crustal carbon *via* volcanism or metamorphic decarburization over geological timescales (Dasgupta and Hirschmann, 2010; Plank and Langmuir, 1993). This process is responsible for the recycling of a great amount of carbon and consequently, exerts profound influence upon the terrestrial ecosystem functions. In recent decades, the carbon balance between the Earth's surface and the interior is wrecked. It has become our urgent desire to examine carbon sequestration capacity of different reservoirs and strive for a balance of carbon income and outcome.

Extensive studies have been carried out on carbon flux from the Earth's surface to the interior but obtained totally different results (Gorman et al., 2006; Johnston et al., 2011). Estimation on the removal amount of the subducted carbon from slabs varies from 35 to 100% (Kelemen and Manning, 2015). The large inconsistency is due mainly to our limited knowledge on behaviors of carbonates in subduction zones.

Carbonates (e.g. calcite $CaCO_3$, magnesite $MgCO_3$ and dolomite $(Ca, Mg)CO_3$) are predominantly carbon species in the Earth's crust. Their structural stability in subduction zones is a key to measuring carbon flux. On the one hand, with the increase of the subduction depth, the pressure-temperature and the oxygen fugacity conditions become more and more favorable for reduced carbon species. In this respect, carbonates would be overtaken by diamond or graphite at mantle depths in excess of ~250 km where the redox state begins to be buffered by iron-wüstite equilibrium due to disproportionation of Fe^{2+} to Fe^{3+} and metallic Fe^0 (Frost et al., 2004). At greater depths, Fe^{2+} disproportionation to Fe^{3+} and Fe^0 progressively increases, which likely results to diamond domains in the deep Earth (Rohrbach and Schmidt, 2011). On the other hand, however, the possibilities of crustal carbonates in the upper-mid mantle have been suggested by thermodynamic calculations (Sun et al., 2018) and experiments (Ghosh et al., 2009; Litvin et al., 2014). Besides, carbonate associations have been frequently discovered as inclusions in the transition-zone and the lower-mantle diamonds (e.g. Brenker et al., 2007; Kaminsky, 2012; Kaminsky et al., 2013; 2016). This indicates that the crystal chemistry of carbonates and the carbon sequestration mechanism in the deep Earth are far more complicated than previously thought.

In this study, we systematically review the high-pressure behaviors of carbonates along from cold to the hottest subduction geotherms, aiming at three scientific issues: *1*) Establishing a comprehensive phase relation of main carbonates in the Earth's mantle. Our first concern is whether carbonates will melt and breakdown at high-pressure and high-temperature conditions, or preserve to greater depths even approaching the core-mantle boundary (CMB). *2*) Next, close attention are paid upon the reduction mechanism of carbonates in reactions with the metallic mantle during subducting processes, as that would be an impenetrable barrier to carbonate subduction. *3*) Meanwhile, decarbonization of carbonated peridotites and eclogites (including mid-ocean ridge basalt, MORB) by the surrounding silicates should also be examined, as these processes exhibit the possibility of CO_2 release as an equilibrium phase in the deep mantle, which sets fundamental control on mantle metasomatism.

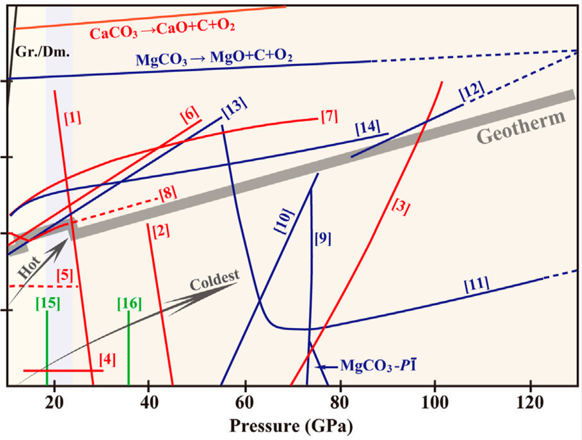

FIGURE 1 | Phase diagram of $CaCO_3$, $MgCO_3$, $(Ca,Mg)CO_3$ and the ferrous series under high pressures and temperatures. Equilibrium boundary between Gr. and Dm. is based on Bundy et al. (1996). Pressure-Temperature-profiles of hot subduction slab (red arrow) stagnant in the transition zone and the coldest slab (navy-blue arrow) penetrating into the lower mantle (an extrapolated curve) are referred to Syracuse et al. (2010). The gray zone indicates the Mantle Geotherm (Katsura et al., 2010). Curve [1] represents the phase boundary between Arag. and $CaCO_3$-VII and Curve [2] between $CaCO_3$-VII and Post-Arag. (Gavryushkin et al., 2017; Li et al., 2018). Transformation from Post-Arag. to $P2_1/c$-*h* is indicated by Curve [3] (Gavryushkin et al., 2017; Zhang ZG. et al., 2018). Phase relation between $CaCO_3$-VI (*P*-1) and Arag. (13.5–25 GPa; ~1100 K) is denoted by Curve [4] (Pickard and Needs, 2015; Bayarjargal et al., 2018). Curve [5] is an extrapolated curve showing the transformation from Arag. to $CaCO_3$-V (disordered) (Litasov et al., 2017; Zhao et al., 2019) or an unknown structure. Melting curves of $CaCO_3$ and the boundary of decomposition of $CaCO_3$ melt are referred to Litvin et al. (2014) (Curve [6]), Zhang and Liu, (2015) (Curve [7]) and Li et al. (2017) (Curve [8]). Structural evolution from $MgCO_3$ to *C2/m* (Curve [9]) is based on Oganov et al. (2008) and Boulard et al. (2011). $MgCO_3$-*P*-1 has a limited stable regime between 85 and 101 GPa below ~1100 K (Pickard and Needs, 2015). Spin crossover of Fe^{2+} in ferromagnesite (Curve [10]) is from Liu et al. (2015). Phase boundaries from Fe^{2+}-rich Mg-carbonates-*R*-3*c* to *Pmm*2 (Curve [11]) is plotted by Liu et al. (2015) and to *C2/m* (Curve [12]) by Boulard et al. (2011; 2012; 2015). $MgCO_3$ melt and the decomposition to diamond are measured from Litvin et al. (2014) (Curve [13]) and Solopova et al. (2015) (Curve [14]). Phase transition from Fe-Dol. to Fe-Dol.-II is denoted by Curve [15] and further to Fe-Dol.-III by Curve [16] (Merlini et al., 2012). Abbreviations: Gr., graphite; Dm., diamond; Arag., aragonite; Post-Arag., post-aragonite; Fe-Dol., Fe^{2+}-bearing dolomite; Fe-Dol.-II, Fe^{2+}-bearing dolomite-II; Fe-Dol.-III, Fe^{2+}-bearing dolomite-III.

PHASE DIAGRAM OF CARBONATES IN THE MANTLE

$CaCO_3$, $MgCO_3$, $(Ca,Mg)CO_3$ are three main inorganic carbon substances in the Earth's crust. They are also dominant carbon species recovered in sublithospheric diamonds. Carbonates show versatile behaviors such as phase transition, dissolution, melting, decomposition and decarburization at mantle conditions. For example, $CaCO_3$ exhibits exceeding solubility in aqueous fluids and may extract a considerable portion of carbon from slabs. But Ca^{2+} in carbonates would be replaced by Mg^{2+} upon sinking, and the solubility of dolomite reduces significantly if carbonates become Mg-rich (Farsang et al., 2021). Naturally Fe^{2+} substituting Mg^{2+} forms a complete $MgCO_3$-$FeCO_3$ solid solution, and a minor addition of Fe^{2+} significantly affect the phase boundary of carbonates especially at lower-mantle pressures (Liu et al., 2015; Tao et al., 2014). The following section presents a summary of phase relation of $CaCO_3$, $MgCO_3$ and $(Ca,Mg)CO_3$ and their ferrous series at depths.

Calcite $CaCO_3$

The stable polymorph of $CaCO_3$ at ambient conditions is calcite (R-3c, $Z = 6$) where $[CO_3]^{2-}$ species form parallel layers and Ca^{2+} are six-fold coordinated by O^{2-}. Upon pressures above ~2 GPa, calcite reconstructively converts to aragonite ($Pmcn$, $Z = 4$) with $[CaO_6]$-octahedra turning into $[CaO_9]$-polyhedra. Aragonite has long been considered as the dominant $CaCO_3$-structure in the Earth's interior from the upper mantle to the top of the lower mantle. Yet its density is lower than the principle constituents of the mantle (Litasov et al., 2007), which casts doubts on the presence of $CaCO_3$ in the deep Earth. Accumulations of experimental and theoretical data lately, however, create a whole new landscape of $CaCO_3$ inside the Earth. One significant finding is $CaCO_3$-VII ($P2_1/c$-l, $Z = 4$), which was put forward by Gavryushkin et al. (2017) as favorable in the pressure range of 30–50 GPa below1200 K (**Figure 1**). Bayarjargal et al. (2018) and Li et al. (2018) subsequently expanded its temperature scope to the melting point and suggest $CaCO_3$-VII as a predominant candidate at mantle depths of 690–1010 km. Increasing temperature would lower the pressure of aragonite → $CaCO_3$-VII transformation (Zhang ZG. et al., 2018). $CaCO_3$-VII is characterized with non-planar $[CO_3]^{2-}$ units that are rotated by ~45° relative to those in calcite/aragonite and are tilted ~90° to one another. It is considered as an intermediate in the aragonite → post-aragonite transformation wherein the $[CO_3]^{2-}$ units undergo a ~90° rotation (Pickard and Needs, 2015; Smith et al., 2018). Conversion of aragonite to $CaCO_3$-VII is accompanied by an uprush of 2% for density, and an increase of 9, 2 and 8% for shear, longitudinal and average sound velocities. The difference in wave velocities increase by ~6% when 10% $CaCO_3$ is present with respect to a pure pyrolitic composition (Bayarjargal et al., 2018). Therefore, the potential preferred orientation of $CaCO_3$-VII may contribute to seismic discontinuities at ~700 km in the vicinity of slabs (Kaneshima, 2013; Yang and He, 2015; Bayarjargal et al., 2018).

In the meanwhile, Gavryushkin et al. (2017) took the initiative in observing the occurrence of aragonite-II ($P2_1/c$), another model structurally relevant to aragonite at 35 GPa and its absence at 50 GPa. The phase domain of aragonite-II was reproduced by Bayarjargal et al. (2018) under non-hydrostatic pressures of 30–38 GPa. Yet never aragonite-II was a pure phase in both studies. By contrast, at pressures of 23–38 GPa, Li et al. (2018) observed only $CaCO_3$-VII generation at temperatures up to 2300 K. Zhang ZG. et al. (2018) provided thermodynamic arguments for the marginal metastability of aragonite-II at 30–40 GPa, and with temperature rising, aragonite-II became increasingly unfavorable. It is open to question for the presence and stability of aragonite-II, which is subjected to kinetic barriers of equilibrium phase transformations in experiments and uncertainties in calculations.

At 42 GPa and 1400 K, a further phase transition occurs from $CaCO_3$-VII to post-aragonite ($Pmmn$, $Z = 2$) with the Clapeyron slope of the phase boundary being -233 K/GPa (Bayarjargal et al., 2018; Li et al., 2018). Post-aragonite exhibits much higher wave velocity anisotropies than major silicates and other carbonates (Huang et al., 2017). This reconstructive transformation leads to measurable decreases in shear (−7.0%) and longitudinal (−4.7%) wave velocities around 1010 km in consideration of the pyrolitic mantle composition with 10% $CaCO_3$ (Li and Yuen, 2014; Niu, 2014; Bayarjargal et al., 2018). Post-aragonite was once believed as the best host structure for $CaCO_3$ in the bulk of the lower mantle and it transformed to a pyroxene-like structure $C222_1$ at the CMB (Oganov et al., 2008). This notion, however, should be deliberated. Another pyroxene-phase $P2_1/c$-h as recommended above ~65 GPa, which was evolved from collapse of $P2_1/c$-l without energy barriers (Pickard and Needs, 2015; Huang et al., 2017; Zhang ZG. et al., 2018). Both $P2_1/c$-h and $C222_1$ are featured with $[CO_4]^{4-}$ species, but the former is made up of pyroxene chains stacked out-of-phase while the latter of parallel chains. In spite of pyroxene-phases, Lobanov et al. (2017) insisted that post-aragonite perseveres until ~105 GPa, afterwards it undergoes the lowest-enthalpy path to become $P2_1/c$-h along with conversion of sp^2-to sp^3-hybridized carbon. But Smith et al. (2018) documented that $CaCO_3$-VII itself is capable of sp^2-sp^3 hybridization exchange and rather than any known $CaCO_3$-polymorphs, an entirely new phase came in above ~50 GPa. There exist remarkable discrepancies as to the stability of $CaCO_3$-polymorphs under mid-mantle pressures as well as the phase boundaries, due likely to the kinetic hindrance of the transformations or limitations of different approaches, but sp^3-hybridized carbon does merit special notice because of its thermodynamical stability in the megabar regime.

Melting of $CaCO_3$ was observed at ~1880 K at 3 GPa (Irving and Wyllie, 1975) and monitored using Raman Spectroscopy above ~1900 K at 10 GPa (Litvin et al., 2014), with a smoother slope by conductivity measurement (Li et al., 2017). The melting curve derived from First-principles calculations shifted slightly to lower temperatures, where a knee point occurred at 13 (1) GPa and 1970 (40) K that was attributed to conversion between $CaCO_3$-V and aragonite. Aragonite was detected in the recovered products in the pressure-temperature region where $CaCO_3$-V is supposed to be stable (Zhang and Liu, 2015; Li et al., 2017) due likely to the unquenchable character of $CaCO_3$-V. $CaCO_3$ had a broad area of congruent melting up to ~3500 K, above which, it started to decompose. Decomposition of $CaCO_3$ resulted in generation of graphite that transformed to diamond if annealed to lower temperatures of 700–2700 K (Bayarjargal et al., 2010; Spivak et al., 2011). All these studies pointed out that melting and decomposition of $CaCO_3$ were realized at temperatures above most subduction geotherms. That is, almost the whole mantle falls into the solid regime of $CaCO_3$ polymorphs.

$CaCO_3$ with complex structural chemistry can be understood from the following two perspectives. *1*) In calcite-members ($CaCO_3$, $CdCO_3$, $MnCO_3$, $FeCO_3$, $ZnCO_3$, $MgCO_3$, etc), $CaCO_3$ has the largest ionic radius of Ca^{2+} that can bear various pressures by adjusting coordination numbers (Oganov et al., 2008). *2*) In aragonite-family ($CaCO_3$, $SrCO_3$, $PbCO_3$, $BaCO_3$, etc), $CaCO_3$ contains the closest matching in distance between Ca^{2+} and $[CO_3]^{2-}$ species that results to the most variation in C-O bond lengths and deviation from $[CO_3]^{2-}$-coplane (Antao and Hassan, 2009). The great variety of $CaCO_3$ polymorphs opens possibilities of stable $CaCO_3$ component in the deep mantle. According to the results above, we plot **Figure 1** for to obtain an overview of phase evolution of $CaCO_3$ to be aragonite (≤~25 GPa) → $CaCO_3$-VII (25–42 GPa) → post-aragonite (42–80 GPa) → $P2_1/c$-h or $C222_1$ (80–137 GPa), which is dominantly affected by pressure.

Magnesite $MgCO_3$ and Ferromagnesite

$MgCO_3$ maintained its rhombohedral structure (R-3c; Z = 6) up to at least ~80 GPa and ~2300 K, thereafter it turned into $MgCO_3$-II ($C2/m$; Z = 6) until the CMB (Isshiki et al., 2004; Maede et al., 2017) (**Figure 1**). $MgCO_3$-II is featured with $[C_3O_9]^{6-}$-rings that consists of three $[CO_4]^{4-}$-tetrahedra with asymmetric C-O bonds, and Mg^{2+} are in eight- or ten-fold coordination (Oganov et al., 2008; Boulard et al., 2011). Another silicate-like polymorph $C222_1$ was once proposed as the most thermodynamically favorable for $MgCO_3$ above ~102 GPa (Panero and Kabbes, 2008), but it was dismissed later. By calculations, Pickard and Needs (2015) suggested a new phase of P-1 to be the best candidate at pressures of 85–101 GPa in a limited temperature regime that is slightly lower than the coldest subduction geotherm. That is the reason why in most attempts we observed $MgCO_3$ directly transformed to $MgCO_3$-II (Boulard et al., 2011; Maeda et al., 2017; Martirosyan et al., 2018). The stability of $C2/m$ was also confirmed in Fe^{2+}-rich $MgCO_3$ (Ferromagnesite-II) above 80 GPa between 1850 and 2500 K. Ferromagnesite-II hasd a higher density and was temperature quenchable. Especially it could accommodate a considerable amount of Fe^{3+} (magnetite Fe_4O_3 and/or a new phase of $Fe_4(CO_4)_3$) that resulted from self-redox reaction between Fe^{2+} and $[CO_3]^{2-}$ (Boulard et al., 2011, 2012, 2015; Chen et al., 2018). Special attention has been paid on spin transition of Fe^{2+} that drives a prior-transformation of ferromagnesite from R-3c to $Pmm2$ at ~50 GPa and 1400 K (Liu et al., 2015), along with an abrupt volume collapse. The phase boundary of ferromagnesite from high spin to low spin state was tightly constrained around 60 GPa for temperatures above ~1000 K (Liu et al., 2015). There might be a positive correlation between the Fe^{2+}-content and the spin transition pressure (Spivak et al., 2014). Or there is just a negligible compositional effect due to the long Fe^{2+}-Fe^{2+} distances in the structure separated by $[CO_3]^{2-}$ species (Lin et al., 2012; Hsu and Huang, 2016; Weis et al., 2017). Some doubts remain regarding the presence of intermediate-spin state (Hsu and Huang, 2016; Weis et al., 2017).

$MgCO_3$ melt congruently at temperatures above the Mantle Geotherm (Litvin et al., 2014; Solopova et al., 2015). An increasing separation in melting points between $CaCO_3$ and $MgCO_3$ with pressure was expected to partially account for the majority of carboantitic melt found on the Earth's surface being highly calcic (Hammouda et al., 2015; Li et al., 2017). $MgCO_3$ decomposed to oxides and diamond above ~3000 K (Spivak et al., 2013; Litvin et al., 2014; Solopova et al., 2015), and the energy cost for $CaCO_3$ is much higher (Santos et al., 2019). Melting curve of ferromagnesite deviated seriously from that of pure $MgCO_3$. Similar to $FeCO_3$, melting loop of ferromagnesite was asymmetrical and had a thermal minimum for Fe^{2+}-rich compositions (Tao et al., 2014; Kang et al., 2015). At mantle conditions, ferromagnesite was energetically advantageous over decomposition (Boulard et al., 2011; 2012), which generated magnetite-magnesioferrite solid solution, graphite and CO_2 (Kang et al., 2016). So melting and decomposition of $CaCO_3$-$MgCO_3$ series bounded the phase fields of these carbonates, and that cast doubts on releasing free CO_2 in the deep Earth.

The elastic behaviors of $MgCO_3$ associate closely to its structural chemistry, which besides, helps to locate the presence of subducted carbonates in the mantle. At mantle pressures, the shear wave velocities in $MgCO_3$ were smaller than those in silicates. Marcondes et al. (2016) thus associated the low-velocity zones near the bottom of the lower mantle with the presence of $MgCO_3$. In the light of the density reduction, Litasov et al. (2008) announced that $MgCO_3$ had a limited effect on seismic profiles of principle assemblages in the mantle, but Yang et al. (2014)proposed to detect its presence by regionally seismic anisotropies because of its unusual high compressional (V_P) and shear (V_S) anisotropies. Existence of minor Fe^{2+} as well as the spin transition opened a new window on the elastic properties of ferromagnesite (Fu et al., 2017; Stekiel et al., 2017). For high spin state, the sound velocities decreased with Fe^{2+}-content, whereas the anisotropy of the sound velocities increased. Upon pressure, anisotropies of V_P and V_S increased until spin transition occurred and decreased afterwards. So a drastic softening of sound velocities across spin transition may occur in slabs enriched with ferromagnesite in the mid-lower mantle. Increases of both V_P and V_S velocities were observed after spin transition. Enrichment of Fe^{2+} led to larger differences in sound velocities and velocity anisotropies for low spin state as well. In this regard, Fe^{2+}-rich $MgCO_3$ regions may show higher seismic contrast compared with principle minerals in the deep mantle.

To sum up (**Figure 1**), along subduction geotherms $MgCO_3$ maintains initial R-3c structure up to ~80 GPa and hereafter converts to $C2/m$, with sp^2-sp^3 transition further upholding the phase in the lowermost mantle. Ferromagnesite undergoes spin transition in the mid-mantle and changes to $Pmm2$-structure subsequently. The drop in the unit-cell and the accordingly uprush of the density expand the stability field of ferromagnesite to higher pressures, yet disproportionation of Fe^{2+} could highly disintegrate the structure at lower-mantle conditions. Temperature exerts a greater impact on phase relations of ferromagnesite relative to $MgCO_3$. Neither melting nor decomposition occurs in $MgCO_3$ or ferromagnesite over the entire mantle.

Dolomite (Ca,Mg)CO_3 and Ankerite

Dolomite-(Ca,Mg)CO_3 is a common carbonate mineral in marine sediments, carbonated eclogite and ophiolite (Tao et al., 2020; Shatskiy et al., 2021). At the topmost of the upper mantle, dolomite broke down into a mixture of magnesite-$MgCO_3$ and aragonite-$CaCO_3$, the field of the coexistence opening towards higher temperature with pressure (Tao et al., 2014). A monoclinic phase (dolomite-II) set in driven by rotation of $[CO_3]^{2-}$ groups at 14–20 GPa under ambient temperature (Santillán et al., 2003; Merlini et al., 2019; Stekiel et al., 2019). This new phase was expected to enhance the thermodynamic stability of (Ca,Mg)CO_3 up to 40 GPa over $MgCO_3$+$CaCO_3$. Above 41 GPa, a triclinic structure (dolomite-III, Z = 8) formed (Merlini et al., 2019).

Naturally Fe^{2+} substitutes Mg^{2+} in dolomite with various contents. Incorporation of Fe^{2+} strongly decreased the order degree of the structure (Tao et al., 2014) and helprf maintain its stability to higher pressures and temperatures (Stekiel et al., 2019). A trigonal → orthorhombic transformation was firstly observed in $(Ca,Mg)_{1.9}Fe_{0.1}(CO_3)_2$ at ~17 GPa and 300 K (Mao et al., 2011). This new orthorhombic phase persisted in upon laser-heating to ~1600–1700 K at 27–31 GPa. At 36–83 GPa, it further transformed to a monoclinic structure. The pressure-induced spin transition of Fe^{2+} was manifested by a drop in the unit-cell volume at ~47 GPa. This observation, however, was not reproduced in Fe-richer counterparts. A similar experimental study on a Fe^{2+}-richer crystal $CaMg_{0.6}Fe_{0.4}(CO_3)_2$, suggested formation of two triclinic structures under pressures (Merlini et al., 2012). One was Fe-dolomite-II (*P*-1; Z = 4), a distortion of the dolomite structure associated by rotation of $[CO_3]^{2-}$ groups, existing between 17 and 35 GPa. The coordination number of Ca^{2+} increased from six in Fe-dolomite to eight in Fe-dolomite-II. The other was Fe-dolomite-III that adopted the same *P*-1 symmetry but had eight formula units in the primitive cell. It exhibited structural relations to $CaCO_3$-III, as the $[CO_3]^{2-}$ units are non-planar with carbon partly in four-fold coordination, some of which edge-shared with Ca^{2+} and Fe^{2+} polyhedra. Fe-dolomite-III had a broad stability domain to 43 GPa and the melting point (~2600 K). Its density was demonstrably comparable to that of the mixture $MgCO_3$+$CaCO_3$ if taking into account the $FeCO_3$ component. The second-order transformation from Fe-dolomite to Fe-dolomite-II was similar to that of dolomite → dolomite-II, and it had been strongly confirmed by Merlini et al. (2019). But above 36 GPa, Merlini et al. (2019) suggested a first-order transition to a rhombohedral symmetry (*R*3) (Fe-dolomite-IIIb). In the pressure range of 70–120 GPa and at 2500 K, Fe-dolomite-IV with an orthorhombic symmetry (*Pnma*) formed. It was charactered with corner-sharing $[CO_4]^{4-}$ units in three-fold rings, similar to $MgCO_3$-*C*2/*m* (Oganov et al., 2008). Different Fe^{2+} contents could be responsible for the disagreement. Previously, Solomatova and Asimow (2016) predicted a monoclinic phase *C*2/*c*as the stable structure for more Fe^{2+}-enriched samples $Ca(Mg_{0.5},Fe_{0.5})(CO_3)_2$ and $CaFe(CO_3)_2$ up to 60 GPa. The *C*2/*c* phase cannot be achieved experimentally due to the large energy barrier and the correspondingly large volume collapse, resulting in conversion from dolomite to metastable structures.

Existing data has revealed the high-pressure behaviors of dolomite, as is summarized in **Figure 1**, but it is limited to draw a full understanding of the structural evolution of Fe-dolomite at pressures and temperatures. Issues deserve evaluation with respect to the effect of Fe^{2+}-content and its spin transition on the thermal and elastic properties and the stability fields (Tao et al., 2014; Merlini et al., 2016), and possibility of energetically competitive structures. Besides, there remains a large area uncovered for pressures above ~60 GPa. We now reach agreements on *1*) a minor addition of Fe^{2+} stabilizes the rhombohedral structure of dolomite against decomposition and transformation under upper mantle conditions; *2*) there stands a good chance for fine changes occurring at ~17 and ~35 GPa, and a decrease trend of crystal symmetry is expected with pressure.

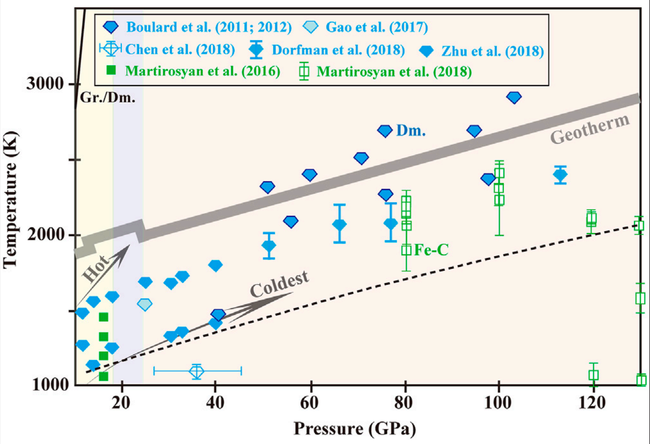

FIGURE 2 | Experimental pressure-temperature conditions and run products of carbonates-Fe^0 system. Blue diamond and green square represent formation of diamond (Dm.) and iron carbide (Fe-C), respectively, with uncertainties estimated for conditions marked. Diamond formation is always along with graphite generation. The dashed black curve is extrapolated from Zhu et al. (2018) for indicating the onset boundary of $MgCO_3$-Fe^0 interaction.

CARBONATES REDUCTION BY REDUCED MANTLE

Given most subduction geotherms, $CaCO_3$, $MgCO_3$, (Ca,Mg)CO_3 and their ferrous series maintain solid polymorphs over a wide range of depths down to the CMB. But their presence in the mantle depends highly as well on oxygen fugacity, which is controlled by oxidation state of iron in minerals and melts (e.g. sulfides and silicates) (Bataleva et al., 2017). A large part of the mantle below 250 km is thought to be Fe^0-sufficient and favorable for reductions of carbonates or carbonatitic melts, which is a potential barrier to carbonates further-subduction and a promising mechanism for sublithospheric diamond formation (Rohrbach and Schmidt, 2011; Stagno et al., 2011). Several carbon species uncovered from the lower-mantle diamonds, vary from oxidized phases (e.g. carbonates) to the reduced (e.g. methane, graphite and iron carbide) (Brenker et al., 2007; Kaminsky and Wirth, 2011; Kaminsky, 2012; Kaminsky et al., 2013, 2016; Smith et al., 2016). That strongly indicates that the redox reactions between subducted carbonates (oxidized) and metallic mantle (reduced) is responsible for sublithospheric diamond genesis (**Figure 2**).

Several studies have been conducted in petrologic context of subducted carbonate assemblages in contact with metallic mantle. One representative study (Palyanov et al., 2013) at 6.5–7.5 GPa and 1273–1873 K documented that $(Mg_{0.9}Ca_{0.1})CO_3$-Fe^0 interaction generated carbonatitic melts, magnesiowustite

(Mg,Fe)O, cohenite Fe_3C and metastable graphite. Increasing temperature led to a higher degree of partial melting but a decrease in Ca^{2+}-component in carbonate melt. Diamonds nucleation from carbonatitic melts (≥1673 K) was expected with heavier carbon isotope relative to the initial carbonate and high concentrations of nitrogen (1000–1500 ppm). In contrast, at iron front where carbide (Fe-C) melt formed, diamond crystallized with lower $\delta^{13}C$ value and only 100–200 ppm of nitrogen mostly in the form of single substitutional aggregation. These chemical characters are analogous to that of natural sublithospheric diamonds. Besides, the accompanying products, iron carbide, graphite and (Mg,Fe)O are characteristic inclusions in natural stones. For simplicity, at the topmost of the upper mantle, $MgCO_3$ reduction by Fe^0 is described as:

$$MgCO_3\,(\text{magnesite}) + Fe^0\,(\text{metal}) \rightarrow (Mg,Fe)O + Fe_3C + C\,(\text{diamond}) \tag{R3 – 1}$$

Thermodynamic calculations showed that over the entire mantle pressure range, C+(Mg,Fe)O is more stable than $MgCO_3$+Fe-C. Thus, presence of residual carbides in the run products is due to incomplete reaction. A similar experimental work (Martirosyan et al., 2015) later reproduced this observation but for only formation of graphite rather than diamond. That can be accounted for by kinetic impeding for graphite-to-diamond conversion. Increase of temperature and addition of catalysts are two effective methods for diamond formation (Tomlinson et al., 2011; Palyanov et al., 2013).

At higher pressure-temperature conditions, the onset boundary of $MgCO_3$-Fe^0 interaction was defined linearly crossing 1100 K at ~14 GPa and 1375 K at ~40 GPa. The onset of the reaction and diamond nucleation seemed to have nothing to do with partial melting of Fe-C, whichrequired much higher temperatures (Morard et al., 2017). Crystallization of diamond slowed down drastically in 14–18 GPa, corresponding to the mantle depths of 410–525 km (Zhu et al., 2018). That implied a high-pressure kinetic for the reaction and accordingly, a huge reduction in diamond production at the transition zone. The mechanism of the high-pressure kinetic was unknown but it provided a plausible explanation for the abundance of sublithospheric diamond at 250–450 km in contrast to the rarity below. In a broader pressure-temperature range of 70–150 GPa and 1500–2600 K, $MgCO_3$-Fe^0 interaction was exemplified by (Martirosyan et al., 2018):

$$MgCO_3\,(\text{magnesite}) + Fe\,(\text{metal}) \rightarrow FeO + (Mg,Fe)O + Fe_7C_3 + C\,(\text{diamond}) \tag{R3 – 2}$$

Transformation from $MgCO_3$-R-$3c$ to $C2/m$ around 80 GPa exerted little effect on the reaction path. Diamonds nucleated and grew directly from carbonates at subsolidus conditions. Coexistence of FeO+(Mg,Fe)O in the run products suggested an immiscibility gap in MgO-FeO system (Dorfman et al., 2018; Martirosyan et al., 2018). Naturally for worldwide sublithospheric diamonds, (Mg,Fe)O solid solution is the dominant (50–56%) lower-mantle inclusions which presents a broad range in magnesium index ($Mg\# = Mg/(Mg+Fe)_{at.}$, 0.36–0.90). Brazil, the most productive for population of transition zone and lower mantle diamonds, however, possesses (Mg,Fe)O of severely Fe^{2+}-rich, up to $Mg\# = 0.36$ (Kaminsky, 2012). An origin from the D″ layer was proposed as a mechanism to explain this discrepancy (Kaminsky and Wirth, 2011), but it seemed at odds with the immiscibility gap in MgO-FeO system. Factors such as temperature (Palyanov et al., 2013) and oxygen fugacity (Martirosyan et al., 2015) may be more possible to account for the variations of (Mg,Fe)O composition.

In comparison with $MgCO_3$, $CaCO_3$ reacting with Fe^0 proceeded much slower. For $CaCO_3$-Fe^0 coupling in closed systems, Ca-wüstites were identified after reactions at 3–5.5 GPa and 1573–1673 K (5–48 h) with solid carbon in the form of graphite (Chepurov et al., 2011). Similarly for deeper subduction geotherms, interaction of $CaCO_3$-Fe^0 system at 4–16 GPa and 923–1673 K was established as (Martirosyan et al., 2016):

$$CaCO_3\,(\text{aragonite}) + Fe^0\,(\text{metal}) \rightarrow Fe_7C_3 + CaFe_2O_3\,(\text{Ca} - \text{wűstite}) \tag{R3 – 3}$$

The sluggish kinetics of established $CaCO_3$-Fe^0 interaction suggested that significant amount of carbonates could survive and sink to the transition zone (Martirosyan et al., a 2016). At 6 GPa and 1273–1473 K, redox reaction between $CaCO_3$+$MgCO_3$ mixture and metallic iron resulted in formation of Ca-(Mg,Fe)O and Fe_3C (Martirosyan et al., 2015). But under higher pressure-temperature conditions of 51–113 GPa and 1800–2500 K, the $CaCO_3$ component in $(Mg_{0.38}Ca_{0.59}Fe_{0.03})CO_3$ seemed unresponsive in the reactions but remained in the phase of post-aragonite (Dorfman et al., 2018). Model of carbonates-Fe^0 interaction was applicable to Fe^{2+}-carbonates self-reduction, where Fe^{2+} disproportionated and reacted with C^{4+} to form diamond and Fe^{3+}-oxides at lower mantle pressures (*see* **Section 2.2**; Boulard et al., 2011; 2012; 2015; Chen et al., 2018). But diamonds nucleated from Fe^{2+}-carbonates self-reduction were too tiny to be analyzed.

For all the carbon-phases during carbonates-Fe^0 interaction, a closer look leads us to check the behaviors of iron carbide (e.g. cohenite Fe_3C, Fe_7C_3). Iron carbide has been discovered as inclusions in sublithospheric diamonds (Kaminsky and Wirth, 2011) and silicates which are believed to originate at various depths spanning from the upper mantle to possibly the CMB. That indicates an active participation of iron carbide in deep carbon cycle. Iron carbides could form by solid-solid reaction in portions of the Earth's interior where metallic iron and elemental carbon or carbonateare in mutual contact (Palyanov et al., 2013). It dissolves carbon with bulk content as high as ~300 ppm, and maintains stable in the reduced mantle environments with oxygen fugacity values close to or below IW buffer equilibrium. Besides, multiple lines of evidence suggest a mantle with sulfide-rich metallic melt (Stachel and Harris, 2008; Zhang Z. et al., 2018). Owing to strong non-ideal mixing between carbon and sulfur in Fe-bearing alloy, the presence of sulfur significantly lower the solubility of carbon and trigger carbon exsolution from the carbide (Zhang Z. et al., 2018). The discovery of a carbide+sulfide+metal assemblage in sublithospheric diamonds shed lights on mechanism of diamond formation from Fe-C-S melt (Smith et al., 2016). Here we evaluate the phase relations of Fe-C-S systems in the mantle focusing on exsolution of diamond. Chemical reactions involving:

$$2Fe_3C + 3S_2 \rightarrow 6FeS + 2C^0 \qquad (R3-4)$$

$$Fe_3C + 3FeS_2 \rightarrow 6FeS + C^0 \qquad (R3-5)$$

Most studies on Fe-C-S systems were performed at pressures ≤8 GPa (Bataleva et al., 2017). These studies reported efficient capabilities of Fe_3C to generate graphite (1473–1873 K), diamond (1573–1873 K) and pyrrhotite (FeS) in the presence of sulfur-bearing metasomatic agents; further temperature increase led to higher efficiency of diamond crystallization. The established Fe-C-S model was applicable to Fe-Ni-C-S system, where Fe-Ni alloy showed a greater accommodation of dissolved carbon with temperature up to 2600 K but at lower pressures (≤20 GPa) (Narygina et al., 2011).

Redox reactions between subducted carbonates and Fe^{2+}-peridotites/eclogites can be taken as a simplified model of slab-mantle interactions processing in the deep zones. It was mainly controlled by low concentrations of carbonates and metallic iron at the CMB as well as low diffusion of chemical components (e.g. O^{2-}, Fe^{2+}) among silicates and carbonates. This is a limited process and set constraints for carbon speciation and protections for carbonates from reduction (**Figure 2**). Likely that a significant amount of (Ca,Mg,Fe)-carbonates may survive from Fe^0-saturation boundary (Martirosyan et al., a 2016) at the upper mantle and the transition zone. But at the top of the lower mantle due to stagnation of subducting slabs, carbonates accumulate and are heated up. Carbonates-Fe^0 interaction would be more probable for diamond production. The rate of graphite-to-diamond transformation was higher in a FeNi system. Higher pressure appeared to favor growth of cubo-octahedral diamonds, whereas octahedral diamonds grow at lower pressure conditions (≤10 GPa in $MgCO_3$ and ≤15 GPa in FeNi). The run products lacked the slip planes and lamination lines commonly associated with superdeep diamonds, and we may suggest that these deformation features are due to transport instead of growth conditions (Tomlinson et al., 2011). Accompanying with carbon freezing in the Earth, carbon isotope fractionation occurs. The carbon isotope composition in the mantle displays a well-defined peak around $\delta^{13}C = -5‰$ in an extensive range to the lowest of ~−40‰. Subduction of organic carbon was advocated for the mantle regions with ^{13}C depletion. Relatively, reduction of carbonates extracted ^{12}C to a greater degree and it was more likely to contribute to the broad distribution of carbon in the mantle (Horita and Polyakov, 2015).

CARBONATES DECARBONIZATION BY SILICATES

In consideration of major minerals in basaltic plates and the mantle, carbonate stability should also be inspected by carbonates-silicates interactions under mantle conditions. This reaction sets fundamental control not merely on subduction limit of carbonate or CO_2 release in the mantle, but on physicochemical properties of the mantle such as initiation of melting by lowering the mantle solidus, generation of alkalic magma in oceanic islands and carbonate metasomatism in cratonic mantle. Two typical chemical reactions are appraised here:

$$CaCO_3 + SiO_2 \rightarrow CaSiO_3 + CO_2 \qquad (R4-1)$$

$$MgCO_3 + SiO_2 \rightarrow MgSiO_3 + CO_2 \qquad (R4-2)$$

SiO_2 is one of the abundant components in MORB. Along subduction geotherms, SiO_2 changes to its high-pressure polymorphs as coesite, stishovite, $CaCl_2$-type and seifertite successively (Murakami et al., 2003; Grocholski et al., 2013). According to experimental and theoretical results, even for the temperature profiles in cold subduction slabs, $CaCO_3$-VII reacted with SiO_2-stishovite above 23 GPa and 1500 K to produce $CaSiO_3$-perovskite and possibly free CO_2. High temperature greatly increased the tendency of partitioning Ca^{2+} from carbonates $CaCO_3$ to silicates $CaSiO_3$ (Zhang ZG. et al., 2018; Li et al., 2018), accounting for the observation of abundance of $CaSiO_3$-perovskite in sublithospheric diamonds compared to typical mantle mineralogy. Decarbonation of $MgCO_3$ by SiO_2-coesite was confirmed beginning at 6–7 GPa and above 1600 K, and the decarbonatation temperature increased sharply with pressure (Palyanov et al., 2002; Kakizawa et al., 2015). An addition of alkali-component to $MgCO_3$-SiO_2 system negligibly changed the reaction path, and the output diamond was close to the initial $MgCO_3$ in terms of carbon isotopic composition (Palyanov et al., 2002). At 28–62 GPa and 1490–2000 K (770–1500 km), $MgSiO_3$-perovskite and solid CO_2 (V or VI) formed from interactions between $MgCO_3$ and SiO_2-stishovite (Takafuji et al., 2006). With this regard, both $CaCO_3$ and $MgCO_3$ was unstable and would release CO_2 to the lower mantle for SiO_2-rich subducted basalts.

Calculations carried out at higher pressures of 50–200 GPa under static conditions (0 K) showed that $CaCO_3$ (post-aragonite) and $MgCO_3$ ($R\text{-}3c$) maintained stable but react with SiO_2 at closely the CMB (Oganov et al., 2008; Pickard and Needs, 2015; Santos et al., 2019). This was contradictory to the experimental observations (Maeda et al., 2017) where the reaction of $MgCO_3$-SiO_2 occurred at mantle depth beginning from ~1000 km and that held true for all the mantle regions below. Different results could be due to different conditions in these studies. $MgCO_3$-$R\text{-}3c$ reacted with SiO_2-stishovite for formation of $MgSiO_3$-bridgmanite and CO_2-VI (six-fold coordinated of carbon) at depths around 1700 km (83 GPa; 1780 K). Internal production of CO_2 from $MgCO_3$-SiO_2 system was thus, possible in the middle of the lower mantle (1700–1900 km) and at greater depths CO_2-VI would decompose

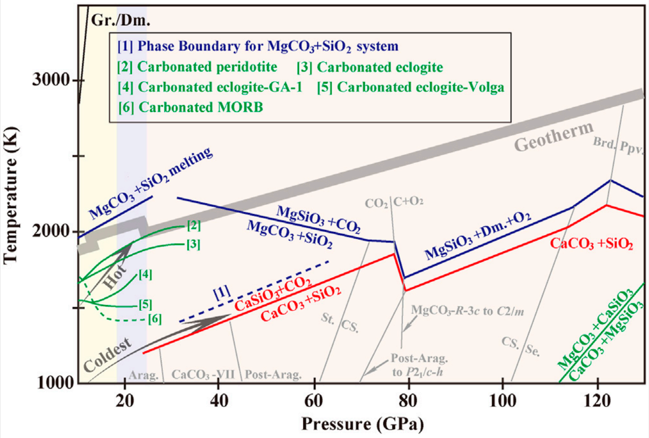

FIGURE 3 | Schematic reaction line of carbonate-silicate at the Earth's mantle conditions. The black lines representing $CaCO_3$-SiO_2 reaction is measured according to Li et al. (2018) and Zhang and Liu (2015). The dark-blue lines indicate phase boundaries for $MgCO_3$-SiO_2 system (solid: Maeda et al., 2017; dotted [1]: Takafuji et al., 2006). Partial melting of $MgCO_3$-SiO_2 series produces a simple eutectic system (Kakizawa et al., 2015). Curve [2] represents solidus curve of carbonated peridotite (Litasov and Ohtani, 2009). Solidus curves of carbonated eclogites are plotted according to Litasov and Ohtani (2010) (Curve [3]) and Kiseeva et al. (2013) (Curve [4], [5]). The melting curve of carbonated MORB (Curve [6]) according to Thomson et al. (2016). Phase diagram for the stability of $MgCO_3$+$CaSiO_3$ versus $CaCO_3$+$MgSiO_3$ is referred to Santos et al. (2019). Phase boundaries of $CaCO_3$- and $MgCO_3$-polymorphs follow the references in **Section 2.1**. The phase diagrams of SiO_2 (Murakami et al., 2003; Grocholski et al., 2013), CO_2 (Litasov et al., 2011) and $MgSiO_3$ (Komabayashi et al., 2008) are included with gray solid lines. Abbreviations: Gr., graphite; Dm., diamond; St., stishovite; CS., $CaCl_2$-type SiO_2; Se., seifertite; Brd., $MgSiO_3$ bridgmanite; Ppv., $MgSiO_3$ post-perovskite.

to diamond. If survived, $MgCO_3$-*R*-3*c* changed to *C*2/*m* and reacted with SiO_2-seifertite to generate $MgSiO_3$-post-perovskite and diamond at the lowermost mantle.

Figure 3 summarizes the phase relations of carbonate-silicate system at mantle conditions. The solidus of the carbonated MORB intersected most subduction geotherms at mantle depths of 300–700 km, creating a focused region of melt at the top of the transition zone and producing a barrier to carbonate recycling into the deep mantle (Thomson et al., 2016). But in super-cold slabs, carbonated MORB would survive from the melting process and sink further. Carbonation reactions involving olivine or pyroxene tended to react with CO_2 to form carbonate without dissociation into a CO_2-bearing assemblage, so present-day subduction of oceanic crust likely introduced carbon into the mantle in the form of carbonated eclogite. Phase relations of CaO-MgO-Al_2O_3-SiO_2-CO_2 system exhibited a substantial increase in $MgCO_3$ component in melt compositions from lower pressures (12–16 GPa) to the higher (20–25 GPa). That may be due to $CaSiO_3$-perovskite formation at 20 GPa but $MgSiO_3$-perovskite required higher pressures (Keshav and Gudfinnsson, 2010). For carbonates with high bulk alkali contents, the alkali-rich carbonates tended to form a solid solution with Ca^{2+} but left Mg^{2+} incorporating into majorite. What is striking was that most carbon in SiO_2-rich melts partitioned into alkali-rich aragonite and diamond, whereas little diamond formed in SiO_2-deficient melts. It may be accounted for by more progressive Fe^{2+}-Fe^{3+} transformation with pressure in SiO_2-rich melts (Kiseeva et al., 2013). Along subduction geotherms from the upper mantle to the transition zone, carbon-phases in alkali-rich carbonated eclogites evolve following the route of "$MgCO_3$+$CaCO_3$ (aragonite) or $MgCO_3$-$CaCO_3$ (calcite) solid solution → $MgCO_3$+alkali-rich $CaCO_3$ (aragonite) → alkali-rich $CaCO_3$ (aragonite) → graphite and diamond."

$$CaCO_3 + MgO \rightarrow CaO + MgCO_3 \qquad (R4-3)$$

$$CaCO_3 + MgSiO_3 \rightarrow CaSiO_3 + MgCO_3 \qquad (R4-4)$$

Calculations indicated that the reaction R4-3 was energetically unfavorable over the entire mantle. That is, $CaCO_3$ is stable under thermodynamic conditions if there is MgO in excess as expected in a pyrolitic mantle (Oganov et al., 2008; Pickard and Needs, 2015; Santos et al., 2019). For the conditions of $MgSiO_3$ in excess (R4-4), which was the main mineral in the lower mantle, $CaCO_3$ would be consumed and the $MgCO_3$+$CaSiO_3$ association was more favorable to the mid-mantle, hereafter $CaCO_3$ became restabilized over $MgCO_3$ (Oganov et al., 2008; Pickard and Needs, 2015; Zhang ZG. et al., 2018; Santos et al., 2019). The higher densities of the $CaCO_3$-polymorphs relative to the $MgCO_3$-polymorphs could be responsible for the free energy change of the reaction. However, temperature and chemical potentials need to be taken into account further as they can shift the phase relations conceivably. Santos et al. (2019) believed that an increase in temperature increased the pressure at which the reaction becomes unfavorable. That is, $MgCO_3$ was the main host of oxidized carbon over almost the mantle. But for super-cold subduction geotherms, $CaCO_3$ was more stable than $MgCO_3$.

As is highlighted in **Figure 3**, during deep-subduction processes, $MgCO_3$ exhibits much higher stability relative to $CaCO_3$ in consideration of existence of subducted SiO_2 and $MgSiO_3$ in a pyrolitic mantle model. Only for locally regions where MgO is in excess, $CaCO_3$ could be preserved to the CMB. Carbonatitic melts reacting with SiO_2 would release CO_2 (solid) into the lower mantle, which will eventually decompose to diamond.

CONCLUSIONS AND PROSPECTS

Carbonates play a key role in the recycling of carbon from the Earth's crust to the interior *via* subduction processes, producing one of the carbon budgets in the entire Earth's system. In light of the striking discoveries above, we now have a much clearer picture of behaviors of carbonates in the deep Earth.

First, several new polymorphs have been identified as stable of $CaCO_3$, $MgCO_3$ and (Ca,Mg)CO_3 and their ferrous series (**Figure 1**), which improve our expectations for their possibilities in the mantle. Existence of carbonates and the occurrence of the phase transitions may correlate with the discontinuities in the Earth's seismic profile. Carbonates of $CaCO_3$-$MgCO_3$-$FeCO_3$ series remain in solid phases along most modern subduction geotherms. So liberation of carbonatitic melts or CO_2 owing to carbonate decomposition seems unlikely, with such possibility restricted merely for conditions in hot zones. However, decarbonization of $CaCO_3$ and $MgCO_3$ takes place in SiO_2-rich subducted basalts under the lower-mantle conditions (**Figure 3**). CO_2 decomposing to diamond is energetically favored in the region from the middle of the lower mantle to the CMB. Meanwhile, carbonates in slabs tend to be reduced to diamond at metal-saturation boundary at the topmost of the lower mantle (**Figure 2**). Diamonds produced from slab-mantle interactions are similar to natural stones in terms of chemical composition and inclusion characteristics. So far the existing data have covered almost the entire mantle conditions for decarbonization and reduction of carbonates and documented diamond nucleation. In this regard, carbonates reduction and decarbonization are effective mechanisms of carbon sequestration at the top-mid region of the lower mantle.

Researches on carbon cycle throughout the Earth's system have long represented an interesting frontier. One fundamental goal of carbon cycle research is to know the balance between income and outcome global carbon fluxes as well as the carbon fluxes change in space and time. But many details of the processes remain unclear for the lack of intensive monitoring. Three issues may be worth of particular considerations in the future work:

(1) Besides carbonates, CO_2 and iron carbides mentioned above, there could exist other chemical forms of carbon in the mantle that has been uncovered, for example, a new carbon phase of $Fe_4(CO_4)_3$ derived from decomposition of Fe-bearing carbonates (Boulard et al., 2015). So a critical and pressing task is to search for these undiscovered carbon. Given the scarcity of natural samples, we may gain insights by thermodynamic calculations and experiments. These efforts will shed new lights on our view on deep carbon reservoirs, for example, how they form and under what conditions are they stable for long.

(2) Existing experiments have confirmed the possibility of redox reactions between subducted carbonates and metallic mantle to produce sublithospheric diamonds and other reduced carbon species. However, it is not yet clear whether carbonates-Fe^0 processes generate significant amounts of diamonds. To what extent do carbonates turn into diamonds? And what role has the remaining carbonatitic melts played in deep carbon cycle and besides, in mantle metasomatism. These questions are basically related to the kinetics of carbonates-Fe^0 interactions that set constraints on sequestration efficiency directly of deep carbon. Besides, carbon isotope fractionation during slab-mantle interactions is also an essential part in the study of deep carbon cycle. However, previous insights have been gained from theoretical calculations (Horita and Polyakov, 2015), as natural samples are too scarce. Experiments conducted at high-pressure and high-temperature conditions may be a favor to synthesize large samples.

(3) Now we have a better knowledge of carbon recycle in the carbonated MORB during deep subduction processes. Yet there is an increasing recognition that continental crust carrying sedimentary carbonate rocks can subduct to the upper mantle (Zhu et al., 2009). With depth, a certain amount of CO_2 is released from carbonatitic components *via* progressive metamorphism. Moreover, higher metamorphic temperatures enhance the activity of fluids in subduction zones, which significantly promotes decarbonization of carbonates (Zhang ZG. et al., 2018; Li et al., 2018). We believe that such reactions are a widespread process and exert an assignable effect upon carbon flux between the Earth's surface and the interior. So equally important are efforts to be made on processes and rates by which carbon cycle in continental subduction zones.

AUTHOR CONTRIBUTIONS

JG wrote the original draft. XW, XY, and WS were responsible for the review and modification.

ACKNOWLEDGMENTS

The authors are thankful to the reviewers.

REFERENCES

Antao, S. M., and Hassan, I. (2009). The Orthorhombic Structure of CaCO3, SrCO3, PbCO3 and BaCO3: Linear Structural Trends. *Can. Mineral.* 47 (5), 1245–1255. doi:10.3749/canmin.47.5.1245

Bataleva, Y. V., Palyanov, Y. N., Borzdov, Y. M., Bayukov, O. A., and Zdrokov, E. V. (2017). Iron Carbide as a Source of Carbon for Graphite and Diamond Formation Under Lithospheric Mantle P-T Parameters. *Lithos* 286-287, 151–161. doi:10.1016/j.lithos.2017.06.010

Bayarjargal, L., Fruhner, C.-J., Schrodt, N., and Winkler, B. (2018). CaCO3 Phase Diagram Studied with Raman Spectroscopy at Pressures up to 50 GPa and High Temperatures and DFT Modeling. *Phys. Earth Planet. Interiors* 281, 31–45. doi:10.1016/j.pepi.2018.05.002

Bayarjargal, L., Shumilova, T. G., Friedrich, A., and Winkler, B. (2010). Diamond Formation from CaCO3 at High Pressure and Temperature. *ejm* 22, 29–34. doi:10.1127/0935-1221/2010/0021-1986

Boulard, E., Menguy, N., Auzende, A. L., Benzerara, K., Bureau, H., Antonangeli, D., et al. (2012). Experimental Investigation of the Stability of Fe-Rich Carbonates in the Lower Mantle. *J. Geophys. Res.* 117, B02208. doi:10.1029/2011jb008733

Boulard, E., Gloter, A., Corgne, A., Antonangeli, D., Auzende, A.-L., Perrillat, J.-P., et al. (2011). New Host for Carbon in the Deep Earth. *Proc. Natl. Acad. Sci.* 108 (13), 5184–5187. doi:10.1073/pnas.1016934108

Boulard, E., Pan, D., Galli, G., Liu, Z., and Mao, W. L. (2015). Tetrahedrally Coordinated Carbonates in Earth's Lower Mantle. *Nat. Commun.* 6, 6311. doi:10.1038/ncomms7311

Brenker, F. E., Vollmer, C., Vincze, L., Vekemans, B., Szymanski, A., Janssens, K., et al. (2007). Carbonates from the Lower Part of Transition Zone or Even the Lower Mantle. *Earth Planet. Sci. Lett.* 260, 1–9. doi:10.1016/j.epsl.2007.02.038

Bundy, F. P., Bassett, W. A., Weathers, M. S., Hemley, R. J., Mao, H. U., and Goncharov, A. F. (1996). The Pressure-Temperature Phase and Transformation Diagram for Carbon; Updated Through 1994. *Carbon* 34, 141–153. doi:10.1016/0008-6223(96)00170-4

Chen, M., Shu, J., Xie, X., Tan, D., and Mao, H.-k. (2018). Natural Diamond Formation by Self-Redox of Ferromagnesian Carbonate. *Proc. Natl. Acad. Sci. USA* 115 (11), 2676–2680. doi:10.1073/pnas.1720619115

Chepurov, A. I., Sonin, V. M., Zhimulev, E. I., Chepurov, A. A., and Tomilenko, A. A. (2011). On the Formation of 621 Element Carbon During Decomposition of CaCO3 at High P-T Parameters Under Reducing Conditions. *622 Doklady Earth Sciences* 441 (2), 1738–1741.

Dasgupta, R., and Hirschmann, M. M. (2010). The Deep 623 Carbon Cycle and Melting in Earth's Interior. *Earth Planet. Sci. Lett.* 298, 1–13.

Dorfman, S. M., Badro, J., Nabiei, F., Prakapenka, V. B., Cantoni, M., and Gillet, P. (2018). Carbonate Stability in the Reduced Lower Mantle. *Earth Planet. Sci. Lett.* 489, 84–91. doi:10.1016/j.epsl.2018.02.035

Farsang, S., Louvel, M., Zhao, C. S., Mezouar, M., Rosa, A. D., Widmer, R. N., et al. (2021). Deep Carbon Cycle Constrained by Carbonate Solubility. *Nature Communications* 12, 4311.

Frost, D. J., Liebske, C., Langenhorst, F., McCammon, C. A., Trønnes, R. G., and Rubie, D. C. (2004). Experimental Evidence for the Existence of Iron-Rich Metal in the Earth's Lower Mantle. *Nature* 428, 409–412. doi:10.1038/nature02413

Fu, S., Yang, J., and Lin, J. F. (2017). Abnormal Elasticity of Single-Crystal Magnesiosiderite Across the Spin Transition in Earth's Lower Mantle. *Phys. Rev. Lett.* 118, 036402. doi:10.1103/PhysRevLett.118.036402

Gavryushkin, P. N., Martirosyan, N. S., Inerbaev, T. M., Popov, Z. I., Rashchenko, S. V., Likhacheva, A. Y., et al. (2017). Aragonite-II and CaCO3-VII: New High-Pressure, High-Temperature Polymorphs of CaCO3. *Cryst. Growth Des.* 17, 6291–6296. doi:10.1021/acs.cgd.7b00977

Ghosh, S., Ohtani, E., Litasov, K. D., and Terasaki, H. (2009). Solidus of Carbonated Peridotite from 10 to 20 GPa and Origin of Magnesiocarbonatite Melt in the Earth's Deep Mantle. *Chem. Geology.* 262, 17–28. doi:10.1016/j.chemgeo.2008.12.030

Gorman, P. J., Kerrick, D. M., and Connolly, J. A. D. (2006). Modeling Open System Metamorphic Decarbonation of Subducting Slabs. *Geochem. Geophys. Geosystems* 7 (4), Q04007. doi:10.1029/2005gc001125

Grocholski, B., Shim, S.-H., and Prakapenka, V. B. (2013). Stability, Metastability, and Elastic Properties of a Dense Silica Polymorph, Seifertite. *J. Geophys. Res. Solid Earth* 118, 4745–4757. doi:10.1002/jgrb.50360

Hammouda, T., Chantel, J., Manthilake, G., Guignard, J., and Crichton, W. (2015). Hot Mantle Geotherms Stabilize Calcic Carbonatite Magmas up to the Surface. *Geology* 42, 911–914. doi:10.1130/G35778.1

Horita, J., and Polyakov, V. B. (2015). Carbon-bearing Iron Phases and the Carbon Isotope Composition of the Deep Earth. *Proc. Natl. Acad. Sci. USA* 112 (1), 31–36. doi:10.1073/pnas.1401782112

Hsu, H., and Huang, S-C. (2016). Spin Crossover and Hyperfine Interactions of Iron in (Mg,Fe)CO_3 Ferromagnesite. *Phys. Rev. B* 94, 060404. doi:10.1103/physrevb.94.060404

Huang, D., Liu, H., Hou, M.-Q., Xie, M.-Y., Lu, Y.-F., Liu, L., et al. (2017). Elastic Properties of CaCO 3 High Pressure Phases from First Principles. *Chin. Phys. B* 26 (8), 089101. doi:10.1088/1674-1056/26/8/089101

Irving, A. J., and Wyllie, P. J. (1975). Subsolidus and Melting Relationships for Calcite, Magnesite and the Join CaCO3-MgCO3 36 Kb. *Geochimica et Cosmochimica Acta* 39 (1), 35–53. doi:10.1016/0016-7037(75)90183-0

Isshiki, M., Irifune, T., Hirose, K., Ono, S., Ohishi, Y., Watanuki, T., et al. (2004). Stability of Magnesite and its High-Pressure Form in the Lowermost Mantle. *Nature* 427, 60–63. doi:10.1038/nature02181

Johnston, F. K. B., Turchyn, A. V., and Edmonds, M. (2011). Decarbonation Efficiency in Subduction Zones: Implications for Warm Cretaceous Climates. *Earth Planet. Sci. Lett.* 303, 143–152. doi:10.1016/j.epsl.2010.12.049

Kakizawa, S., Inoue, T., Suenami, H., and Kikegawa, T. (2015). Decarbonation and Melting in MgCO3-SiO2 System at High Temperature and High Pressure. *J. Mineralogical Petrological Sci.* 110, 179–188. doi:10.2465/jmps.150124

Kaminsky, F. (2012). Mineralogy of the Lower Mantle: A Review of 'super-Deep' mineral Inclusions in Diamond. *Earth-Science Rev.* 110, 127–147. doi:10.1016/j.earscirev.2011.10.005

Kaminsky, F. V., Ryabchikov, I. D., and Wirth, R. (2016). A Primary Natrocarbonatitic Association in the Deep Earth. *Miner Petrol.* 110, 387–398. doi:10.1007/s00710-015-0368-4

Kaminsky, F. V., and Wirth, R. (2011). Iron Carbide Inclusions in Lower-Mantle diamond from Juina, Brazil. *Can. Mineral.* 49, 555–572. doi:10.3749/canmin.49.2.555

Kaminsky, F. V., Wirth, R., and Schreiber, A. (2013). Carbonatitic Inclusions in Deep Mantle diamond from Juina, Brazil: New Minerals in the Carbonate-Halide Association. *Can. Mineral.* 51, 669–688. doi:10.3749/canmin.51.5.669

Kaneshima, S. (2013). Lower Mantle Seismic Scatterers below the Subducting Tonga Slab: Evidence for Slab Entrainment of Transition Zone Materials. *Phys. Earth Planet. Interiors* 222, 35–46. doi:10.1016/j.pepi.2013.07.001

Kang, N., Schmidt, M. W., Poli, S., Connolly, J. A. D., and Franzolin, E. (2016). Melting Relations in the System FeCO3-MgCO3 and Thermodynamic Modelling of Fe-Mg Carbonate Melts. *Contrib. Mineral. Petrol.* 171, 74. doi:10.1007/s00410-016-1283-3

Kang, N., Schmidt, M. W., Poli, S., Franzolin, E., and Connolly, J. A. D. (2015). Melting of Siderite to 20GPa and Thermodynamic Properties of FeCO3-Melt. *Chem. Geology.* 400, 34–43. doi:10.1016/j.chemgeo.2015.02.005

Katsura, T., Yoneda, A., Yamazaki, D., Yoshino, T., and Ito, E. (2010). Adiabatic Temperature Profile in the Mantle. *Phys. Earth Planet. Interiors* 183, 212–218. doi:10.1016/j.pepi.2010.07.001

Kelemen, P. B., and Manning, C. E. (2015). Reevaluating Carbon Fluxes in Subduction Zones, What Goes Down, Mostly Comes up. *Proc. Natl. Acad. Sci. USA* 112 (30), E3997–E4006. doi:10.1073/pnas.1507889112

Keshav, S., and Gudfinnsson, G. H. (2010). Experimentally Dictated Stability of Carbonated Oceanic Crust to Moderately Great Depths in the Earth: Results from the Solidus Determination in the System CaO-MgO-Al2O3-SiO2-CO2. *J. Geophys. Res.* 115, B05205. doi:10.1029/2009jb006457

Kiseeva, K., Litasov, K. D., Yaxley, G. M., Ohtani, E., and Kamenetsky, V. S. (2013). Melting and Phase Relations of Carbonated Eclogite at 9-21GPa and the Petrogenesis of Alkali-Rich Melts in the Deep Mantle. *J. Petrology* 54, 1–29. doi:10.1093/petrology/egt023

Komabayashi, T., Hirose, K., Sugimura, E., Sata, N., Ohishi, Y., and Dubrovinsky, L. S. (2008). Simultaneous Volume Measurements of Post-perovskite and Perovskite in MgSiO3 and Their Thermal Equations of State. *Earth Planet. Sci. Lett.* 265, 515–524. doi:10.1016/j.epsl.2007.10.036

Li, J., and Yuen, D. A. (2014). Mid-mantle Heterogeneities Associated with Izanagi Plate: Implications for Regional Mantle Viscosity. *Earth Planet. Sci. Lett.* 385, 137–144. doi:10.1016/j.epsl.2013.10.042

Li, X. Y., Zhang, Z. G., Lin, J. F., Ni, H. W., Prakapenka, V. B., and Mao, Z. (2018). New High Pressure Phase of $CaCO_3$ at the Topmost Lower Mantle: Implication for the Deep Mantle Carbon Transportation. *Geophys. Res. Lett.* 45, 1335–1360. doi:10.1002/2017gl076536

Li, Z., Li, J., Lange, R., Liu, J., and Militzer, B. (2017). Determination of Calcium Carbonate and Sodium Carbonate Melting Curves up to Earth's Transition Zone Pressures with Implications for the Deep Carbon Cycle. *Earth Planet. Sci. Lett.* 457, 395–402. doi:10.1016/j.epsl.2016.10.027

Lin, J.-F., Liu, J., Jacobs, C., and Prakapenka, V. B. (2012). Vibrational and Elastic Properties of Ferromagnesite Across the Electronic Spin-Pairing Transition of Iron. *Am. Mineral.* 97, 583–591. doi:10.2138/am.2012.3961

Litasov, K. D., Fei, Y., Ohtani, E., Kuribayashi, T., and Funakoshi, K. (2008). Thermal Equation of State of Magnesite to 32GPa and 2073K. *Phys. Earth Planet. Interiors* 168, 191–203. doi:10.1016/j.pepi.2008.06.018

Litasov, K. D., Goncharov, A. F., and Hemley, R. J. (2011). Crossover from Melting to Dissociation of CO2 Under Pressure: Implications for the Lower Mantle. *Earth Planet. Sci. Lett.* 309, 318–323. doi:10.1016/j.epsl.2011.07.006

Litasov, K. D., Ohtani, E., Ghosh, S., Nishihara, Y., Suzuki, A., and Funakoshi, K. (2007). Thermal Equation of State of Superhydrous Phase B to 27GPa and 1373K. *Phys. Earth Planet. Interiors* 164, 142–160. doi:10.1016/j.pepi.2007.06.003

Litasov, K. D., and Ohtani, E. (2009). Solidus and Phase Relations of Carbonated Peridotite in the System CaO-Al2O3-MgO-SiO2-Na2O-CO2 to the Lower Mantle Depths. *Phys. Earth Planet. Interiors* 177, 46–58. doi:10.1016/j.pepi.2009.07.008

Litasov, K. D., Shatskiy, A., Gavryushkin, P. N., Bekhtenova, A. E., Dorogokupets, P. I., Danilov, B. S., et al. (2017). P-V-T Equation of State of CaCO 3 Aragonite to 29 GPa and 1673 K: In Situ X-ray Diffraction Study. *Phys. Earth Planet. Interiors* 265, 82–91. doi:10.1016/j.pepi.2017.02.006

Litasov, K., and Ohtani, E. (2010). The Solidus of Carbonated Eclogite in the System CaO-Al2O3-MgO-SiO2-Na2O-CO2 to 32GPa and Carbonatite Liquid in the Deep Mantle. *Earth Planet. Sci. Lett.* 295, 115–126. doi:10.1016/j.epsl.2010.03.030

Litvin, Y., Spivak, A., Solopova, N., and Dubrovinsky, L. (2014). On Origin of Lower-Mantle Diamonds and Their Primary Inclusions. *Phys. Earth Planet. Interiors* 228, 176–185. doi:10.1016/j.pepi.2013.12.007

Liu, J., Lin, J.-F., and Prakapenka, V. B. (2015). High-pressure Orthorhombic Ferromagnesite as a Potential Deep-Mantle Carbon Carrier. *Sci. Rep.* 5, 7640. doi:10.1038/srep07640

Lobanov, S. S., Dong, X., Martirosyan, N. S., Samtsevich, A. I., Stevanovic, V., Gavryushkin, P. N., et al. (2017). Raman Spectroscopy and X-ray Diffraction of sp3CaCO3 at Lower Mantle Pressures. *Phys. Rev. B* 96, 104101. doi:10.1103/physrevb.96.104101

Maeda, F., Ohtani, E., Kamada, S., Sakamaki, T., Hirao, N., and Ohishi, Y. (2017). Diamond Formation in the Deep Lower Mantle: A High-Pressure Reaction of MgCO3 and SiO2. *Sci. Rep.* 7, 40602. doi:10.1038/srep40602

Mao, Z., Armentrout, M., Rainey, E., Manning, C. E., Dera, P., Prakapenka, V. B., et al. (2011). Dolomite III: A New Candidate Lower Mantle Carbonate. *Geophys. Res. Lett.* 38, L22303. doi:10.1029/2011gl049519

Marcondes, M. L., Justo, J. F., and Assali, L. V. C. (2016). Carbonates at High Pressures: Possible Carriers for Deep Carbon Reservoirs in the Earth's Lower Mantle. *Phys. Rev. B* 94, 104112. doi:10.1103/physrevb.94.104112

Martirosyan, N. S., Litasov, K. D., Lobanov, S. S., Goncharov, A. F., Shatskiy, A., Ohfuji, H., et al. (2018). The Mg-Carbonate-Fe Interaction: Implication for the Fate of Subducted Carbonates and Formation of Diamond in the Lower Mantle. *Geosci. Front.* 10, 1–10.

Martirosyan, N. S., Litasov, K. D., Shatskiy, A., and Ohtani, E. (2015). The Reactions Between Iron and Magnesite at 6 GPa and 1273-1873 K: Implication to Reduction of Subducted Carbonate in the Deep Mantle. *J. Mineralogical Petrological Sci.* 110, 49–59. doi:10.2465/jmps.141003a

Martirosyan, N. S., Yoshino, T., Shatskiy, A., Chanyshev, A. D., and Litasov, K. D. (2016). The CaCO3-Fe Interaction: Kinetic Approach for Carbonate Subduction to the Deep Earth's Mantle. *Phys. Earth Planet. Interiors* 259, 1–9. doi:10.1016/j.pepi.2016.08.008

Merlini, M., Cerantola, V., Gatta, G. D., Gemmi, M., Hanfland, M., Kupenko, I., et al. (2019). Dolomite-IV: Candidate Structure for a Carbonate in the Earth's Lower Mantle. *Am. Mineral.* 102 (8), 1763–1766. doi:10.2138/am-2017-6161

Merlini, M., Crichton, W. A., Hanfland, M., Gemmi, M., Muller, H., Kupenko, I., et al. (2012). Structures of Dolomite at Ultrahigh Pressure and Their Influence on the Deep Carbon Cycle. *Proc. Natl. Acad. Sci.* 109 (34), 13509–13514. doi:10.1073/pnas.1201336109

Merlini, M., Sapelli, F., Fumagalli, P., Gatta, G. D., Lotti, P., Tumiati, S., et al. (2016). High-temperature and High-Pressure Behavior of Carbonates in the Ternary Diagram CaCO3-MgCO3-FeCO3. *Am. Mineral.* 101, 1423–1430. doi:10.2138/am-2016-5458

Morard, G., Andrault, D., Antonangeli, D., Nakajima, Y., Auzende, A. L., Boulard, E., et al. (2017). Fe-FeO and Fe-Fe3C Melting Relations at Earth's Core-Mantle Boundary Conditions: Implications for a Volatile-Rich or Oxygen-Rich Core. *Earth Planet. Sci. Lett.* 473, 94–103. doi:10.1016/j.epsl.2017.05.024

Murakami, M., Hirose, K., Ono, S., and Ohishi, Y. (2003). Stability of $CaCl_2$-type and PbO_2-type SiO_2 at High Pressure and Temperature Determined by In-Situ X-ray Measurements. *Geophys. Res. Lett.* 30, 1207. doi:10.1029/2002gl016722

Narygina, O., Dubrovinsky, L. S., McCammon, C. A., Kurnosov, A., Kantor, I. Y., Prakapenka, V. B., et al. (2011). X-ray Diffraction and Mössbauer Spectroscopy Study of Fcc Iron Hydride FeH at High Pressures and Implications for the Composition of the Earth's Core. *Earth Planet. Sci. Lett.* 307, 409–414. doi:10.1016/j.epsl.2011.05.015

Niu, F. (2014). Distinct Compositional Thin Layers at Mid-mantle Depths beneath Northeast China Revealed by the USArray. *Earth Planet. Sci. Lett.* 402, 305–312. doi:10.1016/j.epsl.2013.02.015

Oganov, A. R., Ono, S., Ma, Y., Glass, C. W., and Garcia, A. (2008). Novel High-Pressure Structures of MgCO3, CaCO3 and CO2 and Their Role in Earth's Lower Mantle. *Earth Planet. Sci. Lett.* 273, 38–47. doi:10.1016/j.epsl.2008.06.005

Palyanov, Y. N., Sokol, A. G., Borzdov, Y. M., Khokhryakov, A. F., and Sobolev, N. V. (2002). Diamond Formation Through Carbonate-Silicate Interaction. *Am. Mineral.* 87, 1009–1013. doi:10.2138/am-2002-0726

Palyanov, Y. N., Bataleva, Y. V., Sokol, A. G., Borzdov, Y. M., Kupriyanov, I. N., Reutsky, V. N., et al. (2013). Mantle-slab Interaction and Redox Mechanism of Diamond Formation. *Proc. Natl. Acad. Sci.* 110 (51), 20408–20413. doi:10.1073/pnas.1313340110

Panero, W. R., and Kabbes, J. E. (2008). Mantle-wide Sequestration of Carbon in Silicates and the Structure of Magnesite II. *Geophys. Res. Lett.* 35, L14307. doi:10.1029/2008gl034442

Pickard, C. J., and Needs, R. J. (2015). Structures and Stability of Calcium and Magnesium Carbonates at Mantle Pressures. *Phys. Rev. B* 91, 104101. doi:10.1103/physrevb.91.104101

Plank, T., and Langmuir, C. H. (1993). Tracing Trace Elements from Sediment Input to Volcanic Output at Subduction Zones. *Nature* 362, 739–743. doi:10.1038/362739a0

Rohrbach, A., and Schmidt, M. W. (2011). Redox Freezing and Melting in the Earth's Deep Mantle Resulting from Carbon-Iron Redox Coupling. *Nature* 472, 209–212. doi:10.1038/nature09899

Santillán, J., Williams, Q., and Knittle, E. (2003). Dolomite-II: A High-Pressure Polymorph of $CaMg(CO_3)_2$. *Geophys. Res. Lett.* 30 (2), 1054. doi:10.1029/2001GL016018

Santos, S. S. M., Marcondes, M. L., Justo, J. F., and Assali, L. V. C. (2019). Stability of Calcium and Magnesium Carbonates at Earth's Lower Mantle Thermodynamic Conditions. *Earth Planet. Sci. Lett.* 506, 1–7. doi:10.1016/j.epsl.2018.10.030

Shatskiy, A., Bekhtenova, A., Podborodnikov, I. V., Arefiev, A. V., Vinogradova, Y. G., and Litasov, K. D. (2021). Solidus of Carbonated Phlogopite Eclogite at 3-6 GPa: Implications for Mantle Metasomatism and Ultra-high Pressure Metamorphism. *Gondwana Res.* 103, 188–204. doi:10.1016/j.gr.2021.10.016

Smith, D., Lawler, K. V., Martinez-Canales, M., Daykin, A. W., Fussell, Z., Alexander, S. G., et al. (2018). Postaragonite Phases of $CaCO_3$ at Lower Mantle Pressures. *Phys. Rev. Mater.* 2, 013605. doi:10.1103/physrevmaterials.2.013605

Smith, E. M., Shirey, S. B., Nestola, F., Bullock, E. S., Wang, J., Richardson, S. H., et al. (2016). Large Gem Diamonds from Metallic Liquid in Earth's Deep Mantle. *Science* 354 (6318), 1403–1405. doi:10.1126/science.aal1303

Solomatova, N. V., and Asimow, P. D. (2016). *Ab Initio Study of the Structure and Stability of High-Pressure Iron-Bearing Dolomite*. American Geophysical Union, Fall Meeting.

Solopova, N. A., Dubrovinsky, L., Spivak, A. V., Litvin, Y. A., and Dubrovinskaia, N. (2015). Melting and Decomposition of MgCO3 at Pressures up to 84 GPa. *Phys. Chem. Minerals* 42, 73–81. doi:10.1007/s00269-014-0701-1

Spivak, A., Solopova, N., Litvin, L., and Dubrovinsky, L. (2013). Chemical Interaction of Mg-Carbonate and the Earth's Lower Mantle Minerals. EGU General Assembly. *Geophys. Res. Abstr.* 15, EGU2013–44741.

Spivak, A., Solopova, N., Cerantola, V., Bykova, E., Zakharchenko, E., Dubrovinsky, L., et al. (2014). Raman Study of MgCO3-FeCO3 Carbonate Solid Solution at High Pressures up to 55 GPa. *Phys. Chem. Minerals* 41, 633–638. doi:10.1007/s00269-014-0676-y

Spivak, A. V., Dubrovinskii, L. S., and Litvin, Y. A. (2011). Congruent Melting of Calcium Carbonate in a Static experiment at 3500 K and 10-22 GPa: Its Role in the Genesis of Ultradeep Diamonds. *Dokl. Earth Sc.* 439 (2), 1171–1174. doi:10.1134/s1028334x11080319

Stachel, T., and Harris, J. W. (2008). The Origin of Cratonic Diamonds - Constraints from Mineral Inclusions. *Ore Geology. Rev.* 34, 5–32. doi:10.1016/j.oregeorev.2007.05.002

Stagno, V., Tange, Y., Miyajima, N., McCammon, C. A., Irifune, T., and Frost, D. J. (2011). The Stability of Magnesite in the Transition Zone and the Lower Mantle as Function of Oxygen Fugacity. *Geophys. Res. Lett.* 38, L19309. doi:10.1029/2011gl049560

Stekiel, M., Girard, A., Nguyen-Thanh, T., Bosak, A., Milman, V., and Winkler, B. (2019). Phonon-driven Phase Transitions in Calcite, Dolomite, and Magnesite. *Phys. Rev. B* 99, 054101. doi:10.1103/physrevb.99.054101

Stekiel, M., Nguyen-Thanh, T., Chariton, S., McCammon, C., Bosak, A., Morgenroth, W., et al. (2017). High Pressure Elasticity of FeCO 3 -MgCO 3 Carbonates. *Phys. Earth Planet. Interiors* 271, 57–63. doi:10.1016/j.pepi.2017.08.004

Sun, W.-d., Hawkesworth, C. J., Yao, C., Zhang, C.-c., Huang, R.-f., Liu, X., et al. (2018). Carbonated Mantle Domains at the Base of the Earth's Transition Zone. *Chem. Geology.* 478, 69–75. doi:10.1016/j.chemgeo.2017.08.001

Syracuse, E. M., van Keken, P. E., and Abers, G. A. (2010). The Global Range of Subduction Zone Thermal Models. *Phys. Earth Planet. Interiors* 183, 73–90. doi:10.1016/j.pepi.2010.02.004

Takafuji, N., Fujino, K., Nagai, T., Seto, Y., and Hamane, D. (2006). Decarbonation Reaction of Magnesite in Subducting Slabs at the Lower Mantle. *Phys. Chem. Minerals* 33, 651–654. doi:10.1007/s00269-006-0119-5

Tao, R., Zhang, L., Fei, Y., and Liu, Q. (2014). The Effect of Fe on the Stability of Dolomite at High Pressure: Experimental Study and Petrological Observation in Eclogite from Southwestern Tianshan, China. *Geochimica Et Cosmochimica Acta* 143, 253–267. doi:10.1016/j.gca.2014.02.031

Tao, R., Zhang, L., and Zhang, L. (2020). Redox Evolution of Western Tianshan Subduction Zone and its Effect on Deep Carbon Cycle. *Geosci. Front.* 11 (3), 915–924. doi:10.1016/j.gsf.2019.09.007

Thomson, A. R., Walter, M. J., Kohn, S. C., and Brooker, R. A. (2016). Slab Melting as a Barrier to Deep Carbon Subduction. *Nature* 529, 76–79. doi:10.1038/nature16174

Tomlinson, E. L., Howell, D., Jones, A. P., and Frost, D. J. (2011). Characteristics of HPHT Diamond Grown at Sub-lithosphere Conditions (10-20GPa). *Diamond Relat. Mater.* 20, 11–17. doi:10.1016/j.diamond.2010.10.002

Weis, C., Sternemann, C., Cerantola, V., Sahle, C. J., Spiekermann, G., Harder, M., et al. (2017). Pressure Driven Spin Transition in Siderite and Magnesiosiderite Single Crystals. *Sci. Rep.* 7, 16526. doi:10.1038/s41598-017-16733-3

Yang, J., Mao, Z., Lin, J.-F., and Prakapenka, V. B. (2014). Single-crystal Elasticity of the Deep-Mantle Magnesite at High Pressure and Temperature. *Earth Planet. Sci. Lett.* 392, 292–299. doi:10.1016/j.epsl.2014.01.027

Yang, Z., and He, X. (2015). Oceanic Crust in the Mid-mantle Beneath West-central Pacific Subduction Zones: Evidence fromStoPconverted Waveforms. *Geophys. J. Int.* 203 (1), 541–547. doi:10.1093/gji/ggv314

Zhang, Z. G., Mao, Z., Liu, X., Zhang, Y. G., and Brodholt, J. (2018b). Stability and Reactions of $CaCO_3$ Polymorphs in the Earth's Deep Mantle. *J. Geophys. Research-Solid Earth* 123, 6491–6500. doi:10.1002/2017jb015019

Zhang, Z., Hastings, P., Von der Handt, A., and Hirschmann, M. M. (2018a). Experimental Determination of Carbon Solubility in Fe-Ni-S Melts. *Geochimica Et Cosmochimica Acta* 225, 66–79. doi:10.1016/j.gca.2018.01.009

Zhang, Z., and Liu, Z. (2015). High Pressure Equation of State for Molten CaCO3 from First Principles Simulations. *Chin. J. Geochem.* 34 (1), 13–20. doi:10.1007/s11631-015-0036-8

Zhao, S., Schettino, E., Merlini, M., and Poli, S. (2019). The Stability and Melting of Aragonite: An Experimental and Thermodynamic Model for Carbonated Eclogites in the Mantle. *Lithos* 324-325, 105–114. doi:10.1016/j.lithos.2018.11.005

Zhu, F., Li, J., Liu, J. C., Lai, X. J., Chen, B., and Meng, Y. (2018). Kinetic Control on the Depth Distribution of Superdeep Diamonds. *Geophys. Res. Lett.* 46, 1984–1992. doi:10.1029/2018GL080740

Zhu, Y.-F., Massonne, H.-J., and Men-Fan Zhu, M. F. (2009). Petrology of Low-Temperature, Ultrahigh-Pressure Marbles and Interlayered Coesite Eclogites Near Sanqingge, Sulu Terrane, Eastern China. *Mineral. Mag.* 73 (2), 307–332. doi:10.1180/minmag.2009.073.2.307

Conflict of Interest: The authors declare that the research was conducted in the absence of any commercial or financial relationships that could be construed as a potential conflict of interest.

frontiers
in Earth Science

ORIGINAL RESEARCH
published: 29 March 2022
doi: 10.3389/feart.2022.860057

New Insight From the First Application of Ti-in-Quartz (TitaniQ) Thermometry Mapping in the Eastern Khondalite Belt, North China Craton

***Yuanyuan Zheng*[1,2,3]*, Yang Qi*[1,2,3]*, Di Zhang*[1,2]*, Shujuan Jiao*[1,2]**, Guangyu Huang*[1,2] *and Jinghui Guo*[1,2]**

[1]State Key Laboratory of Lithospheric Evolution, Institute of Geology and Geophysics, Chinese Academy of Sciences, Beijing, China, [2]Innovation Academy for Earth Science, CAS, Beijing, China, [3]College of Earth and Planetary Sciences, University of Chinese Academy of Sciences, Beijing, China

The thermal regime of the lower crust is a critical factor that controls crustal anatexis, high-grade metamorphism, and granite formation, which finally results in crustal differentiation. However, the large-scale thermal regime in the Precambrian continental crust is generally not well established. In this study, we first applied Ti-in-quartz (TitaniQ) thermometer to map the temperature variation in the lower crust within an area of ~10,000 km^2 in the Paleoproterozoic eastern Khondalite Belt, North China Craton. The studied rocks are aluminous gneisses/granulites, which contain abundant quartz that generally coexists with rutile. The results show that matrix-type quartz with substantial rutile exsolution generally contains the maximum Ti concentration, which is <300 ppm higher than that of inclusion-type quartz. This result suggests that two quartz types probably formed at the prograde and near-peak to early cooling metamorphic stages, respectively. Therefore, the temperature mapping result based on the maximum Ti concentrations of the matrix-type quartz can better represent the thermal regime than inclusion-type quartz. Our regime shows that the hottest Paleoproterozoic lower crust is underneath the Liangcheng-Heling'er-Zhuozi area, where ultrahigh-temperature (UHT) metamorphism is closely associated with abundant charnockite. The hottest region may represent the root of an ancient large hot orogeny. Our study provides a new insight into the formation of UHT metamorphism.

Keywords: Ti-in-quartz (TitaniQ) thermometer, aluminous gneiss/granulite, UHT metamorphism, thermal regime, the khondalite belt, North China Craton

Edited by:
Guibin Zhang,
Peking University, China

Reviewed by:
Shengyao Yu,
Ocean University of China, China
Chang Whan Oh,
Jeonbuk National University, South Korea

****Correspondence:***
Shujuan Jiao
jiaoshujuan0215@126.com

Specialty section:
This article was submitted to Petrology,
a section of the journal
Frontiers in Earth Science

Received: *22 January 2022*
Accepted: *01 March 2022*
Published: *29 March 2022*

Citation:
Zheng Y, Qi Y, Zhang D, Jiao S, Huang G and Guo J (2022) New Insight From the First Application of Ti-in-Quartz (TitaniQ) Thermometry Mapping in the Eastern Khondalite Belt, North China Craton.
Front. Earth Sci. 10:860057.
doi: 10.3389/feart.2022.860057

INTRODUCTION

Ultrahigh-temperature (UHT) metamorphism occurs at temperatures of ≥900°C (0.7–1.3 GPa; Harley, 1998), and is the hottest metamorphism in the lower crust. The first UHT metamorphism was reported over 50 years ago. Numbers of UHT localities have been discovered worldwide, and detailed studies have laid the foundation for a complete understanding of the crustal thermal regime (Harley, 1998; Sajeev et al., 2004; Santosh et al., 2007a; Harley, 2008; Janwari et al., 2012). Study of UHT metamorphism facilitates interpreting the lithospheric evolution throughout Earth's history, especially the crust–mantle interaction and tectonic evolution.

The Khondalite Belt within the North China Craton (NCC) was formed by the collision of the Yinshan Block in the north and the Ordos Block in the south at ca. 1.95 Ga (Zhao et al., 2005). Since the first identification of two typical UHT metamorphic localities at Dongpo in the Daqingshan terrane (Guo et al., 2012) and Tuguiwula in the Jining terrane (Santosh et al., 2006), investigations have discovered new localities of UHT rocks, for example, Tuguishan, Xuwujia, Hongsigou, Zhaojiayao, Xumayao, Nantianmen, and Xiaonangou (Jiao et al., 2011; Jiao and Guo, 2011; Liu et al., 2012; Zhang et al., 2012; Yang et al., 2014; Li and Wei, 2016; Wang et al., 2020). However, their spatial relationship, especially the distribution area of UHT metamorphism, is ambiguous.

Numerous methods have been applied to estimate the peak metamorphic temperature of UHT granulites, including thermometers and phase equilibria modeling. The thermometers of two-feldspar, Zr-in-rutile, Ti-in-zircon, and Al-in-orthopyroxene performed well in the UHT temperature estimates. Titanium in quartz was also calibrated as a Ti-in-quartz (TitaniQ) thermometer (Ostapenko et al., 1987; Wark and Watson, 2006; Thomas et al., 2010; Huang and Audétat, 2012; Zhang et al., 2020), which has been applied to various rock types and proved to be valid (Spear and Wark, 2009; Storm and Spear, 2009; Thomas and Bruce Watson, 2012; Kidder et al., 2013; Tual et al., 2018). Quartz is ubiquitous in many UHT rocks, and the application of the TitaniQ thermometer is convenient because only the quartz phase needs to be analyzed. In addition, quartz internal structures revealed by cathodoluminescence (CL) images can assist in interpreting the mechanism of quartz formation (Sprunt et al., 1978; Müller et al., 2002; Kendrick and Indares, 2018). Therefore, the application of the TitaniQ thermometer in combination with quartz CL imaging can potentially indicate the metamorphic evolution of UHT granulites.

In this study, we applied the TitaniQ thermometer and CL imaging of quartz to metapelites (including UHT granulites) in the eastern Khondalite Belt for the first time. The samples were collected from an area of ~10,000 km^2 to conduct regional temperature mapping. Our approach provides a new simple method for calculating metamorphic temperature in this region. Our temperature mapping shows the regional thermal regime of the lower crust and provides a new insight into the formation of UHT metamorphism.

GEOLOGICAL SETTING AND SAMPLING LOCALITY

The formation and evolution of the NCC have been topics of ongoing debates for many decades. As the oldest craton in China with an age record of up to 3.8 Ga (Liu et al., 1992; Wan et al., 2005), the NCC has experienced complicated geological processes. The model ages from zircon Hf isotope and whole-rock Nd isotope in TTG gneisses suggest that the formation age of the continental crust of NCC is 2.8–2.7 Ga and ca. 2.5 Ga (Wu et al., 2005; Geng et al., 2012).

A suggestion has been that the NCC could be divided into three major tectonic units: The Western block, the Eastern block, and the collisional belt of the Trans-North China Orogen (Zhao et al., 2011). There are two other recognized orogens: the Jiao-Liao-Ji Belt in the Eastern Block, formed by the collision between the Nangrim Block and Longgang Block at ca. 1.95–1.90 Ga and the Khondalite Belt in the Western Block, formed by the collision between the Yinshan Block and Ordos Block at ca. 1.95 Ga, which is related to the assembly of the Columbia supercontinent (Zhao et al., 1998; Zhao et al., 2001; Zhao et al., 2003; Zhao et al., 2005; Zhao et al., 2011).

The east-west trending Khondalite Belt is located in the north-central part of the Western Block, NCC. It can be divided into three terranes from west to east: Helanshan-Qianlishan (H-Q), Wulashan-Daqingshan (W-D), and Jining (JN) terranes (**Figure 1A**). The rock types of the belt are composed of khondalite series rocks (aluminum-rich meta-sedimentary rocks), garnet-cordierite granites, charnockites, meta-gabbros, and a small amount of TTG gneisses. Zircon geochronological results suggest that detrital materials in the Khondalite Belt were derived from Archean and Paleoproterozoic magmatism (Zhai and Peng, 2007; Zhai, 2009). The protolith of the Khondalite series is considered to have been deposited between 2.00 and 1.95 Ga, which represents the deposition of an active continent margin, instead of an Archean cratonic basin (Wan et al., 2009; Dan et al., 2012).

The whole Khondalite Belt has experienced upper amphibolite- to granulite-facies metamorphism, including high-pressure metamorphism between 1.96 and 1.94 Ga and an overprinted HT-UHT metamorphism event at 1.94–1.80 Ga (Santosh et al., 2007b; Santosh et al., 2009; Yin et al., 2011; Jiao et al., 2020; Jiao and Guo, 2020; Jiao et al., 2021).

In the Helanshan-Qianlishan terrane of western Khondalite Belt, the calculated peak temperature and pressure conditions are 850–870°C and 1.4–1.5 GPa, within a clockwise P–T path, and this high-pressure metamorphism suggests the occurrence of continent-continent collision in the Khondalite Belt (Yin et al., 2009; Yin et al., 2011; Yin et al., 2015; Zhou et al., 2010). In the Wulashan-Daqingshan terrane, rock types are variable and contain meta-sedimentary rocks, Archean TTG gneisses, and mafic granulites, with varying degrees of multi-metamorphism (Jiang et al., 2022).

Rock types in the Jining terrane of eastern Khondalite Belt are khondalite series rocks associated with a small amount of quartzite, graphite gneiss, marble, calc-siliceous gneiss, potassic garnet-bearing granite, and intrusive meta-gabbro and –norite (**Figure 1B**). The distribution area of the potassic garnet-bearing granite is large: 40% of the rock exposed (**Figure 1A**). The potassic garnet-bearing granite is dominated by abundant charnockite associated with minor leucogranites, which represent two periods of magmatic events (Peng et al., 2012; Wang et al., 2017; Wang et al., 2018). The distribution area of intrusive meta-gabbros and norites is small. A suggestion has been that the formation of meta-gabbros and meta-norites provides a heat source for UHT metamorphism (Peng et al., 2010; Peng et al., 2012), which leads to the formation of garnet-bearing granite by *in-situ* anatexis of khondalite series rocks. The volume of granites is one third to one half of the khondalite series rocks, and the age

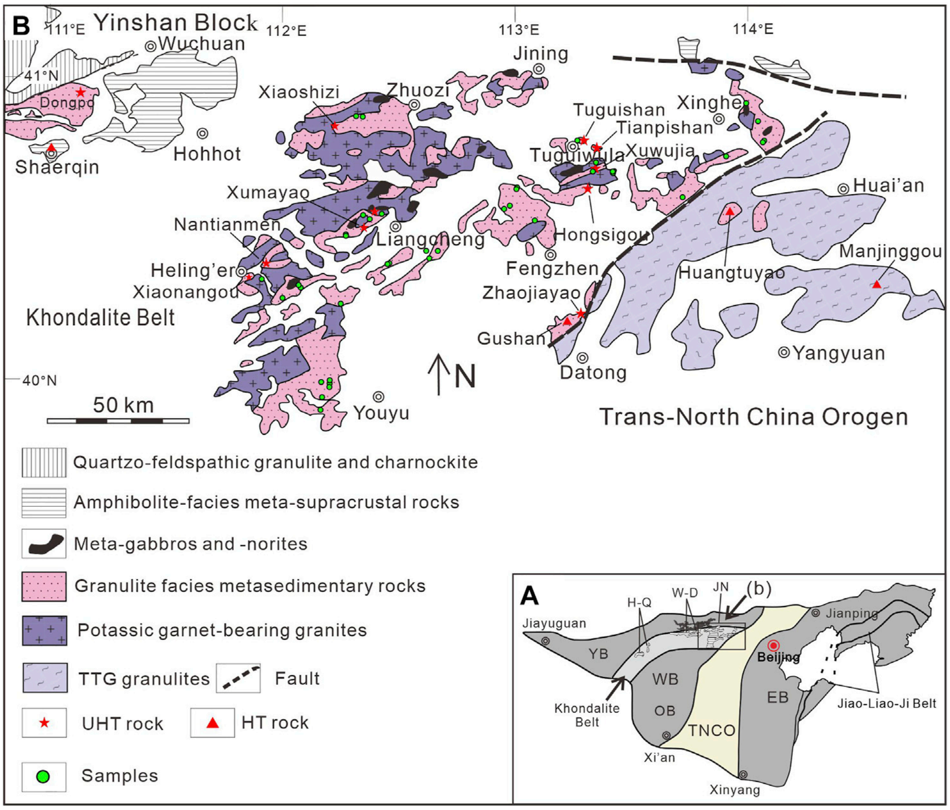

FIGURE 1 | (A) Tectonic subdivision of the basement in the North China Craton; **(B)** Distribution of the exposed rocks in the eastern Khondalite Belt, North China Craton. Samples are distributed throughout the whole research region. Abbreviations of areas: WB, Western Block; EB, Eastern Block; TNCO, Trans-North China Orogen; YB, Yinshan Block; OB, Ordos Block; H-Q, Helanshan-Qianlishan; W-D, Wulashan-Daqingshan; JN, Jining.

of granite formation is coeval with the metamorphic age of khondalite series rocks (Zhai, 2009).

Sapphirine-bearing metapelites or residual granulites have been discovered at the Dongpo and Shaerqin localities in the Wulashan-Daqingshan terrane, recording HT-UHT conditions of 910–980°C and 860–890°C, respectively (Guo et al., 2012; Jiao et al., 2015). The sapphirine-bearing UHT granulites were reported from the Tuguiwula (Tianpishan) locality (Santosh et al., 2007a), which preserves the diagnostic UHT mineral assemblages of Spr + Qz and Opx + Sil + Qz (Mineral abbreviations follow Warr, 2021), and the near-peak temperature of 900–1,000°C was recorded. Subsequently, additional UHT granulite localities have been reported in the Jining terrane, such as Tuguishan, Xuwujia, Nantianmen, Xiaonangou, and Xumayao (Santosh et al., 2007a; Jiao et al., 2011; Jiao and Guo, 2011; Liu et al., 2012; Zhang et al., 2012). In Helanshan terrane, UHT metamorphism was reported in spinel-bearing granulites, with peak conditions of ~960–1,030°C and 6.3–7.3 kbar (Gou et al., 2018). Generally, the UHT granulites in the Khondalite Belt have experienced complex clockwise *P*–*T* paths, including decompression-heating, nearly isobaric cooling (IBC), and nearly isothermal decompression/decompression-heating stages, although anticlockwise *P*–*T* paths were also proposed (**Figure 2**; Liu et al., 2010; Jiao et al., 2011; Jiao and Guo, 2011; Li and Wei, 2016).

Our research region is the Jining-Tuguiwula-Liangcheng-Heling'er-Youyu area located within the Jining terrane of the eastern Khondalite Belt (**Figure 1B**), which contains several UHT localities. Forty-four representative samples throughout this region were studied using a TitaniQ thermometer to constrain the occurrence and spatial scale of the UHT metamorphism.

PETROGRAPHY

The studied samples were mostly aluminous gneisses (or granulites). The major minerals in these samples are quartz, plagioclase, K-feldspar, garnet, sillimanite, and biotite. These samples were classified into four groups. The first group is characterized by a Grt + Sil + Bt + Qz + Pl/Kfs mineral assemblage, which can be subdivided into coarse-grained and fine-grained according to the granularity of garnet grains (**Figures 3A,B**). Thirty-two samples belong to this group, accounting for the majority of the samples. In addition, four samples in this group had distinct foliation structures (samples 20HL19, 20HL39, 20HL89, 20HL143) (**Figure 3C**). The oriented arrangement of sillimanite composes the foliation. Except for sillimanite, minerals such as quartz, biotite, and resorbed garnet can also compose the foliation. The second group was characterized by a Grt + Bt + Qz + Pl/Kfs mineral assemblage and comprised four samples (**Figure 3D**). In this group, the volume proportion of sillimanite was relatively low to none, and biotite was the main aluminous-rich mineral. The third group was characterized by a Grt + Sil + Qz + Pl/Kfs mineral assemblage and comprised three samples (**Figure 3E**). In this group, the size of the biotite was small, and the main aluminous-rich mineral was sillimanite. The fourth group was characterized by a Grt + Qz + Pl/Kfs mineral assemblage and comprised five samples (**Figure 3F**).

Garnet occurs as porphyroblasts in all samples, which contain quartz, plagioclase, biotite, and rutile as inclusions. Garnet in some samples had been resorbed and broken into small pieces. Plagioclase and K-feldspar are commonly present in the matrix. K-feldspar had been altered in some samples. Sillimanite mainly occurs in the matrix in the needle-and-column shape. Lamellar biotite mainly disperses in the matrix: Some grains are distributed around garnet, and some occur as inclusions in garnet. Quartz exists in two forms: Matrix-type quartz and quartz inclusions in garnet. In some samples, rutile needles are within quartz grains, which can be observed in the photomicrographs. In some samples, rutile grew along three directions, which may represent the crystallization direction. We observed that the occurrence of rutile needles in quartz grains from the northern part is more general than that in the southern part of the studied region.

Rutile exists as an accessory phase in all the samples. Most of the rutile grains occur in the matrix surrounded by quartz, and the others occur as inclusions in garnet. The volume proportion and grain size of rutile differ. In five samples from south of Heling'er (samples 20HL49, 20HL59, 20HL64, 20HL73, and 20HL89), rutile was 50–200 μm in size and had an extremely low volume percentage. By contrast, rutile in samples from the Xinghe area was 100–800 μm and occupied a higher volume percentage (samples 09XH07, 09XH16, 09XH21, and 09XH32). In samples from Tuguishan locality, a few spinel grains with grain sizes of 100–250 μm were observed (samples 09TGS01, 09TGS18, and 18TG01), which is distinct from the other samples.

ANALYTICAL METHODS

Electron Microprobe Analysis

Concentrations of major (Si) and minor (Al and Ti) elements in quartz grains were all determined by CAMECA SXFive electron probe micro-analyzer at the Institute of Geology and Geophysics, Chinese Academy of Sciences (IGGCAS) in Beijing, China. Accelerating voltage was 15 kV and beam currents were 30 and 300 nA for major and minor elements. The peak counting times were 20s for Si and 120s for Al and Ti. Rhodonite, albite and rutile were used as standards for calibration. Standardization was performed with a beam current of 20 nA and with a peak counting time of 20s. Data were obtained by the X-PHI matrix correction (Merlet, 1994). Oxygen was calculated by cation stoichiometry and included in the matrix correction. The following detection limits were based on a 3σ estimate of the measured background variance: ~210 ppm for Si, ~12 ppm for Al and ~13 ppm for Ti.

A large spot size of 50 μm was used for all analyses in order to involve the composition of substantial rutile needles in the measurement, because TiO_2 in these rutile needles might have once occupied by pre-existing quartz that is before rutile exsolution (See *Section Discussion*). The natural smoky quartz crystal was used as a secondary standard, which has reproducible Ti concentration (57 ± 4 ppm; Audétat et al., 2015). Our averaged Ti concentration ($N = 55$) of the quartz standard is 58 ± 3 ppm, which is consistent with the recommended value within error. Our analyzed quartz grains in the matrix are all far away from other major Ti-bearing minerals, such as rutile and biotite, to avoid secondary fluorescence effect.

Cathodoluminescence Imaging

The Cathodoluminescence (CL) images of quartz were observed using a Nova NanoSEM 450 (FSEM) scanning electron microscope at the IGGCAS. The Nova NanoSEM 450 was equipped with a Gatan Instrument "MonoCL14" detector. An accelerating voltage of 10 kV and a beam current of 1.1 nA were used during the analysis, and the working distance was 27–29 mm.

Thermometry

The titanium concentration in quartz was first proposed as a geological thermometer in 1987 (Ostapenko et al., 1987). The thermodynamic principle of the TitaniQ thermometer depends on the titanium equilibrium between quartz and rutile, which can be expressed in an exchange reaction: $TiO_2^{Qz} = TiO_2^{Rt}$. The calibration experiments suggest that titanium solubility in quartz depends on the pressure and temperature conditions in the case that quartz crystallizes coexisting with rutile, and titanium contents of quartz (in ppm by weight) would increase exponentially with T. Similar to other trace-element thermometers, TitaniQ thermometer has several calibrations (Wark and Watson, 2006; Thomas et al., 2010; Huang and Audétat, 2012; Thomas et al., 2015). Within these models, the experiments were set to high pressure (5–20 kbar) and high temperature (700–940°C) conditions in the Thomas et al. (2010) model, which is the most suitable for the metamorphic conditions of our studied samples. Hence, we used the model calibrated by Thomas et al. (Thomas et al., 2010) in this study. And the pressure we have chosen for all calculations is 8 kbar based on couples of previous studies in the eastern Khondalite Belt (**Figure 2**; e.g., Santosh et al., 2007a; Santosh et al., 2012; Jiao et al., 2013a; Yang et al., 2014; Li and Wei, 2016; Li and Wei, 2018).

When applying the TitaniQ thermometer, the activity of TiO_2 should be accurately estimated. The value is generally 1 if rutile exists in the studied rocks, which means that the system is TiO_2 saturated (Ghent and Stout, 1984). There are also methods for calculating TiO_2 activity if the rocks do not contain rutile, which are mainly based on different solution models and compositions of Fe-Ti oxides (Hayden and Watson, 2007; Hildreth and Wilson, 2007; Kularatne and Audétat, 2014).

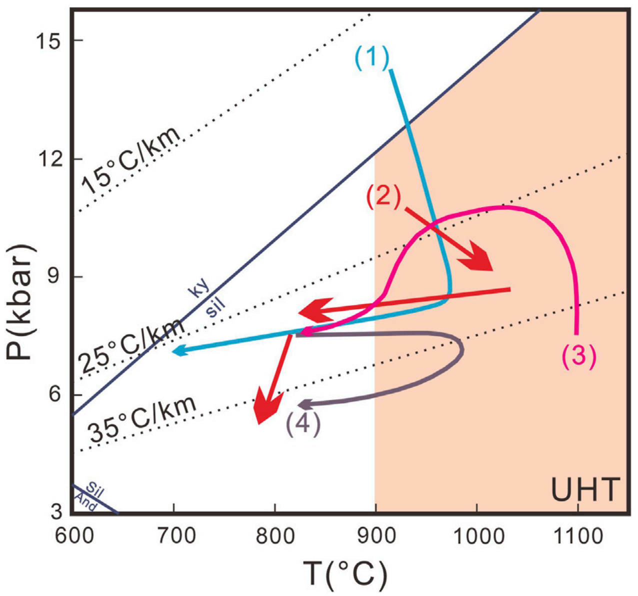

FIGURE 2 | Previously reported *P–T* paths of UHT granulites in the Khondalite Belt. (1) is from Li and Wei (2016), (2) is from Li and Wei (2018), (3) is from Santosh et al. (2012) and (4) is from Yang et al. (2014).

All samples in this study contain rutile, although the grain size and volume percentage vary. For example, five samples from south of Heling'er (samples 20HL49, 20HL59, 20HL64, 20HL73, and 20HL89) contain few tiny rutile. A study suggested that fluid remains saturated with respect to rutile once the fluid is rutile-saturated, and subsequent rutile growth is not sufficient to drive the liquid to rutile-undersaturation (Acosta et al., 2020). Although the absence of rutile does not necessarily imply quartz growth from a rutile-undersaturated liquid, researcher interpreted it as a liquid that was near saturation but below the critical supersaturation required to nucleate new rutile crystals (Acosta et al., 2020). Because of the aforementioned reasons, we used a TiO_2 activity of 1 for all samples.

TitaniQ temperature mapping was conducted using ArcGIS with the inverse distance weighted interpolation method.

RESULT

Quartz Ti Concentrations and Temperatures by TitaniQ

A total of 463 spots were analyzed in 44 samples. Analyses with unacceptable total SiO_2 content (>105 or <95) were discarded. We finally obtained 417 valid data points (**Supplementary Tables S1, S2**), among which 182 were quartz inclusions within garnet from 42 samples (**Supplementary Table S1**), and 235 were of matrix-type quartz from 43 samples (**Supplementary Table S2**).

Within quartz inclusions of garnet, Ti concentrations range from 40 to 550 ppm. We calculated the average Ti concentrations for each sample, which range from 58 to 420 ppm, and four data points of extremely high Ti concentrations far from the others within several samples (samples 20HL34, 20HL59, 20HL64, and 09TGS01) were not included and regarded as outlier data (**Figure 3A**). Temperatures calculated by the TitaniQ thermometer for these quartz average Ti concentrations range from 654°C (sample 20HL89) to 891°C (sample 18LC01), all below UHT conditions (**Figure 4A**). The maximum Ti concentrations of each sample range from 65 to 550 ppm, the corresponding TitaniQ temperatures range from 665 to 934°C, and the highest temperatures are from samples in the Liangcheng and Zhuozi areas (**Figure 4B**).

Within matrix-type quartz, Ti concentrations range from 30 to 1,000 ppm. The calculated average Ti concentrations for each sample, range from 100 to 528 ppm, and six data points of extremely high Ti concentrations far from the others within several samples (i.e., samples 18ZZ01, 20HL104, 18TG01, 18TG04, and 09XH32) were not included, and were regarded as outlier data (**Figure 4C**). Temperatures calculated by the TitaniQ thermometer for these quartz average Ti concentrations range from 685 to 917°C (**Figure 4D**), and some of them have recorded UHT metamorphic conditions. The maximum Ti concentrations of each sample range from 156 to 680 ppm (**Figure 4C**), and the corresponding TitaniQ temperatures are 760–970°C, and the highest temperatures are also from samples in the Liangcheng and Zhuozi areas (**Figure 4D**).

We compared the difference in average Ti concentrations between the matrix-type quartz and quartz inclusions for each sample, without considering the outlier data (**Figure 5A**). The matrix-type quartz contains Ti concentrations <180 ppm higher than that of quartz inclusions, and only five samples show an inverse trend (**Figure 5A**). Therefore, the temperature calculated for the matrix-type quartz is generally <120°C higher than that of quartz inclusions (**Figure 5B**).

We also compared the difference in maximum Ti concentrations between the matrix-type quartz and quartz inclusions for each sample, without considering the outlier data (**Figure 5C**). The matrix-type quartz also contains Ti concentrations <300 ppm higher than that of quartz inclusions. The temperature calculated for matrix-type quartz is generally <160°C higher than that of quartz inclusions (**Figure 5D**).

Quartz Internal Structures

The CL images revealed types of quartz internal structures not observed in the photomicrographs. We divided quartz according to internal structure into four types: 1) Non-structure with homogeneous luminescence, 2) linear structure with low luminescence, 3) sealed fractures, and 4) reticular structures.

The non-structure with homogeneous luminescence is the simplest CL image in our samples and displays uniform luminescence without a special structure (**Figure 6**). It is more common in quartz inclusions than in matrix-type quartz. Quartz inclusions with non-structure contain low Ti concentrations, generally 100–200 ppm, and TitaniQ temperatures are 700–800°C (**Figures 6A,B**). Matrix-type quartz with non-structure has different Ti concentrations, which could be as low as 225 ppm with a TitaniQ temperature of 805°C

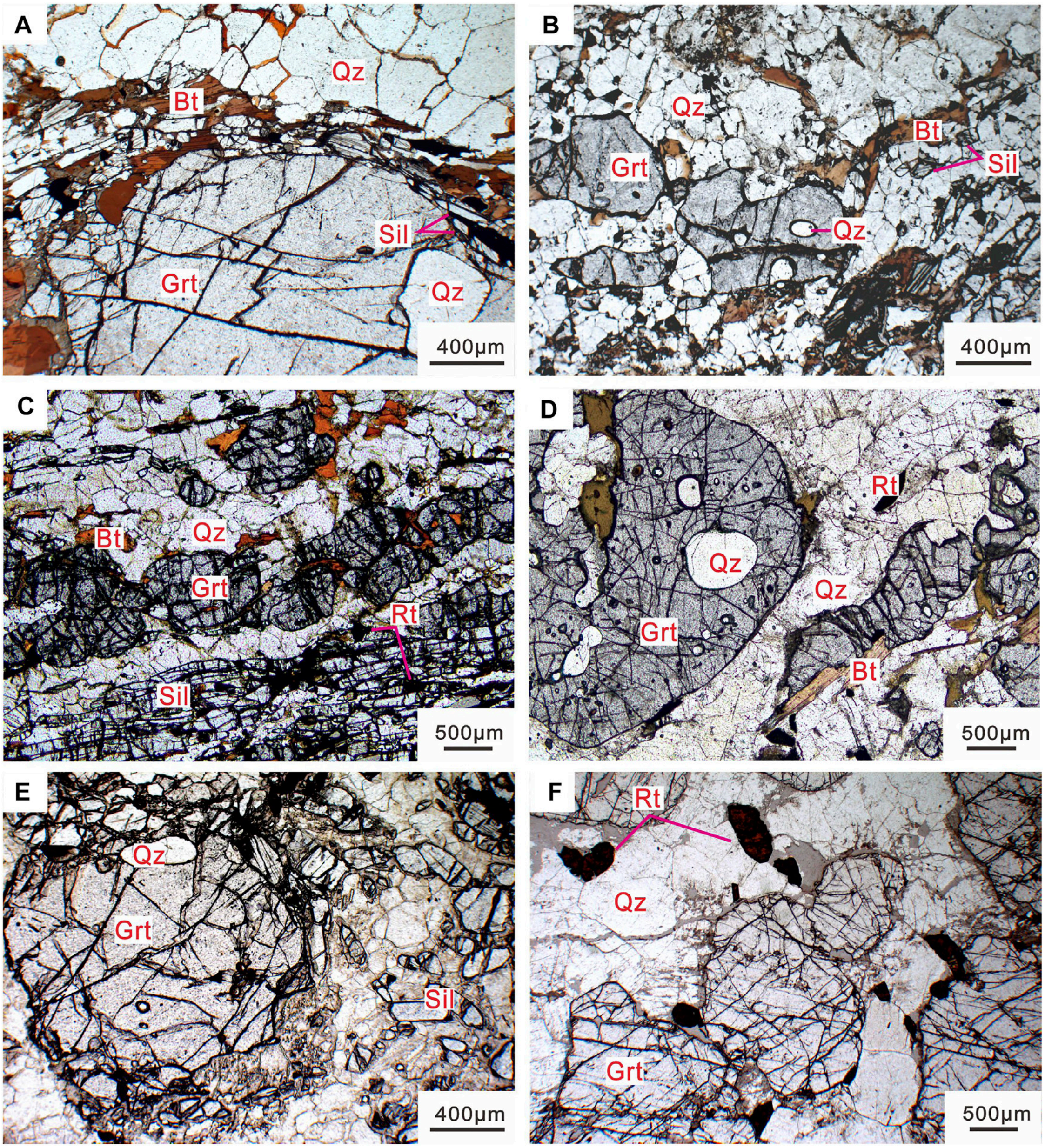

FIGURE 3 | Photomicrographs showing the typical mineral assemblages and quartz micro-textures of samples from the eastern Khondalite Belt, North China Craton. **(A)** Quartz occurs as inclusions in rims of coarse-grained garnet, and in the matrix from Grt-Sil-Bt gneiss (sample 20HL64); **(B)** Quartz is included by fine-grained garnet and occurs in the matrix from Grt-Sil-Bt gneiss (sample 20HL39); **(C)** Quartz occurs in the matrix from fine-grained Grt-Sil-Bt gneiss (sample 20HL19), the oriented arrangement of sillimanite defines the foliation; **(D)** Quartz occurs as inclusions in rims of coarse-grained garnet, and in the matrix from Grt-Bt gneiss/granulite (sample 18LC21), with rutile in the matrix; **(E)** Quartz occurs as inclusions in rim of coarse-grained garnet, and in the matrix from Grt-Sil gneiss (sample 20HL123); **(F)** Garnet occurs as porphyroblast with quartz and rutile in the matrix from garnet-bearing gneiss/granulite (sample 09XH21). Mineral abbreviations follow Warr (2021).

(**Figure 6D**) and as high as 490 ppm with a TitaniQ temperature of 917°C (**Figure 6F**).

A linear structure with low luminescence occurs in both quartz inclusions and matrix-type quartz (**Figure 7**). These dark linearities within quartz generally correspond to the rutile needles shown in the photomicrographs. Rutile is rare and barely visible under photomicrographs but distinct in CL images. The occurrence of rutile needles is more common in quartz inclusions than in matrix-type quartz but generally occurs in the cores of the grains. Quartz Ti concentrations within rutile needle-rich domains are commonly high (>250 ppm), and the corresponding temperatures are >820°C (**Figure 7**).

Healed fractures characterized by healed microcracks and dark patches occur in both quartz inclusions and matrix-type quartz (**Figure 8**). The dark patches grew around and extended along the cracks. Healed fractures generally occur simultaneously with

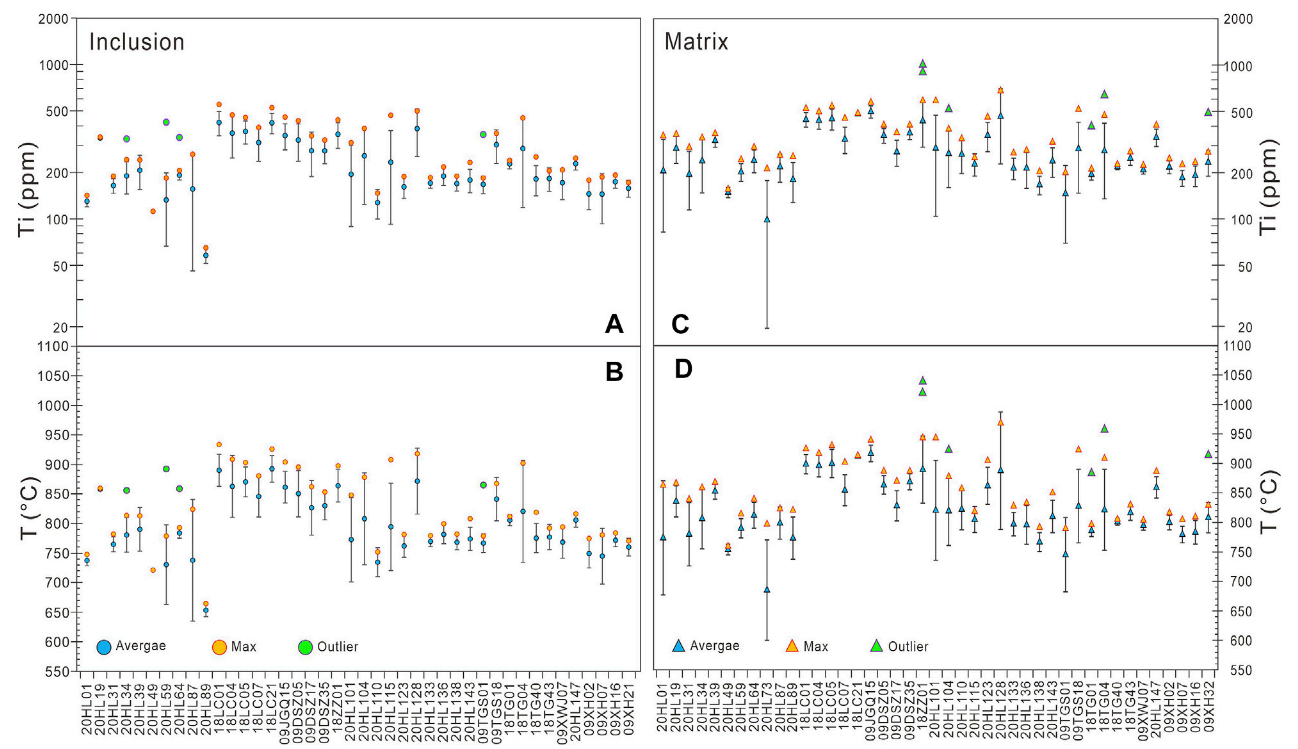

FIGURE 4 | The titanium concentrations of quartz and the calculated temperatures by TitaniQ thermometer in Grt-Sil-Bt and Grt-Bt gneisses (or granulites) from the eastern Khondalite Belt. **(A,B)** The titanium concentrations of quartz inclusions in garnet and the calculated temperatures. **(C,D)** The titanium concentrations of matrix-type quartz and the calculated temperatures. We have three series of data: the average data, the maximum data and the outlier data. The average concentration of titanium and the temperature were calculated without the outlier data. The temperatures were calculated at pressure = 8 kbar and a_{TiO2} = 1. The error is 1SD of the dataset in each sample. The TitaniQ model we used here was calibrated by Thomas et al. (2010).

rutile needles (i.e., linear structures with low luminescence). Thus, quartz with healed fractures also has high Ti concentrations of >200 ppm and corresponding temperatures of >790°C (**Figures 8B,D**).

Reticular structures only occur in a few quartz grains (**Figure 9**). An irregular pattern of differential CL forms an enigmatic reticular microstructure. It is likely that a large single quartz crystal with bright luminescence is separated by dark stringers into numerous sub-crystals. However, this structure occurs differently in quartz inclusions and matrix-type quartz; in the former, the dark stringers are relatively blurry and disappear in the rim of the grain (**Figure 9B**). By contrast, the stringers are more fully developed in the matrix-type quartz (**Figure 9D**). Quartz grains with this internal structure generally contain low Ti concentrations of <250 ppm and corresponding temperatures of <820°C (**Figure 9**).

DISCUSSION

Multi-Stage Quartz Formation/Alteration During Metamorphism

Studies have constrained the metamorphic age and *P*–*T* path of aluminous gneisses/granulites in the eastern Khondalite Belt. Zircon U-Pb dating and detailed petrological investigations in combination with phase equilibria modeling have constrained the timing of UHT metamorphism at 1.94–1.80 Ga, following the prior HP metamorphism (Santosh et al., 2007b; Jiao et al., 2013b; Li and Wei, 2016). The *P*–*T* paths involved post-peak cooling and decompression stages, although the prograde stages were variable (**Figure 2**; Santosh et al., 2007a; Santosh et al., 2012; Yang et al., 2014; Li and Wei, 2016; Li and Wei, 2018). We interpret the quartz formation based on the aforementioned metamorphic evolution history.

Quartz inclusions in garnet generally contain less Ti concentrations than matrix-type quartz, and the TitaniQ temperature is <160°C lower (**Figure 5**). This result suggests that the quartz inclusions probably grew during prograde metamorphism. Garnet may protect quartz inclusions from later resetting. However, quartz inclusions have a wide range of Ti concentrations, which may represent quartz inclusions that formed during different periods of prograde metamorphism, or are reset by later retrogression. Quartz inclusions with homogeneous luminescence CL images have low Ti concentrations, which may form at relatively low temperatures during the early prograde period, and others with rutile needles have high Ti concentrations and may form at relatively higher temperature conditions of the prograde metamorphism.

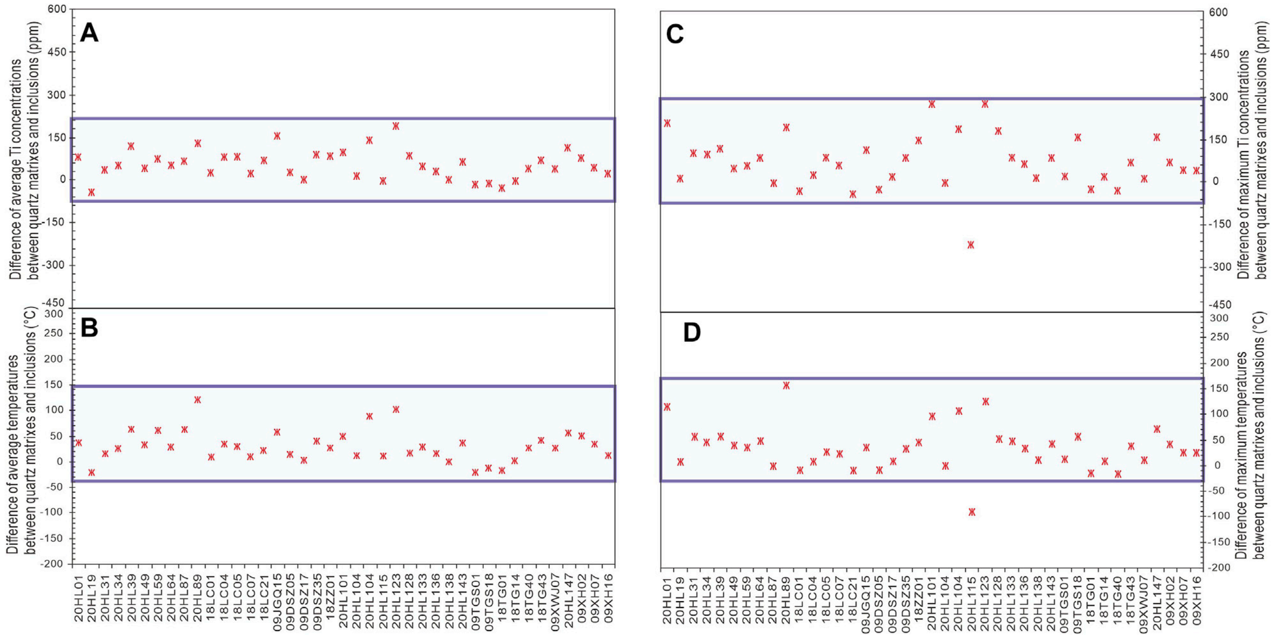

FIGURE 5 | Comparison of quartz titanium concentrations and the calculated temperatures by TitaniQ thermometer between matrix-type quartz and quartz inclusions in garnet. **(A)** Difference of the average quartz titanium concentrations between matrix-type quartz and quartz inclusions; **(B)** Difference of the average calculated temperatures between matrix-type quartz and quartz inclusions; **(C)** Difference between the maximum titanium concentrations between matrix-type quartz and quartz inclusions; **(D)** Difference between maximum calculated temperatures between matrix-type quartz and quartz inclusions; The *Y* axes are that Ti concentrations of quartz or calculated temperatures of matrix-type quartz minus those of quartz inclusions in garnet in each sample.

Matrix-type quartz was dominant in the studied rocks. The grains with homogeneous luminescence CL images and rutile needle structures that contain high Ti concentrations probably formed during the near-peak or early cooling stage. It was suggested that the high-temperature quartz that crystallized from the residual melt during early cooling is characterized by non-structure homogeneous luminescence CL (Storm and Spear, 2009).

The occurrence of rutile needles has been observed in Ti-rich quartz interiors of medium- to high-grade metamorphic rocks, such as quartz in migmatites and UHT metamorphic rocks (Cherniak et al., 2007; Sato and Santosh, 2007; Storm and Spear, 2009). Two mechanisms have been proposed to explain these features: 1) The entrapment of preexisting acicular rutile by growing quartz and 2) the exsolution of high-Ti quartz into low-Ti quartz and acicular rutile. In our samples, rutile needles are generally restricted to grain cores and are consistent with quartz crystallographic orientations, which strongly proves the second mechanism (Storm and Spear, 2009; Thomas and Nachlas, 2020). The dark "spots" in the CL images observed by Cherniak et al. (2007) were also interpreted as the feature of rutile exsolution during the post-peak cooling.

For both quartz inclusions and matrix-type quartz, especially the latter without garnet protection, some grains contain low Ti concentrations, which suggest the occurrence of later resetting. Healed fracture structures exist in both quartz inclusions and matrix-type quartz, which are similar to filled fractures in plutonic quartz and fluid-controlled quartz recovery in granulites (Seyedolali et al., 1997; Van den Kerkhof et al., 2004). Quartz first formed with non-healed fractures owing to the stresses imposed on the grains and decrepitation of fluid inclusions caused by the pressure difference between fluid inclusions and host quartz, probably by tectonic settings, such as uplift. Subsequently, the fractures were filled with secondary quartz or quartz nuclei by precipitation of non-luminescing SiO_2. Quartz with such structures commonly contains high Ti concentrations and yields high TitaniQ temperatures. Thus, we propose that quartz with such fractures within our samples grew or recrystallized during post-peak nearly isothermal decompression.

The occurrence of reticular structure in quartz is less common in our samples, and quartz with such structures contains relatively low Ti concentrations and accordingly records low TitaniQ temperatures. Many studies have verified a positive correlation between Ti concentrations in quartz and CL intensity (Sprunt et al., 1978; Müller et al., 2002; Spear and Wark, 2009). Thus, the Ti concentrations are heterogeneously distributed. Reticular zoning might indicate the pathway of fluid infiltration.

In summary, we posit that matrix-type quartz with extensive rutile exsolution most probably grew during the near-peak to the early cooling stage and can better constrain the near-peak conditions of the studied samples than inclusion-type quartz. Therefore, the variation in the maximum TitaniQ temperatures of matrix-type quartz in these samples can better show the thermal regime of the studied region.

Validity of the TitaniQ Thermometer

Another major question can be posed to interpret the meaning of TitaniQ temperature: *Can the matrix-type quartz that formed*

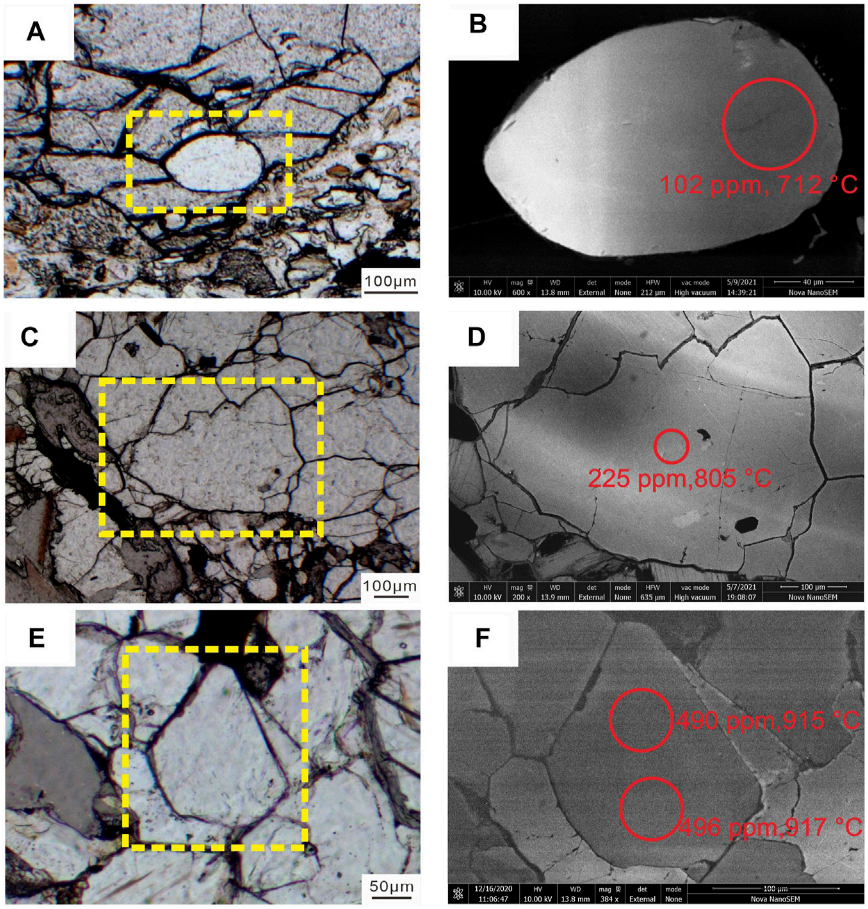

FIGURE 6 | Representative photomicrographs and CL images of the analyzed quartz grains showing non-structure with homogeneous luminescence. **(A)** Quartz inclusion within garnet rim in sample 20HL101, and CL image is shown in **(B)**; **(C,E)** Matrix-type quartz in samples 09XH07 and 09JGQ15, and CL images are shown in **(D,F)**, respectively. The red circle marks the analyzed EPMA spot.

during near-peak or early cooling preserve the original Ti concentrations? Mechanisms for quartz Ti re-equilibrium are diffusion (e.g., both lattice and grain boundary diffusion) and recrystallization during deformation and/or retrogression.

Experimental studies have shown that Ti diffusion is slow in quartz (Cherniak et al., 2007; Jollands et al., 2020). According to Cherniak et al. (2007), the diffusion distance of Ti-in-quartz is 0.05, 2, and 5 μm at 0.001, 1.0, and 10 Ma at 500°C. However, the diffusion distances increased to 16 μm, 500 μm, and 1,600 μm over the same time range at 800°C. Nevertheless, experiments under anhydrous conditions suggest that grain boundary diffusion is 3–4 orders of magnitude faster than lattice diffusion (Bromiley and Hiscock, 2016). Therefore, the grain boundary acts as an efficient conduit for Ti equilibrium, especially in fine-grained rocks. Studies have shown an increasing trend of Ti concentrations from the core toward the rim in quartz inclusions of garnet, interpreted as an exchange with the host garnet (Spear et al., 2012), but we did not recognize such features in our samples.

Many studies have suggested that dynamic recrystallization is an efficient mechanism for Ti re-equilibrium, especially fast grain boundary migration, which is crucial for Ti re-equilibrium at high temperatures (Stipp et al., 2002; Grujic et al., 2011). Generally, recrystallized quartz, which has well-developed facets impinging on the preliminary quartz, results in cuspate, serrated, and irregular grain boundaries of preliminary quartz (Thomas and Nachlas, 2020). Typical serrated boundaries from matrix-type quartz shown in **Figures 5C,D** suggest incomplete re-equilibration and would contain low Ti concentrations; thus, we did not select domains near the serrated boundaries for analysis.

Despite the aforementioned factors, the highest TitaniQ temperatures (ca. 960–970°C) are broadly consistent with the reported temperatures calculated by other methods in the studied region (Santosh et al., 2007a; Jiao et al., 2013a; Jiao et al., 2013b; Li and Wei, 2016; Li and Wei, 2018), for example, 966–1,096°C by a two-feldspar thermometer in Xuwujia, 850–1,000°C by a Zr-in-rutile thermometer in Tuiguishan, 940–1,030°C by Ti-in-zircon and a ternary feldspar thermometer in Nantianmen and Xiaonangou, ~975°C based on phase equilibria modeling in Xumayao, and 930–1,050°C by pseudosection in Hongsigou (Jiao et al., 2011; Jiao and Guo, 2011; Liu et al., 2012; Zhang et al., 2012; Yang et al., 2014). This result confirms the validity of the TitaniQ thermometer in

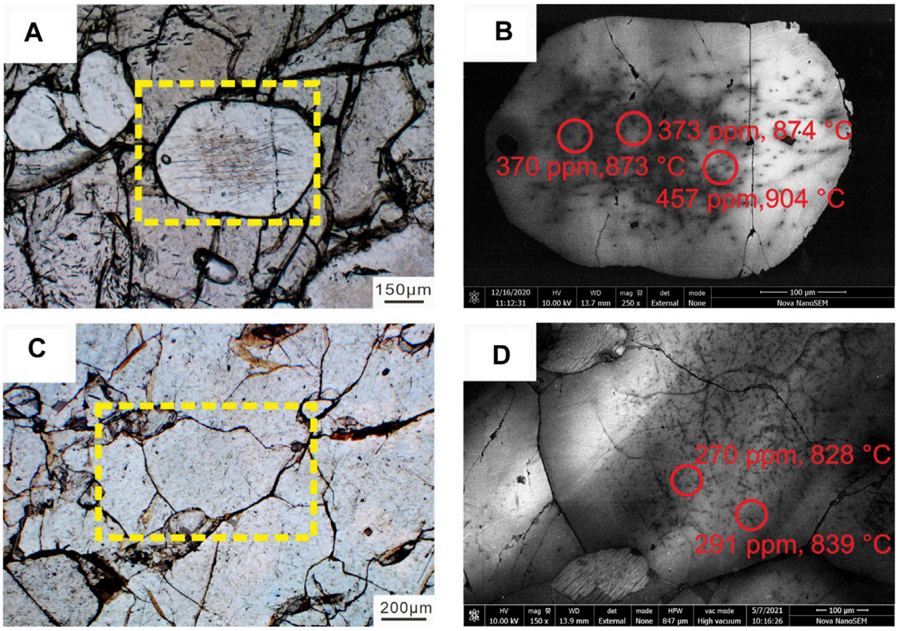

FIGURE 7 | Representative photomicrographs and CL images of the analyzed quartz grains showing linear structure with low luminescence. **(A)** Quartz inclusion within garnet in sample 09JGQ15 and CL image is shown in **(B)**; **(C)** Matrix-type quartz in sample 09DSZ17 and CL image is shown in **(D)**.

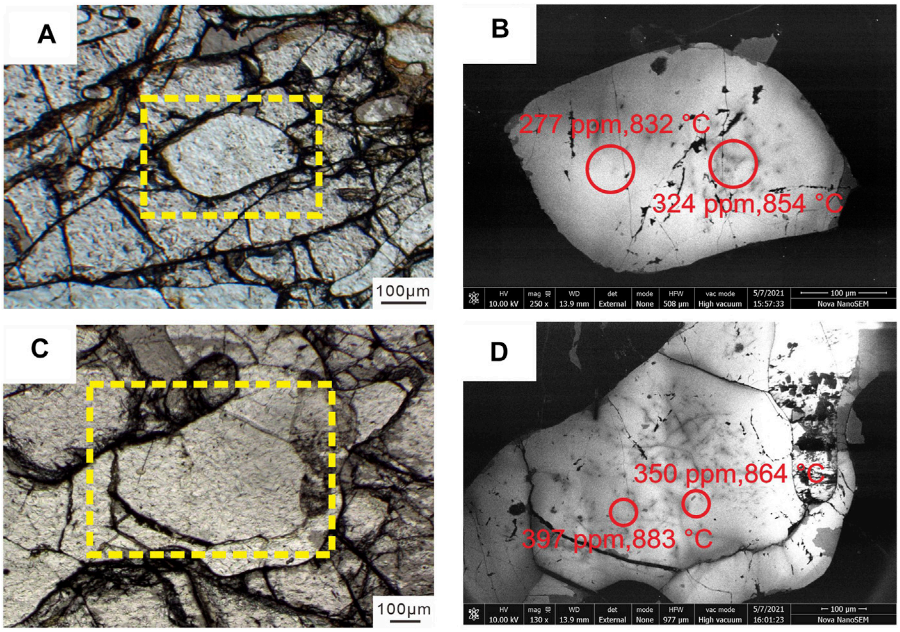

FIGURE 8 | Representative photomicrographs and CL images of the analyzed quartz grains showing healed fractures. **(A,C)** Quartz inclusion within garnet and matrix-type quartz both in sample 09DSZ35, and CL image is shown in **(B,D)**, respectively.

high-grade rocks, and TitaniQ temperatures may represent the minimum estimates of the peak temperatures.

Other possible influences on our calculated temperatures were 1) the pressure estimation, 2) the location of selected analytical spots, and 3) sample bias. We set a pressure of 8 kbar for all calculations in this study. Pressure at 1 kbar higher would result in a 30°C higher calculated temperature. The analyzed domains with abundant rutile needles contain higher Ti concentrations

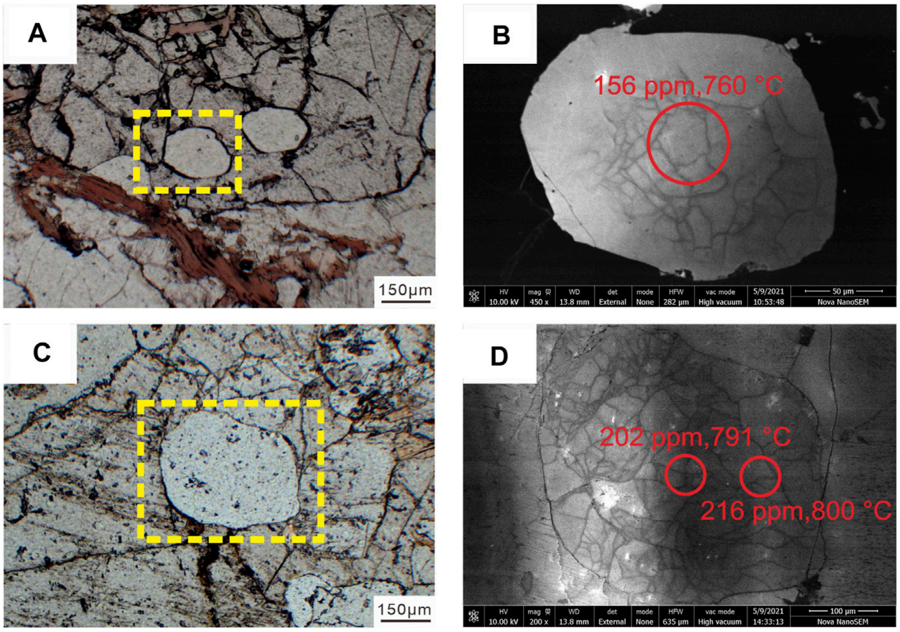

FIGURE 9 | Representative photomicrographs and CL images of the analyzed quartz grains showing reticular structure. **(A)** Quartz inclusion within garnet in sample 20HL59 and CL image is shown in **(B)**; **(C)** Matrix-type quartz in sample 20HL89 and CL image is shown in **(D)**.

than the domains without rutile needles; therefore, if any, we generally selected domains with the most abundant rutile needles for analysis. However, quartz and rutile have different crystal structure, which result in different characteristic X-ray efficiencies. This effect might influence the measured Ti concentrations. The EMP analytical spots are actually in two-dimension, which may underestimate the real volume percentage of rutile needles in quartz. Finally, we must acknowledge that in some samples we probably missed the quartz grain that contains the highest Ti concentrations, and in this case, the maximum TitaniQ temperatures for such samples would be underestimated.

Thermal Regime of the Eastern Khondalite Belt

In **Figure 10A**, the mapping is based on the temperature calculated from the maximum Ti concentrations of matrix-type quartz in each sample; for comparison, that in **Figure 10B** is based on the temperature calculated from the average Ti concentrations of matrix-type quartz in each sample. Sample localities are marked in the picture to show the distribution of the samples and the effect of sample bias.

Both temperature mapping results show that the large-scale and extremely hot regions are surrounded by Liangcheng, Heling'er, and Zhuozi. The maximum TitaniQ temperatures were >900°C, suggesting the occurrence of UHT metamorphism. This phenomenon is consistent with those of several UHT metamorphic localities reported in this area (e.g., Liu et al., 2012; Jiao et al., 2013a; Jiao et al., 2013b). This hottest area was also consistent with the region where extensive charnockite occurred (**Figure 1**). Our results also show that Tuguiwula area, where typical UHT granulites with diagnostic Spr + Qz and Opx + Sil + Qz mineral assemblages have been reported, are hot, but the scale of the hot region is limited and surrounded by a relatively cold region. It might imply that the surrounding area is probably located at a higher crustal level. Alternatively, it is noticed that we have not collected samples from Zhuozi to Jining and further to Tuguiwula because of the thick sediment cover. The variation of temperatures in this region is probably caused by sample bias. Therefore, it is also possible that the whole area of Heling'er-Liangcheng-Tuguiwula-Jining-Zhuozi have experienced UHT metamorphism. It requires confirmation in future research.

In contrast, the Youyu and Xinghe areas are not as hot as the Liangcheng-Heling'er-Zhuozi area, although the major mineral assemblages are mostly the same. The maximum TitaniQ temperature is below 900°C, implying that these two areas probably do not experience UHT metamorphism. Alternatively, the analyzed quartz probably crystallized during the later stage of post-peak cooling. Quartz from these areas generally shows a non-structure with homogeneous luminescence structures, and rutile needles cannot be observed.

The thermal regime of the eastern Khondalite Belt, established by the TitaniQ thermometer in this case, is consistent with the results of another independent study using Zr-in-rutile thermometry mapping (Qi et al., unpublished). This particular case study further confirms the validity of the TitaniQ thermometer in recognizing UHT metamorphism and constraining its thermal conditions and spatial scales.

Several models have been proposed to interpret the formation of UHT metamorphism in the eastern Khondalite Belt, including radiogenic heat production (Jiao et al., 2013a), post-collisional

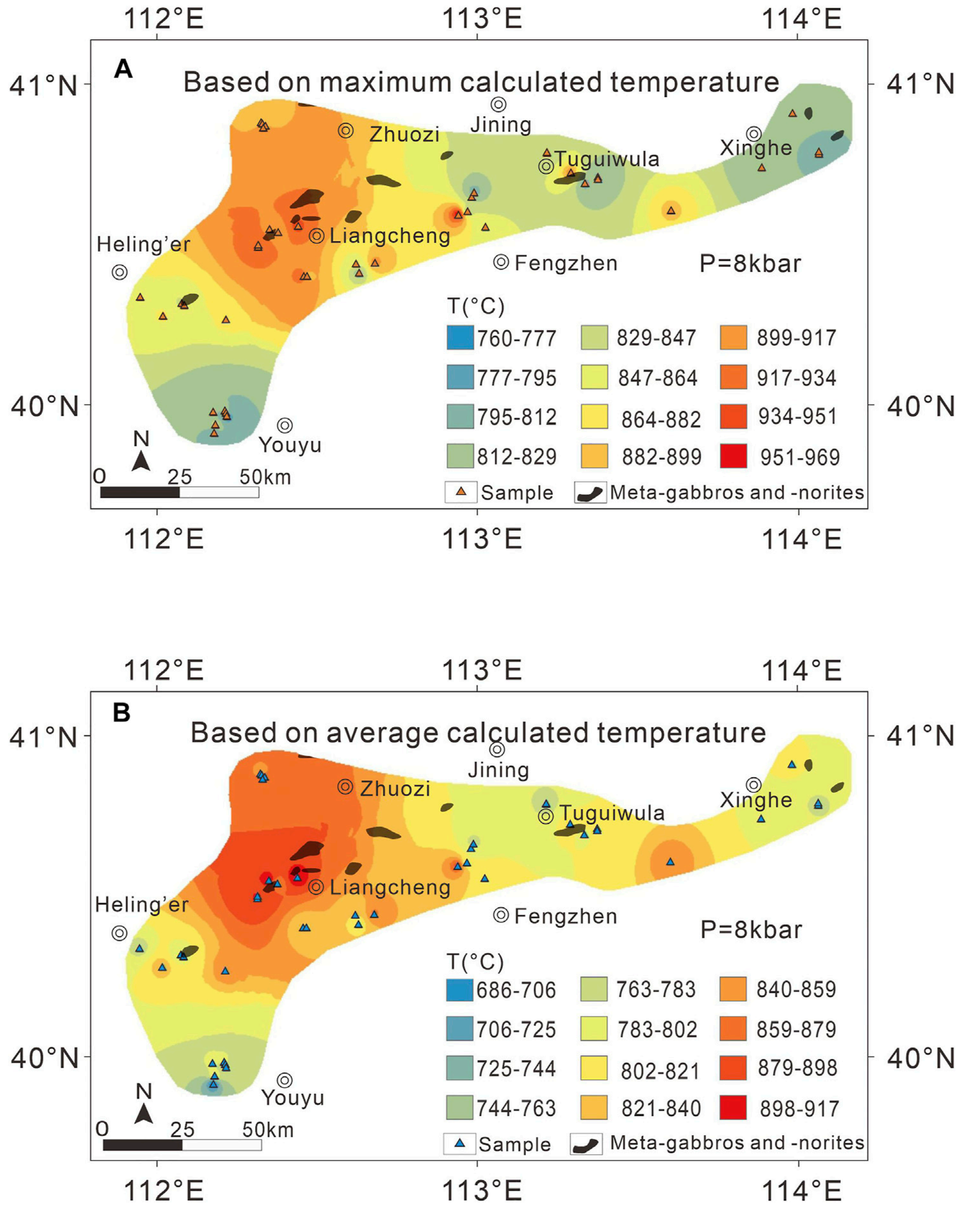

FIGURE 10 | The thermal regime of the lower crust of the eastern Khondalite Belt, North China Craton, constrained by TitaniQ thermometer in this study. **(A)** Metamorphic temperature mapping with the maximum calculated temperatures of matrix-type quartz. **(B)** Metamorphic temperature mapping with the average calculated temperatures of matrix-type quartz. The mapping was conducted by ArcGIS, with inverse distance weighted (IDW) method. Sample localities are marked as triangle labels.

lithosphere extension due to asthenospheric upwelling (Zhao, 2009; Li and Wei, 2018; Jiao et al., 2021), ridge subduction (Santosh and Kusky, 2009; Peng et al., 2011; Santosh et al., 2012), mantle plume (Santosh et al., 2008), and emplacement of mantle-derived mafic magma (Huang et al., 2019). In addition, a back-arc setting has also been proposed to explain UHT metamorphism in other regions (Brown, 2006; Brown and Johnson, 2018). Our study certifies the regional distribution of UHT metamorphism in the eastern Khondalite Belt, and the large-scale hottest region is the Liangcheng-Heling'er-Zhuozi area, which is consistent with the occurrence of extensive charnockite. This result implies that the formation of UHT metamorphism is closely related to charnockite. This extremely hot metamorphism and magmatism might be the coupling effect of the same mechanism, which probably formed in the root of a Paleoproterozoic large hot orogeny. However, we could not distinguish these UHT formation models in this study, and the potential model should be able to explain the spatially close relationship between UHT metamorphism and charnockite.

CONCLUSION

In this study, we first applied TitaniQ thermometer to 44 aluminous gneisses/granulites in the Paleoproterozoic eastern Khondalite Belt, collected from an area of ~10,000 km^2. Our results show that matrix-type quartz with substantial rutile exsolution generally yielded the maximum TitaniQ temperatures, and that of quartz inclusions in garnet was <160°C lower. These results implied that quartz inclusions probably formed during the prograde metamorphism, and matrix-type rutile needle-rich quartz formed during the near-peak to early cooling stages. The temperature mapping result based on the maximum TitaniQ temperatures of matrix-type quartz indicates that the hottest Paleoproterozoic lower crust is beneath the Liangcheng-Heling'er-Zhuozi area, where UHT metamorphism is closely associated with abundant charnockite. This region may represent the root of an ancient large hot orogeny.

DATA AVAILABILITY STATEMENT

The original contributions presented in the study are included in the article/**Supplementary Material**, further inquiries can be directed to the corresponding author.

AUTHOR CONTRIBUTIONS

SJ designed the research plan. SJ, YQ, and YZ went to the fieldtrip and collected the samples. DZ and YZ analyzed the samples. YZ wrote the original manuscript. All authors revised the manuscript.

FUNDING

Funding came from the National Natural Science Foundation of China (NSFC; No. 41890832, 42122018 and 41672189), the Youth Innovation Promotion Association of the Chinese Academy of Sciences (CAS; No. 2018089).

ACKNOWLEDGMENTS

We thank Qian Mao for EPMA analysis. We appreciate constructive comments from CWO and SY.

SUPPLEMENTARY MATERIAL

The Supplementary Material for this article can be found online at: https://www.frontiersin.org/articles/10.3389/feart.2022.860057/full#supplementary-material

REFERENCES

Acosta, M. D., Watkins, J. M., Reed, M. H., Donovan, J. J., and DePaolo, D. J. (2020). Ti-in-quartz: Evaluating the Role of Kinetics in High Temperature crystal Growth Experiments. *Geochimica et Cosmochimica Acta* 281, 149–167. doi:10.1016/j.gca.2020.04.030

Audétat, A., Garbe-Schönberg, D., Kronz, A., Pettke, T., Rusk, B., Donovan, J. J., et al. (2015). Characterisation of a Natural Quartz crystal as a Reference Material for Microanalytical Determination of Ti, Al, Li, Fe, Mn, Ga and Ge. *Geostand Geoanal Res.* 39 (2), 171–184. doi:10.1111/j.1751-908X.2014.00309.x

Bromiley, G. D., and Hiscock, M. (2016). Grain Boundary Diffusion of Titanium in Polycrystalline Quartz and its Implications for Titanium in Quartz (TitaniQ) Geothermobarometry. *Geochimica et Cosmochimica Acta* 178, 281–290. doi:10.1016/j.gca.2016.01.024

Brown, M. (2006). Duality of thermal Regimes Is the Distinctive Characteristic of Plate Tectonics since the Neoarchean. *Geol.* 34 (11), 961–964. doi:10.1130/G22853A.1

Brown, M., and Johnson, T. (2018). Secular Change in Metamorphism and the Onset of Global Plate Tectonics. *Am. Mineral.* 103 (2), 181–196. doi:10.2138/am-2018-6166

Cherniak, D. J., Watson, E. B., and Wark, D. A. (2007). Ti Diffusion in Quartz. *Chem. Geology* 236 (1–2), 65–74. doi:10.1016/j.chemgeo.2006.09.001

Dan, W., Li, X.-H., Guo, J., Liu, Y., and Wang, X.-C. (2012). Integrated *In Situ* Zircon U-Pb Age and Hf-O Isotopes for the Helanshan Khondalites in North China Craton: Juvenile Crustal Materials Deposited in Active or Passive continental Margin? *Precambrian Res.* 222-223, 143–158. doi:10.1016/j.precamres.2011.07.016

Geng, Y., Du, L., and Ren, L. (2012). Growth and Reworking of the Early Precambrian continental Crust in the North China Craton: Constraints from Zircon Hf Isotopes. *Gondwana Res.* 21, 517–529. doi:10.1016/j.gr.2011.07.006

Ghent, E. D., and Stout, M. Z. (1984). TiO2 Activity in Metamorphosed Pelitic and Basic Rocks: Principles and Applications to Metamorphism in southeastern Canadian Cordillera. *Contr. Mineral. Petrol.* 86 (3), 248–255. doi:10.1007/BF00373670

Gou, L., Li, Z., Liu, X., Dong, Y., Zhao, J., Zhang, C., et al. (2018). Ultrahigh-temperature Metamorphism in the Helanshan Complex of the Khondalite Belt, North China Craton: Petrology and Phase Equilibria of Spinel-Bearing Pelitic Granulites. *J. Metamorph Geol.* 36, 1199. doi:10.1111/jmg.12442

Grujic, D., Stipp, M., and Wooden, J. (2011). Thermometry of Quartz Mylonites: Importance of Dynamic Recrystallization on Ti-in-quartz Reequilibration. *Geochem. Geophys. Geosys.* 12. doi:10.1029/2010GC003368

Guo, J., Peng, P., Chen, Y., Jiao, S., and Windley, B. F. (2012). UHT Sapphirine Granulite Metamorphism at 1.93-1.92Ga Caused by Gabbronorite Intrusions: Implications for Tectonic Evolution of the Northern Margin of the North China Craton. *Precambrian Res.* 222-223, 124–142. doi:10.1016/j.precamres.2011.07.020

Harley, S. L. (1998). On the Occurrence and Characterization of Ultrahigh-Temperature Crustal Metamorphism. *Geol. Soc. Lond. Spec. Publications* 138, 81–107. doi:10.1144/GSL.SP.1996.138.01.06

Harley, S. L. (2008). Refining the P-T Records of UHT Crustal Metamorphism. *J. Metamorph Geol.* 26, 125–154. doi:10.1111/j.1525-1314.2008.00765.x

Hayden, L. A., and Watson, E. B. (2007). Rutile Saturation in Hydrous Siliceous Melts and its Bearing on Ti-Thermometry of Quartz and Zircon. *Earth Planet. Sci. Lett.* 258 (3–4), 561–568. doi:10.1016/j.epsl.2007.04.020

Hildreth, W., and Wilson, C. J. N. (2007). Compositional Zoning of the Bishop Tuff. *J. Petrol.* 48 (5), 951–999. doi:10.1093/petrology/egm007

Huang, G., Guo, J., Jiao, S., and Palin, R. (2019). What Drives the Continental Crust to Be Extremely Hot So Quickly? *J. Geophys. Res. Solid Earth* 124 (11), 11218–11231. doi:10.1029/2019JB017840

Huang, R., and Audétat, A. (2012). The Titanium-In-Quartz (TitaniQ) Thermobarometer: A Critical Examination and Re-calibration. *Geochimica et Cosmochimica Acta* 84, 75–89. doi:10.1016/j.gca.2012.01.009

Jiang, X., Yu, S., Liu, Y., Li, S., Lv, P., Peng, Y., et al. (2022). Episodic Metamorphism and Anatexis within the Khondakite Belt, North China Craton: Constraint from Late-Paleoproterozoic Fluid-Fluxed Melting of the Daqingshan Complex. *Precambrian Res.* 369, 106504. doi:10.1016/j.precamres.2021.106504

Jiao, S.-J., Guo, J.-H., Wang, L.-J., and Peng, P. (2015). Short-lived High-Temperature Prograde and Retrograde Metamorphism in Shaerqin Sapphirine-Bearing Metapelites from the Daqingshan Terrane, North China Craton. *Precambrian Res.* 269, 31–57. doi:10.1016/j.precamres.2015.08.002

Jiao, S., Evans, N. J., Guo, J., Fitzsimons, I. C. W., Zi, J.-W., and McDonald, B. J. (2021). Establishing the P-T Path of UHT Granulites by Geochemically Distinguishing Peritectic from Retrograde Garnet. *Am. Mineral.* 106, 1640–1653. doi:10.2138/am-2021-7681

Jiao, S., Fitzsimons, I. C. W., Zi, J.-W., Evans, N. J., Mcdonald, B. J., and Guo, J. (2020). Texturally Controlled U-Th-Pb Monazite Geochronology Reveals Paleoproterozoic UHT Metamorphic Evolution in the Khondalite Belt, North China Craton. *J. Petrol.* 61 (1), egaa023. doi:10.1093/petrology/egaa023

Jiao, S., and Guo, J. (2011). Application of the Two-Feldspar Geothermometer to Ultrahigh-Temperature (UHT) Rocks in the Khondalite belt, North China Craton and its Implications. *Am. Mineral.* 96 (2–3), 250–260. doi:10.2138/am.2011.3500

Jiao, S., Guo, J., Harley, S. L., and Peng, P. (2013a). Geochronology and Trace Element Geochemistry of Zircon, Monazite and Garnet from the Garnetite And/or Associated Other High-Grade Rocks: Implications for Palaeoproterozoic Tectonothermal Evolution of the Khondalite Belt, North China Craton. *Precambrian Res.* 237, 78–100. doi:10.1016/j.precamres.2013.09.008

Jiao, S., Guo, J., Harley, S. L., and Windley, B. F. (2013b). New Constraints from Garnetite on the P-T Path of the Khondalite Belt: Implications for the Tectonic Evolution of the North China Craton. *J. Petrol.* 54 (9), 1725–1758. doi:10.1093/petrology/egt029

Jiao, S., Guo, J., Mao, Q., and Zhao, R. (2011). Application of Zr-In-Rutile Thermometry: a Case Study from Ultrahigh-Temperature Granulites of the Khondalite belt, North China Craton. *Contrib. Mineral. Petrol.* 162 (2), 379–393. doi:10.1007/s00410-010-0602-3

Jiao, S., and Guo, J. (2020). Paleoproterozoic UHT Metamorphism with Isobaric Cooling (IBC) Followed by Decompression-Heating in the Khondalite Belt (North China Craton): New Evidence from Two Sapphirine Formation Processes. *J. Metamorph Geol.* 38 (4), 357–378. doi:10.1111/jmg.12525

Jollands, M. C., Bloch, E., and Müntener, O. (2020). New Ti-in-Quartz Diffusivities Reconcile Natural Ti Zoning with Time Scales and Temperatures of Upper Crustal Magma Reservoirs. *Geology* 48, 654–657. doi:10.1130/G47238.1

Kendrick, J., and Indares, A. (2018). The Ti Record of Quartz in Anatectic Aluminous Granulites. *J. Petrol.* 59 (8), 1493–1516. doi:10.1093/petrology/egy070

Kidder, S., Avouac, J.-P., and Chan, Y.-C. (2013). Application of Titanium-In-Quartz Thermobarometry to Greenschist Facies Veins and Recrystallized Quartzites in the Hsüehshan Range, Taiwan. *Solid Earth* 4 (1), 1–21. doi:10.5194/se-4-1-2013

Kularatne, K., and Audétat, A. (2014). Rutile Solubility in Hydrous Rhyolite Melts at 750-900°C and 2kbar, with Application to Titanium-In-Quartz (TitaniQ) Thermobarometry. *Geochimica et Cosmochimica Acta* 125, 196–209. doi:10.1016/j.gca.2013.10.020

Li, X., and Wei, C. (2018). Ultrahigh-temperature Metamorphism in the Tuguiwula Area, Khondalite Belt, North China Craton. *J. Metamorph. Geol.* 36 (4), 489–509. doi:10.1111/jmg.12301

Li, X. W., and Wei, C. J. (2016). Phase Equilibria Modelling and Zircon Age Dating of Pelitic Granulites in Zhaojiayao, from the Jining Group of the Khondalite Belt, North China Craton. *J. Metamorph. Geol.* 34 (6), 595–615. doi:10.1111/jmg.12195

Liu, D. Y., Nutman, A. P., Compston, W., Wu, J. S., and Shen, Q. H. (1992). Remnants of ≥3800 Ma Crust in the Chinese Part of the Sino-Korean Craton. *Geol.* 20 (4), 339–342. doi:10.1130/0091-7613(1992)020<0339:romcit>2.3.co;2

Liu, S. J., Li, J. H., and Santosh, M. (2010). First Application of the Revised Ti-In-Zircon Geothermometer to Paleoproterozoic Ultrahigh-Temperature Granulites of Tuguiwula, Inner Mongolia, North China Craton. *Contrib. Mineral. Petrol.* 159 (2), 225–235. doi:10.1007/s00410-009-0425-2

Liu, S., Tsunogae, T., Li, W., Shimizu, H., Santosh, M., Wan, Y., et al. (2012). Paleoproterozoic Granulites from Heling'er: Implications for Regional Ultrahigh-Temperature Metamorphism in the North China Craton. *Lithos* 148, 54–70. doi:10.1016/j.lithos.2012.05.024

Merlet, C. (1994). An Accurate Computer Correction Program for Quantitative Electron Probe Microanalysis. *Mikrochim Acta* 114-115, 363–376. doi:10.1007/BF01244563

Müller, A., Lennox, P., and Trzebski, R. (2002). Cathodoluminescence and Micro-structural Evidence for Crystallisation and Deformation Processes of Granites in the Eastern Lachlan Fold Belt (SE Australia). *Contrib. Mineral. Petrol.* 143 (4), 510–524. doi:10.1007/s00410-002-0361-x

Ostapenko, G. T., Gamarnik, M. Y., Gorogotskaya, L. I., Kuznetsov, G. V., Tarashchan, A. N., and Timoshkova, L. P. (1987). Isomorphism of Titanium Substitution for Silicon in Quartz: Experimental Data. *Mineral. Zh* 9, 30–40.

Peng, P., Guo, J.-H., Windley, B. F., and Li, X.-H. (2011). Halaqin Volcano-Sedimentary Succession in the central-northern Margin of the North China Craton: Products of Late Paleoproterozoic ridge Subduction. *Precambrian Res.* 187, 165–180. doi:10.1016/j.precamres.2011.03.006

Peng, P., Guo, J. H., Windley, B. F., Liu, F., Chu, Z., and Zhai, M. G. (2012). Petrogenesis of Late Paleoproterozoic Liangcheng Charnockites and S-type Granites in the central-northern Margin of the North China Craton: Implications for ridge Subduction. *Precambrian Res.* 222-223, 107–123. doi:10.1016/j.precamres.2011.06.002

Peng, P., Guo, J., Zhai, M., and Bleeker, W. (2010). Paleoproterozoic Gabbronoritic and Granitic Magmatism in the Northern Margin of the North China Craton: Evidence of Crust-Mantle Interaction. *Precambrian Res.* 183, 635–659. doi:10.1016/j.precamres.2010.08.015

Sajeev, K., Osanai, Y., and Santosh, M. (2004). Ultrahigh-temperature Metamorphism Followed by Two-Stage Decompression of Garnet-Orthopyroxene-Sillimanite Granulites from Ganguvarpatti, Madurai Block, Southern India. *Contrib. Mineral. Petrol.* 148 (1), 29–46. doi:10.1007/s00410-004-0592-0

Santosh, M., and Kusky, T. (2010). Origin of Paired High Pressureâ€"ultrahigh-Temperature Orogens: a ridge Subduction and Slab Window Model. *Terra Nova* 22 (1), 35–42. doi:10.1111/j.1365-3121.2009.00914.x

Santosh, M., Liu, S. J., Tsunogae, T., and Li, J. H. (2012). Paleoproterozoic Ultrahigh-Temperature Granulites in the North China Craton: Implications for Tectonic Models on Extreme Crustal Metamorphism. *Precambrian Res.* 222-223 (223), 77–106. doi:10.1016/j.precamres.2011.05.003

Santosh, M., Sajeev, K., Li, J. H., and Liu, S. J. (2006). Extreme Crustal Metamorphism during Columbia Supercontinent Assembly: Evidence from North China Craton. *Gondwana Res.* 10 (3–4), 256–266. doi:10.1016/j.gr.2006.06.005

Santosh, M., Tsunogae, T., Li, J. H., and Liu, S. J. (2007a). Discovery of Sapphirine-Bearing Mg-Al Granulites in the North China Craton: Implications for Paleoproterozoic Ultrahigh Temperature Metamorphism. *Gondwana Res.* 11 (3), 263–285. doi:10.1016/j.gr.2006.10.009

Santosh, M., Tsunogae, T., Ohyama, H., Sato, K., Li, J. H., and Liu, S. J. (2008). Carbonic Metamorphism at Ultrahigh-Temperatures: Evidence from North China Craton. *Earth Planet. Sci. Lett.* 266 (1–2), 149–165. doi:10.1016/j.epsl.2007.10.058

Santosh, M., Wan, Y., Liu, D., Chunyan, D., and Li, J. (2009). Anatomy of Zircons from an Ultrahot Orogen: the Amalgamation of the North China Craton within the Supercontinent Columbia. *J. Geology* 117 (4), 429–443. doi:10.1086/598949

Santosh, M., Wilde, S., and Li, J. (2007b). Timing of Paleoproterozoic Ultrahigh-Temperature Metamorphism in the North China Craton: Evidence from SHRIMP U-Pb Zircon Geochronology. *Precambrian Res.* 159 (3–4), 178–196. doi:10.1016/j.precamres.2007.06.006

Sato, K., and Santosh, M. (2007). Titanium in Quartz as a Record of Ultrahigh-Temperature Metamorphism: the Granulites of Karur, Southern India. *Mineral. Mag.* 71 (2), 143–154. doi:10.1180/minmag.2007.071.2.143

Seyedolali, A., Krinsley, D. H., Boggs, S., Jr., O'Hara, P. F., Dypvik, H., and Goles, G. G. (1997). Provenance Interpretation of Quartz by Scanning Electron Microscope–Cathodoluminescence Fabric Analysis. *Geology* 25, 787–790. doi:10.1130/0091-7613(1997)025<0787:PIOQBS>2.3.CO;2

Shazia, J. R., Santosh, M., and Sajeev, K. (2012). Peraluminous Sapphirine-Cordierite Pods in Mg-Rich Orthopyroxene Granulite from Southern India: Implications for Lower Crustal Processes. *J. Asian Earth Sci.* 58, 88–97. doi:10.1016/j.jseaes.2012.06.020

Spear, F. S., Ashley, K. T., Webb, L. E., and Thomas, J. B. (2012). Ti Diffusion in Quartz Inclusions: Implications for Metamorphic Time Scales. *Contrib. Mineral. Petrol.* 164 (6), 977–986. doi:10.1007/s00410-012-0783-z

Spear, F. S., and Wark, D. A. (2009). Cathodoluminescence Imaging and Titanium Thermometry in Metamorphic Quartz. *J. Metamorphic Geology* 27 (3), 187–205. doi:10.1111/j.1525-1314.2009.00813.x

Sprunt, E. S., Dengler, L. A., and Sloan, D. (1978). Effects of Metamorphism on Quartz Cathodoluminescence. *Geol.* 6 (5), 305–308. doi:10.1130/0091-7613(1978)6<305:eomoqc>2.0.co;2

Stipp, M., Stünitz, H., Heilbronner, R., and Schmid, S. M. (2002). Dynamic Recrystallization of Quartz: Correlation between Natural and Experimental Conditions. *Geol. Soc. Lond. Spec. Publications* 200, 171–190. doi:10.1144/GSL.SP.2001.200.01.11

Storm, L. C., and Spear, F. S. (2009). Application of the Titanium-In-Quartz Thermometer to Pelitic Migmatites from the Adirondack Highlands, New York. *J. Metamorphic Geology* 27 (7), 479–494. doi:10.1111/j.1525-1314.2009.00829.x

Thomas, J. B., and Bruce Watson, E. (2012). Application of the Ti-in-quartz thermobarometer to rutile-free systems. Reply to: a comment on: 'TitaniQ under pressure: the effect of pressure and temperature on the solubility of Ti in quartz' by Thomas et al. *Contrib. Mineral. Petrol.* 164 (2), 369–374. doi:10.1007/s00410-012-0761-5

Thomas, J. B., Bruce Watson, E., Spear, F. S., Shemella, P. T., and Lanzirotti, S. K. A. (2010). TitaniQ under Pressure: the Effect of Pressure and Temperature on the Solubility of Ti in Quartz. *Contrib. Mineral. Petrol.* 160 (5), 743–759. doi:10.1007/s00410-010-0505-3

Thomas, J. B., and Nachlas, W. O. (2020). Discontinuous Precipitation of Rutilated Quartz: Grain-Boundary Migration Induced by Changes to the Equilibrium Solubility of Ti in Quartz. *Contrib. Mineral. Petrol.* 175 (4), 38. doi:10.1007/s00410-020-01676-2

Thomas, J. B., Watson, E. B., Spear, F. S., and Wark, D. A. (2015). TitaniQ Recrystallized: Experimental Confirmation of the Original Ti-in-Quartz Calibrations. *Contrib. Mineral. Petrol.* 169 (3), 27. doi:10.1007/s00410-015-1120-0

Tual, L., Möller, C., and Whitehouse, M. J. (2018). Tracking the Prograde P-T Path of Precambrian Eclogite Using Ti-in-Quartz and Zr-In-Rutile Geothermobarometry. *Contrib. Mineral. Petrol.* 173 (7), 56. doi:10.1007/s00410-018-1482-1

Van den Kerkhof, A. M., Kronz, A., Simon, K., and Scherer, T. (2004). Fluid-Controlled Quartz Recovery in Granulite as Revealed by Cathodoluminescence and Trace Element Analysis (Bamble Sector, Norway). *Contrib. Mineral. Petrol.* 146 (5), 637–652. doi:10.1007/s00410-003-0523-5

Wan, Y., Liu, D., Dong, C., Xu, Z., Wang, Z., Wilde, S. A., et al. (2009). The Precambrian Khondalite Belt in the Daqingshan Area, North China Craton: Evidence for Multiple Metamorphic Events in the Palaeoproterozoic Era. *Geol. Soc. Lond. Spec. Publications* 323, 73–97. doi:10.1144/SP323.4

Wan, Y., Liu, D., Song, B., Wu, J., Yang, C., Zhang, Z., et al. (2005). Geochemical and Nd Isotopic Compositions of 3.8Ga Meta-Quartz Dioritic and Trondhjemitic Rocks from the Anshan Area and Their Geological Significance. *J. Asian Earth Sci.* 24, 563–575. doi:10.1016/j.jseaes.2004.02.009

Wang, B., Wei, C.-J., Tian, W., and Fu, B. (2020). UHT Metamorphism Peaking Above 1100 °C with Slow Cooling: Insights from Pelitic Granulites in the Jining Complex, North China Craton. *J. Petrol.* 61, egaa070. doi:10.1093/petrology/egaa070

Wang, L.-J., Guo, J.-H., Yin, C., and Peng, P. (2017). Petrogenesis of Ca. 1.95 Ga Meta-Leucogranites from the Jining Complex in the Khondalite Belt, North China Craton: Water-Fluxed Melting of Metasedimentary Rocks. *Precambrian Res.* 303, 355–371. doi:10.1016/J.PRECAMRES.2017.04.036

Wang, L.-J., Guo, J.-H., Yin, C., Peng, P., Zhang, J., Spencer, C. J., et al. (2018). High-temperature S-type Granitoids (Charnockites) in the Jining Complex, North China Craton: Restite Entrainment and Hybridization with Mafic Magma. *Lithos* 320-321, 435–453. doi:10.1016/j.lithos.2018.09.035

Wark, D. A., and Watson, E. B. (2006). TitaniQ: a Titanium-In-Quartz Geothermometer. *Contrib. Mineral. Petrol.* 152 (6), 743–754. doi:10.1007/s00410-006-0132-1

Warr, L. N. (2021). Thousands of New and Improved mineral Symbols. *Nature* 598 (7882), 566. doi:10.1038/d41586-021-02884-x

Wu, F., Zhao, G., Wilde, S. A., and Sun, D. (2005). Nd Isotopic Constraints on Crustal Formation in the North China Craton. *J. Asian Earth Sci.* 24 (5), 523–545. doi:10.1016/j.jseaes.2003.10.011

Yang, Q.-Y., Santosh, M., and Tsunogae, T. (2014). Ultrahigh-temperature Metamorphism under Isobaric Heating: New Evidence from the North China Craton. *J. Asian Earth Sci.* 95, 2–16. doi:10.1016/j.jseaes.2014.01.018

Yin, C., Zhao, G., Guo, J., Sun, M., Xia, X., Zhou, X., et al. (2011). U-pb and Hf Isotopic Study of Zircons of the Helanshan Complex: Constrains on the Evolution of the Khondalite Belt in the Western Block of the North China Craton. *Lithos* 122 (1–2), 25–38. doi:10.1016/j.lithos.2010.11.010

Yin, C., Zhao, G., and Sun, M. (2015). High-pressure Pelitic Granulites from the Helanshan Complex in the Khondalite Belt, North China Craton: Metamorphic P-T Path and Tectonic Implications. *Am. J. Sci.* 315, 846–879. doi:10.2475/09.2015.03

Yin, C., Zhao, G., Sun, M., Xia, X., Wei, C., Zhou, X., et al. (2009). LA-ICP-MS U-Pb Zircon Ages of the Qianlishan Complex: Constrains on the Evolution of the Khondalite Belt in the Western Block of the North China Craton. *Precambrian Res.* 174, 78–94. doi:10.1016/j.precamres.2009.06.008

Zhai, M., and Peng, P. (2007). Paleoproterozoic Events in the North China Craton. *Acta Petrologica Sinica* 23, 2665–2682. (In Chinese with English Abstract).

Zhai, M. (2009). Two Kinds of Granulites (HT-HP and HT-UHT) in North China Craton: Their Genetic Relation and Geotectonic Implications. *Acta Petrologica Sinica* 25, 1753–1771. (In Chinese with English Abstract).

Zhang, C., Li, X., Almeev, R. R., Horn, I., Behrens, H., and Holtz, F. (2020). Ti-in-quartz Thermobarometry and TiO2 Solubility in Rhyolitic Melts: New Experiments and Parametrization. *Earth Planet. Sci. Lett.* 538, 116213. doi:10.1016/j.epsl.2020.116213

Zhang, H., Li, J., Liu, S., Li, W., Santosh, M., and Wang, H. (2012). Spinel + Quartz-Bearing Ultrahigh-Temperature Granulites from Xumayao, Inner Mongolia Suture Zone, North China Craton: Petrology, Phase Equilibria and Counterclockwise *P-T* Path. *Geosci. Front.* 3, 603–611. doi:10.1016/j.gsf.2012.01.003

Zhao, G., Li, S., Sun, M., and Wilde, S. A. (2011). Assembly, Accretion, and Break-Up of the Palaeo-Mesoproterozoic Columbia Supercontinent: Record in the North China Craton Revisited. *Int. Geology Rev.* 53 (11–12), 1331–1356. doi:10.1080/00206814.2010.527631

Zhao, G. (2009). Metamorphic Evolution of Major Tectonic Units in the Basement of the North China Craton: Key Issues and Discussion. *Acta Petrologica Sinica* 25, 1772–1792. (In Chinese with English Abstract).

Zhao, G., Sun, M., Wilde, S. A., and Li, S. (2003). Assembly, Accretion and Breakup of the Paleo-Mesoproterozoic Columbia Supercontinent: Records in the North China Craton. *Gondwana Res.* 6 (3), 417–434. doi:10.1016/S1342-937X(05)70996-5

Zhao, G., Sun, M., Wilde, S. A., and Sanzhong, L. (2005). Late Archean to Paleoproterozoic Evolution of the North China Craton: Key Issues Revisited. *Precambrian Res.* 136 (2), 177–202. doi:10.1016/j.precamres.2004.10.002

Zhao, G., Wilde, S. A., Cawood, P. A., and Lu, L. (1998). Thermal Evolution of Archean Basement Rocks from the Eastern Part of the North China Craton and its Bearing on Tectonic Setting. *Int. Geology Rev.* 40, 706–721. doi:10.1080/00206819809465233

Zhao, G., Wilde, S. A., Cawood, P. A., and Sun, M. (2001). Archean Blocks and Their Boundaries in the North China Craton: Lithological, Geochemical, Structural and P-T Path Constraints and Tectonic Evolution. *Precambrian Res.* 107 (1–2), 45–73. doi:10.1016/S0301-9268(00)00154-6

Zhou, X., Zhao, G., and Geng, Y. (2010). Helanshan High Pressure Politic Granulite: Petrologic Evidence for Collision Event in the Western Block of the North China Craton. *Acta Petrologica Sinica* 26, 2113–2121. (In Chinese with English abstract).

Conflict of Interest: The authors declare that the research was conducted in the absence of any commercial or financial relationships that could be construed as a potential conflict of interest.

frontiers
in Earth Science

ORIGINAL RESEARCH
published: 31 March 2022
doi: 10.3389/feart.2022.817682

Two Phases of Metamorphism in the High-Pressure Schists in Central Inner Mongolia, China: Implications for the Tectonic Transition From Terminal Subduction of the Paleo-Asian Ocean to Continental Collision

Jinrui Zhang[1], Shuang Tang[1], Chunjing Wei[2], Hang Chu[3], Wenliang Xu[1] and Ling Jiang[1]*

[1]School of Earth Sciences, Jilin University, Changchun, China, [2]School of Earth and Space Sciences, Peking University, Beijing, China, [3]Tianjin Institute of Geology and Mineral Resources, Tianjin, China

OPEN ACCESS

Edited by:
Yi Chen,
Chinese Academy of Sciences (CAS), China

Reviewed by:
Laixi Tong,
Northwest University, China
Jia Cai,
Chinese Academy of Geological Science, China

****Correspondence:***
Jinrui Zhang
jerryzhang@jlu.edu.cn

Specialty section:
This article was submitted to Petrology, a section of the journal Frontiers in Earth Science

Received: *18 November 2021*
Accepted: *25 February 2022*
Published: *31 March 2022*

Citation:
Zhang J, Tang S, Wei C, Chu H, Xu W and Jiang L (2022) Two Phases of Metamorphism in the High-Pressure Schists in Central Inner Mongolia, China: Implications for the Tectonic Transition From Terminal Subduction of the Paleo-Asian Ocean to Continental Collision.
Front. Earth Sci. 10:817682.
doi: 10.3389/feart.2022.817682

High-pressure (HP) rocks exhumed from subduction zones usually record much warmer geotherms than numerical modelling results, as their peak mineral assemblages are always modified during the exhumation process. The decompressional metamorphic evolution of HP rocks should be considered carefully if using their P–T records to constrain the thermal structure of a subduction zone. The Ondor Sum Group, known as mélanges containing various high P/T metamorphic rocks in central Inner Mongolia, represents a fragment of subducted oceanic crust in the Early Paleozoic, However, the thermal structure of the subduction zone is unavailable due to an absence of exhumed HP rocks with P–T estimates. In this study, the HP schists were newly discovered in the Ondor Sum Group at Airgin Sum in the central Inner Mongolia. The HP schists include a garnet–phengite schist (sample EL01) and a garnet–amphibole schist (sample EL08). The petrography of these rocks and phase equilibrium modelling using THERMOCALC suggest two phases of metamorphism, both of which are characterized by clockwise P–T evolutions involving pre-peak prograde stage, peak-stage, and post-peak decompression stage. The peak P–T conditions of the early-phase metamorphism are constrained by P–T pseudosections to be ~18 kbar/~535°C for sample EL01 and 18 kbar/~500°C for sample EL08. The peak P–T conditions of the late-phase metamorphism are constrained by P–T pseudosections to be ~8 kbar/532°C in EL01 and ~7.0 kbar/495°C in EL08. Available U–Pb data of zircons from the HP schists and a granodiorite vein using LA–ICP–MS constrain the timing of early-phase HP metamorphism in the early Paleozoic and the late-phase metamorphism supposed to be in the Devonian based on the previous reported ages. The peak P–T conditions for the early-phase metamorphism were high-P/T conditions with a thermal gradient of ~8°C/km, pointing to a warm oceanic subduction. The overprinting late-phase metamorphism represents medium-P/T conditions with a geothermal gradient of 22–25°C/km, which we attribute to a collisional thickening process. As a result, we suggest that the HP schists in the Ondor Sum Group represent the terminal stage of subduction of the Paleo-Asian oceanic plate, and that the schists were involved in the continental collision after the closure of the Paleo-Asian Ocean in the Devonian.

Keywords: high-pressure schist, ondor sum group, pseudosection, tectonic transition, paleo-asian ocean

1 INTRODUCTION

The thermal structure of subduction zones is controversial as different insights are acquired from geological observations (Tsujimori et al., 2006; Groppo et al., 2009; Penniston–Dorland et al., 2015; Agard et al., 2018; Brown and Johnson, 2018; Holder et al., 2019; Tamblyn et al., 2019) and numerical modelling (e.g., Peacock, 1996; Peacock and Wang, 1999; Syracuse et al., 2010; van Keken et al., 2011; van Keken et al., 2018; van Keken et al., 2019). According to the previous geological studies, metamorphism during oceanic plate subduction is typically of high-P type with geothermal gradients within 5–15°C/km, based mainly on the P–T estimates using traditional methods of high-pressure (HP) rocks exhumed from ancient subduction zones (Miyashiro, 1961, 1994). However, using kinematically defined slabs for obtaining a comprehensive suite of thermal models suitable for the current global subduction system, Syracuse et al. (2010) simulated the thermal structure in 56 segments of active subduction zones. The results suggested that the geothermal gradients along slab surfaces in most oceanic subduction zones range from 3 to 10°C/km, with the P–T conditions mainly located in the metamorphic "forbidden zone" of <5°C/km. Although the numerical modelling results are subject to argument and discussion (Penniston–Dorland et al., 2015; Kohn et al., 2018; van Keken et al., 2018), it is a fact that the HP rocks exhumed from ancient subduction zones generally record much warmer geotherms than numerical modelling results. The mismatch forces us to reevaluate the rigidity and rationality of the P–T estimates for exhumed HP rocks. One uncertainty should be taken into account as the peak mineral assemblages in the exhumed HP rocks are always

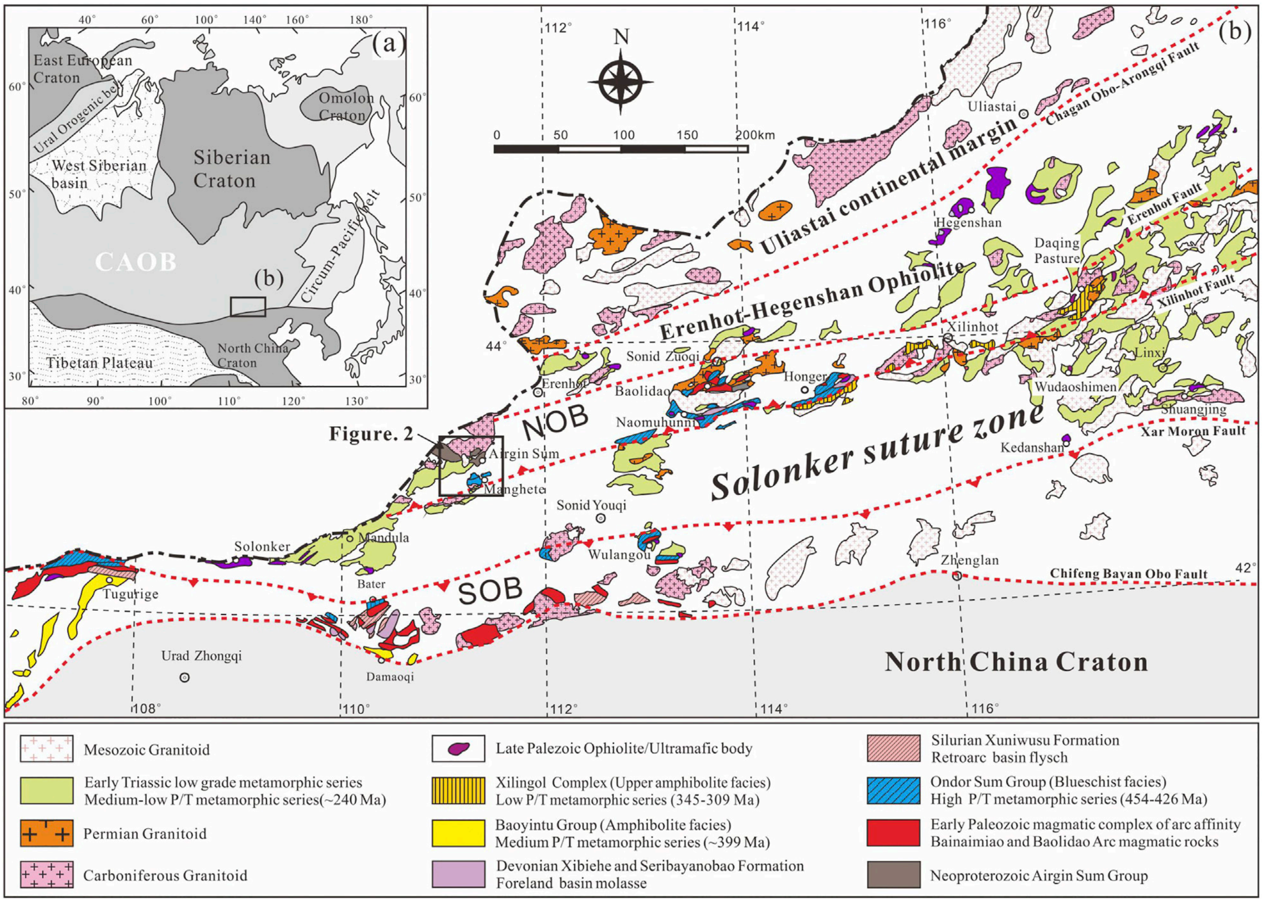

FIGURE 1 | (A) Location of the Central Asian Orogenic Belt (modified after Xu et al., 2013). **(B)** Geological sketch map of the central Inner Mongolia showing the subdivided tectonic units (compiled from IMBGMR, 1991; Jian et al., 2008; Xiao et al., 2003; Xu et al., 2013), and distribution of the Ondor Sum Group.

modified during decompression (Whitney and Davis, 2006; Wei and Clarke, 2011; Tsujimori and Ernst, 2014; Wei and Tian, 2014; Hernánde–Uribe et al., 2018), and this may result in underestimation of the peak pressure or overestimation of the peak temperature related to the metamorphism. Therefore, the decompressional metamorphic evolution of HP rocks should be considered carefully if using their P–T records to constrain thermal structure of a subduction zone.

The early Paleozoic subduction and accretion of the Paleo-Asian oceanic system resulted in various HP metamorphic belts in the Central Asian Orogenic Belt (CAOB) domain. In central Inner Mongolia, the Ondor Sum Group comprises subduction-related mélanges with strongly foliated quartz schists and minor blocks of intermediate–felsic volcanic rocks, pyroclastic tuffs, meta-gabbro, ultramafic rocks, blueschist, chert, and marble (Tang et al., 1983; Tang and Yan, 1993; Xu et al., 2001, 2013; Xiao et al., 2003), which are distributed at Wulangou, Airgin Sum and Naomuhunni (**Figure 1**). At Wulangou, the quartz schists contain high-P/T minerals in an assemblage that includes deerite, glaucophane, lawsonite, phengite, minnesotaite, piemontite, and stilpnomelane (Tang et al., 1983; Tang, 1990). The meta-gabbro also contains sodic amphibole, stilpnomelane, and phengite with a Si content of 3.64 (De Jong et al., 2006). Estimates of the blueschist P–T conditions are 6.0–7.5 kbar/250–300°C, based on the experimental data of Liou et al. (1987) and Maresch (1977) for the stability of lawsonite and glaucophane (Tang and Yan, 1993). At Naomuhunni, an epidote–blueschist block is constrained to be metamorphosed in P–T condition of 6.6–8.1 kbar/420–470°C based on phase equilibria modelling (Xu et al., 2001; Jinrui Zhang et al., 2015). At Airgin Sum, a sodic amphibole-bearing quartzite records P–T conditions of 7–10 kbar/400–450°C (Li et al., 2014) using the garnet–phengite thermometer of Krogh and Råheim (1978). Moreover, a garnet-bearing barroisite schist from the same area records a nearly isothermal decompression from 8.2 to 9.3 kbar/450–500°C to 6–8 kbar/470–500°C, followed by cooling decompression to 2.8 kbar/435°C (Jinrui Zhang et al., 2015). The reported P–T conditions of the above metamorphic rocks indicate medium-P/T facies series rather than the high-P/T facies series. This is attributed to two possibilities: 1) the reported medium-P/T rocks might be the shallower products of subduction other than the exhumed high-P/T products; 2) the absence of peak P–T conditions may be attributed to retrograde metamorphism during uplift or overprinting by tectonic thermal events. Consequently, these reported P-T conditions cannot reveal the thermal structure and evolution of the subduction zone. Moreover, the significance of the corresponding geochronological data needs to be further determined.

In this paper, we report new discoveries of HP schists in the Ondor Sum Group at Airgin Sum in the central Inner Mongolia, including garnet–mica and garnet–amphibole schists. We successfully identify the high-P/T metamorphism and geotherm from the new HP schists using phase equilibria modeling and distinguish it from late decompressional thermal imprint to help construct thermal structure of subduction zones from petrological view. Moreover, based on the zircon U-Pb ages and the previous reported ages, the tectonic significance of the HP schists is also well illustrated.

2 GEOLOGICAL SETTING

The central Inner Mongolia orogenic domain of the Xing' an-Inner Mongolia Orogenic Belt (XIMOB) belongs to the eastern part of the CAOB (**Figure 1**). Multiple tectonic belts/units, including suture zones, accretionary complexes, orogenic belts, and microcontinental blocks have been proposed (e.g., Xiao et al., 2003; Jian et al., 2008, 2010, 2012; Miao et al., 2008; Xu et al., 2013, 2014). However, the schemes of subdivision in terms of the tectonic architecture of this domain remain poorly understood (Xiao et al., 2003; Jian et al., 2008; Xu et al., 2013). In this paper, a preferred alternative scheme is presented based on recent studies of the metamorphism (Zhang et al., 2018b). The major belts include the Southern and Northern Orogenic Belts (SOB and NOB) indicated by Xu et al. (2013), the Solonker suture zone flanked by the SOB and NOB, and the Erenhot–Hegenshan ophiolite belt to the north of the NOB (Xiao et al., 2003), as shown on **Figure 1B**. Their geological characteristics are summarized below.

The SOB consists of subduction-related mélanges, magmatic complexes of arc-affinity, sedimentary sequences of retro-arc and foreland basins, and various metamorphic rocks. The mélanges are known as the Ondor Sum Group, and it has been suggested to be metamorphosed during subduction at 454–426 Ma (^{40}Ar/^{39}Ar ages) (Tang and Yan, 1993; De Jong et al., 2006). The magmatic complex of arc-affinity includes a volcanic sequence of basic to acidic rocks (499–440 Ma) known as the Bainaimiao Group (Zhang et al., 2010), as well as plutons of diorite, gabbro, and granitoid with ages of 490–425 Ma (Liu et al., 2003; Jian et al., 2008; Xu et al., 2013). The sedimentary sequences comprise the Silurian flysch of the Xuniwusu Formation and the Lower Devonian molasse of the Xibiehe Formation, which are respectively interpreted to represent deposition in retro-arc and foreland basins (Xu et al., 2013). The medium-P/T metamorphic rocks located in the west Tugurige area are grouped together as the Baoyintu Group, and it has been proposed recently that they are the products of a collisional process at ca. 399 Ma (Chen et al., 2015). These units in the SOB have been interpreted in terms of a tectonic evolution during the early Paleozoic from southward subduction of the Paleo-Asian oceanic plate to subsequent collision (Jian et al., 2008; Xu et al., 2013; Chen et al., 2015).

The NOB has similar configuration to the SOB. The mélanges are also known as the Ondor Sum Group, and a blueschist block at Naomuhunni yielded a glaucophane ^{40}Ar/^{39}Ar age of 383 ± 13 Ma (Xu et al., 2001). The magmatic complexes with arc affinities are distributed from Baolidao through Xilinhot to Daqing Pasture, and they consist of cumulate gabbros, gabbro-diorites, quartz diorites, tonalites, and granites with ages of 482–428 Ma (Chen et al., 2000; Shi et al., 2004, 2005; Jian et al., 2008; Xue et al., 2009). The foreland molasse sequences are grouped together as the Devonian Seribayanobao Formation, and they unconformably overlie the mélanges (Xu et al., 2013).

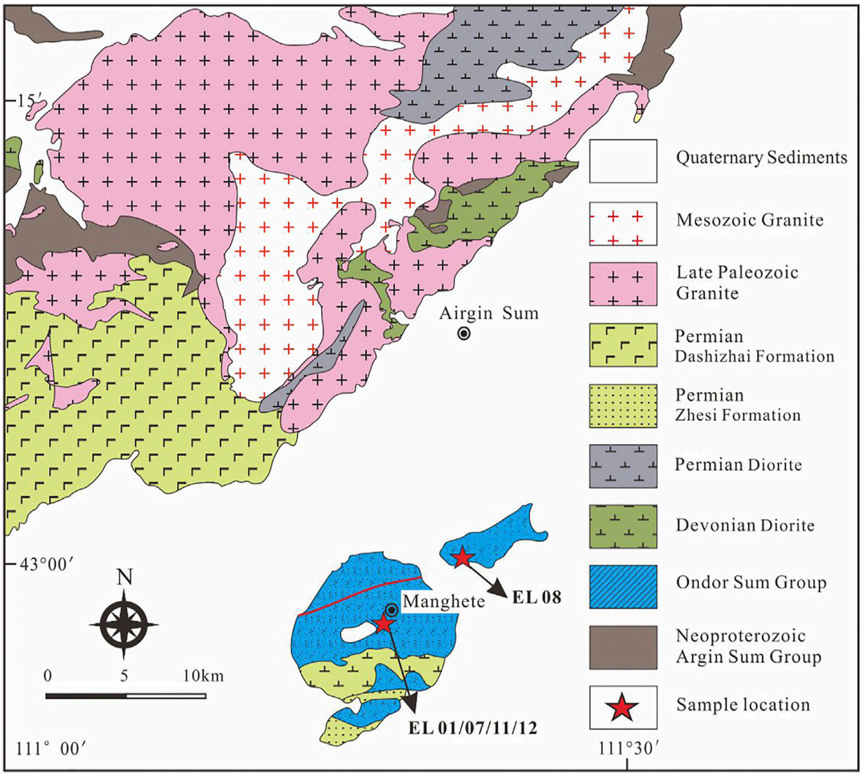

FIGURE 2 | Geological map of Airgin Sum area (modified after Li et al., 2014) showing lithological distribution of the Ondor Sum Group and sampling localities.

The Xilingol Complex of metamorphic rocks underwent HT–LP metamorphism at 345–309 Ma in relation to the extensional processes of a previous orogeny (Zhang et al., 2018b). It has been suggested that these tectonic units represent a northward subduction–collision system in central Inner Mongolia (Xu et al., 2013). Precambrian terranes in the area include the Airgin Sum Group, which is composed mainly of low-grade mica-schists and metasandstones with an upper intercept age of 952 ± 8 Ma (IMBGMR, 1991) and an age peak at 1,180 Ma (Xu et al., 2014), as well as 1,516 ± 31 Ma gneissic granites at Sunidzuoqi (Sun et al., 2013), and together these Precambrian rocks are classified as part of the Southern Mongolian Block (Badarch et al., 2002; Yarmolyuk et al., 2005, 2008; Xu et al., 2014).

The Solonker suture zone and the Erenhot–Hegenshan ophiolite belt are both marked by sporadic distributions of various ophiolitic fragments such as metabasalts, serpentinized harzburgites, dunites, and gabbroic cumulates. The suture zone has an age of 297–250 Ma (Xiao et al., 2003; Miao et al., 2008; Jian et al., 2010, 2012) and the Erenhot–Hegenshan ophiolite belt an age of 354–300 Ma (Liu et al., 2012; Zhang et al., 2014; Song et al., 2015; Zhicheng Zhang et al., 2015). They were once considered evidence of the continuous evolution of the Paleo-Asian oceanic system during the late Paleozoic (Xiao et al., 2003). However, more recent studies have indicated that the basic rocks exhibit characteristics of N-MORB and E-MORB, or supra-subduction zone-type oceanic crust that might have formed in back-arc basins (Song et al., 2015) or limited ocean basins (Chu et al., 2013; Jinrui Zhang et al., 2015; Wang et al., 2015).

The tectonic belts mentioned above were extensively intruded by the late Paleozoic granitic plutons including the Carboniferous and Permian granitoids (**Figure 1B**). However, these plutons are still variously and controversially interpreted as the products of subduction (Zhang et al., 2007, 2009; Liu et al., 2009) or post-orogenic extension (Shi et al., 2003; Zhang et al., 2014; Tong et al., 2015; Qiao et al., 2017). Recent research has revealed that the widely distributed Carboniferous–Permian volcanic and sedimentary sequences along the Solonker suture zone were metamorphosed to greenschist and local amphibolite facies low–medium-P series rocks in the Early Triassic (~240 Ma), and it was suggested that this metamorphism resulted from the closure of limited ocean basins (Chen et al., 2012; Zhang et al., 2016). Moreover, it has been suggested that the 222–204 Ma monzogranites and syenogranites at Xilinhot and Sunidzuoqi (Liu et al., 2005) and the 238–204 Ma peraluminous granites at Shuangjing formed in a setting of crustal thickening (Li et al., 2007).

The Ondor Sum Group is characterized by typical configurations containing various blocks and heterogeneously deformed matrix (Xu et al., 2013). The matrix consists mainly of interbedded sericite–quartz schist, chlorite–quartz schist, and mica-schist, and the blocks include quartzite (sodic-amphibole-bearing locally), ultramafic rocks,

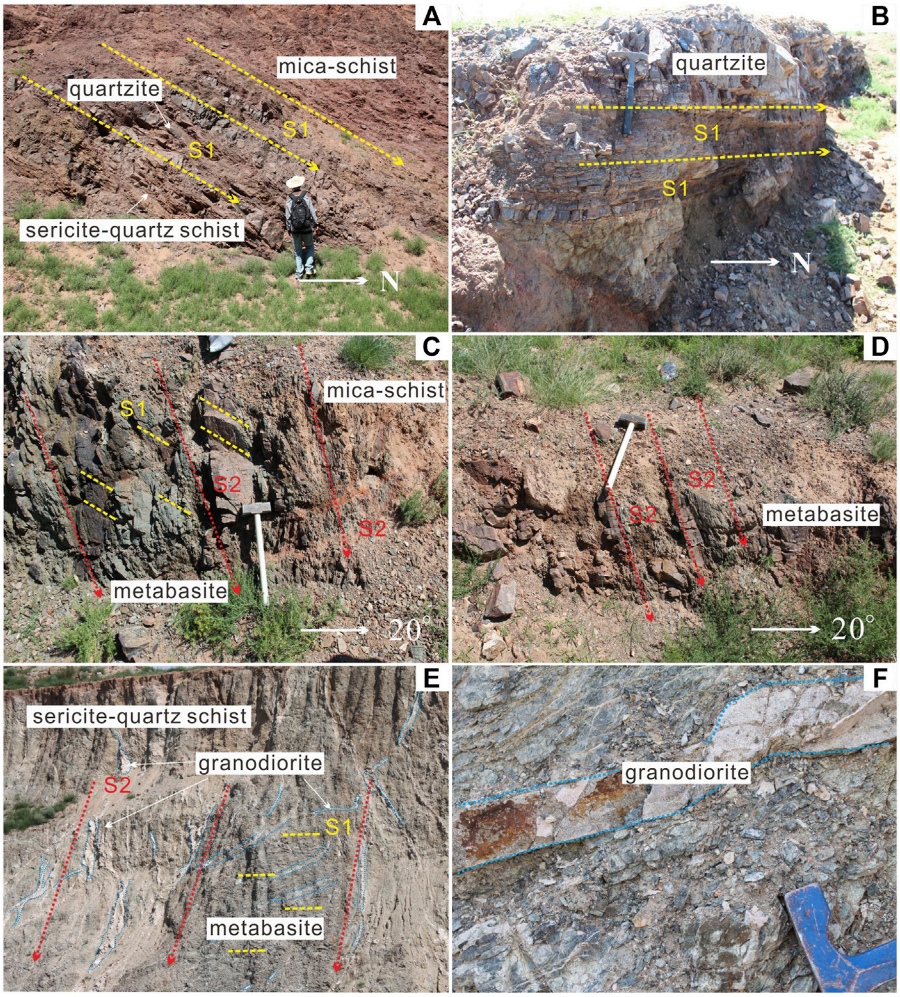

FIGURE 3 | Field photographs showing rocks of different types in the Ondor Sum Group at Airgin Sum, including quartzite **(A,B)**, sericite-quartz schist **(A)**, mica-schist **(A,C)** and metabasite **(C,D)**, and granodiorite veins **(E,F)**. Two phases of foliations (S1 and S2) are observed in the outcrops.

limestone, and metabasite as well as barroisite schist. Along with the Ondor Sum Group also distributes the Airgin Sum Group, Permian volcanic and sedimentary sequences such as the Dashizhai and Zhesi formations, and late Paleozoic and Mesozoic plutons (**Figure 2**). In the field of Airgin Sum, the matrix is composed dominantly of sericite–quartz schist, intercalated with minor amounts of garnet mica-schist (HP rocks in this study) that runs in strips parallel to the foliation of the sericite–quartz schist. Several blocks within the matrix are quartzites and metabasites, found mostly through exploratory drilling. The quartzites had already been reported by Li et al. (2014) to locally contain sodic-amphibole. The metabasites are garnet amphibole schists (HP rocks in this study) along with minor greenschist. Multiphase deformations have been recorded in the Ondor Sum Group, including the early S1 foliation that dips mainly to the north in the quartzite, mica-schist, sericite–quartz schist, and metabasite outcrops (Xu et al., 2013; **Figures 3A–C**), and the nearly-vertical late S2 foliation that displaces the early S1 foliation (Xu et al., 2013; **Figures 3D,E**). Moreover, the HP schists are intruded by granodiorite veins locally. These veins are observed to be striking parallel to S1 foliation initially but modified later by S2 foliation, indicating that the granodiorite veins were formed later than S1 but earlier than S2 (**Figure 3F**).

Samples for this study were collected from the Ondor Sum group in Manghete, ~20 km south of the Airgin Sum area (**Figure 2**). They include different HP schist samples such as two garnet–mica schist samples (EL01 and EL07), a garnet–amphibole schist sample (EL08) and a sericite–quartz schist sample (EL11) intercalated with the garnet-mica schist. Moreover, a granodiorite sample (EL12) intruding in the HP schist was also selected. It should be noted that the HP samples EL01 and EL08 are for petrological analyses and phase equilibria modeling as these two samples are observed to preserve multistage mineral assemblages and deformations which are available to better reveal the metamorphic evolution. Other samples are only for zircon U-Pb dating.

TABLE 1 | Bulk-rock compositions of the HP schists at Airgin Sum.

ICP–OES whole rock compositions (wt%)

Sample	SiO_2	TiO_2	Al_2O_3	$Fe_2O_3^T$	FeO	MnO	MgO	CaO	Na_2O	K_2O	P_2O_5	LOT	Total	$Mg^{\#}$	A/CNK
EL01	69.86	0.79	12.57	5.66	0.00	0.28	2.73	1.10	1.43	2.57	0.21	2.99	100.19	0.49	1.76
EL08	48.52	1.76	13.48	12.72	0.00	0.20	6.50	10.43	2.63	0.21	0.22	3.63	100.30	0.51	

Normalized molar proportion used for phase equilibria modeling (mole%)

Sample	Figs	SiO_2	Al_2O_3	CaO	MgO	FeO	K_2O	Na_2O	TiO_2	MnO	O
EL01	**Figures 6,7**	77.33	8.20	0.98	4.50	4.71	1.81	1.53	0.66	0.26	0.10
EL08	**Figures 8,9**	53.46	8.75	10.63	10.68	10.55	0.14	2.81	1.46	0.19	2.33

LOI, loss on ignition; $Fe_2O_3^T$: total Fe_2O_3 in ICP–OES, analyses; $Mg^{\#}$ = MgO/(MgO + FeO) in mole.
A/CNK, $Al_2O_3/(^{CaO}$ + Na_2O+ K_2O) in mole.

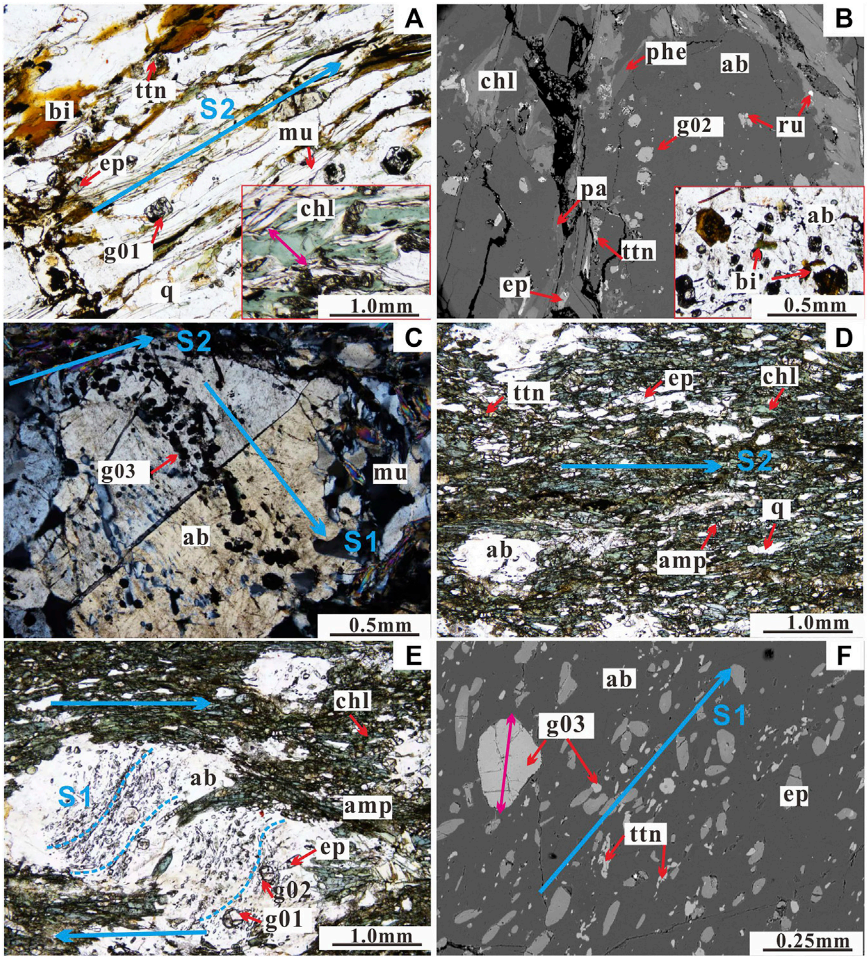

FIGURE 4 | Microphotographs of newly discovered schists from the Ondor Sum Group at Airgin Sum, central Inner Mongolia. **(A)** The foliated matrix composed of phengite, biotite, epidote, chlorite and titanite (S2 foliation) in sample EL01; **(B)** The BSE images showing albite porphyroblasts enclosing the early fine-grained garnet and the matrix minerals such as phengite, paragonite, biotite, quartz and rutile as inclusions; **(C)** The oriented garnet inclutions in albite porphyroblasts showing the early foliation (S1) in sample EL04; **(D)** The foliated matrix composed of amphibole, albite, chlorite, epidote and titanite (S2 foliation) in sample EL08; **(E)** The syntectonic albite porphyroblast showing dextral movement along foliation S2 with oriented inclusions (S1) in sample EL08; **(F)** The BSE images showing inclusions of albite porphyroblast such as garnet, epidote, amphibole and titanite in sample EL08. The measured garnet grains are shown with double sided arrow. Mineral abbreviations: bi, biotite; mu, muscovite; ep, epidote; chl, chlorite; amph, amphibole; g, garnet; phe, phengite; ab, albite; q, quartz; ttn, titanite; ru, rutile; pa, paragonite; q, quartz.

3 PETROLOGICAL ANALYSES

3.1 Analytical Methods

The bulk-rock compositions of samples EL01 and EL08 were determined by a Leeman Prodigy inductively coupled plasma optical emission spectrometer (ICP–OES) system with high dispersion Echelle optics at China University of Geoscience (Beijing). Standard basalt GSR3 was used for calibration. The loss on ignition was determined routinely and the relative analytical uncertainties for all elements are <3%. The results are presented in **Table 1**. Mineral microprobe analyses were carried out at the Key Laboratory of Orogenic Belts and Crustal Evolution of Peking University. The minerals were analyzed using a JXA-8100 electron microprobe in wavelength-dispersive mode with 15 kV acceleration potential, 15 nA beam current, and a counting time of 20–30 s. The beam diameter was set to 1 μm for all phases except for muscovite, which was analyzed using a 5 μm beam diameter. Natural and synthetic minerals were used for standardization. Relative analytical uncertainties are <2% for major elements. The analyses of samples EL01 and EL08 are presented in **Supplementary Appendixs S1, S2**. Photomicrographs of the two samples are shown in **Figure 4**.

3.2 Bulk-Rock Compositions

The garnet–mica schist EL01 has content of SiO_2 = 69.86 wt%, Na_2O = 1.43 wt%, K_2O = 2.57 wt%, CaO = 1.10 wt%, A/CNK = 1.76, and $Mg^{\#}$ = 0.49, which is likely to represent an aluminum-rich graywacke or volcanic sedimentary rock from an ocean trench (Li et al., 2014). The garnet–amphibole schist EL08 is a typical basic rock with contents of SiO_2 = 48.52 wt%, Al_2O_3 = 13.48 wt%, $Fe_2O_3{}^T$ = 12.72 wt%, MgO = 6.50 wt%, CaO = 10.43 wt%, and Na_2O = 2.63 wt%, with an $Mg^{\#}$ value of 0.51 (Zhang et al., 2014).

3.3 Petrography and Mineral Compositions

Sample EL01 contains garnet (5 vol%), white mica (30 vol%, muscovite and phengite), biotite (10 vol%), albite (16 vol%), quartz (28 vol%), and chlorite (6 vol%) along with minor paragonite (2 vol%), epidote (2 vol%), and accessory titanite, and rutile (**Figure 4A**). Albite occurs as porphyroblasts that are 2–3 mm across (**Figure 4B**) that grew over a fine-grained and well foliated matrix defined by oriented muscovite, biotite, quartz, and chlorite (S2, **Figure 4A**). A few albite porphyroblasts contain numerous inclusions of garnet, phengite, biotite, paragonite, and rutile that are oriented to form an early-phase foliation (S1 in **Figures 4B,C**). The albites commonly have low values of X_{An} (0.01–0.03) in cores and mantles, but high values of X_{An} (0.06) in the rims. Garnet occurs as inclusions in albite and as subhedral to euhedral grains of 0.05–0.20 mm in the matrix, and they exhibit different compositions in these two places. A measured garnet in the matrix (g01) exhibits asymmetric zoning. The right half of **Figure 5A** shows increasing almandine from core to rim (0.41→0.58, = $Fe^{2+}/(Fe^{2+} + Mg + Ca + Mn)$, others are defined accordingly), increasing pyrope (0.06→0.07), but decreasing spessartine (0.33→0.19) and grossular (0.20→0.16). The left half of **Figure 5A** shows a similar core-to-mantle trend as the right half but is rimmed by a precipitous increase of grossular (0.23–0.28) and decrease of spessartine (0.10–0.06), coupled with pyrope (0.08–0.10) and almandine (0.56–0.57). Two measured garnet grains (g02 and g03) from within an albite porphyroblast show increasing grossular from cores to rims (0.14→0.27 in g02 and 0.17→0.29 in g03) coupled with decreasing spessartine (0.17→0.09 in g02 and 0.16→0.06 in g03). Their almandine

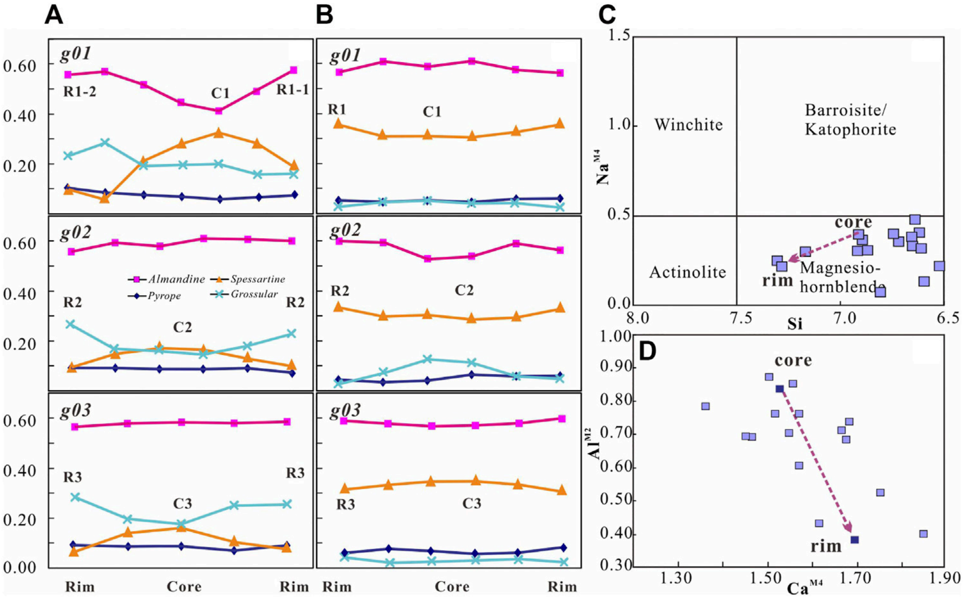

FIGURE 5 | The zoning profiles of almandine, pyrope, grossular and spessartine for the representative garnet grains in sample EL01 **(A)** and sample EL08 **(B)**, and the Si *vs*. Na^{M4} p. f.u. **(C)** and Ca^{M4} *vs*. Al^{M2} **(D)** diagram showing the compositions of amphibole in the sample EL08 (after Leake et al., 1997).

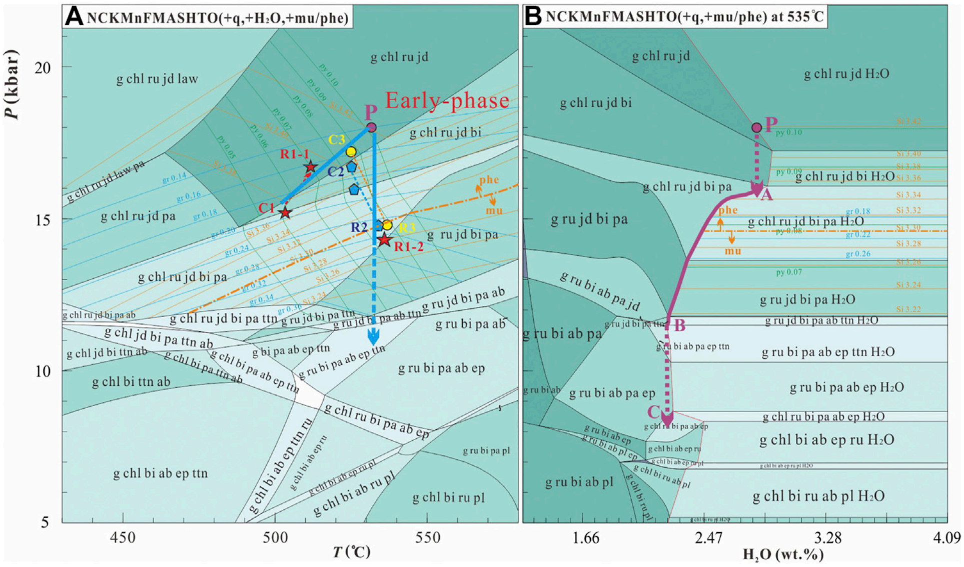

FIGURE 6 | (A) *P–T* pseudosection for sample EL01 calculated in the system NCKMnFMASHTO (+q, H_2O, mu/phe) using the modified bulk-rock composition from Table 1, and **(B)** P-M(H_2O) pseudosection calculated at temperature of 535°C. The pseudosections show isopleths of *py* (pyrope) and *gr* (grossular) in garnet and Si content in phengite for relevant mineral assemblages. The plots of the measured pyrope and grossular in the core and rim of different garnet grains (g01, g02, and g03) are shown as different shapes marked with C (C1, C2, and C3) and R (R1, R2, and R3). The R1-1 and R1-2 represent right and left rim of the grain g01. Mineral abbreviations: law, lawsonite; ctd, chloritoid; o, omphacite; jd, jadeite, pl, plagioclase others are the same as in **Figure 3**.

(0.55–0.61 in g02 and 0.56–0.59 in g03) and pyrope (0.07–0.09 in g02 and 0.07–0.09 in g03) contents are nearly constant, although some analyses show slight fluctuations (**Figure 5A**). Biotite in the matrix and as inclusions are both found altered to chlorite with X_{Mg} values of 0.54–0.61 and small amounts of K = 0.37–0.52 p.f.u. (per formulae unit). Phengite generally occurs as inclusions in the albite and has Si = 3.31–3.42 p.f.u. and Mg = 0.26–0.34 p.f.u., while muscovite in the matrix has lower values of Si = 3.19–3.26 p.f.u. and Mg = 0.23–0.24 p.f.u. Paragonite flakes mostly intergrown with phengite have Na = 0.82–0.93 p.f.u. Chlorite forms either large porphyroblasts 1–2 mm across or micro-flakes in the matrix. Most have X_{Mg} values [= $Mg/(Fe^{2+} + Mg)$] of 0.58–0.66. A measured chlorite flake shows an increase in X_{Mg} from core to rim of 0.59–0.64. Epidote has pistacite contents (Ps = $Fe^{3+}/(Fe^{3+} + Al)$) of 0.15–0.19. According to the above observations, two phases of mineral assemblage can be inferred: an early phase that is characterized by the coexistence of garnet and phengite together with paragonite, biotite, and rutile as inclusions, and a late phase that is marked by the formation of albite porphyroblasts together with muscovite, biotite, chlorite, epidote, and titanite. Moreover, we suggest that these two phases of mineral assemblage correspond to the two phases of foliations.

Sample EL08 contains amphibole (37 vol%), albite (20 vol%), garnet (4 vol%), epidote (16 vol%), chlorite (8 vol%), and quartz (12 vol%) together with minor titanite (**Figure 4D**). Albite occurs as porphyroblasts 1–3 mm across that grew over a well-foliated matrix defined by oriented amphibole, titanite, epidote, and chlorite (S2, **Figure 4E**). The albite porphyroblasts locally developed pressure shadows that indicate dextral shearing (**Figure 4E**). The albites have X_{An} < 0.05 and contain numerous inclusions of garnet, epidote, titanite, and quartz that are oriented, forming an early-phase foliation (S1 in **Figure 4F**). The S1 foliation commonly displays S-shapes: the part that is in the core domain of an albite shows a uniform orientation, but this is gradually deflected outside the core to be consistent with S2 near the rim, indicating a syntectonic origin for the albite. The amphiboles are deep to light blue–green and form prismatic crystals in the matrix and inclusions in the outer rims of the albite porphyroblasts (**Figure 4E**). Two occurrences of amphibole show magnesio-hornblende compositions (Leake et al., 1997) with Si = 7.30–6.44 p.f.u., Al^{M2} = 0.87–0.38 p.f.u., Na^{M4} = 0.49–0.08 p.f.u., and Ca^{M4} = 1.75–1.36 p.f.u. (**Figures 5C,D**). Moreover, one measured amphibole grain exhibits zoning with Al^{M2} decreasing from 0.85 p.f.u. to 0.43 p.f.u. from core to rim and Na^{M4} decreasing from 0.37 p.f.u. to 0.25 p.f.u. Garnets only occur as 0.05–0.2 mm inclusions within the albite porphyroblasts. Three analyzed grains display increasing pyrope from core to rim (0.04→0.06 in g01 and g02, 0.05→0.08 in g03), coupled with fluctuations in grossular (0.31→0.36 in g01, 0.30→0.29 in g02, and 0.35→0.33 in g03), spessartine (0.04→0.02 in g01, 0.13→0.06 in g02, and ~0.02 in g03), and almandine (0.61→0.56 in g01, 0.53–0.59 in g02, and 0.57→0.58 in g03, **Figure 5B**). Epidote is present in the matrix and as inclusions within the albite porphyroblasts, and they all have similar compositions with Ps ($Fe^{3+}/(Fe^{3+} + Al)$) = 0.16–0.24. Chlorite also occurs both in the matrix and as inclusions in the albite, and its values of X_{Mg} ($Mg/(Fe^{2+} + Mg)$) = 0.59–0.60. The above observations suggest two phases of mineral assemblage: an early phase represented by the garnet-bearing inclusions within albite, and a late phase marked by the formation of albite porphyroblasts together with the matrix minerals, and these two phases of mineral assemblage also correspond to the two phases of foliation development.

4 PHASE EQUILIBRIA MODELLING AND P–T CONDITIONS

Phase equilibria were modeled for samples EL01 and EL08 in the system NCKMnFMASHTO (Na_2O–CaO–K_2O–MnO–FeO $_{total}$–MgO–Al_2O_3–SiO_2–H_2O–TiO_2–Fe_2O_3). This system provides a realistic compositional approximation of the studied rocks, within which the early-phase assemblages with garnet can be calculated. The pseudosection modelling was done for the garnet–phengite schist EL01 and the garnet–amphibole schist EL08 using THERMOCALC 3.45 with the internally consistent thermodynamic dataset (ds62) of Holland and Powell (2011). The mixing models were those presented for clinopyroxene and amphibole (Green et al., 2016), garnet, orthopyroxene, and biotite (White et al., 2014), plagioclase (Holland and Powell, 2003), muscovite (Coggon and Holland, 2002), chlorite (Holland and Powell, 1998), ilmenite (White et al., 2000), and epidote (Holland and Powell, 1998). Rutile, titanite, and paragonite are pure end-member phases. Quartz and the fluid phase (assumed to be pure H_2O) were in excess.

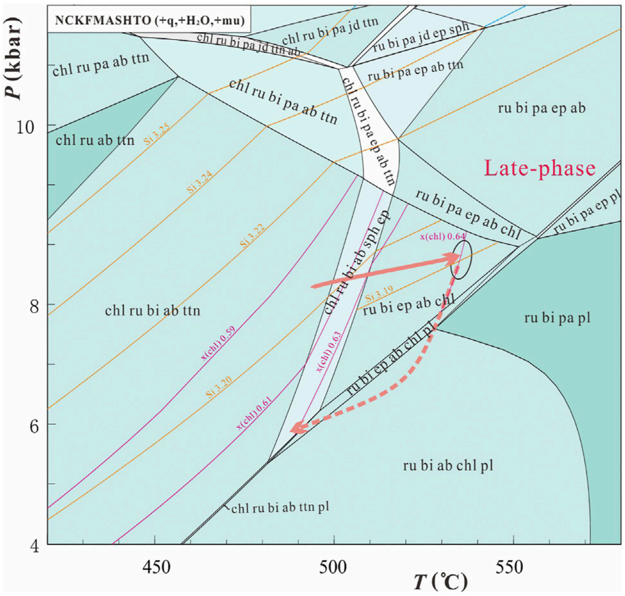

FIGURE 7 | *P–T* pseudosection for sample EL01 calculated in the NCKFMASHTO (+q, H_2O, mu) using an effective bulk composition generated according to mass balance constraints by excluding the composition of garnet and integrating mineral compositions and modal abundance data of the other phases, normalized on the basis of mole-proportions as: SiO_2 = 79.44, Al_2O_3 = 7.95, CaO = 0.52, MgO = 4.57, FeO = 3.60, K_2O = 1.93, Na_2O = 1.63, TiO_2 = 0.68, and O = 0.09 (mol%). The pseudosections show isopleths of Si content in muscovite and x (chl) { = Mg/(Fe^{2+} + Mg)} for relevant mineral assemblages.

For the modelling of the early-phase assemblages of sample EL08, the bulk-rock compositions given by the ICP–OES analyses were used, normalized to mole proportions according to the model system. The O (Fe_2O_3) values were estimated on the basis of mass balance constraints by adding up the Fe^{3+} contents of each mineral (**Table 1**). However, in sample EL01, the chloritization of biotite resulted in a loss of a certain amount of K_2O from the bulk-rock compositions given by ICP–OES analyses, which therefore may not be appropriate for modelling the early phase metamorphism. Thus, an effective bulk composition was generated for sample EL01 following the method of Carson et al. (1999) by integrating mineral compositions (using a standard biotite composition with X_{Mg} = 0.60 after Li et al., 2014) and modal abundance data for the phases present. The bulk-rock compositions for the calculated pseudosections are listed in **Table 1**.

4.1 Pseudosections for Sample EL01

The P–T pseudosection calculated for sample EL01 in the NCKMnFMASHTO system is presented in **Figure 6A**. The albite-absent assemblages occur at higher pressures above 10–13 kbar, and the titanite-present assemblages occur in the lower P–T range of <8–12 kbar/500°C. The inferred early-phase assemblage of garnet, phengite, paragonite, biotite, and rutile without albite cannot match any predicted assemblage in the pseudosection. However, the pyrope and grossular compositions of the garnet constrain P–T conditions in jadeite-bearing assemblages. The matrix-garnet defined prograde P–T vector from ~15 kbar/~503°C to ~17 kbar/~515°C (C1→R1-1) is based on the core-to-rim zoning shown in the right part of **Figure 5A**, and the retrograde P–T condition of ~14 kbar/~540°C (R1-2) is based on the rim in the left part of the diagram. Moreover, the core–rim zoning of two garnet grains included within albite defines a dominantly decompressional P–T path from ~16 to ~14 kbar at a temperature of ~530°C (C2→R2 and C3→R3). The plotting of the measured Si = 3.34–3.31 p.f.u in phengite is roughly consistent with the P–T conditions defined by the garnet cores. However, the measured Si = 3.42–3.38 p.f.u in phengite indicates a higher pressure that is more likely to represent the peak condition. This peak P–T condition can be constrained to ~18 kbar/~535°C, based on the maximum Si content in phengite and pyrope in garnet, while the grossular content of the garnet was likely modified during the decompressional stages.

To illustrate the post-peak decompressional metamorphic evolution, a P–M (H_2O) pseudosection was calculated at T = 535°C (**Figure 6B**), which shows that the predicted peak assemblage contains 2.82 wt% H_2O. The decompressional path from the inferred peak condition (P) deviates from the H_2O-saturated curve, and proceeds in H_2O-absent conditions. At ~16 kbar (A), the path returns to H_2O-saturated conditions and evolves along the H_2O-saturation line to lower M (H_2O), and with successive dehydration the modes of paragonite and biotite growth increase together with decreasing modes of jadeite, chlorite, and phengite. The final disappearance of jadeite

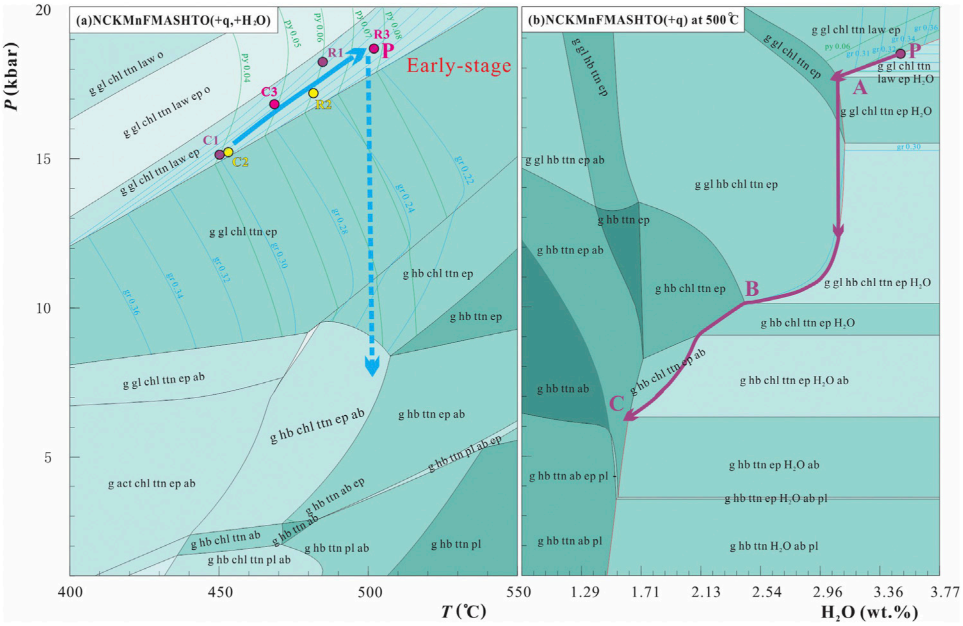

FIGURE 8 | (A) *P–T* pseudosection for sample EL08 calculated in the system NCKMnFMASHTO (+q, H_2O) using the modified bulk-rock composition from **Table 1** and **(B)** P–M (H_2O) pseudosection calculated at temperature of 500°C. The pseudosection is contoured with isopleths of pyrope (py) and grossular (gr) in garnet. The plots of the measured pyrope and grossular in the core and rim of different garnet grains (g01, g02, and g03) are shown as different shapes marked with C (C1, C2, and C3). It is noted that the subtypes of amphibole used in pseudosections follow those in Diener et al. (2007) where glaucophane (gl) refers to sodic amphibole, actinolite (act) refers to calcic amphibole and hornblende (hb) refers to sodic-calcic amphibole or calcic amphibole. Others are the same as in **Figures 4**, **7**.

occurs in a narrow pressure range with the presence of both jadeite and epidote at ~11.8 kbar (B), accompanied by a pronounced release of water with H_2O down to ~2.23 wt%. As further decompression may occur under fluid-absent conditions if there is no infiltration of water to saturate the rock, the mineral assemblage (g + chl + pa + bi + ru + ep) at this point tends to be preserved (Guiraud et al., 2001; Wei and Clarke, 2011). In this case, the metamorphic evolution may continue with the formation of a late-phase mineral assemblage represented by the S2 foliation and especially the growth of albite porphyroblasts, which possibly represent the overprinting of a separate metamorphic–deformational event.

The inferred late-phase assemblage that is marked by the presence of albite porphyroblasts together with chlorite, epidote, and titanite is predicted to stabilize under P–T conditions of <10 kbar and <520°C (**Figure 6A**). However, this prediction may not be valid, because the post-peak metamorphic evolution would have been controlled by local equilibrium domains as a result of the widespread preservation of early-phase minerals. To investigate the metamorphic evolution of the late-phase assemblage, an alternative P–T pseudosection was calculated in the system NCKFMASHTO, using an effective bulk composition that was generated following Carson et al. (1999) by excluding the components frozen in the early-phase assemblage. As shown in **Figure 7**, the inferred late-phase assemblage that includes muscovite, biotite, epidote, chlorite, and rutile is predicted to stabilize in the P–T range of 5–9 kbar/500–550°C. The isopleths of the measured Si = 3.19 in muscovite and x (chl) = 0.64 in chlorite can yield a P–T condition of ~8 kbar/532°C, which is in good agreement with that defined from the inferred assemblage. Under this condition, the rock may contain 2.69–3.05 wt% H_2O, which is a much higher value than when jadeite disappears (~2.23 wt%), and this indicates that infiltration of water occurred during the late-phase metamorphic evolution. Moreover, the core–rim increase in chlorite X_{Mg} from 0.59 to 0.64 predicts a prograde metamorphic evolution characterized by increasing temperature, and the measured rims of albite with higher X_{An} probably indicate decompression to the plagioclase-stable assemblage.

4.2 Pseudosections for Sample EL08

The *P–T* pseudosection for sample EL08 is presented in **Figure 8A**. The inferred early-phase garnet-bearing and albite-absent assemblages can occur at high pressures above 8–10 kbar. The contours of the measured core–rim zoning in garnet grains yield a prograde *P–T* vector from 15 kbar/~450°C to 18 kbar/~500°C (C1→R1 for g01, C2→R2 for g02, and C3→R3 for g03 in **Figure 5B**) in the assemblage with lawsonite and glaucophane, neither of which have been observed in the rock. If it is assumed the post-peak decompression was isothermal, the metamorphic evolution can be documented in the P–M (H_2O) pseudosection at 500°C (**Figure 8B**). The decompressional path from the peak condition (P) may evolve along the H_2O-saturation line to lower M (H_2O), characterized by lawsonite decomposition through successive dehydration reactions, and releasing a large amount of H_2O (3.52→3.10 wt%). On the disappearance of lawsonite at

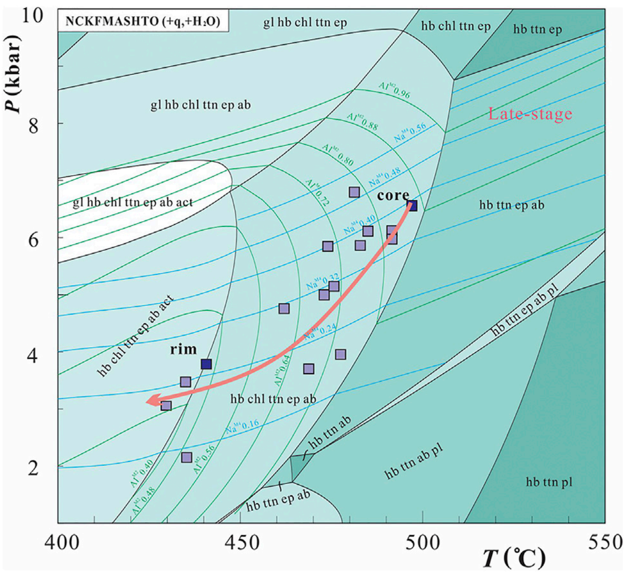

FIGURE 9 | *P–T* pseudosection for sample EL08 calculated in the NCKFMASHTO (+q, H_2O) using an effective bulk composition generated by the same method as in **Figure 7**, normalized on the basis of mole-proportions as: $SiO_2 = 54.07$, $Al_2O_3 = 8.60$, CaO = 10.47, MgO = 10.92, FeO = 9.98, $K_2O = 0.15$, $Na_2O = 2.92$, $TiO_2 = 1.52$, and O = 2.40 (mol%). The pseudosection is contoured with isopleths of Al^{M2} and Na^{M4} in calcic-amphibole. Plots of cacic-amphibole compositions are shown as squares and labels C and R correspond to those in **Figure 5**.

~17.5 kbar (A), the decompressional path may deviate from the H_2O-saturated curve and proceed under H_2O-absent conditions. At ~12 kbar (B), the path will return to H_2O-saturated conditions. Further decompression would see equilibria evolving along the H_2O-saturation line to lower M (H_2O), resulting in glaucophane giving way to hornblendic amphibole (C). Thus, a prediction of the decompressional path P→C is that both lawsonite- and glaucophane-bearing assemblages are unlikely to be preserved due to a series of dehydration reactions, and the inclusions in albite are more likely to be g + hb + chl + ttn + ep than other higher pressure phases. A further notable dehydration reaction is predicted to be hb + ep = chl + q + ab + H_2O, responsible for the formation of albite at 6–9 kbar. Albite growing as coarse-grained porphyroblasts may contribute to the abundant fluids that resulted from dehydration reactions and deformation during the formation of the S2 foliation. Thus, it is reasonably clear that the early-phase assemblage cannot be preserved in the matrix.

To investigate the metamorphic evolution of the inferred late-phase assemblage, a P–T pseudosection was calculated in the NCKFMASHTO system using the effective bulk composition generated by excluding garnet (**Figure 9**). The inferred late-phase mineral assemblage is predicted to match the stability field of the assemblage hb + chl + ttn + ep + ab at <9 kbar and 400–500°C. The isopleths of Al^{M2} and Na^{M4} for the measured zoning values of 0.87–0.38 and 0.40–0.22 in magnesio-hornblende yield a P–T vector from ~7.0 kbar/495°C to ~3 kbar/430°C, which is characteristic of cooling decompression. The cooling decompression is predicted to have the rock evolving towards higher water contents (from 1.89 to 2.46 wt%), indicating the infiltration of water during the late-phase metamorphic evolution (Guiraud et al., 2001).

5 ZIRCON U–PB AGE DATA

To obtain the protolith and metamorphism-related ages, the sericite–quartz schist sample EL11, the garnet–mica schist sample EL07 and the granodiorite sample EL12 are for zircon U-Pb dating respectively. Zircon grains in these samples were separated using standard heavy-liquid and magnetic techniques followed by handpicking under a binocular microscope at the Langfang Regional Geological Survey, China. The grains were embedded in epoxy resin discs and polished down to about half-sections to expose the grain interiors. To reveal the internal structures of the zircon grains, cathodoluminescence (CL) images were obtained using a Quanta 200F environmental scanning electron microscope housed at the State Key Laboratory of Orogenic Belts and Crustal Evolution of Peking University. The zircon U–Pb dating was carried out with a quadrupole ICP–MS (Agilent 7500a) connected to an UP-193 Solid-State laser (193 nm, New Wave Research Inc.) at the Ministry of Education Key Laboratory of Orogenic Belts and Crustal Evolution, School of Earth and Space Sciences, Peking University. The laser spot diameters were 25 μm and the laser frequency 10 Hz. The calibrations for the zircon analyses were done using NIST 610 glass as an external standard and Si as an internal standard. The standard zircon 91,500 (1,063 ± 14 Ma, n = 13) was used as an external standard for correcting the effects of U–Pb isotope fractionation. The standard zircon Plesovice (337.3 ± 0.7 Ma) was also used as an external standard to monitor the deviations of age measurements and calculations. The isotopic ratios and elemental contents of the zircons were calculated using GLITTER ver. 4.4 (Van Achterbergh et al., 2001). The concordia ages and diagrams were obtained using Isoplot/Ex (3.0) (Ludwig, 2003). Common lead was corrected using ComPbCorr# (ver. 3.15, Andersen, 2002). The errors given on individual analyses are at the 1σ level, but the weighted mean ages and their errors are reported at the 2σ level. $^{207}Pb/^{206}Pb$ ages were accepted for grains older than 1,000 Ma and $^{206}Pb/^{238}U$ ages for grains younger than 1,000 Ma (Sircombe, 1999). The analytical data are shown in **Supplementary Appendixs S3–S5**.

Zircon grains from sample EL11 are mostly euhedral and subhedral with lengths range from 120 to 80 μm. They mostly show high luminescence and simple oscillatory zoning in the CL images, suggesting their detrital origin mainly from igneous sources (**Figure 10A**). The detrital zircons have concordant ages ranging from 453 ± 9 Ma to 2,583 ± 40 Ma (**Figure 11A**). Four age populations can be discriminated including 2,583–1,532 Ma, 1,401–807 Ma, 701–667 Ma, and 569–453 Ma. Conspicuous age peaks are located at 1,176, 689, and 456 Ma (**Figure 11B**). The youngest coeval zircon grains between 453 ± 9 and 462 ± 5 Ma yield a weighted mean age of 456 ± 5 Ma (MSWD = 0.3, 2σ) which constrains the youngest depositional age of protolith to be 456 ± 5 Ma (**Figure 11A**). It needs to be noted that some zircons are characterized by metamorphic rims with high luminescence brightness in CL images, however, they were beyond analysis due to the widths of <10 μm.

Zircon grains from sample EL07 are mostly euhedral–subhedral with lengths ranging from 120 to 80 μm. They generally exhibit typical oscillatory or planar zoning with relatively low luminescence brightness in CL images (**Figure 10B**), suggesting their detrital origin was mainly from igneous sources. Most zircons have metamorphic rims with relatively high luminescence brightness, however, they were too narrow for analysis due to the widths of <10 μm. The detrital zircons have a concentrated concordant $^{206}Pb/^{238}U$ age range between 438 ± 6 Ma and 454 ± 6 Ma with Th/U ratios of 0.23–0.97. Thus, we suppose that the protolith of the garnet–mica schist sample is proximal sedimentary rock or volcanic sedimentary rock. The concentrated zircon ages yield a weighted mean $^{206}Pb/^{238}U$ age of 445 ± 2 Ma and MSWD = 0.76 (**Figure 11C**).

Zircon grains from sample EL12 are mostly euhedral–subhedral with lengths ranging from 120 to 80 μm. They generally exhibit typical oscillatory or planar zoning with relatively low luminescence brightness in CL images (**Figure 10C**), suggesting a magmatic origin. Thirty-five analyses show Th/U ratios between 0.39 and 1.18 and define concordant ages which yield a weighted mean $^{206}Pb/^{238}U$ age of 427 ± 2 Ma and MSWD = 0.84 (**Figure 11D**).

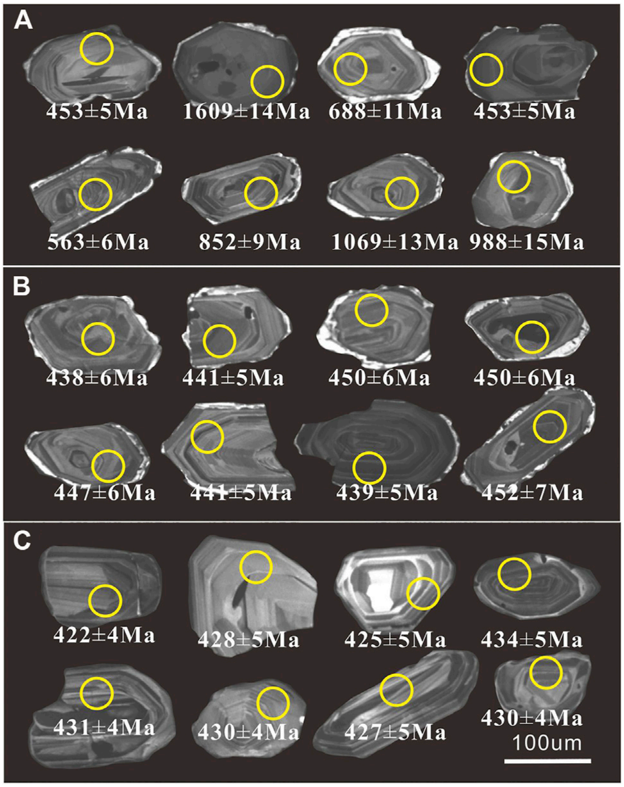

FIGURE 10 | Cathodoluminescence (CL) images of selected zircons from samples EL11 **(A)**, EL07 **(B)**, and EL12 **(C)** at Airgin Sum. Solid circles show positions of LA-ICP-MS analytical sites and ages in Ma.

6 DISCUSSION

6.1 Metamorphic Evolution

Petrographic observations and phase equilibria modelling indicate that both the garnet–phengite schist (EL01) and the garnet–amphibole schist (EL08) record two P/T series of metamorphic evolution including an early high-P/T series and a late medium-P/T series.

6.1.1 The Early-phase HP Evolution

Phase equilibria modelling suggests that both samples underwent a clockwise P–T evolution involving the prograde, peak, and post-peak isothermal decompression stages. The peak conditions were ~18 kbar/~535°C for EL01 and 18 kbar/~500°C for EL08. For both samples, the observed early-phase assemblages cannot match those predicted at their peak conditions because the post-peak decompressional evolution was dominated by dehydration reactions. As indicated in the P–M (H_2O) pseudosections (**Figures 6B**, **8B**), the peak HP minerals of jadeite in EL01 and lawsonite and glaucophane in EL08 could not survive during decompression. Moreover, as the contents of the jadeite and lawsonite reactants would have been rather low, no idiomorphic pseudomorphs of these minerals are likely to be found. Mostly, the metamorphic evolution that was dominated by dehydration in the HP rocks could be triggered by decompression, even with cooling, and in general it will not reach a state of full equilibrium. Thus, in most cases, garnet and phengite can preserve their compositions of the peak condition (or close to it), and their composition isopleths in P–T pseudosections can provide informative peak P–T estimates (Wei and Tian, 2014).

6.1.2 The Late-phase MP Metamorphism

The late-phase metamorphic evolution of samples EL01 and EL08 is characterized by the formation of albite and the S2 foliation. Sample EL01 is characterized by a clockwise P–T vector including a nearly heating path until the P–T condition of ~8 kbar/532°C, constrained by chlorite and muscovite compositions, and a retrograde path of decompression constrained by higher values of X_{An} in the rims of albite porphyroblasts. For sample EL08, only a retrograde path from ~7.0 kbar/495°C to ~3 kbar/430°C with cooling and decompression can be recovered from the Na^{M4} and Al^{M2} isopleths in the hornblende (**Figure 9**), and this needs to be addressed for the genetic connection between the late-phase medium-P/T and the early-phase high-P/T series mineral assemblages. Three vital pieces of evidence are presented. First, the late-phase assemblage in EL01 has a clockwise P–T path, which indicates a complete cycle of compression–exhumation that corresponds to a separate tectonic process. Second, the two-phases of foliation, especially in sample EL08, where the matrix minerals developed an independent foliation and the albite porphyroblasts are observed to be syntectonic, suggest that the early-phase foliation has been displaced. Third, in sample EL01, the formation of the late-phase mineral assemblage with albite requires the ingress of fluids, which is more likely to have

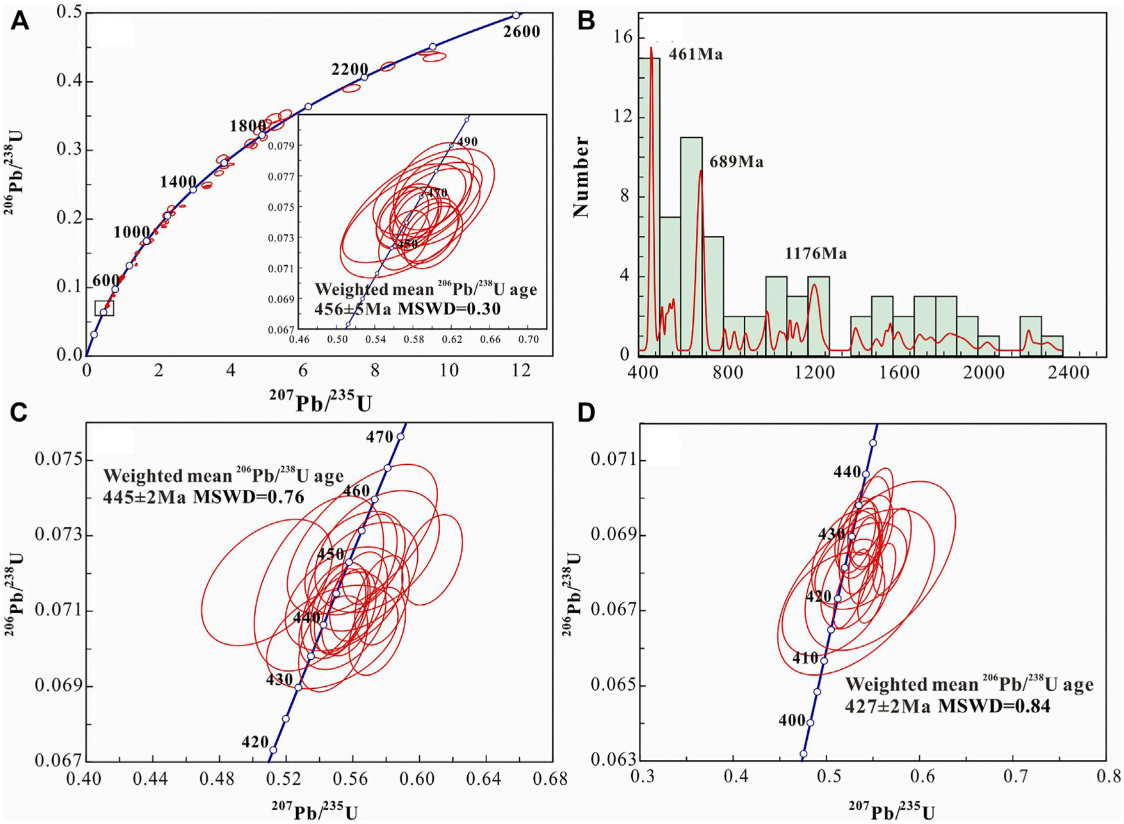

FIGURE 11 | (A) Concordia diagrams showing zircon U-Pb data of sample EL11; **(B)** Relative probability histogram of U–Pb ages of the detrital zircons in sample EL11; **(C)** Concordia diagrams showing detrital zircon U-Pb data in sample EL07; **(D)** Concordia diagrams showing magmatic zircon U-Pb data in sample EL12.

been triggered during the development of the late-phase foliation. As a consequence, we suggest that the late-phase assemblages in the two samples record a metamorphism that overprinted the early-phase HP assemblages, but preceded the later decompressional exhumation. Moreover, the two-phases of metamorphic evolution were accompanied by different foliations, indicating the superimposition of different tectonic activities.

The two phases of metamorphism are suggested to be regional in the studied area as they are consistent to the two phases of deformations (S1 and S2) which are generally observed in the Ondor Sum Group. Due to the modification of the early-phase decompression and late-phase metamorphism, the peak mineral assemblages in the exhumed HP rocks in the Ondor Sum Group mostly failed to be preserved. However, the exception for the garnet–phengite schist and garnet–amphibole schist in the Ondor Sum Group are probably due to the lack of fluid during the metamorphism as indicated above.

6.2 Ages of Protolith and Metamorphism of the Ondor Sum Group in Argin Sum

Different ages were abtained in the Ondor Sum Group in the previous research. In Wulangou, meta-andesites of arc type yielded a protolith age of 470 ± 2 Ma using the zircon U–Pb method (Li et al., 2012), and sodic amphibole from the blueschists and phengite from the quartz schists yielded ^{40}Ar/^{39}Ar ages of 426 ± 15 and 454–453 Ma, respectively (Tang and Yan, 1993; De Jong et al., 2006). At Naomuhunni, an epidote–blueschist block reported by Xu et al. (2001) yielded a glaucophane ^{40}Ar/^{39}Ar age of 383 ± 13 Ma.

Comparison of zircon age spectrum (**Figure 12**) shows that the detrital zircon ages of the HP schist samples at Airgin Sum are consistent with those at Naomuhunni, both of which belong to the northern Ondor Sum Group in NOB. Moreover, they are consistent with the age patterns of the Mongolia and the northeastern China plot. Their zircon ages suggest multiple sources contributed to the sediment formation. For instance, the major age peak at 456–442 Ma are supposed to reflect the early Paleozoic arc magmatism in the XIMOB (Chen et al., 2000; Shi et al., 2003; Jian et al., 2008; Chen et al., 2009; Xue et al., 2009; Li et al., 2012). The age groups with peaks of ~689 and ~1,176 Ma are consistent with those reported in the Ergun and Xing' an blocks (Zhou and Wilde (2013); Zhou et al., 2014) and the Southern Mongolian block (Badarch et al., 2002; Yarmolyuk et al., 2005). And the other older ages should be derived from the North China Craton (NCC, Zhao et al., 2001; Zhao et al., 2002; Wilde et al., 2002). The age groups of the Ondor Sum

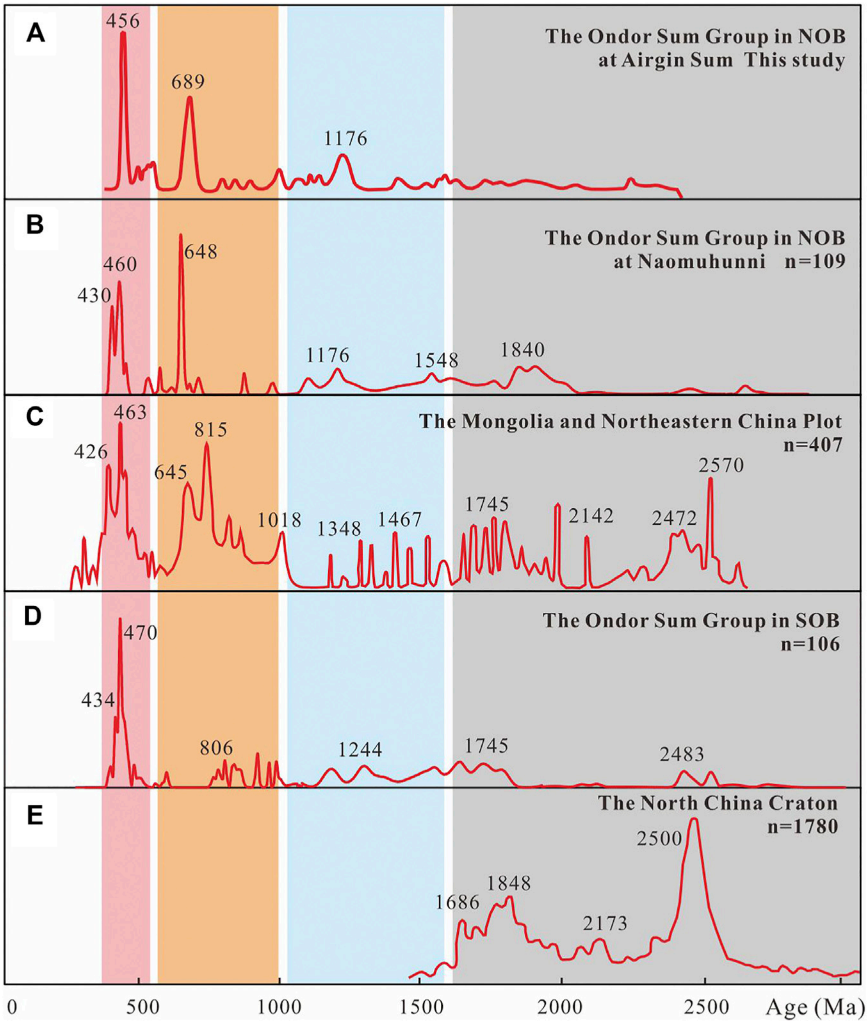

FIGURE 12 | Relative probability diagrams showing age distribution of Ondor Sum Group in central Inner Mongolia **(A,B,D)**, the Mongolia and Northeastern China Plot **(C)** and the NCC **(E)**. Data are cited from Zhou and Wilde (2013), Zhou et al. (2014), Xu et al. (2013, 2014), and Rojas-Agramonte et al. (2011).

Group in the SOB are mostly the same as the NOB except a conspicuous absence of ~689 Ma peak and ~1,176 Ma, which is probably attributed to the absence or decrease of detrital contribution from the blocks in the north.

No available metamorphic age data have been obtained in the samples, which, however, can be alternatively constrained between ca. 442 and ca. 425 Ma, on the basis of the youngest detrital age group of ca. 442 Ma and the ages of ca. 425 Ma for the granodiorite intrusions. This estimate is consistent with the reported $^{40}Ar/^{39}Ar$ ages of 454–453 Ma in the phengite schist (De Jong et al., 2006) and $^{40}Ar/^{39}Ar$ age of ~426 Ma in the blueschist in Ondor Sum Group (Tang and Yan, 1993). It needs to be noted that the glaucophane $^{40}Ar/^{39}Ar$ age of 383 ± 13 Ma was obtained in the blueschists in Ondor Sum Group (Xu et al., 2001). Based on the two phases of metamorphic evolution indicated above, we suggest, therefore, that the metamorphic age of 383 ± 13 Ma records the overprinting of the late-phase medium-P/T series metamorphism and not the early-phase high-P/T series metamorphism. In the context of the geological setting, this age seems to be consistent with the 399 ± 8 Ma age of the Barrovian metamorphic belt within the limit of error.

6.3 Geological Implication for the Metamorphism

As indicated above, the HP rocks exhumed from ancient subduction zones have been controversially argued to record much warmer geotherms than numerical modelling results.

Although the Syracuse models were argued to have underestimated the temperatures of subduction zones, they have been well matched by the peak P–T conditions reported for the exhumed HP rocks (Brown and Johnson, 2018), including those of the Franciscan at Jenner, United States (Krogh Ravna and Terry, 2004), southwest Tianshan belt (Wei C. J. et al., 2009;

Tian and Wei, 2013), the north Qilian belt (Wei C. J. et al., 2009), and the Yuli belt in China (Huang et al., 2021). The numerical modelling results of Syracuse et al. (2010) seem to be well consistent with the records from natural HP rocks if their peak pressure conditions are well recovered.

The investigated garnet–phengite schist (EL01) and garnet–amphibole schist (EL08) in the Ondor Sum Group are interpreted to have experienced HP metamorphism along clockwise P–T paths in the early phase, with a thermal gradient of 8°C/km at peak conditions, and they can be classified as typical high-P/T types (**Figure 13**). According to the numerical modelling of Syracuse et al. (2010), the prograde P–T paths are apparently warmer than those in most subduction zones. Thermal structure of subduction zones is controlled by various factors including the age of subducted oceanic crust, the convergent rate, the subduction dip angle and the thicknesses of both subducting and overriding lithospheres (Kirby et al., 1991; van Hunen et al., 2002; Gerya and Meilick, 2011; van Keken et al., 2011; Leng and Mao, 2015). Nevertheless, on the context of field tectonic evolution, the HP schists of the Ondor Sum Group at Airgin Sum seem to be related to a warm subduction at the terminal evolution of the Paleo-Asian Ocean, which we suggest may correspond to the subduction of a young slab (Syracuse et al., 2010), or a low-rate of subduction (<2 cm/yr, van Keken et al., 2002). This interpretation is suggested by several lines of evidence, including: 1) the protoliths of the metabasite in this study showing affinities between N-MORB and E-MORB which has been previously suggested to represent environment of limited intercontinental ocean basins (Zhang et al., 2014), 2) the high P/T metamorphism in the garnet–phengite schist which has occurred soon after formation of the protolith; 3) the absence of arc magmatic activity since ~420 Ma which probably indicates termination of subduction process (Song et al., 2015). The P–T conditions of the late-phase metamorphism that was overprinted on our HP schist sample EL08 indicate a thermal gradient of 22–25°C/km, which is typical of the medium-P/T facies series (Miyashiro, 1994). We suppose that the late-phase metamorphism is consistent with the metamorphism of the Baoyintu Group, in which the near-peak of a typical medium-P/T Barrovian metamorphism took place at 399 ± 8 Ma, corresponding to an orogenic thickening process (Chen et al., 2015). This sequence of events can be supported by other lines of evidence, including: 1) the development of the Upper Devonian molasses formation that unconformably overlies early Paleozoic mélanges and flysch in both the NOB and SOB (Xu et al., 2013), 2) the gap in magmatic activity between 420 and 360 Ma (Xu et al., 2013; Song et al., 2015), corresponding to the collisional orogeny and 3) the development of collision-related biotite monzogranites of high-K calc-alkaline series of 423–392 Ma in Sunidzuoqi and Xilinhot (Shi et al., 2004; Xu et al., 2015).

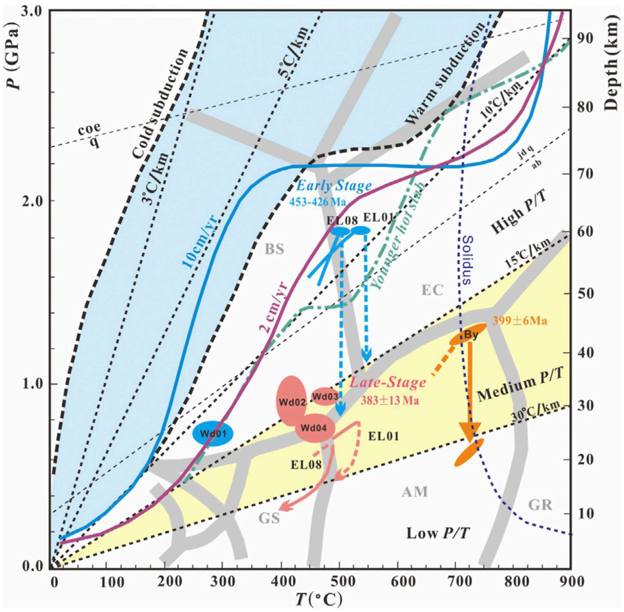

FIGURE 13 | The summarized P–T conditions and paths of the high-pressure rocks in the Ondor Sum Group. Wd01 refer to the P–T results of the blueschist at Wulangou cited from Tang and Yan (1993). Wd02 and Wd03 refer to the P–T results of sodic-amphibolite bearing quartzite (Li et al., 2014b) and barroisite schist (Zhang et al., 2015) at Airgin Sum respectively. Wd04 refer to the P–T result of epidote-blueschist at Naomuhunni (Zhang et al., 2015). By refers to the P–T path of the Barrovian metamorphism the Baoyintu Group in Chen et al. (2015). EL01 and EL08 refer to the P–T paths of HP schists in this study. The bold dotted curves indicate the approximate range of the geothermal gradient at slab surface between cold and hot subduction zones simulated in Syracuse et al. (2010). The thick curves indicate P–T paths predicted for differing convergence velocities of the incoming plate (van Keken et al., 2002, 20 Ma, 30 dip). In general, slower convergence velocities (2 cm/yr) are predicted to result in higher temperatures at a given depth compared to faster convergence velocities (van Keken et al., 2002, 10 cm/yr). The thick chain-dotted line refers to a younger slab have higher geothermal gradients at both the surface as indicated in Wei and Zheng et al. (2020). The reaction ab = jd + q and the transition lines of Al_2SiO_5 were calculated using THERMOCALC. The division of the metamorphic facies series is after Miyashiro (1961, 1994). The metamorphic facies boundaries are after Maruyama et al. (1996) and Oh and Liou (1998).

Consequently, a preliminary tectonic reconstruction may be achieved for the evolution of the Paleo-Asian Ocean in central Inner Mongolia although our results are temporarily representative of a local area and more researches are still needed. The Paleo-Asian Ocean was initiated at ca. 500 Ma in central Inner Mongolia with bidirectional subduction, both northward beneath the Southern Mongolia Block (SMB) and southward beneath the NCC (e.g., Xiao et al., 2003; Xu et al., 2013; Song et al., 2015). This resulted in the formation of the 499–425 Ma Bainaimiao Arc complexes in the south and the 482–428 Ma Baolidao Arc complexes in the north, as well as contemporaneous high-P/T mélanges represented by the Ondor Sum Group. From ~420 Ma, the Paleo-Asian oceanic system came to an end and collision resulted in orogenic processes. The Ondor Sum Group at Airgin Sum was supposed to be involved in the collision with overprinting by the medium-P/T metamorphism. We thus suggest that the HP schists of the Ondor Sum Group at Airgin Sum record the tectonic transition from terminal subduction of the Paleo-Asian Ocean to continental collision.

7 CONCLUSION

Our field observations, petrographic observations, phase equilibria modelling, and zircon U–Pb dating for the samples of Ondor Sum Group in the Airgin Sum area, have led to the following conclusions:

1) Both HP schists record two phases of metamorphism and two phases of foliation development, based on their mineral assemblages and petrography.

2) Both phases of metamorphism were characterized by clockwise P–T evolutions involving pre-peak prograde, peak, and post-peak decompression stages. The peak P–T conditions of the early phase were ~18 kbar/~535°C for sample EL01 and 18 kbar/~500°C for EL08, and the modeled peak mineral assemblage that contained jadeite, lawsonite, and glaucophane could not survive the isothermal decompression, which was dominated by dehydration reactions. The peak P–T conditions of the late-phase metamorphism were ~8 kbar/532°C and ~7.0 kbar/495°C, respectively, and this metamorphism overprinted the early-phase metamorphism.

3) Available zircon ages data suggest that the early-phase HP metamorphism occurs in the early Paleozoic.

4) The data for the two phases of metamorphism indicate two entirely different P/T series, an early high-P/T series with a thermal gradient of ~8°C/km, pointing to the subduction of a warm subduction enviroment, and a late medium-P/T series with a geothermal gradient of 22–25°C/km that was related to collisional thickening of the crust. We suggest that the early high-P/T metamorphism represents the terminal subduction of the Paleo-Asian oceanic plate, and that the later medium-P/T metamorphism represents the involvement of these schists in the continental collision that took place after the closure of the Paleo-Asian Ocean in the Devonian.

DATA AVAILABILITY STATEMENT

The original contributions presented in the study are included in the article/**Supplementary Material**, further inquiries can be directed to the corresponding author.

AUTHOR CONTRIBUTIONS

JZ: Methodology, Software, Writing Original Draft, Resourses, Formal analysis, Validation. WX, CW: Conceptualization. HC, LJ: Investigation. ST: Data Curation.

FUNDING

This work was financially supported by the National Natural Science Foundation of China (Grant Numbers 42072073 and 41702049), Opening Foundation of Key Laboratory of Mineral Resources Evaluation in Northeast Asia, Ministry of Natural Resources (DBY-ZZ-19-08), the Major State Basic Research Development Program of China (2013CB429801), and the China Survey of Geology (121201091100).

ACKNOWLEDGMENTS

We thank Bei Xu and Pohung Huang for their constructive comments of the manuscript, and thank Hong Qing and Xiaoli Li for their help in experimental analyses. We also thank anonymous reviewers for their thoughtful and constructive reviews on the manuscript.

SUPPLEMENTARY MATERIAL

The Supplementary Material for this article can be found online at: https://www.frontiersin.org/articles/10.3389/feart.2022.817682/full#supplementary-material

REFERENCES

Agard, P., Plunder, A., Angiboust, S., Bonnet, G., and Ruh, J. (2018). The Subduction Plate Interface: Rock Record and Mechanical Coupling (From Long to Short Timescales). *Lithos* 320-321, 537–566. doi:10.1016/j.lithos.2018.09.029

Andersen, T. (2002). Correction of Common lead in U-Pb Analyses that Do Not Report 204Pb. *Chem. Geology.* 192, 59–79. doi:10.1016/s0009-2541(02)00195-x

Badarch, G., Dickson Cunningham, W., and Windley, B. F. (2002). A New Terrane Subdivision for Mongolia: Implications for the Phanerozoic Crustal Growth of Central Asia. *J. Asian Earth Sci.* 21, 87–110. doi:10.1016/s1367-9120(02)00017-2

Brown, M., and Johnson, T. (2018). Secular Change in Metamorphism and the Onset of Global Plate Tectonics. *Am. Mineral.* 103 (2), 181–196. doi:10.2138/am-2018-6166

Carson, C. J., Powell, R., and Clarke, G. L. (1999). Calculated mineral Equilibria for Eclogites in CaO-Na_2O-FeO-MgO-Al_2O_3-SiO_2-H_2o: Application to the Pouébo Terrane, Pam Peninsula, New Caledonia. *J. Metamorphic Geology.* 17, 9–24. doi:10.1046/j.1525-1314.1999.00177.x

Chen, B., Jahn, B.-m., Wilde, S., and Xu, B. (2000). Two Contrasting Paleozoic Magmatic Belts in Northern Inner Mongolia, China: Petrogenesis and Tectonic Implications. *Tectonophysics* 328, 157–182. doi:10.1016/s0040-1951(00)00182-7

Chen, B., Jahn, B. M., and Tian, W. (2009). Evolution of the Solonker Suture Zone: Constraints from Zircon U-Pb Ages, Hf Isotopic Ratios and Whole-Rock Nd-Sr Isotope Compositions of Subduction- and Collision-Related Magmas and Forearc Sediments. *J. Asian Earth Sci.* 34, 245–257. doi:10.1016/j.jseaes.2008.05.007

Chen, C., Zhang, Z., Guo, Z., Li, J., Feng, Z., and Tang, W. (2012). Geochronology, Geochemistry, and its Geological Significance of the Permian Mandula Mafic Rocks in Damaoqi, Inner Mongolia. *Sci. China Earth Sci.* 55, 39–52. doi:10.1007/s11430-011-4277-z

Chen, Y., Wei, C., Zhang, J., and Chu, H. (2015). Metamorphism and Zircon U-Pb Dating of Garnet Amphibolite in the Baoyintu Group, Inner Mongolia. *Sci. Bull.* 60, 1698–1707. doi:10.1007/s11434-015-0890-0

Chu, H., Zhang, J., Wei, C., Wang, H., and Ren, Y. (2013). A New Interpretation of the Tectonic Setting and Age of Meta-Basic Volcanics in the Ondor Sum Group, Inner Mongolia. *Chin. Sci. Bull.* 58, 3580–3587. doi:10.1007/s11434-013-5862-7

Coggon, R., and Holland, T. J. B. (2002). Mixing Properties of Phengitic Micas and Revised Garnet-Phengite Thermobarometers. *J. Metamorph Geol.* 20, 683–696. doi:10.1046/j.1525-1314.2002.00395.x

De Jong, K., Xiao, W., Windley, B. F., Masago, H., and Lo, C.-h. (2006). Ordovician ^{40}Ar/^{39}Ar Phengite Ages from the Blueschist-Facies Ondor Sum Subduction-Accretion Complex (Inner Mongolia) and Implications for the Early Paleozoic History of continental Blocks in China and Adjacent Areas. *Am. J. Sci.* 306, 799–845. doi:10.2475/10.2006.02

Diener, J. F. A., Powell, R., White, R. W., and Holland, T. J. B. (2007). A New Thermodynamic Model for Clino- and Orthoamphiboles in the System Na_2O–CaO–FeO–MgO–Al_2O_3–SiO_2–H_2O–O. *J. Metamorph. Geol.* 25, 631–656. doi:10.1111/j.1525-1314.2007.00720.x

Gerya, T. V., and Meilick, F. I. (2011). Geodynamic Regimes of Subduction Under an Active Margin: Effects of Rheological Weakening by Fluids and Melts. *J. Metamorph. Geol.* 29 (1), 7–31. doi:10.1111/j.1525-1314.2010.00904.x

Green, E. C. R., White, R. W., Diener, J. F. A., Powell, R., Holland, T. J. B., and Palin, R. M. (2016). Activity-composition Relations for the Calculation of Partial Melting Equilibria in Metabasic Rocks. *J. Metamorph. Geol.* 34, 845–869. doi:10.1111/jmg.12211

Groppo, C., Beltrando, M., and Compagnoni, R. (2009). TheP-Tpath of the Ultra-high Pressure Lago Di Cignana and Adjoining High-Pressure Meta-Ophiolitic Units: Insights into the Evolution of the Subducting Tethyan Slab. *J. Metamorph. Geol.* 27 (3), 207–231. doi:10.1111/j.1525-1314.2009.00814.x

Guiraud, M., Powell, R., and Rebay, G. (2001). H2 O in Metamorphism and Unexpected Behaviour in the Preservation of Metamorphic mineral Assemblages. *J. Metamorph. Geol.* 19, 445–454. doi:10.1046/j.0263-4929.2001.00320.x

Hernández–Uribe, D., Mattinson, C. G., and Zhang, J. X. (2018). Phase Equilibrium Modelling and Implications for P –T Determinations of Medium-temperature UHP Eclogites, North Qaidam Terrane, China. *J. Metamorph. Geol.* 36 (9), 1237–1261. doi:10.1111/jmg.12444

Holder, R. M., Viete, D. R., Brown, M., and Johnson, T. E. (2019). Metamorphism and the Evolution of Plate Tectonics. *Nature* 572 (7769), 378–381. doi:10.1038/s41586-019-1462-2

Holland, T. J. B., and Powell, R. (1998). An Internally Consistent Thermodynamic Data Set for Phases of Petrological Interest. *J. Metamorph. Geol.* 16, 309–343.

Holland, T., and Powell, R. (2003). Activity?composition Relations for Phases in Petrological Calculations: an Asymmetric Multicomponent Formulation. *Contrib. Mineral. Petrol.* 145, 492–501. doi:10.1007/s00410-003-0464-z

Holland, T. J. B., and Powell, R. (2011). An Improved and Extended Internally Consistent Thermodynamic Dataset for Phases of Petrological Interest, Involving a New Equation of State for Solids. *J. Metamorph. Geol.* 29, 333–383. doi:10.1111/j.1525-1314.2010.00923.x

Huang, P. H., Wei, C., and Zhang, J. (2021). High- P Metamorphism of Garnet-Epidote-Amphibole Schists from the Yuli Belt, Eastern Taiwan: Evidence Related to Warm Subduction. *J. Metamorph. Geol.* 39, 675–693. doi:10.1111/jmg.12577

IMBGMR (Inner Mongolian Bureau of Geology and Mineral Resources) (1991). *Regional Geology of Inner Mongolian Autonomous Region*. Beijing: Geological Publishing House, 726. (in Chinese with English abstract).

Jian, P., Liu, D., Kröner, A., Windley, B. F., Shi, Y., Zhang, F., et al. (2008). Time Scale of an Early to Mid-paleozoic Orogenic Cycle of the Long-Lived Central Asian Orogenic Belt, Inner Mongolia of China: Implications for Continental Growth. *Lithos* 101, 233–259. doi:10.1016/j.lithos.2007.07.005

Jian, P., Liu, D., Kröner, A., Windley, B. F., Shi, Y., Zhang, W., et al. (2010). Evolution of a Permian Intraoceanic Arc-Trench System in the Solonker Suture Zone, Central Asian Orogenic Belt, China and Mongolia. *Lithos* 118, 169–190. doi:10.1016/j.lithos.2010.04.014

Jian, P., Kröner, A., Windley, B. F., Shi, Y., Zhang, W., Zhang, L., et al. (2012). Carboniferous and Cretaceous Mafic-Ultramafic Massifs in Inner Mongolia (China): A SHRIMP Zircon and Geochemical Study of the Previously Presumed Integral "Hegenshan Ophiolite". *Lithos* 142-143, 48–66. doi:10.1016/j.lithos.2012.03.007

Zhang, J., Wei, C., and Chu, H. (2015). Blueschist Metamorphism and its Tectonic Implication of Late Paleozoic-Early Mesozoic Metabasites in the Mélange Zones, central Inner Mongolia, China. *J. Asian Earth Sci.* 97, 352–364. doi:10.1016/j.jseaes.2014.07.032

Kirby, S. H., Durham, W. B., and Stern, L. A. (1991). Mantle Phase Changes and Deep-Earthquake Faulting in Subducting Lithosphere. *Science* 252 (5003), 216–225. doi:10.1126/science.252.5003.216

Kohn, M. J., Castro, A. E., Kerswell, B. C., Ranero, C. R., and Spear, F. S. (2018). Shear Heating Reconciles thermal Models with the Metamorphic Rock Record of Subduction. *Proc. Natl. Acad. Sci. USA* 115 (46), 11706–11711. doi:10.1073/pnas.1809962115

Krogh, E. J., and Råheim, A. (1978). Temperature and Pressure Dependence of Fe-Mg Partitioning between Garnet and Phengite, with Particular Reference to Eclogites. *Contr. Mineral. Petrol.* 66, 75–80. doi:10.1007/bf00376087

Krogh Ravna, E. J., and Terry, M. P. (2004). Geothermobarometry of UHP and HP Eclogites and Schists - an Evaluation of Equilibria Among Garnet-Clinopyroxene-Kyanite-Phengite-Coesite/quartz. *J. Metamorph. Geol.* 22 (6), 579–592. doi:10.1111/j.1525-1314.2004.00534.x

Leake, B., Woolley, A., Arps, C., Birch, W., Gilbert, M., Grice, J., et al. (1997). Nomenclature of Amphiboles: Report of the Subcommitee on Amphiboles of the International Mineralogical Association, Commission on New Minerals and Mineral Names. *Can. Mineral.* 35, 219–246.

Leng, W., and Mao, W. (2015). Geodynamic Modeling of thermal Structure of Subduction Zones. *Sci. China Earth Sci.* 58, 1070–1083. doi:10.1007/s11430-015-5107-5

Li, J. Y., Gao, L. M., and Sun, G. H. (2007). Shuangjingzi Middle Triassic Syn-Collisional Crust-Derived Granite in the East Inner Mongolia and its Constraint on the Timing of Collision between Siberian and Sino-Korean Paleo-Plates (In Chinese). *Acta Geol. Sin.* 23, 565–582. doi:10.1631/jzus.2007.B0900

Li, C. D., Zhao, L. G., Wang, H. C., Zhang, K., Xu, Y. W., Gu, C. Y., et al. (2012). LA-ICP MS U-Pb Geochronology of Zircons from the Wenduermiao Group and its Tectonic Significance. *Acta Petrol. Sin.* 28, 3705–3714. (in Chinese with English abstract).

Li, R. B., Xu, B., Zhao, P., Tong, Q. L., and Zhang, J. R. (2014). The Discovery of Blueschist-Facies Rock in Airgin Sum Area, Erenhot, Inner Mongolia and its Tectonic Significance. *Chin. Sci. Bull.* 59, 66–71. doi:10.1360/972012-1670

Liou, J. G., Maruyama, S., and Cho, M. (1987). Very Low-Grade Metamorphism of Vocanic and Volcaniclastic Rocks-mineral Assemblages and mineral Facies. *Low Temper. Metamorph.* 59, 113.

Liu, D. Y., Jian, P., Zhang, Q., Zhang, F., Shi, Y., Shi, G., et al. (2003). SHRIMP Dating of Adakites in the Tulinkai Ophiolite, Inner Mongolia: Evidence for the Early Paleozoic Subduction. *Acta Geol. Sin.* 77, 317–326.

Liu, W., Siebel, W., Li, X.-j., and Pan, X.-f. (2005). Petrogenesis of the Linxi Granitoids, Northern Inner Mongolia of China: Constraints on Basaltic Underplating. *Chem. Geology*. 219, 5–35. doi:10.1016/j.chemgeo.2005.01.013

Liu, J. F., Chi, X. G., Zhang, X. Z., Ma, Z. H., Zhao, Z., Wang, T. F., et al. (2009). Geochemical Characteristic of Carboniferous Quartzdiorite in the Southern Xiwuqi Area, Inner Mongolia and its Tectonic Significance. *Acta Geol. Sin.* 83, 365–376. (in Chinese with English abstract). doi:10.1016/S1874-8651(10)60080-4

Liu, J., Li, J., Chi, X., Qu, J., Hu, Z., Fang, S., et al. (2012). A Late-Carboniferous to Early Early-Permian Subduction–Accretion Complex in Daqing Pasture, southeastern Inner Mongolia: Evidence of Northward Subduction beneath the Siberian Paleoplate Southern Margin. *Lithos* 177, 285–296. doi:10.1016/j.lithos.2013.07.008

Ludwig, K. R. (2003). *ISOPLOT 3.0: A Geochronological Toolkit for Microsoft Excel*, Vol. 4. Berkeley, CA: Berkeley Geochronology Center Special Publication.

Maruyama, S., Liou, J. G., and Terabayashi, M. (1996). Blueschists and Eclogites of the World and Their Exhumation. *Int. Geol. Rev.* 38 (6), 485–594. doi:10.1080/00206819709465347

Maresch, W. V. (1977). Experimental Studies on Glaucophane: an Analysis of Present Knowledge. *Tectonophysics* 43, 109–125. doi:10.1016/0040-1951(77)90008-7

Miao, L., Fan, W., Liu, D., Zhang, F., Shi, Y., and Guo, F. (2008). Geochronology and Geochemistry of the Hegenshan Ophiolitic Complex: Implications for Late-Stage Tectonic Evolution of the Inner Mongolia-Daxinganling Orogenic Belt, China. *J. Asian Earth Sci.* 32, 348–370. doi:10.1016/j.jseaes.2007.11.005

Miyashiro, A. (1961). Evolution of Metamorphic Belts. *J. Petrol.* 2 (3), 277–311. doi:10.1093/petrology/2.3.277

Miyashiro, A. (1994). *Metamorphic Petrology*. London: UCL Press Limited.

Oh, C. W., and Liou, J. G. (1998). A Petrogenetic Grid for Eclogite and Related Facies Under High-Pressure Metamorphism. *Island Arc* 7 (1-2), 36–51. doi:10.1046/j.1440-1738.1998.00180.x

Peacock, S. M., and Wang, K. (1999). Seismic Consequences of Warm versus Cool Subduction Metamorphism: Examples from Southwest and Northeast Japan. *Science* 286 (5441), 937–939. doi:10.1126/science.286.5441.937

Peacock, S. M. (1996). Thermal and Petrologic Structure of Subduction Zones. *Subduction: Top. Bottom* 96, 119–133.

Penniston-Dorland, S. C., Kohn, M. J., and Manning, C. E. (2015). The Global Range of Subduction Zone thermal Structures from Exhumed Blueschists and Eclogites: Rocks Are Hotter Than Models. *Earth Planet. Sci. Lett.* 428, 243–254. doi:10.1016/j.epsl.2015.07.031

Qiao, X., Li, W., Zhong, R., Hu, C., Zhu, F., and Li, Z. (2017). Elemental and Sr-Nd Isotopic Geochemistry of the Uradzhongqi Magmatic Complex in Western Inner Mongolia, China: A Record of Early Permian post-collisional Magmatism. *J. Asian Earth Sci.* 144, 171–183. doi:10.1016/j.jseaes.2016.12.002

Rojas-Agramonte, Y., Kröner, A., Demoux, A., Xia, X., Wang, W., Donskaya, T., et al. (2011). Detrital and Xenocrystic Zircon Ages from Neoproterozoic to Palaeozoic Arc Terranes of Mongolia: Significance for the Origin of Crustal Fragments in the Central Asian Orogenic Belt. *Gondwana Res.* 19, 751–763. doi:10.1016/j.gr.2010.10.004

Shi, G., Liu, D., Zhang, F., Jian, P., Miao, L., Shi, Y., et al. (2003). SHRIMP U-Pb Zircon Geochronology and its Implications on the Xilin Gol Complex, Inner Mongolia, China. *Chin. Sci. Bull.* 48, 2742–2748. doi:10.1016/j.sedgeo.2003.12.012

Shi, Y. R., Liu, D. Y., Zhang, Q., Zhang, F. Q., Miao, L. C., Shi, G. H., et al. (2004). SHRIMP Dating of Diorites and Granites in Southern Suzuoqi, Inner Mongolia. *Acta Geol. Sin.* 78, 789–799. (in Chinese with English abstract). doi:10.1007/BF02873097

Shi, Y. R., Liu, D. Y., Zhang, Q., Jiang, P., Zhang, F. Q., Miao, L. C., et al. (2005). The Petrogenesis and SHRIMP Dating of the Baiyinbaolidao Adakitic Rocks in Southern Suzuoqi, Inner Mongolia. *Acta Petrol. Sin.* 21, 143–150. (in Chinese with English abstract).

Sircombe, K. N. (1999). Tracing Provenance through the Isotope Ages of Littoral and Sedimentary Detrital Zircon, Eastern Australia. *Sediment. Geology.* 124, 47–67. doi:10.1016/s0037-0738(98)00120-1

Song, S. G., Wang, M. M., Xu, X., Wang, C., Niu, Y. L., and Allen, M. B. (2015). Ophiolites in the Xing'an-Inner mongolia Accretionary belt of the CAOB: Implications for Two Cycles of Seafloor Spreading and Accretionary Orogenic Events. *Tectonics* 34, 1371–1385. doi:10.1002/2015tc003948

Sun, L. X., Ren, B. F., Zhao, F. Q., Gu, Y. C., Li, Y. F., and Liu, H. (2013). Zircon U-Pb Dating and Hf Isotopic Compositions of the Mesoporterozoic Granitic Gneiss in Xilinhot Block, Inner Mongolia. *Geol. Bull. China* 32, 327–340.

Syracuse, E. M., van Keken, P. E., and Abers, G. A. (2010). The Global Range of Subduction Zone thermal Models. *Phys. Earth Planet. Interiors* 183 (1–2), 73–90. doi:10.1016/j.pepi.2010.02.004

Tamblyn, R., Zack, T., Schmitt, A. K., Hand, M., Kelsey, D., Morrissey, L., et al. (2019). Blueschist from the Mariana Forearc Records Long-Lived Residence of Material in the Subduction Channel. *Earth Planet. Sci. Lett.* 519, 171–181. doi:10.1016/j.epsl.2019.05.013

Tang, K., and Yan, Z. (1993). Regional Metamorphism and Tectonic Evolution of the Inner Mongolian Suture Zone. *J. Metamorphic Geology.* 11, 511–522.

Tang, K. D., Yan, Z. J., Zhang, R. P., Xu, D. K., Tchi, Y., Su, Y. Z., et al. (1983). On Wentermiao Group and its Tectonic Significance. *Contrib. Project Plate Tectonic North. China* 1, 186–208. (in Chinese).

Tang, K. (1990). Tectonic Development of Paleozoic Foldbelts at the north Margin of the Sino-Korean Craton. *Tectonics* 9, 249–260. doi:10.1029/tc009i002p00249

Tian, Z. L., and Wei, C. J. (2013). Metamorphism of Ultrahigh-Pressure Eclogites from the Kebuerte Valley, South Tianshan, NW China: Phase Equilibria and P-T Path. *J. Metamorph. Geol.* 31, 281–300. doi:10.1111/jmg.12021

Tong, Y., Jahn, B.-m., Wang, T., Hong, D.-w., Smith, E. I., Sun, M., et al. (2015). Permian Alkaline Granites in the Erenhot-Hegenshan belt, Northern Inner Mongolia, China: Model of Generation, Time of Emplacement and Regional Tectonic Significance. *J. Asian Earth Sci.* 97, 320–336. doi:10.1016/j.jseaes.2014.10.011

Tsujimori, T., and Ernst, W. G. (2014). Lawsonite Blueschists and Lawsonite Eclogites as Proxies for Palaeo-Subduction Zone Processes: a Review. *J. Meta. Geol.* 32 (5), 437–454. doi:10.1111/jmg.12057

Tsujimori, T., Sisson, V., Liou, J., Harlow, G., and Sorensen, S. (2006). Very-low-temperature Record of the Subduction Process: A Review of Worldwide Lawsonite Eclogites. *Lithos* 92, 609–624. doi:10.1016/j.lithos.2006.03.054

Van Achterbergh, E., Ryan, C., Jackson, S., and Griffin, W. L. (2001). *Data Reduction Software for LA-ICP-MS in Laser-Ablation-ICP MS in the Earth Sciences*. Editor P. Sylvester (Sylvester: Mineralogical Association of Canada Short Course), 29, 239–243.

van Hunen, J., van den Berg, A. P., and Vlaar, N. J. (2002). On the Role of Subducting Oceanic Plateaus in the Development of Shallow Flat Subduction. *Tectonophysics* 352, 317–333. doi:10.1016/s0040-1951(02)00263-9

van Keken, P. E., Hacker, B. R., Syracuse, E. M., and Abers, G. A. (2011). Subduction Factory: 4. Depth-dependent Flux of H_2O from Subducting Slabs Worldwide. *J. Geophys. Res.-Solid Earth*, 116. doi:10.1029/2010jb007922

van Keken, P. E., Wada, I., Abers, G. A., Hacker, B. R., and Wang, K. (2018). Mafic High-Pressure Rocks Are Preferentially Exhumed from Warm Subduction Settings. *Geochem. Geophys. Geosyst.* 19 (9), 2934–2961. doi:10.1029/2018gc007624

van Keken, P. E., Wada, I., Sime, N., and Abers, G. A. (2019). Thermal Structure of the Forearc in Subduction Zones: A Comparison of Methodologies. *Geochem. Geophys. Geosyst.* 20, 3268–3288. doi:10.1029/2019gc008334

Wang, X. C., Wilde, S. A., Xu, B., and Pang, C. J. (2015). Origin of Arc-like continental Basalts: Implications for Deep-Earth Fluid Cycling and Tectonic Discrimination. *Lithos* 261, 5–45.

Wei, C. J., and Clarke, G. L. (2011). Calculated Phase Equilibria for MORB Compositions: a Reappraisal of the Metamorphic Evolution of Lawsonite Eclogite. *J. Metamorph. Geol.* 29 (9), 939–952. doi:10.1111/j.1525-1314.2011.00948.x

Wei, C., and Tian, Z. (2014). Modelling of the Phase Relations in High-Pressure and Ultrahigh-Pressure Eclogites. *Isl. Arc.* 23 (4), 254–262. doi:10.1111/iar.12087

Wei, C. J., and Zheng, Y. F. (2020). Metamorphism, Fluid Behavior and Magmatism in Oceanic Subduction Zones. *Sci. China (Earth Sciences)* 63 (01), 56–81. doi:10.1007/s11430-019-9482-y

Wei, C. J., Wang, W., Clarke, G., Zhang, L. F., and Song, S. G. (2009a). Metamorphism of High/ultra-High-Pressure Pelitic–Felsic Schist in the South Tianshan Orogen, NW China: Phase Equilibria and P-T Path. *J. Petrol.* 50, 1973–1991. doi:10.1093/petrology/egp064

Wei, C. J., Yang, Y., Su, X. L., Song, S. G., and Zhang, L. F. (2009b). Metamorphic Evolution of Low-Teclogite from the North Qilian Orogen, NW China: Evidence from Petrology and Calculated Phase Equilibria in the System NCKFMASHO. *J. Metamorphic Geology.* 27, 55–70. doi:10.1111/j.1525-1314.2008.00803.x

White, R. W., Powell, R., Holland, T. J. B., and Worley, B. A. (2000). The Effect of TiO_2 and Fe_2O_3 on Metapelitic Assemblages at Greenschist and Amphibolite Facies Conditions: Mineral Equilibria Calculations in the System K_2O-FeO-MgO-Al_2O_3 -SiO_2 -H_2O-TiO_2 -Fe_2O_3. *J. Metamorphic Geology.* 18, 497–511. doi:10.1046/j.1525-1314.2000.00269.x

White, R. W., Powell, R., Holland, T. J. B., Johnson, T. E., and Green, E. C. R. (2014). New mineral Activity-Composition Relations for Thermodynamic Calculations in Metapelitic Systems. *J. Meta. Geol.* 32, 261–286. doi:10.1111/jmg.12071

Whitney, D. L., and Davis, P. B. (2006). Why Is Lawsonite Eclogite So Rare? Metamorphism and Preservation of Lawsonite Eclogite, Sivrihisar, Turkey. *Geol* 34 (6), 473–476. doi:10.1130/g22259.1

Wilde, S. A., Zhao, G., and Sun, M. (2002). Development of the North China Craton during the Late Archaean and its Final Amalgamation at 1.8 Ga: Some Speculations on its Position within a Global Palaeoproterozoic Supercontinent. *Gondwana Res.* 5, 85–94. doi:10.1016/s1342-937x(05)70892-3

Xiao, W. J., Windley, B. F., Hao, J., and Zhai, M. G. (2003). Accretion Leading to Collision and the Permian Solonker Suture, Inner Mongolia, China: Termination of the central Asian Orogenic belt. *Tectonics* 22, 1069–1088. doi:10.1029/2002tc001484

Xu, B., Charvet, J., and Zhang, F. Q. (2001). Primary Study on Petrology and Geochronology of the Blueschist in Sunidzuoqi, Northern Inner Mongolia. *Chin. J. Geology.* 36, 424–434. (in Chinese with English abstract).

Xu, B., Charvet, J., Chen, Y., Zhao, P., and Shi, G. (2013). Middle Paleozoic Convergent Orogenic Belts in Western Inner Mongolia (China): Framework, Kinematics, Geochronology and Implications for Tectonic Evolution of the Central Asian Orogenic Belt. *Gondwana Res.* 23, 1342–1364. doi:10.1016/j.gr.2012.05.015

Xu, B., Zhao, P., Bao, Q. Z., Zhou, Y. H., Wang, Y. Y., and Luo, Z. W. (2014). Preliminary Study on the Pre-Mesozoic Tectonic Unit Division of the Xing-Meng Orogenic Belt (XMOB). *Acta Petrol. Sin.* 30, 1841–1857. (in Chinese with English abstract). doi:10.1016/j.pgeola.2014.02.004

Xu, B. W., Xi, A. H., Ge, Y. H., Liu, J., Wang, M. Z., and Fang, C. (2015). Zircon U-Pb Ages of the Late Paleozoic A-Type Granites in Chifeng, Inner Mongolia and its Tectonic Significance. *Acta Geol. Sin.* 1, 58–69. (in Chinese with English abstract). doi:10.3321/j.issn:1000-0569.2005.03.006

Xue, H. M., Guo, L. J., Hou, Z. Q., Zhou, X. W., Tong, Y., and Pan, X. F. (2009). The Xilingele Complex from the Eastern Part of the Central Asian-Mongolia Orogenic Belt, China: Products of Early Variscan Orogeny Other Than Ancient Block: Evidence from Zircon SHRIMP U–Pb Ages. *Acta Petrol. Sin.* 25, 2001–2010.

Yarmolyuk, V. V., Kovalenko, V. I., Sal'nikova, E. B., Kozakov, I. K., Kotov, A. B., Kovach, V. P., et al. (2005). U-pb Age of Syn- and Postmetamorphic Granitoids of South Mongolia: Evidence for the Presence of Grenvillides in the Central Asian Fold belt. *Doklady Earth Sci.* 404, 986–990.

Yarmolyuk, V. V., Kovalenko, V. I., Sal'nikova, E. B., Kovach, V. P., Kozlovsky, A. M., Kotov, A. B., et al. (2008). Geochronology of Igneous Rocks and Formation of the Late Paleozoic South Mongolian Active Margin of the Siberian Continent. *Stratigr. Geol. Correl.* 16, 162–181. doi:10.1134/s0869593808020056

Zhang, S.-H., Zhao, Y., Song, B., Yang, Z.-Y., Hu, J.-M., and Wu, H. (2007). Carboniferous Granitic Plutons from the Northern Margin of the North China Block: Implications for a Late Palaeozoic Active continental Margin. *J. Geol. Soc.* 164, 451–463. doi:10.1144/0016-76492005-190

Zhang, S. H., Zhao, Y., Song, B., Hu, J. M., Liu, S. W., Yang, Y. H., et al. (2009). Contrasting Late Carboniferous and Late Permian-Middle Triassic Intrusive Suites from the Northern Margin of the north China Craton. *Geol. Soc. Am. Bull.* 121, 181–200. doi:10.1130/B26157.1

Zhang, Y. P., Su, Y. Z., and Li, J. C. (2010). Regional Tectonic Significance of the Late Silurian Xibiehe Formation in central Inner Mongolia, China. *Geol. Bull. China* 29, 1599–1605. (in Chinese with English abstract). doi:10.1017/S0004972710001772

Zhang, J. R., Chu, H., Wei, C. J., and Wang, K. (2014). Geochemical Characteristics and Tectonic Significance of Meta-Basic Volcanics in the Ondor Sum Group, Central Inner Mongolia. *Acta Petro. Sin.* 30, 1935–1947.

Zhang, J., Wei, C., Chu, H., and Chen, Y. (2016). Mesozoic Metamorphism and its Tectonic Implication along the Solonker Suture Zone in central Inner mongolia, china. *Lithos* 261, 262–277. doi:10.1016/j.lithos.2016.03.014

Zhang, J.-R., Wei, C.-J., and Chu, H. (2018b). High-temperature and Low-pressure metamorphism in the Xilingol Complex of central Inner Mongolia, China: An Indicator of Extension in a Previous Orogeny. *J. Metamorph Geol.* 36, 393–417. doi:10.1111/jmg.12297

Zhao, G., Wilde, S. A., Cawood, P. A., Sun, M., and Lu, L. Z. (2001). Archean Blocks and Their Boundaries in the North China Craton: Lithological, Geochemical, Structural and P-T Path Constraints and Tectonic Evolution. *Precambrian Res.* 107, 45–73. doi:10.1016/s0301-9268(00)00154-6

Zhao, G., Cawood, P. A., Wilde, S. A., and Sun, M. (2002). Review of Global 2.1-1.8 Ga Orogens: Implications for a Pre-Rodinia Supercontinent. *Earth-Sci. Rev.* 59, 125–162. doi:10.1016/s0012-8252(02)00073-9

Zhicheng Zhang, Z., Li, K., Li, J., Tang, W., Chen, Y., and Luo, Z. (2015). Geochronology and Geochemistry of the Eastern Erenhot Ophiolitic Complex: Implications for the Tectonic Evolution of the Inner Mongolia-Daxinganling Orogenic Belt. *J. Asian Earth Sci.* 97, 279–293. doi:10.1016/j.jseaes.2014.06.008

Zhou, J.-B., and Wilde, S. A. (2013). The Crustal Accretion History and Tectonic Evolution of the NE China Segment of the Central Asian Orogenic Belt. *Gondwana Res.* 23, 1365–1377. doi:10.1016/j.gr.2012.05.012

Zhou, J. B., Wang, B., Zeng, W. S., and Cao, J. L. (2014). Detrital Zircon U-Pb Dating of the Zhalantun Metamorphic Complex and its Tectonic Implications, Great Xing'an, NE China. *Acta Petrol. Sin.* 30, 1879–1888.

Conflicts of Interest: The authors declare that the research was conducted in the absence of any commercial or financial relationships that could be construed as a potential conflict of interest.

frontiers | Frontiers in Earth Science

ORIGINAL RESEARCH
published: 27 April 2022
doi: 10.3389/feart.2022.866375

Evolution of the Continental Crust in the Northern Tibetan Plateau: Constraints From Geochronology and Hf Isotopes of Detrital Zircons

Zeyu Liu, Guibin Zhang*, Lu Xiong, Feng Chang and Shuaiqi Liu

The Key Laboratory of Orogenic Belts and Crustal Evolution, MOE, School of Earth and Space Sciences, Peking University, Beijing, China

To investigate the evolution of the continental crust in the northern Tibetan Plateau, detrital zircon U–Pb geochronology and Hf isotopes analysis were performed on two fluvial sand samples from North Qaidam (the Yuka and Shaliu rivers). A total of 443 detrital zircon U–Pb ages and 244 Hf isotopic results were obtained and reveal that the South Qilian, North Qaidam, and East Kunlun terranes show affinity to the western Yangtze Block. Age distributions of detrital zircons from the Yuka River cluster mainly in two age intervals of 1,000–700 and 480–400 Ma. The corresponding $\varepsilon_{Hf}(t)$ values are mostly negative, with depleted two-stage Hf model ages (T_{DM2}) of 2.1–1.6 Ga. In contrast, age data for the Shaliu River fall in the ranges of 1,000–700, 460–380, and 260–200 Ma, with T_{DM2} ages of 2.0–1.6 and 1.6–1.2 Ga. In addition, zircons with Neoproterozoic ages from both river samples possess common Paleoproterozoic T_{DM2} ages (2.0–1.6 Ga, with a peak of 1.8–1.7 Ga), indicating that the South Qilian, North Qaidam and East Kunlun terranes were probably part of the same Neoproterozoic continent. The East Kunlun and North Qaidam terranes are inferred to include Mesoproterozoic continental crust (1.6–1.0 Ga), suggesting differences in crustal evolution between the East Kunlun–North Qaidam and Qilian terranes. Phanerozoic magmatism in these three terranes was sourced mainly from the recycling of ancient continental crust with minor contributions from the juvenile crust.

Keywords: south qilian, north qaidam, east kunlun, detrital zircon, zircon U-Pb geochronology, hf isotopes

OPEN ACCESS

Edited by:
Michel Grégoire,
Géosciences Environnement Toulouse (GET), France

Reviewed by:
Simon Johnson,
Geological Survey of Western Australia, Australia
Oscar Laurent,
Géosciences Environnement Toulouse (GET), France

****Correspondence:***
Guibin Zhang
gbzhang@pku.edu.cn

Specialty section:
This article was submitted to Petrology, a section of the journal Frontiers in Earth Science

Received: *31 January 2022*
Accepted: *06 April 2022*
Published: *27 April 2022*

Citation:
Liu Z, Zhang G, Xiong L, Chang F and Liu S (2022) Evolution of the Continental Crust in the Northern Tibetan Plateau: Constraints From Geochronology and Hf Isotopes of Detrital Zircons. Front. Earth Sci. 10:866375. doi: 10.3389/feart.2022.866375

1 INTRODUCTION

The northern Tibetan Plateau is an ideal place to understand plate collision, interactions of tectonic uplift and crustal evolution. Although Tibetan Plateau has been studied for decades, most studies focus on the Cenozoic tectonic uplift (Tapponnier et al., 2001; Yin et al., 2008; Clark et al., 2010; Rohrmann et al., 2012; Wang et al., 2014; Botsyun et al., 2019), while rarely studying the crustal evolution from Proterozoic to Paleozoic by using the detrital zircon in the northern Tibetan Plateau.

Zircon is one of the most robust accessory minerals with refractory nature during weathering and transportation, meaning that the U–Pb isotope system of detrital zircons can be used to obtain reliable chronological information, which in turn can be used to track the source region of the host clastic sedimentary rocks. Combined with the stable Lu–Hf isotope compositions, analysis of detrital zircons from modern river sediments can lead to a better understanding of the history of continental growth (Belousova et al., 2010; Kröner et al., 2014; Chen et al., 2015; Xu et al., 2016; Gong et al., 2017).

Thus, detrital zircons can be used to help establish the geological history of regions through which rivers flow, and may record information about the evolution of magmatism and metamorphism in these regions (Lease et al., 2007; Nie et al., 2012; Blayney et al., 2016; Song et al., 2019).

Numerous studies have used detrital zircon U–Pb ages and Hf isotopes to track the continental growth (e.g., Condie et al., 2005; Liu et al., 2008; Yang et al., 2009; Geng et al., 2011; Sun et al., 2012), although data are scarce for the area of the northern Tibetan Plateau investigated in this study. The North China block and the Yangtze block are two stable cratons adjacent to the northern Tibetan Plateau. It is generally considered that 2.9–2.4 Ga were the main periods of crustal growth in the North China Craton, but thermal events from the Mesoproterozoic to early Paleozoic are missing (Yang et al., 2009). The Yangtze Craton records two Precambrian periods of growth at 3.8–3.2 and 0.91–0.72 Ga, which are consistent with detrital zircon ages obtained from the South Qilian and North Qaidam terranes located on the northern Tibetan Plateau (Liu et al., 2008). Thus, the high degree of similarity of detrital zircon ages between the western Yangtze Craton and South Qilian–North Qaidam terranes reveals their close affinity. However, there have been insufficient studies of the overall crustal evolution of the South Qilian, North Qaidam, and East Kunlun terranes, which are key areas for understanding the tectonic evolution of the northern Tibetan Plateau.

The North Qaidam ultra-high pressure metamorphic (UHPM) belt has attracted considerable research attention regarding the evolution of the adjacent Qilian and East Kunlun orogenic belts (Zhang et al., 2008; Song et al., 2011, Song et al., 2019.; Liu et al., 2012; Gao and Zhang, 2017; Gong et al., 2017; Jian et al., 2020; Wu et al., 2020). Gao and Zhang, 2017 conducted zircon U–Pb dating of metapelite from Lüliangshan and Dulan in the North Qaidam UHPM belt and concluded that the North Qilian was an active continental margin, and the North Qaidam was a passive continental margin during the early Paleozoic; then the North Qaidam changed to be an active continental margin after the closure of ancient Qilian Ocean. Liu et al. (2012) conducted U–Pb isotope dating of detrital zircons from Cenozoic sediments in the Lulehe section and modern river sands in the North Qaidam, revealing a record of Rodinia supercontinent break-up, Pan-African regional metamorphism related to the subduction and collision in the Nouth Qaidam–South Qilian area. It is generally considered that multi-stage arc magmatism and continental-collision felsic intrusive magmatism occurred in the South Qilian, North Qaidam, and East Kunlun terranes from the Paleozoic to Triassic during subduction in the Proto-Tethys and Paleo-Tethys oceans. However, relationships among these three terranes during the Paleozoic–Mesozoic multiple Wilson cycles remain debated. Two popular tectonic models for the Paleozoic–Mesozoic tectonic configuration of the South Qilian, North Qaidam, and East Kunlun terranes follow: 1) the archipelago model, which proposes that the three terranes were separated from each other by ocean basins during the early Paleozoic and amalgamated during the mid-to-late Paleozoic (Kang et al., 2019; Zhang et al., 2020); and 2) the continuous continent model, in which during the early Paleozoic, the continuous "North Qaidam-South Qilian" terrane were sandwiched between the North Qilian arc to the north and the Kunlun arc to the south (Cheng et al., 2017; Gehrels et al., 2003; Song et al., 2013, 2014), or the continuous "North Qaidam–East Kunlun" terrane and Qilian Terrane were separated by the Qilian Ocean (Jian et al., 2020).

Here we present results of detrital zircon U–Pb ages, trace-elements, and Hf isotopes collected from sediments of the Yuka and Shaliu rivers on the northern Tibetan Plateau with the aim of tracking the crustal growth and tectonic evolution of the South Qilian, North Qaidam, and East Kunlun terranes, which the three terranes dominated by the Paleoproterozoic-Mesoproterozoic continental crust, and support the archipelago model during the early Paleozoic.

2 GEOLOGICAL SETTING AND SAMPLES

The Paleozoic North Qaidam UHPM belt lies between the Qaidam and South Qilian terranes in the northern margin of the Tibetan Plateau (**Figures 1A–C**). It extends northwestward from Dulan, through Xitieshan and Lüliangshan, to Yuka over an overall length of ~400 km (**Figure 1D**). From the Neoproterozoic to the middle Permian, tectonic–thermal activities in North Qaidam were very intense (Li et al., 1999; Wu, 2008). The intense Neoproterozoic magmatic activity was most likely associated with the assemble and subsequent break-up of the Rodinia supercontinent, whereas the Paleozoic magmatic activity was probably related to the transition of the North Qaidam UHP belt from oceanic subduction to a continental collision regime (Wu et al., 2004; Song et al., 2009b; Zhang et al., 2013). Along the North Qaidam UHPM belt, eclogites are found as NW–SE-oriented boudins and interlayers within para- and orthogneisses in several localities (e.g., Dulan, Xitieshan, and Yuka) and garnet peridotite crops out in the Lüliangshan area (Song et al., 2009b; Zhang et al., 2013). The early stage of eclogite-facies metamorphism was at 473–443 Ma, representing the early oceanic subduction; then followed the continental deep subduction at 426–420 Ma. The reconstruction of Shaliuhe relict oceanic lithology provides evidence for oceanic subduction in the North Qaidam UHPM belt (Song et al., 2003, 2006, 2009a; Zhang et al., 2005, Zhang et al., 2008, 2009; Zhang and Zhang, 2011). Both coesite and diamond inclusions were found from eclogite, garnet peridotite, and country gneisses (Zhang et al., 2016 and references therein).

Dulan is located in the southeastern North Qaidam UHPM belt–northern Kunlun, which is located at the intersection of the South Qilian belt to the north, the East Kunlun Orogenic belt to the south-southeastward, and the Qinling to the east. The Dulan area was affected by multiple orogenic events during the Paleozoic–early Mesozoic, accompanied by tectonic–magmatic activities and granite intrusions. Three stages of Paleozoic granitic magmatism in Dulan had been identified, with S-type affinity: 434–432, 407–397, and 383–373 Ma (Yu et al., 2011), in which the early stage at 434–432 Ma formed more or less simultaneously with the North Qaidam HP/UHP metamorphism responded to

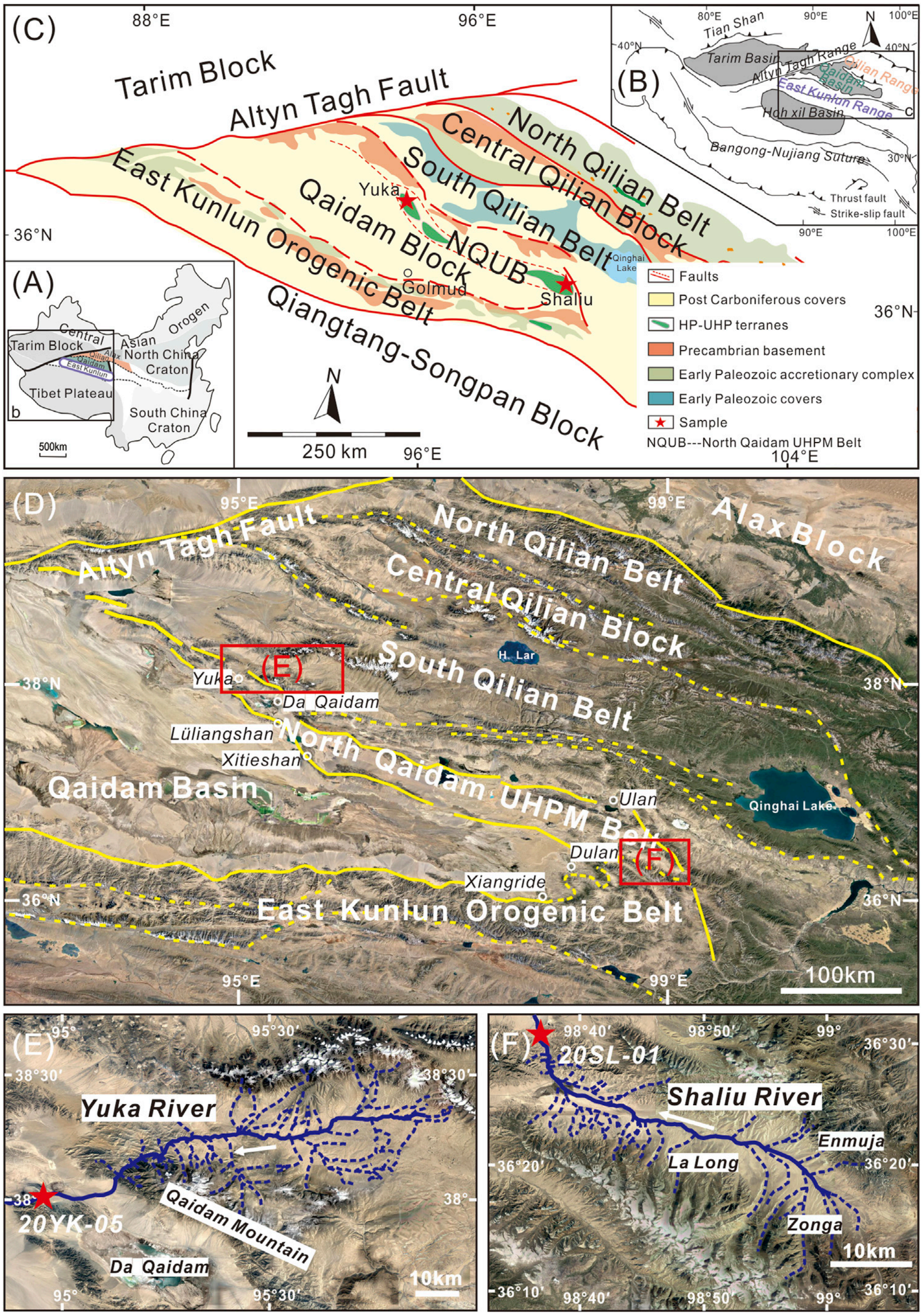

FIGURE 1 | (A) Location of the Tibetan Plateau within China; **(B)** Location of the Qilian Range, Qaidam Basin, and East Kunlun Orogenic Belt in the northern Tibetan Plateau (modified from Yin et al., 2008); **(C)** Simplified geologic maps of the northern Tibetan Plateau (modified from Song et al., 2018); **(D)** Satellite image of the study area showing the two sampling locations; **(E)** Close up view of the catchment area of the Yuka river and sample location of 20YK-05 (red star); **(F)** Close up view of the catchment area of the Shaliu river and sample location of 20SL-01 (red star).

the continental deep subduction and collision (Song et al., 2009b). While the others at 407–397 and 383–373 Ma may have been formed in association with break-off and exhumation of the subducted South Qilian slab and delamination of the lithospheric mantle, respectively (Yu et al., 2011). In addition, the Yematan granitoid represents an event spanning ~30 Myr, ranging from granodiorite with I-type affinities and biotite monzogranite (386–379 Ma), porphyritic biotite granite (367 ± 3 Ma), to diorite (374–360 Ma) (Wu et al., 2007; Wang et al., 2014). Post-collisional magmatic rocks in Dulan occurred

~20–30 Myr later than peak UHP metamorphism (ca. 420 Ma) of continental collision are highly diverse in age and composition, indicating multiple stages of magmatism, melting of various magma sources, and variable degrees of interaction between crust and mantle associated with a complex tectonic evolution from exhumation to orogenic collapse (Wang et al., 2014). Moreover, late Permian–Triassic granites are widely distributed in the eastern part of East Kunlun Terrane (Yuan et al., 2000). Late Triassic granites are widely developed in east of Dulan–Xiangride (Kui et al., 2010).

The Yuka area is part of the North Qaidam UHPM belt and is located between the South Qilian Terrane and the Qaidam Basin. Intermediate–felsic intrusive rocks are widely exposed in the Yuka area, and granites accompanied by UHP metamorphic rocks are well developed. Magmatic rocks are voluminous and represent multiple events, with more intense magmatism during the Caledonian event (early Paleozoic, at about 600–405 Ma) compared with Hercynian (late Paleozoic, at about 386–257 Ma) and Indosinian events (early Mesozoic, at about 257–205 Ma). The largest Paleozoic granite intrusion in the Yuka area is the Qaidamshan pluton, which is composed mainly of porphyritic monzonitic granite, granite porphyry, and granodiorite (He et al., 2020). The crystallization age of the Qaidamshan pluton was early Silurian–early Devonian (ca. 440–400 Ma), formed during continental collision (Wu et al., 2001; Lu et al., 2007; Wu, 2008).

Samples of modern river sediments collected during this study were obtained from the Yuka and Shaliu rivers. Sample 19YK-05 was taken from the Yuka River (**Figure 1E**), at a point located northwest of Dachaidan, west of the Qaidam mountains (38°0.2998′N, 94°56.8398′E). Sample 19SL-01 was taken from the Shaliu River (**Figure 1F**), at a point located in northeastern Dulan County, next to the G109 National Highway (36°31.2211′N, 98°36.6588′E).

3 ANALYTICAL METHODS

Zircon grains were separated using magnetic and heavy-liquid separation techniques and then handpicked under a binocular microscope. Zircon grains were set in an epoxy mount and polished to half thickness. Cathodoluminescence (CL) images were conducted with a Quanta 200F scanning electron microprobe (SEM) at the Key Laboratory of Orogenic Belts and Crustal Evolution, Ministry of Education, School of Earth and Space Sciences (SESS), Peking University (PKU), Beijing, China with conditions of 15 kV and 120 nA.

Zircon U–Pb geochronological and trace-element analyses were performed using a ThermoFisher iCapRQ ICP-MS coupled with a 193 nm GeoLas laser system at the SESS, PKU. The operating conditions are a laser spot diameter of 32 μm, a laser fluence of 5 J cm^{-2}, and a repetition rate of 5 Hz. The aerosol produced by ablation was carried by helium (0.70 L/min) mixed with argon and a small amount of nitrogen (each gas purity is >99.999%). Data reduction was conducted using Iolite software (Paton et al., 2011). Zircon 91,500 was used as an external standard, while GJ-1 and Plešovice were utilized as unknowns to monitor the precision and accuracy of U–Pb dating. Analysis of GJ-1 and Plešovice zircon standards yielded Concordia ages of 599.2 ± 1.2 Ma (2σ, n = 35, MSWD = 2.1) and 337.5 ± 0.7 Ma (2σ, n = 31, MSWD = 0.12), consistent with the recommended values reported in Jackson et al. (2004) and Sláma et al. (2008). The adopted U–Pb ages were $^{206}Pb/^{238}U$ ages for zircon grains with ages of ≤1.0 Ga and $^{207}Pb/^{206}Pb$ ages for grains with ages of >1.0 Ga. Ages with degrees of discordance of >10% were excluded from age calculations. Concordia diagrams were plotted using Isoplot 4.15 (Ludwig, 2003). Trace-element contents were analyzed from the same ablation crater as U-Pb dating and calibrated by ^{29}Si and NIST SRM 610, while NIST SRM 612 was used as a secondary standard (Pearce et al., 1997). Accuracy and precision were better than 5% for most elements. Analytical results for zircon dating and trace-element contents are presented in **Supplementary Tables S1. S2**. Analytical results for standard zircon dating are presented in **Supplementary Table S4**.

In-situ zircon Lu–Hf analyses were conducted using a Nu Plasma II MC–ICPMS coupled with a 193 nm GeoLas laser system at SESS, PKU. Analyses were performed with a laser energy of 8 J cm^{-2}, a repetition rate of 5 Hz, a spot diameter of 44 μm, and helium carry gas (0.63 L/min). Laser spots were positioned to half overlap or lie as close as possible to domains used for zircon U–Pb dating. Zircon 91,500 was analyzed as a calibration standard, and Plešovice and Penglai were adopted as secondary standards to monitor analytical quality. Data reduction was performed using Iolite software (Paton et al., 2011). Mass-dependent fractionation of Hf was corrected by internal normalization relative to a $^{179}Hf/^{177}Hf = 0.73250$ (Patchett and Tatsumoto, 1980) and Yb fractionation was corrected using the constant $^{173}Yb/^{172}Yb = 0.73925$ (Vervoort et al., 2004) and an exponential law. The isobaric interferences of ^{176}Lu and ^{176}Yb on ^{176}Hf were corrected by measuring the intensity of the interference-free ^{175}Lu and ^{172}Yb isotopes with the recommended $^{176}Yb/^{172}Yb$ ratio of 0.5887 and $^{176}Lu/^{175}Lu$ ratio of 0.02655 and assuming the fractionation factor $\beta_{Lu} = \beta_{Yb}$ (Vervoort et al., 2004). The analytical values of $^{176}Hf/^{177}Hf$ for the standard zircons were 0.282307 ± 0.000065 (2σ, n = 24) for 91,500, 0.282482 ± 0.000037 (2σ, n = 22) for Plešovice, and 0.282925 ± 0.000062 (2σ, n = 21) for Penglai, consistent with recommended values reported by Wu et al. (2006), Sláma et al. (2008), and Li et al. (2010), respectively. Present-day chondrite $^{176}Lu/^{177}Lu$ ratio of 0.0332 and $^{176}Hf/^{177}Hf$ ratio of 0.282772 (Blichert-Toft et al., 1997), and present-day depleted mantle values of $(^{176}Lu/^{177}Hf)_{DM} = 0.0384$ and $(^{176}Hf/^{177}Hf)_{DM} = 0.28325$ (Griffin et al., 2000) were used for the calculation of ε_{Hf} (t) values and two-stage Hf model ages (T_{DM2}), respectively. Data for Lu–Hf isotopes of the samples and standard zircons are listed in **Supplementary Tables S3, S5**, respectively.

4 RESULTS

4.1 Detrital Zircon U–Pb Dating and Trace-Element Contents

CL images show that most zircons (>99%) have well-developed oscillatory zoning (**Figure 2**), suggesting a magmatic origin

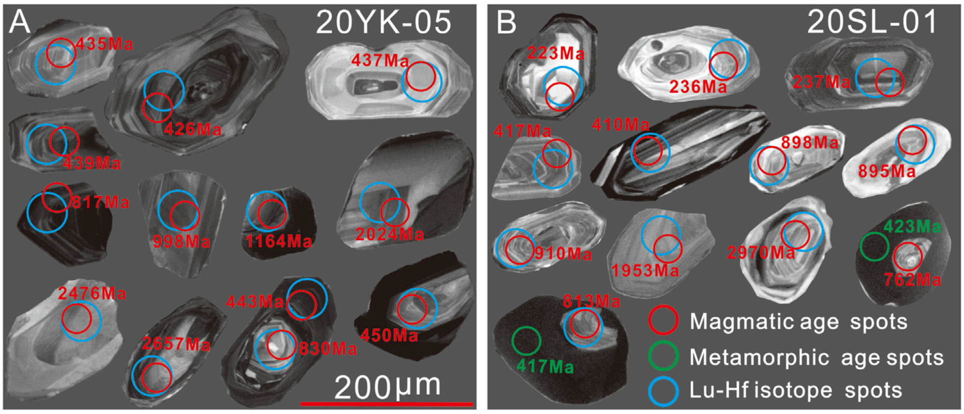

FIGURE 2 | Representative cathodoluminescence (CL) images for detrital zircon crystals of Sample 20YK-05 **(A)** and Sample 20SL-01 **(B)** from North Qaidam.

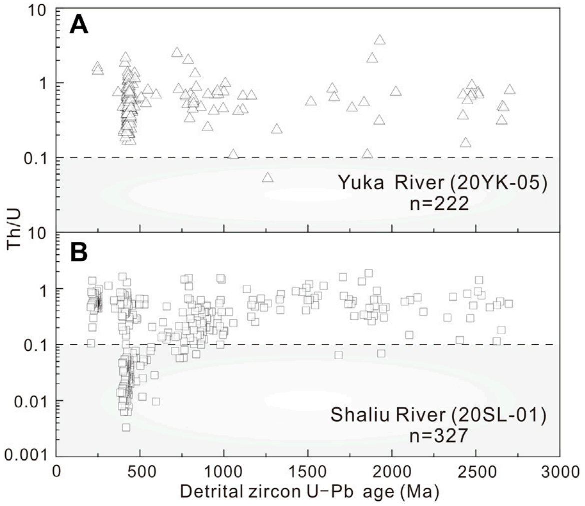

FIGURE 3 | Plot of Th/U ratios versus U-Pb ages of detrital zircons from the river sands of Sample 20YK-05 **(A)** and Sample 20SL-01 **(B)** from North Qaidam.

(Hoskin and Black, 2000; Corfu et al., 2003). Plots of Th/U versus U–Pb ages of detrital zircons and U–Pb age cumulative probability distributions for each sample are presented in **Figures 3**, **5A,B**, respectively.

On the basis of the substitution of (REE^{3+} + Y^{3+}) for Zr in zircon from S-type granites being charge-balanced by P^{5+}, leading to a near 1:1 correlation between (REE + Y) and P, thus plots of (REE + Y) versus molar P can be used to distinguish the S-type and I-type zircons (Burnham and Berry., 2017; Zhu et al., 2020). Applying this classification method (S-type granites, i.e., $0.77*P< [REE + Y] <1.23*P$ for zircons with molar P > 15 μmol/g) to those zircons from the two samples with degrees of discordance of <10% shows that S-type granite zircons account for the majority (56.3%) of the Yuka River detrital zircons (**Figure 4A**), whereas I-type granite zircons account for the majority (73.8%) of the Shaliu River detrital zircons (**Figure 4B**). U–Pb age cumulative probability distributions and U–Pb Concordia diagrams for each age peak of S- and I-type zircons of the two samples are shown in **Figures 5C**,D, **6**. Selected detrital zircons with representative age peaks and mean values of age are given in **Supplementary Table S2**, and chondrite-normalized REE patterns are presented in **Figure 7**.

Zircons from the Yuka river (20YK-05) are characterized by oscillatory zoning textures and high Th/U ratio (mostly >0.1) (**Figures 2A**, **3A**), indicating a magmatic origin (Belousova et al., 2002; Corfu et al., 2003; Hoskin and Black, 2000; Rubatto, 2002). Some grains display core–rim zonation, with an oscillatory-zoned core and an un-zoned or oscillatory-zoned rim in CL images (**Figure 2A**). Of the 258 analyzed detrital zircon U–Pb ages from the Yuka River sample, 86.0% are concordant. Of these analyses, only one has Th/U ratio of <0.10 (0.05, 1,261 Ma), but it has likely a magmatic origin, as inferred from the oscillatory zoning texture. Detrital zircon U–Pb ages obtained for this sample cluster into two main ranges at 1,000–700 Ma and 480–400 Ma with peaks centering at 820 and 433 Ma, and two secondary ranges at 2800–2400 Ma and 2,100–1,500 Ma, respectively (**Figure 5A**). Compositionally, S-type zircon dominates ages of 460–402 Ma (**Figure 6A**), whereas I-type zircon dominates ages of 961–720 Ma and 472–412 Ma (**Figures 6B,C**). REE contents of sample 20YK-05 shows that S-type zircon has stronger negative Eu and Ce anomalies relative to I-type (**Figure 7A**), consistent with the known REE patterns of typical S- and I-type zircons (Burnham and Berry, 2017; Zhu et al., 2020).

Most analyzed zircons from the Shaliu river (20SL-01) are characterized by oscillatory zoning textures (Hoskin and Black, 2000; Corfu et al., 2003). About one-third of the analyzed grains have core–rim structures, with a core of oscillatory zoning and an un-zoned rim in CL images (**Figure 2B**), with Th/U ratios range of 0.01–1.87 (**Figure 3B**). Of the 336 detrital zircon U–Pb ages from the Shaliu River, 93.8% are concordant, with 223 data points are of magmatic origin and 92 data points are of metamorphic origin which distinguished by Th/U < 0.10 and un-zoned CL images; and three main ranges at 1,000–700 Ma, 460–380 Ma, and 260–200 Ma with peaks centering at 870 Ma, 420 Ma, and

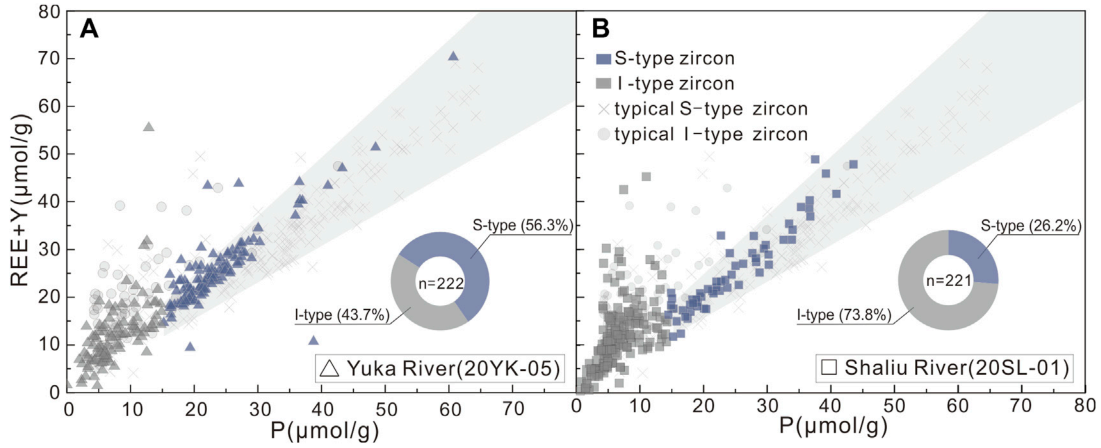

FIGURE 4 | Binary plot of molar *p* concentrations versus (REE + Y) for zircons of Sample 20YK-05 **(A)** and Sample 20SL-01 **(B)**. The gray-shaded area shows the field used to define zircon derived from S-type granites, i.e., 0.77**p*< (REE + Y) <1.23**p* for zircons with molar *p* > 15 μmol/g. The typical S and I-type zircon are collected from Burnham and Berry (2017) and Zhu et al. (2020).

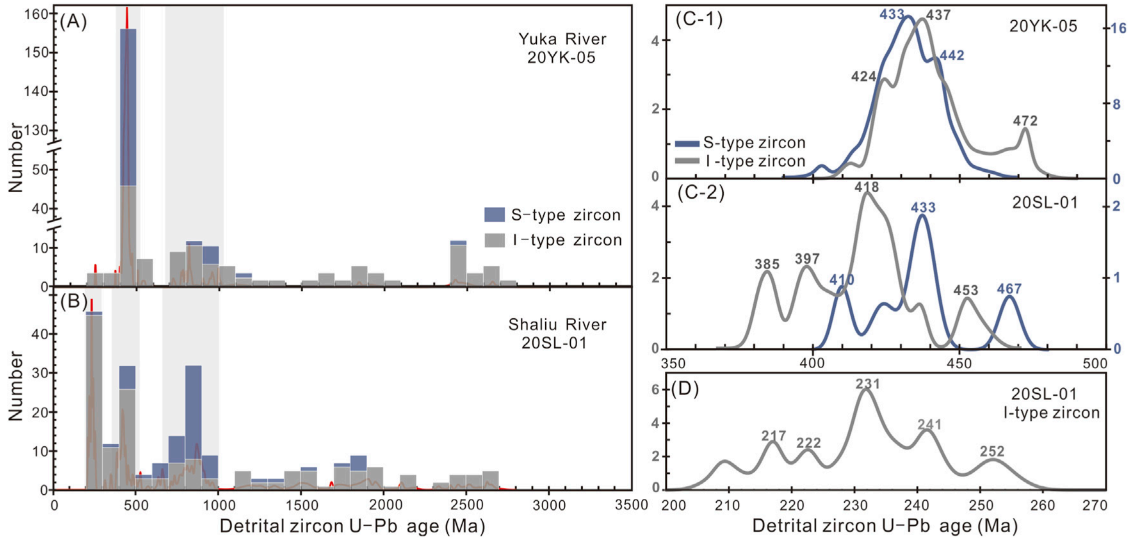

FIGURE 5 | (A) Histograms of detrital zircon U-Pb ages of sample 20YK-05, **(B)** Histograms of detrital zircon U-Pb ages of sample 20SL-01, **(C)** Relative probability plot for Early Paleozoic dates, **(D)** Relative probability plot for Late Paleozoic - Early Mesozoic dates.

232 Ma, and three secondary ranges at 2700–2300 Ma, 2000–1700 Ma, and 1,600–1,100 Ma, respectively (**Figure 5B**). With respect to composition, S-type zircon dominates ages of 915–776 Ma (**Figure 6D**), whereas I-type zircon dominates ages of 927–775 Ma, 458–381 Ma, and 256–207 Ma (**Figures 6E–G**). After excluding 16 mixed ages, the vast majority of the remaining 76 metamorphic zircons fall within the range of 456–383 Ma (**Figure 6H**). Analysis of REE contents for sample 20SL-01 shows the same characteristics as 20YK-05. Metamorphic zircons display flat HREE patterns with weak negative Eu anomalies (**Figure 7B**).

4.2 Lu–Hf Isotopes

Results of 224 Hf isotopic determinations are presented in **Supplementary Table S3** and **Figure 8**. **Figure 9** shows the distribution of T_{DM2} ages (Wu et al., 2007; Yang et al., 2009).

Zircons from sample 20YK-05 (117 analyses) yield ε_{Hf} (t) values of −29.1–16.2 (**Figure 8A**), and T_{DM2} ages in the range of 3.8–1.3 Ga (**Figures 9A-1**), with a peak at 2.1–1.7 Ga. Zircon crystals with U–Pb ages of >1,000 Ma yield values of ε_{Hf} (t) in the range of −12.8–16.2 (**Figure 8A**) and T_{DM2} ages varying from 3.8 to 1.8 Ga (**Figures 9A-2**). Zircons in the age range of 1,000–700 Ma yield ε_{Hf} (t) in the range of −17.1–2.3

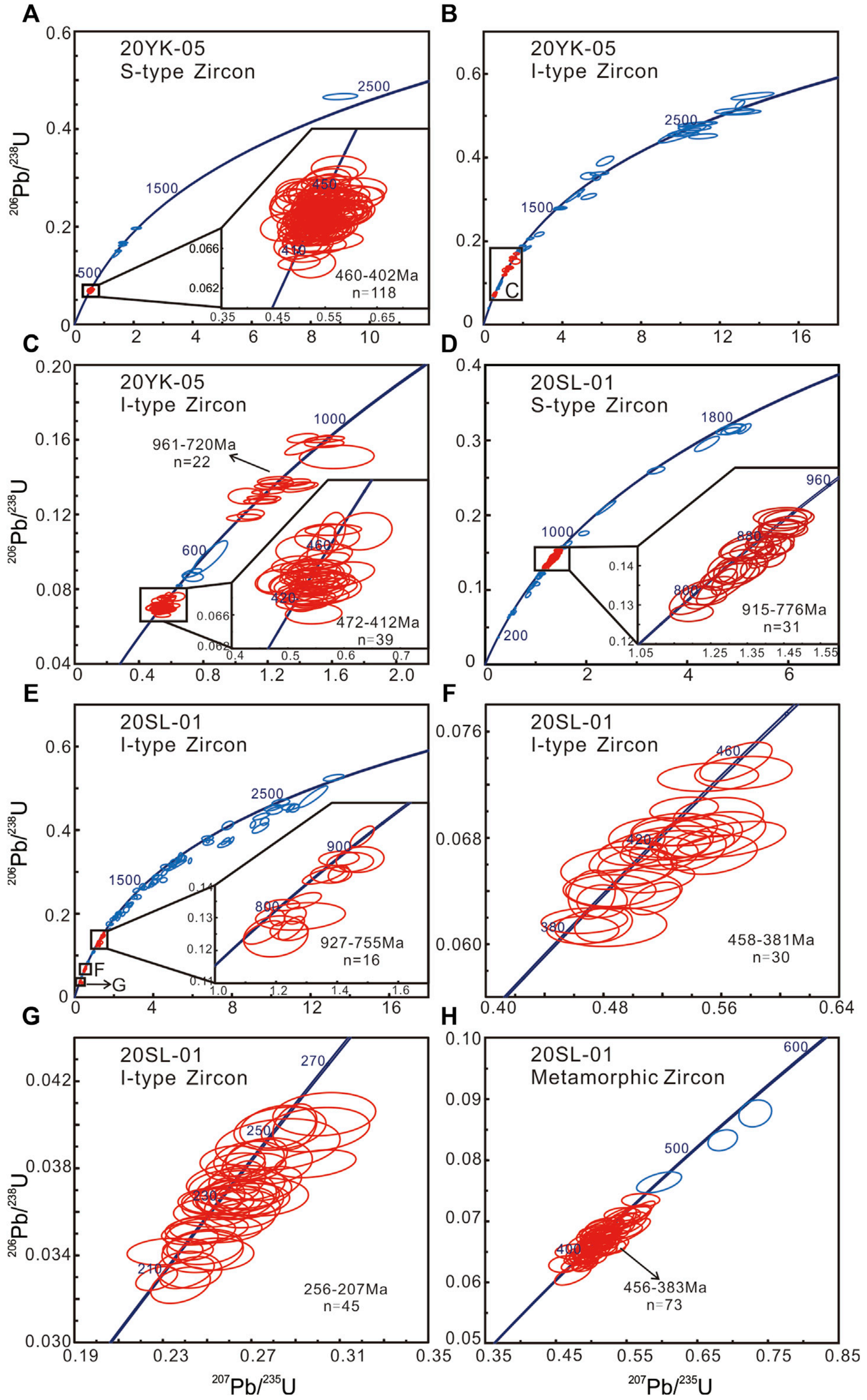

FIGURE 6 | U-Pb concordia plots for the main peaks of detrital zircon dates identified in **Figure 5**. **(A–C)** I- and S-Type zircon U-Pb concordia plots of Sample 20YK-05, **(D–G)** I- and S-Type zircon U-Pb concordia plots of Sample 20SL-01; **(H)** Metamorphic zircon U-Pb concordia plots of Sample 20SL-01.

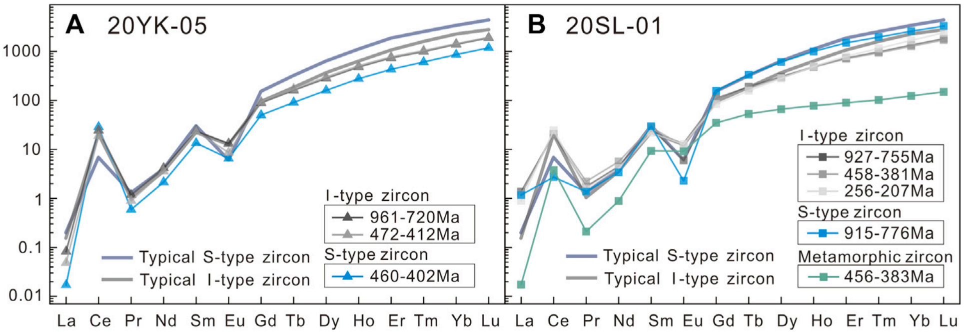

FIGURE 7 | REE in detrital zircons normalized to chondrite (normalization values from Sun and McDonough, 1989). **(A)** Sample 20YK-05, **(B)** Sample 20SL-01. The typical S and I-type zircon are collected from Burnham and Berry (2017) and Zhu et al. (2020).

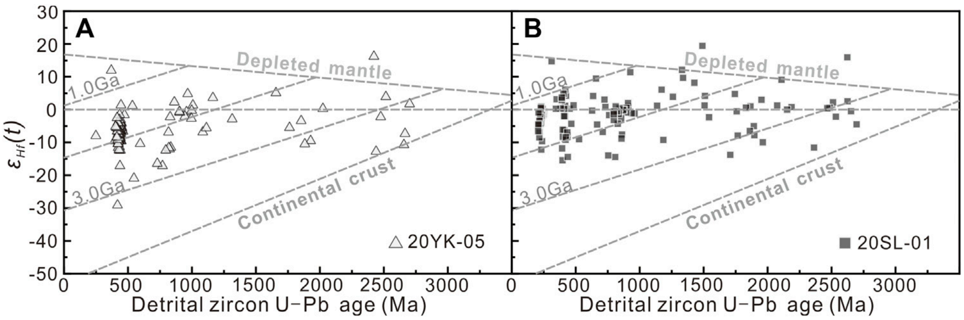

FIGURE 8 | (A) U-Pb age versus ε_{Hf} (t) value plots of concordant detrital zircons of sample 20YK-05; **(B)** U-Pb age versus ε_{Hf} (t) value plots of concordant detrital zircons of sample 20SL-01.

(**Figure 8A**), with only two grains with ε_{Hf} (t) > 0, and T_{DM2} in the range of 2.8–1.6 Ga (**Figures 9A-3**). Zircons in the range of 480–400 Ma yield values of ε_{Hf} (t) in the range of −29.1–1.4 (**Figure 8A**), with only one grain with ε_{Hf} (t) >0, and T_{DM2} in the range of 3.3–1.3 Ga (**Figures 9A-4**).

Zircons from sample 20SL-01 (117 valid analyses) yield ε_{Hf} (t) values in the range of −15.4–19.4 (**Figure 8B**), and T_{DM2} ages in the range of 3.6–0.4 Ga (**Figures 9B-1**), with a peak in the range of 2.5–1.2 Ga. Zircon crystals with U–Pb ages of >1,000 Ma yield ε_{Hf} (t) in the range of −13.8–15.9 (**Figure 8B**) and T_{DM2} in the range of 3.6–1.4 Ga (**Figures 9B-2**). Zircons in the age range of 1,000–700 Ma yield ε_{Hf} (t) in the range of −14.5–11.4 (**Figure 8B**) and T_{DM2} varying from 2.6 to 1.1 Ga (**Figures 9B-3**). Zircons in the range of 460–380 Ma yield ε_{Hf} (t) in the range of −14.5–6.1 (**Figure 8B**), with T_{DM2} in the range of 2.4–1.0 Ga (**Figures 9B-4**). Zircons in the range of 260–200 Ma yield ε_{Hf} (t) in the range of −12.2–0.9 (**Figure 8B**), with T_{DM2} in the range of 2.1–1.2 Ga (**Figures 9B-5**).

5 DISCUSSION

5.1 Potential Source of the Detrital Zircons

Both samples were collected from the North Qaidam UHPM belt, but the upper reaches of the rivers extend beyond this belt. Therefore, analysis of the source(s) of the zircons should consider the contributions made by the upstream portions of the rivers. The Yuka River flows northeast to southwest, from the Qilian Terrane to the Qaidam Basin (**Figure 1E**). Its main tributaries are located in the Yuka area of Qaidam and the South Qilian Terrane. Therefore, investigation of provenance must consider the contribution of the South Qilian Terrane. While the Shaliu River flows southeast to northwest (**Figure 1F**), and its main tributaries are located in the eastern part of the East Kunlun orogenic belt and the North Qaidam UHPM belt. Provenance analysis therefore needs to combine the East Kunlun and North Qaidam.

Combining knowledge of the location of the ancient continents (Gehrels et al., 2003; Song et al., 2014; Wan et al., 2001; Wan et al., 2006), Nd isotopic data (Wan et al., 2006), and especially detrital zircon data (Tung et al., 2007; Xu et al., 2007; Liu et al., 2008; Sun et al., 2008; Sun et al., 2009; Wang et al., 2010; Wang et al., 2012; Wang et al., 2013; Chen et al., 2011; Gehrels et al., 2011; He et al., 2016; Yan et al., 2017; Meng et al., 2017; Jian et al., 2020), shows that the Precambrian basement detrital zircon U–Pb age peaks of the South Qilian, North Qaidam, and East Kunlun terranes are identical to those of the western Yangtze Block, indicating that these terranes have affinity to the western Yangtze Block (Gao and Zhang, 2017; Jian et al., 2020). In this

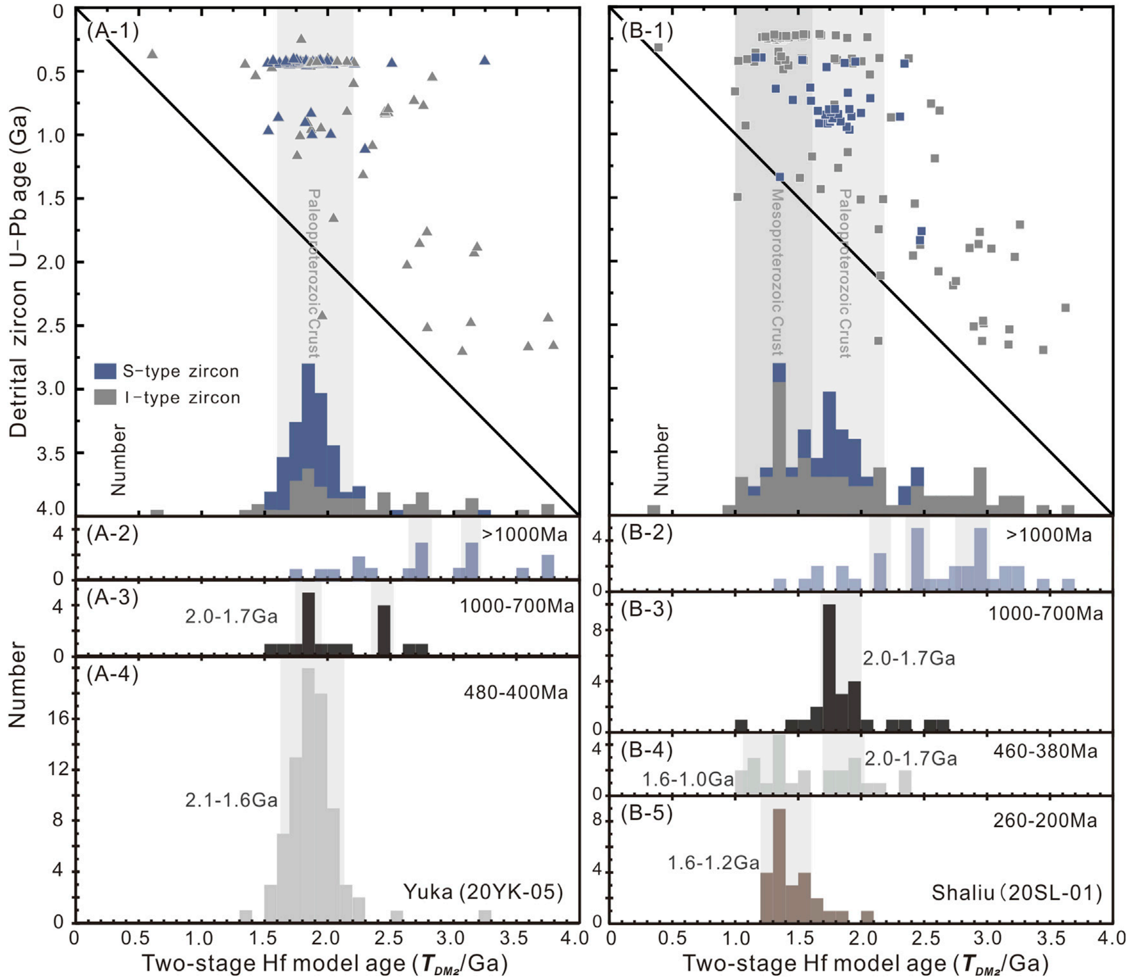

FIGURE 9 | U-Pb age versus two-stage Hf model age (T_{DM2}) value plots of concordant detrital zircons **(A-1)** Sample 20YK-05 **(B-1)** Sample 20SL-01; Relative probability plots of T_{DM2} **(A-2,3,4)** Sample 20YK-05 **(B-2,3,4,5)** Sample 20SL-01.

study, 1,000–700 Ma detrital zircons from the North Qaidam and Qilian terrane (sample 20YK-05) related to the Rodinia supercontinent account for 12% of the sampled grains, and the corresponding 1,000–700 Ma detrital zircons from the North Qaidam and East Kunlun terrane (sample 20SL-01) account for 25%. The detrital zircons of two samples are both partly sourced from the North Qaidam terrane, so the difference in the proportion of Neoproterozoic zircon (13%) may be derived from two different terranes (the South Qilian and the East Kunlun terranes). The detrital zircon of the East Kunlun terrane in this range is significantly more than that in the South Qilian, which is the feature age of the western Yangtze Block (0.91–0.72 Ga, Liu et al., 2008). Therefore, we infer that in the Rodinia supercontinent, the East Kunlun, compared with the South Qilian, show more affinity to the western Yangtze Block.

To track the sources of each identified age range, detrital zircons from the Yuka River were classified into three groups of 961–720 Ma (I-type, n = 22), 472–412 Ma (I-type, n = 39) and 460–402 Ma (S-type, n = 118) based on their ages and compositions, whilst detrital zircons from the Shaliu River were grouped into five groups of 915–776 Ma (S-type, n = 31), 927–755 Ma (I-type, n = 16), 458–381 Ma (I-type, n = 30), 256–207 Ma (I-type, n = 45), and 456–383 Ma (metamorphic age, n = 73; **Figure 6**). Pre-Mesoproterozoic detrital zircons (>1000 Ma) from the Yuka and Shaliu rivers accounted for a small part of the total grains and derived from the ancient crystalline basement.

The South Qilian and North Qaidam terranes record break-up of the Rodinia supercontinent (900–800 Ma), Pan-African regional metamorphism (600–500 Ma), and subduction–collision metamorphism (ca. 450 Ma) (Liu et al., 2012). The zircon U–Pb geochronology of Yuka (Lin et al., 2006) and Xitieshan (Zhang et al., 2003) granitic gneisses in the North Qaidam suggests that a Neoproterozoic granite belt formed during the break-up of Rodinia, implying that Yuka detrital zircons with ages of 961–720 Ma (**Figure 6C**) may be related to the syn- or post-break-up period of the Rodinia supercontinent. Coincides with the ca. 430 Ma continental subduction involving the South Qilian terrane (Song et al., 2009b), the age of subduction–collision metamorphism is consistent with the main age ranges of the Yuka detrital zircons (S-type, 460–402 and I-type, 472–412 Ma), with a peak of 433 Ma (**Figure 5A**). In addition, early Paleozoic magmatic activity in South Qilian–North Qaidam was characterized by myr and multiple episodes. He et al. (2020) divided the magmatism into five periods, namely, 470–450, 450–430, 430–410, 410–400, and 400–370 Ma; with 450–430 Ma as the peak period of granitoid intrusions, which is consistent with the Paleozoic age peak of the studied Yuka River detrital zircons (**Figure 5A**). Meanwhile, this Paleozoic age peak is also consistent with the peak metamorphic age of the Yuka eclogite (435–430 Ma, Song et al., 2009b), indicating that some of the detrital zircons in the Yuka River may have originated from syn-collision magmatic activity.

For the Shaliu River, the age distribution of zircons is more complex, suggesting that they have multiple sources. In the East Kunlun orogenic belt, Mesoproterozoic to Neoproterozoic magmatic intrusions are mainly S-type granites, which are considered to be related to the assembly and break-up of the Rodinia supercontinent (He et al., 2018; Yan et al., 2017). These compositional and temporal features are consistent with the dominance of S-type detrital zircons with Mesoproterozoic to Neoproterozoic ages identified in this study (**Figure 5B**). The geochronology of detrital zircons from gneissic granitoid in Hongshuihe, East Kunlun, indicates crystallization ages of 930–772 Ma (He et al., 2018), which are consistent with the age range of Neoproterozoic S-type zircons of the present study (915–776 Ma; **Figure 6D**). The Shaliu granitic gneiss gave the age of ~920 Ma (Lu, 2002; Chen et al., 2007), being consistent with the Shaliu S-type detrital zircons analyzed for our sample (**Figure 6D**). In summary, the Neoproterozoic detrital zircons analyzed in this study are possibly related to the assembly and break-up of the Rodinia supercontinent at 1,000–700 Ma (Lu, 1998).

Paleozoic intrusions in the East Kunlun orogenic belt are mainly granitic and dioritic, which show a peak crystallization age range of 440–390 Ma (He et al., 2018). UHP metamorphic rocks including eclogite and country paragneiss gave continental deep subduction time of 434–421 Ma for the North Qadaim (Song et al., 2006; 2009b), consistent with the early Devonian ages (433–418 Ma, **Figures 5C-2**) from the Shaliu River sample analyzed in this study. Furthermore, zircons with metamorphic rims constitute a greater proportion of Shaliu River sediments than that of Yuka River sediments, and the main age range of these metamorphic zircons is 456–383 Ma (Zhang et al., 2013, 2014, 2016), which coincides with the timing of oceanic subduction and continental collision and associated syn-metamorphic process in North Qaidam. Therefore, most of the studied detrital zircons in the age range of 458–381 Ma (**Figure 6F**) and with a peak of ca. 422 Ma may have originated from continental syn-collision magmatism, with a few originating from syn-metamorphic processes (**Figure 6H**) related to the above oceanic subduction and continental collision in North Qaidam. While no metamorphic zircons found in the Yuka river due to only a small fraction of its catchment located in the North Qaidam UHPM belt.

The geochronology of Indosinian granites from the East Kunlun orogenic belt can be divided into three stages: formation and expansion of ocean ridges (309–260 Ma); large-scale subduction of the oceanic plate (260–230 Ma); and intracontinental orogenesis (230–190 Ma) (Guo et al., 1998). Mesozoic intrusive rocks are widely distributed throughout the East Kunlun orogenic belt, including granite, granodiorite, and diorite (He et al., 2018), consistent with the 256–207 Ma detrital zircons from the Shaliu River (**Figure 6G**). Moreover, most of the 256–207 Ma zircons are I-type zircons (**Figure 5B**), and such compositions are generally associated with oceanic subduction, which suggests that the 256–207 Ma I-type zircons may have been derived from oceanic subduction and post-orogenic magmatism in East Kunlun during the Indosinian orogenic event.

5.2 Crustal Evolution of the South Qilian, North Qaidam, and East Kunlun Terranes

Zircon Hf isotopes can be used to trace the evolution of the crust. In most cases, a positive $\varepsilon_{\mathrm{Hf}}$ (t) value indicates that the magma was sourced from depleted mantle; if the corresponding T_{DM2} age was close to the crystallization age, the crust can be considered juvenile. In contrast, a negative $\varepsilon_{\mathrm{Hf}}$ (t) indicates that the magma may have included recycled ancient continental crust, and the corresponding T_{DM2} is much older than the crystallization age. For unmixed zircons not derived from a hybrid source with a negative $\varepsilon_{\mathrm{Hf}}$ (t), the T_{DM2} age can be used to estimate the formation time of ancient continental crust (Couzinié, et al., 2016; Geng et al., 2011; Hawkesworth and Kemp, 2006; Iizuka and Hirata, 2005; Kemp et al., 2006; Liu et al., 2008). Accordingly, Hf isotopes of the detrital zircons can help to understand the crustal growth and evolution of the South Qilian, North Qaidam, and East Kunlun terranes. The $\varepsilon_{\mathrm{Hf}}$ (t) values exhibit a wide range from negative to positive for each of the major age ranges of the two samples (**Figures 8A,B**). This value distribution indicates the addition of recycled crustal materials in the magma from which the zircons crystallized; except for several Mesoproterozoic zircons, which show values identical to that of the depleted mantle, indicating the addition of juvenile crust (**Figures 8A,B**).

To facilitate the interpretation of crustal evolution processes in this study, detrital zircons from the Yuka River were classified into three groups with age ranges of >1,000, 1,000–700, and 480–400 Ma, and detrital zircons from the Shaliu River were classified into four groups with age ranges of >1,000, 1,000–700, 460–380, and 260–200 Ma. As shown in relative probability plot histograms of U–Pb ages of Yuka detrital zircons (**Figure 5A**), the >1,000 Ma detrital zircons account for only a small percentage. There is the low proportion of detrital zircon of 1.5–1.0 Ga (both U–Pb ages and two-stage Hf crustal model ages, **Figures 5A, 9A–1**), suggesting that the South Qilian and North Qaidam terranes were tectonically relatively stable during the Mesoproterozoic. The $\varepsilon_{\mathrm{Hf}}$ (t) values of most of the 1,000–700 and 480–400 Ma detrital zircons from the Yuka River are negative (**Figure 8A**), and the T_{DM2} ages are mainly in almost the same ranges of 2.1–1.6 and 2.0–1.7 Ga (**Figures 9A-3, A-4**), respectively, indicating that crustal evolution in the South Qilian—North Qaidam was dominated by recycling of

Paleoproterozoic crust from the Neoproterozoic onward. The two most significant periods of crustal growth in North Qaidam and East Kunlun were 2.2–1.7 and 1.6–1.2 Ga, followed by 3.3–2.7 and 2.5–2.3 Ga (**Figure 9B-1**). Except for the $\varepsilon_{\mathrm{Hf}}$ (t) values of Mesoproterozoic detrital zircons, which are mainly positive, the $\varepsilon_{\mathrm{Hf}}$ (t) values of zircons with other ages are both positive and negative (**Figures 8A,B**), suggesting that the North Qaidam and East Kunlun terranes have been dominated by the remelting and rebuilding of ancient crust, except during the Mesoproterozoic, when the addition of juvenile crust dominated in the East Kunlun Terrane.

In contrast with sample 20YK-05 collected from Yuka river, Mesoproterozoic zircons from sample 20SL-01 are characterized by more depleted Hf isotopes (the $\varepsilon_{\mathrm{Hf}}$ (t) values of zircons of the Shaliu sample at 1.6–1.0 Ga are mostly positive, **Figure 8B**). A comparison of the crustal evolution processes of the South Qilian–North Qaidam and East Kunlun terranes shows that there were differences in crustal growth during 1.6–1.0 Ga (**Figures 9A-1,B-1**). T_{DM2} ages of early Paleozoic detrital zircons (480–400 Ma) from North Qaidam–East Kunlun (2.0–1.7 and 1.6–1.0 Ga, **Figures 9B-4**) are more diverse than those from South Qilian–North Qaidam (2.1–1.6 Ga, **Figures 9A-4**), with a record of Mesoproterozoic continental crust (1.6–1.0 Ga). Moreover, the T_{DM2} ages of 260–200 Ma detrital zircons from the North Qaidam and East Kunlun terranes are Mesoproterozoic (1.6–1.0 Ga, **Figures 9B-5**), also indicating a difference in crustal growth between South Qilian–North Qaidam and North Qaidam–East Kunlun, both of which were located adjacent to the western margin of the Yangtze Block, since at least 1.6 Ga. This difference may be related to the break-up of the Columbian supercontinent during 1.6–1.2 Ga (Hou et al., 2009; Wu et al., 2012; Yin et al., 2012; Wang et al., 2014, 2015; Deng et al., 2020).

5.3 Tectonic Evolution of the Northern Tibetan Plateau

5.3.1 Neoproterozoic Evolution

Jian et al. (2020) has studied detrital zircon U–Pb ages and Hf isotopes of Proterozoic and Paleozoic metamorphic sedimentary rocks from East Kunlun and showed that 1.0–0.9 Ga intrusions in the three terranes of South Qilian, North Qaidam, and East Kunlun are consistent with the age distribution of detrital zircons from East Kunlun and may record the Greenville orogeny. Therefore, these terranes may have been located on the same landmass during the Neoproterozoic. In addition to the above-mentioned evidence for the sources of detrital zircons, U–Pb ages of detrital zircons from Precambrian basement in the South Qilian, North Qaidam, and East Kunlun terranes have similar age clusters in the range of 1,000–700 Ma, which is consistent with the main age interval of 910–720 Ma of magmatic rocks in the western margin of the Yangtze Block (Liu et al., 2008). Moreover, T_{DM2} ages of 1,000–700 Ma detrital zircons of the South Qilian and the East Kunlun terranes are clustered mainly between 2.0 and 1.5 Ga, with a peak of 1.8–1.7 Ga (**Figures 9A-3,B-3**), which also implies that the South Qilian, North Qaidam, and East Kunlun terranes may have been located within the same ancient continent at 1,000–700 Ma, most likely as part of the Rodinia supercontinent.

5.3.2 Early Paleozoic Evolution

Given that the main magmatic period (480–400 Ma) of the South Qilian Terrane preceded than that of the East Kunlun Terrane (460–380 Ma) and that the T_{DM2} ages of early Paleozoic detrital zircons from the East Kunlun Terrane suggest the involvement of Mesoproterozoic continental crust (1.6–1.0 Ga), the East Kunlun and South Qilian terranes may not have been part of the same continent during the early Paleozoic. As such, we propose an archipelago model (Zhang et al., 2020), whereby the terranes were separated from each other by ocean basins during 525–480 Ma. The subduction of the South Qilian Ocean has started by ca. 480 Ma, and the ocean has closed by ca. 420 Ma. Subduction in the Proto-Tethys Ocean in South Qaidam had started by ca. 460 Ma, and the ocean had closed completely by ca. 400 Ma.

Zircon U–Pb ages of I-type granite related to oceanic subduction in the South Qilian–North Qaidam orogenic belt are in the range of 470–460 Ma (Wu et al., 2007), which is consistent with the age peak of I-type detrital zircons in the present study (472 Ma; **Figures 5C-1**) and with 473–443 Ma Shaliuhe oceanic eclogite representing the subduction of oceanic crust (Song et al., 2009b; Zhang et al., 2013). Therefore, subduction-related magmatism occurred at ca. 470 Ma in the North Qaidam UHPM belt. As the temperature increased, the subducted slabs were dehydrated and melted to form magmas, which assimilated continental crust during ascent to form I-type granitic magmas (negative $\varepsilon_{\mathrm{Hf}}$ (t) values; **Figure 8A**) at ca. 470 Ma (**Figures 5C-1**). As the Proto-Tethys ocean closed, the subducting oceanic plate dragged the continental crust downward to also be subducted, and the Qilian Terrane was thrust southward over the Qaidam Terrane. The increase in the thickness of the continental crust caused by continental collision, coupled with the fluid formed by slab dehydration, caused partial melting of the continental crust, forming syn-orogenic S-type granitic magma at ca. 442 Ma (**Figures 5C-1**).

In most cases, the collision margin of the South Qilian–North Qaidam orogenic belt was irregular, and the pole of convergence of the collision was oblique rather than normal (Xu et al., 2013). Therefore, these oblique and irregular edges would have caused asynchronous timings of collision in different parts of the collision zone, which may have led to multiple episodes of magmatism in the orogenic belt. This is reflected in the multiple age peaks of detrital zircons (**Figures 5C,D**). From 437 to 424 Ma, I-type granitic magmatism related to oceanic subduction occurred in the Yuka area (**Figures 5C-1**). In addition to the 442 Ma S-type granitic magmatism, 433 Ma S-type granitic magmatism is also recorded in the South Qilian and North Qaidam terranes (**Figures 5C-1**). Asynchronous collision caused the I-type granitic magmatism related to oceanic subduction in the North Qaidam and East Kunlun terranes (started at 453 Ma) to occur 17 Myr later than that in the South Qilian Terrane, and the major I-type peak of Shaliu sample (ca. 418 Ma, **Figure 5C**) are decoupled with the major I-type peak of Yuka sample (ca. 437 Ma). The oceanic subduction was still occurring in some localities at 418 Ma (**Figures 5C-2**). However, a few S-type granites in the North Qaidam and East Kunlun terranes were formed at 433 Ma (**Figures 5C-2**), which is consistent with the 433 Ma S-type granites in the Yuka area, indicating that large-scale granites were produced in North Qaidam during continental collision.

Zhou et al. (2021) showed that mafic dikes with ages of 393–375 Ma were derived from the melting of the lithosphere mantle in Dulan, North Qaidam. These dikes were derived from the melting of the mantle peridotite, which mark the initiation of post-collisional magmatism in an orogen. The timing of the formation of these mafic dikes coincides with I-type magmatism (ca. 397 and ca. 385 Ma; **Figures 5C-2**) during the middle Devonian in the North Qaidam and East Kunlun terranes. Therefore, we speculate that the I-type granite of the middle Devonian (ca. 397–385 Ma) was the product of the partial melting of the lithospheric mantle which assimilated the continental crust during the late magmatic evolution.

5.3.3 Late Paleozoic–Early Mesozoic Evolution

Late Paleozoic to early Mesozoic granitic intrusions are widely distributed in the eastern part of the East Kunlun Terrane, and their formation might be related with the Paleo-Tethyan oceanic subduction (Li et al., 2012a, b; Ma et al., 2015). This subduction occurred during the late Permian to Middle Triassic and eventually led to closure of the Paleo-Tethys Ocean (Buqingshan Ocean) in southern East Kunlun. In this study, 260–200 Ma I-type magmatic zircons, with peak ages of ca. 252 Ma, ca. 241 Ma, ca. 231 Ma, ca. 222 Ma, and ca. 217 Ma, could be formed by multi-stage magmatism associated with this oceanic subduction process. According to the zircon probability density plots (**Figure 5D**), northward Paleo-Tethys oceanic plate subduction (Cheng et al., 2017; Gehrels et al., 2011; Jian et al., 2020; Xiong et al., 2014; Zhang et al., 2020) started during the late Permian (ca. 260–252 Ma) and continued intensely through to the middle Triassic (ca. 231 Ma), and in a more subdued manner until the Late Triassic (ca. 217–200 Ma).

In summary, the South Qilian, North Qaidam, and East Kunlun terranes have undergone multiple Wilson cycles since the Paleoproterozoic. These terranes/microcontinents were located on the same major ancient continent during 2.1–1.6 Ga and subsequently separated during 1.6–1.2 Ga. The East Kunlun Terrane was augmented by the juvenile crust at this stage, whereas the Qilian Terrane was relatively stable in tectonic and magmatic terms. By ca. 1,000 Ma, as a result of the assembly of the Rodinia supercontinent, the three microcontinents (South Qilian, North Qaidam, and East Kunlun) reassembled on the western Yangtze block, while the East Kunlun terrane was closer than other two terranes, and then became separated by the Proto-Tethys Ocean during the break-up of Rodinia. Later, the Proto-Tethys Ocean began to close, and the three continents collided with each other after closure of the Paleo-Tethys Ocean, forming the current configuration and structure of the South Qilian, North Qaidam, and East Kunlun terranes.

6 CONCLUSION

To investigate the evolution of continental crust of the northern Tibetan Plateau, detrital zircon U–Pb geochronology and Hf isotope analysis by LA-(MC)-ICPMS was performed on two fluvial sand samples from North Qaidam (the Yuka and Shaliu rivers). The main conclusions of the study are as follows.

1) Age distributions of detrital zircons from the Yuka River cluster mainly in two ranges of 1,000–700 and 480–400 Ma, with age peaks at 820 and 433 Ma, respectively. Corresponding data for Shaliu River falls in the ranges of 1,000–700, 460–380, and 260–200 Ma, with peaks of 875, 422, and 232 Ma, respectively.
2) Detrital zircon U–Pb geochronology and Hf isotope analysis show that the Qilian, North Qaidam, and East Kunlun terranes show affinity to the western Yangtze Block.
3) The presence of Mesoproterozoic continental crust (1.6–1.0 Ga) in the East Kunlun and North Qaidam terranes indicate differences in crustal evolution between the East Kunlun–Qaidam terranes and the Qilian Terrane. Phanerozoic magmatic records for the South Qilian, North Qaidam, and East Kunlun terranes suggest that the magmas were mainly sourced from recycled ancient continental crust with minor contributions from the juvenile crust.
4) The Qilian, North Qaidam, and East Kunlun terranes have undergone multiple Wilson cycles since the Paleoproterozoic. We suggest an archipelago model for part of their evolution, which proposes that the terranes were separated from each other by ocean basins during 525–480 Ma.

DATA AVAILABILITY STATEMENT

The original contributions presented in the study are included in the article/**Supplementary Material**, further inquiries can be directed to the corresponding author.

AUTHOR CONTRIBUTIONS

GZ designed this project, GZ, LX, FC and SL collected all samples of this study and field investigation, ZL conducted most of laboratory analysis and data explanation, GZ and ZL wrote the manuscript.

FUNDING

This study is supported by the National Natural Science Foundation of China (Grants 91755206, 41972056, and 41622202).

SUPPLEMENTARY MATERIAL

The Supplementary Material for this article can be found online at: https://www.frontiersin.org/articles/10.3389/feart.2022.866375/full#supplementary-material

REFERENCES

Belousova, E. A., Kostitsyn, Y. A., Griffin, W. L., Begg, G. C., O'Reilly, S. Y., and Pearson, N. J. (2010). The Growth of the Continental Crust: Constraints from Zircon Hf-Isotope Data. *Lithos* 119, 457–466. doi:10.1016/j.lithos.2010.07.024

Belousova, E., Griffin, W., O'Reilly, S. Y., and Fisher, N. (2002). Igneous Zircon: Trace Element Composition as an Indicator of Source Rock Type. *Contrib. Mineral. Petrol.* 143, 602–622. doi:10.1007/s00410-002-0364-7

Blayney, T., Najman, Y., Dupont-Nivet, G., Carter, A., Millar, I., Garzanti, E., et al. (2016). Indentation of the Pamirs with Respect to the Northern Margin of Tibet: Constraints from the Tarim Basin Sedimentary Record. *Tectonics* 35, 2345–2369. doi:10.1002/2016TC004222

Blichert-Toft, J., Chauvel, C., and Albarède, F. (1997). Separation of Hf and Lu for High-Precision Isotope Analysis of Rock Samples by Magnetic Sector-Multiple Collector ICP-MS. *Contrib. Mineralogy Petrology* 127, 248–260. doi:10.1007/s004100050278

Botsyun, S., Sepulchre, P., Donnadieu, Y., Risi, C., Licht, A., and Caves Rugenstein, J. K. (2019). Revised Paleoaltimetry Data show low Tibetan Plateau Elevation during the Eocene. *Science* 363, eaaq1436. doi:10.1126/science.aaq1436

Burnham, A. D., and Berry, A. J. (2017). Formation of Hadean Granites by Melting of Igneous Crust. *Nat. Geosci* 10, 457–461. doi:10.1038/ngeo2942

Chen, J.-F., Han, B.-F., Zhang, L., Xu, Z., Liu, J.-L., Qu, W.-J., et al. (2015). Middle Paleozoic Initial Amalgamation and Crustal Growth in the West Junggar (NW China): Constraints from Geochronology, Geochemistry and Sr-Nd-Hf-Os Isotopes of Calc-Alkaline and Alkaline Intrusions in the Xiemisitai-Saier Mountains. *J. Asian Earth Sci.* 113, 90–109. doi:10.1016/j.jseaes.2014.11.028

Chen, N., Xia, X., Li, X., Sun, M., Xu, P., Liu, X., et al. (2007). Timing of Magmatism of the Gneissic-Granite Plutons along North Qaidam Margin and Implications for Precambrian Crustal Accretions: Zircon U-Pb Dating and Hf Isotope Evidences. *Acta Petrol. Sin.* 23, 501–512. in Chinese with English abstract.

Chen, Y., Pei, X., Li, R., Liu, Z., Li, Z., Zhang, X., et al. (2011). Zircon U-Pb Age of Xiaomiao Formation of Proterozoic in the Eastern Section of the East Kunlun Orogenic Belt. *Geoscience* 25, 510–521. in Chinese with English abstract.

Cheng, F., Jolivet, M., Hallot, E., Zhang, D., Zhang, C., and Guo, Z. (2017). Tectono-Magmatic Rejuvenation of the Qaidam Craton, Northern Tibet. *Gondwana Res.* 49, 248–263. doi:10.1016/j.gr.2017.06.004

Clark, M. K., Farley, K. A., Zheng, D., Wang, Z., and Duvall, A. R. (2010). Early Cenozoic Faulting of the Northern Tibetan Plateau Margin from Apatite (U-Th)/He Ages. *Earth Planet. Sci. Lett.* 296, 78–88. doi:10.1016/j.epsl.2010.04.051

Condie, K. C., Beyer, E., Belousova, E., Griffin, W. L., and O'Reilly, S. Y. (2005). U-pb Isotopic Ages and Hf Isotopic Composition of Single Zircons: The Search for Juvenile Precambrian continental Crust. *Precambrian Res.* 139, 42–100. doi:10.1016/j.precamres.2005.04.006

Corfu, F., Hanchar, J. M., Hoskin, P. W. O., and Kinny, P. (2003). 16. Atlas of Zircon Textures. *Rev. Mineral. Geochem.* 53, 469–502. doi:10.2113/0530469

Couzinié, S., Laurent, O., Moyen, J.-F., Zeh, A., Bouilhol, P., and Villaros, A. (2016). Post-collisional Magmatism: Crustal Growth Not Identified by Zircon Hf-O Isotopes. *Earth Planet. Sci. Lett.* 456, 182–195. doi:10.1016/j.epsl.2016.09.033

Deng, Q., Wang, Z., Ren, G., Cui, X., Cao, H., Ning, K., et al. (2020). Identification of the ∼2.09 Ga and ∼1.76 Ga Granitoids in the Northwestern Yangtze Block: Records of the Assembly and Break-Up of Columbia Supercontinent. *Earth Sci.* 45, 3295–3312. in Chinese with English abstract. doi:10.3799/dqkx.2020.182

Gao, Z., and Zhang, G. (2017). Geochronology of Detrital Zircons from Metapelite of the North Qaidam UHPM Belt and its Geological Implications. *Acta Petrol. Sin.* 33, 1775–1788. in Chinese with English abstract.

Gehrels, G. E., Yin, A., and Wang, X.-F. (2003). Detrital-zircon Geochronology of the Northeastern Tibetan Plateau. *Geol. Soc. Am. Bull.* 115, 881–896. doi:10.1130/0016-7606(2003)115<0881:dgotnt>2.0.co;2

Gehrels, G., Kapp, P., DeCelles, P., Pullen, A., Blakey, R., Weislogel, A., et al. (2011). Detrital Zircon Geochronology of Pre-tertiary Strata in the Tibetan-Himalayan Orogen. *Tectonics* 30, a–n. doi:10.1029/2011TC002868

Geng, X., Gao, S., and Chen, C. (2011). Crustal Growth of the Eastern North China Craton and Sulu Orogen as Revealed by U-Pb Dating and Hf Isotopes of Detrital Zircons from Modern Rivers. *Earth Sci.* 36, 483–499. in Chinese with English abstract. doi:10.3799/dqkx.2011.050

Gong, H., Zhao, H., Xie, W., Kang, W., Zhang, R., Yang, L., et al. (2017). Tectono-Thermal Events of the North Qilian Orogenic Belt, NW China: Constraints from Detrital Zircon U-Pb Ages of Heihe River Sediments. *J. Asian Earth Sci.* 138, 647–656. doi:10.1016/j.jseaes.2017.03.003

Griffin, W. L., Pearson, N. J., Belousova, E., Jackson, S. E., van Achterbergh, E., O'Reilly, S. Y., et al. (2000). The Hf Isotope Composition of Cratonic Mantle: LAM-MC-ICPMS Analysis of Zircon Megacrysts in Kimberlites. *Geochimica et Cosmochimica Acta* 64, 133–147. doi:10.1016/S0016-7037(99)00343-9

Guo, Z., Deng, J., Xu, Z., Mo, X., and Luo, Z. (1998). Late Paleozoic-Mesozoic Intracontinental Orogenic Process and Intermediate-Acidic Igneous Rocks from the Eastern Kunlun Mountains of North Western China. *Geoscience* 12, 344–352. in Chinese with English abstract.

Hawkesworth, C. J., and Kemp, A. I. S. (2006). Evolution of the Continental Crust. *Nature* 443, 811–817. doi:10.1038/nature05191

He, D., Dong, Y., Liu, X., Yang, Z., Sun, S., Cheng, B., et al. (2016). Tectono-thermal Events in East Kunlun, Northern Tibetan Plateau: Evidence from Zircon U-Pb Geochronology. *Gondwana Res.* 30, 179–190. doi:10.1016/j.gr.2015.08.002

He, D., Dong, Y., Liu, X., Zhou, X., Zhang, F., and Sun, S. (2018). Zircon U-Pb Geochronology and Hf Isotope of Granitoids in East Kunlun: Implications for the Neoproterozoic Magmatism of Qaidam Block, Northern Tibetan Plateau. *Precambrian Res.* 314, 377–393. doi:10.1016/j.precamres.2018.06.017

He, X., Yang, X., Wang, Y., Guo, R., Liao, Y., and Fan, Y. (2020). Petrology, Geochemistry and Zircon U-Pb Geochronology of the Chaidamushan Granite from the Southern Margin of Qilianshan. *Acta Geol. Sin.* 94, 1248–1263. in Chinese with English abstract10.1111/1755-6724.14347.

Hoskin, P. W. O., and Black, L. P. (2000). Metamorphic Zircon Formation by Solid-State Recrystallization of Protolith Igneous Zircon. *J. Metamorphic Geology.* 18, 423–439. doi:10.1046/j.1525-1314.2000.00266.x

Hou, G., Halls, H., Davis, D., Huang, B., Yang, M., and Wang, C. (2009). Paleomagnetic Poles of Mafic Dyke Swarms from the North China Craton and Their Relevance to the Reconstruction of the Supercontinent Columbia. *Acta Petrol. Sin.* 25, 650–658. in Chinese with English abstract.

Iizuka, T., and Hirata, T. (2005). Improvements of Precision and Accuracy in *In Situ* Hf Isotope Microanalysis of Zircon Using the Laser Ablation-MC-ICPMS Technique. *Chem. Geology.* 220, 121–137. doi:10.1016/j.chemgeo.2005.03.010

Jackson, S. E., Pearson, N. J., Griffin, W. L., and Belousova, E. A. (2004). The Application of Laser Ablation-Inductively Coupled Plasma-Mass Spectrometry to *In Situ* U-Pb Zircon Geochronology. *Chem. Geology.* 211, 47–69. doi:10.1016/j.chemgeo.2004.06.017

Jian, X., Weislogel, A., Pullen, A., and Shang, F. (2020). Formation and Evolution of the Eastern Kunlun Range, Northern Tibet: Evidence from Detrital Zircon U-Pb Geochronology and Hf Isotopes. *Gondwana Res.* 83, 63–79. doi:10.1016/j.gr.2020.01.015

Kang, H., Chen, Y., Li, D., Bao, C., Chen, Y., Xue, H., et al. (2019). Detrital Zircon Record of Rivers' Sediments in the North Qilian Orogenic Belt: Implications of the Tectonic Evolution of the Northeastern Tibetan Plateau. *Geol. J.* 54, 2208–2228. doi:10.1002/gj.3291

Kemp, A. I. S., Hawkesworth, C. J., Paterson, B. A., and Kinny, P. D. (2006). Episodic Growth of the Gondwana Supercontinent from Hafnium and Oxygen Isotopes in Zircon. *Nature* 439, 580–583. doi:10.1038/nature04505

Kröner, A., Kovach, V., Belousova, E., Hegner, E., Armstrong, R., Dolgopolova, A., et al. (2014). Reassessment of Continental Growth during the Accretionary History of the Central Asian Orogenic Belt. *Gondwana Res.* 25, 103–125. doi:10.1016/j.gr.2012.12.023

Kui, M., Bai, H., Gu, F., and Miao, G. (2010). Division of East Kunlun Tectonic Magmatic Belt and the Rock Tectonic Combination in the Late Variscan-Yanshanian Period. *J. Qinghai Univ. (Nature Science)* 28, 49–55. in Chinese with English abstract.

Lease, R. O., Burbank, D. W., Gehrels, G. E., Wang, Z., and Yuan, D. (2007). Signatures of Mountain Building: Detrital Zircon U/Pb Ages from Northeastern Tibet. *Geol* 35, 239–242. doi:10.1130/g23057a.1

Li, B., Sun, F., Yu, X., Qian, Y., Wang, G., and Yang, Y. (2012a). U-pb Dating and Geochemistry of Diorite in the Eastern Section from Eastern Kunlun Middle Uplifted Basement and Granitic Belt. *Acta Petrol. Sin.* 28, 1163–1172. in Chinese with English abstract.

Li, H., Lu, S., Zhao, F., Li, H., and Yu, H. (1999). Geochronological Framework of the Neoproterozoic Major Geological Events in the Northern Margin of the Qaidam Basin. *Geoscience* 2, 224–225. in Chinese with English abstract.

Li, R., Pei, X., Li, Z., Liu, Z., Chen, G., Chen, Y., et al. (2012b). Geological Characteristics of Late Palaeozoic-Mesozoic Unconformities and Their Response to Some Significant Tectonic Events in Eastern Part of Eastern Kunlun. *Earth Sci. Front.* 19, 244–254. in Chinese with English abstract.

Li, X.-H., Long, W.-G., Li, Q.-L., Liu, Y., Zheng, Y.-F., Yang, Y.-H., et al. (2010). Penglai Zircon Megacrysts: A Potential New Working Reference Material for Microbeam Determination of Hf-O Isotopes and U-Pb Age. *Geostand. Geoanal. Res.* 34, 117–134. doi:10.1111/j.1751-908X.2010.00036.x

Lin, C., Sun, Y., Chen, D., and Diwu, C. (2006). Geochemistry and Zircon LA-ICPMS Dating of Iqe River Granitic Gneiss, Northern Margin of Qaidam Basin. *Geochimica* 5, 489–505. in Chinese with English abstract.

Liu, X., Gao, S., Diwu, C., and Ling, W. (2008). Precambrian Crustal Growth of Yangtze Craton as Revealed by Detrital Zircon Studies. *Am. J. Sci.* 308, 421–468. doi:10.2475/04.2008.02

Liu, Y., Neubauer, F., Li, W., Genser, J., and Li, W. (2012). Tectono-Thermal Events of the Northern Qaidam Margin-Southern Qilian Area, Western China. *J. Jilin Univ. (Earth Sci. Edition)* 42, 1317–1329. in Chinese with English abstract.

Lu, S. N. (1998). A Review of Advance in the Research on the Neoproterozoic Rodinia Supercontinent. *Geol. Rev.* 44, 489–495. in Chinese with English abstract.

Lu, S. N. (2002). *Preliminary Study on Precambrian Geology of Northern Qinghai-Tibet Plateau*. Beijing: Geological Publishing House.

Lu, X., Sun, Y., Zhang, X., Xiao, Q., Wang, X., and Wei, X. (2007). The SHRIMP Age of Tatalin Rapakivi Granite at the North Margin of Qaidam Basin. *Acta Geol. Sin.* 81, 626–634. in Chinese with English abstract.

Ludwig, K. R. (2003). *Isoplot 3.00: A Geochronological Toolkit for Microsoft Excel*. Berkeley CA: Berkeley Geochronology Center. 4, 0-71.

Ma, C., Xiong, F., Yin, S., Wang, L., and Gao, K. (2015). Intensity and Cyclicity of Orogenic Magmatism: An Example from a Paleo-Tethyan Granitoid Batholith, Eastern Kunlun, Northern Qinghai-Tibetan Plateau. *Acta Petrol. Sin.* 31, 3555–3568. in Chinese with English abstract.

Meng, F., Jia, L., Ren, Y., Liu, Q., and Duan, X. (2017). Magmatic and Metamorphic Events Recorded in the Gneisses of the Wenquan Region, East Kunlun Mountains, Northwest China: Evidence from the Zircon U-Pb Geochronology. *Acta Petrol. Sin.* 33, 3691–3709. in Chinese with English abstract.

Nie, J., Horton, B. K., Saylor, J. E., Mora, A., Mange, M., Garzione, C. N., et al. (2012). Integrated Provenance Analysis of a Convergent Retroarc Foreland System: U-Pb Ages, Heavy Minerals, Nd Isotopes, and sandstone Compositions of the Middle Magdalena Valley basin, Northern Andes, Colombia. *Earth-Science Rev.* 110, 111–126. doi:10.1016/j.earscirev.2011.11.002

Patchett, P. J., and Tatsumoto, M. (1981). A Routine High-Precision Method for Lu-Hf Isotope Geochemistry and Chronology. *Contr. Mineral. Petrol.* 75, 263–267. doi:10.1007/BF01166766

Paton, C., Hellstrom, J., Paul, B., Woodhead, J., and Hergt, J. (2011). Iolite: Freeware for the Visualisation and Processing of Mass Spectrometric Data. *J. Anal. Spectrom.* 26, 2508–2518. doi:10.1039/c1ja10172b

Pearce, N. J. G., Perkins, W. T., Westgate, J. A., Gorton, M. P., Jackson, S. E., Neal, C. R., et al. (1997). A Compilation of New and Published Major and Trace Element Data for NIST SRM 610 and NIST SRM 612 Glass Reference Materials. *Geostand. Newsl.* 21, 115–144. doi:10.1111/j.1751-908X.1997.tb00538.x

Rohrmann, A., Kapp, P., Carrapa, B., Reiners, P. W., Guynn, J., Ding, L., et al. (2012). Thermochronologic Evidence for Plateau Formation in central Tibet by 45 Ma. *Geology* 40, 187–190. doi:10.1130/G3253010.1130/g32530.1

Rubatto, D. (2002). Zircon Trace Element Geochemistry: Partitioning with Garnet and the Link between U-Pb Ages and Metamorphism. *Chem. Geology.* 184, 123–138. doi:10.1016/S0009-2541(01)00355-2

Sláma, J., Košler, J., Condon, D. J., Crowley, J. L., Gerdes, A., Hanchar, J. M., et al. (2008). Plešovice Zircon - A New Natural Reference Material for U-Pb and Hf Isotopic Microanalysis. *Chem. Geology.* 249, 1–35. doi:10.1016/j.chemgeo.2007.11.005

Song, B., Zhang, K., Hou, Y., Ji, J., Wang, J., Yang, Y., et al. (2019a). New Insights into the Provenance of Cenozoic Strata in the Qaidam Basin, Northern Tibet: Constraints from Combined U-Pb Dating of Detrital Zircons in Recent and Ancient Fluvial Sediments. *Palaeogeogr. Palaeoclimatol. Palaeoecol.* 533, 109254. doi:10.1016/j.palaeo.2019.109254

Song, S., Bi, H., Qi, S., Yang, L., Allen, M. B., Niu, Y., et al. (2018). HP-UHP Metamorphic Belt in the East Kunlun Orogen: Final Closure of the Proto-Tethys Ocean and Formation of the Pan-North-China Continent. *J. Petrol.* 59, 2043–2060. doi:10.1093/petrology/egy089

Song, S. G., Yang, J. S., Xu, Z. Q., Liou, J. G., and Shi, R. D. (2003). Metamorphic Evolution of the Coesite-Bearing Ultrahigh-Pressure Terrane in the North Qaidam, Northern Tibet, NW China. *J. Metamorph. Geol.* 21, 631–644. doi:10.1046/j.1525-1314.2003.00469.x

Song, S., Niu, Y., Su, L., and Xia, X. (2013). Tectonics of the North Qilian Orogen, NW China. *Gondwana Res.* 23, 1378–1401. doi:10.1016/j.gr.2012.02.004

Song, S., Niu, Y., Su, L., Zhang, C., and Zhang, L. (2014). Continental Orogenesis from Ocean Subduction, Continent Collision/Subduction, to Orogen Collapse, and Orogen Recycling: The Example of the North Qaidam UHPM belt, NW China. *Earth-Science Rev.* 129, 59–84. doi:10.1016/j.earscirev.2013.11.010

Song, S., Niu, Y., Zhang, L., and Zhang, G. (2009b). Time Constraints on Orogenesis from Oceanic Subduction to Continental Subduction, Collision, and Exhumation: An Example from North Qilian and North Qaidam HP-UHP Belts. *Acta Petrol. Sin.* 25, 2067–2077. in Chinese with English abstract.

Song, S., Su, L., Niu, Y., Zhang, G., and Zhang, L. (2009a). Two Types of Peridotite in North Qaidam UHPM belt and Their Tectonic Implications for Oceanic and Continental Subduction: A Review. *J. Asian Earth Sci.* 35, 285–297. doi:10.1016/j.jseaes.2008.11.009

Song, S., Wu, Z., Yang, L., Su, L., Xia, X., Wang, C., et al. (2019b). Ophiolite Belts and Evolution of the Proto-Tethys Ocean in the Qilian Orogen. *Acta Petrol. Sin.* 35, 2948–2970. in Chinese with English abstract.

Song, S., Zhang, C., Li, X., and Zhang, L. (2011). HP/UHP Metamorphic Time of Eclogite in the Xitieshan Terrane, North Qaidam UHPM belt, NW China. *Acta Petrol. Sin.* 27, 1191–1197. in Chinese with English abstract.

Song, S., Zhang, L., Niu, Y., Su, L., Song, B., and Liu, D. (2006). Evolution from Oceanic Subduction to Continental Collision: a Case Study from the Northern Tibetan Plateau Based on Geochemical and Geochronological Data. *J. Petrol.* 47, 435–455. doi:10.1093/petrology/egi080

Sun, J.-F., Yang, J.-H., Wu, F.-Y., and Wilde, S. A. (2012). Precambrian Crustal Evolution of the Eastern North China Craton as Revealed by U-Pb Ages and Hf Isotopes of Detrital Zircons from the Proterozoic Jing'eryu Formation. *Precambrian Res.* 200-203, 184–208. doi:10.1016/j.precamres.2012.01.018

Sun, S.-s., and McDonough, W. F. (1989). Chemical and Isotopic Systematics of Oceanic Basalts: Implications for Mantle Composition and Processes. *Geol. Soc. Lond. Spec. Publications* 42, 313–345. doi:10.1144/gsl.sp.1989.042.01.19

Sun, W.-H., Zhou, M.-F., Gao, J.-F., Yang, Y.-H., Zhao, X.-F., and Zhao, J.-H. (2009). Detrital Zircon U-Pb Geochronological and Lu-Hf Isotopic Constraints on the Precambrian Magmatic and Crustal Evolution of the Western Yangtze Block, SW China. *Precambrian Res.* 172, 99–126. doi:10.1016/j.precamres.2009.03.010

Sun, W., Zhou, M., Yan, D., Li, J., and Ma, Y. (2008). Provenance and Tectonic Setting of the Neoproterozoic Yanbian Group, Western Yangtze Block (SW China). *Precambrian Res.* 167, 213–236. doi:10.1016/j.precamres.2008.08.001

Tapponnier, P., Zhiqin, X., Roger, F., Meyer, B., Arnaud, N., Wittlinger, G., et al. (2001). Oblique Stepwise Rise and Growth of the Tibet Plateau. *Science* 294, 1671–1677. doi:10.1126/science.105978

Tung, K., Yang, H.-J., Yang, H.-Y., Liu, D., Zhang, J., Wan, Y., et al. (2007). SHRIMP U-Pb Geochronology of the Zircons from the Precambrian Basement of the Qilian Block and its Geological Significances. *Chin. Sci Bull* 52, 2687–2701. doi:10.1007/s11434-007-0356-0

Vervoort, J. D., Patchett, P. J., Söderlund, U., and Baker, M. (2004). Isotopic Composition of Yb and the Determination of Lu Concentrations and Lu/Hf Ratios by Isotope Dilution Using MC-ICPMS. *Geochem. Geophys. Geosyst.* 5, a–n. doi:10.1029/2004GC000721

Wang, C., Dai, J., Zhao, X., Li, Y., Graham, S. A., He, D., et al. (2014a). Outward-growth of the Tibetan Plateau during the Cenozoic: A Review. *Tectonophysics* 621, 1–43. doi:10.1016/j.tecto.2014.01.036

Wang, L.-J., Griffin, W. L., Yu, J.-H., and O'Reilly, S. Y. (2013). U-pb and Lu-Hf Isotopes in Detrital Zircon from Neoproterozoic Sedimentary Rocks in the Northern Yangtze Block: Implications for Precambrian Crustal Evolution. *Gondwana Res.* 23, 1261–1272. doi:10.1016/j.gr.2012.04.013

Wang, L.-J., Griffin, W. L., Yu, J.-H., and O'Reilly, S. Y. (2010). Precambrian Crustal Evolution of the Yangtze Block Tracked by Detrital Zircons from Neoproterozoic Sedimentary Rocks. *Precambrian Res.* 177, 131–144. doi:10.1016/j.precamres.2009.11.008

Wang, L.-J., Yu, J.-H., Griffin, W. L., and O'Reilly, S. Y. (2012). Early Crustal Evolution in the Western Yangtze Block: Evidence from U-Pb and Lu-Hf Isotopes on Detrital Zircons from Sedimentary Rocks. *Precambrian Res.* 222-223, 368–385. doi:10.1016/j.precamres.2011.08.001

Wang, W., Zhou, M.-F., Zhao, X.-F., Chen, W.-T., and Yan, D.-P. (2014b). Late Paleoproterozoic to Mesoproterozoic Rift Successions in SW China: Implication for the Yangtze Block-North Australia-Northwest Laurentia Connection in the Columbia Supercontinent. *Sediment. Geology.* 309, 33–47. doi:10.1016/j.sedgeo.2014.05.004

Wang, Z., Wang, J., Deng, Q., Du, Q., Zhou, X., Yang, F., et al. (2015). Paleoproterozoic I-type Granites and Their Implications for the Yangtze Block Position in the Columbia Supercontinent: Evidence from the Lengshui Complex, South China. *Precambrian Res.* 263, 157–173. doi:10.1016/j.precamres.2015.03.014

Wu, C., Gao, Y., Wu, S., Chert, Q. L., Wooden, J. L., Mmdab, F. K., et al. (2007a). Zircon SHRIMP U-Pb Dating of Granites from the Da Qaidam Area in the North Margin of Qaidam Basin. *Acta Petrologica Siniea* 23, 1861–1875. NW Chinain Chinese with English abstract.

Wu, C., Yang, J., Wooden, J., Liou, J., Li, H., and Meng, F. (2001). Zircon SHRIMP Dating of Granite from Qaidam Mountains. *Chin. Sci. Bull.* 46, 1743–1747. in Chinese with English abstract.

Wu, C., Yang, J., Xu, Z., Wooden, J. L., Ireland, T., Li, H., et al. (2004). Granitic Magmatism on the Early Paleozoic UHP Belt of Northern Qaidam, NW China. *Acta Geol. Sin.* 78 (5), 658–674. in Chinese with English abstract.

Wu, F.-Y., Yang, Y.-H., Xie, L.-W., Yang, J.-H., and Xu, P. (2006). Hf Isotopic Compositions of the Standard Zircons and Baddeleyites Used in U-Pb Geochronology. *Chem. Geology.* 234, 105–126. doi:10.1016/j.chemgeo.2006.05.003

Wu, F., Li, X., Zheng, Y., and Gao, S. (2007b). Lu-Hf Isotopic Systematics and Their Applications in Petrology. *Acta Petrol. Sin.* 23, 185–220. in Chinese with English abstract.

Wu, F., Wan, B., Zhao, L., Xiao, W., and Zhu, R. (2020). Tethyan Geodynamics. *Acta Petrol. Sin.* 36, 1627–1674. in Chinese with English abstract. doi:10.1007/s10114-020-9057-2

Wu, S. (2008). *The Petrogenesis of Paleozoic Granitoids in the North Margin of Qaidam Basin and Their Orogenic Response*. Dissertation. Beijing, China: Chinese Academy of Geological Sciences. [in Chinese with English abstract].

Wu, Y., Gao, S., Zhang, H., Zheng, J., Liu, X., Wang, H., et al. (2012). Geochemistry and Zircon U-Pb Geochronology of Paleoproterozoic Arc Related Granitoid in the Northwestern Yangtze Block and its Geological Implications. *Precambrian Res.* 200-203, 26–37. doi:10.1016/j.precamres.2011.12.015

Xiong, F., Ma, C., Zhang, J., Liu, B., and Jiang, H. a. (2014). Reworking of Old continental Lithosphere: an Important Crustal Evolution Mechanism in Orogenic Belts, as Evidenced by Triassic I-type Granitoids in the East Kunlun Orogen, Northern Tibetan Plateau. *J. Geol. Soc.* 171, 847–863. doi:10.1144/jgs2013-038

Xu, W., Zhang, H., and Liu, X. (2007). U-pb Zircon Dating Constraints on Formation Time of Qilian High-Grade Metamorphic Rock and its Tectonic Implications. *Chin. Sci Bull* 52, 531–538. doi:10.1007/s11434-007-0082-7

Xu, Y., Du, Y., and Yang, J. (2013). Tectonic Evolution of the North Qilian Orogenic Belt from the Late Ordovician to Devonian: Evidence from Detrital Zircon Geochronology. *Earth Science-Journal China Univ. Geosciences* 38, 934–946. in Chinese with English abstract.

Xu, Y., Wang, C. Y., and Zhao, T. (2016). Using Detrital Zircons from River Sands to Constrain Major Tectono-Thermal Events of the Cathaysia Block, SE China. *J. Asian Earth Sci.* 124, 1–13. doi:10.1016/j.jseaes.2016.04.012

Yan, Q., Pei, X., Li, R., Li, Z., Pei, L., Liu, C., et al. (2017a). Detrital Zircon U-Pb Age and Geological Significance of Metamorphic Strata at Gouli Area in the Central Tectonic Belt of East Kunlun. *Northwest. Geology.* 50, 165–181. in Chinese with English abstract. doi:10.3799/dqkx.2013.092

Yan, Y., Yang, B., Li, H., Cai, H., Xu, H., and Xu, Y. (2017b). Single-Zircon U-Pb and Geological Significance of Metamorphic and Intrusive System of Nalingele Region in East Kunlun Neo-Proterozoic. *Northwest. Geology.* 50, 33–40. in Chinese with English abstract.

Yang, J., Gao, S., Chen, C., Tang, Y., Yuan, H., Gong, H., et al. (2009). Episodic Crustal Growth of North China as Revealed by U-Pb Age and Hf Isotopes of Detrital Zircons from Modern Rivers. *Geochimica et Cosmochimica Acta* 73, 2660–2673. doi:10.1016/j.gca.2009.02.007

Yin, A., Dang, Y.-Q., Wang, L.-C., Jiang, W.-M., Zhou, S.-P., Chen, X.-H., et al. (2008). Cenozoic Tectonic Evolution of Qaidam basin and its Surrounding Regions (Part 1): The Southern Qilian Shan-Nan Shan Thrust belt and Northern Qaidam basin. *Geol. Soc. America Bull.* 120, 813–846. doi:10.1130/b26180.1

Yin, F., Wang, D., Sun, Z., Ren, G., and Pang, W. (2012). Columbia Supercontinent: New Insights from the Western Margin of the Yangtze Landmass. *Sediment. Geology. Tethyan Geology.* 32, 31–40. in Chinese with English abstract.

Yu, S., Zhang, J., and Hou, K. (2011). Two Constrasting Magmatic Events in the Dulan UHP Metamorphic Terrane: Implication for Collisional Orogeny. *Acta Petrol. Sin.* 27, 3335–3349. in Chinese with English abstract.

Yuan, W., Mo, X., Yu, X., and Luo, Z. (2000). The Record of Indosinian Tectonic Setting from the Granotoid of Eastern Kunlun Mountains. *Geol. Rev.* 46, 203–211. in Chinese with English abstract.

Yusheng, W., Jianxin, Z., Jingsui, Y., and Zhiqin, X. (2006). Geochemistry of High-Grade Metamorphic Rocks of the North Qaidam Mountains and Their Geological Significance. *J. Asian Earth Sci.* 28, 174–184. doi:10.1016/j.jseaes.2005.09.018

Yusheng, W., Zhiqin, X., Jingsui, Y., and Jianxin, Z. (2001). Ages and Compositions of the Precambrian High-Grade Basement of the Qilian Terrane and its Adjacent Areas. *Acta Geol. Sin.-Engl. Ed.* 75, 375–384. doi:10.1111/j.1755-6724.2001.tb00055.x

Zhang, G., Ireland, T., Zhang, L., Gao, Z., and Song, S. (2016). Zircon Geochemistry of Two Contrasting Types of Eclogite: Implications for the Tectonic Evolution of the North Qaidam UHPM Belt, Northern Tibet. *Gondwana Res.* 35, 27–39. doi:10.1016/j.gr.2016.04.002

Zhang, G., Song, S., Zhang, L., Niu, Y., and Shu, G. (2005). Ophiolite-Type Mantle Peridotite from Shaliuhe, North Qaidam UHPM Belt, NW China and its Tectonic Implications. *Acta Petrol. Sin.* 21, 1049–1058. in Chinese with English abstract.

Zhang, G., Song, S., Zhang, L., and Niu, Y. (2008a). The Subducted Oceanic Crust within Continental-Type UHP Metamorphic Belt in the North Qaidam, NW China: Evidence from Petrology, Geochemistry and Geochronology. *Lithos* 104, 99–118. doi:10.1016/j.lithos.2007.12.001

Zhang, G., Zhang, L., and Christy, A. G. (2013). From Oceanic Subduction to continental Collision: An Overview of HP-UHP Metamorphic Rocks in the North Qaidam UHP belt, NW China. *J. Asian Earth Sci.* 63, 98–111. doi:10.1016/j.jseaes.2012.07.014

Zhang, G., Zhang, L., Christy, A. G., Song, S., and Li, Q. (2014). Differential Exhumation and Cooling History of North Qaidam UHP Metamorphic Rocks, NW China: Constraints from Zircon and Rutile Thermometry and U-Pb Geochronology. *Lithos* 205, 15–27. doi:10.1016/j.lithos.2014.06.018

Zhang, G., and Zhang, L. (2011). Rodingite from Oceanic Lithology of Shaliu Terrane in North Qaidam UHPM Belt and its Geological Implication. *Earth Sci. Front.* 18, 151–157. in Chinese with English abstract.

Zhang, G., Zhang, L., Song, S., and Niu, Y. (2009). UHP Metamorphic Evolution and SHRIMP Geochronology of a Coesite-Bearing Meta-Ophiolitic Gabbro in the North Qaidam, NW China. *J. Asian Earth Sci.* 35, 310–322. doi:10.1016/j.jseaes.2008.11.013

Zhang, J., Wan, Y., Meng, F., Yang, J., and Xu, A. (2003). Geochemistry, Sm-Nd and U-Pb Isotope Study of Gneisses (Schists) Enclosing Eclogites in the North Qaidam Mountains - Deeply Subducted Precambrian Metamorphic Basement? *Acta Petrol. Sin.* 19, 443–451. in Chinese with English abstract.

Zhang, J., Yu, S., and Meng, F. (2008b). Metamorphic and Deformational Evolution of the Iqe-Luofengpo Eclogite-Geniss Unit in the North Qaidam Mountains, China. *Geol. Bull. China* 27, 1468–1474. in Chinese with English abstract.

Zhang, S., Jian, X., Pullen, A., Fu, L., Liang, H., Hong, D., et al. (2020). Tectono-Magmatic Events of the Qilian Orogenic Belt in Northern Tibet: New Insights from Detrital Zircon Geochronology of River Sands. *Int. Geology. Rev.* 63, 917–940. doi:10.1080/00206814.2020.1734876

Zhou, C.-A., Song, S., Allen, M. B., Wang, C., Su, L., and Wang, M. (2021). Post-collisional Mafic Magmatism: Insights into Orogenic Collapse and Mantle Modification from North Qaidam Collisional Belt, NW China. *Lithos* 398-399, 106311. doi:10.1016/j.lithos.2021.106311

Zhu, Z., Campbell, I. H., Allen, C. M., and Burnham, A. D. (2020). S-type Granites: Their Origin and Distribution through Time as Determined from Detrital Zircons. *Earth Planet. Sci. LettersSci. Lett.* 536, 116140. doi:10.1016/j.epsl.2020.116140

Conflict of Interest: The authors declare that the research was conducted in the absence of any commercial or financial relationships that could be construed as a potential conflict of interest.

frontiers | Frontiers in Earth Science

ORIGINAL RESEARCH
published: 05 May 2022
doi: 10.3389/feart.2022.891960

Sr-Nd-Hf Isotopic Disequilibrium During the Partial Melting of Metasediments: Insight From Himalayan Leucosome

Lei Yang[1,2,3], *Jia-Min Wang*[2]*, *Xiao-Chi Liu*[2], *Gautam P. Khanal*[3,4] *and Fu-Yuan Wu*[2,3]

[1]*College of Earth Sciences, Chengdu University of Technology, Chengdu, China,* [2]*State Key Laboratory of Lithospheric Evolution, Institute of Geology and Geophysics, Chinese Academy of Sciences, Beijing, China,* [3]*College of Earth and Planetary Sciences, University of Chinese Academy of Sciences, Beijing, China,* [4]*Department of Mines and Geology, Kathmandu, Nepal*

Radiogenic isotopes of granitoids are widely applied to fingerprint the source of granitoids and study the magma mingling and assimilation processes, aiming to decipher the planetary differentiation. This weapon is based on the assumption that crustal melts inherit the radiogenic isotopes of protoliths. However, complicated melting processes in the crust would drive the radiogenic isotopes of melt away from the source, thus calling for a clear understanding of the behaviors of radiogenic isotopes during crustal melting. This study investigated the joint behavior of Rb-Sr, Sm-Nd, and Lu-Hf isotope systems during the melting of metasediments. Leucosome, schist, and leucogranite samples were collected from the Nyalam, South Tibet, where the leucosome was produced by muscovite dehydration melting of metapelites. Results show that the leucosome has a broad range of Sr-Nd-Hf isotopes ($^{87}Sr/^{86}Sr_i$: 0.763,48–0.875321, $\varepsilon Nd_{(t)}$: 14.6–11.6, $\varepsilon Hf_{(t)}$: 15.0–4.4) that deviate from the metasediments. We attributed it to the non-modal or disequilibrium melting of metapelites. The variation of Sr isotopes of leucosome is formed due to preferential entry into the melt of muscovite relative to plagioclase during melting. The changing $^{87}Sr/^{86}Sri$ and $^{87}Rb/^{86}Sr$ of leucosome define an errorchron at ~ 500 Ma indicating an early Paleozoic tectono-thermal event supported by the U-Pb age of zircon cores (~460 Ma) in the leucosome. The Nd isotopes of leucosome are mainly controlled by the preferential dissolution of apatite relative to monazite. The inadequate dissolution of zircon caused more depleted initial Hf isotopes compositions in the leucosome than the source. However, the leucosome with a higher crystallization temperature has radiogenic isotopic composition closer to the source. It indicates that the melting temperature greatly affects the isotope equilibrium between source and melt.

Keywords: radiogenic isotopes, partial melting, isotope disequilibrium, leucosome, leucogranite

Edited by:
Tatsuki Tsujimori,
Tohoku University, Japan

Reviewed by:
Peng Gao,
Sun Yat-sen University, China
Chao Wang,
The University of Hong Kong, Hong Kong SAR, China
Feng Guo,
Guangzhou Institute of Geochemistry (CAS), China

Correspondence:
Jia-Min Wang
wangjm9595@gmail.com

Specialty section:
This article was submitted to Geochemistry,
a section of the journal
Frontiers in Earth Science

Received: *08 March 2022*
Accepted: *06 April 2022*
Published: *05 May 2022*

Citation:
Yang L, Wang J-M, Liu X-C, Khanal GP and Wu F-Y (2022) Sr-Nd-Hf Isotopic Disequilibrium During the Partial Melting of Metasediments: Insight From Himalayan Leucosome. Front. Earth Sci. 10:891960. doi: 10.3389/feart.2022.891960

1 INTRODUCTION

In the Solar System, the planetary Earth is unique in the existence of granite formed and differentiated from the partial melting of continental crust. As a powerful weapon to explore these differentiation processes, radiogenic isotopes are widely applied to fingerprint the magma source and study magma mingling and assimilation processes (DePaolo, 1981; Chappell, 1996; Wu

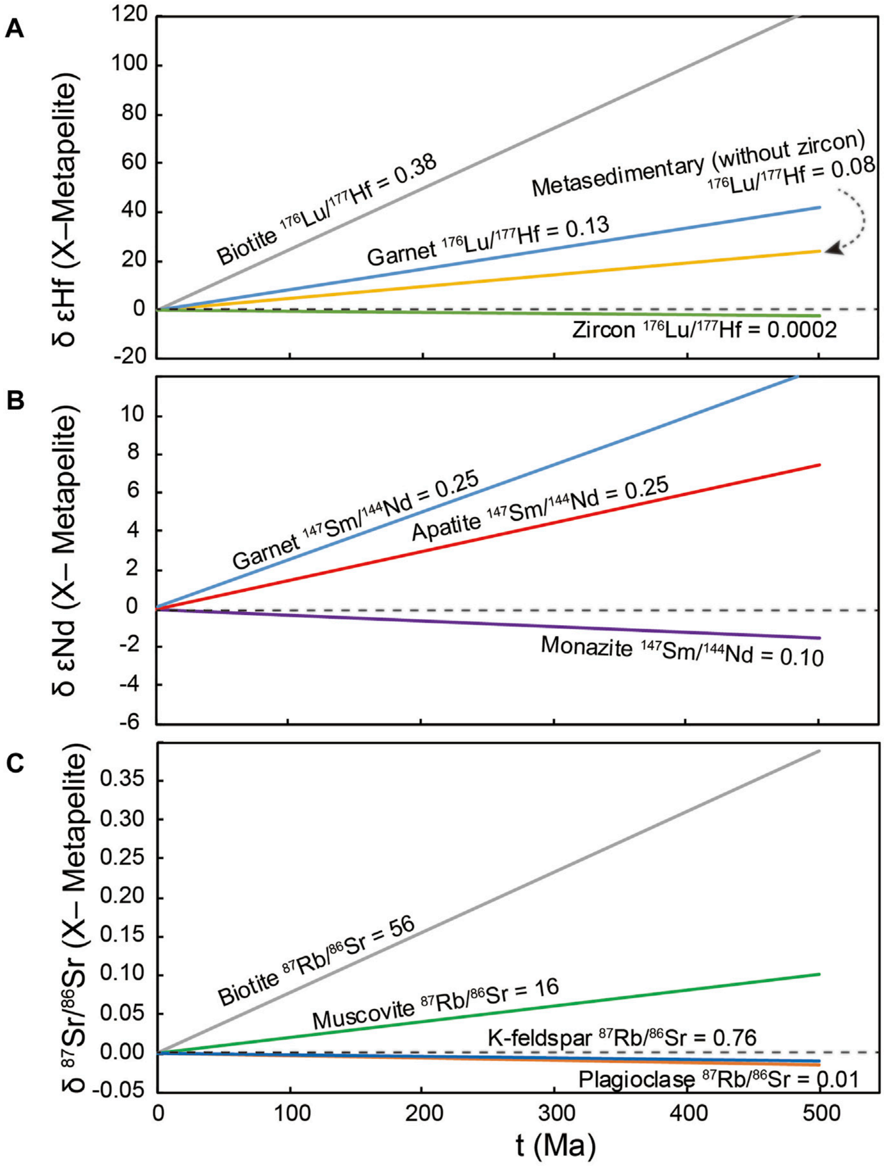

FIGURE 1 | (A) ^{87}Sr/^{86}Sr, **(B)** εNd, and **(C)** εHf isotopic differences of rock-forming and accessory minerals in the metasedimentary rocks relative to the source due to decoupled ingrowth of radiogenic ^{87}Sr, ^{143}Nd, and ^{176}Hf. Rb, Sr, Sm, Nd, Lu and Hf concentration data are adapted from Bea et al. (1994), Faure and Mensing (2005), Zeng et al. (2005), and Rudnick and Gao (2003). Initial Sr, Nd and Hf isotopic compositions are set arbitrarily. We assumed that 90% of the Hf in the metasedimentary is in zircon.

et al., 2014). Theoretically, crustal melt should inherit the radiogenic isotopic compositions of their protoliths. However, an increasing number of studies show that non-modal melting commonly occurs during crustal melting and would deviate the radiogenic isotopes of crustal melt from the source nature (Zeng et al., 2005; Tang et al., 2014). In the source rock, constituent minerals have different parent-to-daughter ratios, and thus the elements with radiogenic ingrowth (e.g., Sr, Nd, and Hf) develop contrasting isotopic compositions with time (**Figure 1**; Wolf et al., 2019). If the isotopic differences among constituent minerals during melting onset were preserved, the melt isotopes could be determined by mineral phases entered into the melt (Knesel and Davidson, 2002; Zeng et al., 2005; Wolf et al., 2019; Xia et al., 2022). Upon the formation of melt, diffusional exchange between the melt and residue will promote isotopic equilibrium, reducing the isotopic difference between the melt and residue until they reach a balance to the source. Residue–melt isotopic equilibrium is controlled by the diffusion rates of the elements, residence time of the melt in the source, equilibrium temperature, and mineral recrystallization (Acosta-Vigil et al., 2017).

Sr, Nd, and Hf isotopes are commonly used to fingerprint the magma source. The analogous behavior of Sm-Nd and Lu-Hf isotopic systems during partial melting leads to a strong

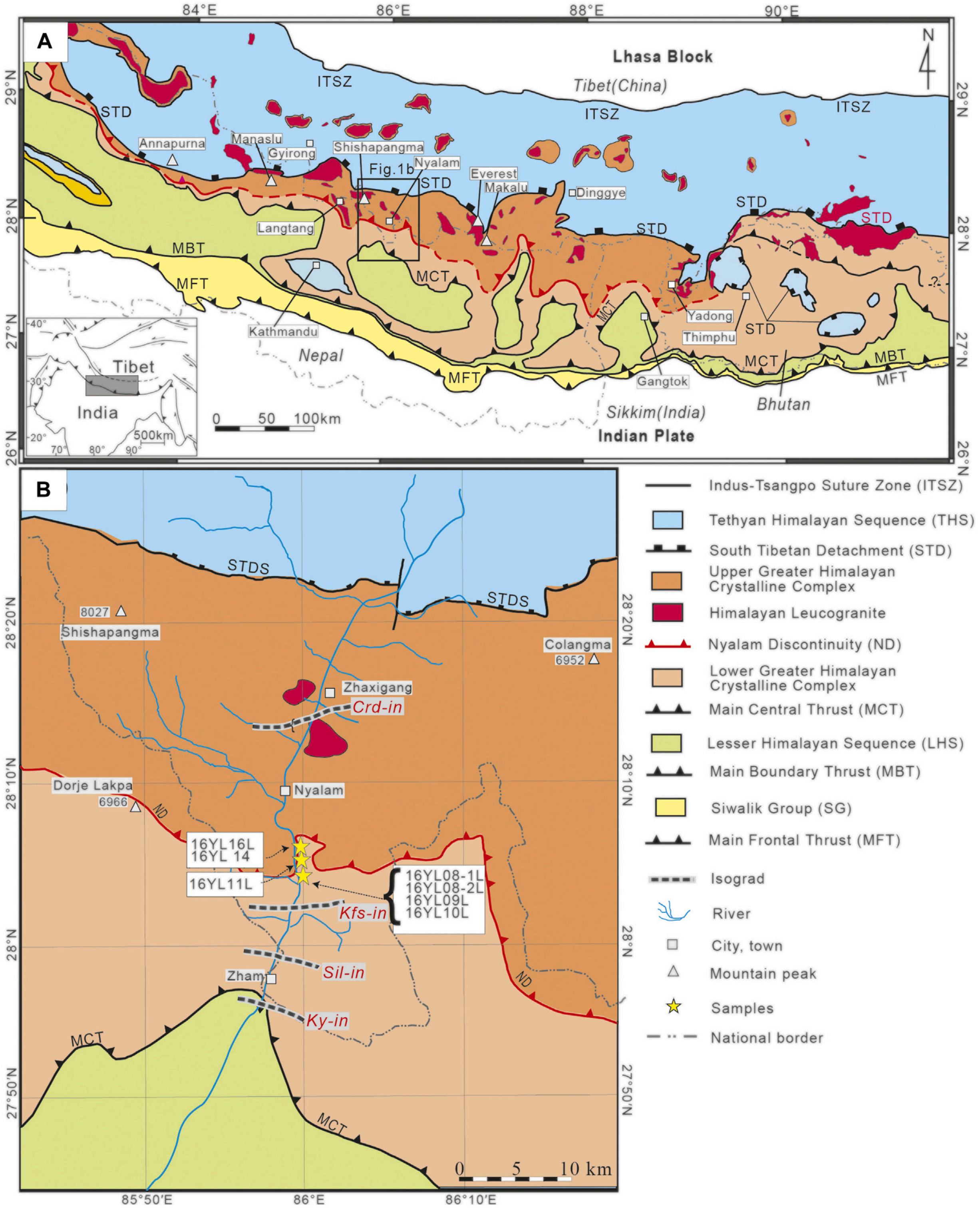

FIGURE 2 | (A) Simplified geological map showing the tectonic framework of the Himalayan orogenic belt. The rectangle indicates the location of the Nyalam. **(B)** Geological sketch map of the Nyalam region (modified after Wang et al., 2015). Mineral abbreviations follow Whitney and Evans (2010).

correlation of the Nd-Hf isotopes that should lie in the Terrestrial Array (Vervoort et al., 2011). Nearly all terrestrial rocks from various sources commonly negative correlates between $^{87}Sr/^{86}Sr$ and $^{143}Nd/^{144}Nd$ isotopic ratios (Clemens et al., 2017). Therefore, the Sr-Nd-Hf isotopes are usually coupled in the crustal rocks. The occurrence of isotopic signatures that deviate from this coupling relationship is thought to be associated with the non-modal or disequilibrium melting processes (Zeng et al., 2005; Zhang et al., 2020). Many studies have identified the isotopic disequilibrium of Sr and Nd during anatexis of metasediments (Knesel and Davidson, 2002; Zeng et al., 2005; Wolf et al., 2019). However, Hf isotopic disequilibrium is mainly found in granitic pluton and is evidenced by modeling (Farina et al., 2014; Tang et al., 2014; Zhang et al., 2020). A reasonable explanation of the anomaly between Sr, Nd, and Hf depends on a clear understanding of the joint behavior of the Sr-Nd-Hf isotopic systems during anatexis of metasediments.

Migmatites, a product of crustal anatexis (Weinberg, 2016), commonly trap *in situ* melt from the source of partial melting and offer an opportunity to study the Sr-Nd-Hf variations during crustal anatexis. In the Himalayas, migmatites are widely exposed, and leucosome within the migmatite is produced by anatectic melting of metasediments (Wang et al., 2015; Wang et al., 2017), making it an ideal material to study the joint behavior of Sr-Nd-Hf isotopic systems during crustal partial melting. This work collected schist, leucosome, and leucogranite from the Great Himalayan Crystalline (GHC) in Nyalam and analyzed their whole-rock Sr-Nd-Hf isotopes. Our work proved that the muscovite dehydration melting reactions and incomplete dissolutions of accessory phases during low-degree partial melting resulted in the deviation of Sr-Nd-Hf isotopes between the melt and the source and their deviation from the array of terrestrial rocks.

2 GEOLOGICAL CONTEXT AND PETROLOGY

The Himalayan orogenic belt in southern Tibet resulted from the India-Asia collision along the Indus–Tsangpo suture zone (Najman et al., 2010). The Indian plate can be divided into the Tethyan Himalayan Sequence (THS), the GHC, and the Lesser Himalayan Series (LHS) from north to south. They were bounded by the Southern Tibetan detachment system (STDS) and the Main Central Thrust (MCT). The GHC consists of late Proterozoic to early Cambrian metasedimentary rocks, which were experienced amphibolite to granulite facies metamorphism. It was intruded by numerous Cambrian–Ordovician plutons (**Figure 2A**).

Nyalam is located in the central Himalaya, southern Tibet, with Shishapangma to the north, Manaslu to the west, and Langtang to the east (**Figure 2B**). The Nyalam Valley is famous for the birth of the concept of Southern Tibet Detachment (Burchfiel et al., 1992) and excellent exposures of the migmatites, leucosome, and leucogranite within the GHC (Wang et al., 2013; Wang et al., 2015; Leloup et al., 2015; Yang et al., 2019). The leucogranite in the Nyalam occurs as sill, small laccolith, and dyke, which was emplaced during Miocene time (27–14 Ma; Yang et al., 2019). Within the GHC, the metamorphic grade increases gradually, indicated by key index metamorphic minerals change from chlorite, garnet, to staurolite in the LHS, and kyanite, sillimanite–muscovite, sillimanite–K-feldspar, and cordierite in the GHC (Wang et al., 2013; Yang et al., 2019). Geothermobarometry data showed that the minimum peak temperature gradually increases from ~580°C in the upper LHS to ~750°C in the upper GHC, whereas metamorphic pressure decreases from 1.0–1.3 to 0.4–0.7 GPa (Wang et al., 2013). Within the sillimanite–K-feldspar zone of the GHC, the internal tectono-metamorphic discontinuity (Nyalam Discontinuity) divides the GHC into lower and upper subunits, with younger ages toward the foreland of the orogenic wedge, forming a duplex structure within the GHC (Wang et al., 2015, 2016). Migmatites are widely distributed in the sillimanite–K-feldspar zone in the middle and upper GHC, where abundant leucosome has been reported with major and trace elements (Yang et al., 2019). In general, leucosome occurs as light-colored layers within stromatic metatexite in the migmatitic paragneiss and orthogneiss. They were produced by muscovite dehydration melting of metasediments according to the petrography, P-T conditions, and geochemistry (Wang et al., 2013; Wang et al., 2015; Yang et al., 2019). Above the cordierite zone, *in situ* leucosome is rare.

In this study, six leucosome samples were separated manually and processed for whole-rock Sr-Nd-Hf isotopic analysis and zircon U-(Th)-Pb dating. The samples were collected mainly from the migmatites of sillimanite–K-feldspar zone around the Nyalam Discontinuity (**Figure 2B**). The migmatite is stromatic metatexite containing centimeter-to decimeter-scale leucosome. Field investigations confirmed that the leucosome is *in situ* (**Figure 3A,B**). The centimeter-scale, layer-parallel leucosome can be traced to their anatectic protoliths. The leucosome has a granoblastic texture and consists of quartz (~30%), K-feldspar (~40%), plagioclase (~20%), biotite (~4%), sillimanite (~3%), garnet (~2%), and accessory (~1%) zircon, monazite, and apatite. In general, the quartz, K-feldspar, and plagioclase are much coarser than in mesosomes or melanosomes. Trace amounts of resorbed muscovite are found in or adjacent to the leucosome, consistent with the formation of K-feldspar and sillimanite during anatexis (**Figures 3D–G**). The melanosomes are composed of alternating layers of sillimanite, biotite, K-feldspar, plagioclase, and ilmenite (**Figure 3G**). The biotite contains numerous inclusions of accessory minerals, e.g., monazite (**Figure 3H**). Monazite U–(Th)–Pb dating indicates that the leucosome was crystallized during 16–14 Ma (Yang et al., 2019). The detailed location and whole-rock geochemistry of the leucosome have been reported in Yang et al. (2019). The schist sample (16YL14) was collected in the sillimanite–K-feldspar zone, a few meters away from sample 16YL12 (GPS: N28°07′02″, E85°59′43″). It consists of quartz (50%), plagioclase (30%), k-feldspar (10%), and biotite (10%). Field and petrographic observations have shown that the schist has not experienced migmatization. We assumed that it represents the protolith corresponding to the leucosome.

The 32 leucogranite samples were collected along a North-South transect across the GHC in Nyalam, from varying occurrences as dikes, sills, and plutons (**Figure 3C**). Like other

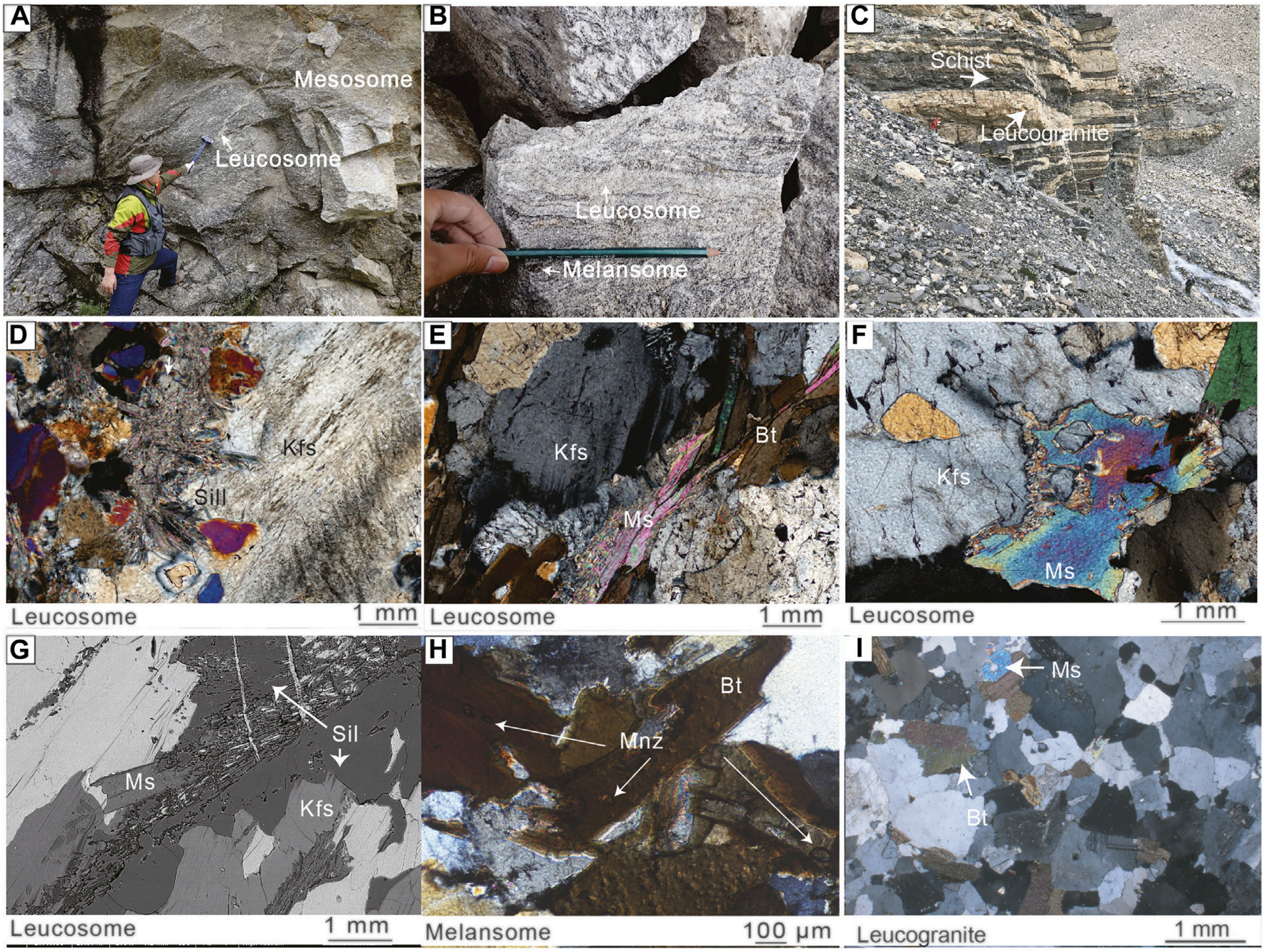

FIGURE 3 | (A and B) Representative outcrop photographs of the leucosome, **(C)** and leucogranite in the Nyalam region. **(D and F)** Microphotographs of leucosome showing the muscovite dehydration melting reactions defined by Ms relicts adjacent to the Kfs and Sil. **(G)** Back-scattered electron image of leucosome showing the muscovite dehydration melting reactions. **(H)** Monazite were wrapped in the biotite of the melansome. **(I)** Microphotographs of the leucogranite..

Himalayan leucogranite (Wu et al., 2020), the principal minerals of the Nyalam leucogranite are quartz, plagioclase, and K-feldspar, with minor varietal muscovite, tourmaline, biotite, and garnet (**Figure 3I**). Principle accessory minerals are zircon, monazite, apatite, and xenotime. Chloritization and sericitization have affected biotite and plagioclase in some leucogranites.

3 ANALYSIS METHOD

3.1 U–(Th)–Pb Zircon Analysis

Zircon laser ablation (LA)–ICP–MS U–(Th)–Pb dating was conducted with an Agilent 7500a quadrupole ICP–MS coupled to a 193-nm excimer laser ablation system. Detailed analytical procedures are provided by Xie et al. (2008). The ^{207}Pb/^{206} Pb, ^{206}Pb/^{238}U, ^{207}U/^{235}U (^{235}U = ^{238}U/137.88), and ^{208}Pb/^{232}Th ratios were corrected using zircon 91,500 as an external standard. The fractionation correction and results were calculated using GLITTER 4.0 (GEMOC, Macquarie University; Griffin et al., 2008). The U–(Th)–Pb dating of standard samples is given in **Supplementary Table S1**.

3.2 Whole-Rock Sr-Nd-Hf Isotope Analysis

High precision isotopic (Sr, Nd, and Hf) measurements were carried out at Nanjing FocuMS Technology Co., Ltd. Geological rock powders were mixed with 60 wt% HNO_3 (0.5 ml) and 40 wt% HF (1.0 ml) in high-pressure PTFE bombs. These bombs were steel-jacketed and placed in the oven at 195°C for 3 days. Digested samples were dried down on a hotplate and reconstituted in a 1.5-ml of 1.5 N HCl before ion exchange purification. The detail of the purification processes of Sr, Nd, and Hf was reported by Ji et al. (2020). Diluted solutions (50 ppb Sr, 50 ppb Nd, and 40 ppb Hf) were introduced into Nu Instruments Nu Plasma II MC–ICP–MS. Raw data of isotopic ratios were internally corrected for mass fractionation by normalizing to ^{86}Sr/^{88}Sr = 0.1194 for Sr, ^{146}Nd/^{144}Nd = 0.7219 for Nd, and ^{179}Hf/^{177}Hf = 0.7325 for Hf with exponential law. International isotopic standards (NIST SRM 987 for Sr, JNdi-1 for Nd, Alfa Hf) were periodically analyzed to correct instrumental drift. Geochemical

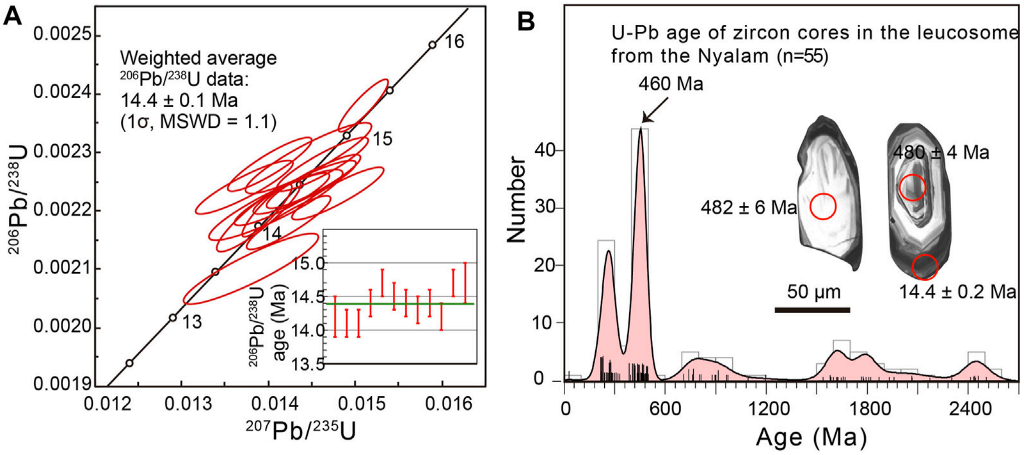

FIGURE 4 | (A) The U–(Th)–Pb dating of zircon rims in the leucosome **(B)** The kernel density estimates of zircon cores ^{207} Pb/^{235}U ages in the leucosome. Inserted images show the represented zircons from the leucosome. The red circle is the laser spot. The data are listed in **Supplementary Table S3**.

reference materials of USGS BCR-2, BHVO-2, AVG-2, RGM-2, and W-2 were treated as quality control. The isotopic compositions of standard samples are given in **Supplementary Table S2**. The values agreed with previous publications within analytical uncertainty (Weis et al., 2006, 2007).

4 RESULT

4.1 U–(Th)–Pb Geochronology of Inherited Zircons

Zircons extracted from the leucosome samples are 100–200 μm in size. Cathodoluminescence (CL) imaging of the zircon internal structures shows euhedral, oscillatory zoned core domains, which are truncated and overgrown by broad, faintly oscillatory zoned rim domains (**Figure 4B**). LA–ICP–MS analyses of the zircon rim domains show lower Th/U ratios relative to the core (rim domains: Th/U = 0.01–0.02; core domains: Th/U = 0.01–1.8). These data are between 95 and 110% concordant. Fourteen spot analyses of the rim yield an age of 14.4 ± 0.1 Ma (1σ; MSWD = 1.1), represent the time of crystallization time (**Figure 4A**). Fifty-five spot analyses of the cores were performed. Except two spots have the age older than Neoproterozoic time, others display scattered ages ranging from 895 ± 10 Ma to 147 ± 1 Ma (^{207}Pb/^{235}U ages with one sigma, **Figure 4B**), which precludes a single-weighted mean age from being calculated. The kernel density estimates (KDE) present a primary age peak at ~460 Ma (**Figure 4B**). The analyses data are shown in **Supplementary Table S3**.

4.2 Whole-Rock Radiogenic Isotopes

The Sr-Nd-Hf isotopes of the leucosome, schist, and leucogranite in this study were listed in **Supplementary Table S4** and plotted in **Figures 5**, **6**. Measured ^{87}Sr/^{86}Sr ratios of leucosome range between 0.764503 ± 5 and 0.879092 ± 3 and the recalculated initial ^{87}Sr/^{86}Sr$_i$ (for ages of each sample were reported by Yang et al. (2019), t = 16–14 Ma) range between 0.763248 ± 4 and 0.875321 ± 3 (**Figures 5A,B**). The initial Sr isotopic composition is correlated with Sr content variation and Rb/Sr ratio (**Figures 5A,B**). In addition, it defines a crude ~500 Ma errorchron with the ^{87}Rb/^{86}Sr ratio, which is consistent with the trend that appears in the Langtang migmatite (**Figure 5B**; Harris and Ayres, 1998). One schist sample from Nyalam has the ^{87}Sr/^{86}Sr ratio 0.729312 and recalculated ^{87}Sr/^{86}Sr$_i$ (t = 15 Ma) ratio 0.729029. Measured ^{87}Sr/^{86}Sr ratios of leucogranite range between 0.744519 ± 5 and 0.771546 ± 4, and recalculated initial ^{87}Sr/^{86}Sr$_i$ range between 0.737481 ± 4 and 0.765985 ± 3 (t = 15 Ma).

Measured ^{143}Nd/^{144}Nd isotopes of leucosome range between 0.511884 ± 4 and 0.512044 ± 5, and recalculated initial εNd$_{(t)}$ range between −11.6 and −14.6 (**Figure 5C**). A remarkable feature is that their initial Sr and Nd isotopic compositions show a positive relationship (**Figure 5D**). The schist from the Nyalam has the ^{143}Nd/^{144}Nd ratio 0.511690 and recalculated εNd$_{(t)}$ (t = 15 Ma) of −18.3. Measured ^{143}Nd/^{144}Nd isotopes of leucogranite range between 0.511817 ± 6 and 0.511912 ± 2, and recalculated initial εNd$_{(t)}$ range between −16.1 and −14.0 (t = 15 Ma).

The measured ^{176}Hf/^{177}Hf isotopes of leucosome range from 0.282350 ± 3 to 0.282654 ± 3. The recalculated initial εHf$_{(t)}$ range between −4.4 and −15.0 (**Figure 6A**). The Hf-Nd isotopes are positively correlated (**Figure 6B**). The schist sample from the Nyalam has the ^{176}Hf/^{177}Hf ratio 0.281965 and recalculated εNd$_{(t)}$ (t = 15 Ma) of −28.7. Measured ^{176}Hf/^{177}Hf isotopes of leucogranite range from 0.282386 ± 2 to 0.282190 ± 2. The recalculated initial εHf$_{(t)}$ range between −13.3 and −20.3 (t = 15 Ma).

5 DISCUSSION

5.1 The Record of the Early Paleozoic Tectono-Thermal Events

Pre-Himalayan evolution is essential to rebuilding the supercontinents (e.g., Gondwana assemblage; Cawood et al., 2007). However, it is much harder to decipher due to this pervasive Cenozoic metamorphic overprint (Palin et al., 2018). In

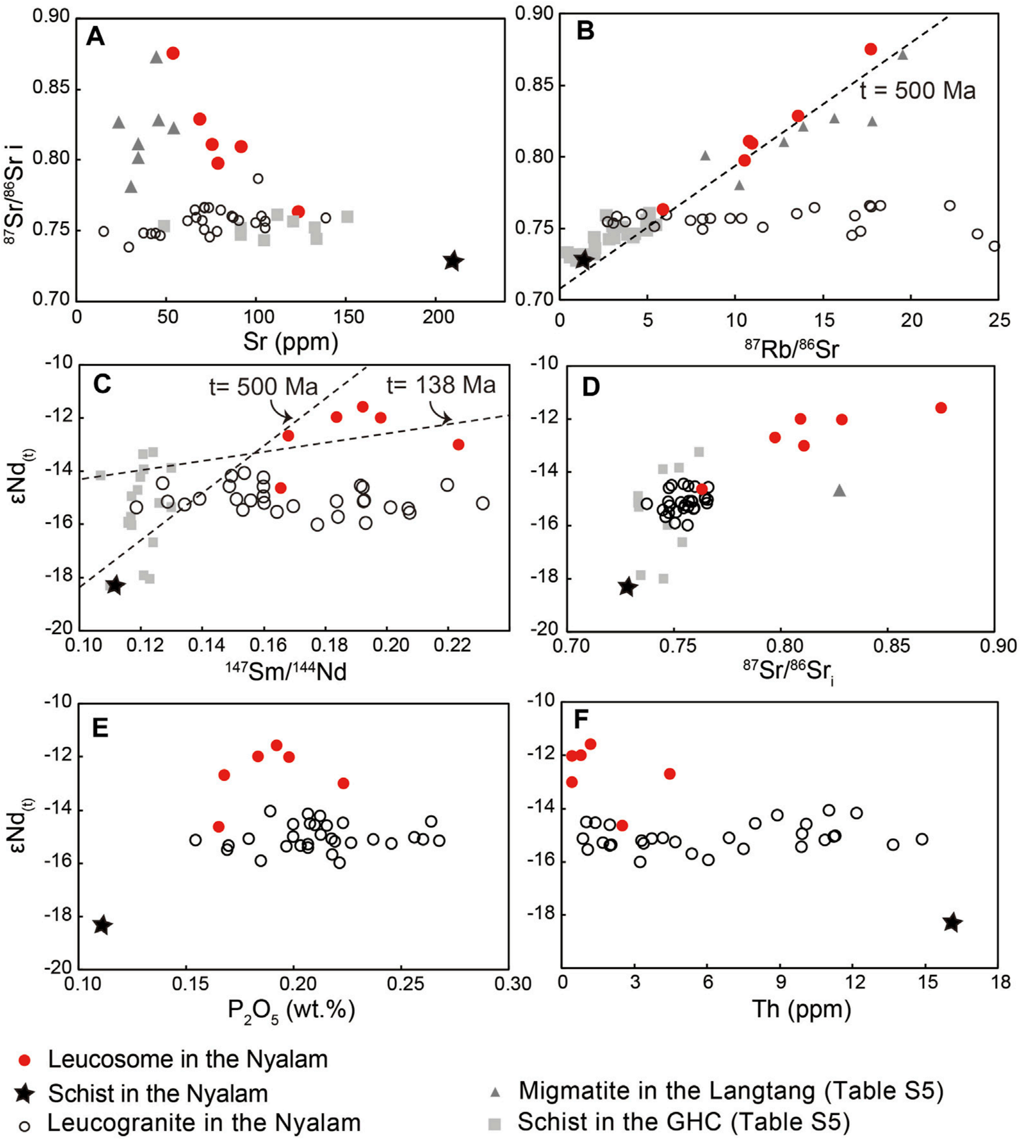

FIGURE 5 | Plots of ^{87}Sr/^{86}Sri vs. **(A)** Sr content, **(B)** ^{87}Rb/^{86}Sr ratios, and εNd(t) vs. **(C)** ^{147}Sm/^{144}Nd ratio, **(D)** ^{87}Sr/^{86}Sr$_i$ ratio, **(E)** P$_2$O$_5$ content, and **(F)** Th content for the Nyalam leucosome, leucogranite, and schist in this study, migmatites in the Langtang (Inger and Harris, 1993), and schists in the GHC (Deniel et al., 1987; Inger and Harris, 1993; Parrish and Hodges, 1996; Robinson et al., 2001). The literature data are listed in **Supplementary Table S5**. The ^{87}Sr/^{86}Sr$_i$ and εNd$_{(t)}$ values of the leucosome and leucogranite are calculated by their crystallization ages reported in Yang et al. (2019). Others are corrected to 15 Ma. The dashed lines in the **(B)** and **(C)** indicate the 500 Ma and 138 Ma errorchrons.

this study, analyses of the zircon rim of leucosome yield an age of 14.4 ± 0.1 Ma, consistent with the monazite age reported by Yang et al. (2019). We suggest that this age represents the timing when anatectic melt crystallization. In the projection of ^{87}Rb/^{86}Sr versus ^{87}Sr/^{86}Sr$_i$, the errorchron is distributed around ~500 Ma. In addition, inherited zircon cores in the leucosome yield a prominent age peak at ~460 Ma (**Figure 4B**). Similar errorchron age in the migmatite was reported by Inger and Harris (1993) from the Langtang to the east of Nyalam. Although such crude "age" has a large uncertainty, it indicates the timing that the GHC were partially homogenized with concerning Sr isotopes (Inger and Harris, 1993). From the Neoproterozoic to early Paleozoic, the GHC is in the northern margin of Gondwana and has experienced a series of orogenic events along with the Andean-type subduction (Cawood et al., 2007). The Cadomian orogeny lasted from ~650 to ~540 Ma (Linnemann et al., 2014; Gao et al., 2019), followed by the ~510–460 Ma Ordovician Bhimpedian (or Kurgiakh) orogeny (Myrow et al., 2006; Cawood et al., 2007), which is most closely related to the age recorded in the leucosome. This early Paleozoic orogeny was accompanied by widespread granitoid magmatism, now exposed in GHC and North Himalayan Gneiss domes aged 520–460 Ma (DeCelles et al., 2000; Cawood et al., 2007; Wang et al., 2012; Gao et al., 2019) and high-grade metamorphism (Cawood et al., 2007; Palin et al., 2018).

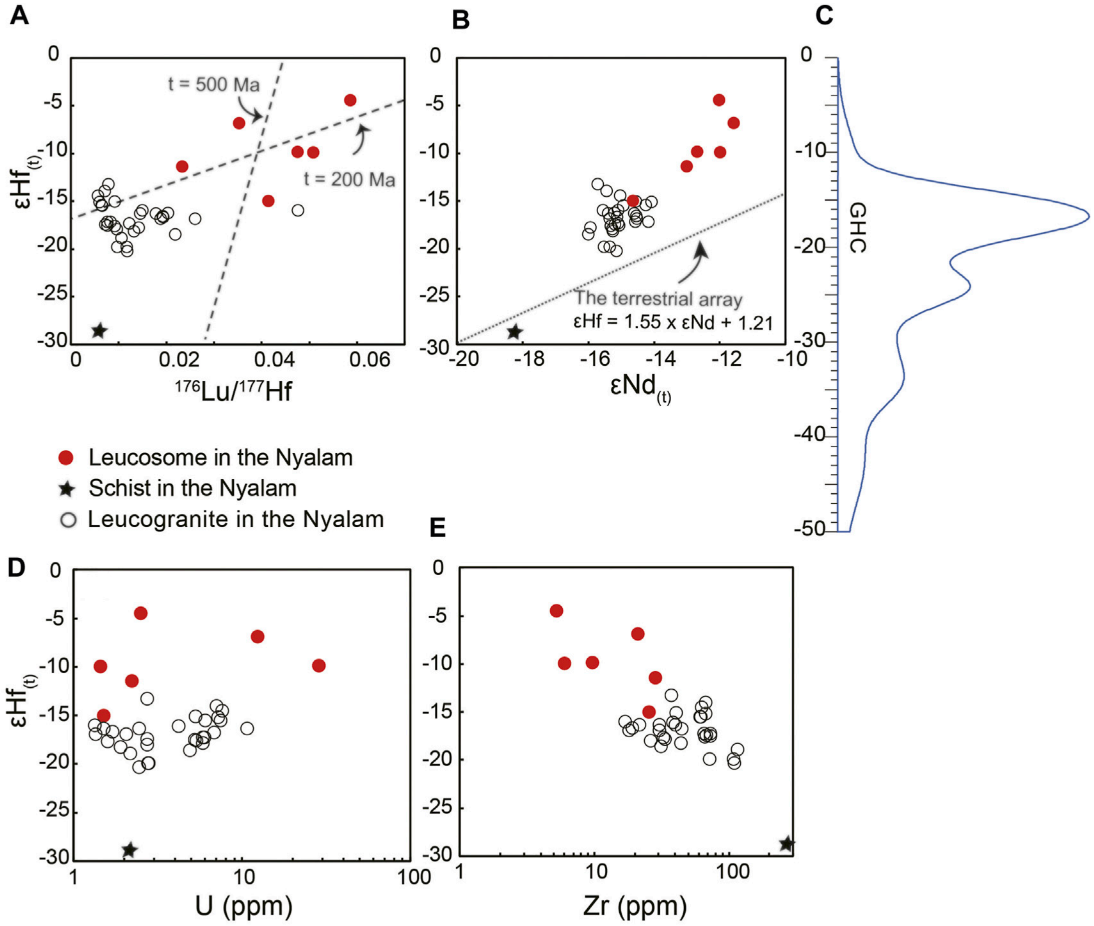

FIGURE 6 | Plots of $\varepsilon Hf_{(t)}$ vs. **(A)** $^{176}Lu/^{177}Hf$, **(B)** $\varepsilon Nd_{(t)}$, **(D)** U, and **(E)** Zr for the leucosome, schist, and leucogranite in the Nyalam. The dashed lines in the **(A)** indicate the 500 Ma and 200 Ma errorchrons. The dotted line in the **(B)** shows the terrestrial array regressed by Vervoort et al. (2011). **(C)** The kernel density estimates of the GHC (Langtang) detrital zircon data, recalculated at 15 Ma, based on the composition of Spencer et al. (2019) (**Supplementary Table S5**).

Unlike the Rb-Sr isotopic system, the Sm-Nd and Lu-Hf isotopic systems in the leucosome present errorchron ages of ~138 Ma and ~200 Ma, respectively (**Figures 5C, 6A**). Such Mesozoic ages are unlikely to be related to any tectonic event because there is no record of Mesozoic metamorphism in the Himalayan orogenic belt (Kapp and DeCelles, 2019). We suggest that these errorchron ages record partially resetting intermediate ages. The absence of early Paleozoic ages in the Sm-Nd and Lu-Hf isotopic systems is perhaps due to the small ranges in $^{147}Sm/^{144}Nd$ and $^{176}Lu/^{177}Hf$ values and variability in the initial Nd and Hf isotopic ratios. The samples in this study were collected from tens of meters to a few kilometers in spatial distance, placing a maximum constraint on the length scale of isotopic re-equilibration during the Himalayan metamorphism.

5.2 The Sr-Nd-Hf Isotopic Disequilibrium of the Leucosome

Enriched $^{87}Sr/^{86}Sr_i$, $\varepsilon Nd_{(t)}$, and $\varepsilon Hf_{(t)}$ compositions in the leucosome indicate its typical crustal origin (**Figures 5, 6**). It is consistent with that the leucosome in this study was produced by muscovite dehydration melting of the GHC metasediments (Yang et al., 2019) However, the leucosome has a broad range of Sr-Nd-Hf isotopes. The origin of the isotopic variability is usually explained in two perspectives: 1) magma mingling and assimilation (DePaolo, 1981; Chappell, 1996); 2) varied crustal sources (Ji et al., 2022); and 3) the isotopic heterogeneity in the source (Deniel et al., 1987). We preclude the first and second assumptions because the leucosome is *in situ* or in-source melt in this study. To discuss the third possibility, we compiled the Sr-Nd-Hf isotopic data of the GHC (**Supplementary Table S5**; Deniel et al., 1987; Inger and Harris, 1993; Parrish and Hodges, 1996; Robinson et al., 2001; Spencer et al., 2019). The compiled data are age-corrected to 15 Ma, the timing of leucosome crystallization. The whole-rock Sr-Nd isotopic data from Manaslu and Langtang show that the GHC has $^{87}Sr/^{86}Sr_i$ from 0.73 to 0.76, and $\varepsilon Nd_{(t)}$ from −15 to −20 (**Figures 5A,B**). The zircon Hf isotopic data from Spence et al. (2019) show that the GHC in the Langtang has $\varepsilon Hf_{(t)}$ values from −8 to −18 (**Figure 6C**). In this study, the schist in the Nyalam has semblable isotopic compositions as those reported in the literature. A remarkable feature of the leucosome is that the Sr-Nd-Hf isotopic compositions deviate in varying degrees from the GHC migmatites (**Figures 5**, **6**). The leucosome yields more radiogenic Sr isotopes composition and less radiogenic Nd and Hf isotopes than the GHC metasediments. It implies that the Nyalam leucosome does not inherit the source isotopic signature of the source, and another process may have driven the isotopes of melt away from the source.

Partial melting in natural rocks always occurs in open systems. The composition of anatectic melts might be affected by melt lost or fractional crystallization, addition of restite, and reverse reaction between melt and restite (Taylor et al., 2014; Brown et al., 2016). Yang et al. (2019) performed detail petrographic and geochemical work to the leucosome in this study, and suggested that the composition of leucosome might be affected by fractionation crystallization and disequilibrium melting. However, it is difficult for the fractional crystallization to affect the isotopic composition of leucosome. For the radiogenic elements, isotopic fractionations are negligible and do not change the isotopes of the melt from the source and crystallized minerals. Another possible process might be non-modal melting or disequilibrium melting (Zeng et al., 2005; Tang et al., 2014; Wolf et al., 2019). Knesel and Davidson (2002) suggested that the various $^{87}Sr/^{86}Sr$ ratios in the melt showed a range of values depending on the mineral phase involved in the melting process. Higher Rb/Sr ratio in the muscovite results in a radiogenic $^{87}Sr/^{86}Sr$, rather than a lower Rb/Sr ratio and unradiogenic $^{87}Sr/^{86}Sr$ in the plagioclase (Knesel and Davidson, 2002). In our study, leucosomes were produced by muscovite dehydration melting (Wang et al., 2013, 2015; Yang et al., 2019), with possible reaction as followings (Patiño Douce and Harris, 1998):

$$22\mathrm{Mus} + 7\mathrm{P1} + 8\mathrm{Qz} \rightarrow 5\mathrm{Kfs} + 5\mathrm{Sill} + 2\mathrm{Bt} + 25\mathrm{L} \tag{1}$$

During muscovite dehydration melting, muscovite is preferentially melted compared with plagioclase. It is accompanied by the growth of peritectic K-feldspar, resulting in a melt with a higher Rb/Sr ratio, lower Sr content, and radiogenic $^{87}Sr/^{86}Sr$ ratio (Harris and Inger, 1992; Patiño Douce and Harris, 1998). It is evidenced by the perfect correlations between $^{87}Sr/^{86}Sr_i$ and Sr ($r^2 = 0.82$), Rb/Sr ratio ($r^2 = 0.99$, **Figures 5A,B**). The $^{87}Sr/^{86}Sr_i$ values of the leucosome increase as the Rb/Sr increases and Sr decreases.

In metasediments, the Sm-Nd system is mainly controlled by apatite and monazite (Rapp et al., 1987). The dissolution of apatite and monazite may play an essential role in shaping the Nd isotopic systematics of anatectic melt (Ayres and Harris, 1997; Zeng et al., 2005). Although Hammerli et al. (2014) argued that metasedimentary rock has reached Nd isotopic equilibrium before 550°C based on *in situ* Sm–Nd isotope study of accessory minerals, we suggest that this scenario does not match with the migmatite in this study. The Nd isotope homogenization between accessory phases in the study of Hammerli et al. (2014) was mainly through recrystallization of detrital accessory minerals. However, if the protolith is dominated by minerals that formed at high-grade metamorphic conditions, prograde metamorphism may not result in significant inter-accessory mineral reactions (Wolf et al., 2019). The migmatite in this study has experienced early Paleozoic metamorphism; therefore, the accessory minerals in the migmatite are difficult to recrystallization during prograde metamorphism.

Zeng et al. (2005) suggested that muscovite dehydration melting occurs at low H_2O activity, which promotes apatite dissolution but inhibits monazite dissolution, resulting in a melt with higher Sm/Nd ratios and more radiogenic Nd isotopic compositions than the source. In **Figure 5C**, it is evident that the leucosome has a higher $^{147}Sm/^{144}Nd$ than the GHC metasedimentary rocks. In addition, the fact that more radiogenic leucosomes in Nd isotope have higher P_2O_5 and lower Th content as well supported the preferable dissolution of apatite during anatexis (**Figures 5E,F**). In the process of crust-mantle differentiation, the crust has higher Rb/Sr and lower Sm/Nd ratios than the mantle. Therefore, the $^{87}Sr/^{86}Sr$ and $^{143}Nd/^{144}Nd$ (or εNd) of terrestrial rocks from various sources are commonly coupled with negative correlation (Clemens et al., 2017). The exceptional example is that the minerals with higher muscovite/plagioclase and apatite/monazite ratios entering the melt during muscovite dehydration melting of metapelite would result in a positive correlation in the Sr-Nd isotope couple, which also occurred in the leucosome (**Figure 5D**).

Since zircon is the primary Hf-bearing mineral in metasedimentary rocks, the Hf isotope of anatectic melt is mainly controlled by the zircon dissolution in the source area (Bea et al., 1994). The variations of Hf isotopes composition in the *in situ* anatectic melt have been attributed to 1) preferential dissolution of uranium-rich zircon (Gao et al., 2021) and 2) disequilibrium melting and peritectic reaction (Farina et al., 2014; Tang et al., 2014; Xia et al., 2022). Gao et al. (2021) reported that the uranium-rich zircons in the Himalayan leucogranite are characterized by higher $\varepsilon Hf_{(t)}$ values. The uranium-rich zircons are preferential entering melt during crust melting because the severe radiation damage reduces their stability (Gao et al., 2021). However, the lack of correlation between U and $\varepsilon Hf_{(t)}$ indicates that the Hf isotope variation in the leucosome is not caused by the preferential dissolution of uranium-rich zircons in the source (**Figure 6D**). The negative correlation between Zr and $\varepsilon Hf_{(t)}$ indicates that the radiogenic Hf isotope in the leucosome was contributed by Zr-poor mineral (**Figure 6E**). With extremely low Lu/Hf ratios, zircon contributes to the unradiogenic Hf, whereas other rock-forming minerals hosting the most Lu contribute to the radiogenic Hf (Tang et al., 2014; Xia et al., 2022). Disequilibrium melting affects retention of unradiogenic Hf in refractory zircon, or release of radiogenic Hf from easily melted minerals, e.g., feldspar and mica, resulting in the melt having a high εHf (the so-called "zircon effect"; Tang et al., 2014). In addition, recent study by *in situ* analyses of zircon in migmatite shows that newly grown zircons have elevation Hf isotope ratios than their protolith zircons (Xia et al., 2022). Xia et al. (2022) attributed to the peritectic reaction of garnet with high Lu/Hf. However, there is no evidence indicates that garnet is involved in the process of muscovite dehydration melting. Hence, we suggest that incomplete dissolution of zircon may contribute to leucosomes with higher εHf. It is supported by the higher $^{176}Lu/^{177}Hf$ ratios in the leucosome than in the source (**Figure 6A**). The trend of Nd-Hf isotopes in the leucosome deviates from the terrestrial array and shows elevated $\varepsilon Hf_{(t)}$ and $\varepsilon Nd_{(t)}$ ratios (**Figure 6B**). In conclusion, we suggest that the incongruent

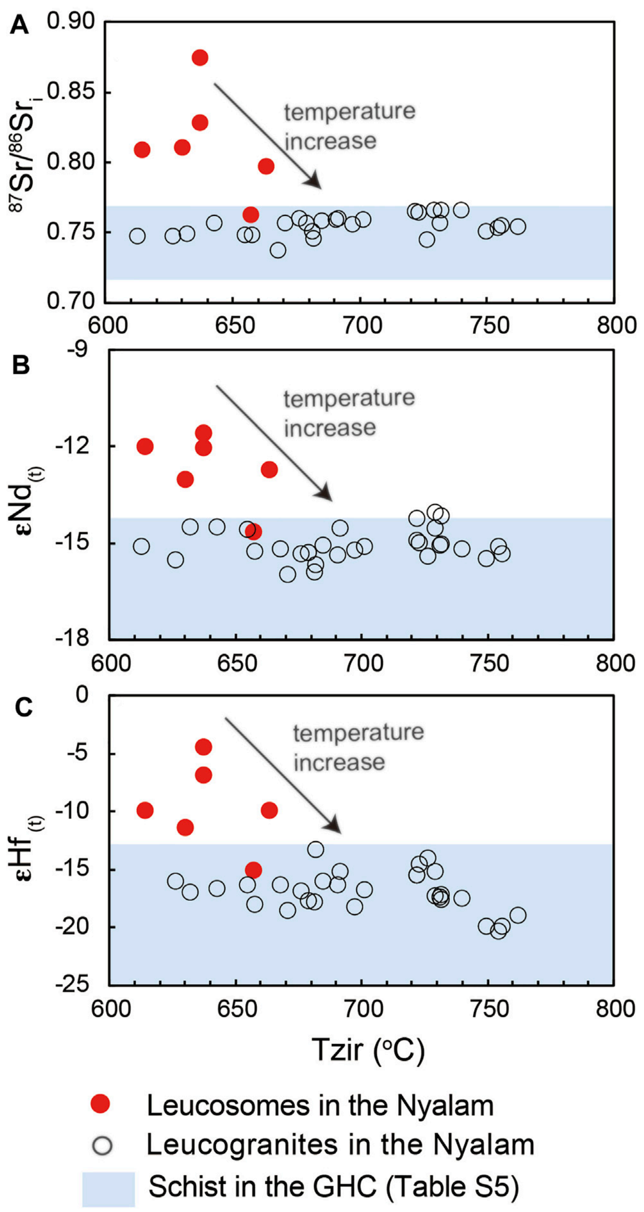

FIGURE 7 | The diagrams show the change of **(A)** $^{87}Sr/^{86}Sri$, **(B)** $εNd_{(t)}$, **(C)** $εHf_{(t)}$ of leucosome and leucogranite with the crystallization temperature. The crystallization temperature was estimated by zircon saturation thermometer (Watson and Harrison, 1983. The blue areas represent the isotope range of the GHC.

trend of Nd-Hf isotopes is resulted from the preferred dissolution of Zr-poor accessory minerals such as mica and feldspar.

5.3 Implications

Based on the zircon saturation thermometer from Watson and Harrison (1983), we estimated the crystallization temperature of the leucosome is 663–614°C, which is consistent with the metamorphism temperature constrained by Wang et al. (2013). The negative correlations between isotopes and crystallization temperatures indicate that temperature has an important effect on the isotopic equilibrium during anatexis (**Figure 7**). It is also supported by the negative correlation between Sr and $^{87}Sr/^{86}Sr_i$ (**Figure 5A**). Because Sr content in the melt increases when melt fraction increases during muscovite dehydration melting of metapelite (Harris and Inger, 1992; Knesel and Davidson, 2002). The leucosome crystallized from higher melt fractions might be produced at higher melting temperatures, has a higher Sr content.

With the temperature increase, the isotopic signature of the leucosome is closer to the source. The rise of temperature during crustal anatexis has three main effects. Firstly, a higher temperature would accelerate the isotopes exchanges, e.g., the diffusion rate of Sr in plagioclase increases exponentially with an increasing temperature (Cherniak and Watson, 1994). Secondly, a higher temperature would prompt the dissolution of accessory minerals because their solubility is a function of temperature (Watson and Harrison, 1983; Montel, 1993). Thirdly, a higher temperature would cause the decomposition of refractory minerals in the metasediments (e.g., biotite and garnet) containing accessory minerals (Bea et al., 2006). These phases are commonly stable under low-degree melting conditions, such as water-saturation melting and muscovite dehydration melting. Therefore, the trapped accessory minerals are difficult to touch the melt to reach an equilibrium.

In conclusion, caution must be taken when using the Sr-Nd-Hf isotopes of low-temperature melt was produced by water-saturated and muscovite dehydration melting to fingerprint the source. The isotopic signatures of high-temperature melt (e.g., the temperature beyond water-saturated and muscovite-dehydration melting) might inherit the isotopic composition of the source more faithfully. It was evidenced by the Nd-Hf isotopic difference between A-type and S-type granite. The Nd-Hf isotopes of S-type granite are deviated from the terrestrial Nd-Hf isotope array compared with A-type granite (Zhang et al., 2020).

The Sr-Nd-Hf disequilibrium revealed by this study has broad implications for the petrogenesis of Himalayan leucogranite. The Himalayan leucogranite might have evolved from a high-temperature magma, which decomposed the biotite, and liberated the accessory minerals to ultimate equilibrium with the melt. The analyzed Sr-Nd-Hf isotopes of leucogranite in the Nyalam present a relatively uniform composition (**Figures 5**, **6**). The $^{87}Sr/^{86}Sr_i$, $εNd_{(t)}$, and $εHf_{(t)}$ of leucogranite do not change with the decreasing crystallization temperature (**Figure 7**). In addition, the $^{87}Sr/^{86}Sr_i$, $εNd_{(t)}$, and $εHf_{(t)}$ of Nyalam leucogranite do not change with the decrease of Sr, P_2O_5, and Zr, indicating that fractional crystallization influences leucogranite composition. The result is consistent with the conclusion of Yang et al. (2019) that the Himalayan leucogranite is the magma produced in the deeper Himalayan orogenic root during peak metamorphism. Subsequently, extensive fractional crystallization occurred through the upward migration of magma along the STDS during the GHC exhumation.

6 CONCLUSION

1) The U-Pb ages of inherited zircon core and Rb-Sr errorchron of the leucosome record an early Paleozoic tectono-thermal

event. Sr-Nd-Hf isotopic homogenization of the leucosome has not been attained during the Himalayan metamorphism.

2) The Sr-Nd-Hf isotopes of the leucosome have a wide range of variations and deviate from the GHC metasediments. During muscovite dehydration melting, preferred consumption of muscovite relative to plagioclase contributed to more radiogenic Sr isotopic compositions in the leucosome, whereas preferable dissolution of apatite and inhibit dissolution of monazite and zircon controlled the less radiogenic Nd-Hf isotopic compositions in the leucosome.
3) The Sr-Nd-Hf isotopic disequilibrium commonly appears in low-temperature partial melting of metasediments. The increase in melting temperature can prompt an isotopic equilibrium between the melt and source.

DATA AVAILABILITY STATEMENT

The original contributions presented in the study are included in the article/**Supplementary Material**, further inquiries can be directed to the corresponding author.

AUTHOR CONTRIBUTIONS

F-YW designed the project. LY, J-MW, X-CL, and F-YW did the fieldwork and collected samples. LY, J-MW, and XL carried out the whole rock Sr-Nd-Hf isotopes analysis. GK carried out the zircon U-Pb dating. All the authors discussed the results and edited the manuscript.

FUNDING

This project received funding from the National Science Foundation of China (Grant number is 41972065, 41888101, and 41772058), the Second comprehensive scientific investigation into Qinghai-Tibet Plateau (Grant number is 2019QZKK0802), and State Key Laboratory of Lithospheric Evolution (E152510201).

ACKNOWLEDGMENTS

We are grateful to Dr. Chao Wang and two anonymous reviewers for their detailed and comprehensive reviews, which improve the quality of the paper significantly.

SUPPLEMENTARY MATERIAL

The Supplementary Material for this article can be found online at: https://www.frontiersin.org/articles/10.3389/feart.2022.891960/full#supplementary-material

REFERENCES

Acosta-Vigil, A., London, D., Morgan, G. B., Cesare, B., Buick, I., Hermann, J., et al. (2017). Primary Crustal Melt Compositions: Insights into the Controls, Mechanisms and Timing of Generation from Kinetics Experiments and Melt Inclusions. *Lithos* 286-287, 454–479. doi:10.1016/j.lithos.2017.05.020

Ayres, M., and Harris, N. (1997). REE Fractionation and Nd-Isotope Disequilibrium during Crustal Anatexis: Constraints from Himalayan Leucogranites. *Chem. Geology.* 139, 249–269. doi:10.1016/S0009-2541(97)00038-7

Bea, F., Montero, P., and Ortega, M. (2006). A LA-ICP-Ms Evaluation of Zr Reservoirs in Common Crustal Rocks: Implications for Zr and Hf Geochemistry, and Zircon-Forming Processes. *Can. Mineral.* 44, 693–714. doi:10.2113/gscanmin.44.3.693

Bea, F., Pereira, M. D., and Stroh, A. (1994). Mineral/leucosome Trace-Element Partitioning in a Peraluminous Migmatite (A Laser Ablation-ICP-MS Study). *Chem. Geology.* 117, 291–312. doi:10.1016/0009-2541(94)90133-3

Brown, C. R., Yakymchuk, C., Brown, M., Fanning, C. M., Korhonen, F. J., Piccoli, P. M., et al. (2016). From Source to Sink: Petrogenesis of Cretaceous Anatectic Granites from the Fosdick Migmatite-Granite Complex, West Antarctica. *J. Pet.* 57, 1241–1278. doi:10.1093/petrology/egw039

Burchfiel, B. C., Zhiliang, C., Hodges, K. V., Yuping, L., Royden, L. H., Changrong, D., et al. (1992). The South Tibetan Detachment System, Himalayan Orogen: Extension Contemporaneous with and Parallel to Shortening in a Collisional Mountain Belt. *Geol. Soc. Am. Spe. Pap.* 269, 1–41. doi:10.1130/SPE269-p1

Cawood, P. A., Johnson, M. R. W., and Nemchin, A. A. (2007). Early Palaeozoic Orogenesis along the Indian Margin of Gondwana: Tectonic Response to Gondwana Assembly. *Earth Planet. Sci. Lett.* 255, 70–84. doi:10.1016/j.epsl.2006.12.006

Chappell, B. W. (1996). Magma Mixing and the Production of Compositional Variation within Granite Suites: Evidence from the Granites of Southeastern Australia. *J. Pet.* 37, 449–470. doi:10.1016/j.epsl.2006.12.00610.1093/petrology/37.3.449

Cherniak, D. J., and Watson, E. B. (1994). A Study of Strontium Diffusion in Plagioclase Using Rutherford Backscattering Spectroscopy. *Geochimica et Cosmochimica Acta* 58, 5179–5190. doi:10.1016/0016-7037(94)90303-410.1016/0016-7037(94)90303-4

Clemens, J. D., Elburg, M. A., and Harris, C. (2017). Origins of Igneous Microgranular Enclaves in Granites: the Example of Central Victoria, Australia. *Contrib. Mineral. Petrol.* 172, 1–27. doi:10.1007/s00410-017-1409-2

DeCelles, P. G., Gehrels, G. E., Quade, J., LaReau, B., and Spurlin, M. (2000). Tectonic Implications of U-Pb Zircon Ages of the Himalayan Orogenic belt in nepal. *Science* 288, 497–499. doi:10.1126/science.288.5465.497

Deniel, C., Vidal, P., Fernandez, A., Le Fort, P., and Peucat, J.-J. (1987). Isotopic Study of the Manaslu Granite (Himalaya, Nepal): Inferences on the Age and Source of Himalayan Leucogranites. *Contr. Mineral. Petrol.* 96, 78–92. doi:10.1007/BF00375529

DePaolo, D. J. (1981). Trace Element and Isotopic Effects of Combined Wallrock Assimilation and Fractional Crystallization. *Earth Planet. Sci. Lett.* 53, 189–202. doi:10.1016/0012-821X(81)90153-9

Farina, F., Stevens, G., Gerdes, A., and Frei, D. (2014). Small-scale Hf Isotopic Variability in the Peninsula Pluton (South Africa): the Processes that Control Inheritance of Source 176Hf/177Hf Diversity in S-type Granites. *Contrib. Mineral. Petrol.* 168, 1065. doi:10.1007/s00410-014-1065-8

Faure, G., and Mensing, T. M. (2005). *Isotopes : Principles and Applications*. Hoboken, NJ: wiley.

Gao, L.-E., Zeng, L., Hu, G., Wang, Y., Wang, Q., Guo, C., et al. (2019). Early Paleozoic Magmatism along the Northern Margin of East Gondwana. *Lithos* 334-335, 25–41. doi:10.1016/j.lithos.2019.03.007

Gao, P., Yakymchuk, C., Zhang, J., Yin, C., Qian, J., and Li, Y. (2021). Preferential Dissolution of Uranium-Rich Zircon Can Bias the Hafnium Isotope Compositions of Granites. *Geology* 50, 336–340. doi:10.1130/G49656.1

Griffin, W. L., Powell, W. J., Pearson, N. J., and O'Reilly, S. Y. (2008). "Glitter: Data Reduction Software for Laser Ablation Icp-Ms," in *Laser Ablation-ICP-MS in the Earth Sciences: Current Practices and Outstanding Issues*. Editor P. J. Sylvester (Mineralogical Association of Canada: Quebec City, QC), 308–311.

Hammerli, J., Kemp, A. I. S., and Spandler, C. (2014). Neodymium Isotope Equilibration during Crustal Metamorphism Revealed by *In Situ* Microanalysis of REE-Rich Accessory Minerals. *Earth Planet. Sci. Lett.* 392, 133–142. doi:10.1016/j.epsl.2014.02.018

Harris, N., and Ayres, M. (1998). The Implications of Sr-Isotope Disequilibrium for Rates of Prograde Metamorphism and Melt Extraction in Anatectic Terrains. *Geol. Soc. Lond. Spec. Publications* 138, 171–182. doi:10.1144/GSL.SP.1996.138.01.10

Harris, N. B. W., and Inger, S. (1992). Trace Element Modelling of Pelite-Derived Granites. *Contr. Mineral. Petrol.* 110, 46–56. doi:10.1007/BF00310881

Inger, S., and Harris, N. (1993). Geochemical Constraints on Leucogranite Magmatism in the Langtang Valley, Nepal Himalaya. *J. Pet.* 34, 345–368. doi:10.1093/petrology/34.2.345

Ji, M., Gao, X.-Y., and Zheng, Y.-F. (2022). Geochemical Evidence for Partial Melting of Progressively Varied Crustal Sources for Leucogranites during the Oligocene-Miocene in the Himalayan Orogen. *Chem. Geology.* 589, 120674. doi:10.1016/j.chemgeo.2021.120674

Ji, W.-Q., Wu, F.-Y., Wang, J.-M., Liu, X.-C., Liu, Z.-C., Zhang, Z., et al. (2020). Early Evolution of Himalayan Orogenic belt and Generation of Middle Eocene Magmatism: Constraint from Haweng Granodiorite Porphyry in the Tethyan Himalaya. *Front. Earth Sci.* 8, 236. doi:10.3389/feart.2020.00236

Kapp, P., and DeCelles, P. G. (2019). Mesozoic-Cenozoic Geological Evolution of the Himalayan-Tibetan Orogen and Working Tectonic Hypotheses. *Am. J. Sci.* 319, 159–254. doi:10.2475/03.2019.01

Knesel, K. M., and Davidson, J. P. (2002). Insights into Collisional Magmatism from Isotopic Fingerprints of Melting Reactions. *Science* 296, 2206–2208. doi:10.1126/science.1070622

Leloup, P. H., Liu, X., Mahéo, G., Paquette, J.-L., Arnaud, N., Aubray, A., et al. (2015). New Constraints on the Timing of Partial Melting and Deformation along the Nyalam Section (central Himalaya): Implications for Extrusion Models. *Geol. Soc. Lond. Spec. Publications* 412, 131–175. doi:10.1144/SP412.11

Linnemann, U., Gerdes, A., Hofmann, M., and Marko, L. (2014). The Cadomian Orogen: Neoproterozoic to Early Cambrian Crustal Growth and Orogenic Zoning along the Periphery of the West African Craton-Constraints from U-Pb Zircon Ages and Hf Isotopes (Schwarzburg Antiform, Germany). *Precambrian Res.* 244, 236–278. doi:10.1016/j.precamres.2013.08.007

Montel, J.-M. (1993). A Model for Monazite/melt Equilibrium and Application to the Generation of Granitic Magmas. *Chem. Geology.* 110, 127–146. doi:10.1016/0009-2541(93)90250-M

Myrow, P. M., Thompson, K. R., Hughes, N. C., Paulsen, T. S., Sell, B. K., and Parcha, S. K. (2006). Cambrian Stratigraphy and Depositional History of the Northern Indian Himalaya, Spiti Valley, north-central India. *Geol. Soc. America Bull.* 118, 491–510. doi:10.1130/B25828.1

Najman, Y., Appel, E., Boudagher-Fadel, M., Bown, P., Carter, A., Garzanti, E., et al. (2010). Timing of India-Asia Collision: Geological, Biostratigraphic, and Palaeomagnetic Constraints. *J. Geophys. Res.* 115, B12. doi:10.1029/2010JB007673

Palin, R. M., Treloar, P. J., Searle, M. P., Wald, T., White, R. W., and Mertz-Kraus, R. (2018). U-pb Monazite Ages from the Pakistan Himalaya Record Pre-himalayan Ordovician Orogeny and Permian continental Breakup. *Geol. Soc. Am. Bull.* 130, 2047–2061. doi:10.1130/B31943.1

Parrish, R. R., and Hodges, V. (1996). Isotopic Constraints on the Age and Provenance of the Lesser and Greater Himalayan Sequences, Nepalese Himalaya. *Geol. Soc. Am. Bull.* 108, 904–911. doi:10.1130/0016-7606(1996)108<0904:icotaa>2.3.co;2

Patino Douce, A. E., and Harris, N. (1998). Experimental Constraints on Himalayan Anatexis. *J. Pet.* 39, 689–710. doi:10.1093/petroj/39.4.689

Rapp, R. P., Ryerson, F. J., and Miller, C. F. (1987). Experimental Evidence Bearing on the Stability of Monazite during Crustal Anaatexis. *Geophys. Res. Lett.* 14, 307–310. doi:10.1029/GL014i003p00307

Robinson, D. M., DeCelles, P. G., Patchett, P. J., and Garzione, C. N. (2001). The Kinematic Evolution of the Nepalese Himalaya Interpreted from Nd Isotopes. *Earth Planet. Sci. Lett.* 192, 507–521. doi:10.1016/S0012-821X(01)00451-4

Rudnick, R. L., and Gao, S. (2003). "Composition of the continental Crust," in *Treatise on Geochemistry*. Editor R. L. Rudnick (Amsterdam: Elsevier), 3, 1–64. doi:10.1016/b0-08-043751-6/03016-4

Spencer, C. J., Dyck, B., Mottram, C. M., Roberts, N. M. W., Yao, W.-H., and Martin, E. L. (2019). Deconvolving the Pre-himalayan Indian Margin - Tales of Crustal Growth and Destruction. *Geosci. Front.* 10, 863–872. doi:10.1016/j.gsf.2018.02.007

Tang, M., Wang, X.-L., Shu, X.-J., Wang, D., Yang, T., and Gopon, P. (2014). Hafnium Isotopic Heterogeneity in Zircons from Granitic Rocks: Geochemical Evaluation and Modeling of "Zircon Effect" in Crustal Anatexis. *Earth Planet. Sci. Lett.* 389, 188–199. doi:10.1016/j.epsl.2013.12.036

Taylor, J., Nicoli, G., Stevens, G., Frei, D., and Moyen, J.-F. (2014). The Processes that Control Leucosome Compositions in Metasedimentary Granulites: Perspectives from the Southern Marginal Zone Migmatites, Limpopo Belt, South Africa. *J. Meta. Geol.* 32, 713–742. doi:10.1111/jmg.12087

Vervoort, J. D., Plank, T., and Prytulak, J. (2011). The Hf-Nd Isotopic Composition of marine Sediments. *Geochimica et Cosmochimica Acta* 75, 5903–5926. doi:10.1016/j.gca.2011.07.046

Wang, J.-M., Wu, F.-Y., Rubatto, D., Liu, S.-R., Zhang, J.-J., Liu, X.-C., et al. (2017). Monazite Behaviour during Isothermal Decompression in Pelitic Granulites: a Case Study from Dinggye, Tibetan Himalaya. *Contrib. Mineral. Petrol.* 172, 1–30. doi:10.1007/s00410-017-1400-y

Wang, J.-M., Zhang, J.-J., Liu, K., Zhang, B., Wang, X.-X., Rai, S., et al. (2016). Spatial and Temporal Evolution of Tectonometamorphic Discontinuities in the central Himalaya: Constraints from P-T Paths and Geochronology. *Tectonophysics* 679, 41–60. doi:10.1016/j.tecto.2016.04.035

Wang, J. M., Zhang, J. J., and Wang, X. X. (2013). Structural Kinematics, Metamorphic P-T Profiles and Zircon Geochronology across the Greater Himalayan Crystalline Complex in South-central Tibet: Implication for a Revised Channel Flow. *J. Meta. Geol.* 31, 607–628. doi:10.1111/jmg.12036

Wang, J., Zhang, J., Wei, C., Rai, S., Wang, M., and Qian, J. (2015). Characterising the Metamorphic Discontinuity across the Main Central Thrust Zone of Eastern-central Nepal. *J. Asian Earth Sci.* 101, 83–100. doi:10.1016/j.jseaes.2015.01.027

Wang, X., Zhang, J., Santosh, M., Liu, J., Yan, S., and Guo, L. (2012). Andean-type Orogeny in the Himalayas of South Tibet: Implications for Early Paleozoic Tectonics along the Indian Margin of Gondwana. *Lithos* 154, 248–262. doi:10.1016/j.lithos.2012.07.011

Watson, E. B., and Harrison, T. M. (1983). Zircon Saturation Revisited: Temperature and Composition Effects in a Variety of Crustal Magma Types. *Earth Planet. Sci. Lett.* 64, 295–304. doi:10.1016/0012-821X(83)90211-X

Weinberg, R. F. (2016). Himalayan Leucogranites and Migmatites: Nature, Timing and Duration of Anatexis. *J. Metamorph. Geol.* 34, 821–843. doi:10.1111/jmg.12204

Weis, D., Kieffer, B., Hanano, D., Nobre Silva, I., Barling, J., Pretorius, W., et al. (2007). Hf Isotope Compositions of U.S. Geological Survey Reference Materials. *Geochem. Geophys. Geosyst.* 8, a–n. doi:10.1029/2006GC001473

Weis, D., Kieffer, B., Maerschalk, C., Barling, J., De Jong, J., Williams, G. A., et al. (2006). High-precision Isotopic Characterization of USGS Reference Materials by TIMS and MC-ICP-MS. *Geochem. Geophys. Geosyst.* 7, a–n. doi:10.1029/2006GC001283

Whitney, D. L., and Evans, B. W. (2010). Abbreviations for Names of Rock-Forming Minerals. *Am. Mineral.* 95, 185–187. doi:10.2138/am.2010.3371

Wolf, M., Romer, R. L., and Glodny, J. (2019). Isotope Disequilibrium during Partial Melting of Metasedimentary Rocks. *Geochimica et Cosmochimica Acta* 257, 163–183. doi:10.1016/j.gca.2019.05.008

Wu, F.-Y., Ji, W.-Q., Wang, J.-G., Liu, C.-Z., Chung, S.-L., and Clift, P. D. (2014). Zircon U-Pb and Hf Isotopic Constraints on the Onset Time of India-Asia Collision. *Am. J. Sci.* 314, 548–579. doi:10.2475/02.2014.04

Wu, F.-Y., Liu, X.-C., Liu, Z.-C., Wang, R.-C., Xie, L., Wang, J.-M., et al. (2020). Highly Fractionated Himalayan Leucogranites and Associated Rare-Metal Mineralization. *Lithos* 352-353, 105319. doi:10.1016/j.lithos.2019.105319

Xia, Q.-X., Chen, Y.-X., Chen, R.-X., and Zheng, Y.-F. (2022). Elevation of Zircon Hf Isotope Ratios during Crustal Anatexis: Evidence from Migmatites Close to the Eastern Himalayan Syntaxis in southeastern Tibet. *Lithos* 412-413, 106592. doi:10.1016/j.lithos.2022.106592

Xie, L., Zhang, Y., Zhang, H., Sun, J., and Wu, F. (2008). *In Situ* simultaneous Determination of Trace Elements, U-Pb and Lu-Hf Isotopes in Zircon and Baddeleyite. *Sci. Bull.* 53, 1565–1573. doi:10.1007/s11434-008-0086-y

Yang, L., Liu, X.-C., Wang, J.-M., and Wu, F.-Y. (2019). Is Himalayan Leucogranite a Product by *In Situ* Partial Melting of the Greater Himalayan Crystalline? A Comparative Study of Leucosome and Leucogranite from Nyalam, Southern Tibet. *Lithos* 342-343, 542–556. doi:10.1016/j.lithos.2019.06.007

Zeng, L., Asimow, P. D., and Saleeby, J. B. (2005). Coupling of Anatectic Reactions and Dissolution of Accessory Phases and the Sr and Nd Isotope Systematics of Anatectic Melts from a Metasedimentary Source. *Geochimica et Cosmochimica Acta* 69, 3671–3682. doi:10.1016/j.gca.2005.02.035

Zhang, C., Liu, D., Zhang, X., Spencer, C., Tang, M., Zeng, J., et al. (2020). Hafnium Isotopic Disequilibrium during Sediment Melting and Assimilations. *Geochem. Persp. Let.* 12, 34–39. doi:10.7185/geochemlet.2001

Conflict of Interest: The authors declare that the research was conducted in the absence of any commercial or financial relationships that could be construed as a potential conflict of interest.

frontiers | Frontiers in Earth Science

ORIGINAL RESEARCH
published: 10 May 2022
doi: 10.3389/feart.2022.892787

Formation of an Intracontinental Orogen Above the Permo-Triassic Mantle Convection Cell in the Paleo-Tethys Tectonic Realm due to Far-Field Stress Derived From Continental Margins

Lei Zhao[1]*, *Mingguo Zhai*[1] and *Xiwen Zhou*[2]

[1]State Key Laboratory of Lithospheric Evolution, Institute of Geology and Geophysics, Chinese Academy of Science, Beijing, China, [2]Institute of Geology, Chinese Academy of Geological Sciences, Beijing, China

OPEN ACCESS

Edited by:
Tatsuki Tsujimori,
Tohoku University, Japan

Reviewed by:
Akira Ishiwatari,
Nuclear Regulation Authority, Japan
Daniel Pastor-Galán,
Tohoku University, Japan

***Correspondence:**
Lei Zhao
zhaolei@mail.iggcas.ac.cn

Specialty section:
This article was submitted to Geochemistry,
a section of the journal
Frontiers in Earth Science

Received: *09 March 2022*
Accepted: *20 April 2022*
Published: *10 May 2022*

Citation:
Zhao L, Zhai M and Zhou X (2022) Formation of an Intracontinental Orogen Above the Permo-Triassic Mantle Convection Cell in the Paleo-Tethys Tectonic Realm due to Far-Field Stress Derived From Continental Margins.
Front. Earth Sci. 10:892787.
doi: 10.3389/feart.2022.892787

The identification of intraplate orogens seemingly poses challenges to the plate tectonic theory. Delineating the formation processes of intraplate orogens can provide clues for the better understandings of the above issue. Although still controversial, the Indosinian (Permo-Triassic) orogeny in the South China Block (SCB) is potentially a good example of intracontinental orogen. In this paper, we carry out studies on the Indosinian high-grade rocks in the northeastern Cathaysia Block of the SCB, hoping to cast light on the features and formation processes of intraplate orogenic belts. These rocks exhibit HP/HT granulite facies mineral assemblages and reaction textures imply that they witnessed eclogite-facies metamorphism. Their clockwise P-T trajectories with isothermal decompression stages suggest significant crustal thickening followed by quick orogenic collapse. Immobile whole-rock trace elements indicate basaltic protoliths features, resembling E-MORB and OIB, respectively. SIMS zircon U-Pb age dating confirms Indosinian metamorphic ages of ~248 Ma and a protolith age of ~953 Ma. The mantle-like O isotopic compositions of the Neoproterozoic magmatic zircon cores further attest that they were primarily mantle derived rocks. The whole-rock Sm-Nd isotopic compositions show more enriched features because of metamorphic alteration, while zircon Lu-Hf isotopic results show primitive characteristics with Neoproterozoic model ages. These features suggest that the high-grade mafic rocks, as well as the metamorphosed early Precambrian metasedimentary rocks hosting them, are all continental crust components and juvenile oceanic crust components featuring plate margins are absent during the SCB Indosinian orogeny. Characteristics of these high-grade rocks and their spatial occurrences are both consistent with the proposal of an intracontinental orogen. After summarizations and comparisons of the Indosinian plate margin activities around the SCB, we suggest that this northeast-southwest trending orogenic belt is geometrically consistent with two mantle convection cells, with one conveying the SCB northward to collide with the North China Craton, and the other conveying the Paleo-Pacific plate northwestwards to form an active continental margin along the southeast SCB. The driving mechanism of the formation of the SCB Indosinian intracontinental orogenic belt could have broad implications for other intraplate orogens around the world.

Keywords: retrograded eclogite, granulite, intraplate orogeny, far-field stress, south China block

INTRODUCTION

The identification of intraplate orogenic belts in different parts of the world posed a challenge to the theory of plate tectonics because according to the theory, compressive stresses concentrate at plate margins where different plates interact while the interior regions of plates are rigid and hard to deform. The intraplate orogens refer to those formed at large distances from active plate boundaries, with driving forces from both plate-boundary and intraplate stress sources (Raimondo et al., 2014). Several examples of intraplate orogens have been proposed and studied in different parts of the world, like central Asia and central Australia (Sandiford and Hand, 1998; Yin et al., 1998; Hand and Sandiford, 1999; Sandiford et al., 2001). Intraplate orogens might also occur in oceanic plates, but examples are difficult to find due to their inaccessibility. Albeit these good examples, the occurrences of large-scale compressional intraplate orogens are relatively rare, especially in the Phanerozoic during which modern plate tectonics dominate geological processes. The Permo-Triassic deformation in the South China Block has long been termed as the Indosinian Movement in the Chinese literature (Cui and Li, 1983; Huang, 1984; Ren, 1984; Wang et al., 2013a; Zhang et al., 2013), and is potentially another good example of intraplate orogenic belt, although different opinions exist (Hsü et al., 1988; Gupta et al., 1989; Rowley et al., 1989; Hsü et al., 1990; Faure et al., 2018; Lin et al., 2018; Shu et al., 2018).

Researchers who proposed the intracontinental setting for the SCB Indosinian orogen believe that the SCB gained and retained its integrity ever since Neoproterozoic, and besides, they found that this orogeny caused mainly thin-skinned tectonics involving reactivation of only ancient continental components (Chen et al., 1991; Li, 1998; Li and Li, 2007; Shu et al., 2008b; Li S. et al., 2012; Shu, 2012; Faure et al., 2016a; Faure et al., 2016b). On the contrary, other researchers suggested a plate margin setting for this orogenic belt (Guo et al., 1984; Hsü et al., 1988; Zhao et al., 1996; Yin et al., 1999; Lin et al., 2018). Hsü et al. (1988) proposed that the SCB Indosinian orogeny was the result of continental collisions between the Yangtze and Cathaysia Blocks, based mainly on the inference that the Banxi Group (mainly in the Jiangnan belt) is a tectonic mélange that accommodated significant crustal shortening through long-distance thrusting. However, other tectonic observations, as well as isotopic ages which show that the Banxi Group represents the Precambrian basement of the SCB, contradict this continental collisional model (Gupta et al., 1989; Rowley et al., 1989; Chen et al., 1991). Due to the lack of high-grade metamorphism, tectonic models like multiple-terrane accretion and soft-collision have also been proposed for the SCB Indosinian orogeny (Guo et al., 1984; Yin et al., 1999). Lin et al. (2018) suggested an Appalachian-style multi-terrane Wilson cycle model for the SCB, in which they argued that the Indosinian orogen was the result of continental collisions between the East and West Cathaysia Blocks. Even though criticisms exist (Faure et al., 2018; Shu et al., 2018), the Triassic high-grade metamorphic rocks, including retrograded eclogites and granulites in the northern Wuyi terrane of the Cathaysia Block, as well as their clockwise P-T trajectories, seem reminiscent those of continental margin orogenic belts (Zhao L. et al., 2017; Xia et al., 2021).

Continental crust, no matter intraplate or proximal to plate margins, will experience crust shortening, thickening, uplifting and exhumation of high-grade metamorphic rocks after accommodating strain (Raimondo et al., 2014). High-grade metamorphism, therefore, can be unhelpful in discriminating intraplate and plate margin orogenic belts. The occurrences of ophiolitic mélange, however, can directly demarcate plate boundaries. Besides, protolith features of high-grade metamorphic rocks and the spatial distributions of orogenic high-grade metamorphic rocks can also provide clues for the discriminating of an orogenic belt. In this paper, we present new studies on the Indosinian high-grade rocks in the northern Wuyi terrane of the Cathaysia Block which represent the uplifted orogenic core components. Based on this new data and a summarization of Indosinian orogenic events around the SCB, we proposed a new interpretation of the SCB Indosinian orogeny and the related deep geodynamic processes for its formation.

GEOLOGICAL BACKGROUND

The SCB situated in the southeastern Eurasia continent is now demarcated by the Central China Orogenic belt in the north from the North China Craton and facing the Tibetan Plateau in the west, the Pacific plate in the east and south (**Figure 1**). Such a triangular region is believed to receive stress from all directions since at least Mesozoic (Li S. et al., 2012), generating the current geometry of the SCB. This continental block is normally believed to have gained its integrity since Neoproterozoic through the amalgamation of the Yangtze and Cathaysia Blocks Li et al., 2009a; Wang X.-L. et al., 2014; Wang Y. et al., 2014; (Li L. et al., 2016; Zhao G. et al., 2018; Zhao J.-H. et al., 2018; Shu et al., 2019). This continental collisional event resulted in the formation of the Jiangnan belt hosting a great amount of the Neoproterozoic sequences of the SCB (Li et al., 2009a; Wang X.-L. et al., 2014; Wang Y. et al., 2014; Li L. et al., 2016; Zhao J.-H. et al., 2018; Shu et al., 2019). Two other episodes of tectonothermal events during Phanerozoic besides the Indosinian orogeny occurred in the SCB, termed as the South China Caledonian orogeny (Paleozoic) and the Yanshanian (Jura-Cretaceous) orogeny in the Chinese literature.

The SCB Caledonian orogeny affected many of the pre-Devonian sequences of the SCB and caused the unconformity

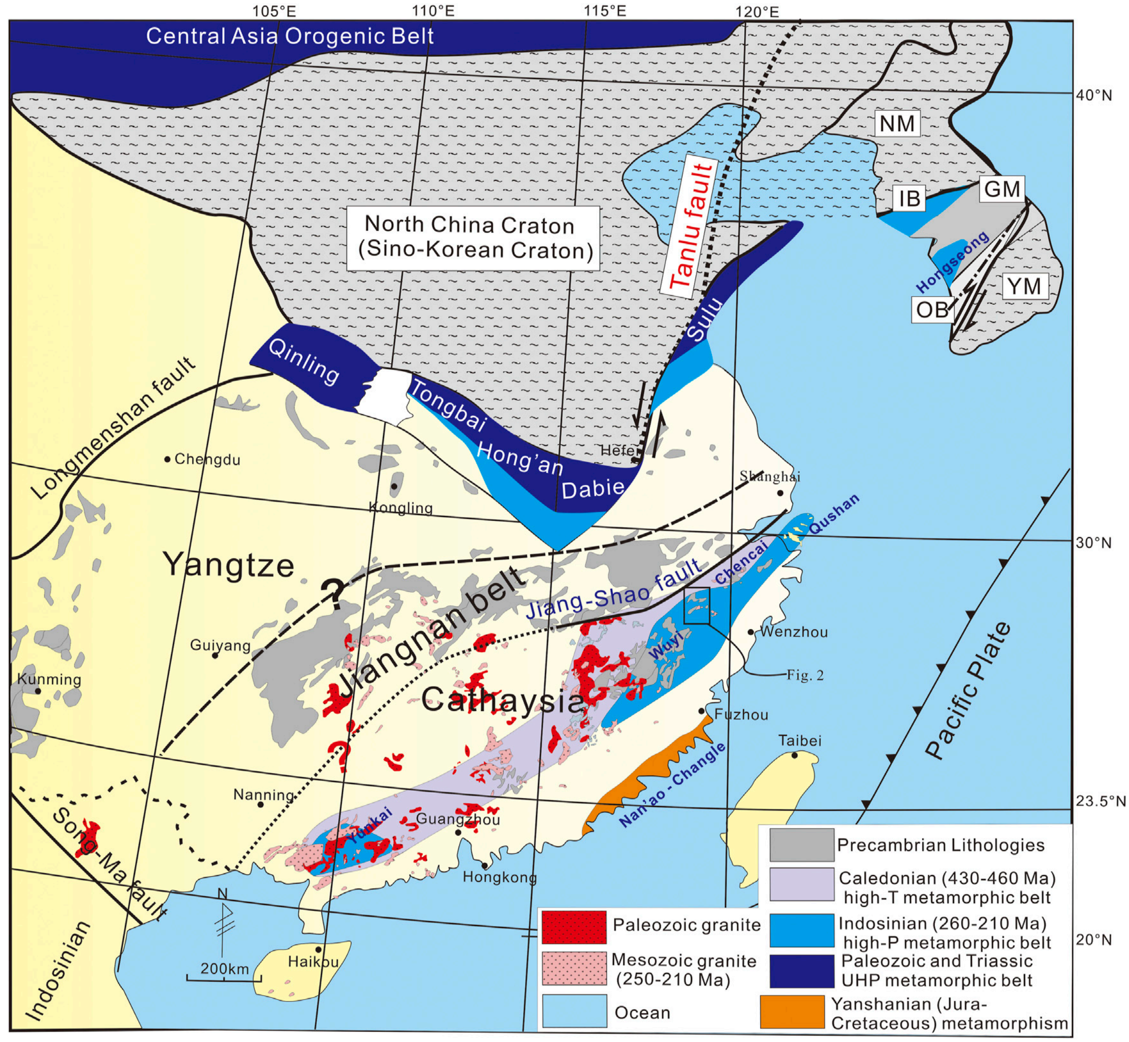

FIGURE 1 | Simplified geological map showing major parts of the east Eurasia continent, with emphasize of the SCB. NM- Nangrim Massif; IB- Imjingang Belt; GM- Gyeonggi Massif; OB- Okcheon Belt; YM- Yeongnam Massif. The map is modified after Oh and Kim (2021), Zhai et al. (2016) and Zhao et al. (2019., 2020).

between the Devonian sequences and the pre-Devonian metamorphic crystalline basement (Chen X. et al., 2012, Chen et al., 2014; Li J. et al., 2016; Wang Y. et al., 2012, Wang et al., 2013a; Zhang et al., 2013; Shu, 2012). Lines of evidence from lithofacies and biofacies suggested that the Paleozoic orogeny was initiated in the southeastern SCB and stepwisely developed toward the northwest direction (Chen X. et al., 2012; Chen et al., 2014). Paleozoic high-grade metamorphism and crustal anatexis widely occur in regions along the Jiangshan-Shaoxing (Jiang-Shao) fault (**Figure 1**, Yu et al., 2003, Yu et al., 2005; Zeng et al., 2008; Zhao et al., 2016, Zhao et al., 2019, Zhao et al., 2020), usually interpreted to be the uplifted orogenic root sequences of the South China Caledonian orogenic belt (Hsü, 1989). Geochronological studies of the Paleozoic metamorphism and anatexis constrain the duration of this event to be between ~460 Ma and 410 Ma, with most metamorphic ages from granulite-facies rocks peaking at ~450 Ma and ~430 Ma (Yu et al., 2003, 2005; Zeng et al., 2008; Zhao et al., 2016; Zhao et al., 2019; Zhao et al., 2020). The metamorphic signatures of the SCB Yanshanian orogeny are mainly preserved along the southeastern coastal regions, represented by extensive migmatitic rocks (**Figure 1**, Liu Q. et al., 2012; Xing et al., 2010, Xing et al., 2014).

The Indosinian orogeny affected large areas of the SCB, but the related high-grade metamorphic signatures occur mainly in the Wuyi terrane of the northeastern Cathaysia Block and are sandwiched by the Caledonian and Yanshanian high-grade metamorphic regions (**Figure 1**). Earlier studies of the Wuyi terrane emphasized mainly the antiquity of the Precambrian sequences (Li, 1997; Yang and Jiang, 2019; Yu et al., 2007, Yu et al., 2009, Yu et al., 2010; Zhao et al., 2014), because they are the critical lithologies that can potentially solve the long-lasting controversy about whether the Cathaysia Block contains “Oldland” (ancient crystalline basement, Grabau, 1924; Hu and Ye, 2006; Lu, 2006; Yu et al., 2006). Besides

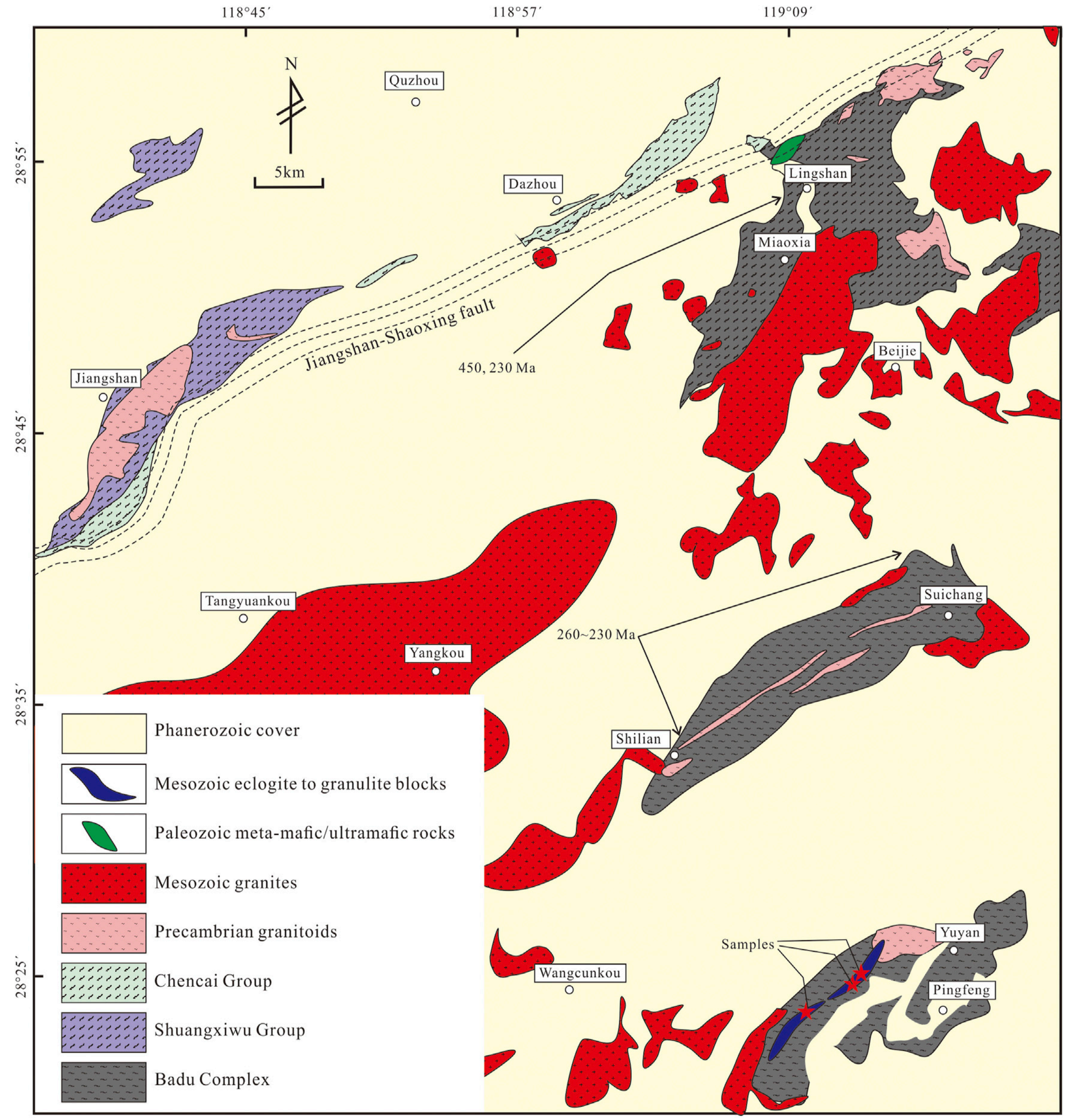

FIGURE 2 | Detailed geological map of the study area showing relations with the Jiang-Shao fault. Right to the south of the fault, both Caledonian and Indosinian metamorphism can be seen. Modified after (Zhejiang GBMR, 1980).

the early Precambrian ages (mainly ~1900–1800 Ma), the Indosinian metamorphic ages are widely identified from these lithologies in these early studies, ranging from 260 Ma to 230 Ma (Xiang et al., 2008; Yu et al., 2009, 2012; Zhao et al., 2014, 2015; Chen et al., 1998). These early Precambrian lithologies have been defined as the Badu and Mayuan complexes and were not found in other parts of the Cathaysia Block (**Figure 1**). Supracrustal sequences, as well as Paleoproterozoic granitoids of these two lithological units, also show Paleoproterozoic metamorphic alterations at ~1.85 Ga, interpreted to be related to the supercontinent Columbia (Yu et al., 2009; Xia et al., 2012; Yu et al., 2012; Zhao et al., 2014). Lin et al. (2018), as mentioned earlier, suggested that the Indosinian metamorphic ages represent the time of a continental collisional event between the East and West Cathaysia.

The Indosinian retrograded eclogites and mafic granulites of the SCB were found to occur mainly in the Wuyi terrane and they are entrained lenticular blocks within the metamorphosed supracrustal rocks of the Badu Complex, which occur to the south of the Jiang-Shao fault (**Figure 2**, Zhao L. et al., 2017; Zhao L. et al., 2018). Rocks of this lithological unit occurring close to the fault exhibit both Paleozoic (~450 Ma) and Indosinian metamorphism (Chen et al., 2015; Zhao et al., 2015; Wang JG. et al., 2014). Rocks occurring further south, like those Paleoproterozoic supracrustal rocks and granitoids

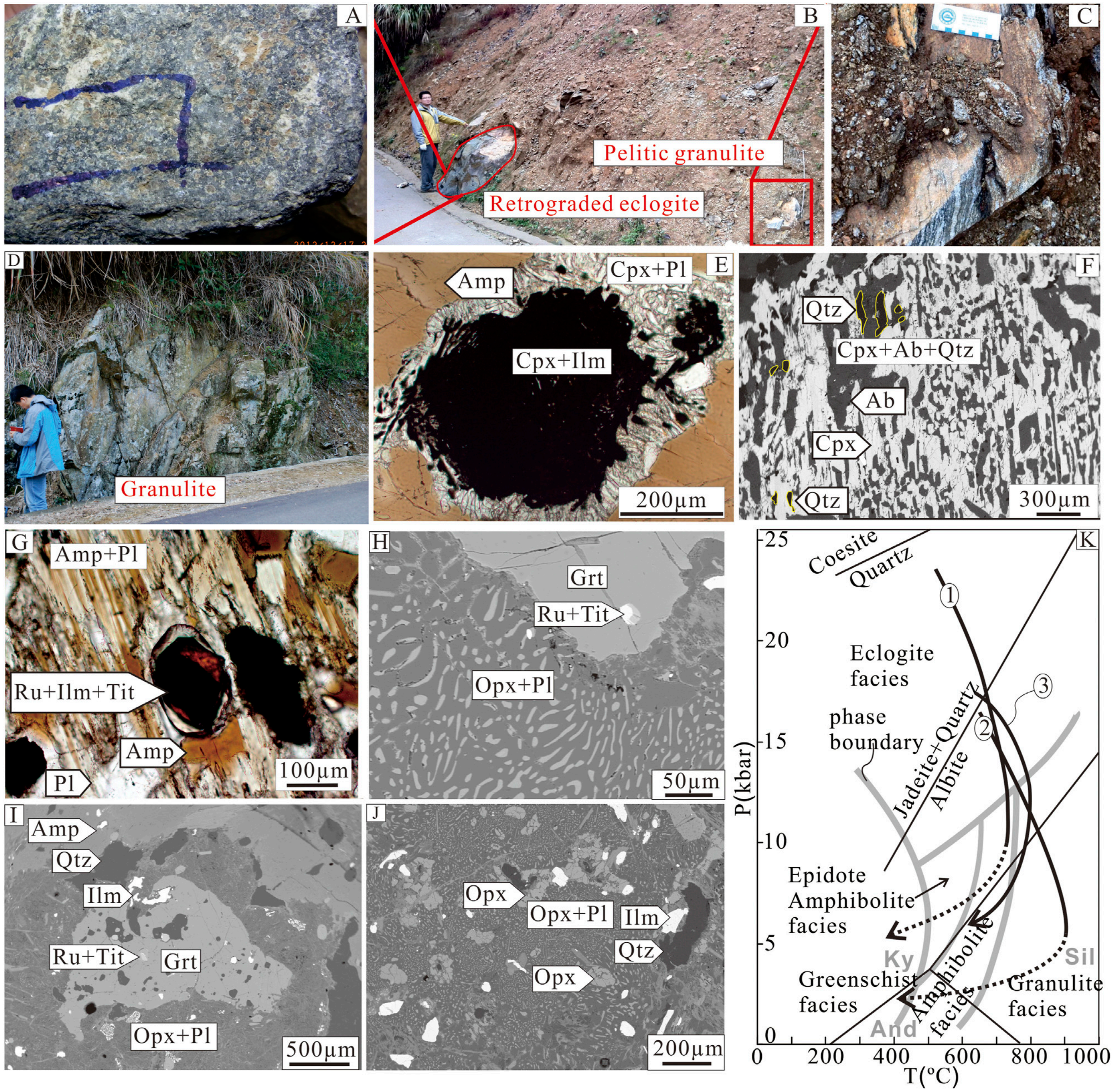

FIGURE 3 | Field photographs **(A–D)**, photomicrographs **(E–J)** showing field occurrences, representative mineral assemblages and reaction textures, and P-T trajectories of the Indosinian high-grade rocks in the Wuyi terrane of the Cathaysia Blocks. Field and micrographic photos are from Zhao L. et al. (2018) and Zhao L. et al. (2017). Numbers in **(K)**, 1 and 2 are P-T trajectories for retrograded eclogite and mafic granulite samples, respectively (from Zhao L. et al., 2017); 3 is P-T trajectory for retrograded eclogite presented by Xia et al. (2021). Mineral abbreviates, Amp, amphibole; Cpx, clinopyroxene; Pl, plagioclase; Ilm, ilmenite; Qtz, quartz; Ab, albite; Ru, rutile; Tit, titanite; Grt, garnet; Opx, orthopyroxene.

in the Suichang-Shilian area, show Indosinian high-grade metamorphism and the Caledonian overprinting is absent (Yu et al., 2012; Zhao et al., 2014). Permo-Triassic (254 Ma, 232–215 Ma) syenites and A-type granites interpreted to represent post-orogenic extensional setting have also been reported from this area within the Indosinian metamorphic belt defined in **Figure 1** (Wang Q. et al., 2005; Sun et al., 2011; Li W. et al., 2012; Sun et al., 2017).

SAMPLES

In order to get a better understanding of the protolith features as well as the driving mechanism of the Indosinian orogenic processes in the SCB, the retrograded eclogite and mafic granulite samples occurring in the Wuyi terrane of the Cathaysia Block were collected and studied in this paper, including five retrograded eclogite samples, and five mafic granulite samples (**Supplementary Table S1**). The metamorphism of these rocks has been presented in a previous paper (Zhao L. et al., 2017). The retrograded eclogite occurs as entrained lenticular blocks within the pelitic granulites of the Badu Complex, whose sizes ranging from tens of centimeters to several meters (**Figure 3**). The long axes of the retrograded eclogite blocks are always parallel with the foliations of the hosting pelitic granulite gneiss. The mafic granulites occur either as deformed dykes or lenticular bodies with varying dimensions hosted by the pelitic granulite gneisses of the Badu Complex (**Figure 3D**).

Mineral assemblages of the retrograded eclogite samples are garnet + plagioclase ± clinopyroxene + amphibole + biotite + quartz and some accessary minerals like ilmenite, rutile, titanite and zircon (**Supplementary Table S1**; **Figures 3E–G**). Two of the retrograded eclogite samples (WY10-1, and -2) experienced stronger metamorphic retrogression whose clinopyroxene grains have been replaced by amphibole. Except for these two samples, clinopyroxene grains are present in all other samples and garnet grains in all the samples develop symplectites composed of fine-grained minerals of clinopyroxene + plagioclase, indicating isothermal decompressions during metamorphism (Zhao L. et al., 2017). Diagnostic eclogite facies mineral of omphacite is absent in all the retrograded eclogite samples, but symplectites of omphacite grains can be seen. The intergrowth of clinopyroxene and albite (**Figure 3F**) imply that they were replacement products of omphacite grains formed through retrograde decompressional metamorphism (Zhao L. et al., 2017). Another petrographic sign implying eclogite facies metamorphism is the absence of plagioclase grains in the matrix. All the observed plagioclase grains occur within the symplectites, either as intergrowths together with clinopyroxene replacing omphacite, or around garnet grains together with clinopyroxene or orthopyroxene or amphibole replacing garnet (**Figures 3E–G**). High-pressure facies minerals like rutile, intergrowth of clinopyroxene and ilmenite can also be seen (**Figures 3E,G**).

The mineral assemblages of the mafic granulite samples are garnet + plagioclase + orthopyroxene + amphibole + biotite + quartz and some accessary minerals like rutile, ilmenite, titanite and zircon (**Supplementary Table S1**). The mafic granulite samples can be further divided into two groups according to their consisting minerals. Compared with group A granulite samples, the two granulite samples in group B contain very few quartz grains and more garnet and amphibole grains. But the mineral assemblages and typical reaction textures of them are the same. The absence of plagioclase in the matrix implies that the mafic granulites might have also experienced eclogite facies metamorphism. Decompressional symplectitic textures can be observed around most garnet grains and they are mainly composed of fine-grained orthopyroxene + plagioclase, and occasionally fine-grained amphibole + plagioclase intergrowths (**Figures 3H–J**).

Previous metamorphic studies on these two kinds of rocks revealed clockwise P-T trajectories and Indosinian metamorphic ages of 251–245 Ma (**Figure 3K**, Zhao L. et al., 2017). Retrograded eclogite samples record metamorphic pressure peak conditions of 500–560°C, 23–24 kbar and these for the granulite samples are 600–720°C, >13 kbar (**Figure 3K**, Zhao L. et al., 2017). High-grade metamorphic rocks with similar metamorphic conditions and P-T trajectories have also been reported from the neighboring regions (Jiang et al., 2016; Xia et al., 2021). The metamorphic conditions of these rocks imply significant crustal thickening (doubled) based on a simple evaluation using lithostatic stresses. Therefore, there might be an orogenic plateau in this region during the Indosinian orogeny. In combination, the spatial occurrences of these Indosinian high-grade rocks define the northeast-southwest striking direction of the Indosinian orogenic belt of the Cathaysia Block, likely representing the uplifted orogenic core (**Figure 1**).

ANALYTICAL TECHNIQUES

Most of the experiments of this study were carried out at the State Key Laboratory of Lithospheric Evolution of the Institute of Geology and Geophysics, Chinese Academy of Sciences (IGGCAS), except for the zircon CL images. The X-ray fluorescence (Shimadzu XRF-1700/1500) was used for major element analyses, after fusion of the samples with lithium tetraborate. After baking the samples for 1 h under a constant temperature at 1000°C, the loss-on-ignition (LOI) was measured as the weight loss of the samples. The Chinese national standard sample GBW07101-07114 is used for corrections. The precision of the results is better than 0.2 wt%. Trace element analyses were performed using an ELEMENT ICP-MS after HNO_3 + HF digestion of about 40 mg sample powder for each specimen in a Teflon vessel. The Chinese national standard samples GSR1 (granite) and GSR3 (basalt) were used during analyses for accuracy and reproducibility. The relative standard deviation was better than 5% above the detection limits.

After crushing the samples, standard heavy-liquid and magnetic techniques were used in zircon grain separation and then the grains were handpicked under a binocular microscope. The zircon grains, together with zircon standards (see detailed descriptions below), were then cast in epoxy discs, and then were ground and polished to expose mid-sections of the grains for CL imaging, U-Pb dating, O (oxygen) and Lu-Hf isotope analyses. The internal zoning of zircons was examined using a CL detector (Garton Mono CL3+) equipped on a Quanta 200F ESEM with 2-min scanning time at conditions of 15 kV and 120 nA at the Peking University.

The zircon oxygen isotope was analyzed using the CAMECA IMS 1280 SIMS. Detailed analytical procedures were described by Li et al. (2010c). The Intensity of ^{16}O was typically no less than 1×10^9 counts per second (cps). The instrumental mass fractionation factor (IMF) is corrected using zircon standard Penglai with a $\delta^{18}O$ (VSMOW) value of 5.3 ± 0.1‰ (2σ) (Li et al., 2010c). The standard data were collected regularly throughout the analytical session as the IMF drifted with time. The Qinghu zircon standard was measured as an unknown and yielded a standard deviation of 0.3 per mil (2σ), which is used for least uncertainty for individual analysis. Uncertainty on individual analysis is usually better than 0.2–0.3‰ (2σ).

SIMS zircon U-Pb dating was conducted using another CAMECA IMS 1280 SIMS. Detailed analytical procedures can be found in Li et al. (2010b) and Li et al. (2009b). During analysis, the O_2^- primary ion beam was accelerated at 13 kv. The ellipsoidal spot size is about 20 × 30 μm. Zircon standard Plešovice, with the age of 337 Ma (Sláma et al., 2008), was used to calibrate the measured Pb/U ratios. A long-term uncertainty of 1.5% (1RSD) for $^{206}Pb/^{238}U$ measurements of the Plešovice standard was propagated to the unknowns, despite that the measured $^{206}Pb/^{238}U$ error in a specific session is generally around 1% (1RSD) or less (Li et al., 2010c). The Pb isotopic compositions of each spot were corrected for common Pb using non-radiogenic ^{204}Pb. An average present-day crustal Pb composition (Stacey and Kramers, 1975) was used for common Pb assuming that the common Pb was largely due to surface contamination introduced during sample preparation. The data were processed using the ISOPLOT program (Ludwig, 2012). The analyzed standard Qinghu zircon as unknown gave a weighted mean $^{206}Pb/^{238}U$ age of 159.9 ± 1.9 Ma (MSWD = 0.87), consistent with the recommended $^{206}Pb/^{238}U$ age of 159.9 ± 0.2 Ma (2 SE) (Li et al., 2009b).

Zircon Hf isotope analyses were carried out using a Neptune MC-ICPMS. The spot size of 40 or 60 μm was applied during ablation with a 193 nm laser, using a repetition rate of 10 Hz in most cases. Detailed descriptions of the instrument and analytical procedures are similar to those in Wu et al. (2006). Two zircon standards, GJ and Mud Tank, whose Hf isotope compositions have been proven to be quite uniform (Woodhead and Hergt, 2005; Zeh et al., 2007; Xie et al., 2008), were used to monitor the stability of the instrument during analyses. In the analytical sessions reported here, the weighted $^{176}Hf/^{177}Hf$ (c) value of GJ is 0.2820035 ± 0.0000041, and the weighted $^{176}Hf/^{177}Hf$ (c) of the Mud tank is 0.282495 ± 0.000005, which, after considering the analytical errors, are consistent with the values recommended previously (Woodhead and Hergt, 2005; Zeh et al., 2007; Xie et al., 2008). Model ages (T_{DM}(Hf)) and $\varepsilon_{Hf}(t)$ of zircon grains were calculated based on depleted mantle and chondrite sources. The value of $^{176}Hf/^{177}Hf$ and $^{176}Lu/^{177}Hf$ of modeled depleted mantle are 0.28325 and 0.0384 (Griffin et al., 2002) and for chondrite 0.282772 and 0.0332, respectively (Blichert Toft and Albarede, 1997). The decay constant of ^{176}Lu adopted in this paper is 1.867 × 10^{-11}per year (Söderlund et al., 2004).

Detailed descriptions of instruments involved and analytical procedures for whole-rock Sm-Nd isotopic analyses are presented in Li C.-f. et al. (2011)), Li et al. (2011 C.-F.) and Yang et al. (2010). Very fine-grained whole-rock powders for Nd isotopic analyses were dissolved in Savillex Teflon screw-top capsules after being spiked with mixed ^{149}Sm-^{150}Nd tracers before HF + HNO_3+$HClO_4$ dissolution. For Sm and Nd separation, we used the classical two-step ion-exchange chromatographic method. The samples were then measured using a Finnigan MAT262 multi-collector thermal ionization mass spectrometer. The blank during the whole procedure was lower than 100 pg. The isotopic ratios were corrected for mass fractionation by normalizing to $^{146}Nd/^{144}Nd$ = 0.7219. The international standard, JNdi-1, was employed to evaluate instrument stability during the period of data collection. The measured values for JNdi-1 were $^{143}Nd/^{144}Nd$ = 0.512104 ± 0.000007 (*n* = 3, MSWD = 0.38). USGS reference material BCR-2 was measured to monitor the accuracy of the analytical procedure, and yielded the following result: $^{143}Nd/^{144}Nd$ = 0.512624 ± 0.000012, which is consistent with the suggested value of BCR-2 yielded by TIMS and MC-ICP-MS techniques (Yang et al., 2010; Li C.-f. et al., 2011; Li C.-F. et al., 2011).

ANALYTICAL RESULTS

All the ten samples in **Supplementary Table S1** were analyzed for whole-rock chemical compositions, while six of them were analyzed for whole-rock Sm-Nd isotopic compositions, and only two representative retrograded eclogite samples (WY1215 and WY1216) and one granulite sample (WY11) were chosen for zircon U-Pb, O and Lu-Hf isotopic analyses.

Whole-Rock Geochemistry

Major and trace element concentrations of the analyzed samples are presented in **Supplementary Table S2** and **Figure 4**. The retrograded eclogite samples have SiO_2, Al_2O_3 contents of 47.52–49.35 wt%, 12.25–15.13 wt%, respectively. They plot within the basalt field and sub-alkaline basalt field in TAS and Nb/Y *vs.* Zr/TiO_2*0.0001 diagrams (**Figures 4A,B**). In other diagrams, the retrograded eclogite samples show tholeiitic and E-MORB compositions (**Figures 4C,D**), and they belong to ocean floor basalts (**Figure 4E**). The spider diagram and chondrite normalized REE distribution patterns of the retrograded eclogite samples exhibit similarities with E-MORB (**Figures 4F,H**).

The mafic granulite samples exhibit large variations in major elements, and they plot in picro-basalt—basalt—andesite fields (**Figure 4A**). Group A granulite samples have higher SiO_2, Al_2O_3, and lower MgO, Fe_2O_3T contents compared with samples of Group B, consistent with the above observations that the ferromagnesian mineral contents of Group A granulite samples are lower than those of Group B. In the Nb/Y *vs.* Zr/TiO_2*0.0001 diagram, these samples plot within the sub-alkaline—andesite—dacite fields (**Figure 4B**). The mafic granulite samples are also tholeiitic and belong to ocean floor basalts as shown in discrimination diagrams (**Figures 4C–E**). The spider diagram and chondrite normalized REE distribution patterns of the mafic granulite samples exhibit similarities with OIB (**Figures 4F,H**).

Zircon U-Pb Age Dating

The three high-grade rocks have all been dated in a previous study, using the LA-ICPMS zircon U-Pb method, which gave metamorphic ages of 245–251 Ma, and also a protolith age of 997 ± 27 Ma for the mafic granulite sample (Zhao L. et al., 2017). In this study, zircons of the two retrograded eclogite samples exhibit similar appearance and internal structures (**Figure 5**). The zircon grains are rounded, small ellipsoidal and are multi-faceted. They are unzoned or show fir-tree zoning patterns, implying metamorphic origins (Vavra, 1990). These two retrograded eclogite samples give uniform apparent $^{206}Pb/^{238}U$ ages with

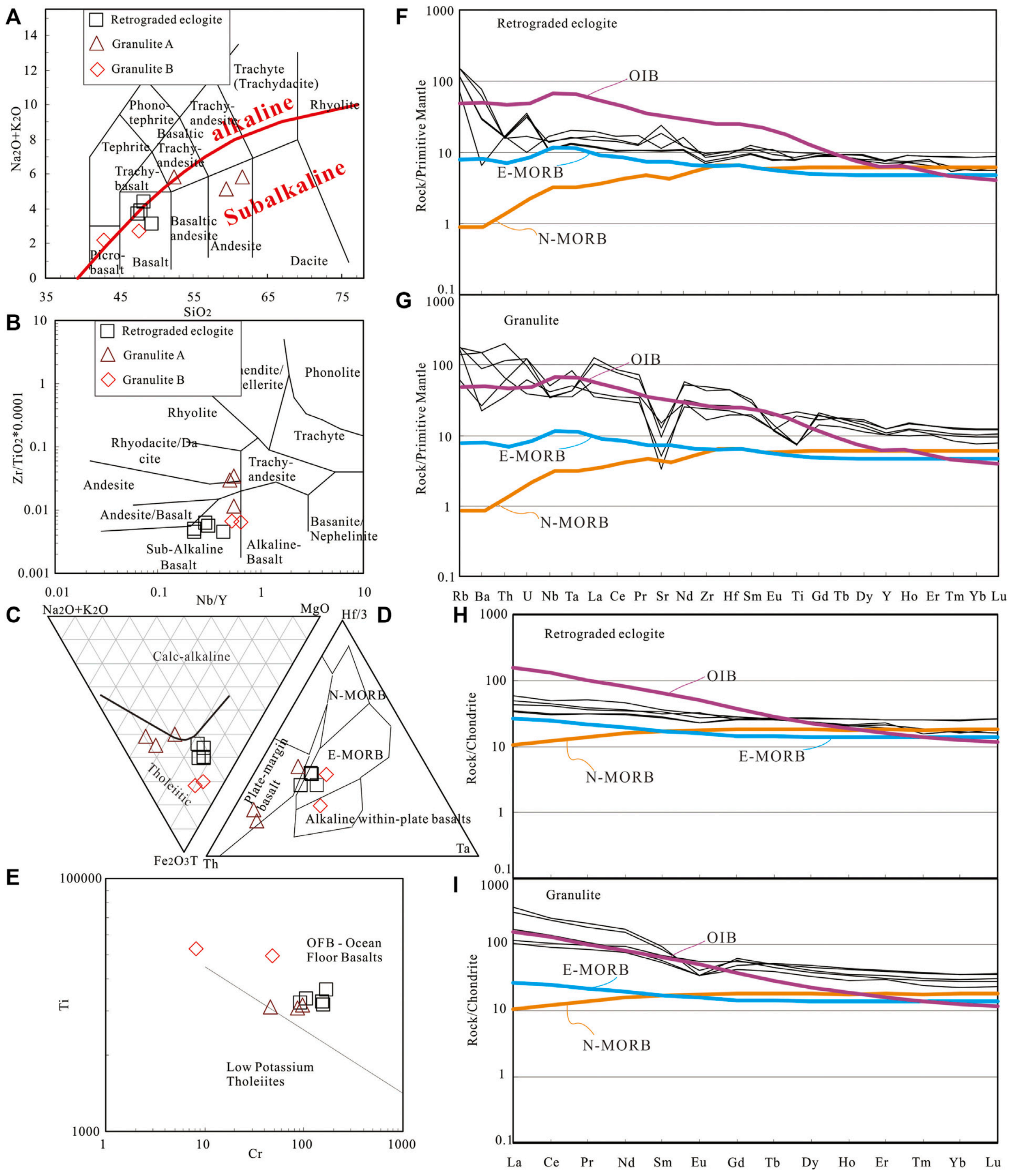

FIGURE 4 | Major and trace element plots of the studied high-grade rocks from the Wuyi terrane of the Cathaysia Block. **(A)** is after Middlemost (1994); **(B)** is after Winchester and Floyd (1977); **(C)** is after Irvine and Baragar (1971); **(D)** is after Wood (1980); **(E)** is after Pearce (1975); Primitive mantle and Chondrite normalization factors, as well as the values for N-MORB, E-MORB and OIB are after Sun and McDonough (1989).

low Th/U ratios and they constrain metamorphic ages of 248–249 Ma (**Figure 5**; **Supplementary Table S3**). Some of the zircon grains of the mafic granulite sample show core-rim structures with cores exhibiting oscillatory zoning while rims without zoning or showing fir-tree zoning (**Figure 5**). The zircon cores that do not show core-rim structures are mostly unzoned or show fir-tree zoning or sector zoning. The analytical results define a Discordia with an upper intercept age at 953 ± 17 Ma and a

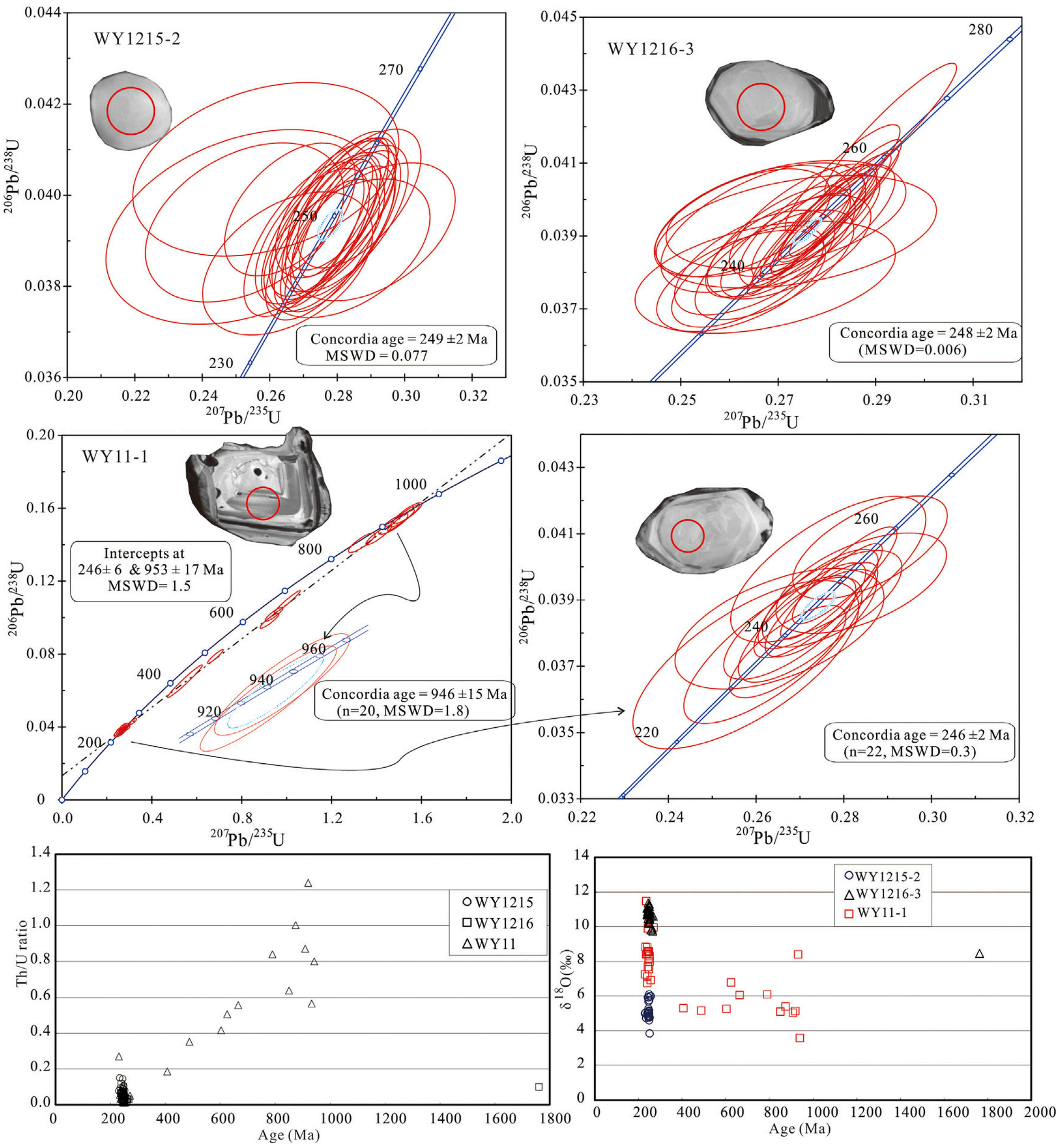

FIGURE 5 | SIMS zircon U-Pb dating results, Th/U ratio *vs*. U-Pb ages plots and zircon O isotopic results of the studies samples.

lower intercept age of 246 ± 6 Ma. The zircon grains with ages of ~246 Ma show uniformly low Th/U ratios while those with older ages have high Th/U ratios (**Figure 5** and **Supplementary Table S3**), which imply their metamorphic and magmatic origins. These results are consistent with previous studies that the high-grade metamorphism occurred during the Early Triassic (Zhao L. et al., 2017; Xia et al., 2021).

Zircon O-Hf Isotopic Compositions

The zircon grains of the two retrograded eclogite samples show significant differences in O isotopic compositions (**Supplementary Table S4** and **Figure 5**). The $\delta^{18}O$ (V-SMOW) values are 3.85–6.08 for zircons from the sample WY1215-2, and 8.46–11.34 for those of the sample WY1216-3. The distinct O isotopic compositions of these metamorphic zircons suggest zircon precipitation from different metamorphic fluids. The $\delta^{18}O$ (V-SMOW) values of zircon cores and rims from the mafic granulite sample show large variations, with cores having low $\delta^{18}O$ values of ~5.5 while rims having high $\delta^{18}O$ values around ~8 (**Supplementary Table S4** and **Figure 5**).

The zircon Hf isotopic compositions of the two retrograded eclogite samples are relatively homogenous, with $^{176}Hf/^{177}Hf$ ratios of 0.282646–0.282521 for WY1215-1 and of 0.281223–0.282806 for WY1216-2 (mostly within the range of 0.282605–0.282798, **Supplementary Table S5**). $\varepsilon_{Hf}(t)$ values are all negative for zircons from the sample WY1215-1 (ranging from −5.9 to −3.4) and mostly positive for zircons from the sample WY1216-2 (ranging

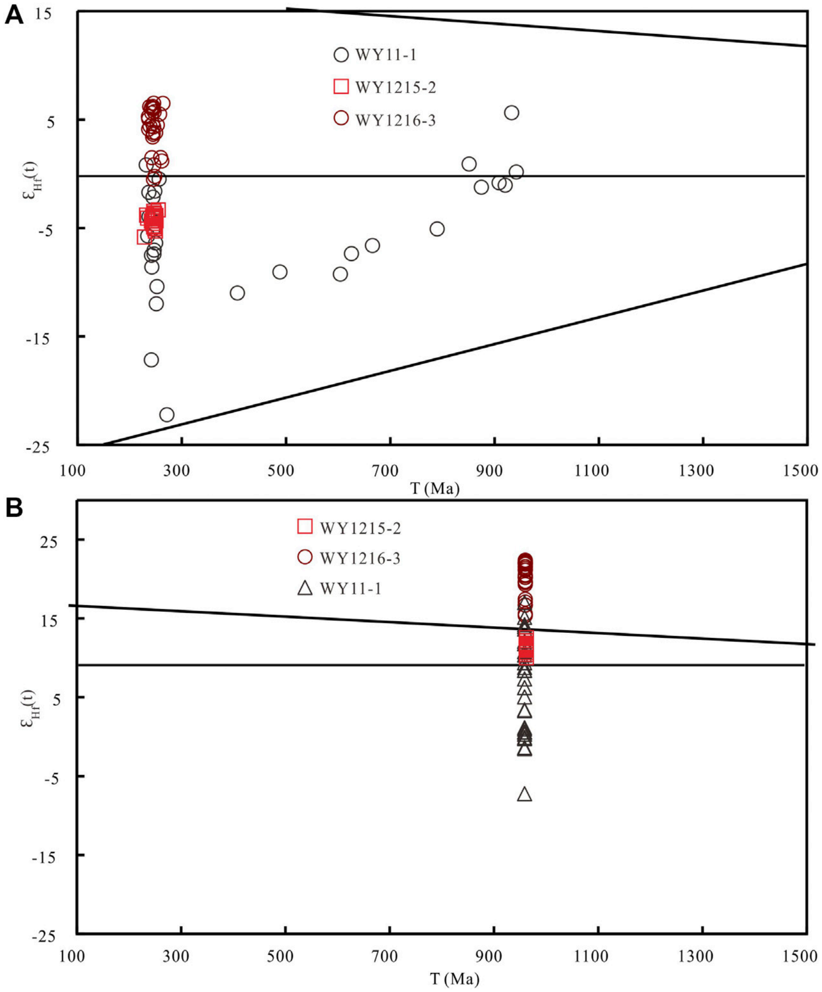

FIGURE 6 | $\varepsilon_{Hf}(t)$ value *vs*. zircon U-Pb age plots of the studied samples.

from −16.1 to +6.6, mostly ranging from 0.9 to 6.6). The single-stage depleted mantle model ages of the sample WY1215-1 are 1011–1088 Ma and 619–2787 Ma (mostly within the range of 619–892 Ma). For the reason that the zircons from the granulite sample exhibit complex internal structures, their Hf isotopic compositions also show large variations, with $^{176}Hf/^{177}Hf$ ratios ranging from 0.281980 to 0.282654 and related $\varepsilon_{Hf}(t)$ values ranging from −22 to +5.6 (**Supplementary Table S5**). The single-stage depleted mantle model ages are 829–1772 Ma. In the zircon U-Pb age *vs.* $\varepsilon_{Hf}(t)$ value diagram, the analyzed results plot above and below the CHUR evolutionary line, based on calculations using apparent zircon U-Pb ages (**Figure 6**). However, if using the protolith age of the mafic granulite (~960 Ma) as the starting age, $\varepsilon_{Hf}(t)$ values of most analyses plot above the CHUR evolutionary line (**Figure 6**).

Whole-Rock Sm-Nd Isotopic Compositions

The six analyzed samples show quite different whole-rock Sm-Nd isotopic compositions (**Supplementary Table S6**). The retrograded eclogite have higher $^{143}Nd/^{144}Nd$ ratios (0.512487–0.512694) than the granulite samples (0.511343–0.512144). The single-stage depleted mantle model ages are mostly Mesoproterozoic for the retrograded eclogite samples (1360–1790 Ma), except one sample with an Archean model age of ~2620 Ma, while those of the mafic granulite samples are older, at 1860–3020 Ma. The $\varepsilon_{Nd}(t)$ values (assuming that the protolith ages are Neoproterozoic based on the protolith age of the mafic granulite, Zhao L. et al., 2017) of the retrograded eclogite samples are positive, ranging from 1.94 to 5.46 while those of the two mafic granulite samples are negative, one at −1.35 and the other at −7.74.

DISCUSSIONS

Indosinian Metamorphism in and Around the SCB

As mentioned earlier, the Indosinian orogeny affected large areas of the SCB. Although previous studies claimed that many of the Neoproterozoic sequences belonging to the Banxi Group

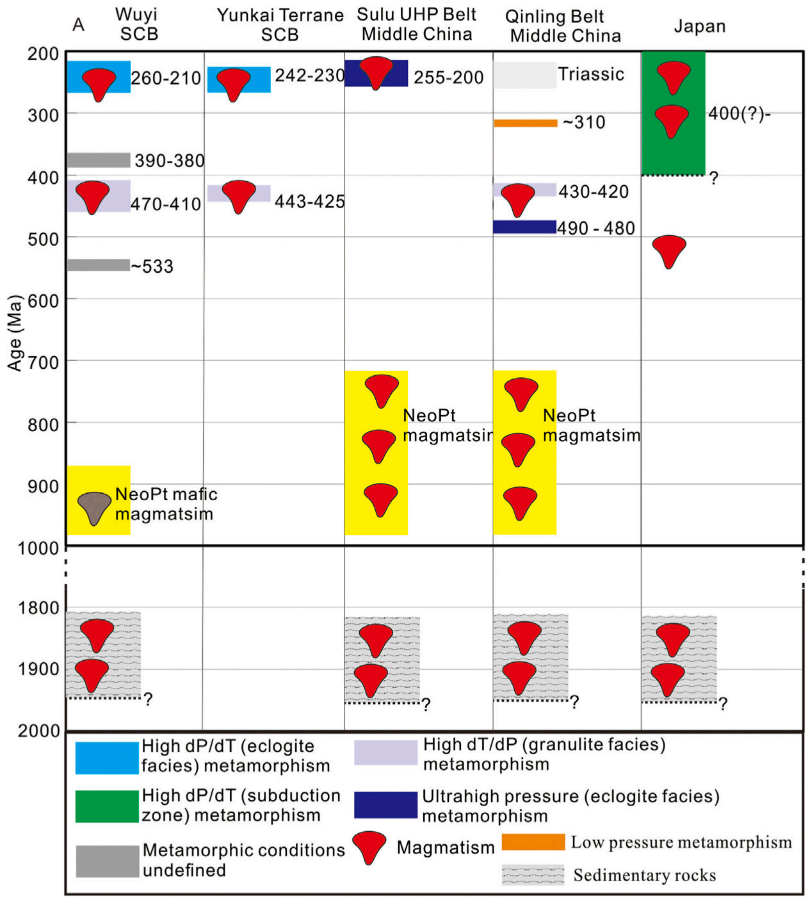

FIGURE 7 | A summarization and comparison of major magmatic, metamorphic and early Precambrian basement rocks in different parts of the orogenic belts in and around the SCB. Related references can be found in the main text.

represent the Precambrian basement of the SCB, Indosinian reworking of these sequences are significant, represented by folding, shearing and long-distance thrusting within the Jiangnan belt (Chu et al., 2012a; Chu et al., 2012b; Chu et al., 2012c; Liu L. et al., 2012; Wang Y. et al., 2005). These deformation features are typical of thin-skinned tectonics, involving only upper crustal components. The occurrences of the high-grade rocks in the northern Wuyi terrane suggest that the orogeny of this region affected deep lower crustal components. The peak pressure conditions of the retrograded eclogite samples indicate the crustal thickness of the northern Wuyi terrane was almost doubled during the orogeny. The decompressional reaction textures and the isothermal (or slow heating) decompressional P-T stage in the P-T trajectories imply that the orogenic belt experienced quick collapse and the high-grade rocks experienced fast uplifting during the late thermal relaxation stage (**Figure 3**, Zhao L. et al., 2017). The metamorphic features of these high-grade rocks are strongly reminiscent of those found in plate margin contractional settings (Brown, 2009; O'Brien, 1993). New SIMS zircon U-Pb dating results confirm the time of metamorphism at 246–249 Ma (**Figure 5**). Indosinian metamorphism has also been reported from the Yunkai terrane in the southwestern Cathaysia Block (**Figures 1**, **7**, Chen C.-H. et al., 2012; Lin et al., 2008; Wan et al., 2010). However, the occurrences of Indosinian metamorphism are not continuous from the Wuyi terrane to the Yunkai terrane, implying that they might not belong to the same Indosinian orogenic belt. Tectonic geometry as well as metamorphic features of the Yunkai terrane exhibit close affinities to the Indosinian tectonothermal events in southwestern SCB and Indochina, which are inconsistent with those of the Wuyi terrane (Lin et al., 2008; Faure et al., 2014; Faure et al., 2016a; Faure et al., 2016b).

The Indosinian high-grade metamorphism in east Eurasia that attracted the most international interests occurs along the Central China Orogenic belt, which is further divided into small segments of the Qinling, Tongbai, Hong'an, Dabie and Sulu (**Figure 1**). This composite orogenic belt records the complete amalgamation history of the two major continental parts of east Eurasia, namely the SCB and the North China Craton, and besides, the identification of ultrahigh-pressure metamorphic minerals like coesite and diamond from eclogites with continental crustal chemical compositions imply deep subduction of the SCB continental crust (Dong et al., 2016; Okay and Celal Şengör,

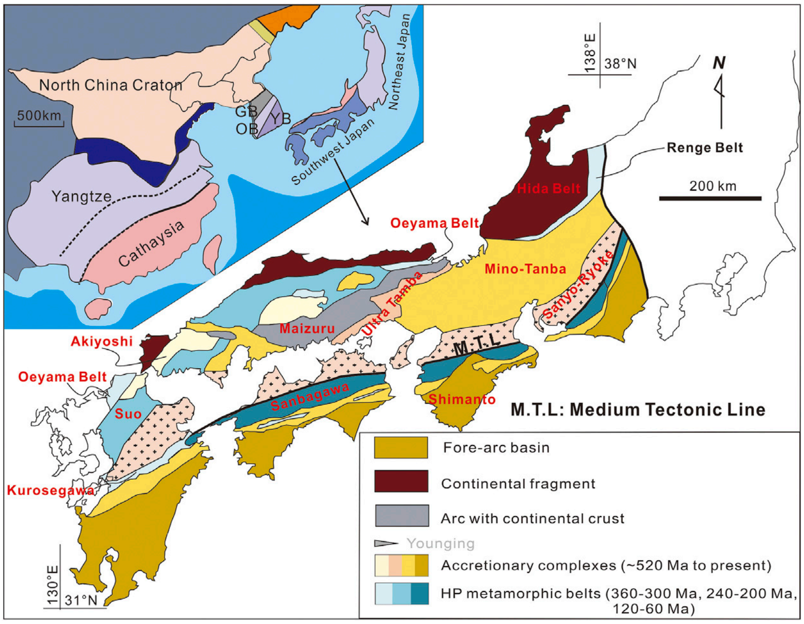

FIGURE 8 | Simplified geological map of major parts of East Asia and Southwest Japan. Modified after Oh and Kim (2021), Tsujimori (2002) and Pastor-Galán et al. (2021).

1992; Wang et al., 1989; Wu and Zheng, 2013; Xu et al., 1992; Zhai et al., 1995; Zhao Z.-F. et al., 2017). Multiple geochronological studies constrain the time of eclogite facies metamorphism of the Sulu and Dabie segments to be at 255–200 Ma, mostly Triassic (**Figure 7**, An et al., 2018; Cheng et al., 2011; Li S. et al., 2017; Liu et al., 2004, Liu et al., 2006; Wu and Zheng, 2013), synchronous with these of the Wuyi terrane. As to the Qinling segment of the Central China Orogenic belt, its high-grade metamorphism occurred mainly during Paleozoic and Triassic overprintings are not very strong (**Figure 7**, Dong et al., 2011). The influence of such an extreme contractional orogen is significant and many of the Indosinian metamorphic events in East Asia have been correlated with this orogenic belt, like those in the Korean Peninsula and Japan (Kwon et al., 2009; Liu, 1993; Oh and Kim, 2021; Ree et al., 1996; Tsujimori, 2002; Ernst et al., 2007). As shown in **Figure 1**, the striking direction of the Sulu segment of the Central China Orogenic belt is parallel with the Indosinian orogenic belt in the Wuyi terrane of the Cathaysia Block, both following northeast-southwest direction. Almost synchronously, the collision between the SCB and the Indochina Peninsula resulted in high-grade metamorphism in southwest SCB and also Indochina (Faure et al., 2014, 2016a, b), whose major tectonic geometry is, however, mainly northwest-southeast (Faure et al., 2016b).

Another important plate that greatly affected the Phanerozoic SCB and which has been overlooked in many previous studies is the one facing its southeastern continental margin, the Paleo-Pacific plate (**Figure 1**). Although still controversial, many geologists suggested the onset of the SCB active continental margin facing the Pacific plate during Mesozoic (Zhou and Li, 2000; Zhou et al., 2006), or during Paleozoic (Li et al., 2006; Li and Li, 2007; Sun et al., 2011). However, pre-Triassic geological records of interactions with the Pacific oceanic plate are now absent in the southeastern SCB continental margin, which is mainly composed of late Mesozoic magmatic rocks (volcanics and intrusive rocks, Shu, 2012; Xu et al., 2007). The Japanese islands, which preserve various geological records of oceanic subduction, accretion, subduction erosion and the formation of the continental crust due to interactions with the Pacific plate, ranging from Paleozoic to Cenozoic, have been suggested to show consanguineous with the SCB (**Figure 8**, Taira, 2001; Wakita, 2013; Pastor-Galán et al., 2021; Isozaki et al., 2010; Wallis et al., 2020). Indeed some of the early Precambrian lithologies in the Hida belt of Southwest Japan show consanguineous with those of the North China Craton as previously suggested (**Figure 8**, Horie et al., 2010; Kawabata et al., 2021; Harada et al., 2021a, 2021b; Kimura et al., 2019), but these sporadically occurred Paleoproterozoic intrusive rocks (~1.85 Ga) as well as the Archean-Paleoproterozoic detrital and/or inherited zircon grains are also comparable to those of the Badu Complex in the Wuyi terrane of the Cathaysia Block (Li et al., 2014; Yu et al., 2009, 2012; Zhao et al., 2015; Isozaki, 2019). Besides, the Paleozoic (~450–410 Ma) and/or Indosinian metamorphic overprintings, as well as the Neoproterozoic lithologies of the Wuyi terrane in northeast Cathaysia Block also provide arguments for a close consanguinity of Japan with the SCB (Zhao et al., 2016, Zhao et al., 2020; Xu et al., 2007; Shu et al., 2008a, Shu et al., 2008b; Horie et al., 2010; Kimura et al., 2019; Harada et al., 2021b). These correlations support the inference that the ancient continental fragments preserved in Japan probably originated from the SCB (Aoki et al., 2015; Isozaki et al., 2010, Isozaki et al., 2014; Tsutsumi et al., 2017; Isozaki, 2019; Pastor-Galán et al., 2021). Besides, the Paleozoic and Mesozoic geological components, like the Paleozoic accretionary complexes, the Mesozoic accretionary complexes, as well as the arc batholiths and ophiolitic mélange in Japan, are quite likely to be the missing continental marginal components of the SCB during the Indosinian orogeny(Isozaki et al., 2010, Isozaki et al., 2014; Isozaki, 2019; Pastor-Galán et al., 2021). Metamorphism of the Japanese islands are mainly low-temperature, high-pressure subduction type and continuous from Paleozoic onwards (**Figure 7**, Ishiwatari and Tsujimori, 2003; Erst et al., 2007; Matsunaga et al., 2021; Takahashi et al., 2018; Tsujimori, 2002; Tsujimori et al., 2006; Tsujimori and Liou, 2004). Alongside with these subduction zone metamorphism, the low (and medium) dP/dT metamorphism can also often be seen (Takahashi et al., 2018), which collectively termed as the 'paired metamorphic belts' (Miyashiro, 1961, 1973). One thing worthy of noticing is the preservation of geological records for an accreted oceanic plateau in Southwest Japan (Tatsumi et al., 2000). These geological records are critical for a better understanding the geological history of the Phanerozoic SCB.

Characteristics of the Protoliths of the High-Grade Rocks

The eclogite and granulite facies mineral assemblages indicate that the studied mafic rocks experienced high-grade metamorphism which might render their whole-rock chemical compositions unreliable, especially the major elements and the fluid-mobile elements like Th, K, etc. The large spread of these samples in **Figure 4A** partly attests to this inference. However, some overall variation trends can still be extracted from the relatively immobile element plots (**Figure 4**), like their sub-alkaline basaltic and tholeiitic compositions. They show close affinities to oceanic crust, with the retrograded eclogite samples resembling E-MORB while the mafic granulite samples resembling OIB. The protoliths of these rocks, therefore, are interpreted to represent the remnants of a disappeared ocean.

Zircon O-Hf isotopic compositions of these metamorphosed mafic rocks exhibit large variations as well, but the magmatic zircon cores preserved in the mafic granulite sample have mantle-like O isotopic signatures (**Figure 5**, Valley et al., 1994). The Neoproterozoic age of 946 Ma constrained by these magmatic zircon cores is interpreted to represent the protolith age of the mafic granulite. Both the zircon Lu-Hf and whole-rock Sm-Nd isotopic compositions of these mafic rocks show large variations. Considering that the hosting rocks of these mafic rocks are the Paleoproterozoic sedimentary rocks of the Badu Complex, any influence from which during high-grade metamorphism will elevate model ages while lowering $\varepsilon(t)$ values for both Lu-Hf and Sm-Nd isotopic systems, the high-grade samples of this study with the youngest single-stage model ages and the highest ε (t) values should be regarded to give the best constraints on the features of these meta-mafic rocks. As described above, the youngest single-stage Hf model ages for both the retrograded eclogite and mafic granulite samples are Neoproterozoic, 619–892 Ma for the retrograded eclogite, and 829—~1000 Ma for the mafic granulite. Whole-rock Sm-Nd isotopic compositions for these high-grade rocks seem to have been disturbed during metamorphism because they exhibit large variations on one hand and on the other hand, the single-stage model ages are Mesoproterozoic to Archean, significantly older than the Hf model ages. The Neoproterozoic protolith ages (990–950 Ma) for these metamorphosed mafic blocks are, therefore, supported by both the magmatic zircon core U-Pb age of the mafic granulite, and the Hf - Nd isotopic compositions.

Previous studies have revealed the occurrences of two episodes of Neoproterozoic magmatism in the Cathaysia Block, one at ~970 Ma and the other at 860–800 Ma (Shu et al., 2008a; Shu et al., 2011; Wang Y. et al., 2014). They have been interpreted to occur in the active continental margin and within plate rifting environments, respectively (Shu et al., 2008a; Shu et al., 2011). If taking the zircon core age of ~950 Ma as the protolith age, the metamorphosed blocks of this study can correlate well with the ~970 Ma magmatism in the Cathaysia Block, representing continental margin components. The protoliths of these metamorphosed mafic blocks, generated during Neoproterozoic, can also be compared with the widespread Neoproterozoic lithologies in the Jiangnan belt (Wang et al., 2013b; Wang Y. et al., 2014; Yao et al., 2014). All these Neoproterozoic magmatic rocks are related to the tectonothermal events that amalgamated the Yangtze and Cathaysia Blocks, and the subsequent rifting (Nanhua Rift) (Li et al., 2009a; Li W. X. et al., 2010; Wang X.-L. et al., 2012). Anyway, the Neoproterozoic magmatic rocks are important components of the continental crust of the SCB during the Indosinian orogeny, rather than newly generated oceanic crustal component (Yu et al., 2008; Shu, 2006, 2012).

Formation of the Indosinian SCB Intraplate Orogenic Belt and Broad International Implications

If based solely on the Indosinian high-grade metamorphism of the Wuyi terrane in northeastern Cathaysia Block, the conclusion of a continental margin orogenic belt can be assigned to the SCB Indosinian orogen, because these metamorphic rocks show identical features with those developed in continental margin orogenic belts (Brown, 2009; O'Brien, 1993). But the geological implications of high-grade metamorphism are not always exclusive and as pointed out by Raimondo et al. (2014), the crustal shortening and thickening, and exhumation high-grade metamorphic rocks from deep crustal levels of intraplate orogens are comparable with their plate-margin counterparts. Therefore, the eclogite and the granulite facies metamorphism such as these of the Wuyi terrane could suggest both intraplate and plate marginal settings.

The spatial occurrence of orogenic metamorphism has been suggested to be a powerful tool in discriminating styles of orogens (Raimondo et al., 2014; Zhai, 2009; Li et al., 2016c, Li et al., 2016d). As summarized by Zhao et al. (2015) and shown in **Figure 1**, the occurrences of the Indosinian high-grade metamorphism are found to occur only in the northeastern Cathaysia Block (Wuyi terrane) and are absent in the Nanling area. In other words, their distribution is not continuous and does

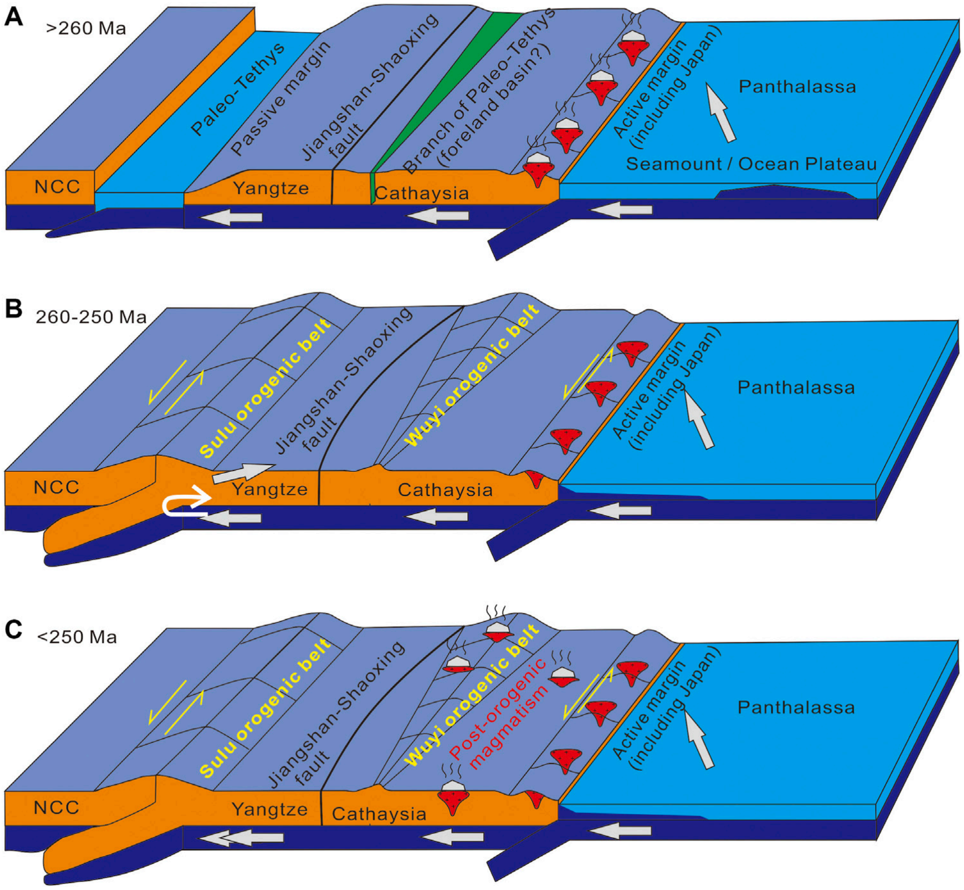

FIGURE 9 | Proposed tectonic evolutionary model for the formation of the Indosinian intraplate orogen in the SCB.

not form a complete belt that can demarcate the continental boundaries. Such a distribution pattern of high-grade metamorphism is inconsistent with those developed in continental marginal settings, but rather indicates an intracontinental setting. Besides the mafic blocks studied in this paper which show continental crust characteristics, other lithologies in the Cathaysia Block exhibiting Indosinian high-grade metamorphic alterations mainly belong to the Paleoproterozoic Badu and Mayuan Complexes of the Wuyi terrane (Yu et al., 2012; Zhao et al., 2015; Zhao L. et al., 2018). The occurrences of all these rocks indicate that the Indosinian orogeny affected only the ancient continental crust components, without the addition of any juvenile components newly generated from mantle which is, however, usually normal for continental marginal orogenic belts due to the consumption of oceanic crust before the final collision (e.g. Jamieson and Beaumont, 2013; Li et al., 2016e; Hou et al., 2021). In summary, although the high-grade rocks in the Wuyi terrane record metamorphism similar to those seen in continental margin settings, they are more likely to have occurred in the intracontinental environment.

The development of intracontinental orogens normally requires the existence of weak lithospheric zones within the continental block (Collins et al., 2011; Raimondo et al., 2014; Sokoutis and Willingshofer, 2011). As mentioned earlier, a Neoproterozoic rifted system termed the Nanhua rift developed in the SCB, as indicated by the wide occurrences of Neoproterozoic magmatism (860–800 Ma) (Shu et al., 2008a, Shu et al., 2011; Li et al., 2005; Wang and Li, 2003; Wang et al., 2007). This rift system is also known to be a failed rift because it aborted soon afterwards and no new ocean was developed. The South China Caledonian orogeny should have solidified most of the failed rift and formed another basin (foreland?) in the Wuyi terrane which behaved as a branch of the Paleo-Tethys Ocean and provided the weak lithospheric zone in the Cathaysia Block (**Figure 9A**). Another critical cause of the intraplate orogen is the driving force. Stress source of orogenic belts, either occurring in the intraplate or plate margin settings, are originally derived from the viscous mantle convections, which operate as conveyors and transport the lithosphere to different places of the Earth, resulting in the formation of convergent and divergent plate margins (Collins, 2003; Collins et al., 2011). The driving forces of intraplate orogens have been more specifically suggested to include far-field stress from plate margins, and intraplate stress largely related to vertical tectonic processes (Raimondo et al., 2014). The geometry of the Indosinian orogen is inconsistent with intraplate stress and implies stress sources from continental margins. The mantle convection cell in the Paleo-Tethys tectonic realm transported the SCB northward (today's orientation), closing the Paleo-Tethys Ocean and forming the Central China Orogenic belt during Permo-Triassic (Collins et al., 2011; Ratschbacher et al., 2003; Wu and Zheng, 2013). The subduction of the paleo-Pacific plate underneath the SCB (including Japan) during the Paleozoic represents another mantle convection cell with a northwestward (today's orientation) conveying direction (**Figure 9A**, Li et al., 2006; Li and Li, 2007). Previous studies on the Indosinian deformation and magmatic activities of the SCB revealed that during ~260–250 Ma, an oceanic plateau arrived at the subduction zone which choked the magmatic arc and besides, the stress, that used to localize on the southeastern continental margin of the SCB, propagated from the continental margin northwestward to inland regions (**Figure 9B**, Li and Li, 2007; Tatsumi et al., 2000). Based on these discussions, we suggest that the far-field stress from the southeast margin of the SCB due to interactions with the paleo-Pacific plate must have facilitated the formation of the SCB Indosinian intraplate orogen. The spatial distribution of the Indosinian high-grade metamorphism in the Cathaysia Block is parallel with the Sulu orogenic belt (**Figure 1**) and the metamorphic ages of the high-grade rocks within these two orogenic belts greatly overlap (**Figure 7**), implying that this segment of the Central China Orogenic belt along the northern margin of the SCB is another stress source for the Indosinian intraplate orogeny of the SCB (**Figure 9B**). This inference is consistent with previous studies which have already proposed that the Indosinian orogeny of the SCB is closely related to the far-field stress from the Central China Orogenic belt (Zhang et al., 2013; Li J. et al., 2017; Wang et al., 2021).

A complete model for the formation of the Indosinian intraplate orogen in the SCB is, therefore, proposed based on the above discussions (**Figure 9**). After the amalgamation of the Yangtze and Cathaysia Blocks during Neoproterozoic, the SCB soon witnessed rifting and formed the Nanhua Rift (Li W. X. et al., 2010; Li et al., 2005; Wang X.-C. et al., 2012, Wang X.-L. et al., 2012). This rift system aborted soon afterwards without the formation of open oceans. During Paleozoic, the South China Caledonian orogeny closed solidified this rift system and likely formed a foreland basin in the Cathaysia Block which remained there until Permo-Triassic (**Figure 9A**, Shu et al., 2008a; Shu et al., 2011), providing the lithospheric weak zone for the intraplate orogenic events. The onset of the active continental margin of the SCB facing the paleo-Pacific (Panthalassa) plate dates back to the Paleozoic and during Permo-Triassic, the arrival of an oceanic plateau at the subduction zone choked the magmatic arc and the stress propagated to the inland regions of the SCB. Almost simultaneously, the collisional events between the SCB and the North China Craton slowed the northward moving of the SCB, providing another retroactive stress source to the SCB (**Figure 9B**). Therefore, stress from both the northwest (Sulu orogenic belt) and southwest (paleo-Pacific) margins during Permo-Triassic acted within the SCB, forming a super-contraction zone in the Wuyi terrane of the northeast Cathaysia Block. The weak lithospheric zone of the Cathaysia Block accommodated the strain and witnessed strong deformation and significant crustal thickening, termed as the Indosinian Wuyi orogenic belt (**Figure 9B**). After the collision of the SCB with the North China Craton, the major driving force for the convergence of these two continental blocks is believed to be the dragging of the eclogitized mafic crust of northern South China (Dong et al., 2013), providing an extensional environment in the Cathaysia Block which resulted in orogenic collapse and the formation of post-orogenic magmatism (**Figure 9C**, Li W. et al., 2012; Sun et al., 2011, Sun et al., 2017). This new model is not only consistent with the geological records in and around the SCB but also has geological implications for interpreting intraplate orogens worldwide.

CONCLUSION

Based on the above descriptions and discussions, the following conclusions can be reached.

1) The occurrences of the Indosinian high-grade metamorphism define the northeast-southwest trending orogenic belt in the Cathaysia Block, southeast SCB, representing the uplifted Indosinian orogenic core components.
2) Whole-rock major and trace element compositions of the high-grade rocks vary significantly, due to metamorphic alterations. The overall trend of their variations constrains the protoliths to be emplaced in plate margin settings, showing E-MORB and OIB compositions by relatively immobile elements.
3) SIMS zircon U-Pb age dating confirm the metamorphic age of 246–249 Ma and an early Neoproterozoic protolith age of 946 Ma. The magmatic zircon cores still preserve mantle-like O isotopic compositions of ~5.5 (δ^{18}O (V-SMOW)). Metamorphic zircons exhibit large variations in O isotopic compositions. Compared with whole-rock Sm-Nd isotopic compositions, zircon Lu-Hf isotopic compositions can better trace the features of the protoliths, confirming their generation during the early Neoproterozoic.
4) The protoliths of these metamorphic rocks were generated during the early Neoproterozoic and were continental crustal components during the Indosinian orogeny. Combined with the spatial distributions of the Indosinian metamorphism in the Cathaysia Block, we suggest that this orogen formed in the intraplate environment.
5) A summarization of Indosinian plate margin activities of the SCB led us to conclude that the driving stress for the formation of the SCB Indosinian orogen in the Wuyi terrane is from both the interactions with the paleo-Pacific plate in the southeast and the North China Craton in the north. In other words, the mantle convection cell that closed the Paleo-Tethys, and the one conveying the paleo-Pacific plate to the SCB continental margin both facilitated the formation of the Indosinian orogen in the Wuyi terrane of the Cathaysia Block. This Indosinian intraplate orogenic belt was primarily a lithospheric weak zone formed during the South China Caledonian orogeny.

DATA AVAILABILITY STATEMENT

The original contributions presented in the study are included in the **Supplementary Material**, further inquiries can be directed to the corresponding author.

AUTHOR CONTRIBUTIONS

LZ carried out all the analyses, processed the data and wrote the manuscript. MZ the leader of the research project, planned the blueprint of the research and provided corrections on the different versions of the manuscript. XZ Initiated the research, funded the field trip and the lab work, and helped preparing the manuscript.

FUNDING

This work was funded by the research programs (Grant Nos. 41872197, 41890832 and 41890834) supported by the National Nature Science Foundation of China and research programs (Grant Nos. DD20201116 and DD20211116) supported by the Chinese Geological Survey.

ACKNOWLEDGMENTS

We are also grateful to Drs. Liu Yu, Tang Guoqiang, Ling Xiao and Prof Yang Yueheng for their help with SIMS zircon U-Pb age dating and O isotopic analysis, as well as zircon Lu-Hf isotopic analyses. Prof. Li Xianhua is greatly thanked for his very helpful discussions.

SUPPLEMENTARY MATERIAL

The Supplementary Material for this article can be found online at: https://www.frontiersin.org/articles/10.3389/feart.2022.892787/full#supplementary-material

Supplementary Table S1 | Information of the studied samples of this study.

Supplementary Table S2 | Whole-rock geochemical compositions of the studied samples.

Supplementary Table S3 | SIMS zircon U-Pb age dating results of the studied samples.

Supplementary Table S4 | SIMS zircon O isotope results of the studied samples.

Supplementary Table S5 | Zircon Lu-Hf isotopic compositions of the studied samples.

Supplementary Table S6 | Whole-rock Sm-Nd isotopic compositions of the studied samples.

REFERENCES

An, S.-C., Li, S.-G., and Liu, Z. (2018). Modification of the Sm-Nd Isotopic System in Garnet Induced by Retrogressive Fluids. *J. Metamorph Geol.* 36, 1039–1048. doi:10.1111/jmg.12426

Aoki, K., Isozaki, Y., Yamamoto, A., Sakata, S., and Hirata, T. (2015). Mid-Paleozoic Arc Granitoids in SW Japan with Neoproterozoic Xenocrysts from South China: New Zircon U-Pb Ages by LA-ICP-MS. *J. Asian Earth Sci.* 97, 125–135. doi:10.1016/j.jseaes.2014.10.018

Blichert-Toft, J., and Albarède, F. (1997). The Lu-Hf Isotope Geochemistry of Chondrites and the Evolution of the Mantle-Crust System. *Earth Planet. Sci. Lett.* 148, 243–258. doi:10.1016/s0012-821x(97)00040-x

Brown, M. (2009). Metamorphic Patterns in Orogenic Systems and the Geological Record. *Geol. Soc.* 318, 37–74. doi:10.1144/sp318.2

Chen, C.-H., Liu, Y.-H., Lee, C.-Y., Xiang, H., and Zhou, H.-W. (2012a). Geochronology of Granulite, Charnockite and Gneiss in the Poly-Metamorphosed Gaozhou Complex (Yunkai Massif), South China: Emphasis on the *In-Situ* EMP Monazite Dating. *Lithos* 144-145, 109–129. doi:10.1016/j.lithos.2012.04.009

Chen, D. F., Li, X. H., Pan, J. M., Dong, W. Q., Chen, G. Q., and Chen, X. P. (1998). Metamorphic Newly Produced Zircons, SHRIMP Ion Microprobe U-Pb Age of Amphibolite of Hexi Group, Zhejiang and its Implications. *Acta Mineral. Sin.* 18, 396–400.

Chen, J., Foland, K. A., Xing, F., Xu, X., and Zhou, T. (1991). Magmatism along the Southeast Margin of the Yangtze Block: Precambrian Collision of the Yangtze and Cathysia Blocks of China. *Geology* 19, 815–818.

Chen, X., Fan, J., Chen, Q., Tang, L., and Hou, X. (2014). Toward a Stepwise Kwangsian Orogeny. *Sci. China Earth Sci.* 57, 379–387. doi:10.1007/s11430-013-4815-y

Chen, X., Tong, L., Zhang, C., Zhu, Q., and Li, Y. (2015). Retrograde Garnet Amphibolite from Eclogite of the Zhejiang Longyou Area: New Evidence of the Caledonian Orogenic Event in the Cathaysia Block. *Chin. Sci. Bull.* 60, 1207–1217. doi:10.1007/s11434-015-0890-0

Chen, X., Zhang, Y., Fan, J., Tang, L., and Sun, H. (2012b). Onset of the Kwangsian Orogeny as Evidenced by Biofacies and Lithofacies. *Sci. China Earth Sci.* 55, 1592–1600. doi:10.1007/s11430-012-4490-4

Cheng, H., Zhang, C., Vervoort, J. D., Wu, Y., Zheng, Y., Zheng, S., et al. (2011). New Lu-Hf Geochronology Constrains the Onset of Continental Subduction in the Dabie Orogen. *Lithos* 121, 41–54. doi:10.1016/j.lithos.2010.10.004

Chu, Y., Faure, M., Lin, W., and Wang, Q. (2012a). Early Mesozoic Tectonics of the South China Block: Insights from the Xuefengshan Intracontinental Orogen. *J. Asian Earth Sci.* 61, 199–220. doi:10.1016/j.jseaes.2012.09.029

Chu, Y., Faure, M., Lin, W., Wang, Q., and Ji, W. (2012b). Tectonics of the Middle Triassic Intracontinental Xuefengshan Belt, South China: New Insights from Structural and Chronological Constraints on the Basal Décollement Zone. *Int. J. Earth Sci. Geol. Rundsch)* 101, 2125–2150. doi:10.1007/s00531-012-0780-5

Chu, Y., Lin, W., Faure, M., Wang, Q., and Ji, W. (2012c). Phanerozoic Tectonothermal Events of the Xuefengshan Belt, Central South China: Implications from UPb Age and LuHf Determinations of Granites. *Lithos* 150, 243–255. doi:10.1016/j.lithos.2012.04.005

Collins, W. J., Belousova, E. A., Kemp, A. I. S., and Murphy, J. B. (2011). Two Contrasting Phanerozoic Orogenic Systems Revealed by Hafnium Isotope Data. *Nat. Geosci.* 4, 333–337. doi:10.1038/ngeo1127

Collins, W. J. (2003). Slab Pull, Mantle Convection, and Pangaean Assembly and Dispersal. *Earth Planet. Sci. Lett.* 205, 225–237. doi:10.1016/s0012-821x(02)01043-9

Cui, S., and Li, J. (1983). On the Indosinian Movement of China's Peri-Pacific Tectonic Belt. *Acta Geol. Sin.* 1, 51–62.

Dong, S., Gao, R., Yin, A., Guo, T., Zhang, Y., Hu, J., et al. (2013). What Drove Continued Continent-Continent Convergence after Ocean Closure? Insights from High-Resolution Seismic-Reflection Profiling across the Daba Shan in Central China. *Geology* 41, 671–674. doi:10.1130/g34161.1

Dong, Y., Safonova, I., and Wang, T. (2016). Tectonic Evolution of the Qinling Orogen and Adjacent Orogenic Belts. *Gondwana Res.* 30, 1–5. doi:10.1016/j.gr.2015.12.001

Dong, Y., Zhang, G., Neubauer, F., Liu, X., Genser, J., and Hauzenberger, C. (2011). Tectonic Evolution of the Qinling Orogen, China: Review and Synthesis. *J. Asian Earth Sci.* 41, 213–237. doi:10.1016/j.jseaes.2011.03.002

Ernst, W. G., Tsujimori, T., Zhang, R., and Liou, J. G. (2007). Permo-Triassic Collision, Subduction-Zone Metamorphism, and Tectonic Exhumation along the East Asian Continental Margin. *Annu. Rev. Earth Planet. Sci.* 35, 73–110. doi:10.1146/annurev.earth.35.031306.140146

Faure, M., Charvet, J., and Chen, Y. (2018). Appalachian-style Multi-Terrane Wilson Cycle Model for the Assembly of South China: COMMENT. *Geology* 46, e446. doi:10.1130/g40222c.1

Faure, M., Lepvrier, C., Nguyen, V. V., Vu, T. V., Lin, W., and Chen, Z. (2014). The South China Block-Indochina Collision: where, when, and How? *J. Asian Earth Sci.* 79, 260–274. doi:10.1016/j.jseaes.2013.09.022

Faure, M., Lin, W., Chu, Y., and Lepvrier, C. (2016a). Triassic Tectonics of the Ailaoshan Belt (SW China): Early Triassic Collision between the South China and Indochina Blocks, and Middle Triassic Intracontinental Shearing. *Tectonophysics* 683, 27–42. doi:10.1016/j.tecto.2016.06.015

Faure, M., Lin, W., Chu, Y., and Lepvrier, C. (2016b). Triassic Tectonics of the Southern Margin of the South China Block. *Comptes Rendus Geosci.* 348, 5–14. doi:10.1016/j.crte.2015.06.012

Grabau, A. (1924). *Stratigraphy of China, Part I, Paleozoic and Older. 1-528.* Peking: Geological Survey and Ministry of Agriculture and Commerce of China.

Griffin, W. L., Wang, X., Jackson, S. E., Pearson, N. J., O'Reilly, S. Y., Xu, X., et al. (2002). Zircon Chemistry and Magma Mixing, SE China: *In-Situ* Analysis of Hf Isotopes, Tonglu and Pingtan Igneous Complexes. *Lithos* 61, 237–269. doi:10.1016/s0024-4937(02)00082-8

Guo, L. Z., Shi, Y. S., Ma, R. S. Y., Shang, F., and Lu, H. F. (1984). Tectonostratigraphic Terranes of Southeast China. *J. Nanjing Univ. Nat. Sci. Ed.* 20, 732–739.

Gupta, S., Rodgers, J., Hsü, K. J., Shu, S., Jiliang, L., Haihong, C., et al. (1989). Comments and Reply on "Mesozoic Overthrust Tectonics in South China". *Geol* 17, 669–673. doi:10.1130/0091-7613(1989)017<0669:caromo>2.3.co;2

Hand, M., and Sandiford, M. (1999). Intraplate Deformation in Central Australia, the Link between Subsidence and Fault Reactivation. *Tectonophysics* 305, 121–140. doi:10.1016/s0040-1951(99)00009-8

Harada, H., Tsujimori, T., Kon, Y., Aoki, S., and Aoki, K. (2021a). Nature and Timing of Anatectic Event of the Hida Belt (Japan): Constraints from Titanite Geochemistry and U-Pb Age of Clinopyroxene-Bearing Leucogranite. *Lithos*, 398–399. doi:10.1016/j.lithos.2021.106256

Harada, H., Tsujimori, T., Kunugiza, K., Yamashita, K., Aoki, S., Aoki, K., et al. (2021b). The δ^{13}C – δ^{18}O Variations in Marble in the Hida Belt, Japan. *Isl. Arc* 30. doi:10.1111/iar.12389

Horie, K., Yamashita, M., Hayasaka, Y., Katoh, Y., Tsutsumi, Y., Katsube, A., et al. (2010). Eoarchean-Paleoproterozoic Zircon Inheritance in Japanese Permo-Triassic Granites (Unazuki Area, Hida Metamorphic Complex): Unearthing More Old Crust and Identifying Source Terrranes. *Precambrian Res.* 183, 145–157. doi:10.1016/j.precamres.2010.06.014

Hou, Q.-L., Guo, Q.-Q., Chen, Y.-C., Cheng, N.-N., Shi, M.-Y., and Li, J.-L. (2021). Discussions on the Mountains and Orogenic Belts and Related Issues. *Acta Petrol. Sin.* 37, 2287–2302. doi:10.18654/1000-0569/2021.08.02

Hsü, K. J. (1989). Geotectonic Structure of South China and its Relations with Japan. *Prog. Earth Sci.* 01, 22–27.

Hsü, K. J., Li, J., Chen, H., Wang, Q., Sun, S., and Sengör, A. (1990). Tectonics of South China: Key to Understanding West Pacific Geology. *Tectonophysics* 183, 9–39.

Hsü, K. J., Sun, S., Li, J., Chen, H., Pen, H., and Sengor, A. (1988). Mesozoic Overthrust Tectonics in South China. *Geology* 16, 418–421.

Hu, S. X., and Ye, Y. (2006). Questions to 'Cathaysia Oldland', 'Cathaysia Block' and 'United Yangtze-Cathaysia Oldland' of South China. *Geol. J. China Univ.* 12, 432–439.

Huang, J. Q. (1984). New Researches on the Tectonic Characteristics of China. *Bull. Chin. Acad. Geol. Sci.* 9, 5.

Irvine, T. N., and Baragar, W. R. A. (1971). A Guide to the Chemical Classification of the Common Volcanic Rocks. *Can. J. Earth Sci.* 8, 523–548. doi:10.1139/e71-055

Ishiwatari, A., and Tsujimori, T. (2003). Paleozoic Ophiolites and Blueschists in Japan and Russian Primorye in the Tectonic Framework of East Asia: A Synthesis. *Isl. Arc* 12, 79–206. doi:10.1046/j.1440-1738.2003.00390.x

Isozaki, Y. (2019). A Visage of Early Paleozoic Japan: Geotectonic and Paleobiogeographical Significance of Greater South China. *Isl. Arc* 28. doi:10.1111/iar.12296

Isozaki, Y., Aoki, K., Nakama, T., and Yanai, S. (2010). New Insight into a Subduction-Related Orogen: A Reappraisal of the Geotectonic Framework and Evolution of the Japanese Islands. *Gondwana Res.* 18, 82–105. doi:10.1016/j.gr.2010.02.015

Isozaki, Y., Aoki, K., Sakata, S., and Hirata, T. (2014). The Eastern Extension of Paleozoic South China in NE Japan Evidenced by Detrital Zircon. *Gff* 136, 116–119. doi:10.1080/11035897.2014.893254

Jamieson, R. A., and Beaumont, C. (2013). On the Origin of Orogens. *Geol. Soc. Am. Bull.* 125, 1671–1702. doi:10.1130/b30855.1

Jiang, Y., Xing, G., Yuan, Q., Zhao, X., Duan, Z., and Dong, X. (2016). The First Discovery of Permian Metamorphic Rocks in Zhoushan Islands, Zhejiang Province. *Geol. Bull. China* 35, 1046–1055.

Kawabata, R., Imayama, T., Kato, T., Oh, C. W., Horie, K., and Takehara, M. (2021). Multi-stage Metamorphic History of the Oki Gneisses in Japan: Implications for Paleoproterozoic Metamorphism and Tectonic Correlations in Northeastern Asia. *J. Metamorph. Geol.* 40, 257–286. doi:10.1111/jmg.12627

Kimura, K., Hayasaka, Y., Shibata, T., Kawaguchi, K., and Fujiwara, H. (2019). Discovery of Paleoproterozoic 1.85 Ga Granitoid Bodies from the Maizuru Terrane in the Tsuwano Area, Shimane Prefecture, Southwest Japan and its Geologic Implications. *Jour. Geol. Soc. Jpn.* 125, 153–165. doi:10.5575/geosoc.2018.0050

Kwon, S., Sajeev, K., Mitra, G., Park, Y., Kim, S. W., and Ryu, I.-C. (2009). Evidence for Permo-Triassic Collision in Far East Asia: The Korean Collisional Orogen. *Earth Planet. Sci. Lett.* 279, 340–349. doi:10.1016/j.epsl.2009.01.016

Li, C.-f., Li, X.-h., Li, Q.-l., Guo, J.-h., and Li, X.-h. (2011a). Directly Determining 143Nd/144Nd Isotope Ratios Using Thermal Ionization Mass Spectrometry for Geological Samples without Separation of Sm-Nd. *J. Anal. At. Spectrom.* 26, 2012. doi:10.1039/c0ja00081g

Li, C.-F., Li, X.-H., Li, Q.-L., Guo, J.-H., Li, X.-H., and Liu, T. (2011b). An Evaluation of a Single-step Extraction Chromatography Separation Method for Sm-Nd Isotope Analysis of Micro-samples of Silicate Rocks by High-Sensitivity Thermal Ionization Mass Spectrometry. *Anal. Chim. Acta* 706, 297–304. doi:10.1016/j.aca.2011.08.036

Li, J., Dong, S., Zhang, Y., Zhao, G., Johnston, S. T., Cui, J., et al. (2016a). New Insights into Phanerozoic Tectonics of South China: Part 1, Polyphase Deformation in the Jiuling and Lianyunshan Domains of the Central Jiangnan Orogen. *J. Geophys. Res. Solid Earth* 121, 3048–3080. doi:10.1002/2015jb012778

Li, J., Zhang, Y., Zhao, G., Johnston, S. T., Dong, S., Koppers, A., et al. (2017a). New Insights into Phanerozoic Tectonics of South China: Early Paleozoic Sinistral and Triassic Dextral Transpression in the East Wuyishan and Chencai Domains, NE Cathaysia. *Tectonics* 36, 819–853. doi:10.1002/2016tc004461

Li, L., Lin, S., Xing, G., Davis, D. W., Jiang, Y., Davis, W., et al. (2016b). Ca. 830 Ma Back-Arc Type Volcanic Rocks in the Eastern Part of the Jiangnan Orogen: Implications for the Neoproterozoic Tectonic Evolution of South China Block. *Precambrian Res.* 275, 209–224. doi:10.1016/j.precamres.2016.01.016

Li, S., Jahn, B.-m., Zhao, S., Dai, L., Li, X., Suo, Y., et al. (2017b). Triassic Southeastward Subduction of North China Block to South China Block: Insights from New Geological, Geophysical and Geochemical Data. *Earth-Science Rev.* 166, 270–285. doi:10.1016/j.earscirev.2017.01.009

Li, S., Santosh, M., Zhao, G., Zhang, G., and Jin, C. (2012a). Intracontinental Deformation in a Frontier of Super-convergence: A Perspective on the Tectonic Milieu of the South China Block. *J. Asian Earth Sci.* 49, 313–329. doi:10.1016/j.jseaes.2011.07.026

Li, S. Z., Li, X. Y., Shu-Juan, Y., Chao, L., Xin, G., Ling-Li, W., et al. (2016e). Global Early Paleozoic Orogens (III): Intracontinental Orogen in South China. *J. Jilin Univ. (Earth Sci. Ed.* 46, 1005–1025. doi:10.13278/j.cnki.jjuese.201604103

Li, S. Z., Yang, C., Zhao, S. J., Li, X. Y., Ling-Li, Y., Shan, L., et al. (2016d). Global Early Paleozoic Orogens (II): Collision-type Orogeny. *J. Jilin Univ. (Earth Sci. Ed.* 46, 946–967. doi:10.13278/j.cnki.jjuese.201604102

Li, S. Z., Yang, C., Zhao, S. J., Li, X. Y., Shu-Yan, G., Ling-Li, Y., et al. (2016c). Global Early Paleozoic Orogens (I): Subduction-accretionary-type Orogeny. *J. Jilin Univ. (Earth Sci. Ed.* 46, 968–1004. doi:10.13278/j.cnki.jjuese.201604101

Li, W., Li, X., and Li, Z. (2005). Neoproterozoic Bimodal Magmatism in the Cathaysia Block of South China and its Tectonic Significance. *Precambrian Res.* 136, 51–66. doi:10.1016/j.precamres.2004.09.008

Li, W., Ma, C., Liu, Y., and Robinson, P. T. (2012b). Discovery of the Indosinian Aluminum A-type Granite in Zhejiang Province and its Geological Significance. *Sci. China Earth Sci.* 55, 13–25. doi:10.1007/s11430-011-4351-6

Li, W. X., Li, X. H., and Li, Z. X. (2010a). Ca. 850 Ma Bimodal Volcanic Rocks in Northeastern Jiangxi Province, South China: Initial Extension during the Breakup of Rodinia? *Am. J. Sci.* 310, 951–980. doi:10.2475/09.2010.08

Li, X.-H., Li, W.-X., Li, Q.-L., Wang, X.-C., Liu, Y., and Yang, Y.-H. (2010b). Petrogenesis and Tectonic Significance of the ~850 Ma Gangbian Alkaline Complex in South China: Evidence from *In Situ* Zircon U-Pb Dating, Hf-O Isotopes and Whole-Rock Geochemistry. *Lithos* 114, 1–15. doi:10.1016/j.lithos.2009.07.011

Li, X.-H., Li, W.-X., Li, Z.-X., Lo, C.-H., Wang, J., Ye, M.-F., et al. (2009a). Amalgamation between the Yangtze and Cathaysia Blocks in South China: Constraints from SHRIMP U-Pb Zircon Ages, Geochemistry and Nd-Hf Isotopes of the Shuangxiwu Volcanic Rocks. *Precambrian Res.* 174, 117–128. doi:10.1016/j.precamres.2009.07.004

Li, X.-H., Li, Z.-X., and Li, W.-X. (2014). Detrital Zircon U-Pb Age and Hf Isotope Constrains on the Generation and Reworking of Precambrian Continental Crust in the Cathaysia Block, South China: A Synthesis. *Gondwana Res.* 25, 1202–1215. doi:10.1016/j.gr.2014.01.003

Li, X.-H., Liu, Y., Li, Q.-L., Guo, C.-H., and Chamberlain, K. R. (2009b). Precise Determination of Phanerozoic Zircon Pb/Pb Age by Multicollector SIMS without External Standardization. *Geochem. Geophys. Geosyst.* 10. doi:10.1029/2009GC002400

Li, X.-H., Long, W.-G., Li, Q.-L., Liu, Y., Zheng, Y.-F., Yang, Y.-H., et al. (2010c). Penglai Zircon Megacrysts: a Potential New Working Reference Material for Microbeam Determination of Hf-O Isotopes and U-Pb Age. *Geostand. Geoanalytical Res.* 34, 117–134. doi:10.1111/j.1751-908x.2010.00036.x

Li, X.-h. (1997). Timing of the Cathaysia Block Formation: Constraints from SHRIMP U-Pb Zircon Geochronology. *Episodes* 20, 188–192. doi:10.18814/epiiugs/1997/v20i3/008

Li, X. H., Li, Z. X., Li, W. X., and Wang, Y. (2006). Initiation of the Indosinian Orogeny in South China: Evidence for a Permian Magmatic Arc on Hainan Island. *J. Geol.* 114, 341–353. doi:10.1086/501222

Li, Z.-X., and Li, X.-H. (2007). Formation of the 1300-km-wide Intracontinental Orogen and Postorogenic Magmatic Province in Mesozoic South China: A Flat-Slab Subduction Model. *Geol* 35, 179–182. doi:10.1130/g23193a.1

Li, Z. X. (1998). "Tectonic History of the Major East Asian Lithospheric Blocks Since the Mid-Proterozoic—A Synthesis," in *Mantle Dynamics and Plate Interactions in East Asia*. Editor M. F. J. Flower, S.-L. Chung, C.-H. Lo, and T.-Y. Lee (Washington, DC: American Geophysical Unio), 221–243. doi:10.1029/GD027p0221

Lin, S., Xing, G., Davis, D. W., Yin, C., Wu, M., Li, L., et al. (2018). Appalachian-style Multi-Terrane Wilson Cycle Model for the Assembly of South China. *Geology* 46, 319–322. doi:10.1130/g39806.1

Lin, W., Wang, Q., and Chen, K. (2008). Phanerozoic Tectonics of South China Block: New Insights from the Polyphase Deformation in the Yunkai Massif. *Tectonics* 27, 1–16. doi:10.1029/2007tc002207

Liu, F. L., Gerdes, A., Liou, J. G., Xue, H. M., and Liang, F. H. (2006). SHRIMP U-Pb Zircon Dating from Sulu-Dabie Dolomitic Marble, Eastern China: Constraints on Prograde, Ultrahigh-Pressure and Retrograde Metamorphic Ages. *J. Metamorph. Geol.* 24, 569–589. doi:10.1111/j.1525-1314.2006.00655.x

Liu, F., Xu, Z., Liou, J. G., and Song, B. (2004). SHRIMP U-Pb Ages of Ultrahigh-Pressure and Retrograde Metamorphism of Gneisses, South-Western Sulu Terrane, Eastern China. *J. Metamorph. Geol.* 22, 315–326. doi:10.1111/j.1525-1314.2004.00516.x

Liu, L., Li, S., Dai, L., Suo, Y., Liu, B., Zhang, G., et al. (2012a). Geometry and Timing of Mesozoic Deformation in the Western Part of the Xuefeng Tectonic Belt, South China: Implications for Intra-continental Deformation. *J. Asian Earth Sci.* 49, 330–338. doi:10.1016/j.jseaes.2011.09.026

Liu, Q., Yu, J.-H., Wang, Q., Su, B., Zhou, M.-F., Xu, H., et al. (2012b). Ages and Geochemistry of Granites in the Pingtan-Dongshan Metamorphic Belt, Coastal South China: New Constraints on Late Mesozoic Magmatic Evolution. *Lithos* 150, 268–286. doi:10.1016/j.lithos.2012.06.031

Liu, X. (1993). High-P Metamorphic Belt in Central China and its Possible Eastward Extension to Korea. *J. Petrological Soc. Korea* 2, 9–18.

Lu, H. F. (2006). On the Cathaysian Oldland. *Geol. J. China Univ.* 12, 413–417.

Ludwig, K. (2012). *User's Manual for Isoplot Version 3.75–4.15: A Geochronological Toolkit for Microsoft Excel.* Berkley: Geochronological Center Special Publication.

Matsunaga, S., Tsujimori, T., Miyashita, A., Aoki, S., Aoki, K., Pastor-Galán, D., et al. (2021). Reappraisal of the Oldest High-Pressure Type Schist in Japan: New Zircon U-Pb Age of the Kitomyo Schist of the Kurosegawa Belt. *Lithos*, 380–381. doi:10.1016/j.lithos.2020.105898

Middlemost, E. A. K. (1994). Naming Materials in the Magma/igneous Rock System. *Earth-Science Rev.* 37, 215–224. doi:10.1016/0012-8252(94)90029-9

Miyashiro, A. (1961). Evolution of Metamorphic Belts. *J. Petrology* 2, 277–311. doi:10.1093/petrology/2.3.277

Miyashiro, A. (1973). Paired and Unpaired Metamorphic Belts. *Tectonophysics* 17, 241–254. doi:10.1016/0040-1951(73)90005-x

O'Brien, P. J. (1993). Partially Retrograded Eclogites of the Münchberg Massif, Germany: Records of a Multi-Stage Variscan Uplift History in the Bohemian Massif. *J. Metamorph. Geol.* 11, 241–260. doi:10.1111/j.1525-1314.1993.tb00145.x

Oh, C. W., and Kim, Y. H. (2021). The Geological Correlation between the Korean Peninsula and China from Paleoproterozoic to Triassic and the Comparative Evaluation Among the Permo-Triassic Collision Models in the Northeast Asia. *jgsk* 57, 369–412. doi:10.14770/jgsk.2021.57.4.369

Okay, A. I., and Celal Şengör, A. M. (1992). Evidence for Intracontinental Thrust-Related Exhumation of the Ultra-high-pressure Rocks in China. *Geol* 20, 411–414. doi:10.1130/0091-7613(1992)020<0411:efitre>2.3.co;2

Pastor-Galán, D., Spencer, C. J., Furukawa, T., and Tsujimori, T. (2021). Evidence for Crustal Removal, Tectonic Erosion and Flare-Ups from the Japanese Evolving Forearc Sediment Provenance. *Earth Planet. Sci. Lett.* 564. doi:10.1016/j.epsl.2021.116893

Pearce, J. A. (1975). Basalt Geochemistry Used to Investigate Past Tectonic Environments on Cyprus. *Tectonophysics* 25, 41–67. doi:10.1016/0040-1951(75)90010-4

Raimondo, T., Hand, M., and Collins, W. J. (2014). Compressional Intracontinental Orogens: Ancient and Modern Perspectives. *Earth-Science Rev.* 130, 128–153. doi:10.1016/j.earscirev.2013.11.009

Ratschbacher, L., Hacker, B. R., Calvert, A., Webb, L. E., Grimmer, J. C., McWilliams, M. O., et al. (2003). Tectonics of the Qinling (Central China): Tectonostratigraphy, Geochronology, and Deformation History. *Tectonophysics* 366, 1–53. doi:10.1016/s0040-1951(03)00053-2

Ree, J.-H., Cho, M., Kwon, S.-T., and Nakamura, E. (1996). Possible Eastward Extension of Chinese Collision Belt in South Korea: the Imjingang Belt. *Geol* 24, 1071–1074. doi:10.1130/0091-7613(1996)024<1071:peeocc>2.3.co;2

Ren, J. S. (1984). The Indosinian Orogeny and its Significance in the Tectonic Evolution of China. *Bull. Chin. Acad. Geol. Sci.* 9, 31–44.

Rowley, D. B., Ziegler, A. M., Gyou, N., Hsü, K. J., Shu, S., Jiliang, L., et al. (1989). Comment and Reply on "Mesozoic Overthrust Tectonics in South China". *Geol* 17, 384–387. doi:10.1130/0091-7613(1989)017<0384:caromo>2.3.co;2

Sandiford, M., and Hand, M. (1998). Controls on the Locus of Intraplate Deformation in Central Australia. *Earth Planet. Sci. Lett.* 162, 97–110. doi:10.1016/s0012-821x(98)00159-9

Sandiford, M., Hand, M., and McLaren, S. (2001). Tectonic Feedback, Intraplate Orogeny and the Geochemical Structure of the Crust: a Central Australian Perspective. *Geol. Soc. Lond. Spec. Publ.* 184, 195–218. doi:10.1144/gsl.sp.2001.184.01.10

Shu, L.-S., Faure, M., Yu, J.-H., and Jahn, B.-M. (2011). Geochronological and Geochemical Features of the Cathaysia Block (South China): New Evidence for the Neoproterozoic Breakup of Rodinia. *Precambrian Res.* 187, 263–276. doi:10.1016/j.precamres.2011.03.003

Shu, L. (2012). An Analysis of Principal Features of Tectonic Evolution of South China Block. *Geol. Bull. China* 31, 1035–1053.

Shu, L., Deng, P., Yu, J., Wang, Y., and Jiang, S. (2008a). The Age and Tectonic Environment of the Rhyolitic Rocks on the Western Side of Wuyi Mountain, South China. *Sci. China Ser. D-Earth Sci.* 51, 1053–1063. doi:10.1007/s11430-008-0078-4

Shu, L., Faure, M., Wang, B., Zhou, X., and Song, B. (2008b). Late Palaeozoic-Early Mesozoic Geological Features of South China: Response to the Indosinian Collision Events in Southeast Asia. *Comptes Rendus Geosci.* 340, 151–165. doi:10.1016/j.crte.2007.10.010

Shu, L. S. (2006). Pre-Devonian Tectonic Evolution of South China: from Cathaysian Block to Caledonian Period Folded Orogenic Belt. *Geol. J. China Univ.* 12, 418–431.

Shu, L., Song, M., and Yao, J. (2018). Appalachian-style Multi-Terrane Wilson Cycle Model for the Assembly of South China: COMMENT. *Geology* 46, e445. doi:10.1130/g40213c.1

Shu, L., Wang, J., and Yao, J. (2019). Tectonic Evolution of the Eastern Jiangnan Region, South China: New Findings and Implications on the Assembly of the Rodinia Supercontinent. *Precambrian Res.* 322, 42–65. doi:10.1016/j.precamres.2018.12.007

Sláma, J., Košler, J., Condon, D. J., Crowley, J. L., Gerdes, A., Hanchar, J. M., et al. (2008). Plešovice Zircon—A New Natural Reference Material for U–Pb and Hf Isotopic Microanalysis. *Chem. Geol.* 249, 1–35. doi:10.1016/j.chemgeo.2007.11.005

Söderlund, U., Patchett, P. J., Vervoort, J. D., and Isachsen, C. E. (2004). The 176Lu Decay Constant Determined by Lu–Hf and U–Pb Isotope Systematics of Precambrian Mafic Intrusions. *Earth Planet. Sci. Lett.* 219, 311–324. doi:10.1016/S0012-821X(04)00012-3

Sokoutis, D., and Willingshofer, E. (2011). Decoupling during Continental Collision and Intra-plate Deformation. *Earth Planet. Sci. Lett.* 305, 435–444. doi:10.1016/j.epsl.2011.03.028

Stacey, J. S., and Kramers, J. D. (1975). Approximation of Terrestrial Lead Isotope Evolution by a Two-Stage Model. *Earth Planet. Sci. Lett.* 26, 207–221. doi:10.1016/0012-821x(75)90088-6

Sun, L.-Q., Ling, H.-F., Shen, W.-Z., Wang, K.-X., and Huang, G.-L. (2017). Petrogenesis of Two Triassic A-type Intrusions in the Interior of South China and Their Implications for Tectonic Transition. *Lithos* 284, 642–653. doi:10.1016/j.lithos.2017.05.006

Sun, S.-S., and McDonough, W. F. (1989). Chemical and Isotopic Systematics of Oceanic Basalts: Implications for Mantle Composition and Processes. *Geol. Soc. Lond. Spec. Publ.* 42, 313–345. doi:10.1144/gsl.sp.1989.042.01.19

Sun, Y., Ma, C., Liu, Y., and She, Z. (2011). Geochronological and Geochemical Constraints on the Petrogenesis of Late Triassic Aluminous A-type Granites in Southeast China. *J. Asian Earth Sci.* 42, 1117–1131. doi:10.1016/j.jseaes.2011.06.007

Taira, A. (2001). Tectonic Evolution of the Japanese Island Arc System. *Annu. Rev. Earth Planet. Sci.* 29, 109–134. doi:10.1146/annurev.earth.29.1.109

Takahashi, Y., Cho, D.-L., Mao, J., Zhao, X., and Yi, K. (2018). SHRIMP U-Pb Zircon Ages of the Hida Metamorphic and Plutonic Rocks, Japan: Implications for Late Paleozoic to Mesozoic Tectonics Around the Korean Peninsula. *Isl. Arc* 27. doi:10.1111/iar.12220

Tatsumi, Y., Kani, T., Ishizuka, H., Maruyama, S., and Nishimura, Y. (2000). Activation of Pacific Mantle Plumes during the Carboniferous: Evidence from Accretionary Complexes in Southwest Japan. *Geology* 28, 580–582. doi:10.1130/0091-7613(2000)028<0580:aopmpd>2.3.co;2

Tsujimori, T., Liou, J. G., Ernst, W. G., and Itaya, T. (2006). Triassic Paragonite- and Garnet-Bearing Epidote-Amphibolite from the Hida Mountains, Japan. *Gondwana Res.* 9, 167–175. doi:10.1016/j.gr.2005.03.001

Tsujimori, T., and Liou, J. G. (2004). Metamorphic Evolution of Kyanite-Staurolite-Bearing Epidote-Amphibolite from the Early Palaeozoic Oeyama Belt, SW Japan. *J. Metamorph. Geol.* 22, 301–313. doi:10.1111/j.1525-1314.2004.00515.x

Tsujimori, T. (2002). Prograde and Retrograde P-T Paths of the Late Paleozoic Glaucophane Eclogite from the Renge Metamorphic Belt, Hida Mountains, Southwestern Japan. *Int. Geol. Rev.* 44, 797–818. doi:10.2747/0020-6814.44.9.797

Tsutsumi, Y., Isozaki, Y., and Terabayashi, M. (2017). The Most Continent-Sided Occurrence of the Phanerozoic Subduction-Related Orogens in SW Japan: Zircon U-Pb Dating of the Mizoguchi Gneiss on the Western Foothill of Mt. Daisen Volcano in Tottori. *J. Asian Earth Sci.* 145, 530–541. doi:10.1016/j.jseaes.2017.06.028

Valley, J. W., Chiarenzelli, J. R., and McLelland, J. M. (1994). Oxygen Isotope Geochemistry of Zircon. *Earth Planet. Sci. Lett.* 126, 187–206. doi:10.1016/0012-821x(94)90106-6

Vavra, G. (1990). On the Kinematics of Zircon Growth and its Petrogenetic Significance: a Cathodoluminescence Study. *Contr. Mineral. Pet.* 106, 90–99. doi:10.1007/bf00306410

Wakita, K. (2013). Geology and Tectonics of Japanese Islands: A Review - the Key to Understanding the Geology of Asia. *J. Asian Earth Sci.* 72, 75–87. doi:10.1016/j.jseaes.2012.04.014

Wallis, S. R., Yamaoka, K., Mori, H., Ishiwatari, A., Miyazaki, K., and Ueda, H. (2020). The Basement Geology of Japan from A to Z. *Isl. Arc* 29, e12339. doi:10.1111/iar.12339

Wan, Y., Liu, D., Wilde, S. A., Cao, J., Chen, B., Dong, C., et al. (2010). Evolution of the Yunkai Terrane, South China: Evidence from SHRIMP Zircon U-Pb Dating, Geochemistry and Nd Isotope. *J. Asian Earth Sci.* 37, 140–153. doi:10.1016/j.jseaes.2009.08.002

Wang, J. G., Yu, S. Q., Zhao, X. D., Wu, M., Gu, G. M., and Hu, Y. H. (2014c). The Discovery of Paleoproterozoic Mafic-Ultramafic Rocks in the Wuyishan Block: Description of Profile and Characteristics of Petrology, Petrography and Isotope Geochronology. *Acta Petrologica Mineralogica* 33, 617–629.

Wang, J., and Li, Z. (2003). History of Neoproterozoic Rift Basins in South China: Implications for Rodinia Break-Up. *Precambrian Res.* 122, 141–158. doi:10.1016/s0301-9268(02)00209-7

Wang, Q., Li, J.-W., Jian, P., Zhao, Z.-H., Xiong, X.-L., Bao, Z.-W., et al. (2005a). Alkaline Syenites in Eastern Cathaysia (South China): Link to Permian-Triassic Transtension. *Earth Planet. Sci. Lett.* 230, 339–354. doi:10.1016/j.epsl.2004.11.023

Wang, X.-C., Li, X.-H., Li, W.-X., and Li, Z.-X. (2007). Ca. 825 Ma Komatiitic Basalts in South China: First Evidence for >1500 °C Mantle Melts by a Rodinian Mantle Plume. *Geol* 35, 1103. doi:10.1130/g23878a.1

Wang, X.-C., Li, X.-h., Li, Z.-X., Li, Q.-l., Tang, G.-Q., Gao, Y.-Y., et al. (2012a). Episodic Precambrian Crust Growth: Evidence from U-Pb Ages and Hf-O Isotopes of Zircon in the Nanhua Basin, Central South China. *Precambrian Res.* 222, 386–403. doi:10.1016/j.precamres.2011.06.001

Wang, X.-L., Shu, L.-S., Xing, G.-F., Zhou, J.-C., Tang, M., Shu, X.-J., et al. (2012b). Post-orogenic Extension in the Eastern Part of the Jiangnan Orogen: Evidence from Ca 800-760Ma Volcanic Rocks. *Precambrian Res.* 222, 404–423. doi:10.1016/j.precamres.2011.07.003

Wang, X.-L., Zhou, J.-C., Griffin, W. L., Zhao, G., Yu, J.-H., Qiu, J.-S., et al. (2014a). Geochemical Zonation across a Neoproterozoic Orogenic Belt: Isotopic Evidence from Granitoids and Metasedimentary Rocks of the Jiangnan Orogen, China. *Precambrian Res.* 242, 154–171. doi:10.1016/j.precamres.2013.12.023

Wang, X., Liou, J. G., and Mao, H. K. (1989). Coesite-bearing Eclogite from the Dabie Mountains in Central China. *Geol* 17, 1085–1088. doi:10.1130/0091-7613(1989)017<1085:cbeftd>2.3.co;2

Wang, Y., Fan, W., Zhang, G., and Zhang, Y. (2013a). Phanerozoic Tectonics of the South China Block: Key Observations and Controversies. *Gondwana Res.* 23, 1273–1305. doi:10.1016/j.gr.2012.02.019

Wang, Y., Wang, Y., Zhang, Y., Cawood, P. A., Qian, X., Gan, C., et al. (2021). Triassic Two-Stage Intra-continental Orogensis of the South China Block, Driven by Paleotethyan Closure and Interactions with Adjoining Blocks. *J. Asian Earth Sci.* 206. doi:10.1016/j.jseaes.2020.104648

Wang, Y., Wu, C., Zhang, A., Fan, W., Zhang, Y., Zhang, Y., et al. (2012c). Kwangsian and Indosinian Reworking of the Eastern South China Block: Constraints on Zircon U-Pb Geochronology and Metamorphism of Amphibolites and Granulites. *Lithos* 150, 227–242. doi:10.1016/j.lithos.2012.04.022

Wang, Y., Zhang, A., Cawood, P. A., Fan, W., Xu, J., Zhang, G., et al. (2013b). Geochronological, Geochemical and Nd-Hf-Os Isotopic Fingerprinting of an Early Neoproterozoic Arc-Back-Arc System in South China and its Accretionary Assembly along the Margin of Rodinia. *Precambrian Res.* 231, 343–371. doi:10.1016/j.precamres.2013.03.020

Wang, Y., Zhang, Y., Fan, W., Geng, H., Zou, H., and Bi, X. (2014b). Early Neoproterozoic Accretionary Assemblage in the Cathaysia Block: Geochronological, Lu-Hf Isotopic and Geochemical Evidence from Granitoid Gneisses. *Precambrian Res.* 249, 144–161. doi:10.1016/j.precamres.2014.05.003

Wang, Y., Zhang, Y., Fan, W., and Peng, T. (2005b). Structural Signatures and 40Ar/39Ar Geochronology of the Indosinian Xuefengshan Tectonic Belt, South China Block. *J. Struct. Geol.* 27, 985–998. doi:10.1016/j.jsg.2005.04.004

Winchester, J. A., and Floyd, P. A. (1977). Geochemical Discrimination of Different Magma Series and Their Differentiation Products Using Immobile Elements. *Chem. Geol.* 20, 325–343. doi:10.1016/0009-2541(77)90057-2

Wood, D. A. (1980). The Application of a ThHfTa Diagram to Problems of Tectonomagmatic Classification and to Establishing the Nature of Crustal Contamination of Basaltic Lavas of the British Tertiary Volcanic Province. *Earth Planet. Sci. Lett.* 50, 11–30. doi:10.1016/0012-821x(80)90116-8

Woodhead, J. D., and Hergt, J. M. (2005). A Preliminary Appraisal of Seven Natural Zircon Reference Materials for *In Situ* Hf Isotope Determination. *Geostand. Geoanalyt Res.* 29, 183–195. doi:10.1111/j.1751-908x.2005.tb00891.x

Wu, F.-Y., Yang, Y.-H., Xie, L.-W., Yang, J.-H., and Xu, P. (2006). Hf Isotopic Compositions of the Standard Zircons and Baddeleyites Used in U-Pb Geochronology. *Chem. Geol.* 234, 105–126. doi:10.1016/j.chemgeo.2006.05.003

Wu, Y.-B., and Zheng, Y.-F. (2013). Tectonic Evolution of a Composite Collision Orogen: An Overview on the Qinling-Tongbai-Hong'an-Dabie-Sulu Orogenic Belt in Central China. *Gondwana Res.* 23, 1402–1428. doi:10.1016/j.gr.2012.09.007

Xia, Y., Xu, X.-S., and Zhu, K.-Y. (2012). Paleoproterozoic S- and A-type Granites in Southwestern Zhejiang: Magmatism, Metamorphism and Implications for the Crustal Evolution of the Cathaysia Basement. *Precambrian Res.* 216, 177–207. doi:10.1016/j.precamres.2012.07.001

Xia, Y., Yin, C., Lin, S., Zhang, J., Qian, J., Wu, S., et al. (2021). Metamorphism and Geochronology of High-Pressure Mafic Granulites (Retrograded Eclogites?) in East Cathaysia Terrane of South China: Implications for Mesozoic Tectonic Evolution. *GSA Bull.* 134, 832. doi:10.1130/B36025.1

Xiang, H., Zhang, L., Zhou, H., Zhong, Z., Zeng, W., Liu, R., et al. (2008). U-pb Zircon Geochronology and Hf Isotope Study of Metamorphosed Basic-Ultrabasic Rocks from Metamorphic Basement in Southwestern Zhejiang: The Response of the Cathaysia Block to Indosinian Orogenic Event. *Sci. China Ser. D-Earth Sci.* 51, 788–800. doi:10.1007/s11430-008-0053-0

Xie, L., Zhang, Y., Zhang, H., Sun, J., and Wu, F. (2008). *In Situ* simultaneous Determination of Trace Elements, U-Pb and Lu-Hf Isotopes in Zircon and Baddeleyite. *Sci. Bull.* 53, 1565–1573. doi:10.1007/s11434-008-0086-y

Xing, G. F., Li, L. M., Jiang, Y., Feng, Y. F., Lu, Q. D., Chen, Z. H., et al. (2014). Petrogenetic Process of Cretaceous 'gneissic' Magma-Mixed Complex in the Changle-Nan'ao Structure Zone, Fujian Province: a Case Study on Xiaocuo Intrusion. *Resour. Surgey Environ.* 35, 79–94.

Xing, G., Lu, Q., Jiang, Y., Nie, T., Chen, R., Feng, Y., et al. (2010). Identification and Significance of "gneissic" Magma-Mixed Complex in the Changle-Nan'ao Fault Zone, Southeastern Fujian, Chian. *Geol. Bull. China* 29, 31–43.

Xu, S., Ai, O., Ji, S., Amc, S., Su, W., Liu, Y., et al. (1992). Diamond from the Dabie Shan Metamorphic Rocks and its Implication for Tectonic Setting. *Science* 256, 80–82.

Xu, X., O'Reilly, S. Y., Griffin, W. L., Wang, X., Pearson, N. J., and He, Z. (2007). The Crust of Cathaysia: Age, Assembly and Reworking of Two Terranes. *Precambrian Res.* 158, 51–78. doi:10.1016/j.precamres.2007.04.010

Yang, Y.-h., Zhang, H.-f., Chu, Z.-y., Xie, L.-w., and Wu, F.-y. (2010). Combined Chemical Separation of Lu, Hf, Rb, Sr, Sm and Nd from a Single Rock Digest and Precise and Accurate Isotope Determinations of Lu-Hf, Rb-Sr and Sm-Nd Isotope Systems Using Multi-Collector ICP-MS and TIMS. *Int. J. Mass Spectrom.* 290, 120–126. doi:10.1016/j.ijms.2009.12.011

Yang, Z.-Y., and Jiang, S.-Y. (2019). Detrital Zircons in Metasedimentary Rocks of Mayuan and Mamianshan Group from Cathaysia Block in Northwestern Fujian Province, South China: New Constraints on Their Formation Ages and Paleogeographic Implication. *Precambrian Res.* 320, 13–30. doi:10.1016/j.precamres.2018.10.004

Yao, J., Shu, L., Santosh, M., and Zhao, G. (2014). Neoproterozoic Arc-Related Mafic-Ultramafic Rocks and Syn-Collision Granite from the Western Segment of the Jiangnan Orogen, South China: Constraints on the Neoproterozoic Assembly of the Yangtze and Cathaysia Blocks. *Precambrian Res.* 243, 39–62. doi:10.1016/j.precamres.2013.12.027

Yin, A., Nie, S., Craig, P., Harrison, T. M., Ryerson, F. J., Xianglin, Q., et al. (1998). Late Cenozoic Tectonic Evolution of the Southern Chinese Tian Shan. *Tectonics* 17, 1–27. doi:10.1029/97tc03140

Yin, H. F., Wu, S. B., Du, Y. S., and Peng, Y. Q. (1999). South China Defined as Part of Tethyan Archipelagic Ocean System. *J. China Univ. Geosciences- Earth Sci.* 24, 3–14.

Yu, J.-H., O'Reilly, S. Y., Wang, L., Griffin, W. L., Zhang, M., Wang, R., et al. (2008). Where Was South China in the Rodinia Supercontinent? *Precambrian Res.* 164, 1–15. doi:10.1016/j.precamres.2008.03.002

Yu, J.-H., O'Reilly, S. Y., Wang, L., Griffin, W. L., Zhou, M.-F., Zhang, M., et al. (2010). Components and Episodic Growth of Precambrian Crust in the Cathaysia Block, South China: Evidence from U-Pb Ages and Hf Isotopes of Zircons in Neoproterozoic Sediments. *Precambrian Res.* 181, 97–114. doi:10.1016/j.precamres.2010.05.016

Yu, J.-H., O'Reilly, S. Y., Zhou, M.-F., Griffin, W. L., and Wang, L. (2012). U-pb Geochronology and Hf-Nd Isotopic Geochemistry of the Badu Complex, Southeastern China: Implications for the Precambrian Crustal Evolution and Paleogeography of the Cathaysia Block. *Precambrian Res.* 222, 424–449. doi:10.1016/j.precamres.2011.07.014

Yu, J.-H., Wang, L., O'Reilly, S. Y., Griffin, W. L., Zhang, M., Li, C., et al. (2009). A Paleoproterozoic Orogeny Recorded in a Long-Lived Cratonic Remnant (Wuyishan Terrane), Eastern Cathaysia Block, China. *Precambrian Res.* 174, 347–363. doi:10.1016/j.precamres.2009.08.009

Yu, J. H., Wei, Z. Y., Wang, L. J., and Sun, T. (2006). Cathaysia Block: a Young Continent Composed of Ancient Materials. *Geol. J. China Univ.* 04, 440–447.

Yu, J., O'Reilly, Y. S., Wang, L., Griffin, W. L., Jiang, S., Wang, R., et al. (2007). Finding of Ancient Materials in Cathaysia and Implication for the Formation of Precambrian Crust. *Chin. Sci. Bull.* 52, 13–22. doi:10.1007/s11434-007-0008-4

Yu, J., Zhou, X., O'Reilly, Y., Zhao, L., Griffin, W., Wang, R., et al. (2005). Formation History and Protolith Characteristics of Granulite Facies Metamorphic Rock in Central Cathaysia Deduced from U-Pb and Lu-Hf Isotopic Studies of Single Zircon Grains. *Chin. Sci. Bull.* 50, 2080–2089. doi:10.1360/982004-808

Yu, J., Zhou, X., Zhao, L., and Chen, X. (2003). Discovery and Implications of Granulite Facies Metamorphic Rocks in the Eastern Nanling, China. *Acta Petrol. Sin.* 19, 461–467.

Zeh, A., Gerdes, A., Klemd, R., and Barton, J. M. (2007). Archaean to Proterozoic Crustal Evolution in the Central Zone of the Limpopo Belt (South Africa-Botswana): Constraints from Combined U-Pb and Lu-Hf Isotope Analyses of Zircon. *J. Petrology* 48, 1605–1639. doi:10.1093/petrology/egm032

Zeng, W., Zhang, L., Zhou, H., Zhong, Z., Xiang, H., Liu, R., et al. (2008). Caledonian Reworking of Paleoproterozoic Basement in the Cathaysia Block: Constraints from Zircon U-Pb Dating, Hf Isotopes and Trace Elements. *Sci. Bull.* 53, 895–904. doi:10.1007/s11434-008-0076-0

Zhai, M., Cong, B., Zhao, Z., Wang, Q., Wang, G., and Jiang, L. (1995). Petrological-tectonic Units in the Coesite-Bearing Metamorphic Terrain of the Dabie Mountains, Central China and Their Geotectonic Implications. *J. Southeast Asian Earth Sci.* 11, 1–13.

Zhai, M. G. (2009). Two Kinds of Granulites (HT-HP and HT-UHT) in North China Craton: Their Genetic Relation and Geotectonic Implications. *Acta Petrol. Sin.* 25, 1753–1771.

Zhai, M., Zhang, Y., Zhang, X., Wu, F., Peng, P., Li, Q., et al. (2016). Renewed Profile of the Mesozoic Magmatism in Korean Peninsula: Regional Correlation and Broader Implication for Cratonic Destruction in the North China Craton. *Sci. China Earth Sci.* 59, 2355–2388. doi:10.1007/s11430-016-0107-0

Zhang, G., Guo, A., Wang, Y., Li, S., Dong, Y., Liu, S., et al. (2013). Tectonics of South China Continent and its Implications. *Sci. China Earth Sci.* 56, 1804–1828. doi:10.1007/s11430-013-4679-1

Zhao, C., He, K., Mo, X., Tai, D., Ye, D., Ye, N., et al. (1996). Discovery and its Significance of Late Paleozoic Radiolarian Silicalite in Ophiolitic Melange of Northeastern Jiangxi Deep Fault Belt. *Chin. Sci. Bull.* 41, 667–670.

Zhao, G., Wang, Y., Huang, B., Dong, Y., Li, S., Zhang, G., et al. (2018a). Geological Reconstructions of the East Asian Blocks: From the Breakup of Rodinia to the Assembly of Pangea. *Earth-Science Rev.* 186, 262–286. doi:10.1016/j.earscirev.2018.10.003

Zhao, J.-H., Zhang, S.-B., and Wang, X.-L. (2018b). Neoproterozoic Geology and Reconstruction of South China. *Precambrian Res.* 309, 1–5. doi:10.1016/j.precamres.2018.02.004

Zhao, L., Cui, X., Zhai, M., Zhou, X., and Liu, B. (2019). Emplacement and Metamorphism of the Mafic Rocks from the Chencai Terrane within the Cathaysia Block: Implications for the Paleozoic Orogenesis of the South China Block. *J. Asian Earth Sci.* 173, 11–28. doi:10.1016/j.jseaes.2019.01.019

Zhao, L., Zhai, M., Santosh, M., and Zhou, X. (2017a). Early Mesozoic Retrograded Eclogite and Mafic Granulite from the Badu Complex of the Cathaysia Block, South China: Petrology and Tectonic Implications. *Gondwana Res.* 42, 84–103. doi:10.1016/j.gr.2016.10.002

Zhao, L., Zhai, M., Zhou, X., Santosh, M., and Ma, X. (2016). Thermal Gradient and Geochronology of a Paleozoic High-Grade Terrane in the Northeastern Cathaysia Block, South China. *Tectonophysics* 691, 311–327. doi:10.1016/j.tecto.2016.10.024

Zhao, L., Zhang, R.-c., Zhai, M.-G., and Zhou, X.-W. (2020). Major Lithologies of the High-Grade Zhoutan Terrane within the Cathaysia Block and Their

Tectonic Implications for the Neoproterozoic - Paleozoic South China. *Lithos* 372, 105664. doi:10.1016/j.lithos.2020.105664

Zhao, L., Zhou, X., Zhai, M., Liu, B., and Cui, X. (2018c). Petrologic and Zircon U-Pb Geochronological Characteristics of the Pelitic Granulites from the Badu Complex of the Cathaysia Block, South China. *J. Asian Earth Sci.* 158, 65–79. doi:10.1016/j.jseaes.2018.02.017

Zhao, L., Zhou, X., Zhai, M., Santosh, M., and Geng, Y. (2015). Zircon U-Th-Pb-Hf Isotopes of the Basement Rocks in Northeastern Cathaysia Block, South China: Implications for Phanerozoic Multiple Metamorphic Reworking of a Paleoproterozoic Terrane. *Gondwana Res.* 28, 246–261. doi:10.1016/j.gr.2014.03.019

Zhao, L., Zhou, X., Zhai, M., Santosh, M., Ma, X., Shan, H., et al. (2014). Paleoproterozoic Tectonic Transition from Collision to Extension in the Eastern Cathaysia Block, South China: Evidence from Geochemistry, Zircon U-Pb Geochronology and Nd-Hf Isotopes of a Granite-Charnockite Suite in Southwestern Zhejiang. *Lithos* 184, 259–280. doi:10.1016/j.lithos.2013.11.005

Zhao, Z.-F., Zheng, Y.-F., Chen, Y.-X., and Sun, G.-C. (2017b). Partial Melting of Subducted Continental Crust: Geochemical Evidence from Synexhumation Granite in the Sulu Orogen. *GSA Bull.* 129, 11. doi:10.1130/B31675.31671

Zhejiang, B. G. M. R. (1980). *Map Report of 1:2,000,000 Geological Map of Shengsi, Yuyao, Dinghai, Ningbo and Shenjiamen*, 7–15.

Zhou, X. M., and Li, W. X. (2000). Origin of Late Mesozoic Igneous Rocks in Southeastern China: Implications for Lithosphere Subduction and Underplating of Mafic Magmas. *Tectonophysics* 326, 269–287. doi:10.1016/s0040-1951(00)00120-7

Zhou, X., Sun, T., Shen, W., Shu, L., and Niu, Y. (2006). Petrogenesis of Mesozoic Granitoids and Volcanic Rocks in South China: a Response to Tectonic Evolution. *Episodes* 29, 26–33. doi:10.18814/epiiugs/2006/v29i1/004

Conflict of Interest: The authors declare that the research was conducted in the absence of any commercial or financial relationships that could be construed as a potential conflict of interest.

frontiers | Frontiers in Earth Science

ORIGINAL RESEARCH
published: 10 May 2022
doi: 10.3389/feart.2022.894353

The Multiple Metamorphism of Mafic Granulites From the East Hebei Terrane, North China Craton: Insights Into the Transition of Tectonic Regimes

Ting Liu[1,2]*, **Chunjing Wei**[2], **Chuan Yang**[3]* and **Zhuang Li**[4]

[1]*College of Earth Sciences, Chengdu University of Technology, Chengdu, China,* [2]*MOE Key Laboratory of Orogenic Belts and Crustal Evolution, School of Earth and Space Sciences, Peking University, Beijing, China,* [3]*China Transport Telecommunications and Information Center, Beijing, China,* [4]*College of Geosciences, China University of Petroleum (Beijing), Beijing, China*

OPEN ACCESS

Edited by:
Yi Chen,
Institute of Geology and Geophysics (CAS), China

Reviewed by:
François Camille,
Commission for the Geological Map of the World, France
Shujuan Jiao,
Institute of Geology and Geophysics (CAS), China

***Correspondence:**
Ting Liu
liuting3624@pku.edu.cn
Chuan Yang
yangchuan@pku.edu.cn

Specialty section:
This article was submitted to Petrology,
a section of the journal Frontiers in Earth Science

Received: *11 March 2022*
Accepted: *07 April 2022*
Published: *10 May 2022*

Citation:
Liu T, Wei C, Yang C and Li Z (2022) The Multiple Metamorphism of Mafic Granulites From the East Hebei Terrane, North China Craton: Insights Into the Transition of Tectonic Regimes.
Front. Earth Sci. 10:894353.
doi: 10.3389/feart.2022.894353

The East Hebei terrane from the North China Craton preserves the dome–and–keel structures, which was transected by a later linear belt in the north margin. Mafic granulites from the linear belt and domes record two groups of metamorphic ages at Neoarchean and Paleoproterozoic, but their accurate metamorphic peak conditions and paths have not been well addressed. Three samples of mafic granulites, including two-pyroxene granulite (JD15120), garnet-bearing two-pyroxene granulite (YC8-43), and garnet clinopyroxene granulite (JD1546), were documented for detailed metamorphic studies. Two-episode metamorphism can be recognized. The first-episode recovered from JD15120 and YC8-43 is represented by peak assemblage of medium-grained clinopyroxene, orthopyroxene, amphibole, plagioclase, and ilmenite, which yields ultrahigh temperature (UHT) conditions of 940–960°C at 7.5–8.5 kbar and 950–990°C at 8 kbar, respectively, constrained by contours of the maximum anorthite (X_{An}) in plagioclase cores. The post-peak evolution is dominated by cooling with decompression, constrained mostly from the measured core-to-rim decreasing X_{An} in plagioclase. By contrast, the second-episode overprinting is recognized in all samples, but exhibits varying textures. In garnet-bearing samples (YC8-43 and JD1546), the overprinting assemblages are characterized by poikilitic garnet that occurs either as coronae around the first-episode pyroxenes, forming “red-eye socket” textures, or as grains in equilibrium with tiny-grained clinopyroxene, plagioclase, amphibole, rutile, and quartz, forming high-pressure (HP) granulite assemblages. These HP granulite assemblages show peak conditions of ~12 kbar/860°C and ~12.6 kbar/835°C, constrained by contours of the maximum grossular (X_{Grs}) in garnet cores and the minimum X_{An} in plagioclase cores. The post-peak evolution is dominated by isothermal decompression, constrained from the outward decreasing X_{Grs} in garnet and increasing X_{An} in plagioclase. LA-ICP-MS U-Pb zircon dating on JD15120 and JD1546 suggests two metamorphic ages of ~2.49 Ga and ~1.78 Ga, being considered to be correlated with the UHT and HP granulite metamorphism, respectively. Tectonically, the late Neoarchean UHT granulite metamorphism may correlate a vertical sagduction regime, whereas the late

Paleoproterozoic HP granulite metamorphism is favored to register the continental collision in the northern margin of the North China Craton. This study may have indications for the Neoarchean–Paleoproterozoic tectonic transition of the craton.

Keywords: Archean supracrustal rocks, Ultra-high temperature granulite, High-pressure granulite, Pseudosection, East Hebei terrane, North China Craton

1 INTRODUCTION

As a window into the lower continental crust, granulites normally record pressure–temperature (*P*–*T*) conditions and *P*–*T* paths being indicative to tectonic models (Harley 1989, Harley 1998). Their secular change in apparent thermal gradients is also suggestive for revealing different heat flow and rheology in distinct tectonics (Brown and Johnson 2018). In the Archean terranes, almost half of the granulites are ultrahigh temperature (UHT) type with high d*T*/d*P* of >22°C/km (Brown 2007; Brown and Johnson 2018), representing extreme thermal conditions related to the coupling between crust, sub-crustal lithosphere, and asthenospheric mantle on a regional scale (Harley 2004; Harley 2008; Kelsey and Hand 2015), whereas the high-pressure (HP) granulites with intermediate d*T*/d*P* of 22–11°C/km became dominant after the Archean Eon (Brown and Johnson 2018), being normally considered as the sign for subduction or collision processes in plate tectonics (O'Brien and Rötzler 2003).

Archean cratons, although featured with thick and depleted lithospheric mantle and relatively stable from subsequent tectonism (Jordan 1978), can have transformation of the cratonic structures and development of multiple metamorphism in response to later reworking events (e.g., Weber 1984; Mahan et al., 2008; Perchuk et al., 2008). For example, the Pikwitonei granulite domain in the Superior Craton, one of the largest Neoarchean high-grade terranes worldwide, was recovered to have undergone multiple metamorphism, involving normal UHT granulite-facies metamorphism with an anticlockwise *P*–*T* path at Neoarchean, and overprinting greenschist to amphibolite-facies metamorphism with local migmatization at Hudsonian. These distinct metamorphic processes suggest different tectonic settings involving magmatic underplating (Mezger et al., 1990) or overthrusting during crustal thickening (Arima and Barnett 1984) for the first-episode metamorphism, and collision between the Superior Craton and the Churchill Province to form the Thompson belt for the second-episode metamorphism (Weber 1984). Therefore, detailed metamorphic studies on Archean cratons can give insights into the tectonic evolution of the early Earth.

The North China Craton (NCC) consists of four Archean blocks including Ordos, Yinshan, Longgang, and Langrim blocks, and three Paleoproterozoic orogenic belts among them (Zhao et al., 2005). These Archean blocks were revealed to record Neoarchean granulite-facies metamorphism with anticlockwise *P*–*T* paths, featured with "red-eye socket" texture in mafic granulites (Zhao et al., 1999; Zhao et al., 2005; Kwan et al., 2016). However, recent studies on mafic granulites from the East Hebei terrane, part of the Longgang block, suggest that some Archean terranes may be subjected to two episodes of granulite-facies metamorphism at late Neoarchean (2.53–2.47 Ga) and late Paleoproterozoic (1.85–1.80 Ga), respectively (Duan et al., 2015; Yang and Wei 2017b; Lu and Wei 2020). The first-episode Neoarchean granulite-facies metamorphism is featured with two-pyroxene granulites, and is argued to have peak conditions of normal UHT granulite facies of 8.0–11.0 kbar/756–940°C using conventional geothermobarometers (He and Ye 1992; Chen and Li 1996; Zhao et al., 1999; Kwan et al., 2016; Yang and Wei 2017a), or 9.0–10.0 kbar/950–1,070°C using rare earth elements (REE)-based geothermometers (Yang and Wei 2017a). On account of that conventional Fe–Mg exchange geothermometers are more likely to record lower temperatures than the peak of granulites as a result of the fast diffusion during cooling (e.g., Frost and Chacko 1989; Pattison et al., 2003), and the REE-based geothermobarometers generally have large uncertainties (Yang and Wei 2017a), the peak conditions for the two-pyroxene granulites remain uncertain. The second-episode Paleoproterozoic metamorphism was first recognized in mafic dykes, characterized by HP granulite-facies assemblages, which record *P*–*T* conditions of 11–12 kbar/790–810°C with clockwise *P*–*T* paths at ~1.82 Ga (Duan et al., 2015). Similar overprinting assemblages were also observed in Neoarchean mafic granulites, which exhibit peak *P*–*T* conditions of 12.5–12.8 kbar/880–900°C, metamorphic zircon ages of 1.83–1.81 Ga, and garnet-whole rock Lu–Hf isochron ages of 1.77–1.79 Ga (Yang and Wei 2017a; Yang and Wei 2017b; Lu and Wei 2020). However, Wang et al. (2018) argued that the HP granulite metamorphism may have occurred at early Paleoproterozoic (~2.46 Ga), which was followed by heating and decompression to form two-pyroxene granulites. Thus, detailed petrological and geochronological studies on both two-pyroxene and HP granulites need to be further conducted to document their metamorphic evolution.

In this article, representative mafic granulites that have been studied using major element- and REE-based geothermobarometers in Yang and Wei (2017a), were selected for constraining their metamorphic *P*–*T* conditions and paths on the basis of the pseudosections calculated using THERMOCALC. Zircon U–Pb dating was also carried out for defining the metamorphic ages.

2 GEOLOGICAL SETTING

The NCC can be normally divided into Eastern and Western Blocks (e.g., Zhao et al., 1998; Zhao et al., 2005; Zhao et al., 2012; **Figure 1A**). It is suggested that the Western Block formed at ~1.95 Ga by the collision between the Yinshan and Ordos Blocks

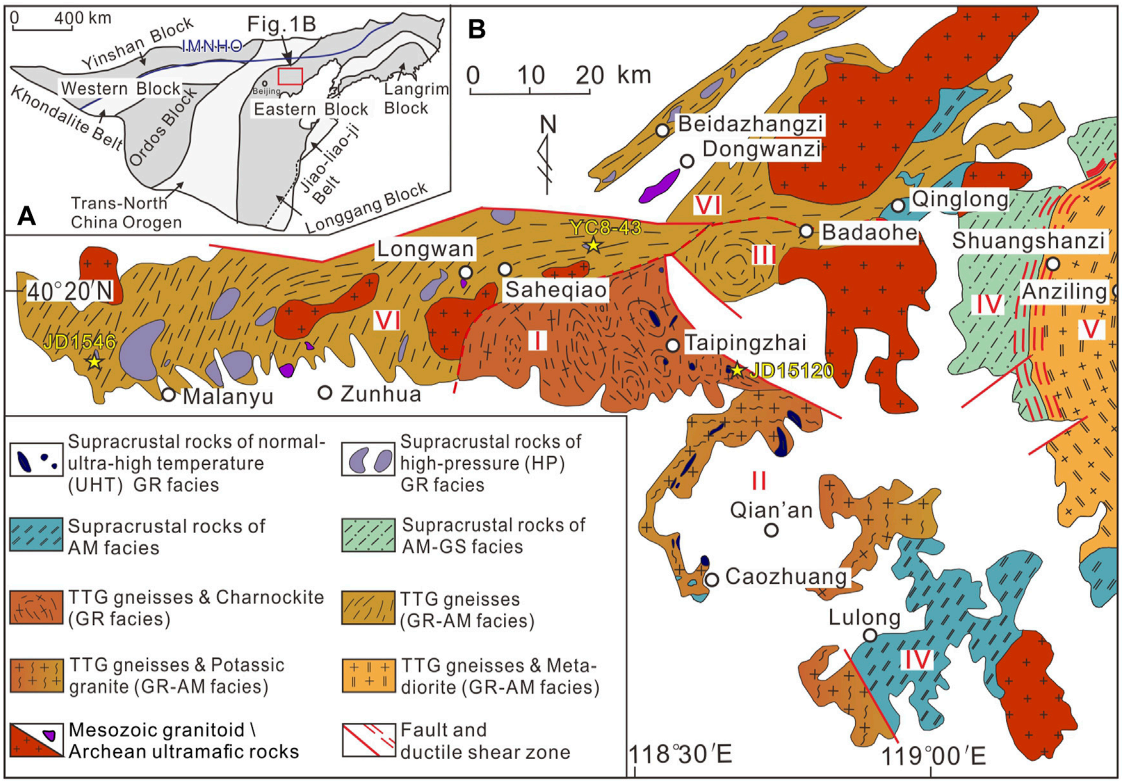

FIGURE 1 | (A) Tectonic subdivision of the North China craton (modified after Zhao et al., 2005; Zhao et al., 2012). **(B)** Geological map of the East Hebei terrane (modified after Wu et al., 1998; Wei 2018) with sample locations. GR-granulite; AM-amphibolite; GS-greenschist.

along the Khondalite Belt, whereas the Eastern Block formed at ~1.90 Ga when the Longgang and Langrim blocks collided along the Jiao–Liao–Ji Belt (e.g., Zhao et al., 1998; Zhao et al., 2005; Zhao et al., 2012). The time of the final amalgamation between Western and Eastern Blocks along the Trans-North China Orogen (TNCO) is controversial: one view suggests that it occurred at ~1.85 Ga (Zhao et al., 1998; Zhao et al., 2005; Zhao et al., 2012), whereas another view favors an older collision age of ~1.95 Ga (Qian et al., 2013; Qian et al., 2015; Qian and Wei 2016), and interprets the age of ~1.85 Ga to represent a separated orogenic event occurred along the northern margin of the NCC (Wei 2018; Qian et al., 2019). In addition, accretionary and collisional tectonics were also proposed for the NCC, including 2.6–2.5 Ga Atlantic-type passive margin on the western side of the Eastern Block, the ~2.5 Ga collision between the arc/accretionary prism and the Eastern Block, ~2.43 Ga amalgamation of Western Block and Eastern Block along the Central Orogenic Belt (COB, approximate TNCO), and the 2.3–1.9 Ga collision along the Inner Mongolia-North Hebei Orogenic Belt (IMNHO) at the north margin of the NCC (Kusky et al., 2016).

The early Precambrian East Hebei terrane, located in the northwestern of the Longgang Block, can be divided into six litho–tectonic units (**Figure 1B**) including the Taipingzhai ovoid-structural domain (I), Qian'an gneiss dome (II), Badaohe gneiss dome (III), Lulong–Shuangshanzi supracrustal belt (IV), Anziling gneiss dome (V) and Saheqiao linear-structural belt (VI), following Wu et al. (1998) and Wei (2018). There is near-vertical normal shear in the Shuangshanzi shear zone between the Anziling dome and the Lulong–Shuangshanzi supracrustal belt formed due to the upwelling of the dome with respect to the down-slipping of the belt (Liu et al., 2017; Zhao et al., 2021). Therefore, the terrane well preserves Archean unique dome–and–keel structure although later deformation marked by numerous NE-to NEE-striking shear zones in the Saheqiao linear-structural belt occurred (Liu and Yang 1994; Kusky et al., 2016; Zhao et al., 2021). As show at **Figure 1B**, the East Hebei terrane mainly consists of Neoarchean TTG gneisses, charnockites, potassic granites, and supracrustal rocks. The TTG gneisses and charnockites show magmatic ages of mostly 2.56–2.48 Ga with a peak at ~2.52 Ga (Liu et al., 1990; Wu and Geng 1991; Geng et al., 2006; Yang et al., 2008; Nutman et al., 2011; Guo et al., 2013; Bai et al., 2014; Bai et al., 2015; Yang et al., 2016a; Yang et al., 2016b), except for a few intrusions in the western margin of Qian'an gneiss dome that have older ages of 3.28–2.94 Ma (Nutman et al., 2011; Sun et al., 2016). They were subjected to amphibolite-to granulite-facies metamorphism at 2.53–2.47 Ga (Geng et al., 2006; Yang et al., 2008; Nutman et al., 2011; Bai et al., 2014; Bai et al., 2015). The supracrustal rocks, mainly comprising metasedimentary and metabasic rocks with a few banded iron formation and ultramafic interlayers (Geng et al., 2006; Polat et al., 2006), commonly occur as rafts within or as

FIGURE 2 | Field occurrence of mafic granulites. **(A,B)** Mafic granulites occurring as rafts or enclaves with clear or blurry boundaries within TTG rocks. **(C)** Mafic granulites with penetrative foliation. **(D)** Heterogeneous mafic granulites with diverse distributions of leucosomes.

belts between TTG gneiss domes (Wei 2018). Most of the metasedimentary rocks share similar protolith deposition ages of 2.53–2.50 Ga (Wan et al., 2015; Sun et al., 2016; Duan et al., 2017; Lu et al., 2017; Liu and Wei 2020), except for fuchsite-bearing quartzite that outcropped at Caozhuang and Luanxian areas having deposition age of >3.5 Ga (Liu et al., 1990; Nutman et al., 2011; Chu et al., 2016). The metabasic rocks were mostly dated to have protolith magmatic ages of 2.61–2.52 Ga with a few at ~2.90 Ga (Zhang et al., 2012; Guo et al., 2013; Fu et al., 2016; Liou et al., 2017). Ultramafic rocks, mostly including serpentinized peridotite, picritic amphibolites, and pyroxenite, are argued to be komatiites (Zhang et al., 1980), intra-oceanic suprasubduction zone ophiolitic rocks (Polat et al., 2006), or remnants of an enriched mantle plume (Wang et al., 2019). These supracrustal rocks were normally dated to have two groups of metamorphic ages at 2.53–2.47 Ga and 1.85–1.80 Ga as have mentioned in introduction (e.g., Yang and Wei 2017b; Lu and Wei 2020). The former episode of metamorphism is widely recorded in the whole East Hebei terrane, corresponding to amphibolite-to greenschist-facies metamorphic conditions in Lulong–Shuangshanzi supracrustal belt (Qi et al., 1999; Guo et al., 2013), amphibolite-facies condition of 10–11 kbar/780–800°C with clockwise P–T path in the Caozhuang area (Liu et al., 2020), and the granulite-facies (9.6–10.3 kbar/860–900°C) to UHT (9–10 kbar/>1,000°C) peak conditions with anticlockwise P–T paths in the western margin of Qian'an gneiss dome, Taipingzhai ovoid-structural domain and Saheqiao linear-structural belt (Kwan et al., 2016; Yang and Wei 2017a; Duan et al., 2017; Lu et al., 2017; Liu and Wei 2018; Lu and Wei 2020; Liu et al., 2021). By contrast, the second-episode metamorphism is locally recognized in the northern part of the terrane, mostly in the Saheqiao linear-structural belt and the Taipingzhai ovoid-structural domain, and dominated by HP granulite-facies metamorphism as have been mentioned in introduction (Duan et al., 2017; Yang and Wei 2017a; Lu and Wei 2020). In addition, there are mafic dykes crosscutting the foliation of Archean TTG gneisses and supracrustal rocks in the Saheqiao linear-structural belt and the Taipingzhai ovoid-structural domain (Chen 1990; Song 1990), and proposed to have experienced HP granulite-facies metamorphism in the later overprinting metamorphism (Duan et al., 2015).

In this study, mafic granulites were collected from the Malanyu, Saheqiao, and Taipingzhai areas. The sample locations are shown on **Figure 1B**. These granulites occur as rafts with clear or blurry boundaries within TTG rocks (**Figures 2A,B**). Most of them have weak or penetrative foliations (**Figure 2C**) and are heterogeneous with the diverse distributions of leucosomes (**Figure 2D**).

3 PETROLOGICAL ANALYSES

3.1 Bulk-Rock Compositions

Among the selected samples, two-pyroxene granulite (JD15120) was collected from the Taipingzhai ovoid-structural domain,

TABLE 1 | Bulk-rock compositions of samples in this study.

Sample	Type	ICP-OES whole rock composition (wt%)										
		SiO_2	TiO_2	Al_2O_3	TFe_2O_3	MnO	MgO	CaO	Na_2O	K_2O	P_2O_5	LOI
JD15120	Two-pyroxene granulite	48.76	0.76	14.06	12.56	0.20	7.90	10.68	2.88	0.90	0.11	0.47
YC8-43	Garnet two-pyroxene granulite	47.74	0.92	13.41	14.14	0.23	7.51	12.64	2.05	0.25	0.08	0.22
JD1546	Garnet clinopyroxene granulite	47.41	0.87	12.02	16.01	0.21	6.86	11.60	2.19	0.81	0.14	1.21
		Normalized molar proportions used for phase equilibria modeling (mole %)										
Sample	**Figure**	H_2O	SiO_2	Al_2O_3	CaO	MgO	FeO	K_2O	Na_2O	TiO_2	O	$Mg^\#$
JD15120	**Figure 6A**	2.51	48.65	8.45	10.84	12.16	12.16	0.69	2.79	0.85	0.91	50
YC8-43	**Figure 7A**	0.70	50.36	8.51	13.20	12.05	11.22	0.18	2.10	0.68	1.00	52
YC8-43 (overprinting)	**Figure 7B**	0.95	50.50	7.93	12.11	10.33	14.09	0.20	1.56	0.84	1.48	42
JD1546	**Figure 8**	1.20	50.23	8.14	13.22	11.15	12.84	0.18	1.64	0.70	0.70	46

Wt%, major element oxides in weight percent; LOI, loss on ignition; mole %, major element oxides in mole percent; $Mg^\#$ *= MgO/(MgO + FeO).*

TABLE 2 | Selected microprobe analyses for sample JD15120.

Mineral	Cpx-1	Opx-1	Amp-1	Pl-1-c	Pl-1-r	Cpx-2	Opx-2	Amp-2	Pl-2
SiO_2	52.25	51.63	42.13	59.06	60.03	52.19	50.97	41.67	59.05
TiO_2	0.08	–	1.59	0.03	0.02	0.14	0.06	1.22	0.04
Al_2O_3	2.21	1.28	11.81	25.03	24.95	2.02	1.40	12.33	24.55
Cr_2O_3	–	0.02	0.03	–	–	–	0.03	0.04	–
Fe2O3	0.47	1.15	1.53	0.18	0.40	1.88	0.79	3.57	1.86
FeO	9.75	25.06	12.98	–	–	7.28	25.34	11.74	–
MnO	0.82	2.45	0.23	–	–	0.35	1.22	0.21	–
MgO	12.28	18.77	11.16	–	0.03	13.08	18.99	11.09	0.10
CaO	21.43	0.46	11.52	8.03	7.30	22.65	0.31	10.83	7.10
Na_2O	0.56	0.03	1.56	6.71	7.17	0.54	0.04	1.38	6.96
K_2O	–	–	1.45	0.31	0.33	0.02	–	1.53	0.29
Total	99.81	100.75	95.84	99.35	100.24	99.97	99.07	95.25	99.95
O	6	6	23	8	8	6	6	23	8
Si	1.963	1.956	6.385	2.655	2.672	1.945	1.956	6.326	2.649
Ti	–	–	0.181	–	–	0.004	0.002	0.139	–
Al	0.098	0.057	2.110	1.327	1.310	0.089	0.063	2.207	1.298
Cr	–	–	0.004	–	–	–	–	0.005	–
Fe^{3+}	0.013	0.033	0.175	0.006	0.013	0.053	0.023	0.408	0.063
Fe^{2+}	0.306	0.794	1.645	–	–	0.227	0.813	1.490	–
Mn	0.026	0.079	0.030	–	–	0.011	0.040	0.027	–
Mg	0.688	1.060	2.521	–	0.002	0.727	1.086	2.509	0.007
Ca	0.863	0.019	1.871	0.387	0.348	0.905	0.013	1.762	0.341
Na	0.041	0.002	0.458	0.585	0.619	0.039	0.003	0.406	0.605
K	0.000	0.000	0.280	0.018	0.019	0.001	0.000	0.296	0.017
X(phase)	0.69	0.57	0.61	0.39	0.35	0.76	0.57	0.63	0.35

X(Cpx) = X(Opx) = X(Amp) = Mg/(Fe^{2+}+Mg); X(Pl) = X_{An} = Ca/(Ca + Na + K); -c, grain core; -r, grain rim. "–" means that the content is below the detection limit. The mineral formulas were calculated with the program AX (Holland; http://www.esc.cam.ac.uk/astaff/holland/ax.html).

while the garnet-bearing two-pyroxene granulite (YC8-43) and clinopyroxene granulite (JD1546) were from the Saheqiao and Malanyu areas, respectively, in the Saheqiao linear-structural belt (**Figure 1B**; Yang and Wei 2017a). Their bulk-rock compositions, being analyzed using a Leeman Prodigy inductively coupled the plasma-optical emission spectroscopy (ICP–OES) system with high-dispersion Echelle optics at China University of Geoscience (Beijing), are presented in **Table 1**. The three samples share similar compositions with SiO_2 of 47.41–48.76 wt%, MgO of 6.86–7.90 wt%, total Fe_2O_3 of 12.56–16.01 wt%, CaO of 10.68–12.64 wt%, and $Mg^\#$ of 46–52.

3.2 Petrography and Mineral Compositions

Mineral compositions were analyzed at the Laboratory of Orogenic Belt and Crustal Evolution of Peking University, China, using a JXA-8100 electron microprobe analyzer (EPM; JEOL). The analyses were conducted under operating conditions of 15 KV accelerating voltage and 10 nA probe current with a

TABLE 3 | Selected microprobe analyses for samples YC8-43 and JD1546.

Mineral	**YC8-43**										**JD1546**					
	Cpx-1	**Opx**	**Amp**	**Pl-1-c**	**Pl-1-r**	**Cpx-2**	**Grt-c**	**Grt-r**	**Pl-2-c**	**Pl-2-r**	**Cpx**	**Grt-c**	**Grt-r**	**Amp**	**Pl-c**	**Pl-r**
SiO_2	51.01	51.29	41.59	54.31	57.23	52.05	36.83	38.72	61.24	59.09	51.99	38.36	37.69	42.23	61.60	60.03
TiO_2	0.22	0.03	2.29	0.06	–	0.20	–	0.09	0.07	0.05	0.25	0.06	0.10	2.07	–	–
Al_2O_3	3.21	2.33	12.61	29.59	27.46	2.72	20.43	20.09	24.35	25.03	3.63	20.30	20.32	12.42	24.42	25.73
Cr_2O_3	–	0.02	0.03	–	–	0.17	–	0.06	0.04	0.04	0.04	–	–	0.02	0.04	0.03
Fe2O3	2.89	1.75	1.89	0.17	0.14	1.52	4.72	0.84	0.09	0.39	1.71	2.17	3.00	2.10	0.09	0.16
FeO	9.07	23.34	13.32	–	–	8.06	21.02	25.47	–	–	9.67	23.29	23.91	13.50	–	–
MnO	0.26	1.08	0.04	–	–	0.17	1.12	1.23	–	0.05	0.09	1.21	1.26	0.09	0.04	0.03
MgO	12.24	20.26	11.22	–	–	12.34	5.45	5.81	0.02	0.05	11.83	5.11	5.73	11.11	–	–
CaO	20.41	0.56	11.58	12.03	9.58	21.90	9.50	7.22	5.97	6.96	20.82	9.47	7.35	11.47	5.79	7.05
Na_2O	0.84	0.02	1.69	4.64	6.04	0.89	–	–	8.44	7.61	1.05	0.03	0.06	1.61	8.47	7.43
K_2O	0.00	0.00	1.71	0.24	0.27	–	–	0.02	0.25	0.27	–	–	0.02	1.72	0.30	0.21
Total	99.86	100.50	97.78	101.04	100.74	99.87	98.61	99.46	100.47	99.54	100.91	99.79	99.14	98.13	100.77	100.67
O	6	6	23	8	8	6	12	12	8	8	6	12	12	23	8	8
Si	1.913	1.924	6.206	2.430	2.551	1.943	2.909	3.040	2.713	2.654	1.927	3.000	2.968	6.274	2.720	2.658
Ti	0.006	–	0.257	–	–	0.006	–	0.005	0.002	0.002	0.007	0.004	0.006	0.231	–	–
Al	0.142	0.103	2.218	1.561	1.443	0.120	1.902	1.859	1.272	1.325	0.159	1.871	1.886	2.175	1.271	1.343
Cr	–	–	0.004	–	–	0.005	–	0.004	–	–	–	–	–	0.002	–	–
Fe^{3+}	0.081	0.049	0.212	0.006	0.005	0.042	0.279	0.049	0.003	0.013	0.048	0.128	0.178	0.235	0.003	0.005
Fe^{2+}	0.284	0.732	1.662	–	–	0.252	1.389	1.672	–	–	0.300	1.523	1.575	1.677	–	–
Mn	0.008	0.034	0.005	–	–	0.005	0.075	0.082	–	0.002	0.003	0.080	0.084	0.011	–	–
Mg	0.684	1.132	2.495	–	–	0.687	0.641	0.680	0.001	0.003	0.653	0.596	0.672	2.460	–	–
Ca	0.820	0.023	1.852	0.577	0.457	0.876	0.804	0.607	0.283	0.335	0.827	0.793	0.620	1.826	0.274	0.334
Na	0.061	0.002	0.489	0.403	0.522	0.064	–	–	0.725	0.663	0.075	0.005	0.009	0.464	0.725	0.638
K	0.000	0.000	0.326	0.014	0.015	–	–	0.002	0.014	0.015	–	–	0.002	0.326	0.017	0.012
X(phase)	0.71	0.61	0.60	0.58	0.46	0.73	0.22	0.22	0.28	0.33	0.69	0.20	0.23	0.59	0.27	0.34
Y(phase)							0.28	0.20				0.27	0.21			

X(Grt) = X_{Py} = $Mg/(Fe^{2+}+Mg + Ca + Mn)$; Y(Grt) = X_{Grs} = $Ca/(Fe^{2+}+Mg + Ca + Mn)$; *others are as in* ***Table 2***.

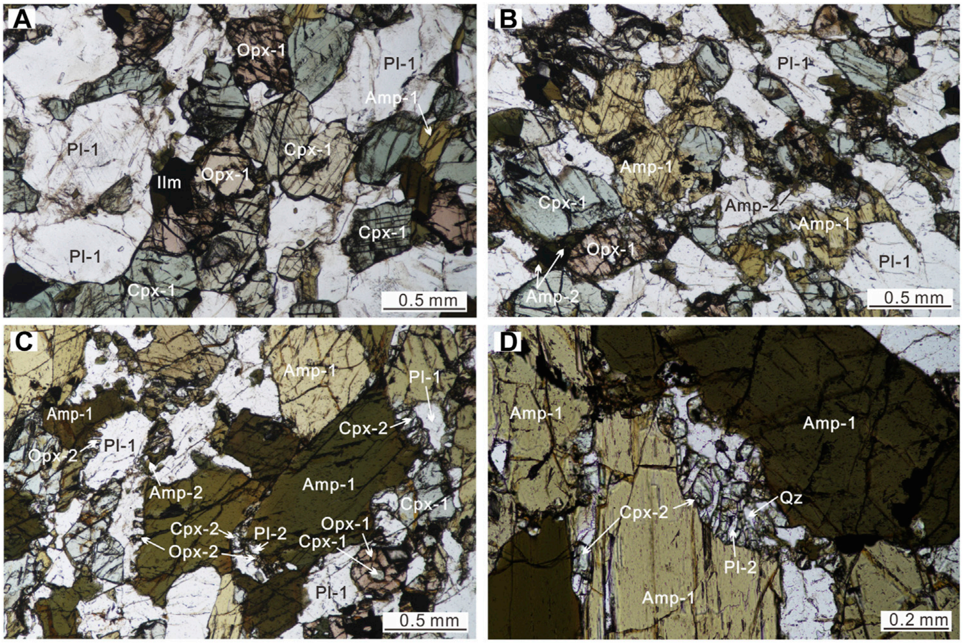

FIGURE 3 | Photomicrographs of sample JD15120. **(A,B)** Coexistence of medium-grained Cpx-1, Opx-1, Pl-1, Amp-1, and ilmenite. **(C,D)** Vermicular minerals of Cpx-2, Opx-2, Amp-2, Pl-2, and quartz along the margin of Amp-1 and Pl-1.

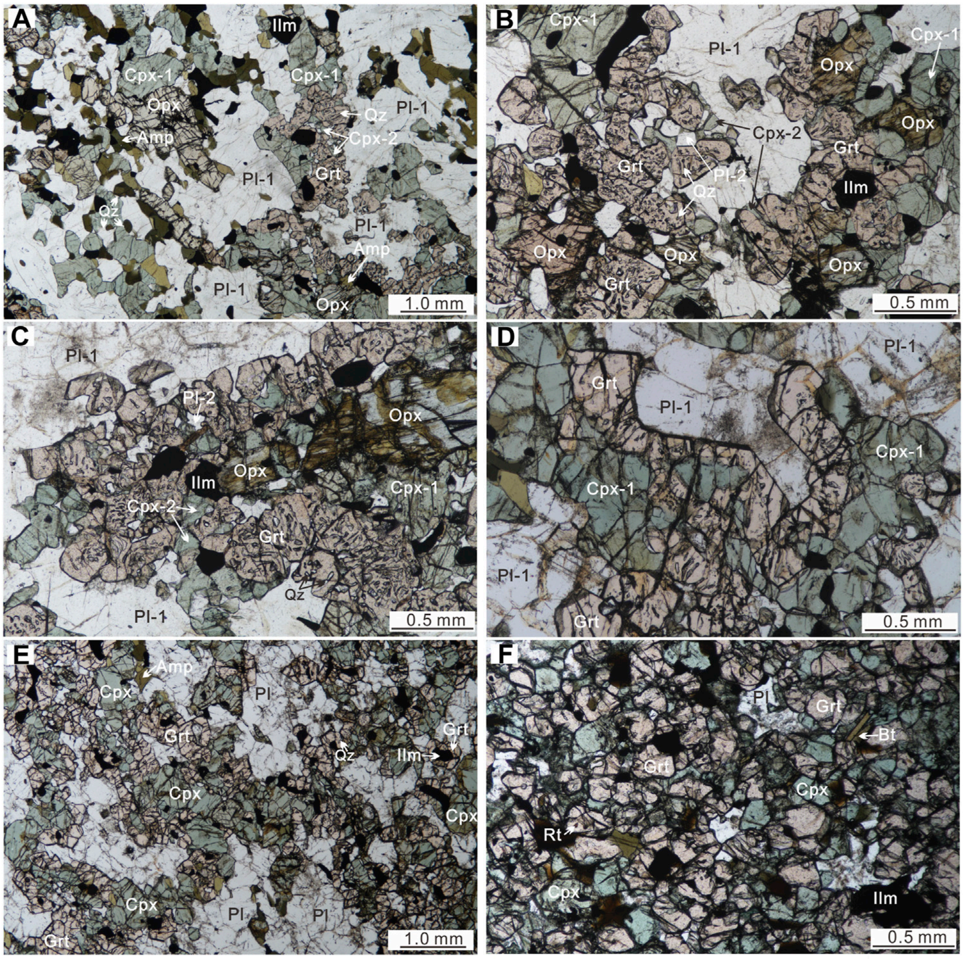

FIGURE 4 | Photomicrographs of samples YC8-43 and JD1546: **(A)** Large-scale photograph showing mineral relations that medium-grained orthopyroxene, Cpx-1, Pl-1, and amphibole are overprinted by fine-grained garnet, Cpx-2, Pl-2, and quartz in YC8-43; **(B,C)** poikilitic garnet with worm-like quartz inclusions occurring with fine-grained Cpx-2 and Pl-2 around medium-grained Cpx-1 and orthopyroxene in YC8-43; **(D)** garnet occurring as "red-eye pocket" separating Cpx-1 from Pl-1 in YC8-43; and **(E,F)** photomicrographs of the sample JD1546 showing the coexistence of fine-grained garnet, clinopyroxene, amphibole, and plagioclase with minor amounts of quartz and biotite.

beam diameter of 2 μm. Natural and synthetic minerals of the SPI Company were used for standardization. Representative mineral analyses are listed in **Tables 2**, **3**. Photomicrographs are shown in **Figures 3**, **4**.

Sample JD15120 is a two-pyroxene granulite with a weak foliation, comprising mostly clinopyroxene (25 vol%), orthopyroxene (15 vol%), amphibole (27 vol%), plagioclase (30 vol%), and minor amounts of biotite, quartz, and ilmenite. It shows overall equigranular texture, where the fine-to medium-grained (0.2–1.0 mm across) clinopyroxene, orthopyroxene, amphibole, and plagioclase directly contact with each other (hereafter Cpx-1, Opx-1, Amp-1, and Pl-1, respectively) (**Figures 3A,B**). Amp-1 can also occur surrounding or replacing clinopyroxene at rims, suggesting later growth (**Figure 3B**). Occasionally, there are vermiform minerals of <0.1 mm, including clinopyroxene, orthopyroxene, amphibole, and plagioclase (hereafter Cpx-2, Opx-2, Amp-2, and Pl-2 respectively), occurring as coronae around Amp-1 or along the boundary between Amp-1 and Pl-1 (**Figures 3C,D**). Clinopyroxene (Cpx-1 and Cpx-2) shows similar diopsidic compositions with En [= Mg/(Ca + Mg + Fe^{2+})] of 0.36–0.39, Fs [= Fe^{2+}/(Ca + Mg + Fe^{2+})] of 0.12–0.16, Wo [= Ca/(Ca + Mg + Fe^{2+})] of 0.46–0.49, and X_{Mg} [= Mg/(Mg + Fe^{2+})] of 0.68–0.76 (Morimoto 1988), but Cpx-1 occasionally has exsolution lamellae of ilmenite in the core. Orthopyroxene (both Opx-1 and Opx-2) has composition of hypersthene with En of 0.52–0.57, Fs of 0.42–0.47, Wo of ~0.01, and X_{Mg} of 0.52–0.67 (Morimoto 1988). Amphibole (Amp-1 and Amp-2) has similar composition of pargasite involving K_2O of 1.45–1.82 wt%, Ca_B = 1.76–1.89, $(Na + K)_A$ = 0.56–0.73, Si = 6.29–6.39, and X_{Mg} = 0.52–0.63 (Leake et al., 2003), but higher Ti of 0.18–0.28 p. f.u. in Amp-1 and lower Ti of 0.10–0.14 p. f.u. in Amp-2. Plagioclase commonly has cuspate boundaries. Pl-1 has chemical zonation with a constant X_{An} = Ca/(Ca + Na + K)] of 0.39–0.41 in the core but outward decreasing to 0.34–0.36 in the rim (**Figure 5A**), while Pl-2 shows slightly lower X_{An} of 0.35–0.39. A few biotite flakes

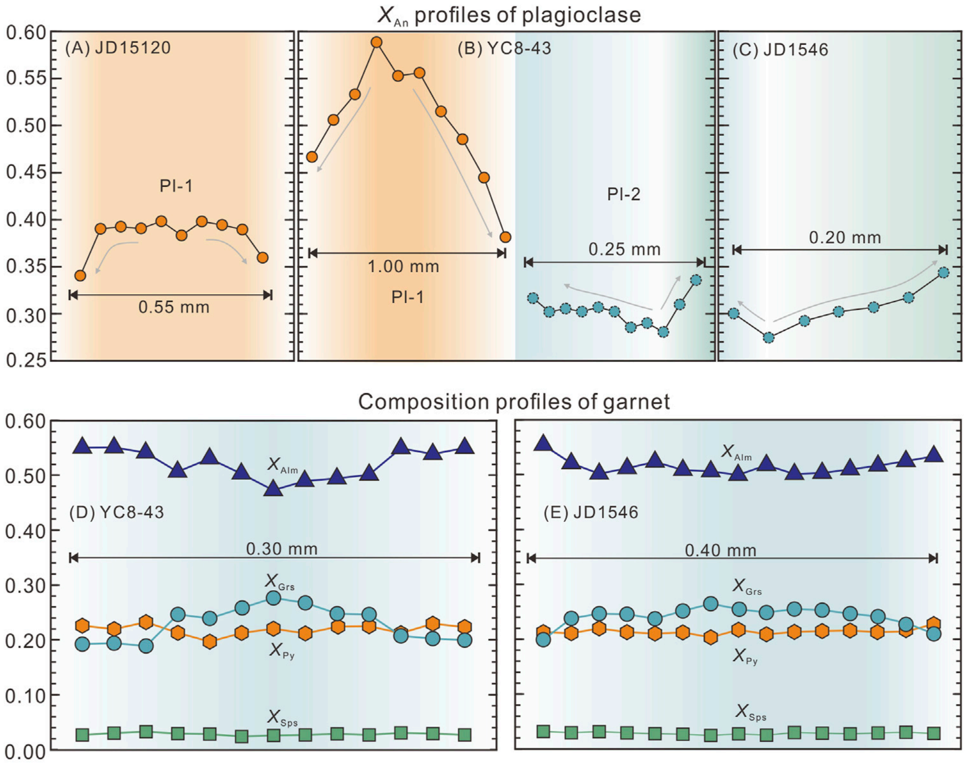

FIGURE 5 | Composition zoning profiles for plagioclase in JD15120 **(A)**, YC8-43 **(B)**, and JD1546 **(C)**, and for garnet in YC8-43 **(D)** and JD1546 **(E)**.

occur around Amp-1 or Cpx-1, suggesting their later growth. Additionally, ilmenite occurs as anhedral grains, and minor amounts of quartz exhibit as irregular shapes coexisting with the rim of Pl-1, or as vermiform grains in coronae. On the basis of the mineral relations and compositions, two generations of assemblage can be inferred for the sample. The first generation comprises the fine-to-medium-grained minerals that include the peak and final stages. The peak assemblage is featured with the coexistence of Cpx-1, Opx-1, Amp-1, Pl-1, and ilmenite, while the final assemblage is characterized by the re-growth of Amp-1 and Pl-1 and the emergence of biotite and quartz. The second generation of assemblage consists of the vermiform minerals of Cpx-2, Opx-2, Amp-2, Pl-2, and Qz in the coronae mostly around Amp-1.

Sample YC8-43 is a garnet-bearing two-pyroxene granulite, comprising clinopyroxene (20 vol%), orthopyroxene (17 vol%), garnet (15 vol%), amphibole (15 vol%), plagioclase (30 vol%), ilmenite (3 vol%), and minor amounts of quartz, biotite, and rutile (**Figures 4A–D**). Clinopyroxene occur either as subhedral to anhedral grains of 0.3–1.2 mm in contact with orthopyroxene (hereafter Cpx-1), or as irregular grains of <0.2 mm coexisting with garnet (hereafter Cpx-2). Both of the two types have similar diopsidic compositions with En of 0.36–0.38, Fs of 0.14–0.17, Wo of 0.46–0.48, and X_{Mg} of 0.67–0.73 (Morimoto 1988). Orthopyroxene shows as anhedral grains of 0.3–1.8 mm and has hypersthene compositions, containing En of 0.60–0.63, Fs of 0.37–0.39, Wo of ~0.01, and X_{Mg} of 0.61–0.63 (Morimoto 1988). Plagioclase is subdivided into tabular grains of 0.3–1.5 mm in diameter (Pl-1) or irregular grains of <0.3 mm (Pl-2). Pl-1 mostly contacts to Cpx-1, orthopyroxene and amphibole, but occasionally be separated from pyroxenes by garnet (**Figures 4C,D**). It exhibits core-to-rim zoning with X_{An} decreasing from 0.56 to 0.59 in the core to 0.38–0.47 in the rim (**Figure 5B**). Pl-2 occurs with garnet and Cpx-2, exhibiting core to rim zoning with increasing X_{An} from 0.28 to 0.34 (**Figure 5B**). Garnet is 0.2–0.5 mm poikilitic grains with numerous quartz inclusions (**Figures 4B–D**). It occurs alone or with Cpx-2 surrounding Cpx-1 and/or orthopyroxene, forming "red-eye socket" textures to separate Cpx-1 and orthopyroxene from Pl-1 (**Figures 4C,D**; Wei et al., 2014). It has almost constant X_{Py} [= Mg/(Ca + Mg + Fe^{2+}+Mn), defined accordingly for other components] mostly of 0.21–0.23 (with a maximum of 0.25) and X_{Sps} of ~0.03, but shows core-to-rim increasing X_{Alm} (0.48→0.56) and decreasing X_{Grs} (0.28→0.20) (**Figure 5D**). Amphibole is mostly anhedral grains with sizes of 0.2–0.8 mm directly contacting to pyroxenes, or irregular shapes surrounding Cpx-1, showing later growth. It has pargasite compositions (Leake et al., 2003) involving K_2O of 1.53–1.71 wt%, Ca_B = 1.83–1.85, $(Na + K)_A$ = 0.60–0.73, Si = 6.21–6.37, Ti = 0.24–0.26 p. f.u. and X_{Mg} = 0.55–0.60 (Yang and Wei 2017a). Biotite occurs around amphibole, indicating their later growth. Ilmenite is irregular grains among minerals or as rounded grains within Cpx-1. It can also be included in garnet. Minor amounts of rutile occur as inclusions in garnet. Quartz occurs as interstitial grains among minerals, or as vermicular inclusions in garnet. Based on petrological observations and mineral compositions, two generations of mineral assemblage can be inferred. The first generation is recognized to involve final and peak stages. The peak stage is marked by the coexistence of Cpx-1, orthopyroxene, Pl-1, amphibole, and ilmenite, while the final is featured with the growth of biotite and quartz. The second generation is characterized by the coexistence of poikilitic garnet, Cpx-2, Pl-2, quartz, and rutile.

Sample JD1546 is a garnet-clinopyroxene granulite, consisting of clinopyroxene (30 vol%), garnet (23 vol%), amphibole (17 vol %), plagioclase (28 vol%), ilmenite (2 vol%), and minor amounts of quartz and biotite (**Figures 4E,F**). The sample has an equigranular texture with grain sizes mostly of 0.1–0.5 mm, except for a few larger-sized clinopyroxene grains of 1.0–1.5 mm. Clinopyroxene has diopsidic compositions with En of 0.37–0.40, Fs of 0.12–0.17, Wo of 0.43–0.50, and X_{Mg} of 0.69–0.77 (Morimoto 1988). Plagioclase is anhedral, and exhibits core-to-rim zoning with increasing X_{An} from 0.27 to 0.35 (**Figure 5C**). Garnet occurs normally with clinopyroxene or as "red-eye socket" textures around clinopyroxene. It exhibits core-to-rim decreasing X_{Grs} of 0.27→0.21 and increasing X_{Alm} of 0.50→0.55, but contains almost constant X_{Py} of 0.20–0.23 and X_{Sps} of ~0.03 (**Figure 5E**). Amphibole is mostly irregular grains with cuspate boundaries, and has pargasite compositions with K_2O of 1.72–1.92 wt%, $Ca_B = 1.78–1.83$, $(Na + K)_A = 0.63–0.68$, Si = 6.16–6.27, Ti = 0.20–0.23 p. f.u., and X_{Mg} = 0.59–0.63 (Leake et al., 2003). Minor amounts of biotite display as irregular flakes or sticks around amphibole or clinopyroxene, suggesting their later formation. Quartz mostly occurs as interstitial grains among other minerals. Ilmenite and rutile occur as irregular grains or as inclusions in garnet. Based on the aforementioned textural relations, the peak assemblage is inferred to involve clinopyroxene, garnet, amphibole, plagioclase, and rutile, and the later growth of amphibole and biotite may represent the post-peak evolution. Presence of the larger-sized clinopyroxene might represent the relicts from an earlier metamorphism.

4 METAMORPHIC *P–T* CONDITIONS

Pseudosection modeling for these samples was conducted using THERMOCALC 3.50 and the internally consistent thermodynamic dataset of Holland and Powell (2011) update (ds62) in the system NCKFMASHTO ($Na_2O–CaO–K_2O–FeO–MgO–Al_2O_3–SiO_2–H_2O–TiO_2–Fe_2O_3$). Mixing models are those presented for garnet, orthopyroxene, and biotite (White et al., 2014), melt, clinopyroxene, and amphibole (Green et al., 2016), plagioclase (Holland and Powell 2003), and ilmenite (White et al., 2000). Among these models, amphibole model "hb" and clinopyroxene model "aug" were used because they are suit for clinoamphibole including pargasite, and for high-temperature clinopyroxene, respectively. As JD15120 and JD1546 are overall homogeneous, the analyzed bulk-rock compositions were used for the phase equilibria modeling. Whereas for YC8-43, the first generation of assemblages was modeled using the analyzed composition, and the second generation of assemblages was calculated based on an effective composition, generated on the basis of mass balance by integrating modal abundance and compositions of relevant minerals together (Carson et al., 1999). The H_2O contents and O (Fe_2O_3) values used in the modeling was defined using *T–M* (H_2O) and *T–M*(O) diagrams (e.g., Korhonen et al., 2011; Korhonen et al., 2012). Compositions used for modeling are presented in **Table 1**.

4.1 Sample JD15120

The *P–T* pseudosection for sample JD15120 was drawn within a *P–T* range of 4–10 kbar and 700–1,100°C (**Figure 6A**), contoured with isopleths of X_{An} in plagioclase and Ti in amphibole. The fluid-absent solidus occurs at temperatures of 830–900°C. The inferred peak assemblage involving medium-grained Cpx-1, Opx-1, Pl-1, Amph-1, and ilmenite is constrained under a large *P–T* condition of <8.5 kbar/900–1,010°C, limited by the garnet-in curve on the high-*P* limit, and biotite-in and orthopyroxene-out curves on the low- and high-*T* limits. The maximum X_{An} of 0.39–0.41 in the core of Pl-1 is plotted in the peak field and constrains a precise peak condition of 7.5–8.5 kbar/940–960°C with a temperature uncertainty of ~6°C (two-sigma level) calculated using THERMOCALC. It needs to be mentioned that this uncertainty should be considered as a minimum because it is propagated from the uncertainty on the enthalpy alone and does not include other sources of uncertainty. The post-peak decompressional cooling is driven by the reaction Cpx + Ilm + Liq = Opx + Pl + Amp + Bt, responsible for later growth of biotite and Amp-1, and also the outward decreasing X_{An} in Pl-1. The measured maximum Ti of 0.28 in Amp-1 is plotted in the biotite-present field, yielding temperatures of >910°C, whereas the lower Ti values were plotted in the sub-solidus fields. However, the observed final assemblage marked by the presence of quartz does not occur in **Figure 6A**, probably because the residual melts that produced the final assemblage were locally segregated and not completely equilibrated with other minerals. Therefore, we calculated a *T–M* (melt) pseudosection at 7 kbar by adding more melts in the final mineral assemblage on **Figure 6A**. As shown in **Figure 6B**, the fluid-absent solidus occurs at lower temperatures as the melt modes increase, and the quartz-present final assemblage appears at ~810°C on the solidus with the melt modes of 10–20 mol%. This field is well consistent with the measured X_{An} of 0.34–0.36 in the rim of Pl-1. Moreover, the measured lower Ti values in amphibole can also plot in the suprasolidus fields. Therefore, a post-peak decompressional cooling process from the peak condition of 7.5–8.5 kbar/940–960°C to the final condition of ~7 kbar/~810°C can be well constrained for JD15120.

4.2 Sample YC8-43

The *P–T* pseudosection for the first-generation of assemblages in YC8-43 was drawn within a *P–T* range of 4–10 kbar and 750–1,000°C (**Figure 7A**), contoured with isopleths of X_{An} in plagioclase and Ti in amphibole. The fluid-absent solidus occurs at temperatures of 860–890°C. The observed peak assemblage involving medium-grained Cpx-1, orthopyroxene, Pl-1, amphibole, and ilmenite is constrained under a large *P–T*

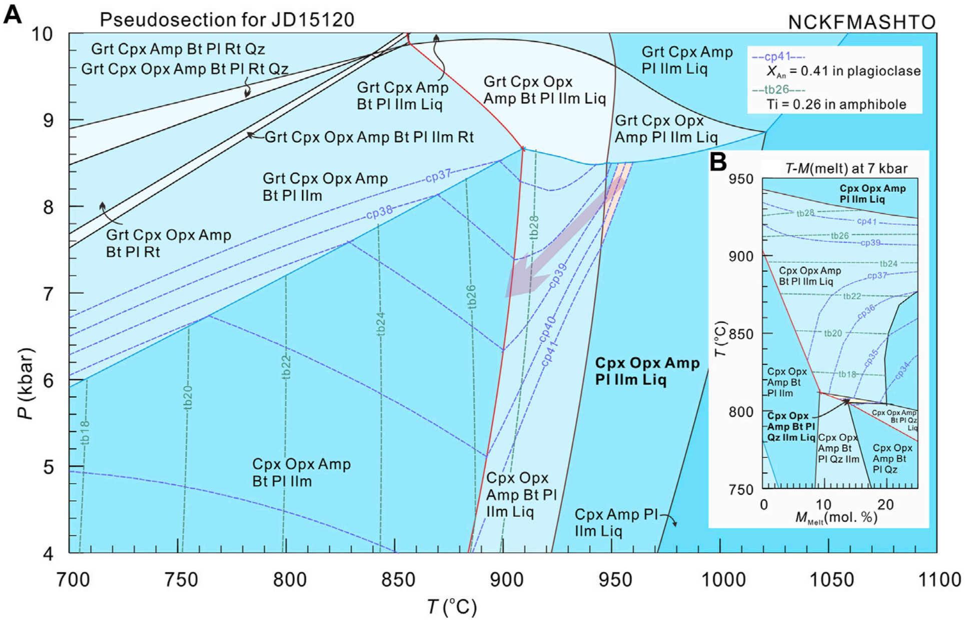

FIGURE 6 | (A) *P–T* pseudosection with proposed *P–T* path for sample JD15120 in the system NCKFMASHTO. Mineral abbreviations follow Whitney and Evans (2010). Composition used for modeling the *P–T* pseudosection is listed in **Table 1**. **(B)** *T–M* (melt) diagram at 7 kbar. The melt composition was defined at 7 kbar and 904°C in **Figure 6A**, and the composition at *M* (melt) = 0 equals to the composition for **Figure 6A**.

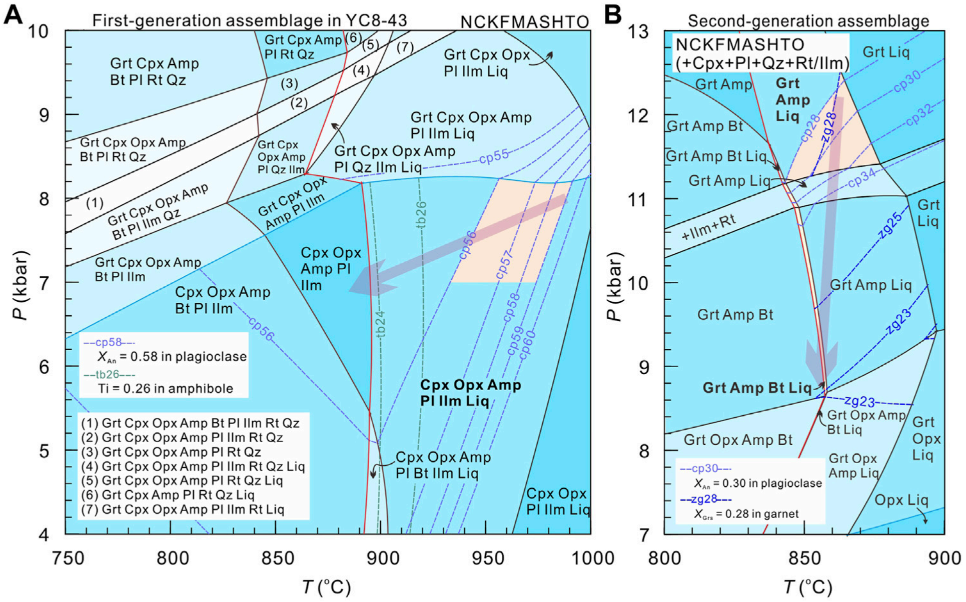

FIGURE 7 | *P–T* pseudosection with the proposed *P–T* path for the first-episode metamorphism **(A)** and second-episode metamorphism **(B)** in the sample YC8-43. Others are same as **Figure 6A**.

condition of <8 kbar/870–1,000°C, limited by the garnet-in curve on the high-*P* limit, and the liquid-out and amphibole-out curves on the low- and high-*T* limits. The measured maximum X_{An} of 0.59–0.56 in the core of Pl-1 is plotted in the peak assemblage field, and yields a peak temperature of 950–990°C at 8 kbar with the uncertainty of ~6°C (two-sigma level). The post-peak decompression cooling is dominated by the reaction of Cpx + Ilm + Liq = Opx + Pl + Amp, being responsible for the observed re-growth of amphibole and the core-to-rim decreasing X_{An} in Pl-1. The measured Ti of 0.24–0.26 in amphibole is consistent with

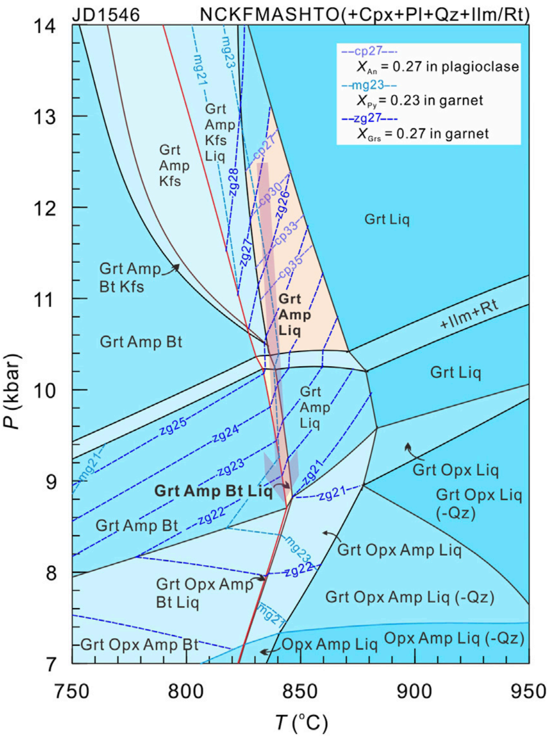

FIGURE 8 | *P–T* pseudosection with the proposed *P–T* path for the sample JD1546. Others are same as **Figure 6A**.

the cooling evolution. Similar to JD15120, the quartz-present final assemblage and the measured X_{An} of 0.38–0.47 in the rim of Pl-1 do not occur in the pseudosection, as a result of local segregation of residual melts. This can be solved using an alternative pseudosection as in **Figure 6B**.

The second-generation of assemblages is modeled over a *P–T* range of 7–13 kbar and 800–900°C (**Figure 7B**), countered with the isopleths of X_{Grs} in garnet and X_{An} in plagioclase. The inferred peak assemblage including garnet, Cpx-2, Pl-2, amphibole, quartz, and rutile occurs within a large *P–T* of >11 kbar/810–880°C, constrained by the rutile-out curve in the low-*P* limit, and the liquid-out and amphibole-out curves in the low- and high-*T* limits. The measured maximum X_{Grs} of 0.28 in the garnet core and the minimum X_{An} of 0.28 in the Pl-2 core yield a precise peak condition of ~12 kbar/860°C within the peak assemblage field with uncertainties of ~1.6 kbar and ~22°C (two-sigma level). The post-peak decompression is dominated by the reaction of Grt + Cpx + Qz + Liq = Amp + Pl, responsible for the formation of outward increasing X_{An} in Pl-2 but decreasing X_{Grs} in garnet.

4.3 Sample JD1546

The *P–T* pseudosection for the sample JD1546 was calculated within a *P–T* range of 7–14 kbar and 750–950°C (**Figure 8**), contoured with isopleths of X_{Py} and X_{Grs} in garnet and X_{An} in plagioclase. The observed peak assemblage involving garnet, clinopyroxene, amphibole, plagioclase, and rutile is constrained under a *P–T* condition of >10.5 kbar/820–870°C, constrained by the rutile-out curve on the low-*P* limit, and the K-feldspar-in and amphibole-out curves on the low- and high-*T* limits. The measured maximum X_{Grs} of 0.27 in the core of garnet and the minimum X_{An} of 0.27 in the core of plagioclase are plotted to yield a precise peak condition at ~12.6 kbar and ~835°C in the peak assemblage field with uncertainties of ~0.6 kbar and ~20°C (two-sigma level). This is almost consistent with the temperature defined by the measured maximum X_{Py} of 0.23 in garnet. The post-peak decompression is dominated by the reaction of Grt + Cpx + Qz + Liq = Amp + Pl ± Bt, in accordance with the outward increasing X_{An} in plagioclase but decreasing X_{Grs} in garnet, and also responsible for the later growth of amphibole and biotite.

5 ZIRCON DATING

Zircon grains from the samples JD15120 (two-pyroxene granulite) and JD1546 (garnet clinopyroxene granulite) were separated by conventional heavy liquid and magnetic separation followed by hand-picking under a binocular microscope. Selected grains were mounted in an epoxy resin, polished down to expose the grain centers, photographed in transmitted and reflected light, and imaged using cathode luminescence (CL). CL imaging was conducted at Peking University on a FEI PHILIPS XL30 SFEG SEM with 2-min scanning time under the condition of 15 kV and 120 μA. The zircon LA–ICP–MS U–Pb isotopic analyses were performed at Peking University using an Agilent 7500c ICP-MS system connected with a 193 nm ArF excimer laser system (COMPexPro 102) with the automatic positioning system. Zircon 91,500 was used as the standard and the standard silicate glass NIST was used to optimize the machine (Wiedenbeck et al., 1995; Wiedenbeck et al., 2004). The concentration of U, Th, and Pb elements were calibrated using ^{29}Si as an internal calibrant and NIST 610 as an external reference standard. ^{207}Pb/^{206}Pb, ^{206}Pb/^{238}U, and ^{207}Pb/^{235}U ratios and apparent ages were calculated using the GLITTER 4.4 (Van Achterbergh et al., 2001; Griffin 2008). The age calculations and plotting of concordia diagrams were carried out using ISOPLOT 3.0 (Ludwig 2003). Analyses described as "concordant" refer to <10% discordance. The results are presented in **Supplementary Tables S1, S2**.

Zircon grains in the sample JD15120 are mostly oval or round in shape and have sizes of 30–150 μm with length/width ratios of 1:1–2:1 (**Figure 9A**). Two groups can be recognized based on their appearances on CL images. Group-1 grains are mostly dim in their luminescence and have a sector, patchy, or fir-tree zones. Group-2 zircons have clear core–rim structures, where the grain cores show similar features with the group-1 zircons, and the rims, mostly 3–20 μm across, are gray in color and have structureless zones. We have conducted only 25 analyses on 25 group-1 grains or group-2 zircon cores, as the rims of group-2 zircons are much smaller than the diameter of the beam spot. The results yield apparent ^{207}Pb/^{206}Pb ages from 2529 ± 31 to 2447 ± 53 Ma. Most of the analyses were plotted on or close to the concordia curve in **Figure 9B** and define an upper intersect age of 2490 ± 19 Ma (MSWD = 0.21), with a weighted

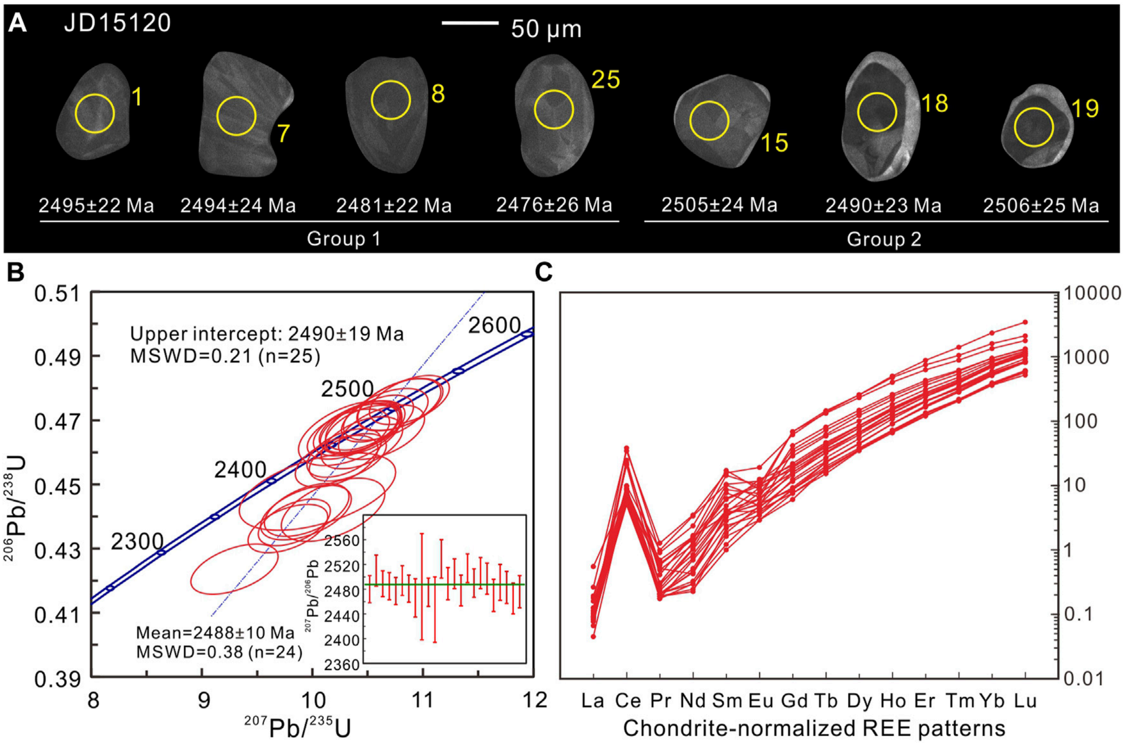

FIGURE 9 | (A) Cathodoluminescence (CL) images of selected zircons from the sample JD15120. Solid circles show the inner positions of LA–ICP–MS analytical sites with their identification numbers as in **Supplementary Table S1**. **(B)** U–Pb isotopic age distributions of analyzed zircons. **(C)** Chondrite-normalized REE patterns (Sun and McDonough 1989).

mean age of 2488 ± 10 Ma (MSWD = 0.38). These zircons were analyzed to have the Th/U ratios of mostly 0.11–1.49, with only one outlier of 3.18. They show left inclined REE patterns with high $(Lu/Gd)_N$ of 25.97–100.00, and exhibit positive Ce anomalies (Ce/Ce* = 11.95–101.29), and mostly negative Eu anomalies (Eu/Eu* = 0.20–1.00) (**Figure 9C**). They are considered to grow from metamorphic melts (Rubatto 2002; Wan et al., 2011).

Zircons in the sample JD1546 are mostly rounded with size range within 20–150 μm and length/width ratios of 1:1–2:1 (**Figure 10A**). They can be subdivided into three groups based on their appearances on CL images. The group-1 zircons are mostly bright in their luminescence and have blurred oscillatory or sector zones. The group-2 accounts for the majority of zircons, and the grains are significantly coarse with sizes of mostly >80 μm and have clear core–rim structures. The grain cores are mostly dim in luminescence and have patchy or sector zones, while the rims are 5–30 μm wide with gray luminescence and structureless zones. The group-3 is rare and small with sizes of <40 μm, featured with dark or gray luminescence and structureless zones. Five analyses were obtained on five group-1 zircons with apparent $^{207}Pb/^{206}Pb$ ages from 2522 ± 22 to 2607 ± 20 Ma (**Figure 10B**). These zircons show the Th/U ratios of 0.35–0.49 and exhibit left inclined REE patterns with $(Lu/Gd)_N$ of 17.24–32.22, positive Ce anomalies (Ce/Ce* = 9.95–17.33), and negative Eu anomalies (Eu/Eu* = 0.20–0.67) on the chondrite-normalized REE patterns (**Figure 10C**). They are considered to be captured zircons of mafic magma. Twenty-seven analyses were conducted on 27 group-2 zircon cores and yielded apparent $^{207}Pb/^{206}Pb$ ages ranging from 2465 ± 9 to 2526 ± 11 Ma. These results were plotted on or close to the concordia curve in **Figure 10B** and defined an upper intersect age of 2494 ± 18 Ma (MSWD = 0.18), with a weighted mean age of 2494 ± 5 Ma (MSWD = 1.5). These zircons have the Th/U ratios of mostly 0.24–0.38 with an outlier of 0.13. On the chondrite-normalized REE patterns, they display left inclined REE patterns with $(Lu/Gd)_N$ of 10.45–131.68, positive Ce anomalies (Ce/Ce* = 2.04–29.25), and positive or negative Eu anomalies (Eu/Eu* = 0.28–2.12) (**Figure 10C**). These zircons were considered to have a metamorphic origin (Corfu et al., 2003). The group-2 zircon rims are smaller than the beam diameter and cannot be analyzed. Only two analyses were obtained on two group-3 zircons. One grain (#12) has apparent $^{207}Pb/^{206}Pb$ age of 1784 ± 20 Ma (**Figure 10B**). It has a low Th/U ratio of 0.07 than other zircons and displays significantly low total REE values, flat HREE pattern with $(Lu/Gd)_N$ of 21.34, positive Ce anomalies (Ce/Ce* = 5.77), and negative Eu anomalies (Eu/Eu* = 0.81) (**Figure 10C**). It is considered to be metamorphic zircons that coexist with garnet (Rubatto 2002). The other grain (#7) has an apparent $^{207}Pb/^{206}Pb$ age of 1922 ± 26 Ma (**Figure 10B**) and the Th/U ratio of 0.30. As it has a flat HREE pattern situated between the REE patterns of group-2 zircon cores and #12 zircon

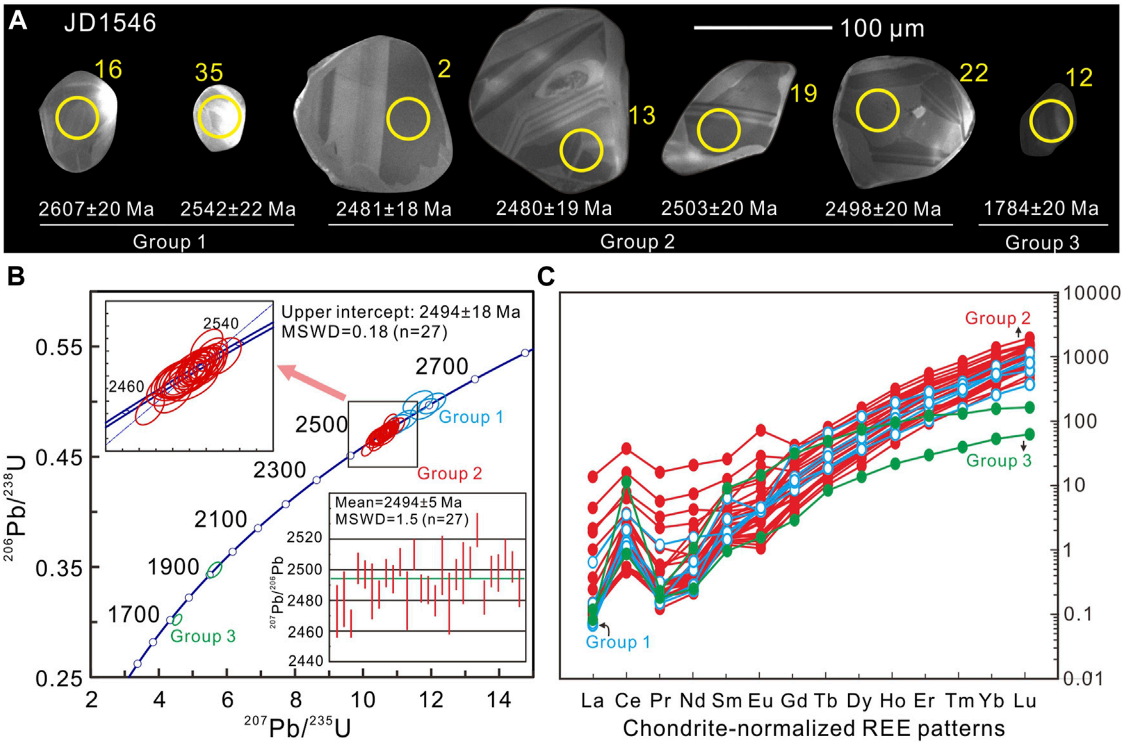

FIGURE 10 | (A) Cathodoluminescence (CL) images of selected zircons from the sample JD1546. Solid circles show the inner positions of LA–ICP–MS analytical sites with their identification numbers as in **Supplementary Table S2**. **(B)** U–Pb isotopic age distributions of analyzed zircons. **(C)** Chondrite-normalized REE patterns (Sun and McDonough 1989).

(**Figure 10C**); we considered that its result would be a mixture of two ages.

6 DISCUSSION

6.1 Metamorphic Evolution of Mafic Granulites

Based on the petrological observations and phase equilibria modeling, two-episode metamorphism can be referred from mafic granulites including the fist-episode UHT metamorphism and the later overprinting metamorphism.

6.1.1 The First-Episode Ultrahigh Temperature Metamorphism

The first-episode metamorphism is inferred in the samples JD15120 and YC8-43, suggesting a *P*–*T* path involving UHT peak conditions and post-peak decompressional cooling under normal granulite-facies conditions. The peak assemblage in both samples is inferred to consist of fine-to-medium-grained clinopyroxene, orthopyroxene, amphibole, plagioclase, and ilmenite. The peak conditions were constrained to be 940–960°C at 7.5–8.5 kbar for the sample JD15120 and 950–990°C at 8 kbar for the sample YC8-43, on the basis of the stability of the peak assemblages in *P*–*T* pseudosections and contours of the measured maximum X_{An} in the core of plagioclase (**Figures 6A**, **7A**). The post-peak evolution is inferred to be dominated by cooling with decompression, which is supported by the later growth of amphibole and biotite, the measured core-to-rim decreasing X_{An} in plagioclase (**Figures 5A,B**), and the measured Ti in amphibole (**Figures 6A**, **7A**). For both of the samples, the observed quartz- and biotite-present final assemblages may represent local segregation of residual melts, and thus, record lower-temperature solidi (~810°C/7 kbar for JD15120 in **Figure 6B**) than those modeled in the *P*–*T* pseudosections in **Figures 6A**, **7A**. The peak UHT conditions are consistent with the REE-based geothermometric results of 948–1,031°C from Yang and Wei (2017a), which are much higher than conventional Cpx–Opx Fe–Mg exchange geothermometric results of 756–940°C (He and Ye 1992; Chen and Li 1996; Zhao et al., 1999; Yang and Wei 2017a). These suggest that both the X_{An} in plagioclase cores and REEs in pyroxenes have high potential for recording the peak temperatures for UHT granulites (Cherniak and Dimanov 2010; Liang et al., 2013; Li and Wei 2016). However, conventional Fe–Mg exchange geothermometers are most likely to record the closure of Fe–Mg diffusion between minerals, with temperatures even lower than the solidus recorded by the quartz-present final assemblages.

Similar UHT peak conditions with post-peak cooling and decompression processes to normal granulite-facies were recovered in mafic and pelitic or greywacke granulites from

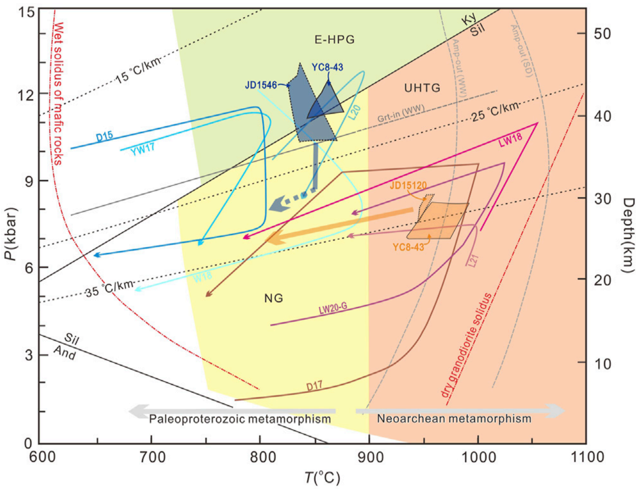

FIGURE 11 | Summarized *P*–*T* conditions and paths for granulites from the East Hebei terrane. Thick arrows represent *P*–*T* paths under peak *P*–*T* conditions in this study. The *P*–*T* paths from literatures are D15, from Duan et al. (2015); D17, from Duan et al. (2017); YW17, from Yang and Wei (2017a); W18, from Wang et al. (2018); LW18, from Liu and Wei (2018); LW20-G, path of meta-greywacke rock from Liu and Wei (2020); L20, from Lu and Wei (2020); and L21, from Liu et al. (2021). Mineral stabilities: Amp-out (WW) and Amp-out (SD) lines from the experiments of Wyllie and Wolf (1993) and Sen and Dunn (1994); Grt-in (WW) line is after Wyllie and Wolf (1993). The wet solidus of mafic rocks is after Lambert and Wyllie (1972) and the dry solidus of granodiorite is cited from Robertson and Wyllie (1971). The transition lines of Al_2SiO_5 are calculated by THERMOCALC. The abbreviations: NG—'normal' granulite; UHTG—ultrahigh-temperature granulite; EHPG—eclogite-high-pressure granulite.

the East Hebei terrane (Duan et al., 2017; Liu and Wei 2018; Liu and Wei 2020; Liu et al., 2021; **Figure 11**). In these granulites, pre-peak up-*P* processes can be inferred on the basis of 1) high-X_{An} plagioclase, spinel, or cordierite inclusions in garnet from pelitic granulites (Duan et al., 2017; Liu and Wei 2020; Liu et al., 2021), 2) orthopyroxene giving way to garnet in greywacke granulites (Liu and Wei 2020), and 3) rounded magnetite–ilmenite inclusions in clinopyroxene from mafic granulites (Liu and Wei 2018), suggesting anticlockwise *P*–*T* paths (**Figure 11**).

6.1.2 The Overprinting Metamorphism

The overprinting metamorphism is recognized in all of the mafic granulites, but exhibits varying textures. In the sample JD15120 from the Taipingzhai ovoid-structural domain, the overprinting assemblages comprise tiny-grained clinopyroxene, orthopyroxene, plagioclase, amphibole, and quartz that occurred as vermicular coronae between medium-grained amphibole and plagioclase. In the sample YC8-43 from the central Saheqiao linear-structural belt, poikilitic garnet occurs as coronae or "red-eye sockets," or aggregates with tiny-grained clinopyroxene, plagioclase, amphibole, rutile, and quartz around the previous two-pyroxenes. Whereas in the sample JD1546 that from the west Saheqiao linear-structural belt, poikilitic garnet-bearing overprinting assemblages have completely replaced the previous UHT assemblages except for a few relicts of medium-grained clinopyroxene. The garnet-bearing assemblages are modeled to have peak *P*–*T* conditions of ~12 kbar/860°C for YC8-43 and ~12.6 kbar/835°C for JD1546, based on the stability of the peak assemblages in the *P*–*T* pseudosections, and the isopleths of the maximum X_{Grs} in garnet cores and the minimum X_{An} in plagioclase cores (**Figures 7B, 8**). The peak *P*–*T* conditions are consistent with the results of 10–14 kbar/800–875°C calculated using REE- and major elements-based geothermobarometers (Yang and Wei 2017a). Similar HP granulite peak conditions of 9–11 kbar/~800°C and 12.5–12.8 kbar/880–900°C are also recovered in mafic granulites from the Malanyu and Beidazhangzi areas in the Saheqiao linear-structural belt (Wang et al., 2018; Lu and Wei 2020). Moreover, the overprinting assemblages in pelitic granulites from the Taipingzhai domain were also constrained to show peak conditions of 10–12 kbar/830–880°C, based on the high X_{Grs} of re-grown garnet (Duan et al., 2017). The post-peak decompression processes are inferred on the basis of the outward decreasing X_{Grs} in garnet and increasing X_{An} in plagioclase in this study and also in other supracrustal rocks (Lu and Wei 2020) and mafic dykes (Duan et al., 2015). In these research works, there are a few coarse-grained plagioclase grains recording a core-to-mantle decreasing X_{An} before the outward increasing X_{An} in the rim, being considered to suggest prograde up-*T* and *P* processes and clockwise *P*–*T* paths (**Figure 11**).

6.2 Significance of Zircon Ages

Most metamorphic zircons from the samples JD15120 and JD1546 yielded ages of 2488 ± 10 Ma (MSWD = 0.38) and 2494 ± 5 Ma (MSWD = 1.5), respectively, which are considered to be related with the early-episode UHT metamorphism. This is because that 1) the zircons with the older ages are mostly large in size, round in shape, and have high Th/U ratios, showing the features of zircons that grew from metamorphic melts (Rubatto 2002; Wan et al., 2011); and 2) they display left-inclined REE patterns with high $(Lu/Gd)_N$ values, suggesting that no garnet was involved with the zircon growth (Rubatto 2002). These features are consistent with the recovered *P*–*T* evolution of the early-episode UHT metamorphism. Moreover, the metamorphic ages are in accordance with the Neoarchean metamorphic ages of 2.55–2.46 Ga with a peak at ~2.50 Ga from supracrustal rocks in the East Hebei terrane (e.g., Nutman et al., 2011) and even in other terranes of the NCC (e.g., Huang et al., 2020).

Only one valid metamorphic age of 1784 ± 20 Ma was obtained from one zircon grain in the sample JD1546, which may correspond to the HP granulite-facies overprinting because that 1) the zircon is small in shape, dark in CL image, and has low Th/U ratio of 0.07, being consistent with zircons that from metamorphic fluid (Rubatto 2002; Wan et al., 2011); and 2) it displays the HREE-flat REE pattern with a low $(Lu/Gd)_N$ value, suggesting its equilibrium with garnet (Rubatto 2002). This age is consistent with the Lu–Hf garnet-whole rock isochron age of 1.77–1.79 Ga in similar granulites from the Saheqiao linear-structural belt (Yang and Wei 2017b). It is worthy to mention that the age of the HP granulite-facies overprinting had well dated to occur at 1.81–1.82 Ga from metabasic dykes (Duan et al., 2015) and other HP granulites (Yang and Wei 2017b; Lu and Wei 2020).

Note that although sample JD1546 is almost completely modified by HP granulite assemblages, its metamorphic zircons are mostly formed during the late Neoarchean UHT metamorphism. This suggests that zircons are more resistant than the major minerals during the lower-temperature overprinting on the higher-temperature UHT granulites. Therefore, it should be careful in linking the metamorphic assemblages with ages, especially for the rocks that have underwent multi-episode metamorphism.

6.3 Tectonic Implications

Two-episode metamorphism has been inferred in the East Hebei terrane, including the late Neoarchean UHT metamorphism and late Paleoproterozoic HP granulite-facies metamorphism, where the first one is featured with anticlockwise *P*–*T* paths whereas the latter one is marked by clockwise *P*–*T* paths (**Figure 11**). These two different metamorphic processes may suggest distinct tectonic settings.

6.3.1 Late Neoarchean Ultrahigh Temperature Metamorphism

The late Neoarchean UHT metamorphism in the East Hebei terrane may attribute from four tectonic models, including amalgamation of microcontinental terranes (e.g., Zhai and Santosh 2011), subduction–collision (e.g., Kusky et al., 2016; Liu et al., 2018), plume-related processes (e.g., Zhao et al., 1999; Geng et al., 2006), and vertical tectonics ("drip tectonics" or "sagduction"; e.g., Duan et al., 2017; Liu and Wei 2018,; Liu and Wei 2020). The Archean vertical tectonism is marked by mantle overturn and crustal delamination in the mantle–crust scale and sagduction within the crust (Johnson et al., 2014; Harris and Bédard 2014; Bédard 2018). A sagduction process, including the diapirism of granitoids and sinking of supracrustal rocks (e.g., Collins et al., 1998; Van Kranendonk et al., 2004), is considered to be the most possible mechanism that accounts for the formation of Archean unique dome–and–keel structures (e.g., Collins et al., 1998; Lin 2005; Lin and Beakhouse 2013; Parmenter et al., 2006), and the simultaneity between the metamorphism of supracrustal rocks and their ambient TTG magmatic activity (François et al., 2014). Thus, a sagduction process is preferred to be responsible for the late Neoarchean UHT metamorphism in the East Hebei terrane, based on the following lines of evidence: 1) the Archean unique dome–and–keel structures are well preserved (**Figure 1**), with the Lulong–Shuangshanzi supracrustal belt distributed between TTG domes and numerous supracrustal rafts within the domes; 2) the determined metamorphic ages of 2.55–2.46 Ga with a peak at ~2.50 Ga are coeval with the final pulse of TTG magmatism that ranging from 2.56 to 2.48 Ga with a peak at ~2.52 Ga (e.g., Wei 2018); and 3) near-vertical normal shear formed due to the upwelling of Anziling dome with respect to the down-slipping of the Lulong–Shuangshanzi supracrustal belt was inferred based on sub-vertical textures including mineral lineations and "S"-type folds in the Shuangshanzi shear zone (Liu et al., 2017; Zhao et al., 2021). The counterclockwise *P*–*T* path in supracrustal rafts can be interpreted in a sagduction process, where the supracrustal rocks were heated first by the intrusion of high-temperature TTG magmas, or more possibly, the mantle-derived magmas, and then dropped to magmas to reach the peak stage, and finally cooled and uplifted during the doming processes.

6.3.2 Late Paleoproterozoic Metamorphism

The late Paleoproterozoic metamorphism is widely observed in the NCC (e.g., Duan et al., 2015; Huang et al., 2016; Yang and Wei 2017b; Zou et al., 2022), and its tectonic setting has been controversially debated. The prevalent view suggests a successive collision model among the Archean blocks, forming the Khondalite belt at ~1.95 Ga, the Jiao-Liao-Ji belt at ~1.90 Ga, and the TNCO at ~1.85 Ga (e.g., Zhao et al., 2005; Zhao et al., 2012). However, the final amalgamation of the NCC along TNCO is argued to occur at ~1.95 Ga, and the dated age of ~1.85 Ga from granulites is interpreted to be correlated with a separated within-plate orogeny (Wei 2018; Qian et al., 2019). Another view contests that there were cold oceanic subduction and collision tectonics occurred in the north margin of the NCC (e.g., Kusky et al., 2016). The oceanic subduction is limited within 1.92–1.85 Ga and supported by the eclogite-facies metamorphism in the Chicheng ophiolitic mélange (Zhang Y. Y. et al., 2020; Zhang et al., 2021), and eclogite xenoliths with superdeep majorite inclusions in the carbonatite from the boundary between the Khondalite belt and TNCO (Xu et al., 2017; Xu et al., 2018), while the collision may occur later at 1.85–1.80 Ga with the similar spatial distribution of the IMNHO, between the NCC and a missing continent (Kusky et al., 2016) or the southwestern margin of the Siberia Craton (Wu et al., 2018).

In this study, late Paleoproterozoic metamorphism was well constrained in the East Hebei terrane, and it becomes weaker from north to south. In the Saheqiao linear-structural belt, HP granulite assemblages are well developed and stronger deformation had mostly removed the Neoarchean fabrics (Yang and Wei 2017a; Lu and Wei 2020; this article). In the Taipingzhai ovoid-structural domain, the Archean domal structures are survived, and the overprinting assemblages are limited in pelitic granulites with the regrowth of garnet (Duan et al., 2017), and in mafic granulites with the formation of vermicular coronae (**Figures 3C,D**), although good HP granulite assemblages are developed in mafic dykes (Duan et al., 2015). While in the Qian'an gneiss dome, overprinting assemblages were reported from the Caozhuang supracrustal rocks that are characterized by staurolite-bearing assemblages of low-amphibolite facies (Liu et al., 2020). Thus, the late Paleoproterozoic overprinting metamorphism in the East Hebei terrane suggests a medium *P*/*T* ratio at 1.78–1.82 Ga (Duan et al., 2015; Duan et al., 2017; Yang and Wei 2017b; Lu and Wei 2020; this article). This is considered to be correlated with intracontinental deformation that triggered by the oceanic subduction-related continental collision in the northern margin of the NCC. The collision event is also favored by the ~1.89 Ga Barrovian-type metamorphism in the Kondalite belt (Huang et al., 2016), the ~1.84 Ga HP granulites from the North Liaoning terrane (Duan et al., 2019), the 1.74–1.83 Ga amphibolite-to-granulite-facies metamorphism in the Miyun complex (He et al., 1993; Zhang H. C. G. et al., 2020; Zou et al., 2022), and the ~1.85 Ga within-plate metamorphism and deformation in the Wutai–Hengshan region (Wei 2018; Qian et al., 2019).

7 CONCLUSION

(1) Two-episode metamorphism can be recognized in mafic granulites from the East Hebei terrane.
(2) The first-episode metamorphism is recovered under UHT conditions of 940–990 °C at 7.5–8.5 kbar and post-peak cooling with the decompression process to ~7 kbar/~810 °C.
(3) The second-episode overprinting metamorphism exhibits varying textures in different samples. In garnet-bearing samples, the overprinting assemblages show HP granulite-facies peak conditions of 12–12.6 kbar/835–860°C, and post-peak isothermal decompression to ~9 kbar.
(4) Zircon dating suggests two metamorphic ages of ~2.49 Ga and ~1.78 Ga, being considered to be correlated with the UHT and HP granulite metamorphism, respectively.
(5) The late Neoarchean UHT granulite metamorphism with a thermal gradient of ~33°C/km may correlate a vertical sagduction regime, whereas the late Paleoproterozoic HP granulite metamorphism with a thermal gradient of ~20°C/km is favored to register the continental collision in the northern margin of the North China Craton.

DATA AVAILABILITY STATEMENT

The original contributions presented in the study are included in the article/**Supplementary Material**, further inquiries can be directed to the corresponding authors.

AUTHOR CONTRIBUTIONS

TL calculated the pseudosections, performed the data analyses, and wrote the manuscript. CY and ZL collected the samples and conducted the experiments. CJW developed the project and revised the manuscript. All authors discussed the results and were involved in writing the paper.

FUNDING

This work was financially supported by the National Natural Science Foundation of China (Grant Nos: 42102062, 42030304).

ACKNOWLEDGMENTS

We thank the editor Yi Chen for his editorial work, and Dr. Camille François and Dr. Shujuan Jiao for their thoughtful and constructive comments, which have greatly improved our manuscript.

SUPPLEMENTARY MATERIAL

The Supplementary Material for this article can be found online at: https://www.frontiersin.org/articles/10.3389/feart.2022.894353/full#supplementary-material

REFERENCES

Arima, M., and Barnett, R. L. (1984). Sapphirine Bearing Granulites from the Sipiwesk Lake Area of the Late Archean Pikwitonei Granulite Terrain, Manitoba, Canada. *Contr. Mineral. Petrol.* 88, 102–112. doi:10.1007/BF00371415

Bai, X., Liu, S., Guo, R., and Wang, W. (2015). Zircon U-Pb-Hf Isotopes and Geochemistry of Two Contrasting Neoarchean Charnockitic Rock Series in Eastern Hebei, North China Craton: Implications for Petrogenesis and Tectonic Setting. *Precambrian Res.* 267, 72–93. doi:10.1016/j.precamres.2015.06.004

Bai, X., Liu, S., Guo, R., Zhang, L., and Wang, W. (2014). Zircon U-Pb-Hf Isotopes and Geochemistry of Neoarchean Dioritic-Trondhjemitic Gneisses, Eastern Hebei, North China Craton: Constraints on Petrogenesis and Tectonic Implications. *Precambrian Res.* 251, 1–20. doi:10.1016/j.precamres.2014.05.027

Bédard, J. H. (2018). Stagnant Lids and Mantle Overturns: Implications for Archaean Tectonics, Magmagenesis, Crustal Growth, Mantle Evolution, and the Start of Plate Tectonics. *Geosci. Front.* 9, 19–49. doi:10.1016/j.gsf.2017.01.005

Brown, M., and Johnson, T. (2018). Secular Change in Metamorphism and the Onset of Global Plate Tectonics. *Am. Mineral.* 103 (2), 181–196. doi:10.2138/am-2018-6166

Brown, M. (2007). Metamorphic Conditions in Orogenic Belts: A Record of Secular Change. *Int. Geol. Rev.* 49, 193–234. doi:10.2747/0020-6814.49.3.193

Carson, C. J., Powell, R., and Clarke, G. L. (1999). Calculated Mineral Equilibria for Eclogites in CaO-Na2O-FeO-MgO-Al2O3-SiO2-H2O: Application to the Pouébo Terrane, Pam Peninsula, New Caledonia. *J. Metamorph. Geol.* 17, 9–24. doi:10.1046/j.1525-1314.1999.00177.x

Chen, M. Y., and Li, S. X. (1996). The Evolution of Granulite Facies Metamorphism in Eastern Hebei Province. *Acta Petrol. Sin.* 12 (2), 343–357. (in Chinese with English abstract).

Chen, M. Y. (1990). Metabasic Dyke Swarms in a High-Grade Metamorphic Terrane: A Case Study in the Taipingzhai–Jinchangyu Area, Eastern Hebei Province. *Acta Geol. Sin.* 3, 427–441. (in Chinese with English abstract). doi:10.1111/j.1755-6724.1990.mp3004006.x

Cherniak, D. J., and Dimanov, A. (2010). Diffusion in Pyroxene, Mica and Amphibole. *Rev. Mineral. Geochem.* 72, 641–690. doi:10.2138/rmg.2010.72.14

Chu, H., Wang, H. C., Rong, G. L., Chang, Q. S., Kang, J. L., Jin, S., et al. (2016). The Geological Significance of the Rediscovered Fuchsite Quartzite with Abundant Eoarchean Detrital Zircons in Eastern Hebei Province. *Chin. Sci. Bull.* 61, 2299–2308. (in Chinese with English abstract). doi:10.1360/N972015-00998

Collins, W. J., Van Kranendonk, M. J., and Teyssier, C. (1998). Partial Convective Overturn of Archaean Crust in the East Pilbara Craton, Western Australia: Driving Mechanisms and Tectonic Implications. *J. Struct. Geology.* 20, 1405–1424. doi:10.1016/S0191-8141(98)00073-X

Corfu, F., Hanchar, J. M., Hoskin, P. W. O., and Kinny, P. (2003). Atlas of Zircon Textures. *Rev. Mineral. Geochem.* 53, 469–500. doi:10.2113/0530469

Duan, Z., Wei, C., and Qian, J. (2015). Metamorphic P–T Paths and Zircon U–Pb Age Data for the Paleoproterozoic Metabasic Dykes of High-Pressure Granulite Facies from Eastern Hebei, North China Craton. *Precambrian Res.* 271, 295–310. doi:10.1016/j.precamres.2015.10.015

Duan, Z., Wei, C. J., and Rehman, H. U. (2017). Metamorphic Evolution and Zircon Ages of Pelitic Granulites in Eastern Hebei, North China Craton: Insights into the Regional Archean P-T-T History. *Precambrian Res.* 292, 240–257. doi:10.1016/j.precamres.2017.02.008

Duan, Z. Z., Wei, C. J., and Li, Z. (2019). Metamorphic P-T Paths and Zircon U–Pb Ages of Paleoproterozoic Metabasic Dykes in Eastern Hebei and Northern Liaoning: Implications for the Tectonic Evolution of the North China Craton. *Precambrian Res.* 326, 124–141. doi:10.1016/j.precamres.2017.11.001

François, C., Philippot, P., Rey, P., and Rubatto, D. (2014). Burial and Exhumation during Archean Sagduction in the East Pilbara Granite-Greenstone Terrane. *Earth Planet. Sci. Lett.* 396, 235–251. doi:10.1016/j.epsl.2014.04.025

Frost, B. R., and Chacko, T. (1989). The Granulite Uncertainty Principle: Limitations on Thermobarometry in Granulites. *J. Geology.* 97, 435–450. doi:10.1086/629321

Fu, J., Liu, S., Chen, X., Bai, X., Guo, R., and Wang, W. (2016). Petrogenesis of Taxitic Dioritic-Tonalitic Gneisses and Neoarchean Crustal Growth in Eastern Hebei, North China Craton. *Precambrian Res.* 284, 64–87. doi:10.1016/j.precamres.2016.08.002

Geng, Y. S., Liu, F. L., and Yang, C. H. (2006). Magmatic Event at the End of the Archean in Eastern Hebei Province and its Geological Implication. *Acta Geol. Sin. (English Edition)* 80, 819–833. doi:10.1111/j.1755-6724.2006.tb00305.x

Green, E. C. R., White, R. W., Diener, J. F. A., Powell, R., Holland, T. J. B., and Palin, R. M. (2016). Activity-Composition Relations for the Calculation of Partial Melting Equilibria in Metabasic Rocks. *J. Metamorph. Geol.* 34, 845–869. doi:10.1111/jmg.12211

Griffin, W. L. (2008). Major Transformations Reveal Earth's Deep Secrets. *Geology* 36, 95–96. doi:10.1130/focus012008.1

Guo, R., Liu, S., Santosh, M., Li, Q., Bai, X., and Wang, W. (2013). Geochemistry, Zircon U-Pb Geochronology and Lu-Hf Isotopes of Metavolcanics from Eastern Hebei Reveal Neoarchean Subduction Tectonics in the North China Craton. *Gondwana Res.* 24, 664–686. doi:10.1016/j.gr.2012.12.025

Harley, S. L. (2004). Extending Our Understanding of Ultrahigh Temperature Crustal Metamorphism. *J. Mineral. Petrol. Sci.* 99, 140–158. doi:10.2465/jmps.99.140

Harley, S. L. (2008). Refining the P-T Records of UHT Crustal Metamorphism. *J. Metamorph. Geol.* 26, 125–154. doi:10.1111/j.1525-1314.2008.00765.x

Harley, S. L. (1989). The Origins of Granulites: A Metamorphic Perspective. *Geol. Mag.* 126, 215–247. doi:10.1017/s0016756800022330

Harley, S. L. (1998). Ultrahigh Temperature Granulite Metamorphism (1050 ˚C, 12 Kbar) and Decompression in Garnet (Mg70)-Orthopyroxene-Sillimanite Gneisses from the Rauer Group, East Antarctica. *J. Metamorph. Geol.* 16 (4), 541–562. doi:10.1111/j.1525-1314.1998.00155.x

Harris, L. B., and Bédard, J. H. (2014). "Interactions between Continent-Like 'Drift', Rifting, and Mantle Flow on Venus: Gravity Interpretations and Earth Analogues," in *Volcanism and Tectonism across the Solar System*. Editors T. Platz, M. Massironi, P. Byrne, and H. Hiesinger (London: Geological Society, Special Publication), 401.

He, G. P., and Ye, H. W. (1992). The Evolution of Metamorphism in Granulite Facies Terrane, Eastern Hebei Province. *Acta Petrol. Sin.* 8 (2), 129–135. (in Chinese with English abstract).

He, G. P., Ye, H. W., and Xia, S. L. (1993). Sm-Nd Isotopic Age of the Metamorphic Basic Dykes in Miyun, Beijing and its Geological Significance. *Acta Petrol. Sin.* 9, 312–317. (In Chinese with English abstract).

Holland, T. J. B., and Powell, R. (2011). An Improved and Extended Internally Consistent Thermodynamic Dataset for Phases of Petrological Interest, Involving a New Equation of State for Solids. *J. Metamorph. Geol.* 29, 333–383. doi:10.1111/j.1525-1314.2010.00923.x

Holland, T., and Powell, R. (2003). Activity-Composition Relations for Phases in Petrological Calculations: An Asymmetric Multicomponent Formulation. *Contrib. Mineral. Petrol.* 145, 492–501. doi:10.1007/s00410-003-0464-z

Huang, B., Kusky, T. M., Johnson, T. E., Wilde, S. A., Wang, L., Polat, A., et al. (2020). Paired Metamorphism in the Neoarchean: A Record of Accretionary-To-Collisional Orogenesis in the North China Craton. *Earth Planet. Sci. Lett.* 543, 116355. doi:10.1016/j.epsl.2020.116355

Huang, G., Jiao, S., Guo, J., Peng, P., Wang, D., and Liu, P. (2016). P-T-t Constraints of the Barrovian-Type Metamorphic Series in the Khondalite Belt of the North China Craton: Evidence from Phase Equilibria Modeling and Zircon U-Pb Geochronology. *Precambrian Res.* 283, 125–143. doi:10.1016/j.epsl.2020.11635510.1016/j.precamres.2016.07.011

Johnson, T. E., Brown, M., Kaus, B. J. P., and VanTongeren, J. A. (2014). Delamination and Recycling of Archaean Crust Caused by Gravitational Instabilities. *Nat. Geosci* 7, 47–52. doi:10.1038/ngeo2019

Jordan, T. H. (1978). Composition and Development of the Continental Tectosphere. *Nature* 274, 544–548. doi:10.1038/274544a0

Kelsey, D. E., and Hand, M. (2015). On Ultrahigh Temperature Crustal Metamorphism: Phase Equilibria, Trace Element Thermometry, Bulk Composition, Heat Sources, Timescales and Tectonic Settings. *Geosci. Front.* 6 (3), 311–356. doi:10.1016/j.gsf.2014.09.006

Korhonen, F. J., Powell, R., and Stout, J. H. (2012). Stability of Sapphirine + Quartz in the Oxidized Rocks of the Wilson Lake Terrane, Labrador: Calculated Equilibria in NCKFMASHTO. *J. Metamorph. Geol.* 30, 21–36. doi:10.1111/j.1525-1314.2011.00954.x

Korhonen, F. J., Saw, A. K., Clark, C., Brown, M., and Bhattacharya, S. (2011). New Constraints on UHT Metamorphism in the Eastern Ghats Province through the Application of Phase Equilibria Modelling and *In Situ* Geochronology. *Gondwana Res.* 20, 764–781. doi:10.1016/j.gr.2011.05.006

Kusky, T. M., Polat, A., Windley, B. F., Burke, K. C., Dewey, J. F., Kidd, W. S. F., et al. (2016). Insights into the Tectonic Evolution of the North China Craton through Comparative Tectonic Analysis: A Record of Outward Growth of Precambrian Continents. *Earth-Science Rev.* 162, 387–432. doi:10.1016/j.earscirev.2016.09.002

Kwan, L. C. J., Zhao, G., Yin, C., and Geng, H. (2016). Metamorphic P-T Path of Mafic Granulites from Eastern Hebei: Implications for the Neoarchean Tectonics of the Eastern Block, North China Craton. *Gondwana Res.* 37, 20–38. doi:10.1016/j.gr.2016.05.004

Lambert, I. B., and Wyllie, P. J. (1972). Melting of a Gabbro (Qtz Eclogite) with Excess H2O to 35 Kbars with Geological Applications. *J. Geol.* 80, 693–708. doi:10.1086/627795

Leake, B. E., Woolley, A. R., Birch, W. D., Burke, E. A. J., Ferraris, G., Grice, J. D., et al. (2003). Nomenclature of Amphiboles: Additions and Revisions to the International Mineralogical Association's 1997 Recommendations. *Can. Mineral.* 41, 1355–1362. doi:10.2113/gscanmin.41.6.1355

Li, X. W., and Wei, C. J. (2016). Phase Equilibria Modelling and Zircon Age Dating of Pelitic Granulites in Zhaojiayao, from the Jining Group of the Khondalite Belt, North China Craton. *J. Metamorph. Geol.* 34, 595–615. doi:10.1111/jmg.12195

Liang, Y., Sun, C., and Yao, L. (2013). A REE-In-Two-Pyroxene Thermometer for Mafic and Ultramafic Rocks. *Geochim. Cosmochim. Acta* 102, 246–260. doi:10.1016/j.gca.2012.10.035

Lin, S., and Beakhouse, G. P. (2013). Synchronous Vertical and Horizontal Tectonism at Late Stages of Archean Cratonization and Genesis of Hemlo Gold deposit, Superior Craton, Ontario, Canada. *Geology* 41, 359–362. doi:10.1130/G33887.1

Lin, S. (2005). Synchronous Vertical and Horizontal Tectonism in the Neoarchean: Kinematic Evidence from a Synclinal Keel in the Northwestern Superior Craton, Canada. *Precambrian Res.* 139, 181–194. doi:10.1016/j.precamres.2005.07.001

Liou, P., Guo, J., Huang, G., and Fan, W. (2017). 2.9 Ga Magmatism in Eastern Hebei, North China Craton. *Precambrian Res.* 326, 6–23. doi:10.1016/j.precamres.2017.11.002

Liu, B., Neubauer, F., Liu, J., Jin, W., Li, W., and Liang, C. (2017). Neoarchean Ductile Deformation of the Northeastern North China Craton: The Shuangshanzi Ductile Shear Zone in Qinglong, Eastern Hebei, North China. *J. Asian Earth Sci.* 139, 224–236. doi:10.1016/j.jseaes.2017.01.014

Liu, D. Y., Shen, Q. H., Zhang, Z. Q., Jahn, B. M., and Auvray, B. (1990). Archean Crustal Evolution in China: U–Pb Geochronology of the Qianxi Complex. *Precambrian Res.* 48, 226–244. doi:10.1016/0301-9268(90)90010-N

Liu, S. W., Wang, W., Bai, X., Guo, R. R., Fu, J. H., Guo, B. R., et al. (2018). Lithological Assemblages of Archean Meta-Igneous Rocks in Eastern Hebei-Western Liaoning Provinces of North China Craton, and Their Geodynamic Implications. *Earth Sci.* 43, 44–56. (in Chinese with English abstract). doi:10.3799/dqkx.2018.003

Liu, T., Wei, C. J., Kröner, A., Han, B. F., and Duan, Z. Z. (2020). Metamorphic P–T Paths for the Archean Caozhuang Supracrustal Sequence, Eastern Hebei Province, North China Craton: Implications for a Sagduction Regime. *Precambrian Res.* 340, 105346. doi:10.1016/j.precamres.2019.105346

Liu, T., Wei, C. J., Johnson, T. E., and Sizova, E. (2021). Newly-Discovered Ultra-High Temperature Granulites from the East Hebei Terrane, North China Craton. *Sci. Bull.* 67, 670–673. in press. doi:10.1016/j.scib.2021.12.023

Liu, T., and Wei, C. J. (2018). Metamorphic Evolution of Archean Ultrahigh-Temperature Mafic Granulites from the Western Margin of Qian'an Gneiss Dome, Eastern Hebei Province, North China Craton: Insights into the Archean Tectonic Regime. *Precambrian Res.* 318, 170–187. doi:10.1016/j.precamres.2018.10.007

Liu, T., and Wei, C. J. (2020). Metamorphic P–T Paths and Zircon U-Pb Ages of Archean Ultra-High Temperature Paragneisses from the Qian'an Gneiss Dome, East Hebei Terrane, North China Craton. *J. Metamorph. Geol.* 38, 329–356. doi:10.1111/jmg.12524

Liu, Z., and Yang, Z. (1994). The Tectonic Evolution of Archean High Grade Metamorphic Terrane, Eastern Hebei, China. *J. Changchun Univ. Earth Sci.* 24, 254–258. (in Chinese with English abstract).

Lu, H., and Wei, C. J. (2020). Late Neoarchean or Late Paleoproterozoic High-Pressure Granulite Facies Metamorphism from the East Hebei Terrane, North China Craton? *J. Asian Earth Sci.* 190, 104195. doi:10.1016/j.jseaes.2019.104195

Lu, J., Zhai, M.-G., Lu, L.-S., and Zhao, L. (2017). P-T-t Evolution of Neoarchaean to Paleoproterozoic Pelitic Granulites from the Jidong Terrane, Eastern North China Craton. *Precambrian Res.* 290, 1–15. doi:10.1016/j.precamres.2016.12.012

Ludwig, K. R. (2003). *User's Manual for Isoplot 3.00: A Geochronological Toolkit for Microsoft Excel (No. 4)*. Berkeley: Berkeley Geochronology Center Special Publication No. 4.

Mahan, K. H., Goncalves, P., Flowers, R., Williams, M. L., and Hoffman-Setka, D. (2008). The Role of Heterogeneous Strain in the Development and Preservation of a Polymetamorphic Record in High-Pgranulites, Western Canadian Shield. *J. Metamorph. Geol.* 26, 669–694. doi:10.1111/j.1525-1314.2008.00783.x

Mezger, K., Bohlen, S. R., and Hanson, G. N. (1990). Metamorphic History of the Archean Pikwitonei Granulite Domain and the Cross Lake Subprovince, Superior Province, Manitoba, Canada. *J. Petrol.* 31, 483–517. doi:10.1093/petrology/31.2.483

Morimoto, N. (1988). Nomenclature of Pyroxenes. *Mineralogy Petrol.* 39, 55–76. doi:10.1007/bf01226262

Nutman, A. P., Wan, Y., Du, L., Friend, C. R. L., Dong, C., Xie, H., et al. (2011). Multistage Late Neoarchaean Crustal Evolution of the North China Craton, Eastern Hebei. *Precambrian Res.* 189, 43–65. doi:10.1016/j.precamres.2011.04.005

O'Brien, P. J., and Rotzler, J. (2003). High-Pressure Granulites: Formation, Recovery of Peak Conditions and Implications for Tectonics. *J. Metamorph. Geol.* 21 (1), 3–20. doi:10.1046/j.1525-1314.2003.00420.x

Parmenter, A. C., Lin, S., and Corkery, M. T. (2006). Structural Evolution of the Cross Lake Greenstone belt in the Northwestern Superior Province, Manitoba: Implications for Relationship between Vertical and Horizontal Tectonism. *Can. J. Earth Sci.* 43, 767–787. doi:10.1139/E06-006

Pattison, D. R. M., Chacko, T., Farquhar, J., and Mcfarlane, C. R. M. (2003). Temperatures of Granulite-Facies Metamorphism: Constraints from Experimental Phase Equilibria and Thermobarometry Corrected for Retrograde Exchange. *J. Geol.* 44, 867–900. doi:10.1093/petrology/44.5.867

Perchuk, L. L., van Reenen, D. D., Varlamov, D. A., van Kal, S. M., TabatabaeimaneshBoshoff, R., and Boshoff, R. (2008). P-T Record of Two High-Grade Metamorphic Events in the Central Zone of the Limpopo Complex, South Africa. *Lithos* 103, 70–105. doi:10.1016/j.lithos.2007.09.011

Polat, A., Kusky, T. M., Li, J. H., Fryer, B. J., Kusky, T., Li, J., et al. (2006). Geochemical and Petrological Evidence for a Suprasubduction Zone Origin of Neoarchean (Ca. 2.5 Ga) Peridotites, central Orogenic belt, North China Craton. *Geol. Soc. America Bull.* 118, 771–784. doi:10.1130/B25845.1

Qi, H. L., Hao, X. H., Zhang, X. D., and Nie, W. D. (1999). The Geological Features of Granite-Greenstone Belts in Qinglong River, Jidong. *Prog. Precambrian Res.* 22, 1–17. (in Chinese with English abstract).

Qian, J. H., and Wei, C. J. (2016). P-T-t Evolution of Garnet Amphibolites in the Wutai-Hengshan Area, North China Craton: Insights from Phase Equilibria and Geochronology. *J. Metamorph. Geol.* 34, 423–446. doi:10.1111/jmg.12186

Qian, J., Wei, C. J., Clarke, G. L., and Zhou, X. (2015). Metamorphic Evolution and Zircon Ages of Garnet-Orthoamphibole Rocks in Southern Hengshan, North China Craton: Insights into the Regional Paleoproterozoic P-T-T History. *Precambrian Res.* 256, 223–240. doi:10.1016/j.precamres.2014.11.013

Qian, J., Wei, C. J., Zhou, X., and Zhang, Y. (2013). Metamorphic P-T Paths and New Zircon U-Pb Age Data for Garnet-Mica Schist from the Wutai Group, North China Craton. *Precambrian Res.* 233, 282–296. doi:10.1016/j.precamres.2013.05.012

Qian, J., Yin, C., Wei, C. J., and Zhang, J. (2019). Two Phases of Paleoproterozoic Metamorphism in the Zhujiafang Ductile Shear Zone of the Hengshan Complex: Insights into the Tectonic Evolution of the North China Craton. *Lithos* 330-331, 35–54. doi:10.1016/j.lithos.2019.02.001

Robertson, J. K., and Wyllie, P. J. (1971). Experimental Studies on Rocks from the Deboullie Stock, Northern Maine, Including Melting Relations in the Water-Deficient Environment. *J. Geology.* 79, 549–571. doi:10.1086/627675

Rubatto, D. (2002). Zircon Trace Element Geochemistry: Partitioning with Garnet and the Link between U-Pb Ages and Metamorphism. *Chem. Geology.* 184, 123–138. doi:10.1016/S0009-2541(01)00355-2

Sen, C., and Dunn, T. (1994). Dehydration Melting of a Basaltic Composition Amphibolite at 1.5 and 2.0 GPa: Implications for the Origin of Adakites. *Contr. Mineral. Petrol.* 117, 394–409. doi:10.1007/BF00307273

Song, S. G. (1990). Metamorphosed Basic and Ultrabasic Dyke Swarms in Taipingzhai Region, East Hebei. *J. Changchun Univ. Earth Sci.* 20, 421–428. (in Chinese with English abstract).

Sun, H., Xie, H. Q., Liu, S. J., Dong, C. Y., Liu, D. Y., and Wan, Y. S. (2016). Archean Magmatism and Metamorphism in the Huangbaiyu-Yangyashan Area, Eastern Hebei Province: Evidence from SHRIMP Zircon U–Pb Dating. *Geol. Bull.* 35, 27–42. (in Chinese with English abstract). doi:10.3969/j.issn.1671-2552.2016.01.004

Sun, S.-S., and McDonough, W. F. (1989). Chemical and Isotopic Systematics of Oceanic Basalts: Implications for Mantle Composition and Processes. *Geol. Soc. Lond. Spec. Publications* 42, 313–345. doi:10.1144/GSL.SP.1989.042.01.19

Van Achterbergh, E., Ryan, C., Jackson, S., and Griffin, W. L. (2001). *Data Reduction Software for LA-ICP-MS*. Ottawa: Mineralogical Society of Canada.

Van Kranendonk, M. J., Collins, W. J., Hickman, A., and Pawley, M. J. (2004). Critical Tests of Vertical vs. Horizontal Tectonic Models for the Archaean East Pilbara Granite-Greenstone Terrane, Pilbara Craton, Western Australia. *Precambrian Res.* 131, 173–211. doi:10.1016/j.precamres.2003.12.015

Wan, Y.-S., Liu, D.-Y., Dong, C.-Y., Xie, H.-Q., Kröner, A., Ma, M.-Z., et al. (2015). "Formation and Evolution of Archean Continental Crust of the North China Craton," in *Precambrian Geology of China*. Editor M Zhai (Berlin, Heidelberg: Springer), 59–136. doi:10.1007/978-3-662-47885-1_2

Wan, Y., Liu, D., Dong, C., Liu, S., Wang, S., and Yang, E. (2011). U-Th-Pb Behavior of Zircons under High-Grade Metamorphic Conditions: A Case Study of Zircon Dating of Meta-Diorite Near Qixia, Eastern Shandong. *Geosci. Front.* 2 (02), 137–146. doi:10.1016/j.gsf.2011.02.004

Wang, C., Song, S., Allen, M. B., Su, L., and Wei, C. J. (2018). High-Pressure Granulite from Jixian, Eastern Hebei, the North China Craton: Implications for Neoarchean to Early Paleoproterozoic Collision Tectonics. *Geol. Soc. Spec. Publ.* 478, 427–448. doi:10.1144/SP478.16

Wang, C., Song, S., Wei, C. J., Su, L., Allen, M. B., Niu, Y., et al. (2019). Palaeoarchaean Deep Mantle Heterogeneity Recorded by Enriched Plume Remnants. *Nat. Geosci.* 12, 672–678. doi:10.1038/s41561-019-0410-y

Weber, W. (1984). The Pikwitonei Granulite Domain: A Lower Crustal Level along the Churchill-Superior Boundary in central Manitoba" in Workshop on: A Cross Section of Archean Crust. LPI Tech. Rep. 83–03, 95–97.

Wei, C. (2018). Neoarchean Granulite Facies Metamorphism and its Tectonic Implications from the East Hebei Terrane. *Acta Petrol. Sin.* 34, 895–912. (in Chinese with English abstract).

Wei, C., Qian, J., and Zhou, X. (2014). Paleoproterozoic Crustal Evolution of the Hengshan-Wutai-Fuping Region, North China Craton. *Geosci. Front.* 5, 485–497. doi:10.1016/j.gsf.2014.02.008

White, R. W., Powell, R., Holland, T. J. B., Johnson, T. E., and Green, E. C. R. (2014). New Mineral Activity-Composition Relations for Thermodynamic Calculations in Metapelitic Systems. *J. Meta. Geol.* 32, 261–286. doi:10.1111/jmg.12071

White, R. W., Powell, R., Holland, T. J. B., and Worley, B. A. (2000). The Effect of TiO2 and Fe2O3 on Metapelitic Assemblages at Greenschist and Amphibolite Facies Conditions: Mineral Equilibria Calculations in the System K2O–FeO–MgO–Al2O3–SiO2–H2O–TiO2–Fe2O3. *J. Metamorph. Geol.* 18, 497–511. doi:10.1046/j.1525-1314.2000.00269.x

Whitney, D. L., and Evans, B. W. (2010). Abbreviations for Names of Rock-Forming Minerals. *Am. Mineral.* 95, 185–187. doi:10.2138/am.2010.3371

Wiedenbeck, M., Allé, P., Corfu, F., Griffin, W. L., Meier, M., Oberli, F., et al. (1995). Three Natural Zircon Standards for U-Th-Pb, Lu-Hf, Trace Element and Ree Analyses. *Geostandards Newsl.* 19, 1–23. doi:10.1111/j.1751-908X.1995.tb00147.x

Wiedenbeck, M., Hanchar, J. M., Peck, W. H., Sylvester, P., Valley, J., Whitehouse, M., et al. (2004). Further Characterisation of the 91500 Zircon Crystal. *Geostand Geoanalyt Res.* 28, 9–39. doi:10.1111/j.1751-908X.2004.tb01041.x

Wu, C., Zhou, Z., Zuza, A. V., Wang, G., Liu, C., and Jiang, T. (2018). A 1.9-Ga Mélange along the Northern Margin of the North China Craton: Implications for the Assembly of Columbia Supercontinent. *Tectonics* 37, 3610–3646. doi:10.1029/2018TC005103

Wu, J. S., Geng, Y. S., Shen, Q. H., Wan, Y. S., Liu, D. H., and Song, B. (1998). *Archean Geology Characteristics and Tectonic Evolution of Sino-Korea Paleo-Continent*. Beijing: Geological Publication House. (in Chinese).

Wu, J. S., and Geng, Y. S. (1991). *The Major Geological Events of the Early Precambrian in the North China Platform*. Beijing: Geological Publication House. (in Chinese).

Wyllie, P. J., and Wolf, M. B. (1993). Amphibolite Dehydration-Melting: Sorting Out the Solidus. *Geol. Soc. Lond. Spec. Publications* 76, 405–416. doi:10.1144/GSL.SP.1993.076.01.20

Xu, C., Kynický, J., Song, W., Tao, R., Lü, Z., Li, Y., et al. (2018). Cold Deep Subduction Recorded by Remnants of a Paleoproterozoic Carbonated Slab. *Nat. Commun.* 9, 2790. doi:10.1038/s41467-018-05140-5

Xu, C., Kynický, J., Tao, R., Liu, X., Zhang, L., Pohanka, M., et al. (2017). Recovery of an Oxidized Majorite Inclusion from Earth's Deep Asthenosphere. *Sci. Adv.* 3, e1601589. doi:10.1126/sciadv.1601589

Yang, C., and Wei, C. (2017b). Two Phases of Granulite Facies Metamorphism during the Neoarchean and Paleoproterozoic in the East Hebei, North China Craton: Records from Mafic Granulites. *Precambrian Res.* 301, 49–64. doi:10.1016/j.precamres.2017.09.005

Yang, C., and Wei, C. (2017a). Ultrahigh Temperature (UHT) Mafic Granulites in the East Hebei, North China Craton: Constraints from a Comparison between Temperatures Derived from REE-Based Thermometers and Major Element-Based Thermometers. *Gondwana Res.* 46, 156–169. doi:10.1016/j.gr.2017.02.017

Yang, J., Wu, F., Wilde, S., and Zhao, G. (2008). Petrogenesis and Geodynamics of Late Archean Magmatism in Eastern Hebei, Eastern North China Craton: Geochronological, Geochemical and Nd-Hf Isotopic Evidence. *Precambrian Res.* 167, 125–149. doi:10.1016/j.precamres.2008.07.004

Yang, Q.-Y., Santosh, M., Collins, A. S., and Teng, X.-M. (2016b). Microblock Amalgamation in the North China Craton: Evidence from Neoarchaean Magmatic Suite in the Western Margin of the Jiaoliao Block. *Gondwana Res.* 31, 96–123. doi:10.1016/j.gr.2015.04.002

Yang, Q.-Y., Santosh, M., and Tsunogae, T. (2016a). High-Grade Metamorphism during Archean-Paleoproterozoic Transition Associated with Microblock Amalgamation in the North China Craton: Mineral Phase Equilibria and Zircon Geochronology. *Lithos* 263, 101–121. doi:10.1016/j.lithos.2015.11.018

Zhai, M.-G., and Santosh, M. (2011). The Early Precambrian Odyssey of the North China Craton: A Synoptic Overview. *Gondwana Res.* 20, 6–25. doi:10.1016/j.gr.2011.02.005

Zhang, H. C. G., Peng, T., Liu, J.-H., Wang, J., Chen, Y.-C., Zhang, Q. W. L., et al. (2020). New Geochronological Evidences of Late Neoarchean and Late Paleoproterozoic Tectono-Metamorphic Events in the Miyun Area, North China Craton. *Precambrian Res.* 345, 105774. doi:10.1016/j.precamres.2020.105774

Zhang, L., Zhai, M., Zhang, X., Xiang, P., Dai, Y., Wang, C., et al. (2012). Formation Age and Tectonic Setting of the Shirengou Neoarchean Banded Iron deposit in Eastern Hebei Province: Constraints from Geochemistry and SIMS Zircon U-Pb Dating. *Precambrian Res.* 222-223, 325–338. doi:10.1016/j.precamres.2011.09.007

Zhang, Y. Y., Wei, C. J., and Chu, H. (2021). Multi-Phase Metamorphism in the Northern Margin of the North China Craton: Records from Metapelite in the Hongqiyingzi Complex. *Gondwana Res.* 98, 289–308. doi:10.1016/j.gr.2021.06.012

Zhang, Y. Y., Wei, C. J., and Chu, H. (2020). Paleoproterozoic Oceanic Subduction in the North China Craton: Insights from the Metamorphic P-T-T Paths of the Chicheng Mélange in the Hongqiyingzi Complex. *Precambrian Res.* 342, 105671. doi:10.1016/j.precamres.2020.105671

Zhang, Y. X., Yan, H. Q., Wang, K. D., and Li, F. Y. (1980). Komatiites from the Qianxi Group in the Eastern Hebei Province, China. *J. Changchun Univ. Earth Sci.* 10, 1–8. (In Chinese with English abstract).

Zhao, C., Zhang, J., Zhao, G., Yin, C., Chen, G., Liu, J., et al. (2021). Kinematics and Structural Evolution of the Anziling Dome-And-Keel Architecture in East China: Evidence of Neoarchean Vertical Tectonism in the North China Craton. *Geol. Soc. Am. Bull.* in press. doi:10.1130/B36225.1

Zhao, G., Cawood, P. A., Li, S., Wilde, S. A., Sun, M., Zhang, J., et al. (2012). Amalgamation of the North China Craton: Key Issues and Discussion. *Precambrian Res.* 222-223, 55–76. doi:10.1016/j.precamres.2012.09.016

Zhao, G., Sun, M., Wilde, S. A., and Sanzhong, L. (2005). Late Archean to Paleoproterozoic Evolution of the North China Craton: Key Issues Revisited. *Precambrian Res.* 136, 177–202. doi:10.1016/j.precamres.2004.10.002

Zhao, G., Wilde, S. A., Cawood, P. A., and Lu, L. (1998). Thermal Evolution of Archean Basement Rocks from the Eastern Part of the North China Craton and its Bearing on Tectonic Setting. *Int. Geol. Rev.* 40, 706–721. doi:10.1080/00206819809465233

Zhao, G., Wilde, S. A., Cawood, P. A., and Lu, L. (1999). Thermal Evolution of Two Textural Types of Mafic Granulites in the North China Craton: Evidence for Both Mantle Plume and Collisional Tectonics. *Geol. Mag.* 136 (3), 223–240. doi:10.1017/S001675689900254X

Zou, L., Guo, J.-H., Huang, G.-Y., Jiao, S.-J., Tian, Z.-H., and Liu, P.-H. (2022). The Effect of Bulk Rock Composition in Phase Equilibria Modelling: A Case Study of Mafic Granulites from the North China Craton. *Contrib. Mineral. Petrol.* 177, 22. doi:10.1007/s00410-022-01887-9

Conflict of Interest: The authors declare that the research was conducted in the absence of any commercial or financial relationships that could be construed as a potential conflict of interest.

frontiers | Frontiers in Earth Science

ORIGINAL RESEARCH
published: 01 July 2022
doi: 10.3389/feart.2022.887154

Metamorphic *P–T* Evolution and *In Situ* Biotite Rb–Sr Geochronology of Garnet–Staurolite Schist From the Ramba Gneiss Dome in the Northern Himalaya

Long-Long Gou[1], Xiao-Ping Long[1], Hao-Yu Yan[1], Tian-Chu Shu[2], Jing-Yu Wang[1], Xiao-Fei Xu[1], Feng Zhou[1] and Zhi-Bo Tian[1]*

[1]State Key Laboratory of Continental Dynamics, Department of Geology, Northwest University, Xi'an, China, [2]Department of Earth and Environmental Sciences, RC Centre of Excellence for Core to Crust Fluid Systems, Macquarie University, Sydney, NSW, Australia

Edited by:
Yi Chen,
Institute of Geology and Geophysics (CAS), China

Reviewed by:
Hao Wang,
Institute of Geology and Geophysics (CAS), China
Jia-Min Wang,
Institute of Geology and Geophysics (CAS), China

***Correspondence:**
Xiao-Ping Long
longxp@nwu.edu.cn

Specialty section:
This article was submitted to Petrology,
a section of the journal Frontiers in Earth Science

Received: *01 March 2022*
Accepted: *23 May 2022*
Published: *01 July 2022*

Citation:
Gou L-L, Long X-P, Yan H-Y, Shu T-C, Wang J-Y, Xu X-F, Zhou F and Tian Z-B (2022) Metamorphic P–T Evolution and In Situ Biotite Rb–Sr Geochronology of Garnet–Staurolite Schist From the Ramba Gneiss Dome in the Northern Himalaya.
Front. Earth Sci. 10:887154.
doi: 10.3389/feart.2022.887154

The North Himalayan gneiss domes provide a window for looking into the deeper crust and record abundant clues of continent collisional orogenesis. This study carried out detailed petrology, *in situ* LA–ICP–MS biotite Rb–Sr dating, and phase equilibrium modeling on garnet–staurolite–two-mica schist in the Ramba gneiss dome in order to constrain metamorphic *P–T* evolution and the timing of metamorphism. A clock-wise *P–T* path, involving an early prograde process that evolves from ~540°C at ~4.4 kbar to ~630°C at ~6.0 kbar, was constructed for garnet–staurolite–two-mica schist in the Ramba gneiss dome. *In situ* LA–ICP–MS biotite Rb–Sr analysis yielded two metamorphic ages of 37.17 ± 5.66 and 5.27 ± 3.10 Ma, corresponding to the timing of retrograde cooling and the cooling age of the dome following the thermal resetting by the emplacement of ca. 8 Ma leucogranite pluton in the core of the dome, respectively. The peak metamorphism is inferred to be older than ca. 37 Ma. Based on these results and the data previously published, the garnet–staurolite–two-mica schist recorded the Eocene crustal thickening, following the India–Asia collision and later the exhumation process.

Keywords: phase equilibrium modeling, P–T path, Ramba gneiss dome, E–W extension, northern Himalaya

INTRODUCTION

Gneiss domes are ubiquitous structures in exhumed orogens (Whitney et al., 2004). During orogenesis, gneiss domes vertically transfer large volumes of deep-seated material into the upper crustal level (Teyssier and Whitney, 2002; Rey et al., 2017) and, thus, provide a window to investigate the orogenic process in the middle-to-lower crust. In addition, gneiss domes are often formed by the superposition of several dome-forming mechanisms or in several different tectonic settings (Yin, 2004). Therefore, gneiss domes were used to investigate the fundamental orogenic process and geodynamics of continental collision orogen, such as crustal thickening or shortening (Yin, 2006; Smit et al., 2014; Ding et al., 2016a) and extension (Lister and Davis, 1989; Chen et al., 1990; Lee and Whitehouse, 2007; Wang et al., 2018).

The Himalayan orogen, as the result of the ongoing collision between the Indian and Asian plates, is one of the largest collisional orogens on the Earth (**Figure 1**), which played a central role in

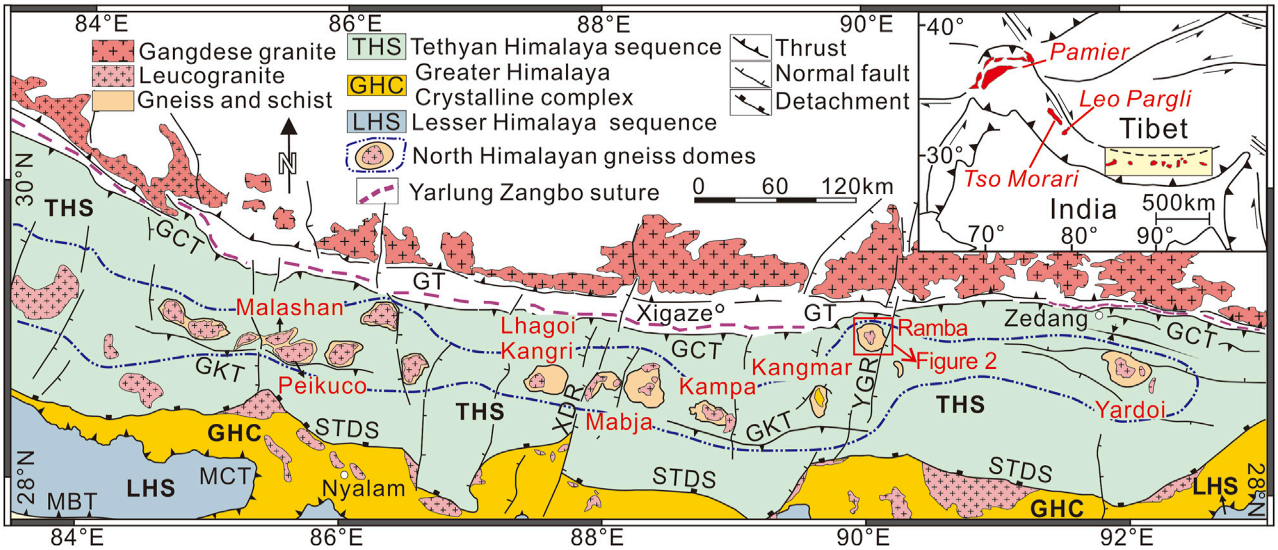

FIGURE 1 | Generalized geological map of the Himalayan orogen (modified from Wang et al., 2018). Abbreviations of metamorphic complexes: GT, Gangdese thrust; GCT, Greater Counter thrust; GKT, Gyirong–Kangmar thrust; STDS, south Tibetan detachment system; MCT, main central thrust; MBT, main boundary thrust.

understanding the continent–continent collisional orogenesis (Yin and Harrison, 2000; Beaumont et al., 2001; Harris, 2007; Searle et al., 2009; Palin et al., 2014; Wang et al., 2016). The northern Himalayan belt is characterized by extension structures, including the north Himalayan gneiss domes (NHGDs), the south Tibet detachment system (STDS), and the north–south trending rifts (NSTR) (Zhang et al., 2012). During the past few decades, the formation mechanisms of the NHGD have been the subject of intensive studies (Chen et al., 1990; Lee et al., 2000, 2004, 2006; Aoya et al., 2006; Quigley et al., 2008; Stearns et al., 2013; Zhang et al., 2004, 2012; Ding et al., 2016a, b; Jessup et al., 2019) as the NHGDs are the window to the middle-to-lower crust in the northern Himalayan belt and are the key to understand not only the tectonic evolution of the Himalayan orogen but also the geodynamic processes within the middle-to-lower crust of continent–continent collisional orogens. Different geodynamic settings have been proposed to interpret the formation of the NHGD, such as north–south extension with the top-to-north movement along the STDS (Chen et al., 1990; Lee et al., 2000, 2004, 2006; Wang et al., 2018), diapirism of buoyant anatexis (LeFort et al., 1987; Harrison et al., 1997), and east–west extension related to the NSTR (Zhang and Guo, 2007; Zhang et al., 2012; Fu et al., 2016).

The Ramba gneiss dome, which is dominated by the top-to-E shear structure, was considered to have been formed by the E–W extension along the NSTR (Guo et al., 2008; Zhang et al., 2012). However, due to the lack of metamorphic data for the Ramba gneiss dome up to now, the similarities and differences of the metamorphic P–T–t evolution between the Ramba gneiss dome and other famous gneiss domes (the Mabja dome and the Yardoi gneiss dome) are unclear.

In this article, the metamorphic P–T evolution and the timing of metamorphism for garnet–staurolite–two-mica schist in the Ramba gneiss dome were constrained, with the evidence from detailed petrology, *in situ* LA–ICP–MS biotite Rb–Sr dating, and phase equilibrium modeling. Based on these results, the tectonic implications and the differences in metamorphic evolution between the E–W and the N–S extensional North Himalayan gneiss domes were discussed.

GEOLOGICAL SETTING AND SAMPLES

The Himalayan orogen includes the northern Himalayas and the southern Himalayas, which are separated by the high crest line (Yin, 2006). The STDS is a network of detachment faults, juxtaposing the Tethys Himalayan sequences (THSs) in the hanging wall over the Greater Himalayan Crystallines (GHC) in the footwall (Searle and Godin, 2003; Zhang et al., 2012). The southern Himalayas is composed of the GHC, the Lesser Himalayan sequences (LHSs), and the Siwalik group (Zhang et al., 2012; **Figure 1**). The GHC is characterized by the ca. 40–30 Ma high pressure (HP) granulite-facies rocks (Kohn and Corrie, 2011; Regis et al., 2014; Iaccarino et al., 2015; Zhang et al., 2015), the ca. 17–14 Ma granulitized eclogites (Wang Y. et al., 2017, 2021; Li et al., 2019; Zhang et al., 2021; Wu et al., 2022), Barrovian metamorphic belts (Wang et al., 2013, 2015; Iaccarino et al., 2017; Shrestha et al., 2017), and abundant ca. 33–7 Ma leucogranites (Searle et al., 1999; Searle and Godin, 2003; Wu et al., 2015 and references therein; Gou et al., 2016; Hopkinson et al., 2017; Liu et al., 2022a). It underwent a long-lived partial melting from ca. 40 to 8 Ma (e.g., Wang et al., 2013, 2015, Wang et al., 2017 J.-M.; Zhang et al., 2015; Tian et al., 2019; Liu et al., 2022b). Within the GHC, tectono-metamorphic discontinuities have been recognized in the recent decade (Wang et al., 2016, and references therein).

The northern Himalayan belt is dominated by the THS, consisting of unmetamorphosed to low-grade metasedimentary rocks (Zhang et al., 2012; **Figure 1**). This belt is characterized by

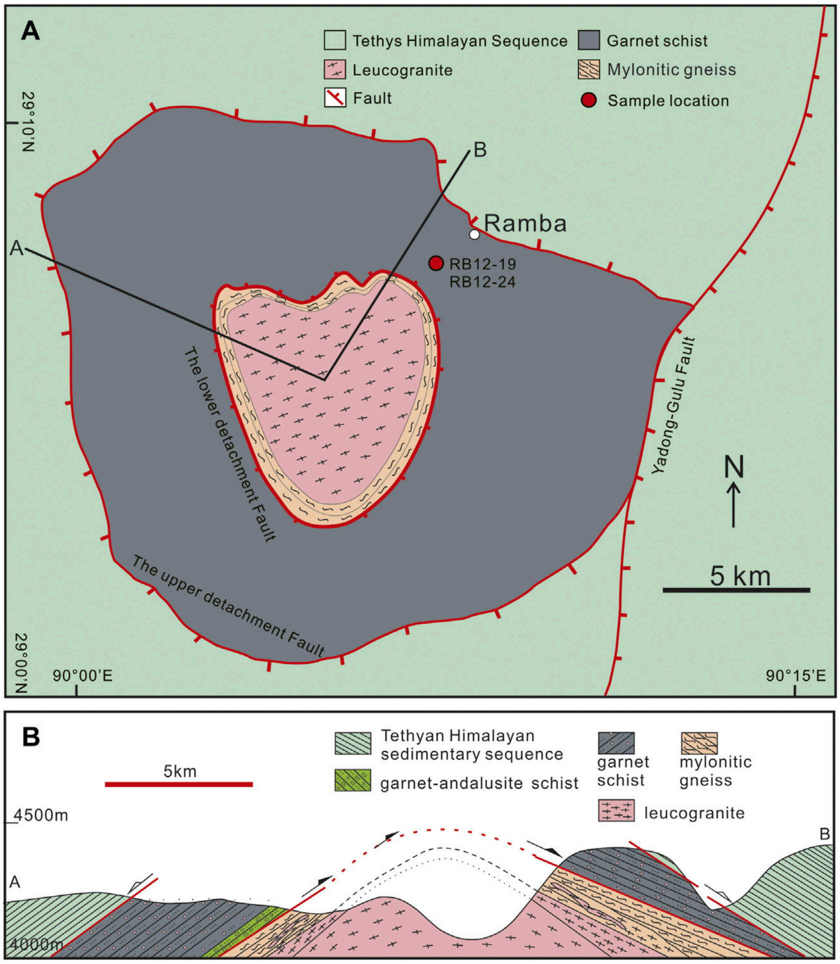

FIGURE 2 | (A) Schematic geological map showing the Ramba gneiss dome and **(B)** cross-section (modified from Zhang et al., 2012).

the NHGD cored by granite plutons (Zhang et al., 2012) and the crystallization ages of granites or leucogranites in the northern Himalayan belt ranging from ca. 48 to 8 Ma (Aikman et al., 2008; Zhang et al., 2012; Liu et al., 2014; Zeng et al., 2011; Gao et al., 2012; Wu et al., 2015; Zeng and Gao, 2017 and references). The dome geometry at the Mabja gneiss dome was formed by middle-Miocene southward-directed thrust faulting upward and southward, which are similar to those of the Kangmar dome (Lee et al., 2000, 2004, 2006). The peak metamorphic condition of the migmatite sample from the sillimanite-zone in the Mabja gneiss dome is 8.2 kbar/705°C (Lee et al., 2004), and the timing of peak metamorphism was constrained to be 35.0 ± 0.8 Ma (Lee and Whitehouse, 2007). The structural, metamorphic, and intrusive histories in middle crustal rocks exposed in these NHGD are similar to those in the GHC, suggesting that the middle crust was continuous from beneath the northern Himalayas southward to the high Himalayas (Lee et al., 2006; Lee and Whitehouse, 2007). The garnet–kyanite–staurolite schists of the Yardoi gneiss dome in the eastern Himalaya record peak P–T conditions of 7–8 kbar and 630–660°C. Zircon U–Pb dating yielded metamorphic ages of 44.8 ± 1.1 Ma, 46.7 ± 1.8 Ma, and 48.2 ± 2.0 Ma (Ding et al., 2016a), which were considered as the timing of prograde metamorphism (Ding et al., 2016b), and Wang et al. (2018) obtained metamorphic ages of 18–17 Ma using SHRIMP monazite U/Th-Pb analysis and suggested that north–south extension in a convergent geodynamic setting during Early Miocene accounts for the formation of the Yardoi dome.

The Ramba gneiss dome is located on the west of the north–south trending Yadong–Gulu rift and near the Yarlung–Zanbo suture (Zhang et al., 2012; Liu et al., 2014, 2019; **Figures 1**, **2**). The dominant deformation was attributed to the E–W extension of the NSTR (Guo et al., 2008; Zhang et al., 2012). Liu et al. (2014) revealed that there were three epidotes (ca. 44 Ma, ca. 28 Ma, and ca. 8 Ma) of granitic magmatism. The granitic rocks of ca. 44 Ma and ca. 28 Ma occur as strongly deformed porphyritic two-mica granite gneiss dykes, which intruded into the margin of the dome (Liu et al., 2014, 2019). The ca. 8 Ma leucogranites include two-mica granite occupying the core of the dome and garnet-bearing granite dykes in the margin of the dome (Liu et al., 2014), and the former has biotite and muscovite ^{40}Ar/^{39}Ar ages of ca. 6 Ma (Guo et al., 2008).

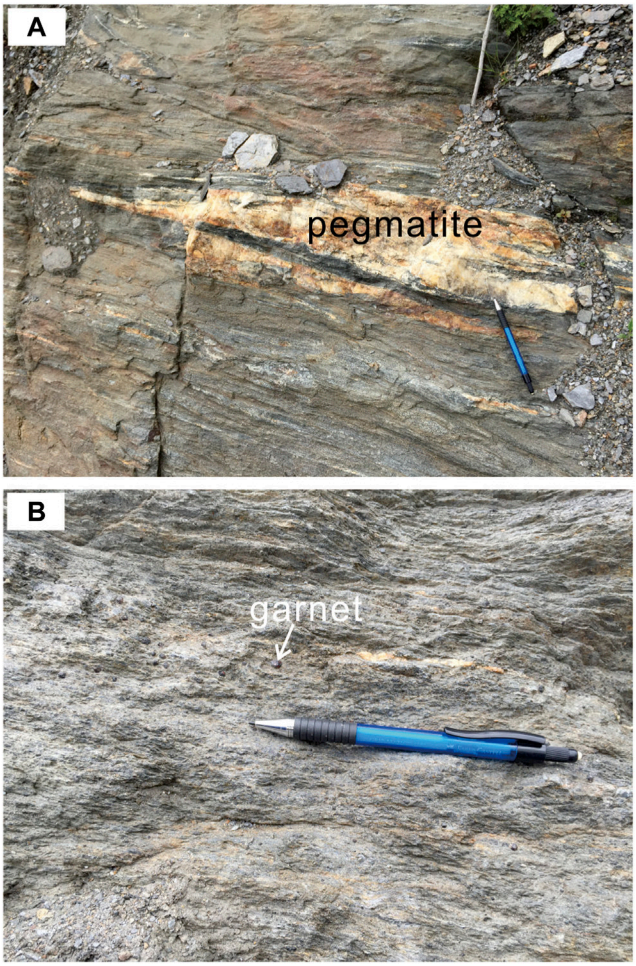

FIGURE 3 | Field photographs of garnet–staurolite–two-mica schist in the Ramba gneiss dome.

Here, two representative samples (RB12-19 and RB12-24) selected for this study are garnet–staurolite–two-mica schist, belonging to the base of the THS on the basis of rock association in a previous study, which experienced detachment shear of STDS (Guo et al., 2008; Zhang et al., 2012). These samples display porphyroblastic texture and are in gray color (**Figure 3**). Pegmatites that are parallel to foliation can be observed (**Figure 3A**), and garnet porphyroblasts are obvious on the outcrop (**Figure 3B**).

PETROGRAPHY AND MINERAL CHEMISTRY

Mineral compositions were analyzed using the JEOL JXA-8230 electron microprobe at the State Key Laboratory of Continental Dynamics (SKLCD), Northwest University, Xi'an. The operating conditions were 2 μm beam size, 15 kV acceleration voltage, and 10 nA beam current. Mineral abbreviations in this study follow Whitney and Evans (2010). Compositional maps illustrating the distributions of Fe, Mg, Ca, and Mn were obtained for representative garnet porphyroblasts using the Quanta450 FEG field-emission environmental scanning electron microscope coupled with the X-MaxN 50 X-ray energy dispersive spectrometer at the SKLCD.

Sample RB12-19

This sample consists of garnet (10%), staurolite (20%), biotite (25%), muscovite (10%), plagioclase (5%), and quartz (30%) and accessory minerals, including zircon, graphite, and ilmenite (**Figures 4A, B**). Garnet occurs as euhedral to subhedral porphyroblasts with grain sizes of 0.4–1.1 mm in diameter (**Figures 4A, B**), with minor quartz inclusions. Staurolite is present as a subhedral porphyroblast with grain sizes of 0.4–1.0 mm and is generally in contact with garnet (**Figures 4A, B**); it displays a yellow-to-black color due to abundant graphite inclusion. Biotite and muscovite occur in the matrix and define the foliation (**Figure 4A**). Plagioclase occurs as relatively small crystals in the matrix, and quartz occurs as small grains in the matrix or as mineral inclusions in garnet (**Figures 4A–C**). As a result, the peak metamorphic mineral assemblage is inferred to be garnet–biotite–muscovite–plagioclase–staurolite–ilmenite–quartz–H_2O.

Mineral compositions and the mole fractions of end-members for sample RB12-19 are given in **Supplementary Table S1**. The garnet is almandine-rich (X_{Alm} = 0.72–0.83), with low concentrations of spessartine (X_{Sps} = 0.07–0.18), pyrope (X_{Prp} = 0.04–0.09), and grossular (X_{Grs} = 0.04–0.06). The zoning profile of a representative garnet grain shows obvious compositional variation from core to rim (**Figure 5A**), with increasing almandine and decreasing spessartine but relatively flat pyrope and grossular, which are consistent with distributions of Fe, Mg, Ca, and Mn on garnet compositional maps (**Figure 6A**). Staurolite has homogeneous compositions, with X_{Mg} of 0.08–0.10. Biotite and muscovite also exhibit homogeneous compositions, with X_{Mg} of 0.40–0.41, Ti of 0.10–0.12 cations per formula unit (cpfu), and Si of 3.09–3.13 cpfu, respectively. Plagioclase displays no compositional variation between different grains, with X_{An} of 0.27–0.31.

Sample RB12-24

Sample RB12-24 is composed of garnet (10%), staurolite (10%), biotite (20%), muscovite (5%), plagioclase (20%), and quartz (35%) and accessory minerals, including zircon, graphite, and ilmenite (**Figures 4C,D**). Garnet occurs as subhedral porphyroblasts with grain sizes ranging from 0.5 to 2.7 mm (**Figure 4D**), larger than garnet in sample RB12-19 (**Figures 4A,B**); it contains mineral inclusions of quartz (**Figure 4D**). Staurolite is present as subhedral porphyroblasts with grain sizes of 0.3–1.4 mm and displays yellow-to-black color due to abundant graphite inclusion (**Figures 4C,E**). Both garnet and staurolite are wrapped by a continuous foliation delineated by biotite and muscovite in the matrix (**Figures 4D,E**). Plagioclase occurs as small grains in the matrix, and quartz occurs as small grains in the matrix or as mineral inclusions in garnet (**Figures 4D,E**). Therefore, the peak metamorphic mineral assemblage is inferred to be garnet–biotite–muscovite–plagioclase–staurolite–ilmenite–quartz–H_2O.

Mineral compositions and the mole fractions of end-members for sample RB12-24 are given in **Supplementary Table S2**. The

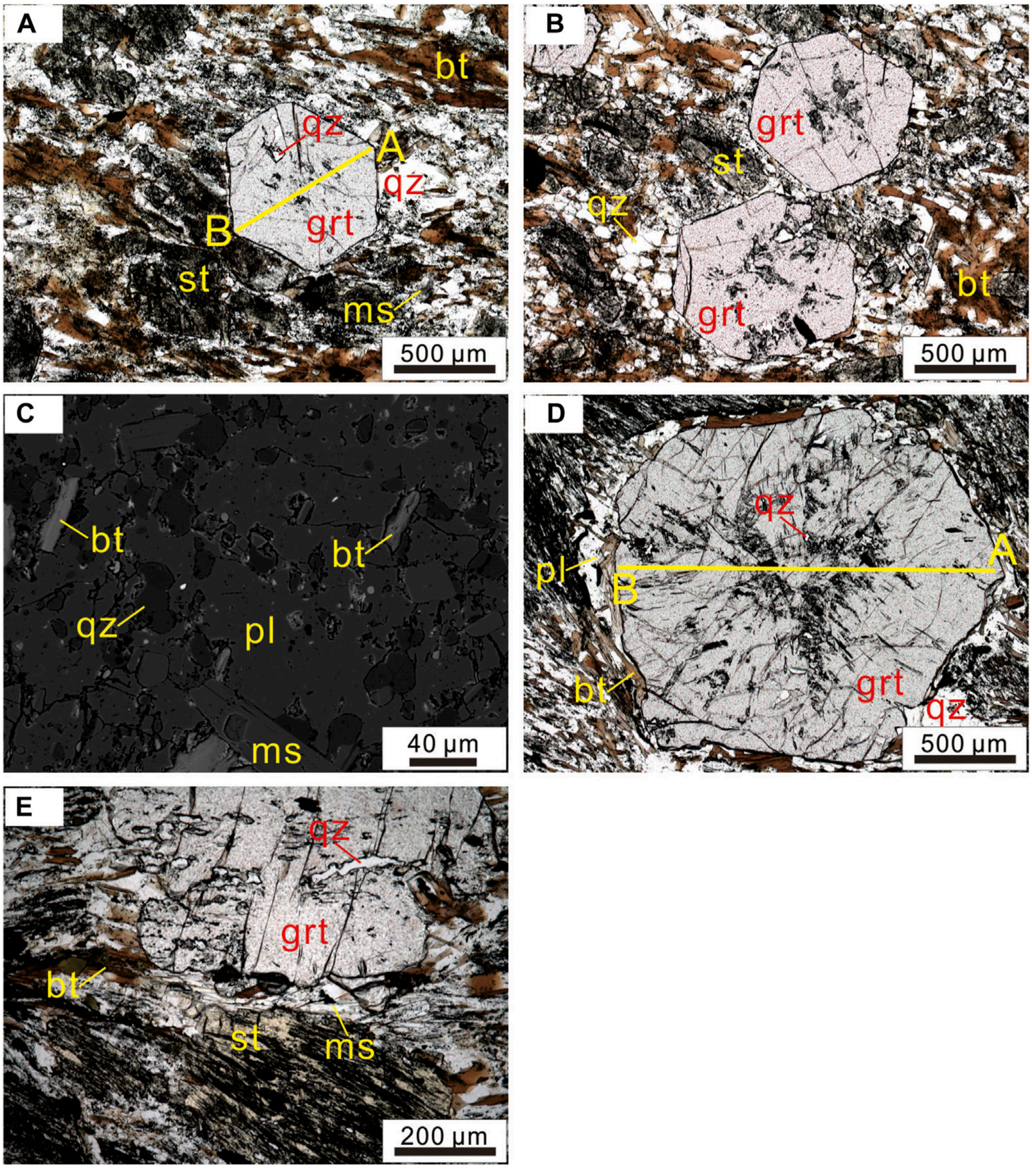

FIGURE 4 | Mineral assemblages and microstructures of garnet–staurolite–two-mica schist in the Ramba gneiss dome. **(A,B)** Photomicrographs to show garnet and staurolite porphyroblasts and matrix minerals, including biotite, muscovite, plagioclase, and quartz in sample RB12-19 (plane-polarized light). **(C)** Photomicrograph to show biotite, muscovite, quartz, and plagioclase in sample RB12-19 (back-scattered electron image). **(D)** Photomicrograph to show garnet porphyroblasts and matrix minerals, including biotite, muscovite, plagioclase, and quartz in the sample RB12-24 (plane-polarized light). **(E)** Photomicrographs to show garnet and staurolite porphyroblasts and matrix minerals, including biotite, muscovite, plagioclase, and quartz in sample RB12-24 (plane-polarized light).

garnet is almandine-rich (X_{Alm} = 0.75–0.87), with low pyrope (X_{Prp} = 0.03–0.04), spessartine (X_{Sps} = 0.01–0.08), and grossular (X_{Grs} = 0.09–0.14) (**Figure 5B**). Compared to those of the sample RB12-19, the pyrope is lower, whereas the grossular is higher (**Figures 5A,B**). The compositional profile of a representative garnet porphyroblast shows moderate variation from the core to the rim (**Figure 5B**), involving increasing almandine and decreasing spessartine but flat pyrope and grossular. These are consistent with distributions of Fe, Mg, Ca, and Mn on garnet compositional maps (**Figure 6B**). Staurolite is uniform in composition, with X_{Mg} ranging from 0.07 to 0.08. Biotite and muscovite also have homogeneous compositions, with X_{Mg} of 0.33–0.35, Ti of 0.10–0.12 cpfu, and Si of 3.08–3.12 cpfu, respectively. Plagioclase displays moderate compositional variation between different grains and is more calcic than that in sample RB12-19, with X_{An} of 0.38–0.53.

PHASE EQUILIBRIUM MODELING

The bulk chemical compositions (**Table 1**) were determined by wavelength-dispersive X-ray fluorescence (XRF) spectrometry on

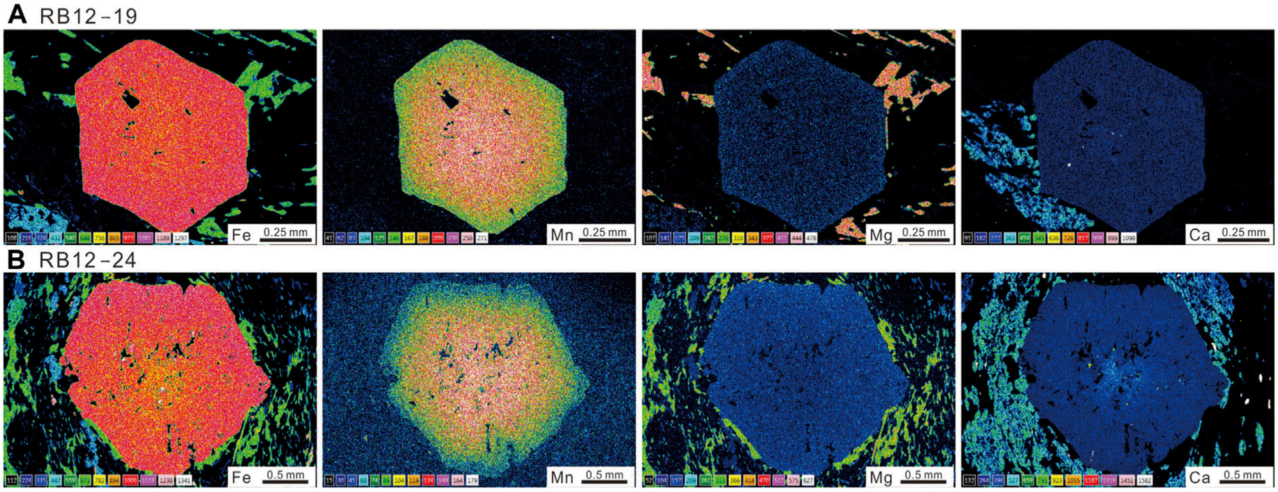

FIGURE 5 | Compositional mapping images of garnets in schist samples RB12-19 **(A)** and RB12-24 **(B)**.

a fused bead at the SKLCD, Northwest University, Xi'an. The normalized molar proportions used for the phase equilibrium modeling are given in **Table 1**. H_2O was set to be in excess. On the basis of low whole-rock Fe^{3+} contents as revealed that garnet, staurolite, biotite, and muscovite in two samples are low in Fe^{3+} (**Supplementary Tables S1, S2**), O = 0.010 was selected. The calculated *P–T* pseudosection allows the mineral assemblages to be evaluated within *P–T* conditions between 450 and 750°C and 3–9 kbar (**Figures 7, 8**). Phase equilibrium calculations were performed using Thermocalc version tc340 (Powell et al., 1998; updated October 2013) in the $MnO–Na_2O–CaO–K_2O–FeO–MgO–Al_2O_3–SiO_2–H_2O–TiO_2–O_2$ (MNCKFMASHTO) system, with the internally consistent thermodynamic dataset ds62 (Holland and Powell, 2011). The activity–composition (*a–x*) models for garnet, staurolite, biotite, cordierite, and chlorite are from White et al. (2014a, b), plagioclase from Holland and Powell (2003), ilmenite from White et al. (2000), epidote from Holland and Powell (2011), and muscovite and paragonite from Smye et al. (2010). Pure phases included sillimanite, kyanite, andalusite, quartz, and rutile. The mineral abbreviations in this study follow those by Whitney and Evans (2010).

Sample RB12-19

The peak phase assemblage is represented by the quinivariant field grt–bt–ms–pl–st–ilm–qz–H_2O, which has a wide *P–T* range, with upper pressure and temperature of 670°C and 7 kbar, respectively (**Figure 7A**). The chlorite-in and plagioclase-out assemblage field boundaries mark the low-temperature limit of this field. The upper temperature and pressure limits are the sillimanite-in and rutile-in assemblage field boundaries, respectively.

Figure 7B shows calculated isopleths of X_{Sps} and X_{Grs} for garnet, X_{Mg} for staurolite, and X_{Ti} for biotite. In the peak phase assemblage field of grt–bt–ms–pl–st–ilm–qz–H_2O, the X_{Sps} in garnet decreases significantly as pressure increases, and X_{Ti} in biotite increases as temperature increases. Isopleths of $X_{Ti(Bt)}$ of 0.10–0.12 are consistent with Ti contents of biotite (**Supplementary Table S1**). The plotted isopleths of X_{Grs} for garnet are close to vertical and decrease as temperature increases. The X_{Mg} in staurolite ranges from 0.08 to 0.10 (**Supplementary Table S1**), with corresponding isopleths plotted in the phase assemblage fields of grt–ms–chl–pl–st–ilm–qz–H_2O and grt–bt–ms–chl–pl–st–ilm–qz–H_2O. As no prograde and retrograde metamorphic mineral assemblages were observed, isopleths of X_{Sps} and X_{Grs} for garnet, X_{Mg} for staurolite, and X_{Ti} for biotite were used to constrain the *P–T* evolution. Plagioclase is stable in the studied sample, and thus, mineral assemblages during the early prograde metamorphic stage should contain plagioclase. Therefore, the X_{Mg} isopleths of staurolite in the mineral assemblage fields that contain plagioclase can be used to constrain the *P–T* conditions in the early stage of prograde metamorphism, although the defined *P–T* range is relatively large (**Figure 7B**). X_{Sps} and X_{Grs} in garnet and X_{Ti} in biotite constrain the peak metamorphic *P–T* conditions to be ~630°C at ~5.8 kbar in the peak mineral assemblage field of grt–bt–ms–pl–st–ilm–qz–H_2O. As a result, a prograde *P–T* path that evolves roughly from ~540°C at ~4 kbar to ~630°C at ~5.8 kbar was defined for the sample RB12-19 (**Figure 7B**).

Sample RB12-24

The peak phase assemblage of grt–bt–ms–pl–st–ilm–qz–H_2O is represented by a quinivariant field, which occurs between 552 and 668°C and 4.7–6.9 kbar (**Figure 8A**). The sillimanite-in assemblage field boundary marks the upper-temperature limit of this field, and the rutile-in assemblage field boundary is the upper-pressure limit. The low temperature and pressure limits are the chlorite-in and muscovite-out assemblage field boundaries, respectively.

Figure 8B shows calculated isopleths of X_{Sps} and X_{Grs} for garnet and X_{Ti} for biotite. The isopleths of X_{Sps} in garnet are horizontal and decrease as pressure increases, and the isopleths of X_{Ti} in biotite are vertical and increase as temperature increases, in the peak phase assemblage field (grt–bt–ms–pl–st–ilm–qz–H_2O).

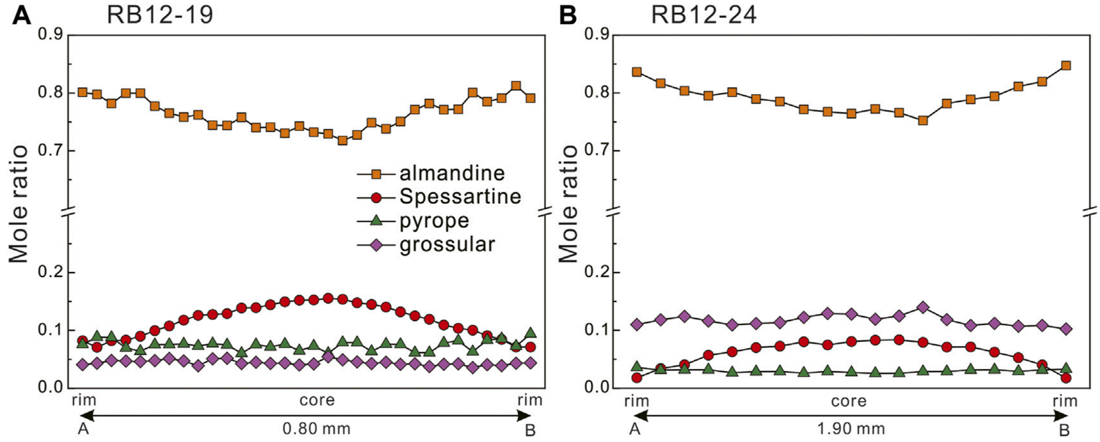

FIGURE 6 | Compositional profiles of garnet porphyroblasts from garnet–staurolite–two-mica schist samples RB12-19 **(A)** and RB12-24 **(B)**. **(A,B)** show garnet compositions matching those at the corresponding locations along the compositional profile of garnet in **Figure 4**.

Ti contents of biotite correspond to isopleths of $X_{Ti(Bt)}$ of 0.10–0.12 (**Supplementary Table S2**). In the phase assemblage field of grt–bt–ms–pl–chl–ilm–qz–H_2O, the isopleths of X_{Sps} in garnet are close to horizontal and decrease as temperature increases. The plotted isopleths of X_{Grs} for garnet are near vertical and decrease as temperature increases. Similar to sample RB12-19, isopleths of X_{Sps} and X_{Grs} for garnet and X_{Ti} for biotite were used to constrain the $P–T$ evolution. The X_{Sps} and X_{Grs} in the garnet core and mantle have crossover points in the mineral assemblage field grt–bt–ms–chl–pl–ilm–qz–H_2O, which constrain the $P–T$ conditions in the early stage of prograde metamorphism to be ~540°C at ~4.4 kbar (**Figure 8B**). In addition, the crossover points of X_{Sps} and X_{Grs} in the garnet rim fall into the peak phase assemblage field of grt–bt–ms–pl–st–ilm–qz–H_2O, which is close to or within the $P–T$ range defined by isopleths of X_{Ti} for biotite (**Figure 8B**). As a result, a prograde $P–T$ path that evolves from ~540°C at ~4.4 kbar to ~620°C at ~6.3 kbar was acquired for the sample RB12-24 (**Figure 8B**).

LA–ICP–MS BIOTITE RB–SR GEOCHRONOLOGY

In situ biotite Rb–Sr dating was conducted on garnet–staurolite–two-mica schist samples RB12-19 and RB12-24. Biotite Rb–Sr isotopic compositions were analyzed on thin sections (**Figure 9**) using an NWR 193-nm ArF excimer laser-ablation (LA) system coupled to an inductively coupled plasma mass spectrometry (ICP-MS, iCAP TQ 00108) at the Guangzhou Tuoyan Analytical Technology Co., Ltd., Guangzhou, China. Ablation material was carried out with high-purity He gas, which was then mixed with Ar gas before introduction into the ICP-MS torch. The reaction gas N_2O was used to suppress isobaric interferences as N_2O is a highly potent reaction gas that reacts efficiently with Sr^+ to form SrO^+ ions but not with Rb^+ (Hogmalm et al., 2017). The reaction rates are optimized by increasing N_2O flow rates in the reaction cell and monitoring the sensitivity of Sr^+ and SrO^+ whilst ablating NIST SRM 610 and mica-Mg. It was found that the signals of SrO^+ achieve maximum without significant loss in the Rb^+ signal when using N_2O at 25–27% flow rates (0.25–0.27 ml min^{-1} of N_2O).

Before sample measurements, N_2O was connected to the 4th mass flow controller in the iCAP TQ, and the lines were purged at a 25% flow rate (0.25 ml min^{-1} of N_2O) for 2 h to maintain stability. This procedure washes out gas impurities and saturates the system, minimizing drift due to variations in the reaction rate. Then, the lens and cell parameters were tuned to maximize sensitivity by ablating NIST SRM 610 in the line scan mode (spot size, 30 μm; pulse repetition rate, 10 Hz; fluence, ~3.5 J/cm^2). Each analysis consists of 30 s of background acquisition followed by 120 s of ablation and 30 s of washout. A dwell time of 50 ms was used for the analysis of on-mass and mass-shifted Sr isotopes (^{86}Sr, ^{87}Sr and ^{88}Sr, $^{86}Sr^{16}O$, $^{87}Sr^{16}O$, and $^{88}Sr^{16}O$) and ^{85}Rb. Typical laser settings during sample analysis are 110-μm spot size, ~7 J/cm^2, and 5-Hz pulse repetition. The detailed instrumentation and analytical conditions were set, following the method described by Gorojovsky and Alard (2020). The raw data were exported offline, and the whole data reduction procedure was performed using an Excel macro program. The Mica-Mg was used as a primary reference standard for calibration of isotopic ratios of the samples. The standard NIST SRM 610 was used as secondary reference material to monitor the data quality, and the measured $^{87}Rb/^{86}Sr$ and $^{87}Sr/^{86}Sr$ ratios are 2.16 ± 0.08 ($n = 2, 2\sigma$) and 0.7110 ± 0.0048 ($n = 2, 2\sigma$), respectively. Compared with the recommended ratios for the standard NIST SRM 610 ($^{87}Rb/^{86}Sr = 2.33$, Gorojovsky and Alard, 2020; $^{87}Sr/^{86}Sr = 0.709699 \pm 0.000018$, Woodhead and Hergt, 2001), the measured $^{87}Sr/^{86}Sr$ ratio is similar within error, whereas the measured $^{87}Rb/^{86}Sr$ ratio is slightly lower, which may be due to that the external standard Mica-Mg has a high $^{87}Rb/^{86}Sr$ ratio (154–155, Gorojovsky and Alard, 2020).

TABLE 1 | Bulk compositions used for phase equilibrium modeling.

Whole-rock compositions (wt.%)

Sample	SiO2	TiO_2	Al_2O_3	Fe_2O_3	MnO	MgO	CaO	Na_2O	K_2O	P_2O_5	LOI	Total
RB12-19	59.37	0.82	20.56	10.10	0.28	1.87	0.50	0.54	3.12	0.11	2.60	99.87
RB12-24	55.45	0.95	21.09	9.47	0.11	1.57	4.31	2.03	1.98	0.13	2.59	99.68

Normalized molar proportion used for phase equilibrium modeling

Sample	Figures	H2O	SiO_2	Al_2O_3	CaO	MgO	FeO	K_2O	Na_2O	TiO_2	MnO	O
RB12-19	7	excess	69.209	14.123	0.624	3.250	8.859	2.320	0.610	0.719	0.276	0.010
RB12-24	8	excess	64.471	14.449	5.369	2.721	8.285	1.468	2.288	0.831	0.108	0.010

Notes: LOI, loss on ignition.

Sample RB12-19

A total of 19 spot analyses were carried out on biotite in sample RB12-19. During a single spot analysis, spots 1, 6, and 7 yielded multiple intervals with obviously different ratios of $^{87}Rb/^{86}Sr$ and $^{87}Sr/^{86}Sr$, which imply biotite may have inhomogeneous Rb–Sr isotopic compositions. Thus, these spot analyses obtained more than one effective data (**Table 2**). The Rb–Sr isotopic data of 3, 6.2, 7.2, 8, 14, 16, 17, and 18 were excluded during age calculation as these data are scattered on the $^{87}Rb/^{86}Sr$ and $^{87}Sr/^{86}Sr$ isochron diagram and cannot be well-included into an isochron (**Figure 9A**). The remaining $^{87}Rb/^{86}Sr$ and $^{87}Sr/^{86}Sr$ ratios are 3.7942–131.847 and 0.7062–0.7866, respectively, which yielded an isochron age of 37.17 ± 5.66 Ma (n = 16, MSWD = 1.5).

Sample RB12-24

Similar to sample RB12-19, 19 spot analyses were carried out on biotite in sample RB12-24. Spot 17 yielded multiple intervals with obviously different ratios of $^{87}Rb/^{86}Sr$ and $^{87}Sr/^{86}Sr$, which obtained two effective datasets (**Table 2**). The $^{87}Rb/^{86}Sr$ and $^{87}Sr/^{86}Sr$ ratios of biotite in sample RB12-24 range from 0.763

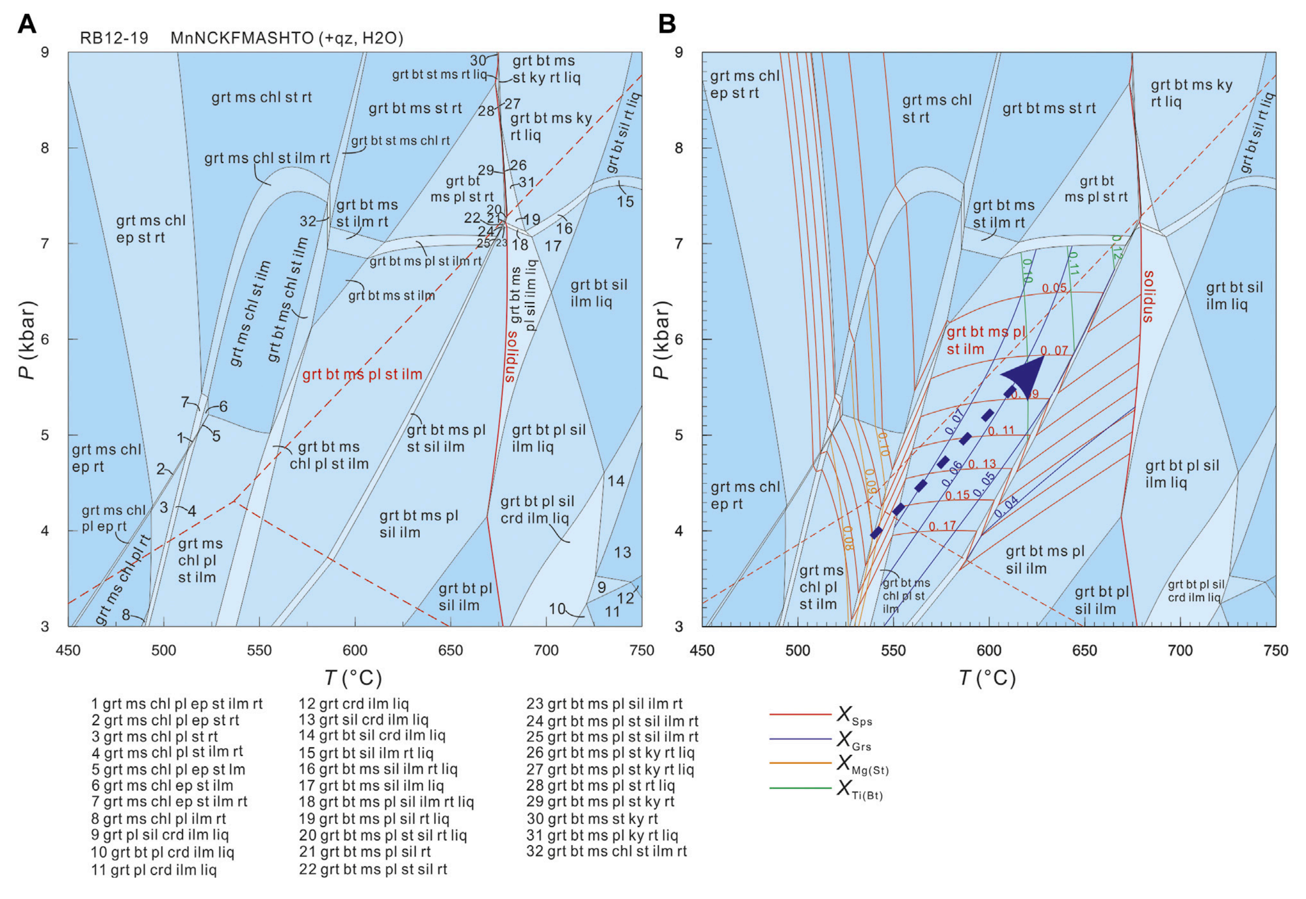

FIGURE 7 | *P–T* pseudosections for the garnet–staurolite–two-mica schist sample RB12-19. **(A)** *P–T* pseudosection that shows mineral assemblages. **(B)** *P–T* pseudosection with isopleths of X_{Sps} and X_{Grs} in garnet, X_{Mg} in staurolite, and X_{Ti} in biotite. The field of peak mineral assemblage is marked by grt–bt–ms–pl–st–ilm–qz–H_2O in red type.

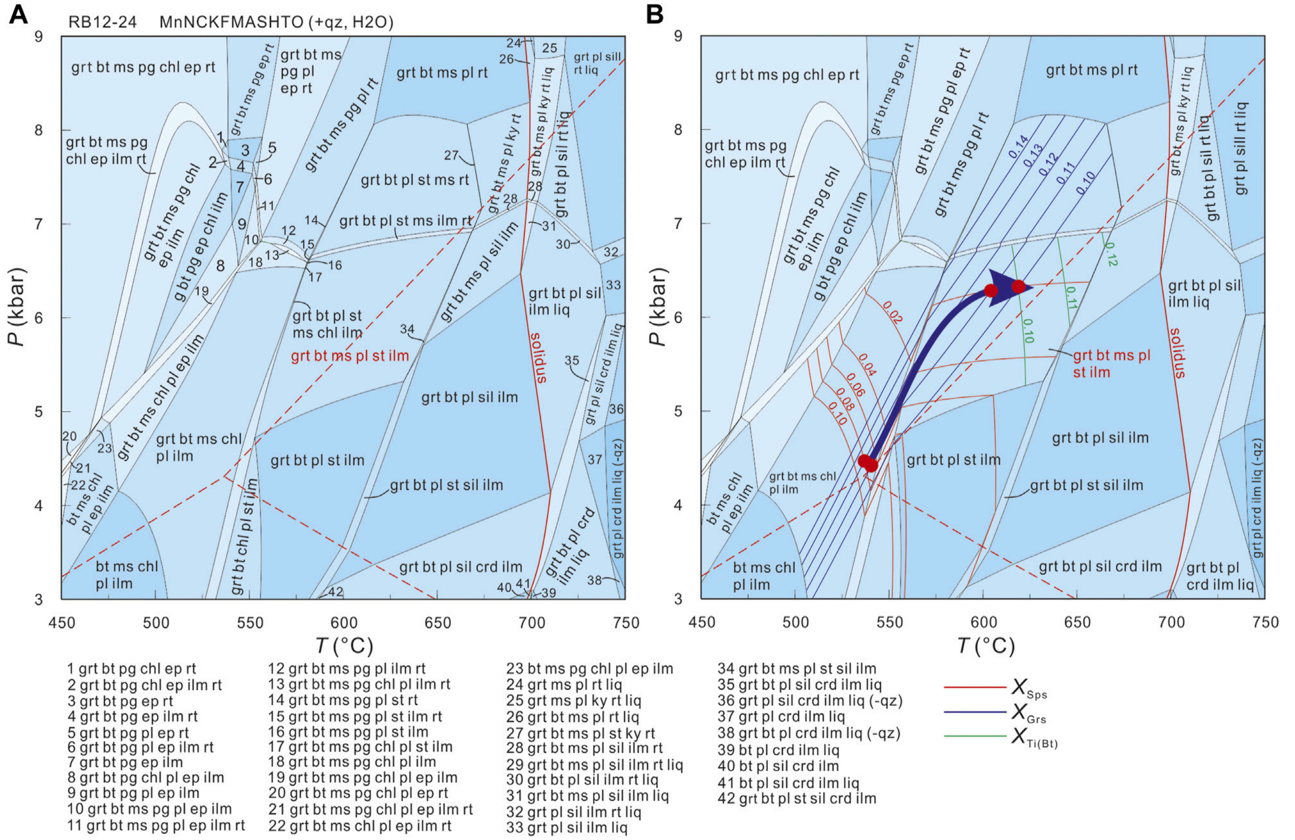

FIGURE 8 | *P–T* pseudosections for the garnet–staurolite–two-mica schist sample RB12-24. **(A)** *P–T* pseudosection that shows mineral assemblages. **(B)** *P–T* pseudosection with isopleths of X_{Sps} and X_{Grs} in garnet and X_{Ti} in biotite. The field of peak mineral assemblage is marked by grt–bt–ms–pl–st–ilm–qz–H_2O in red type.

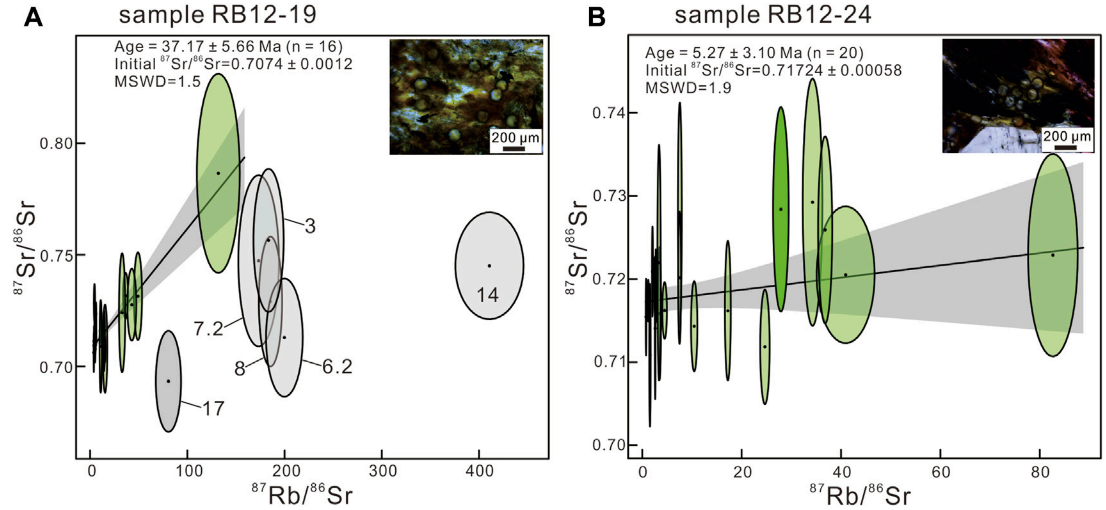

FIGURE 9 | *In situ* LA–ICP–MS biotite Rb–Sr isochron diagrams and photos of biotite with the laser spot: **(A)** sample RB12-19 and **(B)** sample RB12-24.

to 82.637 and 0.711 to 0.729, respectively (**Table 2**). On the ^{87}Rb/^{86}Sr and ^{87}Sr/^{86}Sr isochron diagram, these data yielded an isochron age of 5.27 ± 3.10 Ma (*n* = 20, MSWD = 1.9) (**Figure 9B**). Obviously, this age is younger than that of sample RB12-19, although samples RB12-19 and RB12-24 were collected at the same outcrop, which may be due to

TABLE 2 | LA–ICP–MS biotite Rb–Sr data for the garnet–staurolite–two-mica schist samples RB12-19 and RB12-24 of the Ramba gneiss dome.

Spot number	^{87}Rb/^{86}Sr	±1σ	^{87}Sr/^{86}Sr	±1σ
RB12-19-1.1	4.1439	0.1594	0.7094	0.0024
RB12-19-1.2	5.0593	0.3273	0.7148	0.0041
RB12-19-1.3	3.7942	0.0793	0.7062	0.0036
RB12-19-1.4	15.367	0.931	0.7080	0.0081
RB12-19-2	10.427	0.168	0.7160	0.0023
RB12-19-3	183.523	6.350	0.7565	0.0131
RB12-19-4	49.214	1.695	0.7315	0.0080
RB12-19-5	36.497	1.044	0.7317	0.0042
RB12-19-6.1	10.901	0.480	0.7090	0.0085
RB12-19-6.2	199.794	7.703	0.7130	0.0108
RB12-19-7.1	42.885	1.879	0.7277	0.0066
RB12-19-7.2	173.306	8.544	0.7473	0.0157
RB12-19-8	185.504	4.893	0.7291	0.0119
RB12-19-9	5.0690	0.1682	0.7078	0.0025
RB12-19-10	32.900	1.311	0.7241	0.0109
RB12-19-11	4.0210	0.0361	0.7113	0.0028
RB12-19-12	131.847	9.011	0.7866	0.0182
RB12-19-13	5.8127	0.2173	0.7153	0.0026
RB12-19-14	410.698	14.332	0.7451	0.0098
RB12-19-15	15.153	0.254	0.7078	0.0025
RB12-19-16	4.4781	0.2512	0.7283	0.0035
RB12-19-17	80.555	5.304	0.6933	0.0093
RB12-19-18	5.9343	0.1505	0.7236	0.0021
RB12-19-19	14.368	0.379	0.7115	0.0055
RB12-24-1	27.899	0.641	0.7284	0.0050
RB12-24-2	1.5530	0.0572	0.7108	0.0035
RB12-24-3	82.637	2.040	0.7229	0.0050
RB12-24-4	34.271	0.808	0.7292	0.0061
RB12-24-5	17.226	0.240	0.7162	0.0034
RB12-24-6	10.454	0.259	0.7143	0.0022
RB12-24-7	2.5290	0.0367	0.7194	0.0013
RB12-24-8	0.7626	0.0269	0.7154	0.0019
RB12-24-9	7.5576	0.1586	0.7277	0.0055
RB12-24-10	3.4705	0.1246	0.7159	0.0033
RB12-24-11	40.928	2.385	0.7205	0.0034
RB12-24-12	4.4946	0.1882	0.7162	0.0014
RB12-24-13	24.686	0.388	0.7118	0.0028
RB12-24-14	36.808	0.581	0.7259	0.0046
RB12-24-15	2.5997	0.0296	0.7141	0.0035
RB12-24-16	1.1962	0.0594	0.7174	0.0010
RB12-24-17.1	2.7469	0.0475	0.7192	0.0018
RB12-24-17.2	7.5095	0.1211	0.7202	0.0033
RB12-24-18	2.0603	0.0360	0.7209	0.0022

limited spot analyses for each sample. In fact, sample RB12-19 has two Rb–Sr isotopic trends (**Figure 9A**). The first trend yielded an age of 37.17 ± 5.66 Ma, whereas the second trend did not yield believable age due to the lack of low ^{87}Rb/^{86}Sr data (**Figure 9A**). We found that if the Rb–Sr data within the second trend of sample RB12-19 were pooled together with the data of sample RB12-24, they could give a young age of 4.99 ± 1.30 Ma (not shown), with a small error.

DISCUSSION

Age of Metamorphism

Previous dating on Barrow-type metamorphic rocks in the NHGD generally yielded Oligocene to Miocene ages (Stearns et al., 2013; Wang et al., 2018). For example, LA–ICP–MS monazite U/Th-Pb analysis constrained the timing of metamorphism to be 29–14 Ma for grt + bt ± st ± ky ± sil schists from the Kangmar and Mabja gneiss domes (Stearns et al., 2013), and SHRIMP monazite U/Th-Pb analysis yielded ages of ca. 18 Ma for grt + bt + st ± ky ± sil schists in the Yardoi gneiss dome (Wang et al., 2018). These ages were interpreted as the timing of peak Barrow metamorphism recorded in the NHGD (Stearns et al., 2013; Wang et al., 2018), whereas prograde metamorphism occurred as early as 54–49 Ma based on garnet Lu–Hf analysis (Smit et al., 2014). In addition, monazite U/Th-Pb geochronology of the Gianbul dome in the GHC yielded both Eocene (37–33 Ma) and Miocene (26–22 Ma) ages, which were interpreted as the timing of prograde Barrovian metamorphism and doming driven by upper-crustal extension and positive buoyancy of decompression melts, respectively (Horton et al., 2015).

In this study, *in situ* LA–ICP–MS biotite Rb–Sr dating yielded two metamorphic ages of 37.17 ± 5.66 and 5.27 ± 3.10 Ma for the garnet–staurolite–two-mica schist in the Ramba gneiss dome (**Figure 9**). As the peak metamorphic temperatures of the garnet–staurolite–two-mica schists in the Ramba gneiss dome are higher than the closure temperature of the Rb–Sr system in biotite (~300–400°C) (Verschure et al., 1980; Willigers et al., 2004 and references therein; Scibiorski et al., 2021), the age of 37.17 ± 5.66 Ma is interpreted to represent the timing of retrograde cooling, rather than the peak metamorphism. This interpretation is obviously inconsistent with results from the Kangmar, Mabja, and Yardoi gneiss domes in the Northern Himalayas and the Gianbul dome in the GHC. However, Laskowski et al. (2016) have conducted geochronological research on HP meta-Tethyan rocks in the Lopu Range, located ~600 km west of the city of Lhasa, yielding a garnet Lu-Hf age of 40.4 ± 1.4 Ma and five Ar-Ar phengite ages between 39 and 34 Ma, which were interpreted as the timing of prograde metamorphism and exhumation to mid-crustal depths (~25 km) and concomitant retrogression in the Himalayan orogen, respectively. Khanal et al. (2021) presented new monazite petrochronology for the Kathmandu Klippe in the central Nepalese Himalayas and revealed that Eocene prograde metamorphism and partial melting occurred at 44–38 Ma and 38–35 Ma, respectively (**Figure 10**). Although the meta-Tethyan rocks in the Lopu Range underwent HP metamorphism and the Kathmandu Klippe belong to the upper or uppermost Greater Himalayan Crystallines, these results support that part of the middle-to-lower crustal rocks in the Himalayan orogen underwent exhumation and were not overprinted by Oligocene to Miocene peak Barrow metamorphism.

The age of 5.27 ± 3.10 Ma is significantly younger than the crystallization ages (ca. 44 Ma and ca. 28 Ma) of granitic rocks that intruded into the margin of the Ramba gneiss dome (Liu et al., 2014, 2019). However, this age is slightly younger than the crystallization age (ca. 8 Ma) of the leucogranite pluton occupying the core of the dome (Liu et al., 2014) but is similar to ^{40}Ar/^{39}Ar cooling ages (ca. 6 Ma) of the leucogranite pluton (Guo et al., 2008). Therefore, the age of 5.27 ± 3.10 Ma is

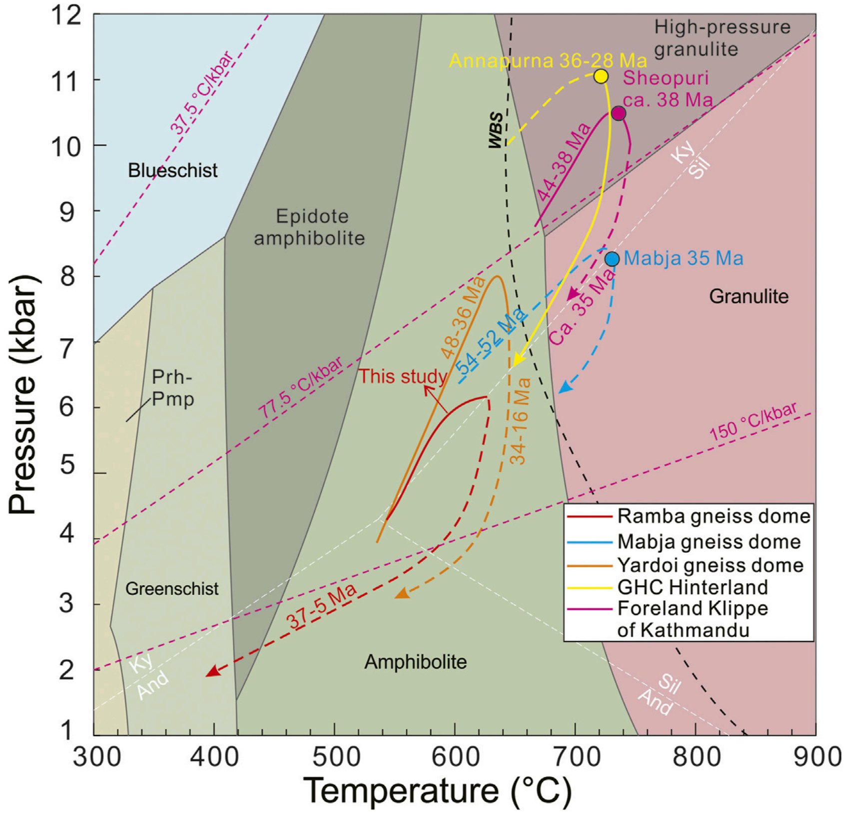

FIGURE 10 | Summary of *P*–*T*–*t* paths of different Eocene units across the Himalayas, including the Ramba gneiss dome in this study, the Majba gneiss dome (Lee et al., 2004; Lee and Whitehouse, 2007; Smit et al., 2014), the Yardoi gneiss dome (Ding et al., 2016b), Hinterland GHC (Iaccarino et al., 2015), and the Kathmandu Klippe (Khanal et al., 2021). The boundary lines for metamorphic facies are modified from Palin et al. (2020). UHT—ultrahigh temperature; WBS—wet basalt solidus.

considered to represent the cooling age of the dome, following the emplacement of the ca. 8 Ma leucogranites.

Metamorphic P–T Paths

In this study, we have determined *P*–*T* paths for the garnet–staurolite–two-mica schists in the Ramba gneiss dome (**Figures 7B, 8B**). Sample RB12-19 recorded a prograde *P*–*T* path that evolves roughly from ~540°C at ~4 kbar to ~630°C at ~5.8 kbar (**Figure 7B**). The prograde *P*–*T* path for sample RB12-24 evolves from ~540°C at ~4.4 kbar to ~620°C at ~6.3 kbar (**Figure 8B**), which displays a slightly higher temperature than those of sample RB12-19 at similar pressure (**Figures 7B, 8**). When the results of the two samples are combined, it is clear that they experienced an obviously early heating burial path (**Figure 10**). It can be noted that sample RB12-24 recorded a nearly isobaric heating path (**Figure 8B**), and thus, a clock-wise *P*–*T* evolution is inferred to the garnet–staurolite–two-mica schist in the Ramba gneiss dome (**Figure 10**).

Here, we compared this *P*–*T* path with those retrieved from the Mabja and Yardoi gneiss domes in the northern Himalaya, the hinterland GHC, and the foreland Kathmandu Klippe (**Figure 10**). The migmatite sample of the sillimanite zone in the Mabja gneiss dome has a peak metamorphic condition of 8.2 kbar/705°C (Lee et al., 2004), which is higher in both pressure and temperature than those of the garnet–staurolite–two-mica schist in the Ramba gneiss dome (**Figure 10**). The garnet–staurolite–kyanite schist in the Yardoi gneiss dome has a peak metamorphic mineral assemblage of grt–bt–ms–pl–st–ky–ilm–qz, occurring in a narrow *P*–*T* condition of 7.2–8.0 kbar and 640–645°C, and the prograde *P*–*T* condition was constrained to be ~540°C at ~4.6 kbar using compositional isopleths X_{Mg} (0.07) and X_{Mn} (0.17) of the garnet core (Ding et al., 2016b). Combined with the retrograde metamorphic process constrained using the occurrence of sillimanite and biotite in the shear bands and the presence of chlorite, Ding et al. (2016b) obtained a clockwise *P*–*T* path for the garnet–staurolite–kyanite schist in the Yardoi gneiss dome, which is similar to that constrained by Wang et al. (2018). This *P*–*T* path is characterized by a prograde process with both P and T increasing and a retrograde process with an early nearly isothermal decompression and late cooling and decompression. It is obvious that the garnet–staurolite–two-mica schist in the Ramba gneiss dome has a similar prograde *P*–*T* condition to that of the schist in the Yardoi gneiss dome but a lower pressure condition at P_{max} (**Figure 10**). In this study, the retrograde *P*–*T* evolution was not supported by the petrological evidence and was only inferred. The *P*–*T* path of the Kathmandu

Klippe in the central Nepalese Himalayas is clockwise, with peak *P–T* conditions of 730–760°C and up to 10.5 kbar, which is higher in both pressure and temperature than those of the garnet–staurolite–two-mica schist in the Ramba gneiss dome but is similar to those from the GHC hinterland (**Figure 10**) (Iaccarino et al., 2015).

Implications for the Formation of the Ramba Gneiss Dome

Ultrahigh pressure (UHP) metamorphic rocks at Kaghan Valley and Tso Morari in the west of the northern Himalayan belt have peak metamorphic ages of 46.2 ± 0.7 Ma and ca. 47–43 Ma, respectively (Kaneko et al., 2003; Donaldson et al., 2013). These suggest deep subduction of the Indian continent at ca. 47–43 Ma. The crustal thickening in the Tibetan Himalaya is broadly synchronous with the Eocene collision between the Indian and Asian plates (Smit et al., 2014). Following the crustal thickening, the deeply buried Indian continental crust underwent a long-lived partial melting (Wang et al., 2013; Zhang et al., 2015), which formed the ca. 48 to 8 Ma granites or leucogranites in the northern Himalayan belt (Aikman et al., 2008; Zhang et al., 2012; Liu et al., 2014; Zeng et al., 2011; Gao et al., 2012; Wu et al., 2015; Zeng and Gao, 2017 and references). In the Ramba gneiss dome, the partial melting is reflected by three epidotes (ca. 44 Ma, ca. 28 Ma, and ca. 8 Ma) of granitic magmatism (Liu et al., 2014, 2019). On the basis of the similarities in Eocene metamorphic conditions and timing of anatexis in the different Eocene units across the Himalayas, Khanal et al. (2021) concluded that an early-stage anatectic response to crustal thickening might be more common than previously thought.

The onset of extensional tectonics of the STDS occurred as early as ca. 36–30 Ma, which marks the initial thinning of thickened crust in the northern Himalayan belt (Zhang et al., 2012; La Roche et al., 2016). In the Ramba gneiss dome, the STDS is represented by the first episode of deformation with top to-NNW sliding, indicated by S–C fabric and NNW-convergent tight folds on the northwestern flank of the dome (Guo et al., 2008; Zhang et al., 2012). The clock-wise *P–T* evolution of the garnet–staurolite–two-mica schist in the Ramba gneiss dome, combined with the age of 37.17 ± 5.66 Ma from the *in situ* LA–ICP–MS biotite Rb–Sr dating, is consistent with the Eocene crustal thickening (**Figure 10**).

The ca. 8 Ma leucogranites occupy the core of the Ramba gneiss dome (Liu et al., 2014) and have ^{40}Ar/^{39}Ar cooling ages of ca. 6 Ma (Guo et al., 2008). The Yadong–Gulu rift, on the east of the dome, was active during the interval ca. 11–5 Ma, with its peak activity at ca. 8 Ma (Pan and Kidd, 1992; Harrison et al., 1995; Zhang et al., 2012), which coincides with the diapir of the ca. 8 Ma leucogranite pluton, formed the shape of the Ramba gneiss dome (Guo et al., 2008; Zhang et al., 2012; Liu et al., 2014).

CONCLUSION

The garnet–staurolite–two-mica schist in the Ramba gneiss dome followed a clock-wise *P–T* path, involving an early prograde process that evolves from ~540°C at ~4.4 kbar to ~630°C at ~6.0 kbar. This prograde evolution is similar to the schist in the Yardoi gneiss dome but with lower T condition at $P_{\max}$ and reflects the crustal thickening, following the Indian-Asian collision. *In situ* LA–ICP–MS biotite Rb–Sr analysis obtained two metamorphic ages of 37.17 ± 5.66 and 5.27 ± 3.10 Ma for the garnet–staurolite–two-mica schist in the Ramba gneiss dome. The former corresponds to the timing of retrograde cooling. The latter is similar to ^{40}Ar/^{39}Ar cooling ages (ca. 6 Ma) of ca. 8 Ma leucogranite and, thus, represents the cooling age of the dome, following the thermal resetting by the emplacement of ca. 8 Ma leucogranite pluton in the core of the dome. The peak metamorphism should be older than ca. 37 Ma.

DATA AVAILABILITY STATEMENT

The original contributions presented in the study are included in the article/**Supplementary Material**; further inquiries can be directed to the corresponding author.

AUTHOR CONTRIBUTIONS

L-LG: investigation, data curation, and writing—original draft preparation. X-PL: conceptualization and investigation. H-YY, T-CS, and J-YW: investigation. X-FX, FZ, and Z-BT: visualization and editing.

FUNDING

This work is supported by a research grant from the State Key Laboratory of Continental Dynamics (SKLCD-04).

ACKNOWLEDGMENTS

The authors thank editor YC for editorial handling work. HW and J-MW for their helpful comments that significantly improved the manuscript.

SUPPLEMENTARY MATERIAL

The Supplementary Material for this article can be found online at: https://www.frontiersin.org/articles/10.3389/feart.2022.887154/full#supplementary-material

REFERENCES

Aikman, A. B., Harrison, T. M., and Lin, D. (2008). Evidence for Early (>44 Ma) Himalayan Crustal Thickening, Tethyan Himalaya, Southeastern Tibet. *Earth Planet. Sci. Lett.* 274, 14–23. doi:10.1016/j.epsl.2008.06.038

Aoya, M., Wallis, S. R., Kawakami, T., Lee, J., Wang, Y., and Maeda, H. (2006). The Malashan Gneiss Dome in South Tibet: Comparative Study with the Kangmar Dome with Special Reference to Kinematics of Deformation and Origin of Associated Granites. *Geol. Soc. Lond. Spec. Publ.* 268, 471–495. doi:10.1144/gsl.sp.2006.268.01.22

Beaumont, C., Jamieson, R. A., Nguyen, M. H., and Lee, B. (2001). Himalayan Tectonics Explained by Extrusion of a Low-Viscosity Crustal Channel Coupled to Focused Surface Denudation. *Nature* 414, 738–742. doi:10.1038/414738a

Chen, Z., Liu, Y., Hodges, K. V., Burchfiel, B. C., Royden, L. H., and Deng, C. (1990). The Kangmar Dome: A Metamorphic Core Complex in Southern Xizang (Tibet). *Science* 250, 1552–1556. doi:10.1126/science.250.4987.1552

Ding, H., Zhang, Z., Dong, X., Tian, Z., Xiang, H., Mu, H., et al. (2016a). Early Eocene (C . 50 Ma) Collision of the Indian and Asian Continents: Constraints from the North Himalayan Metamorphic Rocks, Southeastern Tibet. *Earth Planet. Sci. Lett.* 435, 64–73. doi:10.1016/j.epsl.2015.12.006

Ding, H., Zhang, Z., Hu, K., Dong, X., Xiang, H., and Mu, H. (2016b). P-T-t-D Paths of the North Himalayan Metamorphic Rocks: Implications for the Himalayan Orogeny. *Tectonophysics* 683, 393–404. doi:10.1016/j.tecto.2016.06.035

Donaldson, D. G., Webb, A. A. G., Menold, C. A., Kylander-Clark, A. R. C., and Hacker, B. R. (2013). Petrochronology of Himalayan Ultrahigh-Pressure Eclogite. *Geology* 41, 835–838. doi:10.1130/g33699.1

Fu, J., Li, G., Wang, G., Huang, Y., Zhang, L., Dong, S., et al. (2016). First Field Identification of the Cuonadong Dome in Southern Tibet: Implications for EW Extension of the North Himalayan Gneiss Dome. *Int. J. Earth Sci. Geol. Rundsch)* 106, 1581–1596. doi:10.1007/s00531-016-1368-2

Gao, L., Zeng, L., and Xie, K. (2012). Eocene High Grade Metamorphism and Crustal Anatexis in the North Himalaya Gneiss Domes, Southern Tibet,Southern Tibet. *Chin. Sci. Bull.* 57, 639–650. doi:10.1007/s11434-011-4805-4

Gorojovsky, L., and Alard, O. (2020). Optimisation of Laser and Mass Spectrometer Parameters for the *In Situ* Analysis of Rb/Sr Ratios by LA-ICP-MS/MS. *J. Anal. At. Spectrom.* 35, 2322–2336. doi:10.1039/d0ja00308e

Gou, Z., Zhang, Z., Dong, X., Xiang, H., Ding, H., Tian, Z., et al. (2016). Petrogenesis and Tectonic Implications of the Yadong Leucogranites, Southern Himalaya. *Lithos* 256-257, 300–310. doi:10.1016/j.lithos.2016.04.009

Guo, L., Zhang, J., and Zhang, B. (2008). Structures, Kinematics, Thermochronology and Tectonic Evolution of the Ramba Gneiss Dome in the Northern Himalaya. *Prog. Nat. Sci.* 18, 851–860. doi:10.1016/j.pnsc.2008.01.016

Harris, N. (2007). Channel Flow and the Himalayan-Tibetan Orogen: a Critical Review. *J. Geol. Soc.* 164, 511–523. doi:10.1144/0016-76492006-133

Harrison, T. M., Copeland, P., Kidd, W. S. F., and Lovera, O. M. (1995). Activation of the Nyainqentanghla Shear Zone: Implications for Uplift of the Southern Tibetan Plateau. *Tectonics* 14, 658–676. doi:10.1029/95tc00608

Hogmalm, K. J., Zack, T., Karlsson, A. K.-O., Sjöqvist, A. S. L., and Garbe-Schönberg, D. (2017). *In Situ* Rb-Sr and K-Ca Dating by LA-ICP-MS/MS: an Evaluation of N2O and SF6 as Reaction Gases. *J. Anal. At. Spectrom.* 32, 305–313. doi:10.1039/c6ja00362a

Holland, T. J. B., and Powell, R. (2011). An Improved and Extended Internally Consistent Thermodynamic Dataset for Phases of Petrological Interest, Involving a New Equation of State for Solids. *J. Metamorph. Geol.* 29, 333–383. doi:10.1111/j.1525-1314.2010.00923.x

Holland, T., and Powell, R. (2003). Activity?composition Relations for Phases in Petrological Calculations: an Asymmetric Multicomponent Formulation. *Contributions Mineralogy Petrology* 145, 492–501. doi:10.1007/s00410-003-0464-z

Hopkinson, T. N., Harris, N. B. W., Warren, C. J., Spencer, C. J., Roberts, N. M. W., Horstwood, M. S. A., et al. (2017). The Identification and Significance of Pure Sediment-Derived Granites. *Earth Planet. Sci. Lett.* 467, 57–63. doi:10.1016/j.epsl.2017.03.018

Horton, F., Lee, J., Hacker, B., Bowman-Kamaha'o, M., and Cosca, M. (2015). Himalayan Gneiss Dome Formation in the Middle Crust and Exhumation by Normal Faulting: New Geochronology of Gianbul Dome, Northwestern India. *Geol. Soc. Am. Bull.* 127, 162–180. doi:10.1130/b31005.1

Iaccarino, S., Montomoli, C., Carosi, R., Massonne, H.-J., Langone, A., and Visonà, D. (2015). Pressure-temperature-time-deformation Path of Kyanite-Bearing Migmatitic Paragneiss in the Kali Gandaki Valley (Central Nepal): Investigation of Late Eocene-Early Oligocene Melting Processes. *Lithos* 231, 103–121. doi:10.1016/j.lithos.2015.06.005

Iaccarino, S., Montomoli, C., Carosi, R., Massonne, H.-J., and Visonà, D. (2017). Geology and Tectono-Metamorphic Evolution of the Himalayan Metamorphic Core: Insights from the Mugu Karnali Transect, Western Nepal (Central Himalaya). *J. Metamorph. Geol.* 35, 301–325. doi:10.1111/jmg.12233

Jessup, M. J., Langille, J. M., Diedesch, T. F., and Cottle, J. M. (2019). Gneiss Dome Formation in the Himalaya and Southern Tibet. *Geol. Soc. Lond. Spec. Publ.* 483 (1), 401–422. doi:10.1144/sp483.15

Kaneko, Y., Katayama, I., Yamamoto, H., Misawa, K., Ishikawa, M., Rehman, H. U., et al. (2003). Timing of Himalayan Ultrahigh-Pressure Metamorphism: Sinking Rate and Subduction Angle of the Indian Continental Crust beneath Asia. *J. Metamorph Geol.* 21, 589–599. doi:10.1046/j.1525-1314.2003.00466.x

Khanal, G. P., Wang, J. M., Larson, K. P., Wu, F. Y., Rai, S. M., Wang, J. G., et al. (2021). Eocene Metamorphism and Anatexis in the Kathmandu Klippe, Central Nepal: Implications for Early Crustal Thickening and Initial Rise of the Himalaya. *Tectonics* 40, e2020TC006532. doi:10.1029/2020tc006532

Kohn, M. J., and Corrie, S. L. (2011). Preserved Zr-Temperatures and U-Pb Ages in High-Grade Metamorphic Titanite: Evidence for a Static Hot Channel in the Himalayan Orogen. *Earth Planet. Sci. Lett.* 311, 136–143. doi:10.1016/j.epsl.2011.09.008

La Roche, R. S., Godin, L., Cottle, J. M., and Kellett, D. A. (2016). Direct Shear Fabric Dating Constrains Early Oligocene Onset of the South Tibetan Detachment in the Western Nepal Himalaya. *Geology* 44, 403–406. doi:10.1130/g37754.1

Laskowski, A. K., Kapp, P., Vervoort, J. D., and Ding, L. (2016). High-pressure Tethyan Himalaya Rocks along the India-Asia Suture Zone in Southern Tibet. *Lithosphere* 8, 574–582. doi:10.1130/l544.1

Le Fort, P., Cuney, M., Deniel, C., France-Lanord, C., Sheppard, S. M. F., Upreti, B. N., et al. (1987). Crustal Generation of the Himalayan Leucogranites. *Tectonophysics* 134, 39–57. doi:10.1016/0040-1951(87)90248-4

Lee, J., Hacker, B. R., Dinklage, W. S., Wang, Y., Gans, P., Calvert, A., et al. (2000). Evolution of the Kangmar Dome, Southern Tibet: Structural, Petrologic, and Thermochronologic Constraints. *Tectonics* 19, 872–895. doi:10.1029/1999tc001147

Lee, J., Hacker, B., and Wang, Y. (2004). Evolution of North Himalayan Gneiss Domes: Structural and Metamorphic Studies in Mabja Dome, Southern Tibet. *J. Struct. Geol.* 26, 2297–2316. doi:10.1016/j.jsg.2004.02.013

Lee, J., McClelland, W., Wang, Y., Blythe, A., and McWilliams, M. (2006). Oligocene-Miocene Middle Crustal Flow in Southern Tibet: Geochronology of Mabja Dome. *Geol. Soc. Lond. Spec. Publ.* 268, 445–469. doi:10.1144/gsl.sp.2006.268.01.21

Lee, J., and Whitehouse, M. J. (2007). Onset of Mid-crustal Extensional Flow in Southern Tibet: Evidence from U/Pb Zircon Ages. *Geol* 35, 45–48. doi:10.1130/g22842a.1

Li, Q., Zhang, L., Fu, B., Bader, T., and Yu, H. (2019). Petrology and Zircon U-Pb Dating of Well-preserved Eclogites from the Thongmön Area in Central Himalaya and Their Tectonic Implications. *J. Metamorph Geol.* 37, 203–226. doi:10.1111/jmg.12457

Lister, G. S., and Davis, G. A. (1989). The Origin of Metamorphic Core Complexes and Detachment Faults Formed during Tertiary Continental Extension in the Northern Colorado River Region, U.S.A. *J. Struct. Geol.* 11, 65–94. doi:10.1016/0191-8141(89)90036-9

Liu, S., Zhang, G., Zhang, L., Liu, Z., and Xu, J. (2022a). Boron Isotopes of Tourmalines from the Central Himalaya: Implications for Fluid Activity and Anatexis in the Himalayan Orogen. *Chem. Geol.* 596, 120800. doi:10.1016/j.chemgeo.2022.120800

Liu, S., Zhang, G., Zhang, L., Wang, S., Upreti, B. N., Adhikari, D. P., et al. (2022b). Diverse Anatexis in the Main Central Thrust Zone, Eastern Nepal: Implications for Melt Evolution and Exhumation Process of the Himalaya. *J. Petrology* 63 (3), 1–26. doi:10.1093/petrology/egac003

Liu, Z.-C., Wu, F.-Y., Ji, W.-Q., Wang, J.-G., and Liu, C.-Z. (2014). Petrogenesis of the Ramba Leucogranite in the Tethyan Himalaya and Constraints on the Channel Flow Model. *Lithos* 208-209, 118–136. doi:10.1016/j.lithos.2014.08.022

Liu, Z.-C., Wu, F.-Y., Liu, X.-C., Wang, J.-G., Yin, R., Qiu, Z.-L., et al. (2019). Mineralogical Evidence for Fractionation Processes in the Himalayan Leucogranites of the Ramba Dome, Southern Tibet. *Lithos* 340-341, 71–86. doi:10.1016/j.lithos.2019.05.004

Mark Harrison, T., Lovera, O. M., and Grove, M. (1997). New Insights into the Origin of Two Contrasting Himalayan Granite Belts. *Geol* 25, 899–902. doi:10.1130/0091-7613(1997)025<0899:niitoo>2.3.co;2

Palin, R. M., Santosh, M., Cao, W., Li, S.-S., Hernández-Uribe, D., and Parsons, A. (20202020). Secular Change and the Onset of Plate Tectonics on Earth. *Earth-Science Rev.* 207, 103172. doi:10.1016/j.earscirev.2020.103172

Palin, R. M., Searle, M. P., St-Onge, M. R., Waters, D. J., Roberts, N. M. W., Horstwood, M. S. A., et al. (2014). Monazite Geochronology and Petrology of Kyanite- and Sillimanite-Grade Migmatites from the Northwestern Flank of the Eastern Himalayan Syntaxis. *Gondwana Res.* 26, 323–347. doi:10.1016/j.gr.2013.06.022

Pan, Y., and Kidd, W. S. F. (1992). Nyainqentanglha Shear Zone: A Late Miocene Extensional Detachment in the Southern Tibetan Plateau. *Geol* 20, 775–778. doi:10.1130/0091-7613(1992)020<0775:nszalm>2.3.co;2

Powell, R., Holland, T., and Worley, B. (1998). Calculating Phase Diagrams Involving Solid Solutions via Non-linear Equations, with Examples Using THERMOCALC. *J. Metamorph. Geol.* 16, 577–588. doi:10.1111/j.1525-1314.1998.00157.x

Quigley, M. C., Liangjun, Y., Gregory, C., Corvino, A., Sandiford, M., Wilson, C. J. L., et al. (2008). U-pb SHRIMP Zircon Geochronology and T-T-D History of the Kampa Dome, Southern Tibet. *Tectonophysics* 446, 97–113. doi:10.1016/j.tecto.2007.11.004

Regis, D., Warren, C. J., Young, D., and Roberts, N. M. W. (2014). Tectono-metamorphic Evolution of the Jomolhari Massif: Variations in Timing of Syn-Collisional Metamorphism across Western Bhutan. *Lithos* 190-191, 449–466. doi:10.1016/j.lithos.2014.01.001

Rey, P. F., Mondy, L., Duclaux, G., Teyssier, C., Whitney, D. L., Bocher, M., et al. (2017). The Origin of Contractional Structures in Extensional Gneiss Domes. *Geology* 45, 263–266. doi:10.1130/g38595.1

Scibiorski, E., Jourdan, F., Mezger, K., Tohver, E., and Vollstaedt, H. (2021). Cryptic Excess Argon in Metamorphic Biotite: Anomalously Old 40Ar/39Ar Plateau Dates Tested with Rb/Sr Thermochronology and Ar Diffusion Modelling. *Geochimica Cosmochimica Acta* 315, 1–23. doi:10.1016/j.gca.2021.09.017

Searle, M. P., Cottle, J. M., Streule, M. J., and Waters, D. J. (2009). Crustal Melt Granites and Migmatites along the Himalaya: Melt Source, Segregation, Transport and Granite Emplacement Mechanisms. *Earth Environ. Sci. Trans. R. Soc. Edinb.* 100, 219–233. doi:10.1017/s175569100901617x

Searle, M. P., and Godin, L. (2003). The South Tibetan Detachment and the Manaslu Leucogranite: A Structural Reinterpretation and Restoration of the Annapurna-Manaslu Himalaya, Nepal. *J. Geol.* 111, 505–523. doi:10.1086/376763

Searle, M. P., Noble, S. R., Hurford, A. J., and Rex, D. C. (1999). Age of Crustal Melting, Emplacement and Exhumation History of the Shivling Leucogranite, Garhwal Himalaya. *Geol. Mag.* 136, 513–525. doi:10.1017/s0016756899002885

Shrestha, S., Larson, K. P., Guilmette, C., and Smit, M. A. (2017). The P-T-T Evolution of the Exhumed Himalayan Metamorphic Core in the Likhu Khola Region, East Central Nepal. *J. Metamorph Geol.* 35, 663–693. doi:10.1111/jmg.12250

Smit, M. A., Hacker, B. R., and Lee, J. (2014). Tibetan Garnet Records Early Eocene Initiation of Thickening in the Himalaya. *Geology* 42, 591–594. doi:10.1130/g35524.1

Smye, A. J., Greenwood, L. V., and Holland, T. J. B. (2010). Garnet-chloritoid-kyanite Assemblages: Eclogite Facies Indicators of Subduction Constraints in Orogenic Belts. *Geology* 28, 753–768. doi:10.1111/j.1525-1314.2010.00889.x

Stearns, M. A., Hacker, B. R., Ratschbacher, L., Lee, J., Cottle, J. M., and Kylander-Clark, A. (2013). Synchronous Oligocene-Miocene Metamorphism of the Pamir and the North Himalaya Driven by Plate-Scale Dynamics. *Geology* 41, 1071–1074. doi:10.1130/g34451.1

Teyssier, C., and Whitney, D. L. (2002). Gneiss Domes and Orogeny. *Geol* 30, 1139–1142. doi:10.1130/0091-7613(2002)030<1139:gdao>2.0.co;2

Tian, Z., Zhang, Z., and Dong, X. (2019). Constraining the Age of High-Pressure Metamorphism of Paragneisses from the Eastern Himalayan Syntaxis Using Zircon Petrochronology and Phase Equilibria. *Geol. Soc. Lond. Spec. Publ.* 474, 331–352. doi:10.1144/sp474.11

Verschure, R. H., Andriessen, P. A. M., Boelrijk, N. A. I. M., Hebeda, E. H., Maijer, C., Priem, H. N. A., et al. (1980). On the Thermal Stability of Rb-Sr and K-Ar Biotite Systems: Evidence from Coexisting Sveconorwegian (Ca 870 Ma) and Caledonian (Ca 400 Ma) Biotites in SW Norway. *Contr. Mineral. Pet.* 74, 245–252. doi:10.1007/bf00371694

Wang, J.-M., Lanari, P., Wu, F.-Y., Zhang, J.-J., Khanal, G. P., and Yang, L. (2021). First Evidence of Eclogites Overprinted by Ultrahigh Temperature Metamorphism in Everest East, Himalaya: Implications for Collisional Tectonics on Early Earth. *Earth Planet. Sci. Lett.* 558, 116760. doi:10.1016/j.epsl.2021.116760

Wang, J.-M., Rubatto, D., and Zhang, J.-J. (2015). Timing of Partial Melting and Cooling across the Greater Himalayan Crystalline Complex (Nyalam, Central Himalaya): In-Sequence Thrusting and its Implications. *J. Petrol.* 56, 1677–1702. doi:10.1093/petrology/egv050

Wang, J.-M., Wu, F.-Y., Rubatto, D., Liu, K., Zhang, J.-J., and Liu, X.-C. (2018). Early Miocene Rapid Exhumation in Southern Tibet: Insights from P-T-T-D-Magmatism Path of Yardoi Dome. *Lithos* 304-307, 38–56. doi:10.1016/j.lithos.2018.02.003

Wang, J.-M., Wu, F.-Y., Rubatto, D., Liu, S.-R., Zhang, J.-J., Liu, X.-C., et al. (2017a). Monazite Behaviour during Isothermal Decompression in Pelitic Granulites: a Case Study from Dinggye, Tibetan Himalaya. *Contrib. Mineral. Pet.* 172, 81. doi:10.1007/s00410-017-1400-y

Wang, J.-M., Zhang, J.-J., Liu, K., Zhang, B., Wang, X.-X., Rai, S., et al. (2016). Spatial and Temporal Evolution of Tectonometamorphic Discontinuities in the Central Himalaya: Constraints from P-T Paths and Geochronology. *Tectonophysics* 679, 41–60. doi:10.1016/j.tecto.2016.04.035

Wang, J. M., Zhang, J. J., and Wang, X. X. (2013). Structural Kinematics, Metamorphic P-T Profiles and Zircon Geochronology across the Greater Himalayan Crystalline Complex in South-Central Tibet: Implication for a Revised Channel Flow. *J. Meta. Geol.* 31, 607–628. doi:10.1111/jmg.12036

Wang, Y., Zhang, L., Zhang, J., and Wei, C. (2017b). The Youngest Eclogite in Central Himalaya: P-T Path, U-Pb Zircon Age and its Tectonic Implication. *Gondwana Res.* 41, 188–206. doi:10.1016/j.gr.2015.10.013

White, R. W., Powell, R., Holland, T. J. B., Johnson, T. E., and Green, E. C. R. (2014a). New Mineral Activity-Composition Relations for Thermodynamic Calculations in Metapelitic Systems. *J. Meta. Geol.* 32, 261–286. doi:10.1111/jmg.12071

White, R. W., Powell, R., Holland, T. J. B., and Worley, B. A. (2000). The Effect of TiO2 and Fe2 O3 on Metapelitic Assemblages at Greenschist and Amphibolite Facies Conditions: Mineral Equilibria Calculations in the System K2 O-FeO-MgO-Al2 O3 -SiO2 -H2 O-TiO2 -Fe2 O3. *J. Metamorph. Geol.* 18, 497–511. doi:10.1046/j.1525-1314.2000.00269.x

White, R. W., Powell, R., and Johnson, T. E. (2014b). The Effect of Mn on Mineral Stability in Metapelites Revisited: New a -x Relations for Manganese-Bearing Minerals. *J. Meta. Geol.* 32, 809–828. doi:10.1111/jmg.12095

Whitney, D. L., and Evans, B. W. (2010). Abbreviations for Names of Rock-Forming Minerals. *Am. Mineralogist* 95, 185–187. doi:10.2138/am.2010.3371

Whitney, D. L., Teyssier, C., and Vanderhaeghe, O. (2004). Gneiss Domes and Crustal Flow. *Geol. Soc. Am. Special Pap.* 380, 15–33. doi:10.1130/0-8137-2380-9.15

Willigers, B. J. A., Mezger, K., and Baker, J. A. (2004). Development of High Precision Rb-Sr Phlogopite and Biotite Geochronology; an Alternative to 40Ar/39Ar Tri-octahedral Mica Dating. *Chem. Geol.* 213, 339–358. doi:10.1016/j.chemgeo.2004.07.006

Woodhead, J. D., and Hergt, J. M. (2001). Strontium, Neodymium and Lead Isotope Analyses of NIST Glass Certified Reference Materials: SRM 610, 612, 614. *Geostand. Newsl.* 25, 261–266. doi:10.1111/j.1751-908x.2001.tb00601.x

Wu, C. G., Zhang, L. F., Li, Q. Y., Bader, T., Wang, Y., and Fu, B. (2022). Tectonothermal Transition from Continental Collision to Post-collision: Insights from Eclogites Overprinted in the Ultrahigh-Temperature Granulite Facies (Yadong Region, Central Himalaya). *J. Metamorph. Geol.*, 1–27.

Wu, F. Y., Liu, Z. C., Liu, X. C., and Ji, W. Q. (2015). Himalayan Leucogranites: Petrogenesis and Implications to Orogenesis and Plateau Uplift. *Acta Petrol. Sin.* 31, 1–36. (in Chinese with English abstract).

Yin, A. (2006). Cenozoic Tectonic Evolution of the Himalayan Orogen as Constrained by Along-Strike Variation of Structural Geometry, Exhumation History, and Foreland Sedimentation. *Earth-Science Rev.* 76, 1–131. doi:10.1016/j.earscirev.2005.05.004

Yin, A. (2004). Gneiss Domes and Gneiss Dome Systems. *Geol. Soc. Am. Special Pap.* 380, 1–14. doi:10.1130/0-8137-2380-9.1

Yin, A., and Harrison, T. M. (2000). Geologic Evolution of the Himalayan-Tibetan Orogen. *Annu. Rev. Earth Planet. Sci.* 28, 211–280. doi:10.1146/annurev.earth.28.1.211

Zeng, L., Gao, L.-E., Xie, K., and Liu-Zeng, J. (2011). Mid-Eocene High Sr/Y Granites in the Northern Himalayan Gneiss Domes: Melting Thickened Lower Continental Crust. *Earth Planet. Sci. Lett.* 303, 251–266. doi:10.1016/j.epsl.2011.01.005

Zeng, L. S., and Gao, L. E. (2017). Cenozoic Crustal Anatexis and the Leucogranites in the Himalayan Collisional Orogenic Belt. *Acta Petrol. Sin.* 33, 1420–1444. (in Chinese with English abstract).

Zhang, G. B., Wang, J. X., Webb, A. A. G., Zhang, L. F., Liu, S. Q., Fu, B., et al. (2021). *The Protoliths of Central Himalayan Eclogites*. Geological Society of America Bulletin. doi:10.1130/B36080.1

Zhang, H., Harris, N., Parrish, R., Kelley, S., Zhang, L., Rogers, N., et al. (2004). Causes and Consequences of Protracted Melting of the Mid-crust Exposed in the North Himalayan Antiform. *Earth Planet. Sci. Lett.* 228, 195–212. doi:10.1016/j.epsl.2004.09.031

Zhang, J., and Guo, L. (2007). Structure and Geochronology of the Southern Xainza-Dinggye Rift and its Relationship to the South Tibetan Detachment System. *J. Asian Earth Sci.* 29, 722–736. doi:10.1016/j.jseaes.2006.05.003

Zhang, J., SantoshWang, M. X. X., Wang, X., Guo, L., Yang, X., and Zhang, B. (2012). Tectonics of the Northern Himalaya since the India-Asia Collision. *Gondwana Res.* 21, 939–960. doi:10.1016/j.gr.2011.11.004

Zhang, Z., Xiang, H., Dong, X., Ding, H., and He, Z. (2015). Long-lived High-Temperature Granulite-Facies Metamorphism in the Eastern Himalayan Orogen, South Tibet. *Lithos* 212-215, 1–15. doi:10.1016/j.lithos.2014.10.009

Conflict of Interest: The authors declare that the research was conducted in the absence of any commercial or financial relationships that could be construed as a potential conflict of interest.

Frontiers in
Earth Science

Investigates the processes operating within the major spheres of our planet

Advances our understanding across the earth sciences, providing a theoretical background for better use of our planet's resources and equipping us to face major environmental challenges.

Discover the latest Research Topics

See more →

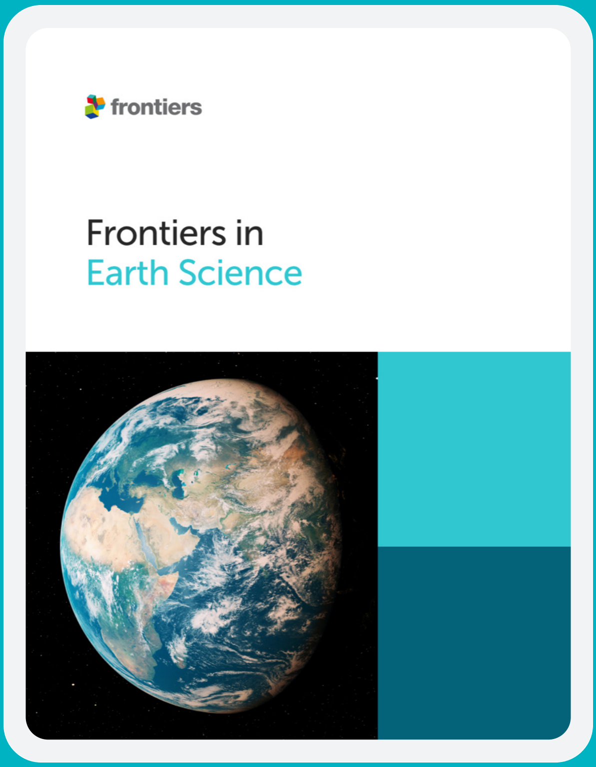

frontiers

Frontiers in
Earth Science

Frontiers

Avenue du Tribunal-Fédéral 34
1005 Lausanne, Switzerland
frontiersin.org

Contact us

+41 (0)21 510 17 00
frontiersin.org/about/contact

frontiers | Research Topics